INFORMATION TO USERS

This manuscript has been reproduced from the microfilm master. UMI films the text directly from the original or copy submitted. Thus, some thesis and dissertation copies are in typewriter face, while others may be from any type of computer printer.

The quality of this reproduction is dependent upon the quality of the copy submitted. Broken or indistinct print, colored or poor quality illustrations and photographs, print bleedthrough, substandard margins, and improper alignment can adversely affect reproduction.

In the unlikely event that the author did not send UMI a complete manuscript and there are missing pages, these will be noted. Also, if unauthorized copyright material had to be removed, a note will indicate the deletion.

Oversize materials (e.g., maps, drawings, charts) are reproduced by sectioning the original, beginning at the upper left-hand corner and continuing from left to right in equal sections with small overlaps.

Photographs included in the original manuscript have been reproduced xerographically in this copy. Higher quality 6" x 9" black and white photographic prints are available for any photographs or illustrations appearing in this copy for an additional charge. Contact UMI directly to order.

ProQuest Information and Learning
300 North Zeeb Road, Ann Arbor, MI 48106-1346 USA
800-521-0600

AN INVESTIGATION OF SHAFT CURRENT

IN

A LARGE SLEEVE BEARING INDUCTION MACHINE

By

RAYMOND ONG K. J. , B.Sc, M.Sc, P.Eng., M.I.E.E.E., A.M.I.E.E

A Thesis

Submitted to the School of Graduate Studies

in Partial Fulfillment of the Requirements

for the Degree

Doctor of Philosophy

McMaster Univeristy

© Copyright by Raymond Ong, March 1999.

SHAFT CURRENT IN A LARGE SLEEVE BEARING INDUCTION MACHINE

DOCTOR OF PHILOSOPHY (1999)
(Electrical Engineering)

McMaster University
Hamilton, Ontario

TITLE: An Investigation of Shaft Current in a Large Sleeve Bearing Induction Machine

AUTHOR: Raymond Ong K.J, B.Sc. (Elect. Eng) (Southampton University, U.K.),
M.Sc (Elect. Eng) (Queen's. University, Canada)

SUPERVISOR: Professor Raymond David Findlay, Ph.D. (University of Toronto)
P.Eng, FIEEE.

NUMBER OF PAGES: XXIV, 332

ABSTRACT

Irregularities in the magnetic circuits of machines may result in spurious voltages that lead to shaft currents through the shaft, bearings, bearing supports and closing through the machine framework. The IEEE Standard Test Procedure for Polyphase Induction Motors and Generators discusses the shaft current and presents a measurement method for recording either the voltage across the ends of the shaft or the current. This thesis discusses an alternative measurement approach and its application to the identification of shaft current in a large induction machine.

Possible causes of shaft current are discussed. The magnetomotive force-permeance approach is used in the determination of the possible causes.

An eight pole 2611 kW oil ring lubricated induction motor which exhibited signs of bearing damage due to shaft current was used in a series of experiments conducted to evaluate the cause(s) of the bearing damage. The new method of shaft current measurement, known as the Rogowski Coil Method, was applied to this machine. The experiments included oil analysis and microscopic analysis of the bearing. The experiments showed that the main cause of the shaft current is the presence of joints between stator lamination segments. Saturation accentuates the magnitude of shaft current. The Rogowski coil method is shown to be reliable; it does not disturb the shaft

current conducting circuit. Furthermore, it requires little maintenance, unlike the ammeter/brush method.

Oil ring delivers oil to the bearing. An oil film will develop between the shaft journal and the bearing. The oil film acts as an insulator against shaft current. It is thus important that sufficient quantity of oil is delivered to the bearing and an oil film is developed as quickly as possible to minimize the shaft current. Hence, the performance of the oil ring is studied. The Rogowski method is used to study the performance of the oil ring. The oil ring is determined to slip early with respect to the shaft. As a result, the amount of oil delivered to the bearing is determined to be less than calculated. The proposed method is simple, reliable and less labor intensive than other methods. Patent application for this method is being filed.

A method of minimizing shaft current is described following the experimental work to determine the cause(s) of the shaft current. Patent application for this method is being filed.

The present on-line monitoring system utilizes the spectral analysis of the stator current to determine stator and rotor faults in alternating current machines. The Rogowski coil method can be used as an alternative on-line monitoring system for such faults.

ACKNOWLEDGMENT

I wish to express my heartfelt gratitude to my supervisor, Prof. R. D. Findlay for his support and encouragement. I would like to thank the other members of my supervisory committee - Prof. B. Szabados, Prof. J. H. Dableh and Mr. J.H. Dymond.

The financial support of General Electric Canada through an award of a study scholarship is deeply appreciated. I would like to thank Mr. Bob Guest for his support of the award and Mr. Ron Osborne for the extension of the award and financial grant to conduct the experimental work at General Electric Peterborough. I would also like to thank the test department of General Electric Peterborough for the support in the conduct of the experimental work. Mr. J. V. Kay and Mr. P. McKenna, my colleagues at General Electric Peterborough, are greatly acknowledged for their co-operation and encouragement.

Last but definitely not the least, I would like to thank my wife, Janice Ong, for her patience and support.

TABLE OF CONTENTS

LIST OF SYMBOLS

A	Cross Section
B	Flux Density
C	Contour
d	Distance between the Rotor Center and the Rotation Center
e	Instantaneous E.M.F.
E	Peak E.M.F.
f	Frequency
H	Magnetic Field Strength
I	Current
J	Number of joints
K_p	Pitch Factor or Chord Factor
K_d	Distribution Factor
m	Number of Phases
MMF	Magnetomotive Force
n_t	Turns Density, Number of Turns Per Unit Length
n_{st}	Stator Winding Spatial Harmonic Order
n_{ws}	Stator Winding Time Harmonic
N	Number of Turns

N_{st}	Number of Turns in Series Per Phase
p	Pole Pairs
P	Poles
R1	Stator Bore Radius
R2	Rotor Outer Radius
R, R_2	Number of Rotor Slots
R_s	Shunt/Ammeter Resistance
R_{sh}	Resistance of the Shaft
R_o	Resistance of the Oil Film
R_b	Bearing Insulation Resistance
R_c	Connection Contact Resistance
S	Number of Stator Slots
S_p	Number of Stator Slots Per Pole Pair
s	Slip
Φ_k	Instantaneous Flux Linking the k^{th} Turn of the N-Turn Coil
Ω	Angular Displacement of the Stator Winding , Electrical Radian; Angle between the Stator Datum and an Arbitrary Point on the Rotor
δ	Length of the Air Gap
q_1	Number of Slots Per Pole Per Phase
υ, η, β, q, h, K_j, z, g	Harmonic Order

α_r	Rotor Slot Angle, $2\pi/R$
β	Pole Pair Harmonic Order
μ_o	Permeability of Free Space, $4\pi \times 10^{-7}$ H/m
$\Im$	Magnetomotive Force (MMF)
$\wp$	Permeance
$\Re$	Reluctance
α_{bb}	Phase Angle between Stator Air Gap Field and Rotor Air Gap Field
δ_m	Mean Air Gap Length
ε	Eccentricity, A Fraction Less than Unity
ϕ	Phase Angle
λ	Coefficient
λ'	Wavelength
ω_r	Rotor Angular Velocity , $\left(\frac{1-s}{p}\right)\omega$
ω	Supply Frequency
k_i , n_s	Saturation Harmonic Order
k_{de}	Dynamic Eccentricity Harmonic Order
k_{se}	Static Eccentricity Harmonic Order
V_i	Induced Shaft Voltage
U_{is}	Speed of Stator Fundamental Field
U_{ks}	Speed of Stator Harmonic Field
U_{kr}	Speed of Rotor Harmonic Field

f_{kr}	Frequency of Induced Rotor Harmonic Current
κ	Spatial Position of the Rotor Bar
DE	Drive End
ODE	Opposite Drive End

LIST OF FIGURES

LIST OF TABLES

CHAPTER 1

INTRODUCTION

1.0 INTRODUCTION

Three phase induction motors are by far the most common prime movers in industry today. Many of these motors which may be as large as 30 MW, are used in critical applications in industries such as petrochemical, pulp and paper, mining and steel manufacture. Any sudden failure of a machine can have a drastic financial loss due to production down time. As well there may be safety implications. The majority of all rotor and stator failures are caused by a combination of various stresses that act on these two components. Austin Bonnett et al [1, 2] categorize these stresses as thermal, magnetic, dynamic, mechanical and environmental. During recent years, there have been improvements in the design and manufacture of windings, accomplished primarily through the development of improved insulation materials and treatment processes. The expected life of the stator has improved significantly. However, the rotor design and manufacture remains basically unchanged. Hence, rotor failures account for a large percentage of the total induction motor failures. One of the principal causes of rotor failures is bearing failures which have increased with change in size and design. A survey of failures in induction machines in the oil industry by O.V. Thorsen et al [3] indicated

bearing failures count for the majority of the failures, at least fifty percent. Many bearings are being operated at increased loads, temperature and speed. The increased operating conditions have resulted in mechanical stress and electrical current failure of the bearings. Shaft current phenomenon is increasingly troubling as the size of the machine has increased and with increased application of variable speed drive.

1.1 SHAFT CURRENT PROBLEM DEFINITION

Shaft voltages which arise from a variety of sources often produce damaging currents in rotating machine components such as the shaft journal, bearings, gears and seals. As the size of the rotating machine increases the magnitudes of the shaft voltage and current increase. Shaft voltage generated in the machine appears across the oil film between the shaft journal and the bearing. The magnitude of this voltage may exceed the breakdown voltage of the oil film resulting in arcing between the shaft journal surface and the bearing babbitt. The main consequence of the arcing is pitting of the shaft and the bearing. An additional consequence of the arcing is the deterioration of the lubricating oil through a carbonization process. The bearing wear and deterioration of the oil accelerate the mechanical wear, hence they aid in further destruction of the bearing. The bearing will then experience increased loading and increased bearing temperature. The bearing capability is further reduced by the higher temperature. Finally, the damaged bearing needs to be replaced, otherwise the process train which includes the electrical machine, will suffer catastrophic failure with consequently severe damage.

In diagnosing shaft currents in electrical machines, research has focused on the machines with anti-friction bearings or high speed turbo-machinery with static excitation. The magnitude of shaft current is measured by a closed circuit involving a shunt or an ammeter [4]. Also, the measurement is usually done during steady state running conditions. It is toward further understanding of the origin of shaft current in machines with medium range speed and oil lubrication that the work of which this thesis is a record, is concerned. There are two primary objectives, the first being the development of an accurate method of measuring the shaft current and second, the development of an analytical basis for the prediction of shaft current. All the tests which were performed were laid out in a systematic approach to validate the causes and measurement of shaft current.

1.2 ORGANIZATION OF THE THESIS

The origins of shaft current are described in Chapter 2. The chapter begins with background materials, reviewing published work on its origin, addressing the different types of shaft current and discussing their effect on the bearing and shaft. Recognition of shaft current is discussed.

Chapter 3 addresses the problem of present state of the art in measuring shaft current accurately. This leads to a novel method of shaft current measurement. The new method is not only reliable but requires little maintenance and is not circuit load dependent. Further the method can be used as part of on-line monitoring system for the electrical machine.

In Chapter 4, with the aid of the magnetomotive force-permeance theory, the possible harmonic contents of the shaft current are determined. Chapter 4 includes a description of armature reaction. This description provides for further development of the shaft voltage prediction rule. The remainder of the chapter is devoted to a discussion of how the effect of non-smooth air gap due to stator and rotor slotting, and non-linear effects may be accounted for in the shaft voltage prediction rule.

Chapter 5 deals with the state of the rotor condition specifically in induction machine. Again using the magnetomotive force-permeance theory, the effect of rotor condition specifically eccentricity and broken bar on shaft current is explained and accounted for in the shaft voltage prediction rule.

In Chapter 6, the design of the experiment is explained, defining the methodology used in the investigative work so as to arrive at the main cause or causes of the bearing damage. Based on the works in the Chapters 4 and 5, the results are analyzed and finally a conclusion is reached.

1.3 CONTRIBUTIONS OF PRESENT WORK

The objectives of the work presented in this thesis includes:

1. Developing an accurate and appropriate method of measuring shaft current. This includes specification for the experimental set-up required to measure the shaft current at all load conditions. It also includes experiments to determine the harmonic contents of shaft current.

2. Developing an analytical theory that assists in shaft voltage prediction.
3. Establishing a systematic methodology to analyze and determine the causes of shaft current.
4. Explaining methodologies to minimize the magnitude of shaft current during transient operation. A proposed method is the subject of a patent application.
5. Developing an accurate method for the determination of the performance of the oil ring. A proposed method is the subject of a patent application. The importance of oil delivery for bearing lubrication by the oil ring is explained.

CHAPTER 2

REVIEW OF THE SHAFT CURRENT PHENOMENON

2.0 INTRODUCTION

In this chapter the current understanding of the shaft current phenomenon is discussed. The possible causes of shaft current are evaluated together with recognized criticisms of each cause. These are followed by discussion on additional factors that could effect the occurrence of shaft current. The characteristics of shaft voltage and current are presented for completeness of understanding of shaft current phenomenon. Finally, to distinguish bearing damage due to shaft current from damages that are of mechanical or chemical nature, recognition of shaft current effect is discussed.

2.1 ORIGIN OF SHAFT CURRENT PHENOMENON

If it were possible to design a perfectly balanced and symmetrical machine, no shaft current would exist. Shaft current exists when flux associated with unbalanced magnetic fields links the shaft and causes shaft voltage. This voltage will tend to circulate the current through the shaft, across the bearing oil film, through the machine base and thence back through the other bearing. The unbalanced magnetic fields may be due to manufacturing variations such as rotor static or dynamic eccentricity, axial cooling holes

in the stator and/or rotor laminations, shaft keyways and joints between segmental laminations. Furthermore, these fields can arise when there is a net current in the stator winding: the current path is axial along the stator frame to one bearing end, via the oil film to the rotor shaft and back to the stator frame and the other bearing end. The net current resulting from the two coil sides of each phase winding having different currents, can be attributed to parasitic capacitive leakage current. The parasitic capacitive leakage current is generally small when the machine is fed from a single frequency sinusoidal voltage source. However, the leakage current must be seriously considered in inverter-fed machines. Unbalanced magnetic fields due to supply unbalance and unbalanced magnetic pull (U.M.P.) generally occur in the transient condition.

The principal causes of shaft current are listed in the sections following.

2.1.1 Shaft Current Due to Alternating Voltages Induced in the Shaft [5 - 14]

Unbalanced magnetic fields in alternating current machines will cause current to be induced in the shaft. This unequal distribution of the magnetic field can result from the introduction of unequal distributions of joints in the stator core. The reluctances of the flux paths through the joints are higher than for other paths. The magnitudes of magnetic field densities in the flux paths through the joints will be less dense than other paths. Thus there will be flux surrounding the shaft, as shown in Figure 2.1. If it varies in density or the shaft rotates, a voltage will be induced. This unequal distribution of flux generally occurs in sectionalized stators. Alger and Samson [5] evolved a shaft current prediction rule. This rule, expressed in equation 2.1, states, " The use of segmental

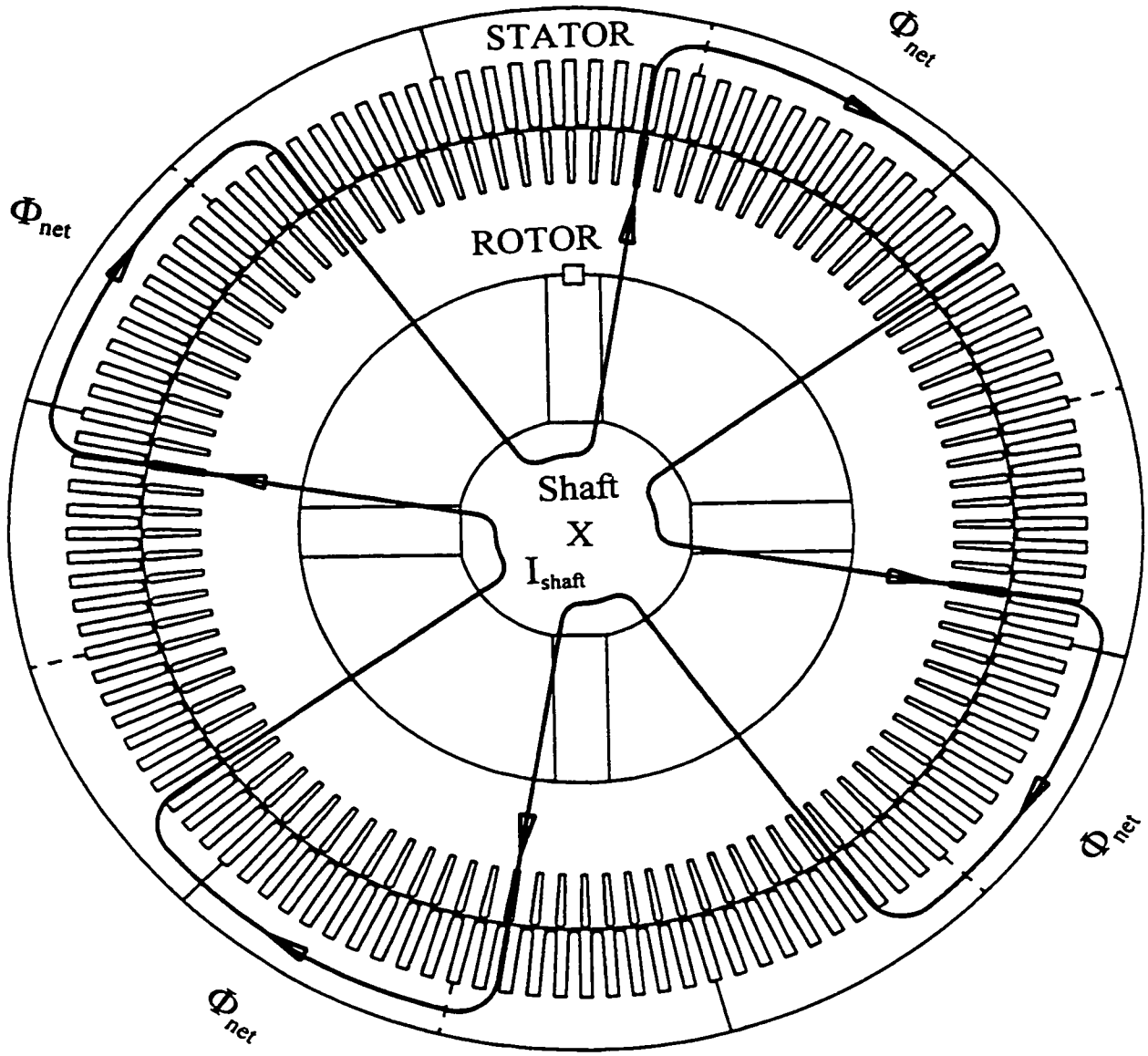

Figure 2.1: Shaft Current Due to Alternating Flux

punching on the stator will cause shaft currents if the ratio of twice the number of joints, J, to the number of poles, P, or four times the number of segments over the number of poles, expressed as a fraction reduced to its lowest terms, has an odd number for its numerator, A ". The number of joints is the number of segments per circle, S_c, times the number of layers before the pattern repeats, generally 2.

We define $$\frac{A}{B} = \frac{2*J}{P} \quad \text{OR} \quad \frac{A}{B} = \frac{4*S_c}{P} \qquad (2.1)$$

where B is the lowest common denominator and A and B are whole numbers.

The frequency of the shaft current is equal to A x f where f is the line frequency. No shaft current will appear if the numerator, A, is even. If the ratio is unity, all poles share equally in the production of the circulating flux and shaft voltage. However, if the ratio is a fraction, only a portion of pole surfaces will be covered, leading to a net circulating flux. The greater the denominator of the fraction the lower will be the shaft voltage. For the case shown in Figure 2.1, with A=3 and B=1 we expect shaft voltage at 180 Hz. Alger did not extend his rule to include spatial and time harmonic effects or saturation effects. In Chapter 4 the harmonic effects and saturation effects are explained and discussed. Negligible shaft current will appear no matter how irregular the flux waveform due to tooth pulsations, harmonics or saturation, if the joints in the stator core are uniform such that the numerator of the ratio, A, is even. There is a lack of detail on the manner in which circulation of flux arises. Hence, the shaft voltage prediction rule as applied to the test machine, will be explained pictorially in Chapter 6.

Asymmetrical magnetic fields may also occur due to differences in the spaces between the ends of laminations and the non symmetrical distribution of slots. The non-symmetrical distribution of slots will result in an unbalanced magnetic field that surrounds the shaft. Buchanan [7] and Lauders [13] remarked that varying punching segment permeabilities can result in magnetic asymmetries in the same manner as joints arising from segmental punching design. Uniform permeability in each flux path is impossible to obtain due to geometry, inconsistencies in manufacturing, etc. and consequently, as the flux pattern shifts around the machine, the varying reluctance will result in changes in the magnitude of the flux. However, we will ignore this factor in this study since there is some evidence that it is insignificant in the occurrence of shaft current [7, 13].

In assembling the stator core and the rotor core, the segments or ring punchings are arranged in such a way that the small variations in thickness which occur during manufacture are equally distributed. Otherwise, spongy sections will result which will basically have the same effect as an uneven air-gap. In practice, the effects of spongy sections are mitigated by rotating the laminations at nine degree steps as the segmental or ring punching is manufactured.

Axial ventilation holes in the stator core are considered as another source of magnetic asymmetries unless they are located symmetrically with respect to the poles.

The fundamental, third, fifth and seventh harmonics are the main frequency components in shaft potentials caused by magnetic asymmetries. The rotor eccentricity

distorts the magnetic field further, contributing to an enhanced effect on the shaft voltage magnitude. Chapter 5 describes the types of rotor conditions such as rotor eccentricity that can cause stray flux in the shaft and resulting in localized bearing current as the shaft rotates.

2.1.2 Shaft Currents due to Shaft Flux [5, 9, 13]

Any unbalanced magnetic field [5] surrounding the shaft will cause the shaft to be magnetized. These shaft fluxes, as shown in Figure 2.2, arise in all electrical machines because of asymmetries in the electrical and magnetic circuits of the machines due to tolerances in the manufacturing process. If a coil is wound around the shaft of an electrical machine, these fluxes will induce in it a voltage by Faraday's Law. The magnetic fluxes will pass from the shaft to the bearing, through the frame of the machine and thence to the other bearing. Hence, these fluxes cut the bearing surface as the shaft rotates, establishing a potential along the length of the journal. A localized bearing current results (See Figure 2.2). This current passes from the shaft at one end of the journal across the oil film to the bearing surface, along the bearing surface, across the oil film and back to the shaft at the other end of the same journal. Insulation of the bearing from the housing will be of little use. It will only increase the magnetic reluctance of the flux path but will not stop the localized current within the bearing [5].

In machine with parallel-connected stator winding, the use of complete circuit rings which surround the shaft may result in shaft magnetization. Generally, these rings are placed at one end of the machine. The shaft flux at this end of the machine will be of

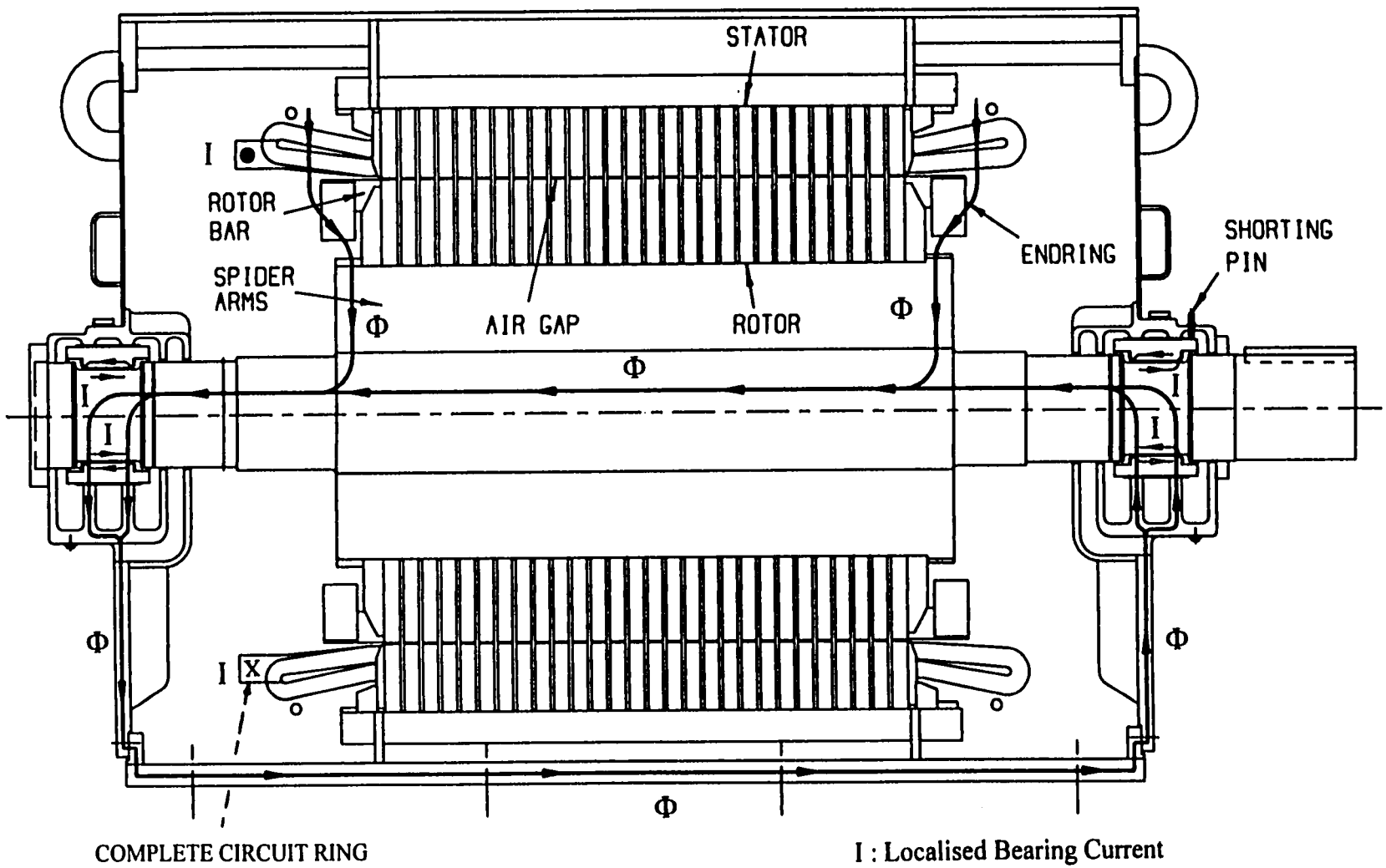

Figure 2.2: Localized Bearing Current Due to Shaft Flux

higher magnitude than that at the other end of the machine. Net shaft flux results. It is thus important that the use of complete circuit rings surrounding the shaft be avoided. Segmental circuit rings are preferred.

Tavner et al [15] examined the importance of winding design on the axial flux in laminated stator core. Three windings designs were studied namely concentric winding, distributed winding with diamond ends and helical winding. In their study, it was clear that with large winding overhang the core end axial flux is large and the flux decreases as the winding overhang or core bore radius is reduced. They found that when the winding overhang is greater than 50% of the core bore radius the internal distribution of the core axial flux is independent of winding geometry and design. This implies that any screening beyond the stator winding will not result in large axial flux densities. For winding overhang less than fifty percent of the core bore radius the distribution is dependent on winding radius. An industrial 8 pole induction machine, described in Appendix 1, was used in the present work. This machine has a stator winding overhang greater than fifty percent of the core bore radius. The rotor bar overhangs the end of the rotor core and is close to the stator overhang as shown in Figure 2.2. There was no screening of the flux from the rotor parts to prevent axial flux in the shaft.

Tavner et al also concluded that the core axial flux penetration increases in a segmented core. This is due to the segmented core current which completes its circuit at the butt joints between segments. Thus, the effectiveness of eddy currents in suppressing axial flux is reduced. Hence, in the 8 pole segmented core induction machine, Appendix

1, the axial flux will penetrate more deeply into the core. However, some of this end winding flux will flow axially in the shaft through the rotor retaining ring, rotor end ring and rotor flange. The stator winding overhang is long and close to these rings. Hence, there will be sufficient amount of end winding flux flowing axially in the shaft to the bearings and then to the frame.

Another source of shaft flux is magnetic particle inspection which is commonly carried out to determine the existence of cracks in the shaft. Magnetic particle inspection tends to generate residual magnetism on the shaft. Without subsequent demagnetization, the shaft may be sufficiently magnetized.

Sohre and Nippes [16, 17] reported that a shaft having a flux density of 0.0003 Tesla will operate satisfactorily without the damaging effect of localized bearing current. They proposed this level of flux density based on their works on high speed turbo-machinery. They pointed out that as the peripheral velocity of shaft increases with size of machine, the induced voltage causing the localized bearing current will increase. The acceptable level of flux density proposed by Sohre and Nippes is relatively close to the level of 0.0002 Tesla proposed by Costello [18].

2.1.3 Shaft Current due to Potential between Shaft and Ground [5, 11, 13, 19 - 23]

It is conceivable that by electrostatic effects, the potential of the rotor of an electric machine can be raised above the ground potential. On reaching a certain value the potential discharges through the oil film of the bearing. If the rotor circuit is grounded elsewhere, a short circuit can occur through the bearings.

In the electrostatic effect, the charges build up on the shaft until the potential is high enough to pierce the oil film [19, 20]. Charge is dissipated through the bearing causing momentary current. If the source of charge is maintained, a process of alternate charging and discharging will continue indefinitely. Constant repetition of such discharge may result in bearing pitting.

Electrostatic effects are greatly influenced by humidity and surface conditions [21-23]. Hence, measurements of the electrostatic potentials are apt to be extremely erratic. Generally, the usual electrostatic potential sources do not produce sustained large currents. The intermittent charging and discharging, if continued for a sufficient period of time. can produce enough bearing damage to cause failure. Some of the most common causes of potential caused by particles impinging are charges that result from moisture particles in wet steam and from dust particles. In this process, charges of opposite sign to the striking particles are left on the object which has been struck.

In the electrostatic case of potential developed by charged lubricant, the lubricant being a relatively poor conductor may become charged as the lubricant passes through a filter with small passages. The molecules may remain charged even after passing through a considerable length of grounded piping system. When the potential becomes high enough the charge may be dissipated through the oil film.

Belt driven machines may be subjected to bearing current damage caused by electrostatic potential build-up by the charged belts. The charges originating at the point where the belt leaves the pulley may be carried on the surface of the belt and deposited

on the load pulley. The rate at which the charge is dissipated is equal to the rate at which the charge is deposited given the same conditions at both pulleys. Should these conditions be different a charge may build up on the shaft if the shaft is insulated by an oil film. The charge developed may dissipate through the bearings. In induction machine, the shaft current originating from electrostatic charge is not usually a concern [21].

2.2 ADDITIONAL FACTORS INFLUENCING SHAFT VOLTAGE AND SHAFT CURRENT

2.2.1 Types of Lubrication

In an alternating current machine, electromotive force may be present whether the machine is running or at rest, its magnitude depending on the relative values of the stator fluxes for the standing and running conditions. The value of bearing current due to shaft E.M.F. will decrease rapidly when the machine is running as the oil film is established. The high proportion of current at low speed can be explained by the fact that the resistance of the oil film decreases with decreasing speed. This oil film resistance does not remain constant. Had it been so, the shaft current could have decreased proportionately with speed or frequency for the constant flux, variable frequency case.

In an oil ring lubricated machine the oil ring rides on the shaft journal, Figure 2.3 and its bottom half is submerged in oil. There is metal-to-metal contact between the shaft journal and the oil ring. Also when the rotor is at rest, there is no oil film between the shaft and the bearing. On energizing the motor, the oil ring initially follows the shaft journal as the shaft rotates. The oil ring carries the oil from the bottom of the bearing

Figure 2.3: Oil Ring on the Shaft Journal.

housing on to the shaft and bearing, thus slowly developing an oil film between the bearing and the shaft journal. As the speed of the shaft increases the oil ring begins to slip. During this slip condition, the portion of the oil ring in contact with the shaft journal may make or break contact with the shaft journal surface, leading to increased probability of arcing between the oil ring and the shaft journal. The arcs may result in carbonization of the oil and pitting of the shaft journal. Fortunately, the shaft tends to be of high strength steel and is able to withstand the sparking without any catastrophic consequence. On this basis, this was not evaluated in this thesis. It is also possible that the oil ring rubs against the bearing housing. The oil ring rubbing the bearing housing makes and breaks the circuit causing a spark that pits the shaft. If the oil ring should touch the bearing housing, a closed circuit for the bearing current will be established.

With an oil ring lubricated bearing system, the oil film is not developed at standstill condition. In fact there is metal-to-metal contact between the journal and the bearing surface. The shaft current circuit will consist of the shaft at one end, the bearing, the frame and shaft at the other end. As the motor runs up to speed, the rotor assembly oscillates in one direction at one instant of time and in the opposite direction at another instant of time. This axial movement continues until the machine is running at its magnetic center during the steady running condition. The oil film builds up on one side of the bearing, opposite to the direction of the motion. Oil is squeezed out of the side of the bearing in the direction of the motion, contributing to thinning of the oil film. The oil ring is not a good carrier of oil and hence the oil film build up will be less than the oil

film thinning. The shaft journal rides on a reduced oil film thickness. The oil film will break and make correspondingly when the rotor assembly is in the opposite direction of motion. The back and forth shaft axial movement will gradually slow down till the machine rotates at its magnetic center. This make and break of oil film phenomenon continues until oil film stability is reached during steady state running condition. This phenomenon is a cause of arcing on the bearing surface. Appendix 2 describes the oil ring performance and lists the factors affecting the life of the bearing. It also includes some of the characteristics of the bearing, lubrication oil and oil ring used in the test machine.

With a forced lubricated bearing system an oil film is developed between the shaft journal and the bearing surface. The bearing current will not damage the bearing as no make and break condition of the current arises. As the motor runs up to speed, the end play movement will cause the oil film thickness to vary until it stabilizes to an average value. It is this oil film variation that could possibly lead to make and break of the shaft current circuit and hence lead to possible arcing at the bearing. However, this possibility is less than for the case of an oil ring lubrication system. In Chapter 6, the importance of build-up of oil film to limit the magnitude of shaft current will be shown.

In machines where the bearing clearance is insufficient, the oil film may not be distributed uniformly. Hence even though the current is small, about one ampere, bearing damage can happen because the oil film may insulate a certain percentage of the bearing, forcing the small current through the remaining non-insulated area. The oil film may not

be thick enough to virtually insulate the shaft from the bearings and prevent the bearing current.

2.2.2 Energy per Square Meter [6, 8, 9]

E.G. Merrick [6] and Adler [8] reported that tests done at A.E.G. in Stadslau showed that when the current density exceeds 15 to 20 amperes per square decimeter of the bearing surface the shaft is damaged. As long as the current density is less than 15 amperes per square decimeter only the bearing is damaged; the shaft will not be harmed. A current density criterion was used because it is difficult to calculate the bearing currents due to varying contact resistance between the shaft and the bearing. Pearce [9] commented that this criterion is a probable means of determining the harmful effect of bearing current. The power energy density criterion was not evaluated as part of the objectives of the thesis. Adler [8] commented that bearing surface is a factor in the determination of the severity of the bearing current. A smooth bearing surface will experience lower bearing current than a rough bearing surface. Furthermore, Adler concluded that bearing current will be larger at rest than when the machine is running. This decrease in current when running is due to increased resistance caused by a better supply of oil between the contact surfaces.

Insulation of over 3.18 millimeters [9] is said to be sufficient to prevent the establishment of current as the shaft voltage never reaches more than 10 volts. This insulation is placed under the pedestal or bracket assembly. However, as can be

demonstrated in an experiment conducted on a 8 pole induction machine, Appendix 1, insulation as thin as 0.762 millimeter may be sufficient.

Bearing damage may occur over a relatively short time of a few seconds, or take several years. The magnitude of the current density dictates the time taken for the bearing destruction. In the experimental work conducted on a 8 pole induction machine, the bearing damage occurred during starting of the machine. In previous work, the steady state phenomenon was assumed. At steady state running condition the oil film stabilizes to an average value. There is no make and break of the flow of current and no arc phenomenon. The bearing is damaged generally due to arcing of the bearing current across the bearing clearance from the journal to the bearing.

2.2.3. Shaft End Play Movement [10, 12, 24]

Wagner [10], Riggs [12] and Rosenberg [24] stated that shaft end-play movement can cause bearing current to occur. During start-up of the machine, the rotor assembly moves axially forward and back as the motor accelerates to rated speed. During this shaft axial movement, if the shaft collar or shoulder runs free of the bearing ends, the oil films in the two bearings are in series. If the oil films are thick enough, they can effectively break the current path. If the collar or shoulder rubs its bearing, only the film in the other bearing offers resistance to shaft current. Hence, the latter oil film may fail and bearing current results. The authors offered no experimental evidence to support the contention that shaft end play movement influences shaft current.

This end play movement effect is not a significant factor as long as the bearings are insulated. In fact, in the 8 pole induction machine with an insulated bearing, as the machine accelerates to steady state running condition with end play movement, the shaft current decays faster to a steady state value than when the machine accelerates with negligible or no end-play movement. The back and forth shaft axial motion probably aids the built-up of the oil film even though there is increased possibility of make and break of the oil film thickness that will cause shaft current to arc across the oil film to the bearing babbitt.

2.2.4 Rotor Construction [5]

Alger [5] considered a segmented type rotor construction to be of little importance in considering how to avoid shaft current as the slip frequency voltage due to the rotor segments is small compared with the line frequency voltage. This is true. However, other considerations of rotor construction must be evaluated such as non-insulated rotor bar, saturation of the bridge above the rotor slot and shaft spider design. Non-insulated rotor bar design is generally a norm. With this design there will be inter-bar current circumferentially, encircling the shaft and hence contributing to shaft flux. In this thesis, the effect of inter-bar current is mentioned in Chapter 5.

2.3 CHARACTERISTICS OF SHAFT VOLTAGE AND CURRENT

A number of characteristics of shaft voltage and current have been observed by previous investigators [5-28]. Characteristics of the shaft voltage are summarized as follows:

1. For a given size of machine and degree of saturation, the magnitude of this voltage will be proportional to the ratio, A/B in equation (2.1) times speed divided by the number of poles. The frequency of the voltage will be equal to the numerator of the segmental punching ratio times line frequency.
2. The shaft voltage will increase rapidly with the rating of the machine, all other factors remaining equal. According to the magnetic equivalent of Ohms' law, flux is proportional to magnetomotive force and inversely proportional to reluctance. As the rating of the machine increases, the core size of the machine increases and hence the reluctance of the stator core decreases. The reluctance of splits in the stator will be a greater proportion of the total stator reluctance. Hence, circulating flux increases and shaft voltage increases correspondingly. As the machine size increases with the rating of the machine, greater constructional asymmetries, sagging of the stator core and the rotor core and saturation arise. These factors influence the increase in the magnitude of shaft voltages.
3. Shaft voltage will be greater in machines with smaller air-gaps. The reluctance of the joint represents a greater proportion of the magnetomotive force for constant flux. The ratio of the magnetic field strength of the air gap to the total magnetic field

strength is small. Thus, the induction machine will be more likely to suffer such currents than the synchronous machine which has a larger air gap. The larger the diameter and the larger the number of poles in the machine the smaller the ratio of $\Re_{sj}$, the reluctance corresponding to the flux in the split stator where the split occurs, to $\Re_{sn}$, the reluctance corresponding to the flux in the split stator where there is no split. Hence, the circulating flux which is proportional to the ratio of $\Re_{sj}/\Re_{sn}$ will decrease. Shaft current due to this effect tends to be more pronounced in high speed machines with few poles.

4. Shaft E.M.F. will build up rapidly with saturation initially until the entire magnetic circuit becomes saturated. As the permeability of the magnetic circuit approaches that of air, the reluctance of the joints has little influence on the total reluctance of the magnetic circuit, and the shaft voltage begins to drop off. For a complete discussion, see Chapter 6. Line frequency shaft currents are nearly proportional to voltage at low flux densities. They decrease less rapidly with saturation. Multiple-frequency shaft currents have low values at reduced voltages.
5. Shaft current is approximately the same at no-load as at the full load condition [21]. Shaft voltages caused by magnetic asymmetries and static-excitation systems do not change in magnitude with changes in the load. This was clearly observed by Verma et al [21-23]. Only shaft potentials of electrostatic origin appear to change considerably with changes in the load. The electrostatic voltage on the shaft decreased linearly with reduction of the load and disappeared completely at about

half of full load in the measurement on a turbo-generator. Electrostatic voltages are erratic in nature. They depend on several factors such as flow and conditions of steam, load changes, source impedance, steam flow rates and many other design variables that determine the resistance in the circuit to ground.

2.4 RECOGNITION OF SHAFT CURRENT

Bearing damage may be of mechanical, chemical or electrical origin. Thus, it is important that an inspection of the damaged bearing be carried out under a microscope. Michael Costello [18] and Boyd and Kaufman [25, 26] provided information on the recognition of bearing current damage, origin and detection of this current and control procedures. Bearing current damage can be classified into four types: 1) Frosting; 2) Pitting; 3) Spark Tracks; 4) Welding.

A frosted surface is characterized by very small individual "craters" which average about 25 micrometers in diameter. This is smaller than many of the surface scratches. The bottoms of these craters are round and shiny. Frosting generally occurs during voltage discharge and is commonly referred to as " electric discharge machining " (EDM) or electrolysis. Frosted surfaces may be of electrical origin or chemical origin. Chemical attack gives a similar appearance to frosting, distinguished by the fact that the arcs are smaller, not as deep and dull. It may be necessary to use X-ray spectroscopy to determine whether the frosting surface is due to chemical contamination or electrolysis.

Pitting results in craters that are generally much larger in size (200 micrometer to about 250 micrometers in diameter) than for frosting. The bottoms of the pits are

rounded and have the smooth shiny appearance of having been melted. Pitting is a more serious form of damage than frosting. Initially, each pit is a separate crater and more or less circular in shape. As the pitting process continues, the pits begin to overlap, tending to destroy the clear evidence of their origin. Pits caused by corrosion or by foreign particles are usually of irregular form and have dull appearance. They are spaced at regular intervals circumferentially over a portion of the bearing. Such pits are almost invariably accompanied by circumferential scratches. Also, although these non-electrical pits have smooth bottoms they do not have the melted appearance of electrical pits. Electrical pits on the journal are usually considerably smaller than those on the bearing. The journal is not readily destroyed by mechanical pitting. This is because the journal is generally harder than the bearing.

Spark tracks are very irregular in nature and are often askew to the direction of rotation. The bottom of the tracks are sometimes melted and they have sharp corners. In contrast, dirt particles would leave rounded corners. The depth of the spark track is generally the same over its entire surface. There are occasions when the shaft journal exhibits absence of electrical discharge marks while electrical discharge is obvious on the bearing surface as shown in Figure 2.4. Figure 2.4 (a) shows uneven darkened thick marks on the upper part of the lower half of the bearing assembly. Microscopic view of the damaged area as shown in Figure 2.4 (b) indicates splatters of bearing babbitt. It appears that the babbitt was blasted out of the bearing surface by momentary electrical

discharge. On further examination of the damaged area, molten crater with spark tracks were observed as shown in Figure 2.4 (c).

Welding of parts such as bearing housing splits and bearing pads occurs when a great amount of current in order of hundreds of amperes passes through these parts. They are obvious to the naked eye.

2.5 SUMMARY

Shaft current generally arises due to asymmetries of the magnetic flux path. The magnitude of the shaft current is measured using an ammeter in the connection between one end of the shaft and its other end. It will be demonstrated in Chapter 3 that this method is fairly inaccurate. A new novel method of shaft current measurement is proposed in Chapter 3.

Equation (2.1) does not take into account harmonics such as stator slot harmonics, rotor slot harmonics and saturation. Furthermore, air gap eccentricities are not considered. The effect of eccentricity was briefly mentioned in the study by Rosenberg [24] and O. Haus [14]. There was no analytical determination of the effect. Hsu [27] reported that shaft voltage increases under greater eccentricities when the stator and rotor axes are parallel. In Chapters 4 and 5, effects of harmonics and air gap eccentricities are considered in the application of equation (2.1) to determine the occurrence of shaft current.

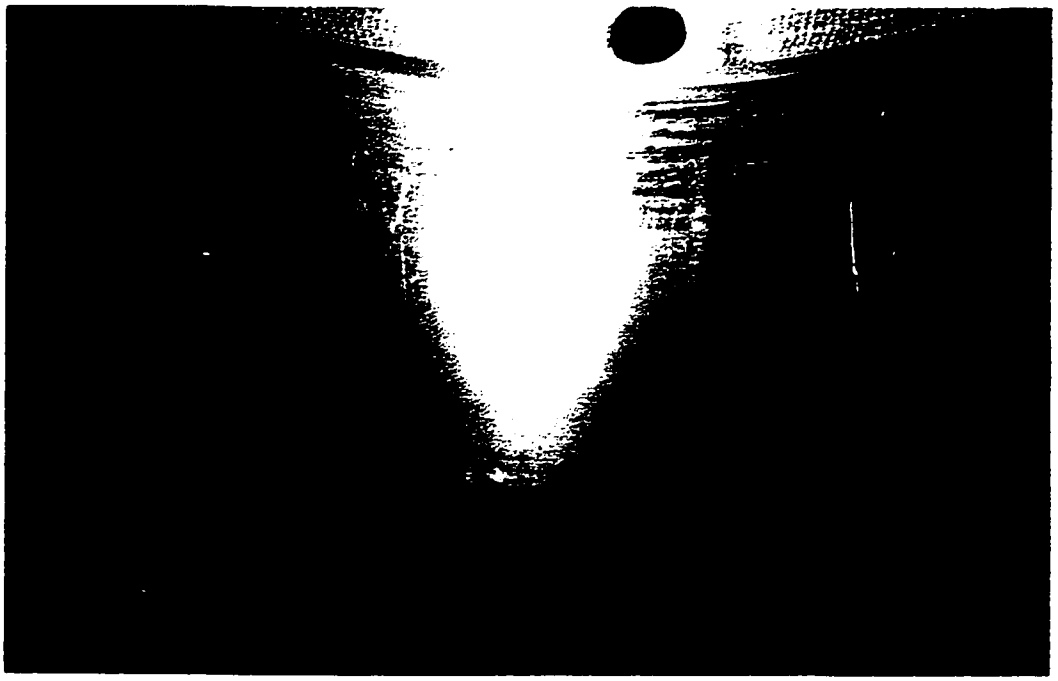

Figure 2.4 (a): A Close-Up View of the Bottom of the Bearing Showing the Damage at the Upper Part of the Bearing.

Figure 2.4: Typical Bearing Damage Due to Shaft Current.

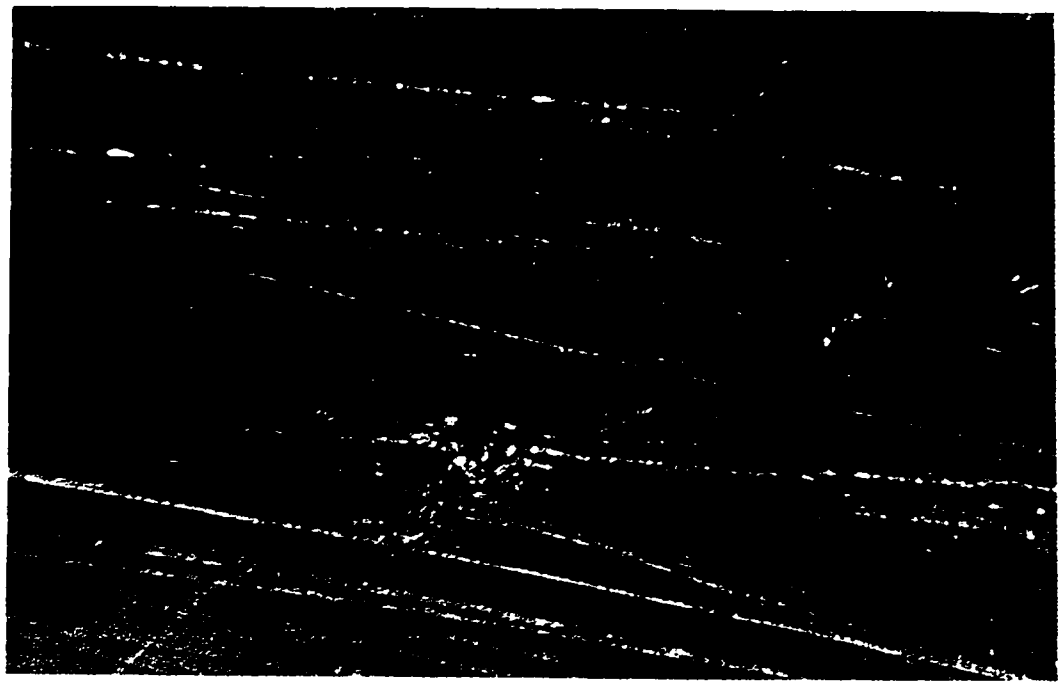

Figure 2.4 (b): A Microscopic View of the Damaged Area Showing Splatter of Babbitt as if It was Blasted by a Momentary Electric Discharge

Figure 2.4 (c) : Another View of the Damaged Area Showing Molten Crater with Spark Track

Figure 2.4: Typical Bearing Damage Due to Shaft Current

It is important to separate mechanical causes from electrical causes of bearing damage. Microscopic inspection of the bearing needs to be carried out to determine the cause of bearing damage. Oil analysis will assist in the determination of the presence of shaft current. However, it will be demonstrated in Chapter 6 that oil analysis can be inconclusive.

The maximum acceptable levels of shaft residual flux proposed by Costello, Sohre and Nippes are the only published values available. These levels were a result of their work on high speed turbo-machinery (speeds equal to or greater than 3600 rpm) and hence for speed equal to or less than 1800 rpm, the level proposed may be on the low side. The levels are only to be used as a guide to minimize localized bearing current.

CHAPTER 3

MEASUREMENT OF SHAFT CURRENT

3.0 INTRODUCTION

Magnetic asymmetries may result in a voltage from end to end of the shaft of a large induction machine. These asymmetries may arise due to the jointing of segmented punchings around the core of the machine, stacking of segments, rotor eccentricity, rotor or stator sag, and other anomalies during manufacture. However, there is evidence that shaft voltage occurs on all rotating electrical machines to a greater or lesser degree. There is also the possibility that other factors such as build-up of electrostatic charge may, in some applications involving PWM inverters, give rise to bearing current.

IEEE Standard 112-1991 [4] describes end-to-end shaft voltage measurement techniques. It states that shaft current can be measured by substituting an ammeter in the circuit. This method yields an incorrect measurement for shaft current. The test machine used for this work is a large, eight pole induction motor. During initial conventional commercial testing, it was found to have discolored oil and damaged bearings. Examination of the bearing babbitt showed the characteristic stitch marks with round shiny bottom craters associated with shaft currents. In this case the oil was clean at the start of the test, and precautions had been taken to insulate the bearings against the

possible development of shaft current. Bearing insulation both before and after the tests was above 10,000 Ω; hence there was no apparent cause for the bearing damage.

However, it is conceivable that a small voltage could be established end-to-end across the shaft. On start-up, before the establishment of an oil film, this small voltage could lead to a relatively high shaft current. On establishment of the oil film, the interruption of the shaft current could then lead to a very high component of induced voltage, resulting in breakdown of the oil film with the consequent damage to the oil and bearing as shown in Figure 2.4. The problem is then to develop a measurement program to establish that shaft voltages did indeed occur and to determine the magnitude of such shaft voltage along with the resulting bearing or shaft current.

In this chapter the different conventional methods of shaft measurement and the proposed Rogowski coil method are discussed. The theory and justification of the proposed Rogowski coil method are described in detail. Finally test results will demonstrate that the Rogowski coil method is a preferred method of shaft current measurement.

3.1 METHODS OF SHAFT CURRENT MEASUREMENT

Two types of shaft current measurement were evaluated. They are the shunt /ammeter method and the Rogowski Coil method.

3.1.1 Shunt/Ammeter Method

The shunt/ammeter method uses a low resistance moving coil type ammeter placed in series with the shaft as illustrated in Figure 3.1.

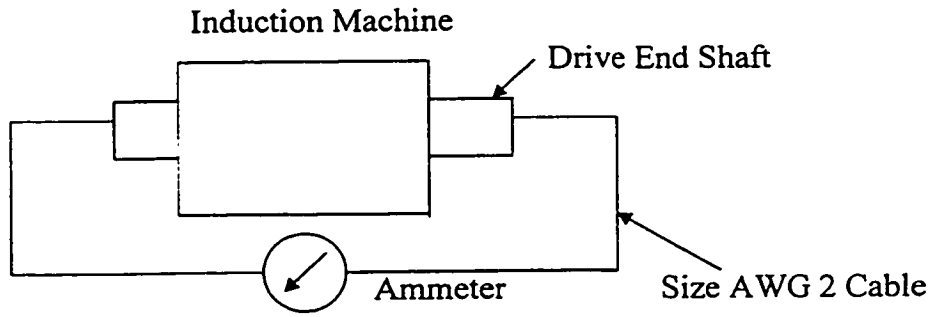

Figure 3.1: Schematic of Ammeter Method

Shaft current measurement varies inversely with the size of the cable. The bigger the size of the cable and hence reduced cable resistance, the larger is the shaft current. The shaft current measured is load dependent. No attempt was made to define a load dependence relationship. After a trial period, a cable of size AWG 2 was determined to be practical and appropriate for stable shaft current measurement. The connection of the cable to the two ends of the shaft can be done through a brush assembly but this is not feasible due to space limitation as a result of the installation of the Rogowski coils on both ends of the motor and a collector ring on the opposite drive end of the shaft. Instead, inch wide copper braided wires wound on the ends of rectangular pieces of wood and connected to the AWG 2 cable, were held in firm contact with the two ends of the shaft. A low resistance ammeter was inserted in the circuit to measure the shaft current. This method is considered unreliable as the introduction of the connection from one end of the

shaft to the ammeter and then to the other end of the shaft results in a low impedance path for the shaft current. Without this external connection there is no path for the shaft current as both bearings are insulated. A detailed explanation is given in Section 3.1.2.

3.1.2 JUSTIFICATION OF THE USE OF ROGOWSKI COIL

IEEE standard 112 indicates the use of a low resistance ammeter in the measurement of shaft current. The ammeter method disturbs the shaft current conducting circuit of the machine as indicated in Figure 3.2 by providing a low resistance path through the shunt resistance or the ammeter resistance.

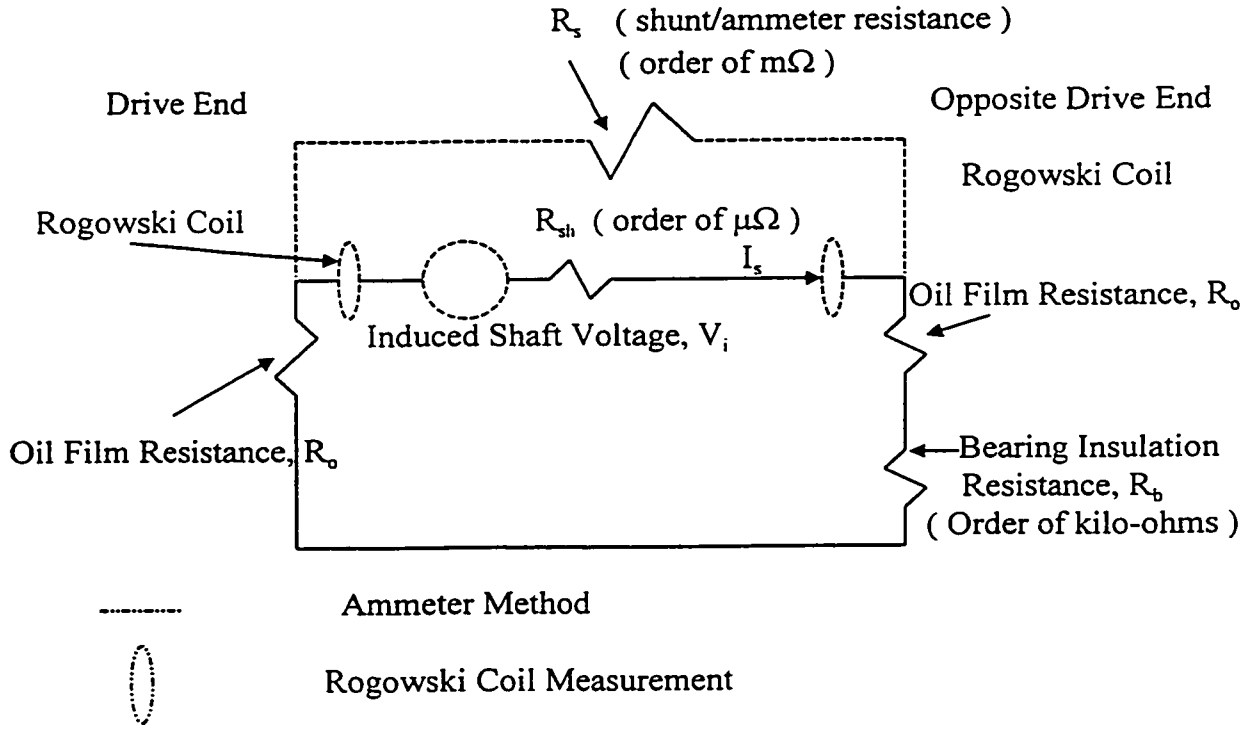

Figure 3.2: Simplified Representation of Machine Under Test

This can be shown as follows:

Applying Kirchhoff's law to the heavy lined circuit in Figure 3.2, we obtain

$$V_i = I_s \left(R_{sh} + R_b + R_o \right) \qquad (3.1)$$

where V_i is the induced shaft voltage,

R_{sh} the resistance of the shaft,

R_o the resistance of the oil film,

and R_b the bearing insulation resistance.

The bearing insulation resistance is at least of the order of kilo-ohms, greater than the shaft resistance and oil film resistance and hence equation (3.1) can be simplified as

$$V_i = I_s \; R_b \qquad (3.2)$$

Equation (3.2) indicates the shaft current to be of small magnitude.

Using the ammeter method, shown in Figure 3.2 as the dashed circuit to measure shaft current, the voltage-current relationship can be obtained as

$$V_i = I_s \left(R_{sh} + R_s + R_c \right) \qquad (3.3)$$

where R_s is the shunt or ammeter resistance and R_c the connection contact resistance. The ammeter resistance is of the order of milli-ohms. With the negligible magnitude of the shaft resistance and ammeter resistance, the shaft current has been amplified. The amplified shaft current does not represent the true value of the machine. The amplification of this current through the ammeter method can cause secondary effects on the shaft and the bearing.

With the Rogowski coil mounted tightly around the shaft on the inboard end of the bearing bracket assembly, the current measured is the true rms current in the shaft. Hence, the direct approach to the measurement of shaft current was abandoned in favor of the Rogowski coil method.

3.1.3 Rogowski Coil Method

In the Rogowski coil method, two Rogowski coils, Figure 3.3, were installed around the shaft close to the rotor bore on both ends of the shaft as shown in Figure 3.4. The voltage outputs from the coils were connected to the collector or slip ring from which connection was made to an isolator and then to a recording system. The isolator is used to ensure that there is no grounding anywhere in the connection from the Rogowski coil to the recording system. A two inch diameter shaft hole was drilled from one end of the shaft to the other end. The insulated coaxial cable extension from the Rogowski coil runs in this hole to the slip ring. In this manner, the influence of interference is further reduced. The slip ring was installed on an insulated adapter on the opposite drive end of the shaft, Figure 3.5. All connection cables are coaxial type to reduce noise interference.

3.2 THEORY OF THE ROGOWSKI COIL [29]

The Rogowski coil consists of a solenoid of fine wire uniformly wound on a flexible non-magnetic tube of which the two ends are brought together to form a butt joint. The coil is basically an air core transformer with a uniformly wound secondary. Hence, the core does not saturate, providing for a linear coil input-output relationship. The coil is

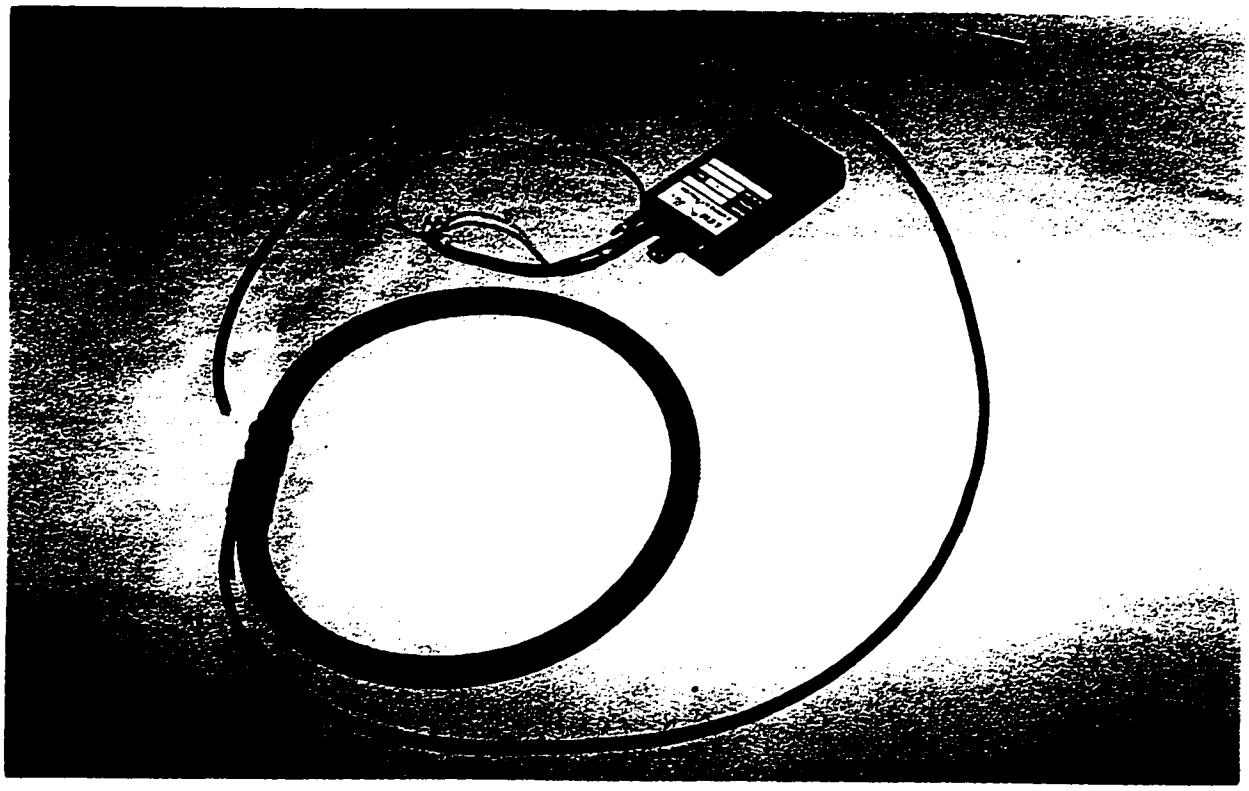

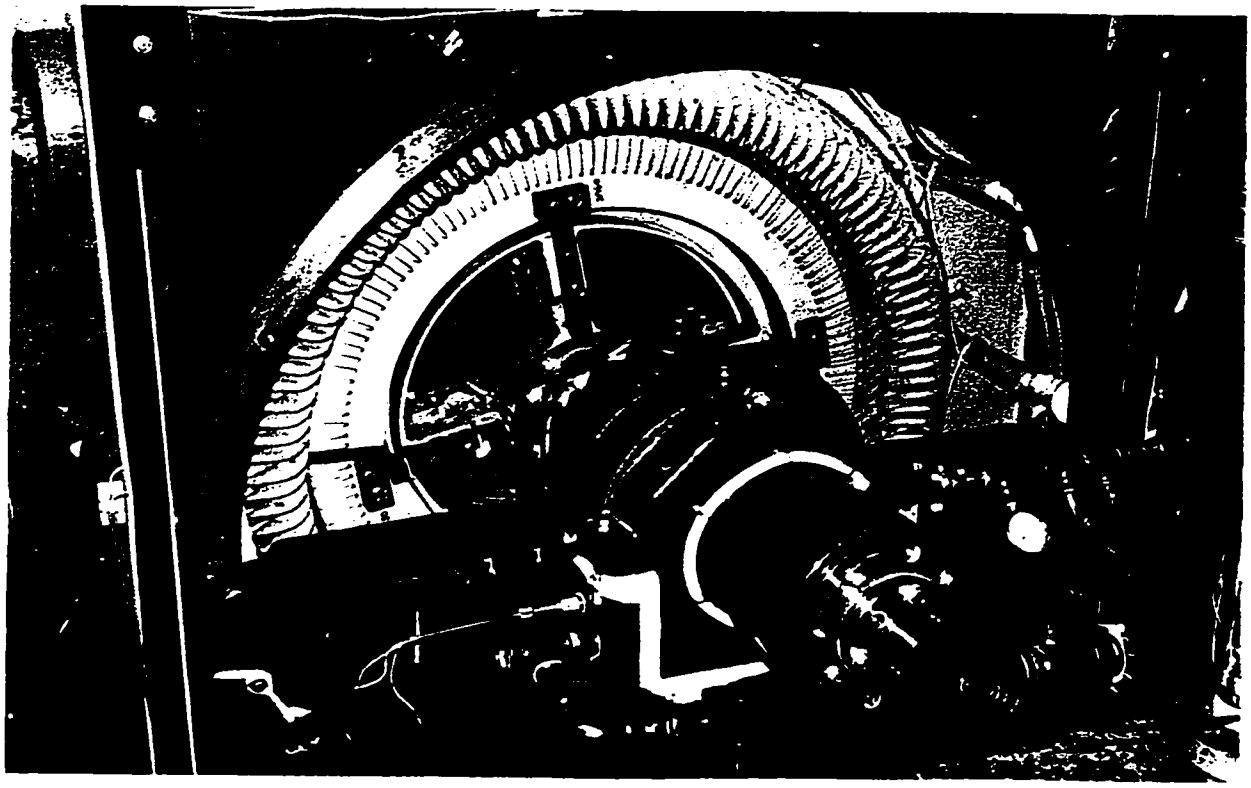

Figure 3.3: Rogowski Coil, Amplifier Unit and Test Machine

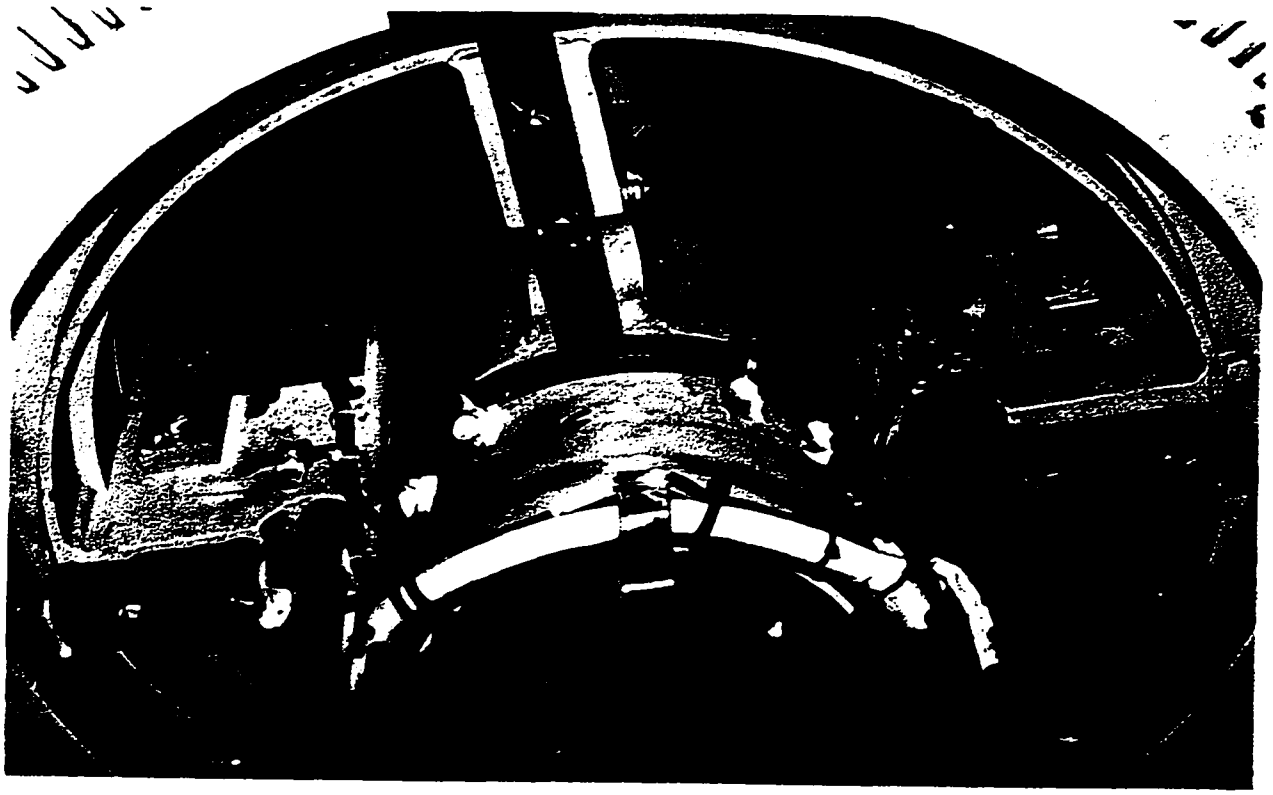

Figure 3.4: Location of Rogowski Coil in the Induction Machine

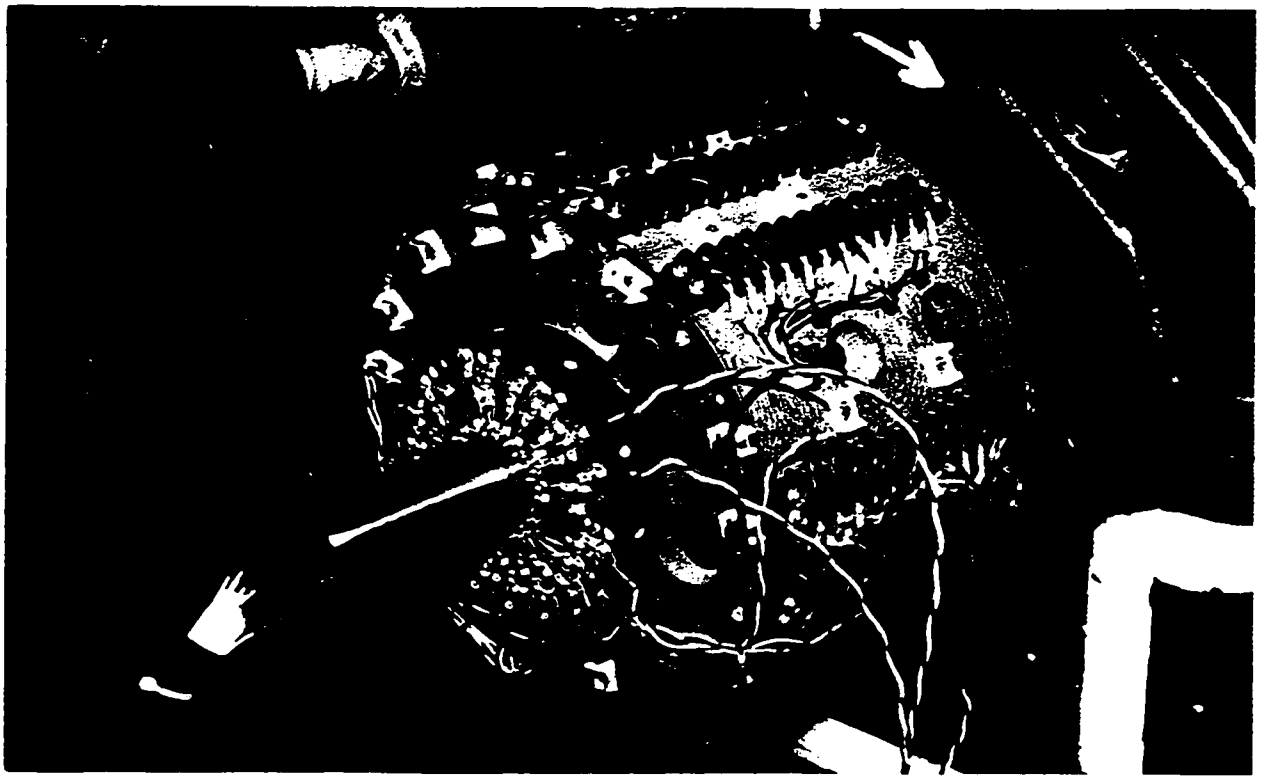

Figure 3.5: Collector Ring Installed on ODE of the Shaft of the Induction Machine

wound tightly around the conductor carrying the current, in this case the shaft. There is no disturbance of the conducting circuit unlike the case when the shunt/ammeter circuit is used. The coil output voltage is proportional to the time rate of change of current. An outline of the Rogowski coil is shown in Figure 3.6.

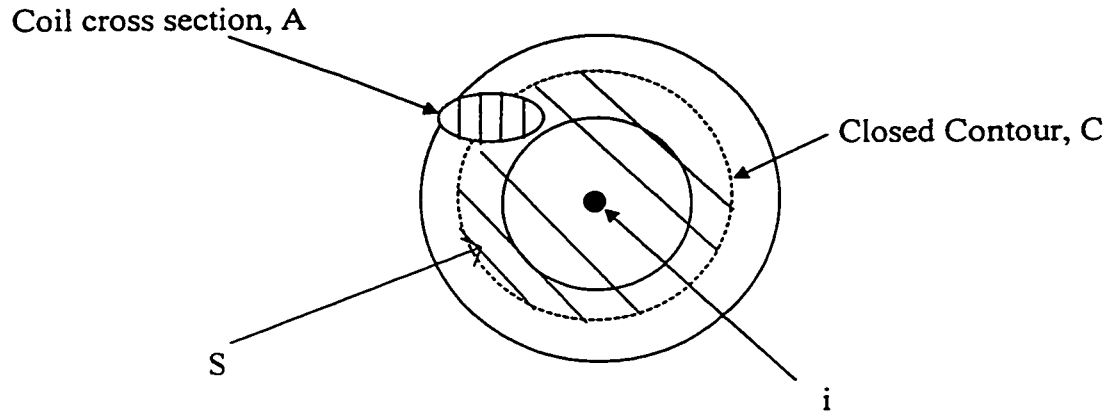

Figure 3.6: Outline of Rogowski Coil

Consider an N turn coil carrying a time varying current i. Let H_t be the component of magnetic field strength tangential to the closed contour and hence normal to the coil cross section A. Also, let H_n be the component of the field normal to surface S. Applying Faraday's law to the Rogowski coil, the induced instantaneous E.M.F. in the coils is given by

$$e = - \frac{d}{dt}\left(\sum_{k=1}^{N} \Phi_k \right) \qquad (3.4)$$

where Φ_k is the instantaneous flux linking the k^{th} turn of the N-turn coil.

Substituting for Φ_k, equation (3.4) becomes

$$e = -\frac{d}{dt}\left(\sum_{k=1}^{N}\left[\iint \mu_o H_{tk}\, dA_k \right] \right) \qquad (3.5)$$

where the permeability in the region of the coil is approximated as that of free space, μ_o and H_{tk} is the magnetic field strength linking the k^{th} turn of the N-turn coil.

The cross section of each turn of the coil, A_k is approximately equal to the coil cross section, A if the coil is constructed of closely wound thin wire. Hence, equation (3.5) can be rearranged to obtain

$$e = -\mu_o \frac{d}{dt}\left(\sum_{k=1}^{N}\left(\iint_A \left(\frac{N}{l} \sum_{k=1}^{N} H_{tk}\, \delta l_k \right) \right) dA \right) \qquad (3.6)$$

where l ($= N\, \delta l_k$) is the length of any closed contour within the coil which is parallel to C, and δl_k is the length of k^{th} turn of the N-turn coil.

For any closed contour within the Rogowski coil, by Ampere's law, the current i, is given by

$$\sum_{k=1}^{N} H_{tk}\, \delta_k \approx \oint H_t dl = i \qquad (3.7)$$

H_t is co-linear with the path everywhere around the closed contour.

Applying equation (3.7) and rearranging, equation (3.6) becomes

$$e = -\mu_o \frac{d}{dt}\left(\iint_A \frac{N\, i}{l} dA \right) \qquad (3.8)$$

The cross section of the coil is small, thus the length, l tends to be close to the length of the axis of the coil, l_c. Hence equation (3.8) can be approximated to equation (3.9).

$$\begin{aligned} e &\approx -\mu_o \frac{NA}{l_c} \frac{di}{dt} \\ &= -\mu_o n_t A \frac{di}{dt} \end{aligned} \qquad (3.9)$$

where n_t is the turns density.

The output e may be affected by induced E.M.F., e′ caused by the magnetic flux crossing the surface, S. The induced E.M.F., e′ is given by

$$e' = -\frac{d}{dt}\left(\iint \mu_o H_n \, dS \right) \qquad (3.10)$$

This induced E.M.F. can be eliminated by having a second layer of winding wound back in the same sense over the first layer of coils or threaded through the center of the tube. Error will not be introduced in the output. Equation (3.9) can be integrated to yield a current-coil output voltage relationship:

$$i = -\frac{\int e \, dt}{\mu_o n_t A} \qquad (3.11)$$

where A is the area of the coil cross-section,

μ_o is the permeability of free space,

and n_t is the number of turns per unit length of the coil.

The relationship in equation (3. 11) is accurate irrespective of whether the coil is placed concentric or non-concentric with the current carrying conductor.

For a sinusoidal current having a peak value I resulting in a peak output voltage, E, of frequency ω, equation (3.11) becomes

$$I = \frac{E}{\omega \mu_0 n_t A} \qquad (3.12)$$

Area A is relatively small compared to the area of the loop formed by the closed coil.

3.3 TEST CONTROL CONDITIONS

Prior to the test, control conditions were set to verify the accuracy of the Rogowski Coil method of shaft current measurement. These conditions were devised to minimize any known extenuating factors on the magnitude of shaft current:

1. The motor bearings have new lead babbitt. Any contamination in the bearing babbitting process was removed by running the motor for four hours a few times. Contamination in the bearing babbitt tends to revise the characteristics of the oil, thus influencing the magnitude of the shaft current. The oil is generally discolored by the contamination.
2. One common barrel of Harmony ISO VG 68 oil was used for all tests. This is to ensure that the oil condition would not constitute a factor in the investigation.
3. The Rogowski coil was calibrated on the shaft prior to the test and after the test. The DE and ODE Rogowski coils have calibration values of 11.02A/V and 13.72A/V, respectively as determined in Appendix 3 compared to the manufacturer's quoted value of 10A/V.

3.4 SET UP FOR THE MEASUREMENT OF SHAFT CURRENT

3.4.1 Rogowski Coil and Flux Coil

The Rogowski coil was wound tightly around the shaft on the inboard end of the bearing bracket assembly at both the drive end and opposite drive end of the machine to measure shaft current. The Rogowski coil output leads are brought through a two inch hole in the shaft, to an eighteen channel slip ring which was mounted on the opposite drive end of the shaft. In addition to the Rogowski coil output leads, leads from the flux coil mounted on the shaft and the spider arms were brought out to terminal blocks and then to the slip ring. The terminal blocks are installed on the outer surface of a textolite mounting adapter. Flux coils were mounted on both the drive end and opposite drive of the shaft to measure shaft flux. The flux coils installed axially on the spider arms measure the radial flux.

3.4.2 Slip Ring and Recording Equipment

A high accuracy, low noise slip ring with thirty six circuits (eighteen channels) as shown in Figure 3.7 was installed on the ODE of the shaft. The slip ring was mounted on an insulating adapter assembly to reduce the effects of possible ground loop. The adapter assembly is made of textolite.

A video cassette recorder as shown in Figure 3.7 was used to store the data throughout the test. The recorder is a compact lightweight fourteen channel system that covers the range from DC to 10 kHz in 7 tape speeds, although a tape speed of 38.1 cm/s was selected. The specifications gave a signal to noise ratio of 49 dB.

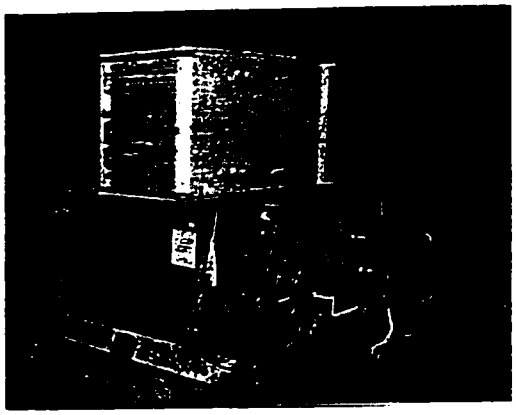

Machine Under Test
Signals From Stationary Sensors

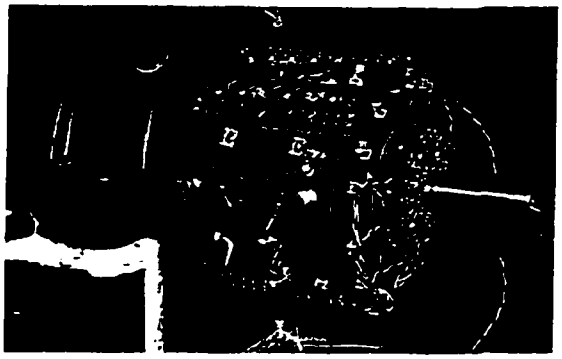

Signals From Rotating Sensors via Slip Ring
Mounted on the ODE of the Machine

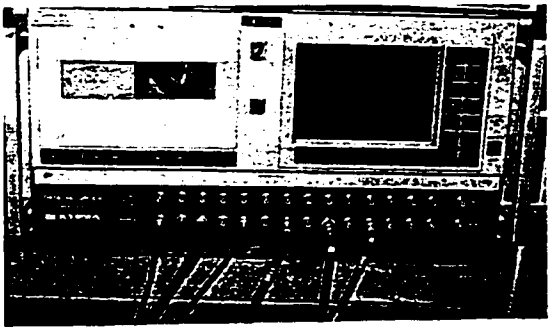

Two 14 Channel Video Cassette Recorders

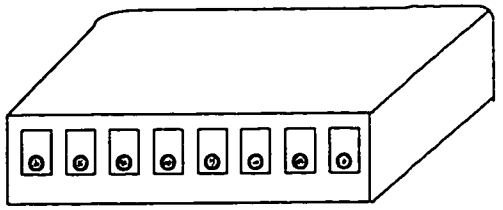

8 Channel Isolation Amplifier

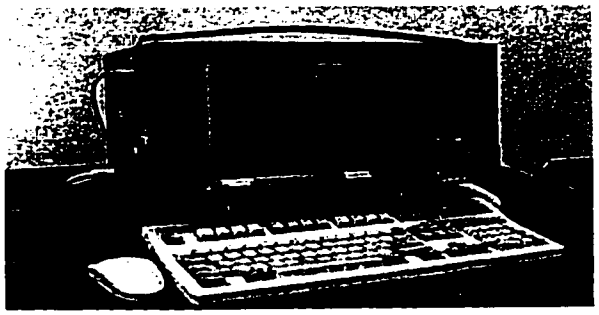

Spectrum Analyzer

Figure 3.7: 2611 kW Induction Machine Experimental Test Set-Up

3.4.3 Spectrum Analyzer

A spectrum analyzer provided for live acquisition, analysis and display of waveform signals. This device is an eight channel 100 kHz dynamic signal analyzer with four selectable frequency resolutions. The noise floor is greater than 90 dB from below full scale 0.1V to 20V full scale. Three types of windows or weighting selections are available - Rectangular, Flat top and Hanning. Rectangular windowing has good frequency resolution but poor amplitude accuracy. The flat top windowing has poor frequency resolution but good amplitude accuracy. Hanning is a good compromise between rectangular and flat top windowing. Details of the specifications of the signal analyzer can be found in [30].

3.4.3 Isolation Amplifier

The Gould 8 channel Isolation Amplifier as shown in Figure 3.7 serves as an interface module between the collector ring and the video cassette recorder and the spectrum analyzer, providing for input-to-output isolation without the worry of creating ground loops. This is especially important as any ground loop will provide a path for the shaft current to flow.

3.5 SHAFT CURRENT MEASUREMENT METHOD TEST RESULTS

In medium and large alternating current machines, both bearings are normally insulated. The test machine bearings are insulated, the insulation material placed on the back of the steel bearing surface which sits on the bearing housing support. During

normal operation, the bearing in the drive end (DE) has its insulation bypassed with a shorting pin. This procedure is to minimize any build-up of electrostatic charges which may occur and hence prevent injury to the machine operator. This shorting pin is a thin steel threaded rod installed on the upper half of the bearing housing assembly. The rod touches the back steel surface of the bearing, bypassing the bearing insulation. A similar shorting pin is installed on the upper half of the opposite drive end bearing housing assembly. A cutaway view of the machine under test is shown in Fig. 3.8 with the cross-section as shown in Figure 3.9.

Both the ammeter method and the Rogowski coil method were conducted at five different voltages when the machine was running at steady state rated speed condition. Condition A as indicated in Tables 3.1, is the Rogowski coil Method with the DE shorting pin down, virtually shorting the insulation while the ODE pin is up and thus maintaining the bearing insulation. Condition B is the ammeter method for the measurement of shaft current with similar bearing insulation conditions as in Condition A. Condition C is the ammeter method for the measurement of shaft current when the shorting pins at both ends are up, hence maintaining the bearing insulation. Condition D is the ammeter method for the measurement of shaft current with the ODE shorting pin down, thus shorting the insulation and the DE bearing insulated. Condition E is the ammeter method for the measurement of shaft current with both bearings non-insulated. Under conditions B, C, D and E, measurements from the Rogowski coil were taken at the

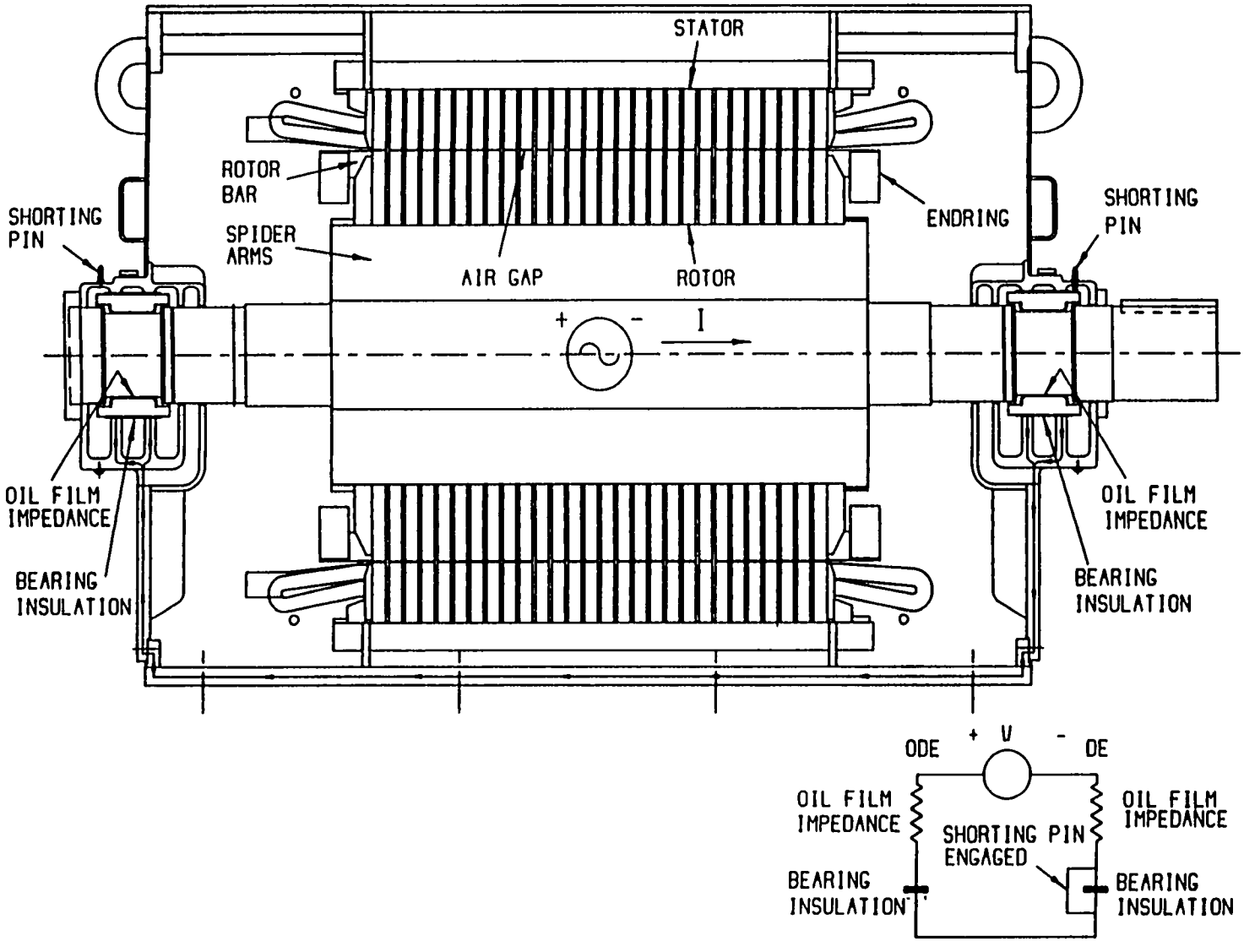

Figure 3.8: Cutaway View of the Machine Under Test

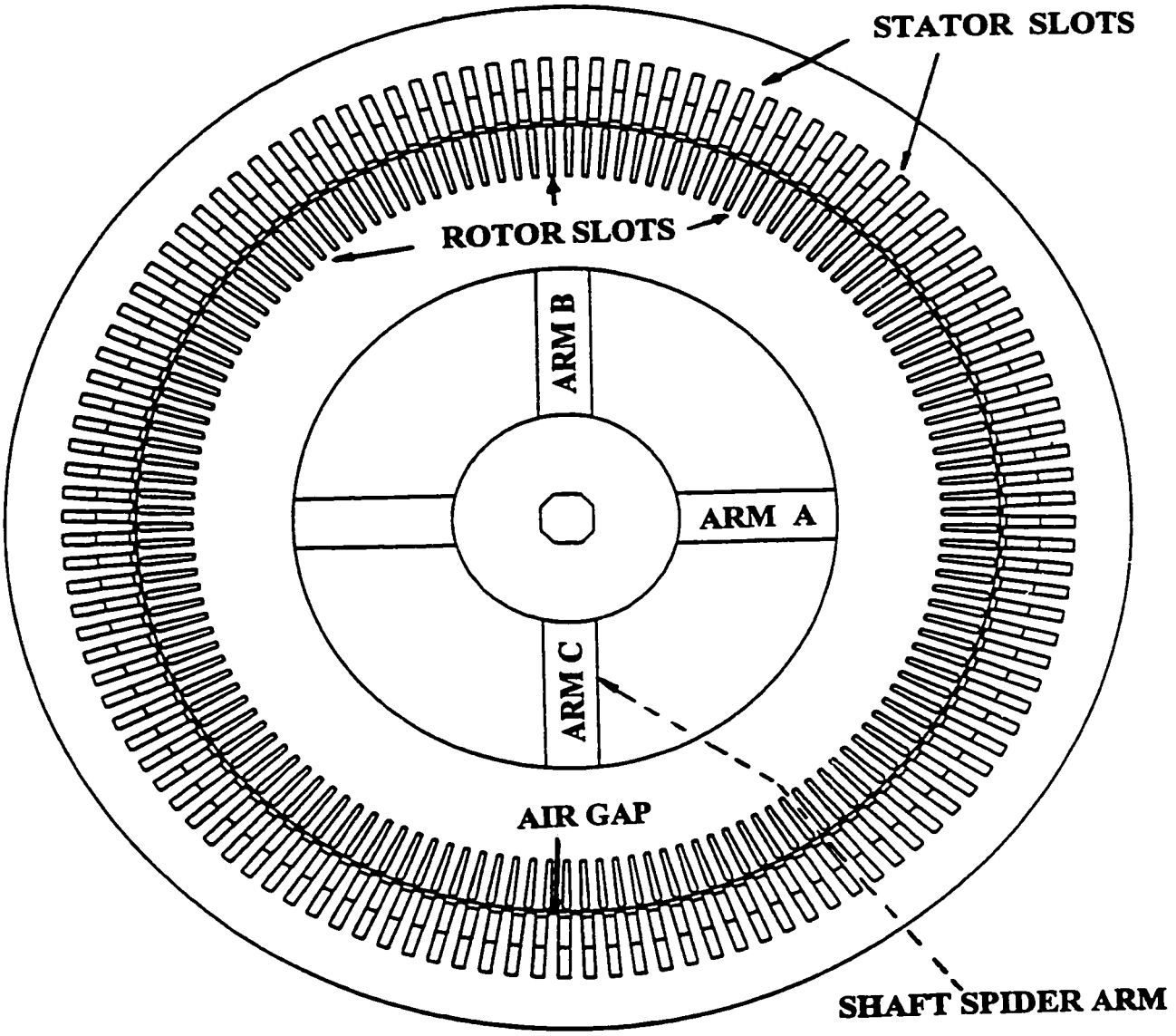

Figure 3.9: Cross Sectional View of the Machine Under Test

same time as the ammeter reading was taken. The measurements shown in Table 3.1, are approximately similar to the ammeter readings, shown in Tables 3.2.

Condition A measurements in Table 3.1 and Condition B measurements in Tables 3.1 and 3.2, clearly indicate the influence of a closed shaft current circuit. Figures 3.10 and 3.11 indicate that the ammeter method provided a path for the zero sequence current which would not have been present in the test machine with either or both bearings insulated. Figure 3.10 (a, i) indicates a non-sinusoidal shaft current waveform whereas Figures 3.10 (b, i) and (c, i) show harmonic sinusoidal waveforms. Figure 3.10 (a, ii), spectral analysis of Figure 3.10 (a, i), indicates dominant frequency components of 60 Hz, 120 Hz and 180 Hz. The 120 Hz component is due to the core vibration. At 20 percent of motor rated line voltage, the stator teeth are not saturated. Hence, the 180 Hz component is not due to saturation but due to joints in the stator core. This conclusion is demonstrated in Chapter 6. Figures 3.10 (b, ii) and (c, ii) show dominant frequency component of 180 Hz. The magnitude of the 180 Hz shaft current component at 80 percent of motor rated line voltage, Figure 3.01 (b, ii), is the maximum value measured using the ammeter method. With the Rogowski coil method, the shaft current measurements indicate a rotor running frequency of 15 Hz as the dominant frequency. The magnitudes of the shaft current in Figures 3.11 (a, i), (b, i) and (c, i) are negligible compared to the values obtained in Figures 3.10 (a, i), (b, i) and (c, i). The dominant 180 Hz frequency components observed in Figures 3.10 (a, ii), (b, ii) and (c, ii) are considerably negligible in Figures 3.11 (a, ii), (b, ii) and (c, ii).

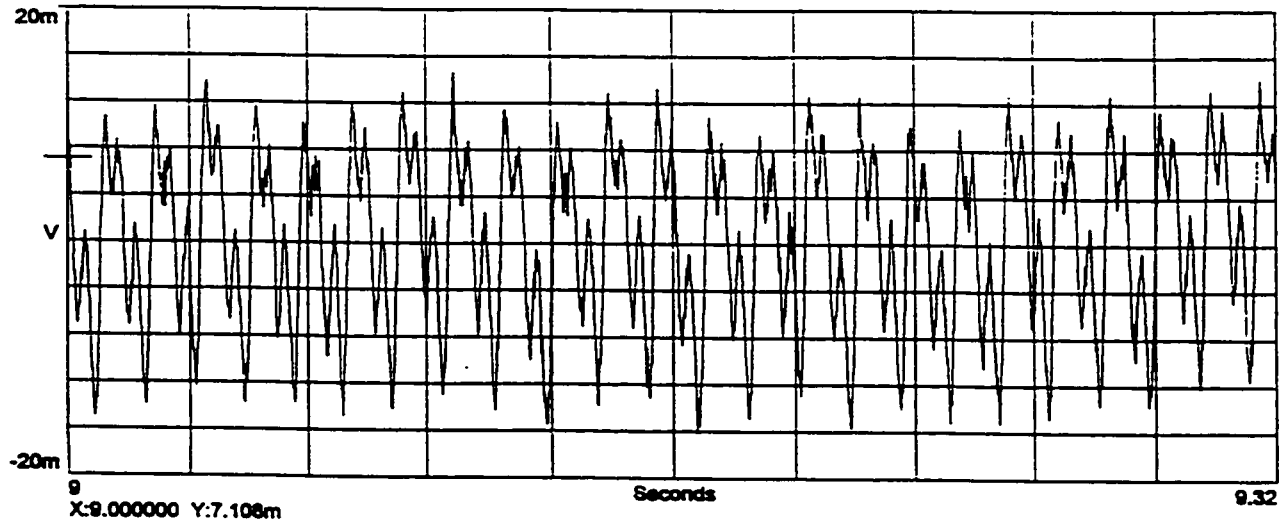

i) Shaft Current Waveform

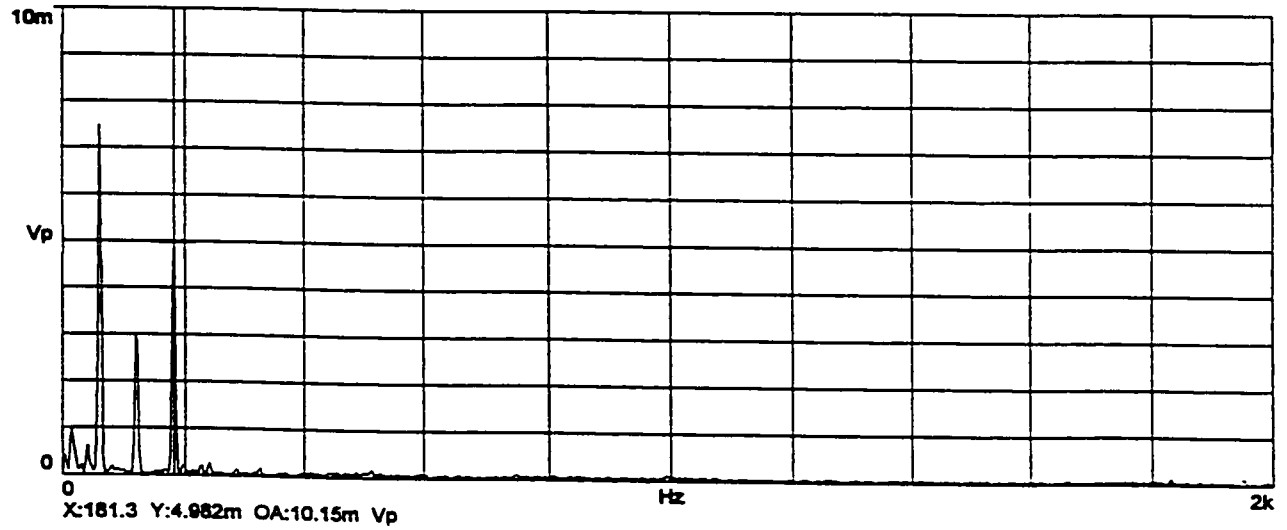

ii) Spectrum Plot

a) Shaft Current Waveform and Spectrum Plot at 20%V

Figure 3.10: Shaft Current Waveform and Spectrum At 20%V, 80%V and 100%V, Measured Using the Shunt/Ammeter Method, Both Bearings Non-Insulated, Oil Ring Lubrication.

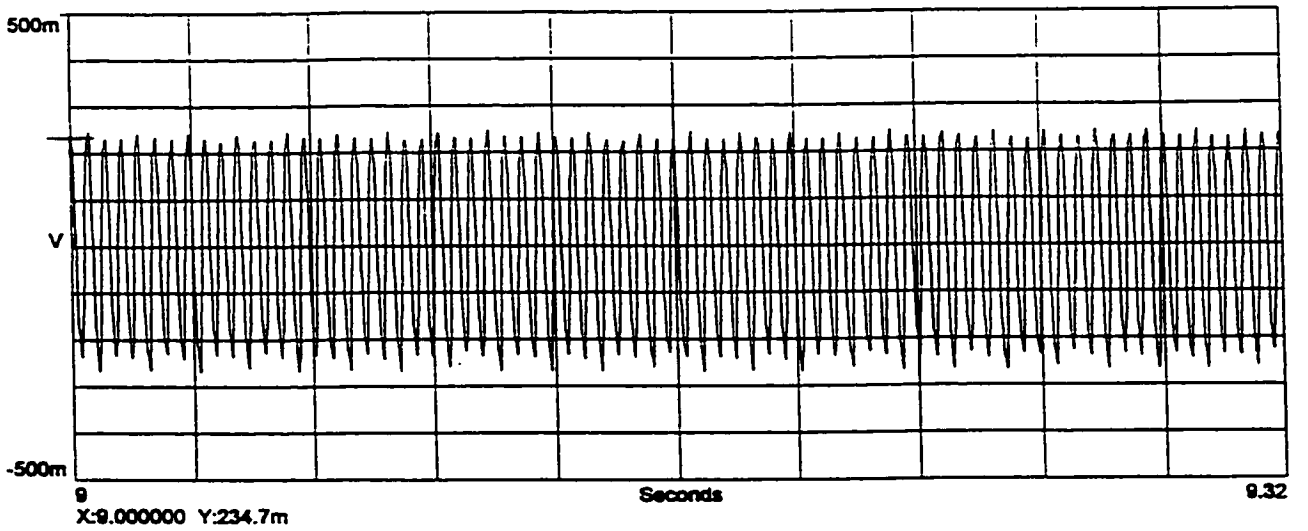

i) Shaft Current Waveform

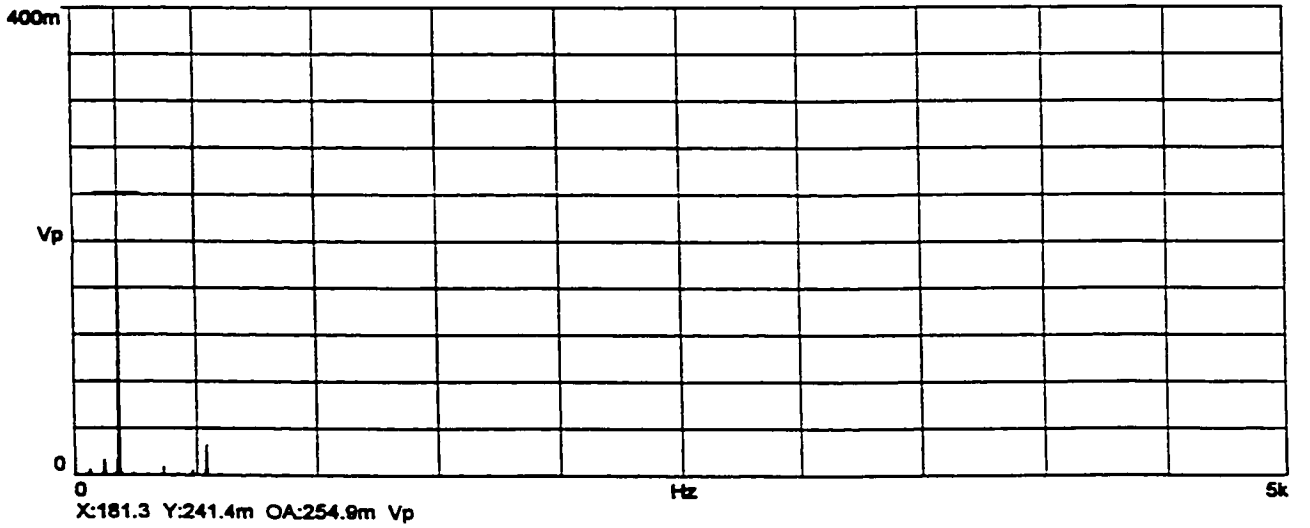

ii) Spectrum Plot

b) Shaft Current Waveform and Spectrum Plot at 80%V

Figure 3.10: Shaft Current Waveform and Spectrum At 20%V, 80%V and 100%V, Measured Using the Shunt/Ammeter Method, Both Bearings Non-Insulated, Oil Ring Lubrication.

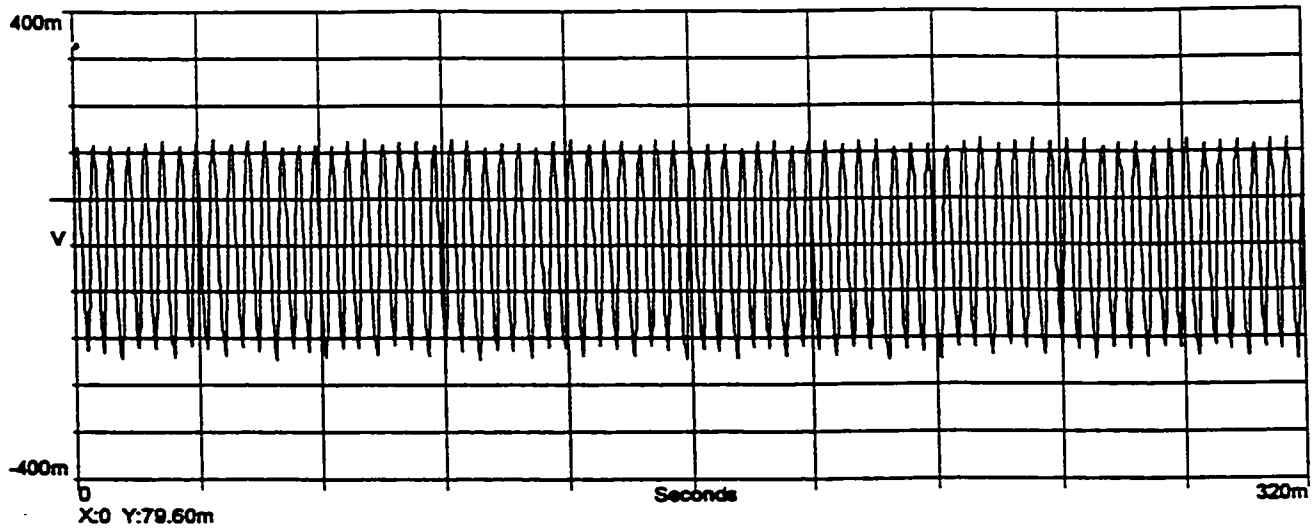

i) Shaft Current Waveform

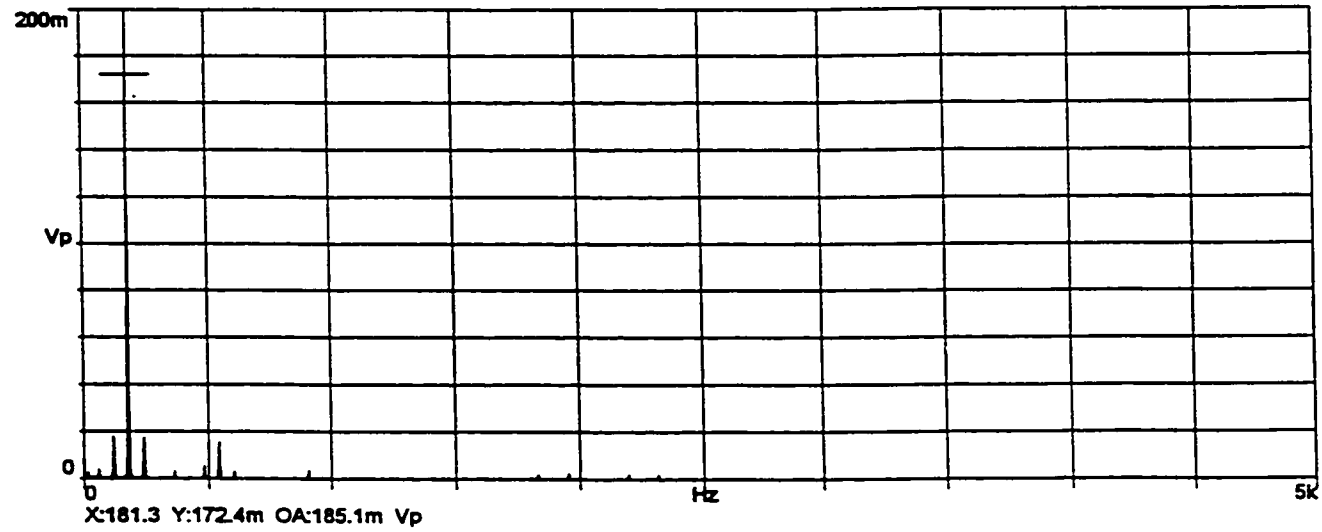

ii) Spectrum Plot

c) Shaft Current Waveform and Spectrum Plot at 100%V

Figure 3.10: Shaft Current Waveform and Spectrum At 20%V, 80%V and 100%V, Measured Using the Shunt/Ammeter Method, Both Bearings Non-Insulated, Oil Ring Lubrication.

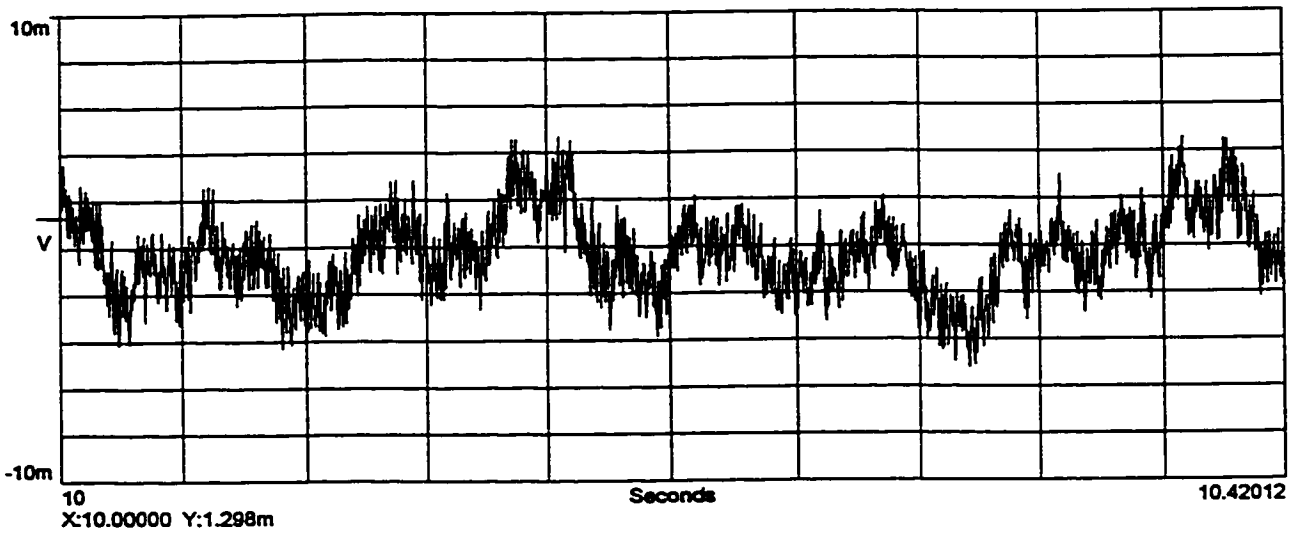

i) Shaft Current Waveform

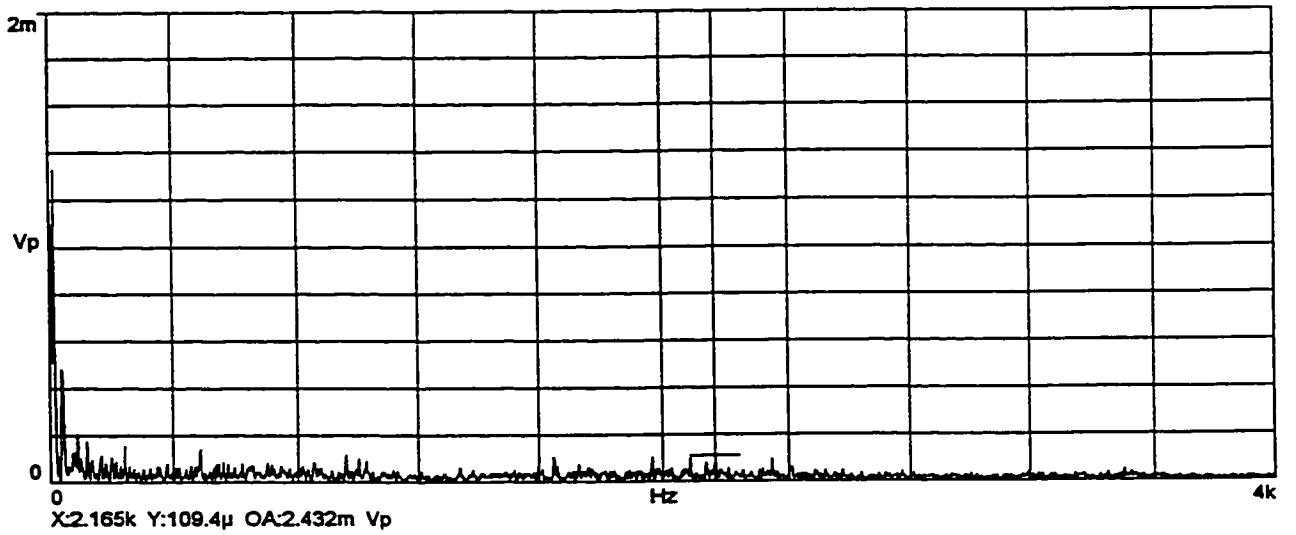

ii) Spectrum Plot

a) Shaft Current Waveform and Spectrum Plot at 20%V

Figure 3.11: Shaft Current Waveform and Spectrum At 20%V, 80%V and 100%V, Measured Using the Rogowski Coil Method, Both Bearings Non-Insulated, Oil Ring Lubrication.

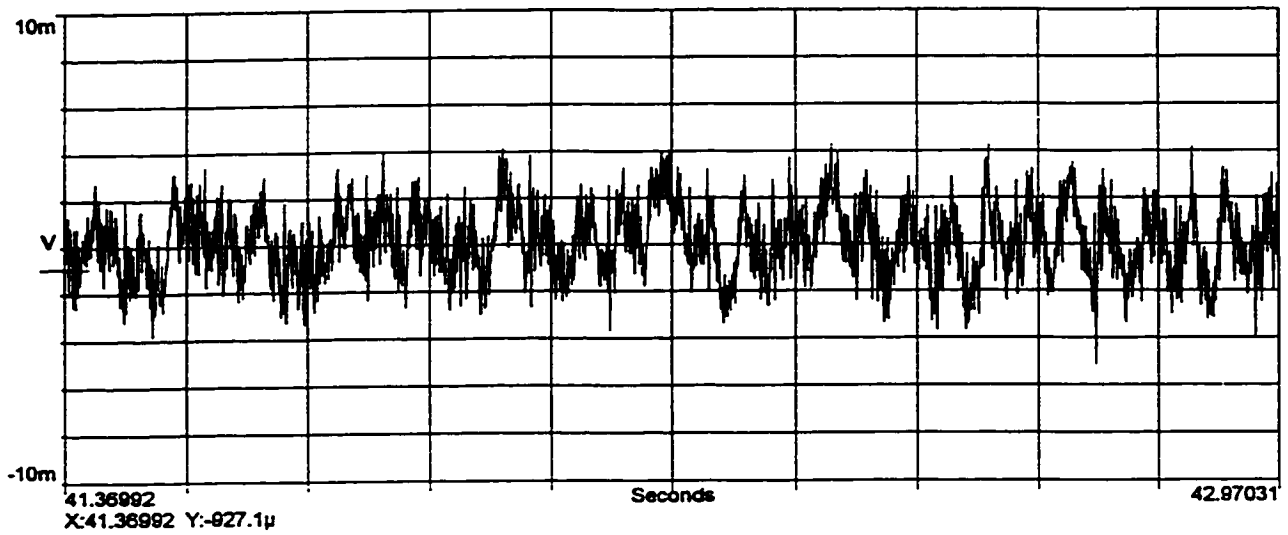

i) Shaft Current Waveform

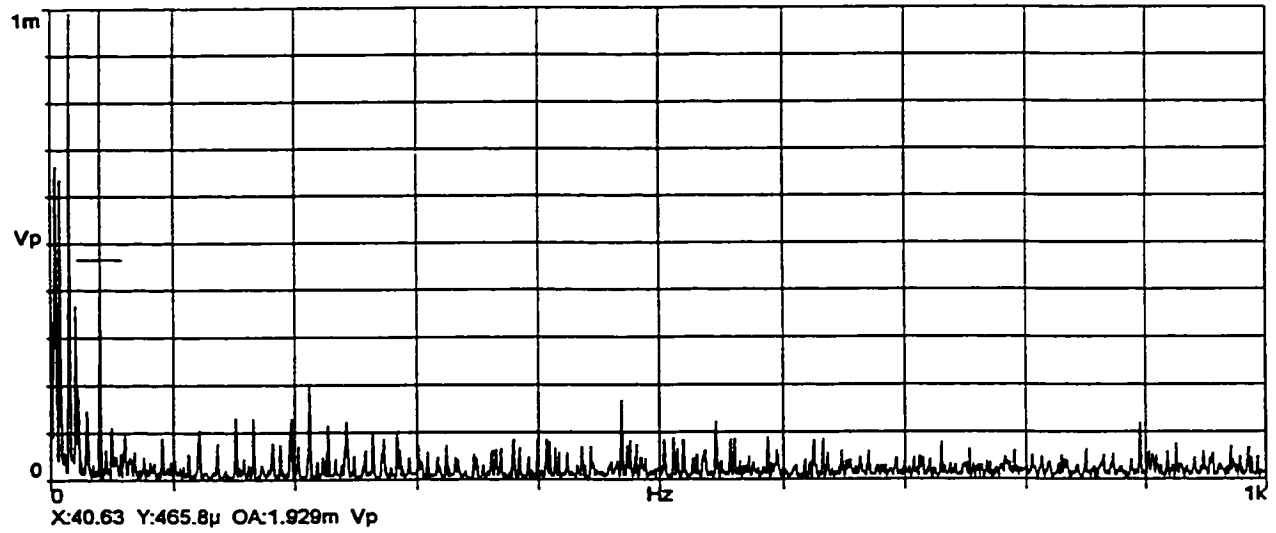

ii) Spectrum Plot

b) Shaft Current Waveform and Spectrum Plot at 80%V

Figure 3.11: Shaft Current Waveform and Spectrum At 20%V, 80%V and 100%V, Measured Using the Rogowski Coil Method, Both Bearings Non-Insulated, Oil Ring Lubrication.

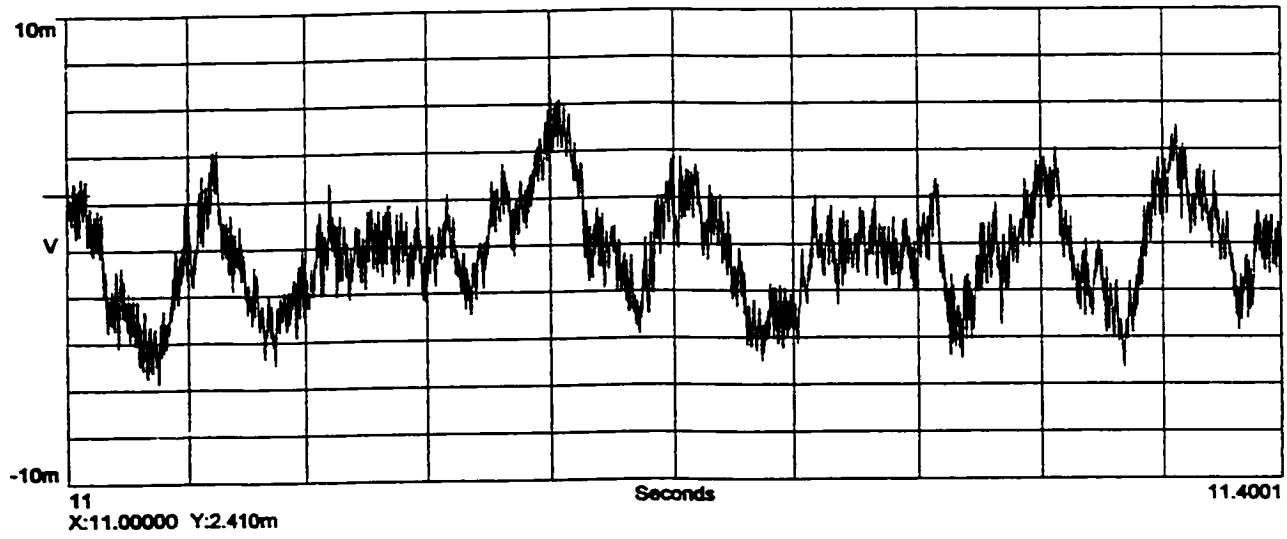

i) Shaft Current Waveform

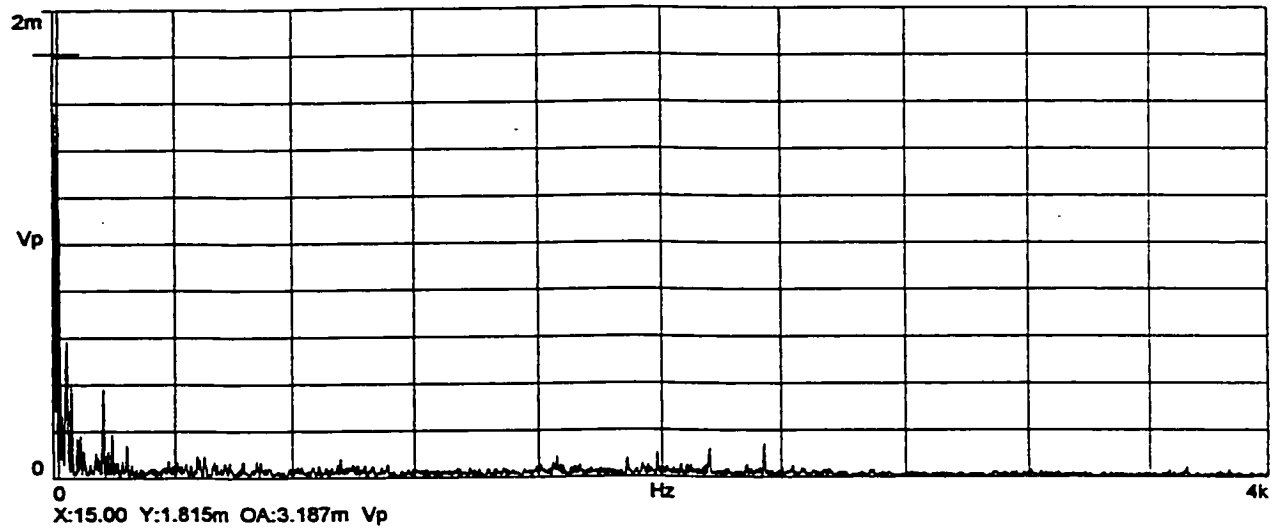

ii) Spectrum Plot

c) Shaft Current Waveform and Spectrum Plot at 100%V

Figure 3.11: Shaft Current Waveform and Spectrum At 20%V, 80%V and 100%V, Measured Using the Rogowski Coil Method, Both Bearings Non-Insulated, Oil Ring Lubrication.

Condition B measurements clearly indicate that the bearing insulation is in good condition, otherwise the readings from the Rogowski coil will be higher than the ammeter reading. Condition C measurements verify the accuracy of the Rogowski coil. The Rogowski coil measures a similar magnitude of shaft current as the ammeter. Condition D measurements verified the conclusion from Condition B measurements.

The oil film behaves as an insulator and limits the magnitude of shaft current to a negligible value; otherwise the Rogowski coil would have indicated a higher shaft current magnitude compared to the reading from the ammeter in Condition E. There is negligible difference between the two values. As the frequency of the shaft current increases, the oil film may break down, hence the oil film alone will not be sufficient to limit the magnitude of shaft current. In this case the bearings need to be insulated or a shaft ground brush installed to bypass the shaft current and limit the amount of shaft current to the bearings.

It is seen from Table 3.1 that the magnitude of shaft current is a maximum at 80 percent of motor rated line voltage. Table 3.2 indicates a similar shaft current phenomenon. Likewise the corresponding shaft voltage magnitude as seen in Table 3.3, is a maximum at that motor line voltage.

3.6 SUMMARY

The Rogowski coil shaft current measurement [31] does not disturb the conducting circuit and is not load dependent. Hence, the shaft current measured is an accurate assessment. Furthermore, this method of measurement can be used as an on-line

monitoring system providing indication of deterioration of bearing insulation or oil. The Rogowski coil shaft current monitoring is inexpensive and does not require periodic maintenance as with the shaft ground brush used in the ammeter method.

	Motor Line Voltage				
Shaft Current (A)	20% Rated Volt	40% Rated Volt	60% Rated Volt	80% Rated Volt	100% Rated Volt
Condition A - DE	0.15	0.16	0.18	0.19	0.13
Condition B - DE	0.85	1.84	12.1	22.20	15.84
Condition C - DE	0.89	1.84	12.03	22.54	15.81
Condition D - DE	0.81	1.86	12.10	22.39	15.85
Condition E - DE	0.88	1.86	12.05	22.45	15.93
Condition A - ODE	0.13	0.15	0.19	0.20	0.14
Condition B - ODE	0.82	1.77	11.98	21.18	15.04
Condition C - ODE	0.84	1.78	11.92	21.21	15.03
Condition D - ODE	0.84	1.78	11.95	21.13	15.05
Condition E - ODE	0.83	1.79	11.93	21.20	15.13

TABLE 3.1 : DE and ODE Rogowski Coil Shaft Current Measurement

	Motor Line Voltage				
Shaft Current (A)	20% Rated Volt	40% Rated Volt	60% Rated Volt	80% Rated Volt	100% Rated Volt
Condition B	0.84	1.84	12.40	22.16	15.60
Condition C	0.88	1.84	12.28	22.28	15.80
Condition D	0.84	1.88	12.28	22.12	15.64
Condition E	0.88	1.84	12.32	22.12	15.76

TABLE 3.2 : Ammeter Method Shaft Current Measurement

	Motor Line Voltage				
Shaft Voltage End-to-End (V)	20% Rated Volt	40% Rated Volt	60% Rated Volt	80% Rated Volt	100 % Rated Volt
Condition A	0.05	0.11	0.66	0.86	0.67

TABLE 3.3 : Shaft Voltage Measurement

CHAPTER 4

HARMONIC WAVEFORMS AND THEIR EFFECTS ON SHAFT CURRENT

4.0 INTRODUCTION

In this chapter, various forms of harmonic waveforms will be evaluated to determine the presence of shaft current. A magnetomotive-permeance wave approach is used in the evaluation. This approach is based on the fact that the magnetomotive force and the air gap permeance can be considered as an infinite series of sinusoidal traveling waves [32]. This approach predicts the order of the harmonics accurately. However, the amplitudes of the traveling wave harmonics computed by this analytical approach is not sufficiently accurate. Furthermore, this approach does not account for the effects of iron saturation. Iron saturation plays an important role in determining the air gap flux density. Hence, this approach is used only to provide quick determination of the presence of shaft current.

4.1 EFFECTS OF STATOR SPATIAL HARMONICS AND ARMATURE REACTION ON SHAFT CURRENT

The magnetic field distribution in the air gap of an electric machine is influenced by several factors such as slotting, saturation and rotor eccentricity. Slotting causes the magnetomotive force (MMF) to stagger around the circumference of the gap,

consequently the MMF wave has harmonic contents superimposed on the fundamental. Rotor eccentricity and iron saturation give rise to air gap permeance harmonics. Figure 4.1 shows the establishment of air gap field in a three phase electrical machine.

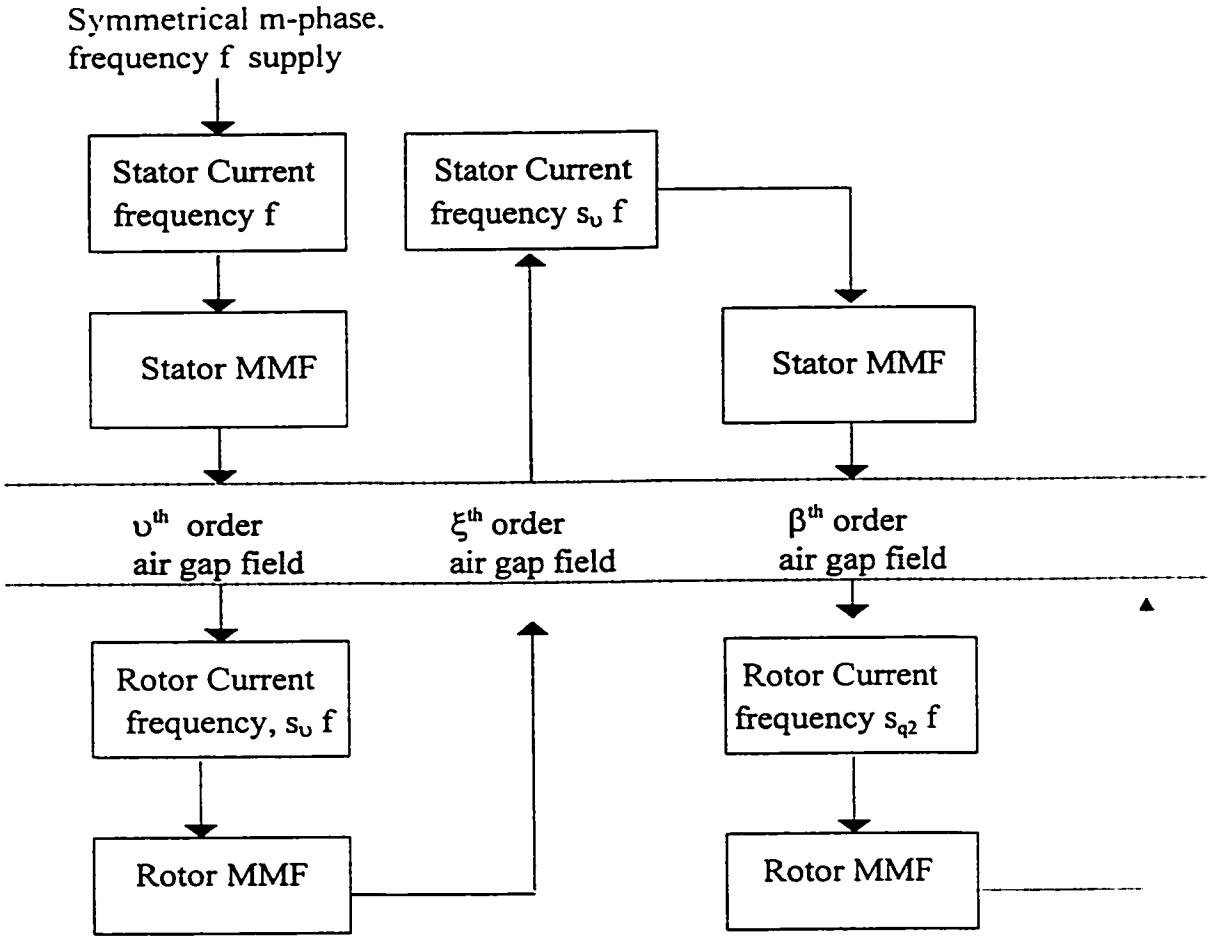

Figure 4.1: Development of Air Gap Field and Armature Reaction in Induction Machine

Consider a three phase electrical machine fed from a symmetrical supply of angular frequency, ω. The three groups of windings of N_{st} turns per phase are mutually displaced

along the circumference by the angle $2\pi/m$. The three phase currents set up an MMF varying with time. This MMF is staggered round the circumference. Thus, in addition to the fundamental pole pair number, p, space harmonics of poles pair number υp is produced. The magnetomotive force, $\Im$ produced by a 3-phase winding [32, 33] is given by

$$\Im_{3\varnothing} = \frac{3\, N_{st}\, I_1 \sqrt{2}}{\pi p} K_{\upsilon p} K_{\upsilon d} \frac{1}{\upsilon} \cos\left(\omega t - \upsilon p\Omega\right) \qquad (4.1)$$

or in general for an m phase winding:

$$\Im_{m\varnothing} = m \frac{4}{\pi} \frac{N_{st}}{p} I_1 \sqrt{2}\, K_{\upsilon p}\, K_{\upsilon d} \frac{1}{\upsilon} \cos\left(\omega t - \upsilon p\Omega\right) \qquad (4.2)$$

where p is the number of pole pairs of the fundamental field,

m is the number of phases of the stator winding,

N_{st} is the number of turns in series per phase,

$K_{\upsilon p}$ is the pitch factor or chording factor for the υ^{th} harmonics,

$K_{\upsilon d}$ is the distribution factor for the υ^{th} harmonics,

υ is the spatial or phase belt harmonic order and

Ω is the angular displacement of the stator winding, electrical radian.

Phase belt harmonics of order 5, 7, 11, etc. are generally present while the third harmonic and its multiples are eliminated. The permeance of the air gap is not uniform, altered by slotting, saturation and rotor position. The constant term of the air gap permeance is given by equation (4.3).

The permeance of the air gap per unit area, $P_{sa} = \frac{\mu_o}{\delta}$ (4.3)

where $\mu_o = 4\pi \times 10^{-7}$ H/m

and δ = length of the air gap, m.

An infinite series of air gap flux density waves produced by the interaction of the MMF waves with the constant term of the permeance wave acts on the rotor winding and induces in the winding voltages having identical order of harmonics. The υ^{th} order air gap flux density is obtained as the product of the corresponding MMF and the air gap permeance per unit area as given in equation (4.4).

$$B_{1,\upsilon} = mq_1 \frac{4}{\pi}\frac{N_{st}}{p} I_1 \sqrt{2}\, K_{\upsilon p} K_{\upsilon d} \frac{1}{\upsilon \delta} \mu_o \cos\left(\omega t - \upsilon p\Omega\right)$$

$$= B_m \frac{1}{\upsilon} \cos\left(\omega t - \upsilon p\Omega\right) \qquad (4.4)$$

where q_1 = the number of slots per pole per phase,

$\upsilon = \left(1 + 2mK_i\right)$ and

$K_i = 0, \pm 1, \pm 2, \ldots$

The air-gap flux density produced by the stator current induces currents in the squirrel cage rotor windings at slip frequency given by

$$s_\upsilon f = \left[1 - \upsilon(1-s)\right] f \qquad (4.5)$$

Space harmonic order, υ is to be taken as positive for forward revolving fields and negative for backward revolving fields [33].

The squirrel cage rotor bars carry equal currents with mutual phase difference as shown in Figures 4.1 and 4.2. The end rings carry the summation of the adjacent bar currents. The currents in the rotor windings produce fields to oppose the flux linkage causing the induced EMF. The distribution of the rotor bars around the periphery of the rotor produces non-sinusoidal current sheet on the rotor. Hence, the air-gap field produced by the rotor will be non-sinusoidal. The fields are stepped in nature. Applying Fourier series, these fields will comprise various sinusoidal components of different orders. Thus, the rotor in addition to producing the harmonic fields of order υ, will also inject air gap harmonic fields of different orders. The current in the n^{th} and $(n-1)^{th}$ rotor mesh at the slip frequency [34] is given by

$$\bar{I}_{r,n}\left(s_\upsilon f\right) = \bar{I}_r \sin\left[s_\upsilon \omega t - \left(n-1\right) \upsilon p \alpha_r \right] \qquad (4.6)$$

$$\bar{I}_{r,n-1}\left(s_\upsilon f\right) = \bar{I}_r \sin\left[s_\upsilon \omega t - \left(n-2\right) \upsilon p \alpha_r \right] \qquad (4.7)$$

where α_r is the rotor slot angle and is equal to ($2\pi / R_2$). R_2 is the number of rotor bars. The current in the rotor bar at slip frequency, $s_\upsilon f$ is given by

$$\bar{I}_{bar,r}\left(s_\upsilon f\right) = \bar{I}_{r,n}\left(s_\upsilon f\right) - \bar{I}_{r,n-1}\left(s_\upsilon f\right) \qquad (4.8)$$

$$= 2\sin\left(\frac{\upsilon p \alpha_r}{2}\right)\bar{I}_r\left(s_\upsilon f\right)\cos\left[s_\upsilon \omega t - \left(n-\frac{3}{2}\right)\upsilon p \alpha_r \right]$$

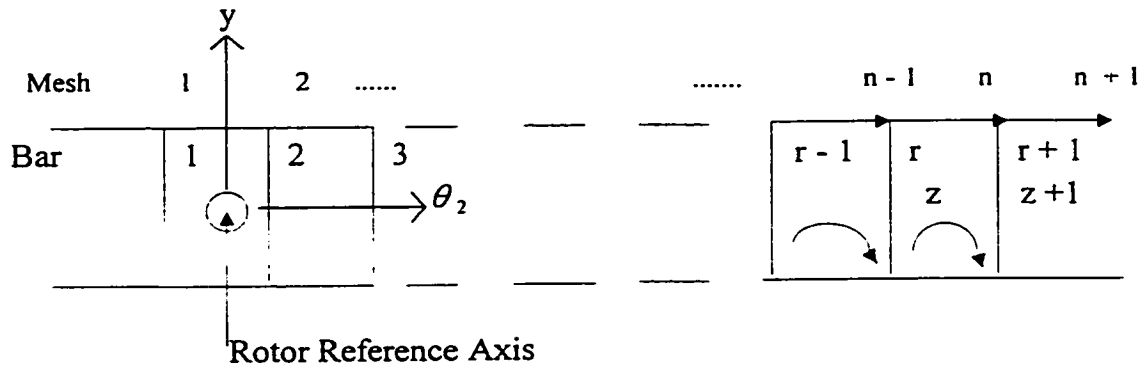

Figure 4.2: Squirrel Cage Winding Mesh Current

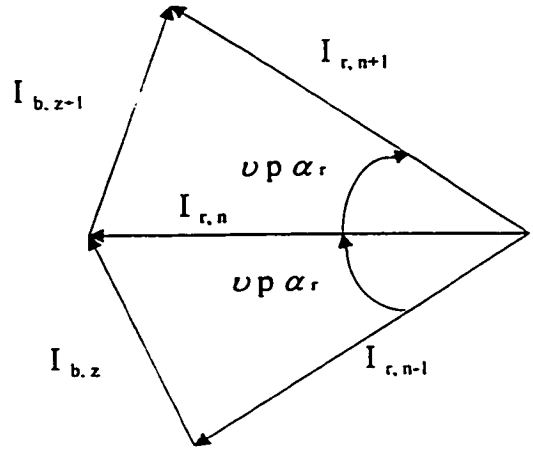

Figure 4.3: Rotor Current Phasor Representation

The incremental change in the flux density distribution at the location of the r^{th} rotor bar is obtained as

$$B_{r,\upsilon} = \frac{\mu_\upsilon}{\delta} \bar{I}_{bar,r}$$

$$= \frac{\mu_o}{\delta} I_r \sqrt{2} \left(2 \sin\left[\frac{\upsilon \; p\alpha_r}{2}\right]\right) \cos\left[s_\upsilon \omega \, t - \left(r - \frac{3}{2}\right) \upsilon \; p \, \alpha_r\right] \qquad (4.9)$$

The resultant stepped flux density distribution produced by the rotor will have harmonic orders ξ

$$B_{2,\upsilon} = \sum_{\xi=-\infty}^{\infty} B_{2,\xi,\upsilon}$$

$$= \sum_{\xi=-\infty}^{\infty} w_{\xi} \cos \xi \theta_2 \qquad (4.10)$$

Resolving into a Fourier series, the coefficient of the ξ^{th} order harmonic term in the series expansion is determined as:

$$w_{\xi} = \frac{1}{2\pi} \int_0^{2\pi} B_{2,\upsilon} (\theta_2) \cos (\xi \, p \theta_2) d\theta_2$$

$$= \frac{1}{2\pi} \left[B_{2,\upsilon}(\theta_2) \frac{\sin(\xi p \theta_2)}{\xi p} \Big|_0^{2\pi} - \int_0^{2\pi} B_{2,\upsilon}(\theta_2) \frac{\sin(\xi p \theta_2)}{\xi p} d\theta_2 \right]$$

$$= \frac{1}{2\pi \xi p} \sum_{r=1}^{R_2} \Delta B_{2,\upsilon} \sin [\xi \, p(r-1.5)\alpha_r] \qquad (4.11)$$

where $\theta_2 = \Omega - \omega \frac{1-s}{p} t$.

The coefficients will have non zero values only when satisfying the following relationship:

$$\xi = \upsilon + K_j \frac{R_2}{p} \qquad (4.12)$$

where $K_j = 0, \pm 1, \pm 2, \ldots$

The induced rotor flux density of ξ^{th} order is given as:

$$B_{2,\xi,\upsilon}(\theta_2) = \frac{\mu_o R_2}{\delta \pi \xi p} \sin\left(\frac{\xi p \pi}{R_2}\right) I_r \sqrt{2} \cos\left[s_\upsilon \omega t - \xi p\left(\Omega - \frac{\omega}{p}(1-s)t\right)\right]$$

$$= \frac{\mu_o R_2}{\delta \pi \xi p} \sin\left(\frac{\xi p \pi}{R_2}\right) I_r \sqrt{2} \cos\left[s_{q_2} \omega t - \xi p \Omega\right] \qquad (4.13)$$

The rotor slot harmonics of the order of

$$\xi_1 = 1 \pm \frac{R_2}{p} \qquad (4.14)$$

are especially disturbing because these harmonics have the same distribution and pitch factor as the main wave, as shown in Appendix 2.

The term ($\upsilon = 1 + 2\,m\,K_i$) in the harmonic order ξ equation is always an odd number. Since υ is also odd, therefore

$$K_j \frac{R_2}{p} = \text{even number} \qquad (4.15)$$

or

$$K_j \frac{R_2}{2p} = \text{integer} \qquad (4.16)$$

in order that out of these rotor flux density waves, those with order equal to that of the stator flux density waves react on the corresponding stator flux density harmonics (armature reaction). The remaining waves are called residual rotor flux density waves. These residual rotor fields will induce currents of different frequencies in the stator

winding. From equations (4.12) and (4.15), only rotor fields with the pole pairs of order ξ_1, can induce current in the stator winding:

$$\xi_1 = \left(1+2mK_i+cK_j\frac{R_2}{p}\right) \qquad (4.17)$$

where c is the lowest denominator of the fraction R_2/p . The larger the value of c, the fewer rotor harmonic fields which induce currents in the stator and the smaller the secondary armature reaction will be. Hence, it is obvious that only for c = 1 or R_2 / p = integer, will the rotor fields induce currents in the series connected stator winding. Table 4.1 demonstrated the condition for armature reaction. The rotor harmonic fields induce currents in the stator windings at a frequency given as:

$$s_{\nu 2} f = \left[1 + K_j \frac{R_2}{p}(1-s)\right] f \qquad (4.18)$$

If the number of rotor bars, R_2 is not divisible by 3, zero sequence currents may be induced in the stator winding. An example of such a case is shown in Table 4.1.

The induced stator currents produce additional harmonic air gap fields of order β. If all the stator winding phase belts are connected in series, the air gap flux density of harmonic order β is determined as:

$$B_{1,\beta} = \frac{mq_1}{2}\frac{4p}{\pi}\frac{N_{ss}}{\beta p} I_1 \sqrt{2}\, K_{w\beta}\, K_{wd} \frac{1}{\delta}\mu_o \cos\left(s_{\nu 2}\,\omega\, t - \beta\, p\Omega\right) \qquad (4.19)$$

where q_1 = number of slots per pole per phase,

$$\beta \quad = \quad \text{harmonic order} = \left(1+2mK_k+K_j\frac{R_2}{p}\right)$$

and $\quad K_k \; = \; 0, \pm 1, \pm 2, \ldots$

The air gap flux density acts on the squirrel cage, inducing in it voltages having identical order of harmonics. The induced voltages drive currents in the closed rotor circuit depending on the impedance of the rotor winding. This impedance is a function of, among other things, the frequency, number of rotor slots, the permeability, shape of the slot, etc. Owing to the rotor slotting and following the procedure from equation (4.4) to equation (4.12) a new set of rotor flux density waves can be obtained. This process of armature reaction continues until the steady state air gap flux distribution is established. Oberretl [34, 35] analyzed this successive interaction of stator and rotor MMFs up to, in some cases, a fourth order of armature reaction However, it is sufficient not to consider other sets of flux density waves beyond that given in equation (4.18) as their magnitudes are negligible. This process of mutual interaction of the stator MMF and rotor MMF, called multiple armature reactions is illustrated in Figure 4.1. The stator air gap harmonics induce currents in the rotor windings at different slip frequencies. Their magnitudes depend on the cage winding arrangement. The non-sinusoidal current distribution of the rotor produces additional harmonics in the air gap. These harmonic air gap fields generated by the rotor induce current in the stator windings at frequencies related to the number of rotor bars and speed of the rotor.

4.2 EFFECTS OF SLOTTED STATOR ON SHAFT CURRENT

Besides the fundamental term the air gap flux density in an induction machine contains higher spatial harmonics. The amplitudes of the higher harmonics of the air gap flux density decrease as the order of harmonics increase because their winding factors decrease. This is, however, not true for slot harmonics. The winding factor [36] for the slot harmonics is equal to the winding factor for the fundamental as shown in Appendix 4. Hence the higher slot harmonic components of the air gap flux density are not negligible. The presence of stator slots bordering the air gap modulates the fundamental flux wave.

The fundamental stator winding MMF [32] is given as:

$$\text{Stator MMF, } \Im(\Omega, t) = \Im_{smf} \cos(\omega t - p\Omega) \qquad (4.20)$$

where Ω is the angle between the stator datum and an arbitrary point on the rotor.

The harmonic permeance wave of slotted stator, $\wp_{ssw} = \wp_{ssh} \cos(h S \Omega)$ (4.21)

where S is the number of stator slots and h is the stator slot harmonic number = 0, ±1, ±2, ±3,...

Hence, the stator slot modulated air gap flux density is given as

$$B_{g,smf,ssph} = \Im_{smf} \cos\{\omega t - p\Omega\} \times \wp_{ssh} \cos\{hS\Omega\}$$

$$= \frac{\Im_{smf}\, \wp_{ssh}}{2}\left[\cos\{\omega t - (hS + p)\Omega\} + \cos\{\omega t + (hS - p)\Omega\}\right] \qquad (4.22)$$

S1 =36, R_2 = 24, m = 3, 2p = 4, c = 1	1+2 m K_i + c K_j R_2/p
K_i = 1, K_j = 1	19
K_i = -1, K_j = -1	-17
K_i = -1, K_j = 1	7
K_i = 1, K_j = -1	-5
K_i = 2, K_j = -1	1
K_i = -2, K_j = 1	1
K_i = -2, K_j = 2	13
K_i = 2, K_j = -2	-11
S1 =36, R_2 = 46 , m = 3, 2p = 4, c = 2	**1+2 m K_i + c K_j R_2/p**
K_i = 1, K_j = 1	53
K_i = -1, K_j = -1	-51
K_i = -1, K_j = 1	41
K_i = 1, K_j = -1	-39
K_i = -2, K_j = 1	35
K_i = 2, K_j = -1	-33
K_i = -3, K_j = 1	29
K_i = 3, K_j = -1	-27
K_i = -4, K_j = 1	23
K_i = 4, K_j = -1	-21
K_i = -5, K_j = 1	17
K_i = 5, K_j = -1	-15
K_i = -6, K_j = 1	11
K_i = 6, K_j = -1	-9
K_i = -7, K_j = 1	5
K_i = 7, K_j = -1	-3

Table 4.1: Harmonic Terms Due to Armature Reaction

The stator fundamental slot harmonic permeance wave has 2S poles and is stationary. The modulation of the fundamental air gap field creates two additional rotating fields, one with (h S - p) pole pairs rotating backward and the other with (h S + p) pole pairs rotating forward. These pole pair fields need to be considered in the determination of the occurrence of shaft currents. Thus, we will have shaft current when the fraction consisting of twice the number of joints divided by the stator slot harmonic field poles, reduced to its lowest term, has an odd number in the numerator. The shaft current frequency is the odd numerator multiple of the supply frequency. That is, equation 2.1 must take into account the additional rotating field created by the stator slots.

These flux density waves could also be produced by the interaction of the component of the MMF wave due to stator current discretization with the average or dc component of the air-gap permeance:

$$B_{g,\,ssmf.\,sspa} = \mathfrak{I}_{ssm} \begin{Bmatrix} \cos\left(\omega t + \left\{ hS - p \right\} \Omega\right) + \\ \cos\left(\omega t - \left\{ hS + p \right\} \Omega\right) \end{Bmatrix} \times \wp_o$$
$$= \mathfrak{I}_{ssm}\, \wp_o \begin{Bmatrix} \cos\left(\omega t + \left\{ hS - p \right\} \Omega\right) + \\ \cos\left(\omega t - \left\{ hS + p \right\} \Omega\right) \end{Bmatrix} \qquad (4.23)$$

The interaction of the MMF wave due to the stator current discretization with variation in the air-gap permeance resulting from stator slots will result in the air-gap flux density waves given by equation (4.24).

$$B_{g,\ ssmf,\ sspf} = \Im_{ssm} \begin{Bmatrix} \cos\left(\omega t + \{ S - p \}\,\Omega\right) + \\ \cos\left(\omega t - \{ S + p \}\,\Omega\right) \end{Bmatrix} \times \wp_{ssf} \cos\left(S\,\Omega \right)$$

$$= \frac{\Im_{ssm}\ \wp_{ssf}}{2} \begin{Bmatrix} \cos\left(\omega t + \{ 2S - p \}\,\Omega\right) + \\ \cos\left(\omega t - \{ 2S + p \}\,\Omega\right) + \\ 2\cos\left(\omega t - p\,\Omega\right) \end{Bmatrix} \qquad (4.24)$$

The first two terms of equation (4.24) are the 2nd order harmonic components of stator slot modulated air gap flux density.

4.3 EFFECTS OF SLOTTED ROTOR ON SHAFT CURRENT

The flux density induced in the slotted rotor by the rotating fundamental stator MMF field is given by the product of this MMF and the permeance wave due to the rotor slotting.

The fundamental stator winding MMF is given as

$$\text{Stator MMF, } \Im(\Omega, t) = \Im_{smf} \cos\left(\omega t - p\Omega\right) \qquad (4.25)$$

where Ω is the angle between the stator datum and an arbitrary point on the rotor,

The harmonic permeance wave of slotted rotor, $\wp_{rsw} = \wp_{rsh} \cos\left(qR\left\{\Omega - \omega_r t\right\}\right)$ (4.26)

where R is the number of rotor slots and q the rotor slot harmonic number = $\pm 1, \pm 2, ..$

Hence, the rotor slot modulated air gap flux density is given by equation (4.27).

$$B_{g,\ smf,\ rsph} = \Im_{smf} \cos\{\omega t - p\Omega\} \times \wp_{rsh} \cos\{qR(\Omega - \omega_r t)\}$$

$$= \frac{\Im_{smf}\ \wp_{rsh}}{2}\begin{bmatrix}\cos\{(-qR\omega_r - \omega)t + (Rq + p)\Omega\} \\ + \\ \cos\{(-qR\omega_r + \omega)t + (Rq - p)\Omega\}\end{bmatrix} \qquad (4.27)$$

The air gap flux density induces corresponding current harmonics in the stationary stator winding:

$$f_g = f\left[\frac{qR(1-s)}{p} \pm 1\right] \qquad (4.28)$$

These harmonics reveal themselves as a pair of 'side frequencies' disposed on either side of the rotor slot ripple carrier frequencies. Harmonic fields as represented by (q R + p) and (q R - p) pole pair fields may give rise to components of shaft voltage and hence shaft current. Hence, we will have shaft current when the ratio of twice the number of joints divided by the harmonic field poles reduced to its lowest term has an odd number in the numerator. The shaft current frequency is the odd numerator multiple of the frequency indicated above. Further to the two additional rotating fields set up by the stator slots, equation (2.1) is to be expanded to include the harmonic fields created by the rotor slots.

Like the stator slot harmonics the rotor slot harmonics are not directly affected by the stator pitch factor. These harmonics however are affected by the rotor skew factor.

The interaction of the component of the MMF wave due to rotor current discretization with the air gap permeance variation due to rotor slotting and rotor motion results in air gap flux density described by equation (4.29)

$$B_{g,rsmh,rspf} = \Im_{rmh}\begin{bmatrix}\cos\left[(\omega t + R\omega_r t) - (R+p)\Omega\right] + \\ \cos\left[(\omega t - R\omega_r t) + (R-p)\Omega\right]\end{bmatrix} \times \wp_{rsf}\cos\{R\Omega - R\omega_r t\}$$

$$= \frac{\Im_{rmh}\,\wp_{rsf}}{2}\begin{bmatrix}\cos(\omega t + p\Omega) + \\ \cos(\omega t - p\Omega) + \\ \cos\left(\{\omega + 2Rq\omega_r\}t - \{2R + p\}\Omega\right) + \\ \cos\left(\{\omega - 2Rq\omega_r\}t + \{2R + p\}\Omega\right)\end{bmatrix} \qquad (4.29)$$

The 3rd and 4th terms in equation (4.29) are the 2nd order harmonic components of the rotor slot modulated air gap flux density.

4.4 EFFECTS OF SLOTTED STATOR AND ROTOR ON SHAFT CURRENT

The flux density induced in the slotted rotor by the rotating stator MMF field is given by the product of this MMF and the permeance wave due the stator and rotor slotting.

The fundamental stator winding MMF is given as:

$$\text{Stator MMF, } \Im(\Omega, t) = \Im_{smf}\cos(\omega t - p\Omega) \qquad (4.30)$$

where Ω is the angle between the stator datum and an arbitrary point on the rotor.

The harmonic permeance of an air gap bounded by a slotted stator and a smooth rotor is given by equation (4.22) and the permeance of air gap bounded by a slotted rotor and a

smooth stator is given by equation (4.26). When both stator and rotor are slotted the total reluctance of the air gap is expressed as

$$\Re_{ssrw} = \frac{1}{\wp_{ssw}} + \frac{1}{\wp_{rsw}} - \frac{1}{\wp_{g}} \qquad (4.31)$$

where $\wp_g = \frac{\mu_0}{g}$ and g is the average air gap.

The corresponding total permeance of the air gap is the reciprocal of its total reluctance

$$\wp_{srsw} = \frac{1}{\Re_{ssrw}} = \frac{\wp_{rsw}\ \wp_{ssw}\wp_{g}}{(\wp_{rsw} + \wp_{ssw})\ \wp_{g} - \wp_{ssw}\ \wp_{rsw}} \qquad (4.32)$$

The first term in the denominator is constant while the second term is a series of variable components. The permeance equation can be reduced approximately to equation (4.33).

$$\wp_{srsw} = K_{ssr}\ \wp_{rsw}\ \wp_{ssw} \qquad (4.33)$$

Hence, the harmonic permeance wave of slotted stator and rotor, $\wp_{srsw}$ can be expressed as equation (4.34).

$$\wp_{srsw} = \wp_{srsh}\left[\cos\left\{-q\,R\,\omega_r\,t + (qR + hS)\,\Omega\right\} + \cos\left\{-q\,R\,\omega_r\,t + (qR - hS)\,\Omega\right\}\right] \qquad (4.34)$$

where R is the number of rotor slots, q is the rotor slot harmonic number = 0, ±1, ±2, ±3,... and h is stator slot harmonic number = 0, ±1, ±2, ±3,...

Hence, the air gap flux density due to the slotted stator and rotor is given by equation (4.35).

$$B_{g,\,smf.\,srsph} = \Im_{smf}\cos\{\omega t - p\Omega\} \times \wp_{srsh}\begin{bmatrix}\cos\{-qR\omega_r t + (qR+hS)\Omega\} + \\ \cos\{-qR\omega_r t + (qR-hS)\Omega\}\end{bmatrix}$$

$$= \frac{\Im_{smf}\,\wp_{srsh}}{2}\begin{bmatrix}\cos\{(-qR\omega_r+\omega)t + (qR+hS-p)\omega\} + \\ \cos\{(-qR\omega_r-\omega)t + (qR+hS+p)\omega\} + \\ \cos\{(-qR\omega_r+\omega)t + (qR-hS-p)\omega\} + \\ \cos\{(-qR\omega_r-\omega)t + (qR-hS+p)\omega\}\end{bmatrix} \qquad (4.35)$$

The stator slot harmonic order h is equal to the rotor slot harmonic order q for interaction to occur. Equation (4.35) can also be produced by the interaction of the stator slot harmonic MMF and the rotor slot harmonic permeance as shown in equation (4.36).

$$B_{g,ssmh,rsph} = \Im_{ssmh}\begin{bmatrix}\cos\{\omega t + (hS-p)\Omega\} + \\ \cos\{\omega t - (hS+p)\Omega\}\end{bmatrix} \times \wp_{rsph}\cos\{qR(\Omega - \omega_r t)\}$$

$$= \frac{\Im_{ssmh}\,\wp_{rsph}}{2}\begin{bmatrix}\cos(\{-qR\omega_r+\omega\}t + \{qR+(hS-p)\}\Omega) + \\ \cos(\{-qR\omega_r-\omega\}t + \{qR-(hS-p)\}\Omega) + \\ \cos(\{-qR\omega_r+\omega\}t + \{qR-(hS+p)\}\Omega) + \\ \cos(\{-qR\omega_r-\omega\}t + \{qR+(hS+p)\}\Omega)\end{bmatrix} \qquad (4.36)$$

The harmonic order h is equal to q so that the interaction can occur.

Furthermore, equation (4.36) can be obtained by considering the interaction of the component of the MMF due to rotor slotting and motion with the permeance wave due to stator slotting as described by equation (4.37).

$$B_{g,\,rsmh,\,ssph} = M_{rmh} \left\{ \begin{array}{l} \cos\left[\left(\omega t + qR\omega_r t \right) - (qR + p)\,\Omega \right] + \\ \cos\left[\left(\omega t - qR\omega_r t \right) + (qR - p)\,\Omega \right] \end{array} \right\} \times \wp_{ssh} \cos\{ hS\Omega \}$$

$$= \frac{M_{rmh}\,\wp_{ssh}}{2} \left[\begin{array}{l} \cos\left(\left\{ \omega + Rq\omega_r \right\} t - \left\{ qR - (hS - p) \right\} \Omega \right) + \\ \cos\left(\left\{ \omega + Rq\omega_r \right\} t - \left\{ qR + (hS + p) \right\} \Omega \right) + \\ \cos\left(\left\{ \omega - Rq\omega_r \right\} t + \left\{ qR + (hS - p) \right\} \Omega \right) + \\ \cos\left(\left\{ \omega - Rq\omega_r \right\} t + \left\{ qR - (hS + p) \right\} \Omega \right) \end{array} \right] \qquad (4.37)$$

where $M_{rmh} = (\Im_{smf}\, \wp_{rsh}) / 2$

4.5 EFFECTS OF SATURATION ON SHAFT CURRENT

Magnetic saturation may be understood graphically by examining Figure 4.4 which shows the mean values of magnetic flux density (B) versus magnetic field intensity (H) for a typical lamination steel. Magnetic field intensity is considered as the input to the system with magnetic flux density as its output. Magnetic field intensity is proportional to the applied current. At any point on the curve, the ratio of magnetic flux density to magnetic field intensity is the permeability, μ. The curve may be divided into several regions. The first part of the curve, the region of low H, is nearly linear, meaning that the flux density is directly proportional to the magnetic field intensity. The permeability is constant. As the magnetic field intensity is increased, the limit of ability of the iron to support the magnetic field is reached, as indicated by the knee of the curve. At

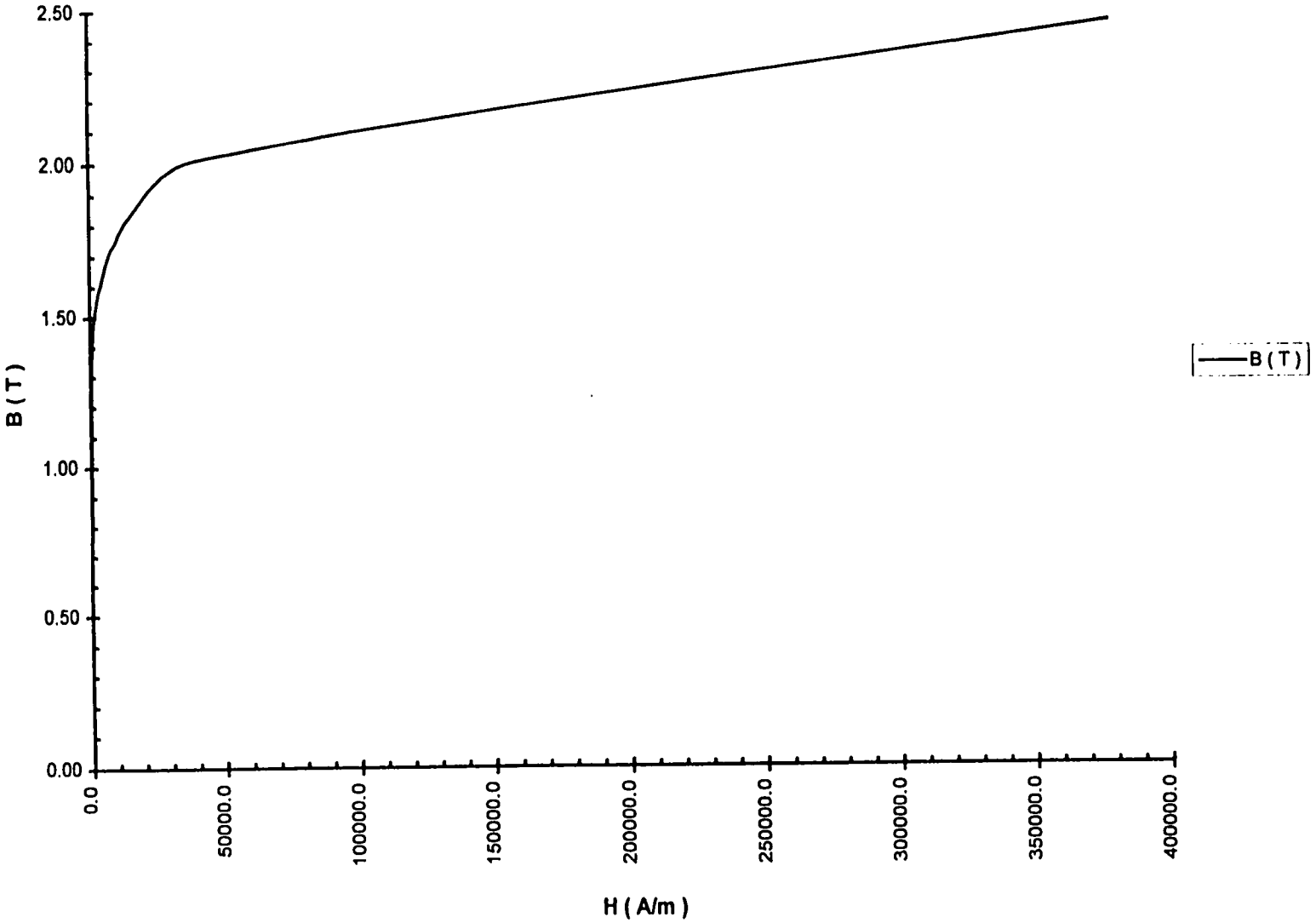

Figure 4.4: Typical B-H Characteristic of Lamination Steel

this point the permeability starts to decrease. Beyond this knee, in the region of high H, the iron becomes saturated, meaning that an increase in magnetic field intensity produces negligible increases in magnetic flux density. A situation may arise when the permeability of the iron is approximately equal to the permeability of air on further increase in magnetic field intensity.

Magnetic saturation [37 - 41] is an inevitable feature in almost all electromagnetic devices. In a polyphase alternating current induction machine, when a sinusoidally distributed magnetomotive (MMF) force wave is applied to its air gap, the waveform of the air gap flux density is not usually sinusoidal as it is distorted by magnetic saturation of the teeth and cores of both stator and rotor. Saturation of the teeth causes the air gap flux density to be flat topped as shown in Figure 4.5. Saturation of the cores tends to produce a flat topped peripheral distribution of the flux density in the core [38] and hence causes the air gap flux density to peak. This can be explained by the fact that the flux in the core is the space integral of the flux in the air gap; that is the air gap flux density is proportional to the space derivative of the core flux. If the derivative of the flat topped core flux distribution peaks so will the air gap flux density. The action of a saturated core in the case where both the core and the teeth are saturated is such that it opposes the effect of the saturated teeth, depending on the relative degrees of saturation of both regions. In all practical machines, the teeth are more saturated than the core [38, 39].

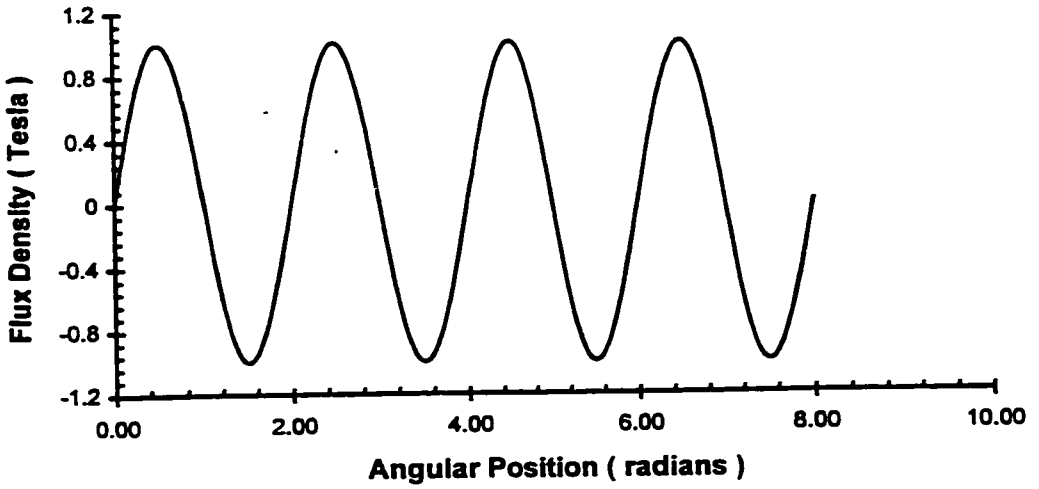

a) Without Saturation

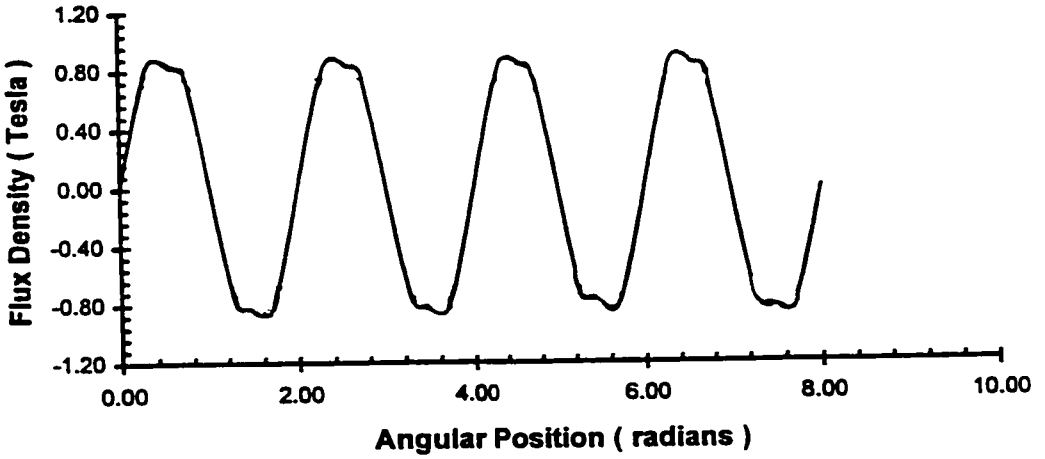

b) With Saturation

Figure 4.5: Air Gap Flux Density Distribution With and Without Saturation

Magnetic saturation causes saturation harmonics [40, 41]. These harmonics are very different from the time harmonics due to solid state power supplies and the spatial harmonics due to non-ideal winding distribution and slotting. They are not excited by a harmonic MMF in the air gap. The flux density produced by the fundamental air gap MMF is by far the largest component present in the teeth and cores. This fundamental MMF wave is therefore responsible for producing the saturation harmonics. The saturation harmonics travel with the same rotational speed in the air gap as the fundamental. They are of odd orders only. The third harmonic is the largest and most important. The 5^{th}, 7^{th} and other non-triplen saturation harmonic effects are dampened by the wye connected stator winding. The wye connected stator winding represents a low impedance circuit to dampen the effect of the non- triplen harmonic air gap flux density. Therefore, the resultant air gap harmonic field due to this interaction is small. For the third harmonic, no stator current exists to counteract the time rate of change of air gap flux density. Hence, rotor third harmonic currents are induced. These induced currents will distort the magnetizing MMF distribution in the air gap. The resultant saturation harmonic air gap flux induces voltages in the stator winding at multiples of supply frequencies. When the stator winding is three phase star connected, the triplen harmonic voltages in each phase are co-phasal and can be ignored.

The saturation harmonic content is high when the teeth are highly saturated and the core is not saturated. Saturation is generally largest at no-load conditions when the slip is small and hence there is negligible damping of these saturation harmonics by these

induced rotor currents. If the supply to the motor is kept constant at the rated values, as the load is increased and the slip increases, the phase difference between the applied load and the primary impedance drop decreases. Hence, the machine becomes less saturated. If, however, the motor is operated at rated voltage and the supply current is allowed to vary with slip from the no-load to the locked rotor condition, saturation harmonics are virtually the same at no-load up to the rated full load but increase as the motor line current increases with increasing slip towards the locked-rotor condition.

The spatial distribution of air-gap flux density influenced by saturation somewhat resembles a square wave as shown in Figure 4.5. This wave can be approximated by a Fourier series with odd spatial harmonics:

$$B_{sat}(\Omega) = B_1 \cos(p\Omega) + B_{sat,3} \cos(3p\Omega) + B_{sat,5} \cos(5p\Omega) + B_{sat,7} \cos(7p\Omega) + \ldots \quad (4.38)$$

Each of these harmonic waves rotates at the same speed and in the same direction as the fundamental. Hence the flux density waveform influenced by saturation is

$$\begin{aligned} B_{sat}(\Omega) = {} & B_1 \cos(\omega t - p\Omega) + B_{sat,3} \cos(3\omega t - 3p\Omega) + \\ & B_{sat,5} \cos(5\omega t - 5p\Omega) + B_{sat,7} \cos(7\omega t - 7p\Omega) + \ldots \end{aligned} \quad (4.39)$$

Ignoring higher harmonics, the flux density wave of harmonic order of 3p due to magnetic saturation is

$$B_{sat}(\Omega) = B_{sat,3} \cos(3\omega t - 3p\Omega) \quad (4.40)$$

The harmonic traveling wave of equation (4.39) can be obtained from the MMF-permeance wave approach. In the 8 pole machine, there are eight regions of high flux density in the stator teeth where saturation is most likely to occur. In each of these areas,

the local effective air gap length is increased, producing low local permeance values. Ninety electrical degrees away from each of the regions of high concentration of flux density are the regions of low flux density. The local air gap permeance in the regions of low flux density is high. Hence, the full spatial permeance wave around the air gap due to saturation [36, 37] consisting of twice the number of pole pairs in space superimposed upon an average component and rotating at twice the frequency of the fundamental wave, can be written as:

$$(\Omega) = \wp_o + \wp_{sat} \cos(2\omega t - 2p\Omega) \qquad (4.41)$$

Equation (4.41) is one case of a general expression of permeance of a smooth and concentric air gap combined with the effects of saturation which is given as

$$_{sa}(\Omega) = \sum_{n_s=0}^{\infty} \wp_{sans} \cos n_s(2\omega t - 2p\Omega) \qquad (4.42)$$

Considering only the fundamental MMF, the flux density traveling wave caused by saturation is given as

$$B_{sat} = \Im \cos(\omega t - p\Omega) \times \wp(\Omega)$$

$$= \wp_o \Im \cos(\omega t - p\Omega) + \frac{\wp_{sat} \Im}{2}[\cos(\omega t - p\Omega) + \cos(3\omega t - 3p\Omega)] \qquad (4.43)$$

The second term of equation (4.43) consists of the contribution to the main flux density wave and the harmonic wave due to saturation, equation (4.40). The saturation harmonic field acts on the rotor winding, inducing in the rotor winding voltages having the identical order of harmonics. The induced voltages drive current in the rotor circuit. Owing to the rotor slotting the rotor current MMF contains harmonics. These induced

rotor harmonic MMF waves interact with the permeance of the air gap to generate a new set of air gap flux density waves. Out of these flux density waves, those waves of order equal to that of the stator saturation harmonic field react on the corresponding stator flux density harmonics. This phenomenon is defined earlier as armature reaction. The remaining waves called residual rotor flux density waves induce voltage in the stator winding with frequency different from that of the supply network frequency. Each current component due to the induced stator winding voltage gives rise to new stator MMF harmonics, a part of which reacts on the residual rotor flux density waves while the remaining part constitutes the stator residual flux density. This armature reaction process [34, 35] continues until the steady state air gap flux density is obtained. The residual rotor slot harmonic fields due to saturation are given as

$$B_{sat} = B_{\lambda sa} \cos(\chi_{sat} \omega t - \lambda_{sat} px) \qquad (4.44)$$

where $\chi_{sat} = 3 + K_j \frac{R_2}{p}(1-s)$

and $\lambda_{sat} = 3 + \frac{K_j R_2}{p}$

In some machines the 5th and 7th harmonic saturation components are significant and must be considered. Hence the residual rotor slot harmonic field will have slot harmonic contents and pole pair numbers given by equation (4.45)

$$\chi_{sat} = K_i + K_j \frac{R_2}{p}(1-s) \qquad (4.45)$$

and $\lambda_{sat} = K_i + \frac{K_j R_2}{p}$

where $K_i = 3, 5$ and 7 and $K_j = 1, 2, 3\ldots$

4.6 SUMMARY

The important harmonics in induction machines are classified as shown in Figure 4.6. These harmonics contribute to the losses of the machine and affect the torque characteristics of the machine. Furthermore these harmonics, as summarized in Tables 4.2 and 4.3 need to be carefully considered in the shaft voltage prediction rule given in equation (2.1).

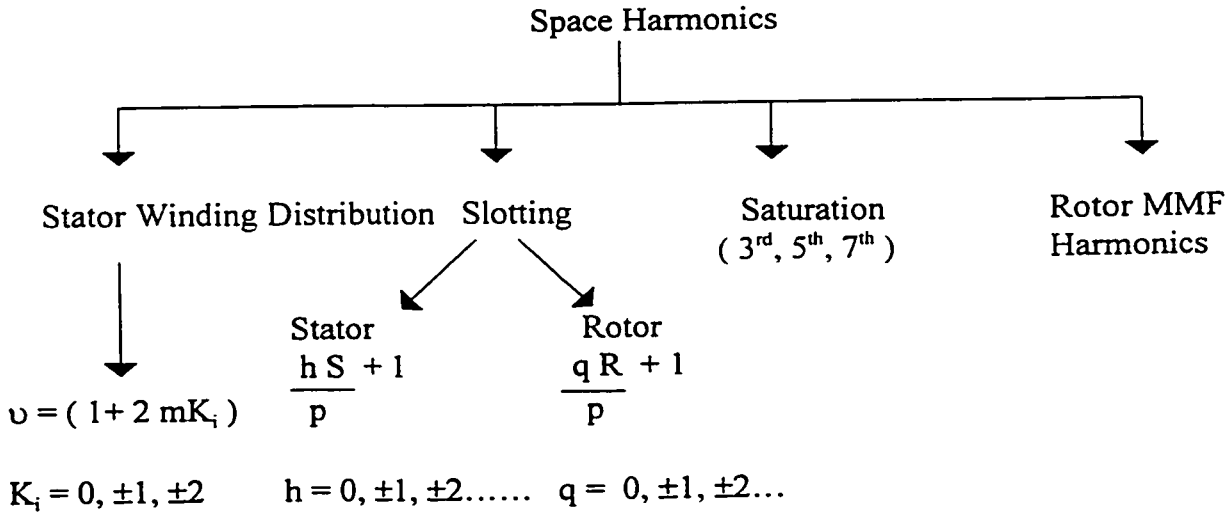

Figure 4.6: Classification of Harmonics in Induction Machine

Origin of Fields	Primary Fields	Harmonic Fields Caused by Damping Rotor Current	
		Pole Pairs	Frequency
Winding fields Equation (4.4)	$B(\Omega, t) = \sum_{\upsilon} B_{\upsilon w} \cos(\omega t - \upsilon p\Omega)$ $\upsilon = 1 + 2mK_i$ $Ki = 0, \pm1, \pm2,\ldots$	ξp $\xi = \upsilon + (K_j R_2/p)$ $K_j = 0, \pm1, \pm2,\ldots$	$\{1+[K_j R_2(1-s)/p]\}f$ $K_j = 0, \pm1, \pm2,\ldots$
Saturation fields Equation (4.43)	$B(\Omega, t) = \sum_{\upsilon_i} B_{\upsilon_s} \cos \upsilon_i(\omega t - p\Omega)$ $\upsilon_i = 1 + 2n_s$ $n_s = 1, 2, 3$	ξp $\xi = \upsilon_i + (K_j R_2/p)$ $K_j = 0, \pm1, \pm2,\ldots$	$\{\upsilon_i + [K_j R_2(1-s)/p]\}f$ $K_j = 0, \pm1, \pm2,\ldots$

Table 4.2: Air Gap Fields of Induction Motor Under Normal Operating Condition.

EQUATIONS	POLE PAIR	FREQUENCY
Armature Reaction Fields Equation (4.19)	βp $\beta = 1 + 2mK_k + \varepsilon R_2/p$ $K_k, \varepsilon = 0, \pm1, \pm2,\ldots$	$\{1 + [K_j R_2 (1-s)/p]\}f$ $K_i = 0, \pm1, \pm2,\ldots$
Stator Slots Modulated Fields Equation (4.22)	$hS \pm p$ $h = 0, \pm1, \pm2,\ldots$	f
Stator Slots Modulated Field and 3rd Harmonic Current	$hS \pm p$ $h = 0, \pm1, \pm2,\ldots$	$3f$
Rotor Slots Modulated Fields Equation (4.28)	$Rq \pm p$ $q = 0, \pm1, \pm2,\ldots$	$\{qR(1-s)/p \pm 1\}f$ $q = 0, \pm1, \pm2,\ldots$
Stator and Rotor Slots Modulated Fields Equation (4.36)	$qR \pm (hS \pm p)$ $h, q = 0, \pm1, \pm2,\ldots$	$\{qR(1-s)/p \pm 1\}f$ $q = 0, \pm1, \pm2,\ldots$

Table 4.3: Other Harmonic Pole Pairs and Corresponding Frequencies.

CHAPTER 5

ROTOR CONDITIONS AND THEIR EFFECTS ON SHAFT CURRENT

5.0 INTRODUCTION

Many failures in squirrel cage induction machine are associated with cage integrity. Bonnett and Soukup [42] cited several kinds of stresses, namely thermal, dynamic and mechanical as reasons for rotor cage failures. A majority of diagnostic techniques developed thus far, are dependent on detecting a twice slip frequency modulation in the speed or torque. This twice slip frequency side- band around the fundamental is also evidently present in the line current of the machine.

This chapter will examine how these three types of rotor conditions, namely the rotor eccentricity condition, non-insulated rotor bar condition and broken bar fault condition may contribute to the magnitude of shaft current. These conditions will also generate stray flux that can circulate around the shaft and hence cause localized bearing current. The broken bar fault condition is an abnormal phenomenon.

5.1 EFFECTS OF ECCENTRICITY ON SHAFT CURRENT

One of the most common problems in rotating machinery installations is vibration. Lateral shaft vibrations - rotor dynamic motions perpendicular to the machine rotational

axis, are the most common type of vibrations. These vibrations generally are due to bearing wear or fracture. bent rotor shaft, shaft misalignment, operation at whirl/whip condition, etc. These causes result in rotor static and dynamic eccentricities as shown in Figures 5.1 and 5.2. Figure 5.3 indicates the operation of a machine with no eccentricity.

Static eccentricity is the condition existing when the axis of the rotor is displaced from the axis of the stator by a distance, $\varepsilon\ \delta_m$ where δ_m is the mean air gap length and ε is a fraction less than unity. A uniform air gap pattern is maintained throughout the rotation. The rotor is turning on its own axis. Static eccentricity can be caused by stator core ovality or incorrect positioning of the rotor or stator. The magnetizing and mutual inductances of the stator phases are different for the three phases but they are constant. However, the rotor magnetizing and mutual inductances will be a function of the rotor position and will be varying with time.

Dynamic eccentricity is present when the air gap length pattern rotates with the rotor. The center of the rotor is not at the center of rotation. Dynamic eccentricity is a function of space and time. A bent shaft, bearing wear or mechanical resonance at critical speeds could result in dynamic eccentricity of the rotor. The magnetizing and mutual inductances of the stator phases will be a function of the rotor position whereas the inductances of the rotor will be a constant but different for the three phases.

Salon et. al. [43] showed that in an induction machine which has a small air gap, a non-uniform air gap due to rotor eccentricity distorts the air gap flux density distribution and results in unbalanced magnetic pull (U.M.P.) and other additional magnetic forces

directed both radially and tangentially. Using the finite element method, they demonstrated that circulating current between parallel windings in an asymmetrical induction machine reduces the U.M.P. and other magnetic forces. The reduction can be explained in that the inductance is lower in those circuits located where the air gap is larger than nominal, relative to the inductance of circuits located where the air gap is smaller than nominal. With the circuits connected to the same voltage, the currents in the circuits facing the larger air gap are slightly larger than those facing the smaller air gap. The circulating current tends to smooth out the distortion in the air gap flux density distribution with the net effect of reduction of additional magnetic flux and magnetic force waves generated by the non-uniform air gap. These circulating damping currents would not be observed in the line current spectrum since they are circulating currents within the stator winding. Stavrou and Penman [44] observed side band currents due to static eccentricity and concluded that the slot harmonics variation, as a function of eccentricity, in the phase currents depends on the combination of stator and rotor slots and the number of poles. It does not depend on the first order permeance. Bradford [45] and Dorrell [46] indicated that the side-band currents increase rapidly as the motor is loaded. Furthermore Dorrell [47] found that the upper side-band currents due to the dynamic eccentricity decrease as the motor is loaded. He also stated that there is a decrease in lower side band current from no-load to full load when there is either a nominal zero dynamic or static eccentricity. If substantial degrees of both types of eccentricity are present, there is little change in the lower side band current

from no-load to full-load. This contrasts with the upper side band which decreases in magnitude when both types of eccentricity are present.

In static eccentricity, a uniform air gap pattern is maintained throughout the rotation. Each point on the stator experiences a constant magnetic pull.

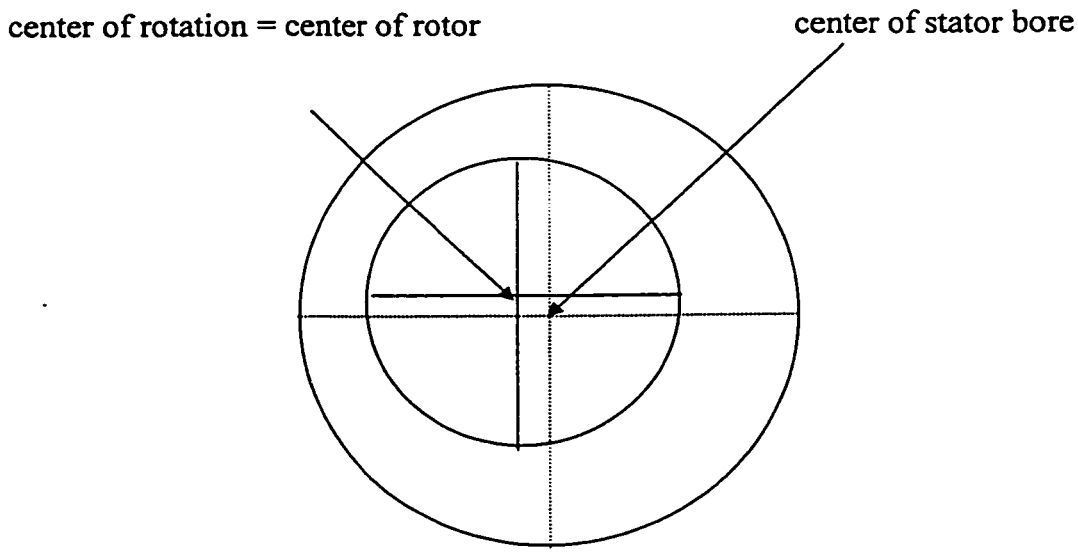

Figure 5.1: Static Eccentricity

In dynamic eccentricity, as the rotor rotates, the air gap length pattern rotates with the rotor such that each point on the stator will experience a strong magnetic pull followed 180 mechanical degree by the weaker magnetic pull.

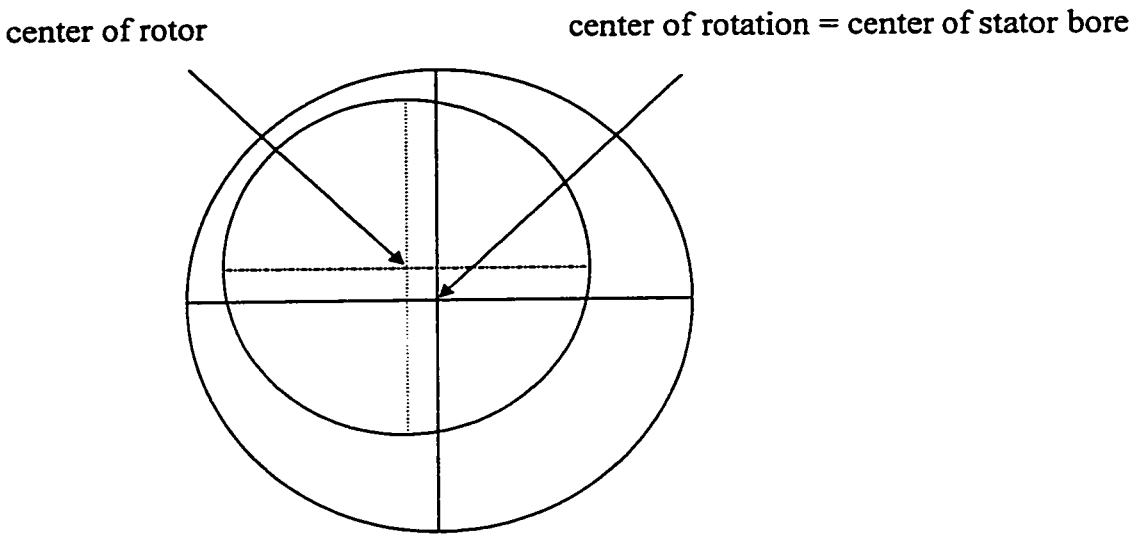

Figure 5.2: Dynamic Eccentricity

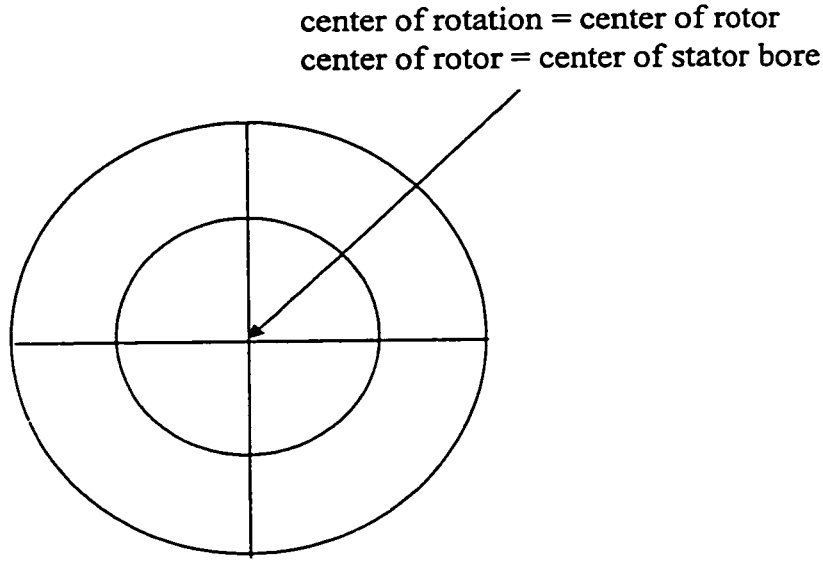

Figure 5.3 : No Eccentricity

The presence of eccentricity gives rise to higher harmonics which are responsible for the following effects:

1. Unbalanced magnetic pull (U.M.P.)
2. Vibration and noise
3. Shaft current
4. Parasitic Torque

A consequence of stationary asymmetry of the air gap will be an unbalanced magnetic pull between rotor and stator surfaces due to the magnetic forces, tending to pull the surfaces together on the side that has the smaller air gap. The unbalanced magnetic pull alters the eccentricity level of the machine. The incremental increase in the eccentricity level, $\Delta\varepsilon$ depends on the extent to which the shaft moves, bends and deforms under the action of forces acting on it. The increase in eccentricity level is considered constant as long as the unbalanced magnetic pull is determined to be a constant force. Robinson [48] explained that though a constant force, the attraction force is greater between the stator and rotor surfaces on the side with the small air gap when the poles of the rotating flux wave are on the eccentricity axis. Furthermore, this attraction force will go through 2 cycles of force for every cycle of voltage; that is the force has a varying component with twice line frequency. The poles of the rotating flux are on the eccentricity axis as long as the inequality of the air gap remains constant, that is the stator and rotor do not move sideways relative to each other under the influence of force.

For small levels of eccentricity, as the force on one side decreases to its minimum value, the rotor moves to the other side under the action of spring and passes the center of the stator bore. As the opposite pole of the flux wave appears on the eccentricity axis the force will be directed to the opposite side. As a result of this effect, the rotor moves once to one side and then to the opposite side in one cycle of voltage. This type of motion constitutes a line frequency vibration. Thus, it is clear that very slight asymmetry of the rotor may not of itself cause anything but a variation of the unbalanced magnetic pull on the eccentricity axis and lead to a change of the eccentricity level as a function of the speed of rotation.

The survey of published work on unbalanced magnetic pull in rotating electric machine by P. Von Kaehne [49] highlighted three causes of unbalanced magnetic pull namely, slot combinations, faults in supply or in machine windings, and eccentricity and saturation.

Unbalanced magnetic pull occurs when the air gap field contains two harmonic fields with pole pairs differing by one. The two harmonic fields could be two stator fields, two rotor fields or one stator with one rotor field. To avoid unbalanced magnetic pull, the slot difference between the stator and rotor slots should avoid certain values as shown in Appendix 5.

5.1.1 Derivation of Air gap Flux Density

The air gap of an eccentric rotor, $\delta(\Omega)$, described in detail in Appendix 6, is given in equation (5.1).

$$\delta(\Omega) = R1 - R2 - d\cos(\Omega) \qquad (5.1)$$

where R1 is the stator bore radius, R2 the rotor outer radius and d the distance between the rotor center and the rotation center

The rotor eccentricity ε is

$$\varepsilon = \frac{d}{\delta_m} \qquad (5.2)$$

where δ_m, the mean or average air gap length is equal to (R1-R2).

Hence, the air gap of an eccentric rotor is described as

$$\delta(\Omega) = \delta_m\left[1 - \varepsilon_s\cos(\Omega) - \varepsilon_d\cos(\Omega - \omega_r t)\right] \qquad (5.3)$$

where ε_s is the rotor static eccentricity and ε_d is the rotor dynamic eccentricity.

The air gap permeance $\wp(\Omega)$ [43] is expressed as:

$$\wp(\Omega) = \frac{1}{\delta(\Omega)}$$

$$= \frac{1}{\delta_m\left[1 - \varepsilon_s\cos(\Omega) - \varepsilon_d\cos(\Omega - \omega_r t)\right]} \qquad (5.4)$$

The air gap permeance function can be developed in terms of a Fourier series. If the function is approximated by the first two harmonic components of the Fourier series, the air gap permeance can be written as:

$$(\Omega) = \frac{1}{\delta_m}\left\{\begin{array}{l}\lambda_0 + \lambda_1\cos(\Omega) + \lambda_2\cos(2\Omega) + \\ \lambda_3\cos(\Omega - \omega_r t) + \lambda_4\cos 2(\Omega - \omega_r t)\end{array}\right\} \qquad (5.5)$$

where

$$\lambda_0 = \left\{1 + \left(\frac{\varepsilon_s^2}{2}\right) + \left(\frac{\varepsilon_d^2}{2}\right)\right\}, \quad \lambda_1 = \left(\varepsilon_s + \left(\frac{3\varepsilon_s^3}{4}\right)\right) \tag{5.5a}$$

$$\lambda_2 = \left(\frac{\varepsilon_s^2}{2}\right), \quad \lambda_3 = \left(\varepsilon_d + \left(\frac{3\varepsilon_d^3}{4}\right)\right) \tag{5.5b}$$

$$\lambda_4 = \left(\frac{\varepsilon_d^2}{2}\right) \tag{5.5c}$$

The complete Fourier series of air gap permeance takes the form

$$(\Omega) = \mu_o \left\{ \begin{array}{l} \frac{1}{\delta_e} + \frac{1}{\delta_e} \sum_{k_{se}=1}^{\infty} 2\,[\lambda_s]^{k_{se}} \cos\, k_{se}\Omega + \\ \frac{1}{\delta_e} \sum_{k_{de}=1}^{\infty} 2\,[\lambda_d]^{k_{de}} \cos\, k_{de}(\Omega - \omega_r t) \end{array} \right\}$$

$$= \frac{\mu_o}{\delta_e} \left\{ \sum_{k_{se}=0}^{\infty} \wp_{se} \cos(k_{se}\,\Omega) + \sum_{k_{de}=1}^{\infty} \wp_{de} \cos(k_{de}(\Omega - \omega_r t)) \right\} \tag{5.6}$$

where

$$\delta_e = \delta_m \sqrt{1 - \varepsilon_s^2 - \varepsilon_d^2}$$

$$\lambda_s = \frac{1 - \sqrt{1 - \varepsilon_s^2}}{\varepsilon_s}, \quad \lambda_d = \frac{1 - \sqrt{1 - \varepsilon_d^2}}{\varepsilon_d} \tag{5.6a}$$

where $0 \le \varepsilon_s, \varepsilon_d \le 1$

In p-pole pair machines, the fundamental component of MMF distribution can be expressed as:

$$\Im(\Omega, t) = \Im_p \cos(\omega t - p\Omega) \qquad (5.7)$$

For p > 1 the fundamental flux density component can be expressed as

$$B_p(\Omega, t) = -\frac{\mu_o R \Im_p}{\delta(\Omega) p} \cos(\omega t - p\Omega) \qquad (5.8)$$

The value of $1/\delta(\Omega)$ in equation (5.5) is substituted into equation (5.8) to obtain

$$B_p(\Omega, t) = -\frac{\mu_o R \Im_p}{\delta_m p} \cos(\omega t - p\Omega) \left\{ \begin{matrix} \lambda_0 + \lambda_1 \cos(\Omega) + \lambda_2 \cos(2\Omega) + \\ \lambda_3 \cos(\Omega - \omega_r t) + \lambda_4 \cos 2(\Omega - \omega_r t) \end{matrix} \right\}$$

$$= -\frac{\mu_o R \Im_p \lambda_0}{\delta_m p} \left\{ \begin{matrix} \cos(\omega t - p\Omega) \\ + \frac{\lambda_1}{2\lambda_0} \left[\begin{matrix} \cos\{\omega t - (p-1)\Omega\} + \\ \cos\{\omega t - (p+1)\Omega\} \end{matrix} \right] \\ + \frac{\lambda_2}{2\lambda_0} \left[\begin{matrix} \cos\{\omega t - (p-2)\Omega\} + \\ \cos\{\omega t - (p+2)\Omega\} \end{matrix} \right] \\ + \frac{\lambda_3}{2\lambda_0} \left[\begin{matrix} \cos\{(\omega - \omega_r)t - (p-1)\Omega\} + \\ \cos\{(\omega + \omega_r)t - (p+1)\Omega\} \end{matrix} \right] \\ + \frac{\lambda_4}{2\lambda_0} \left[\begin{matrix} \cos\{(\omega - 2\omega_r)t - (p-2)\Omega\} + \\ \cos\{(\omega + 2\omega_r)t - (p+2)\Omega\} \end{matrix} \right] \end{matrix} \right\}$$

(5.9)

where the rotor angular velocity $\omega_r = \left(\frac{1-s}{p}\right)\omega$ where ω is the supply frequency and p is the pole pair.

In addition to the main field with p pole pairs there are two additional fields with (p ± 1) and (p ± 2) pole pairs. These pole pairs pulsate at frequencies f, (f ± f_r)and (f ± 2f_r). Looking at the 8 pole machine, we have in addition to the four pole pair field a three pole pair field and a five pole pair field. There will be shaft current due to the harmonic fields when the fraction consisting of the ratio of twice the number of joints to the harmonic field poles when reduced to its lowest terms contains an odd numerator.

The coefficients of the Fourier series produced by the inversion of the air gap length when only static or dynamic eccentricity is present, are expressed in equation (5.6a) and Figure 5.4, where it is clear that at 50% eccentricity the first harmonic has a magnitude of about 0.62 on the normalized plot and the second harmonic is 27% of the first harmonic. Hence only the p and (p ± 1) field components need to be considered.

The p and (p ± 1) fields will induce EMF's into the rotor cage and hence produce rotor MMF waves. In terms of the rotor reference frame the rotor MMF waves can be expressed as:

$$\begin{aligned}\Im_r(\Omega,t) = {} & \Im_r^p \cos(s\omega t - p\Omega_2 - \phi_1) + \Im_{r,s}^{p-1} \cos\left(\frac{1+\{p-1\}s}{p}\omega t - \{p-1\}\Omega_2 - \phi_2\right) + \\ & \Im_{r,s}^{p+1} \cos\left(\frac{-1+\{p+1\}s}{p}\omega t - (p+1)\Omega_2 - \phi_3\right) + \Im_{r,d}^{p-1} \cos(s\omega t - \{p-1\}\Omega_2 - \phi_4) + \\ & \Im_{r,d}^{p+1} \cos(s\omega t - \{p+1\}\Omega_2 - \phi_5)\end{aligned} \qquad (5.10)$$

Equation (5.10) shows that when s << 1, static eccentricity induces (p ± 1) pole pair MMF waves in the rotor with current frequency approximately ω/p while the dynamic

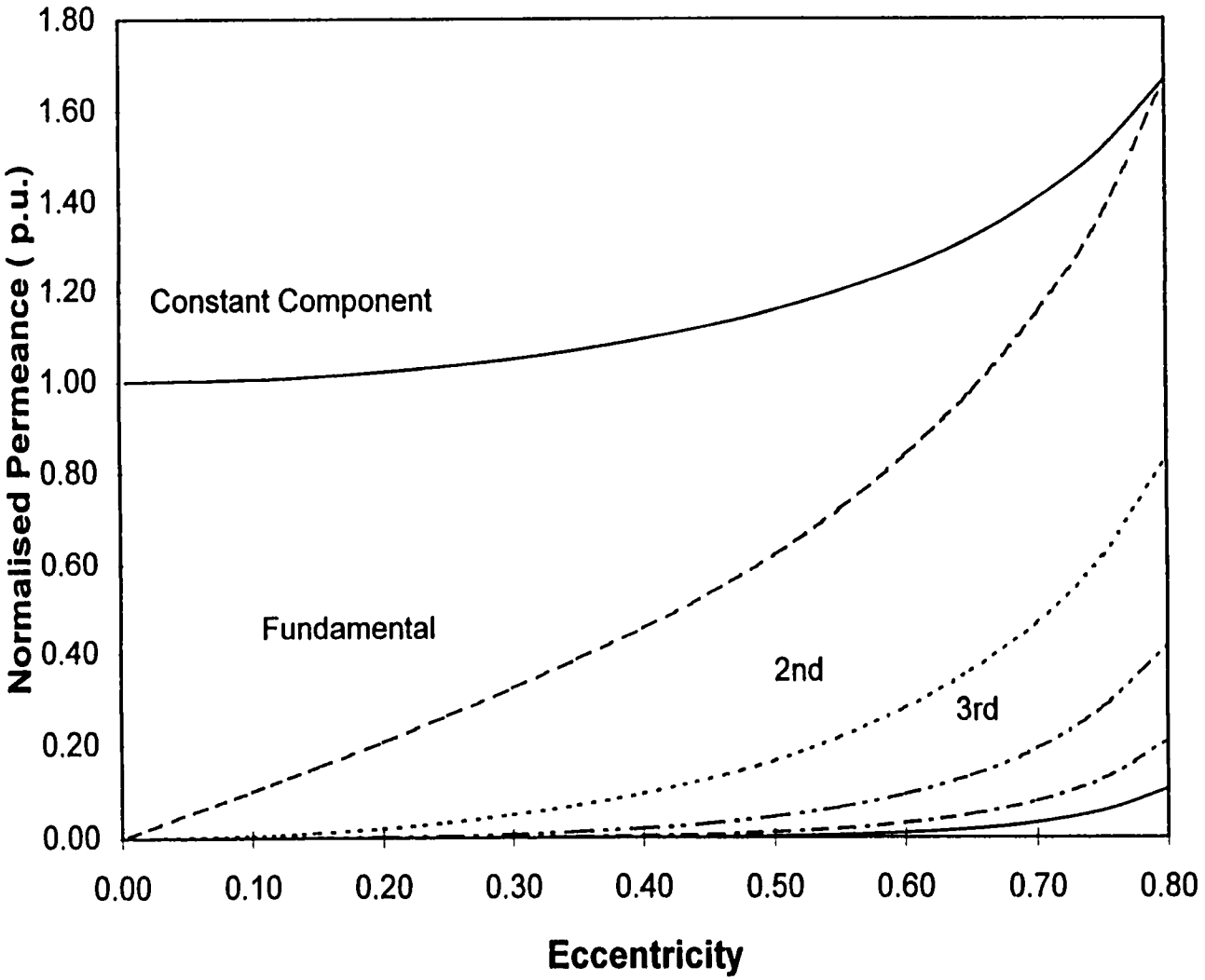

Figure 5.4: Air Gap Permeance Coefficients

eccentricity induced (p ± 1) pole pair MMF waves have slip frequency current components. Thus, at close to synchronous speed, that is at no load, the second term of equation (5.9) is damped by the rotor. The fourth term in equation (5.9) represents the stator fields at close to synchronous speed, not damped by the rotor current. As shown by Dorrell [46], dynamic eccentricity induced unbalanced magnetic pull at no load is much higher than that due to static eccentricity. As the load increases, the unbalance magnetic pull decreases. The fourth term in equation (5.9) is damped by the rotor current.

The rotor MMF waves will generate equivalent field components. When these field components are modulated by the air gap eccentricity, p-pole pair air gap field components are generated which will induce non-supply frequency EMF's in the stator windings. To obtain these components, the rotor (p ± 1) MMF waves in stator coordinates are multiplied by the fundamental air gap permeance. The rotor MMF waves are converted to stator reference frames using the coordinate relationship $\Omega_2 = \Omega - \omega t$. The modulated field components are

$$B_r(\Omega, t) = \begin{Bmatrix} \Im_{r,s}^{p-1} \cos(\omega t - (p-1)\Omega - \phi_2) + \\ \Im_{r,s}^{p+1} \cos(\omega t - (p+1)\Omega - \phi_3) \end{Bmatrix} \lambda_3 \cos(\omega_r t - \Omega) + \begin{Bmatrix} \Im_{r,d}^{p-1} \cos([\omega - \omega_r]t - [p-1]\Omega - \phi_4) + \\ \Im_{r,d}^{p+1} \cos([\omega - \omega_r]t - [p+1]\Omega - \phi_5) \end{Bmatrix} \lambda_1 \cos(\Omega) \qquad (5.11)$$

The rotor MMF waves due to static eccentricity are modulated by the dynamic eccentricity air gap permeance and vice versa in order to obtain the p pole pair field components and the supply frequency side-bands.

5.2 EFFECT OF SPATIAL HARMONICS AND ECCENTRICITIES ON SHAFT CURRENT

The air gap flux density produced by the stepped distribution of the stator MMF is given in equation (4.1) and reiterated below:

$$B_{1,\nu} = mq_1 \frac{4}{\pi}\frac{N_{st}}{p} I_1 \sqrt{2}\, K_{\upsilon p} K_{\upsilon d} \frac{1}{\upsilon \delta}\, \mu_o \cos(\omega t - \upsilon p\Omega) \qquad (5.12)$$

Due to rotor eccentricities, the air gap flux densities on one side of the air gap will be larger than that on the other side of the air gap resulting in a net flux around the shaft. Hence, the air gap flux density is modified by the eccentric air gap permeance as follows:

$$B_{1,\nu} = \frac{mq_1}{2}\frac{4}{\pi}\frac{N_{st}}{P} I_1 \sqrt{2}\, K_{\upsilon p} K_{\upsilon d} \frac{1}{\upsilon}\, \mu_o \cos(\omega t - \upsilon p\Omega) \times \left(\frac{1}{\delta_m}\left\{\begin{array}{l} \lambda_0 + \lambda_1 \cos(\Omega) + \lambda_2 \cos(2\Omega) \\ + \lambda_3 \cos(\Omega - \omega_r t) + \lambda_4 \cos 2(\Omega - \omega_r t) \end{array}\right\}\right) \qquad (5.13)$$

These harmonic air gap fields induce currents in the rotor cage winding at slip frequencies. The induced rotor cage currents are stepped in nature and produce harmonic air gap fields of a different order as given in equation (5.14).

$$B_{2,\xi,\upsilon} = \frac{\mu_o R}{\delta \pi \xi p} \sin\left(\frac{\xi p \pi}{R}\right) I_r \sqrt{2} \cos\left[s_\upsilon \omega t - \xi p\left(\Omega - \frac{\omega}{p}(1-s)t\right)\right]$$

$$= \frac{\mu_o R}{\pi \xi p} \sin\left(\frac{\xi p \pi}{R}\right) I_r \sqrt{2} \cos\left[s_{q2}\, \omega t - \xi p\Omega\right] \times \qquad (5.14)$$
$$\frac{1}{\delta_m}\left\{\begin{array}{l} \lambda_0 + \lambda_1 \cos(\Omega) + \lambda_2 \cos(2\Omega) + \\ \lambda_3 \cos(\Omega - \omega_r t) + \lambda_4 \cos 2(\Omega - \omega_r t) \end{array}\right\}$$

Equation (5.14) is rearranged to obtain equation (5.14a)

$$B_{2,\xi,\upsilon} = \frac{\mu_o R}{\pi \xi p} \sin\left(\frac{\xi p \pi}{R}\right) I_r \sqrt{2} \frac{1}{\delta_m} \times$$

$$= \left(\begin{array}{l} \lambda_0 \cos\left(s_{q2}\,\omega t - \xi p \Omega\right) + \\ \frac{\lambda_1}{2}\left\{ \begin{array}{l} \cos\left(s_{q2}\,\omega t - (\xi p - 1)\Omega\right) \\ + \cos\left(s_{q2}\,\omega t - (\xi p + 1)\Omega\right) \end{array} \right\} + \\ \frac{\lambda_2}{2}\left\{ \begin{array}{l} \cos\left(s_{q2}\,\omega t - (\xi p - 2)\Omega\right) \\ + \cos\left(s_{q2}\,\omega t - (\xi p + 2)\Omega\right) \end{array} \right\} + \\ \frac{\lambda_3}{2}\left\{ \begin{array}{l} \cos\left((s_{q2}\,\omega - \omega_r)t - (\xi p - 1)\Omega\right) \\ + \cos\left((s_{q2}\,\omega + \omega_r)t - (\xi p + 1)\Omega\right) \end{array} \right\} + \\ \frac{\lambda_4}{2}\left\{ \begin{array}{l} \cos\left((s_{q2}\,\omega - 2\omega_r)t - (\xi p - 2)\Omega\right) \\ + \cos\left((s_{q2}\,\omega + 2\omega_r)t - (\xi p + 2)\Omega\right) \end{array} \right\} \end{array} \right)$$

(5.14a)

These rotor fields will induce stator currents of different frequencies in the stator winding.

The induced stator current produces harmonic air gap fields given by equation (5.15).

$$B_{1,\beta} = \frac{m q_1}{2} \frac{4}{\pi} \frac{N_{st}}{P} I_1 \sqrt{2}\, K_{up} K_{ud} \frac{1}{\beta} \mu_o \cos\left(s_{q2}\,\omega t - \beta p \Omega\right) \times \left(\frac{1}{\delta_m} \left\{ \begin{array}{l} \lambda_0 + \lambda_1 \cos(\Omega) + \lambda_2 \cos(2\Omega) \\ + \lambda_3 \cos(\Omega - \omega_r t) + \lambda_4 \cos 2(\Omega - \omega_r t) \end{array} \right\} \right)$$

(5.15)

Equations (5.15) is rearranged to obtain equation (5.15a)

$$B_{1\beta} = \frac{mq_1}{2}\frac{4}{\pi}\frac{N_{st}}{p} I_1\sqrt{2}\, K_{up}K_{ud}\frac{1}{\beta}\mu_o\frac{1}{\delta_m} \times$$

$$\left(\begin{array}{l}
\lambda_0\cos(s_{q2}\,\omega t-\beta p\Omega)+ \\
\frac{\lambda_1}{2}\left[\cos(s_{q2}\,\omega t-(\beta p-1)\Omega)+\cos(s_{q2}\,\omega t-(\beta p+1)\Omega)\right]+ \\
\frac{\lambda_2}{2}\left[\cos(s_{q2}\,\omega t-(\beta p-2)\Omega)+\cos(s_{q2}\,\omega t-(\beta p+2)\Omega)\right]+ \\
\frac{\lambda_3}{2}\left[\cos(s_{q2}\,(\omega-\omega_r)t-(\beta p-1)\Omega)+\cos(s_{q2}\,(\omega+\omega_r)t-(\beta p+1)\Omega)\right]+ \\
\frac{\lambda_4}{2}\left[\cos(s_{q2}\,(\omega-2\omega_r)t-(\beta p-1)\Omega)+\cos(s_{q2}\,(\omega+2\omega_r)t-(\beta p+1)\Omega)\right]
\end{array}\right)$$

(5.15a)

5.3 EFFECTS OF SATURATION AND ECCENTRICITY ON SHAFT CURRENT

Ignoring armature reaction, the residual rotor slot harmonic field due to saturation and eccentricity is given by equation (5.16).

$$B_{sat,ecc} = B_{\lambda sa,ecc}\cos(\chi_{sat,ecc}\,\omega t - \lambda_{sat,ecc}\,p\Omega) \qquad (5.16)$$

where

$$\chi_{sat,ecc} = 3 + K_j\frac{R}{p}(1-s)+\left[1 \pm \frac{q(1-s)}{p}\right] \qquad (5.16a)$$

and

$$\lambda_{sat,ecc} = \frac{K_j R}{p} + 3 + \left(1 \pm \frac{q}{p}\right) \qquad (5.16b)$$

In some machines the 5th and 7th harmonic components are significant and must be

considered. Hence, the residual rotor slot harmonic field will have slot harmonic contents and pole pair numbers given by

$$\chi_{sat,ecc} = k_i + K_j \frac{R}{p}(1-s) + \left[1 \pm \frac{q(1-s)}{p}\right] \qquad (5.16c)$$

$$\lambda_{sat,ecc} = \frac{K_j R}{p} + k_i + \left(1 \pm \frac{q}{p}\right) \qquad (5.16d)$$

where $k_i = 3, 5$ and 7 and $K_j = 1, 2, 3, \ldots$

Equation (5.16) is one component of a generalized set of harmonics that could be obtained from consideration of slotted rotor and stator, saturation and eccentricity.

Following the procedure in Chapter 4 in which the permeances due to rotor and stator slotting were combined, equations (4.33), (4.41) and (5.6) give the general total permeance as

$$\wp_{tot}(\Omega, t) = \sum_{q=0}^{\infty}\sum_{h=0}^{\infty}\sum_{n_s=0}^{\infty}\sum_{k_{se}=0}^{\infty}\sum_{k_{de}=0}^{\infty} \wp_{srsh}\,\wp_{sarus}\,\wp_{se}\,\wp_{de} \times \cos\begin{Bmatrix}(qR \pm hS \pm k_{se} \pm k_{de} \pm 2n_s p)\Omega \\ -((qR \pm k_{de})\omega_r \pm 2n_s\omega)t\end{Bmatrix} \qquad (5.17)$$

The air gap magnetomotive force consists of a series of waves generated by the currents in the stator and rotor, given by equation (5.18). Phase angle and skew are neglected.

$$\Im_{tot} = \sum_{n_{st}=1}^{\infty} \sum_{n_{ws}=-\infty}^{\infty} \Im_{n_{st},n_{ws}} \cos\left(n_{st}\, p\Omega - n_{ws}\, \omega\, t\right) + \sum_{n_{rt}=1}^{\infty} \sum_{n_{wr}=-\infty}^{\infty} \Im_{n_{rt},n_{wr}} \cos\left(n_{rt}\, p\Omega - \left(n_{wr}\, s\omega + n_{rt}\, p\, \omega_r\right)t\right) \qquad (5.18)$$

The air gap flux density distribution [49, 50], given as the product of permeance and MMF is expressed as:

$$B(\omega,t) = \sum_{j_s,\Theta_s} B_{j_s,\Theta_s} \cos\left(j_s\Omega - \Theta_s t\right) + \sum_{j_r,\Theta_r} B_{j_r,\Theta_r} \cos\left(j_r\Omega - \Theta_r t\right) \qquad (5.19)$$

where

$$\begin{aligned} j_s &= qR \pm hS \pm k_{se} \pm k_{de} \pm 2\, n_s\, p \pm n_{st} p \\ \Theta_s &= \left(qR \pm k_{de}\right)\omega_r \pm 2n_s\, \omega \pm n_{ws}\, \omega \\ j_r &= qR \pm hS \pm k_{se} \pm k_{de} \pm 2\, n_s\, p \pm n_{rt} p \\ \Theta_r &= \left(qR \pm k_{de} \pm n_{rt}\, p\right)\omega_r \pm 2n_s\, \omega \pm n_{wr}\, s\omega \end{aligned} \qquad (5.19a)$$

In the case of static eccentricity alone, the use of the first permeance harmonic had been suggested as a means of estimating the degree of eccentricity [51, 52]. This is erroneous because Stavrou et. al. [44] demonstrated that the increase in the slot harmonic components depend on the values of permeances, k_{se} of order | S-R | and | S-R-2p | or | R-S-2p |. For combinations of slots and poles giving a permeance of an order which is greater than 6, Figure 5.4 indicates that the effects will be so small that it is difficult to detect any changes until the levels of eccentricity approach or even exceed seventy percent.

In the case of pure dynamic eccentricity, currents of $\{ [R \pm 1] (1-s)/p \pm 1 \} f$ frequencies do not appear in the stator winding as fields with { p+1 } pole pairs cannot induce such

currents in the stator winding. However, previous research [51, 52] had shown the presence of such harmonics which can only be explained by the fact that a combination of a small amount of static and dynamic eccentricities are usually present and able to induce currents of such frequencies. Stavrou et. al. [44] showed that the side-bands which appear in the stator current are { [R ±(R ± S)] (1-s)/p ± 1 }f and { [R ± (R ±S ±2p)] (1- s)/ p ±1 }f. This means that additional side-bands of slot harmonics that are induced in the stator winding depends on the number of rotor and stator slots, and the number of poles. Their amplitudes depend on the variation of the corresponding permeance components, k_{de} of order | R ± S | and | R ± S ± 2p |. Again from Figure 5.4, it is shown that until a threshold value of dynamic eccentricity is reached, there will be minimal variations of these orders of harmonic components in the phase current.

5.4 EFFECTS OF INTER-BAR CURRENTS ON SHAFT CURRENTS

Inter-bar currents exist in the rotor as long as the bars are not insulated, the end ring resistance is large and the inter-bar impedance is small. The inter-bar currents, also known as cross-path currents do not follow the path in the cage. The current path is from bar to bar or from bar to shaft through the iron. The inter-bar impedance is usually considered as pure uniformly distributed contact resistance between the cage and the lamination. Results of measurements published by Christofides [53] show that the inter-bar impedance is almost independent of frequency for frequencies up to several hundreds of hertz. The reactive component of the inter-bar impedance is small when compared with the resistive

component. Thus, the inter-bar impedance is largely resistive for frequencies within the normal operating condition of the machine. This is especially true in machines with aluminum cages wherein partial insulation is achieved via oxidation of the aluminum. The oxidation may not be uniform and hence there will be large variations in the magnitude of the insulation for different points in the same rotor. The oxidation build up on the bar surfaces gives rise to higher bar/core contact resistance. The contact resistance becomes non-linear [53] when large inter-bar currents flow. When the motor is running at rated speed the contact resistance may be assumed to be linear.

In large machines, the reactive component of the inter-bar impedance may be, in certain cases, of similar magnitude to that of the resistive component and thus may not be neglected [54]. Weppler [54] takes into account the effect of inter-bar currents by using a complex skew factor for the fundamental wave and higher harmonics.

When a squirrel cage machine is running, a net induced voltage exists which acts across the iron between adjacent bars. If the insulation between bars and iron is imperfect, this voltage will cause circulating currents from bar to bar across the rotor iron, resulting in axial flux along the shaft as shown in Figure 5.5.

A study by Kerszenbaum and Landy [55] showed that there is a substantial increase in inter-bar currents in machines with broken bars if the bars are not insulated. The low ratio of inter-bar to rotor bar impedance is shown to be the cause of the large inter-bar currents in non-insulated cages having broken bar and/or end rings. The inter-bar currents vary with the slip and may be large in highly rated machine. This inter-bar current, if substantial, can

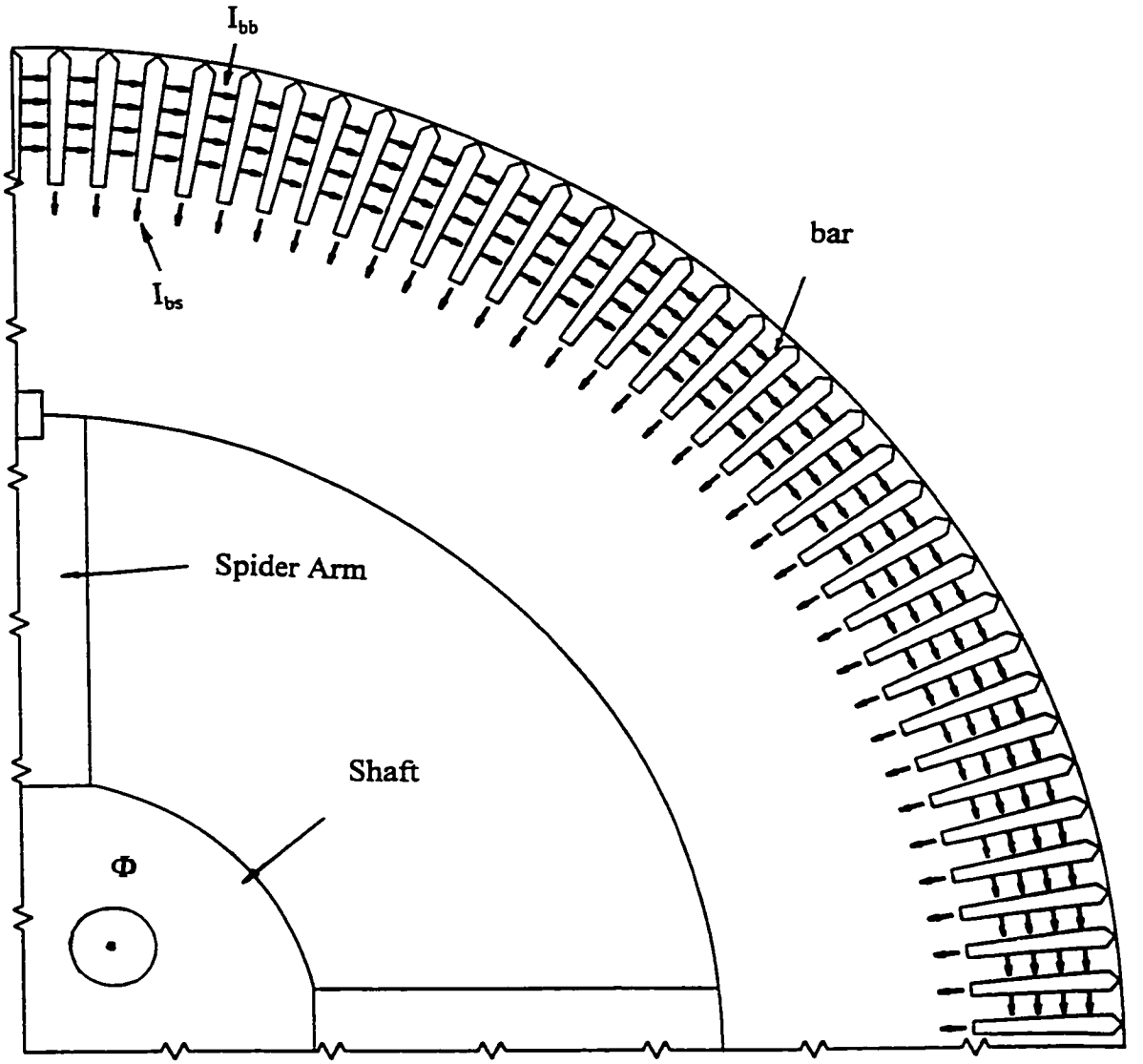

Figure 5.5: Representation of Interbar Current and Axial Flux

result in axial flux flowing in the shaft. Further work by Walliser and Landy [56] showed that the fundamental frequency side-bands do indeed get smaller if the inter-bar currents are present in the rotor. They suggested that current side-bands higher up in the frequency spectrum are present and must be monitored in order to obtain a more accurate indication of the existence of the broken bars.

Bearing insulation is only effective against shaft current but not so with axial flux. Axial flux can be reduced by installation of a copper ring around the shaft. However, this method of axial flux reduction is only effective against the fundamental component of the axial shaft flux; it does not eliminate the high frequency component of the axial flux. Localized bearing current is present in a machine with axial shaft flux. The localized voltage developed across the thin oil film may be sufficient to break down the oil film and hence shaft currents arc across the bearing clearance and damage the babbitt surface.

5.5 EFFECTS OF BROKEN OR FRACTURED ROTOR BARS ON SHAFT CURRENT

Electromagnetic asymmetries in an induction machine give rise to additional time harmonics in the spectrum of the stator winding current. If the rotor of a machine is completely symmetrical with no broken bars as shown in Figure 5.6, the forward rotating fields add while the backward rotating fields cancel. However, an asymmetrical rotor will not result in all the backward rotating fields being canceled. The effects of these backward rotating fields are used to detect broken bars. Broken or fractured bars and end rings as shown in Figure 5.7, induce stray flux mainly at the rotor core end. As a result the motors

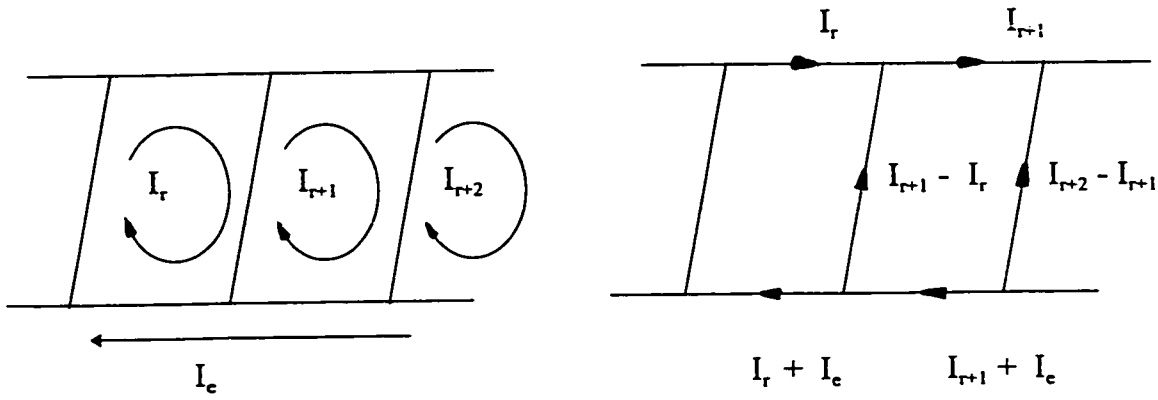

Figure 5.6: Healthy Rotor Bar and Current Distribution

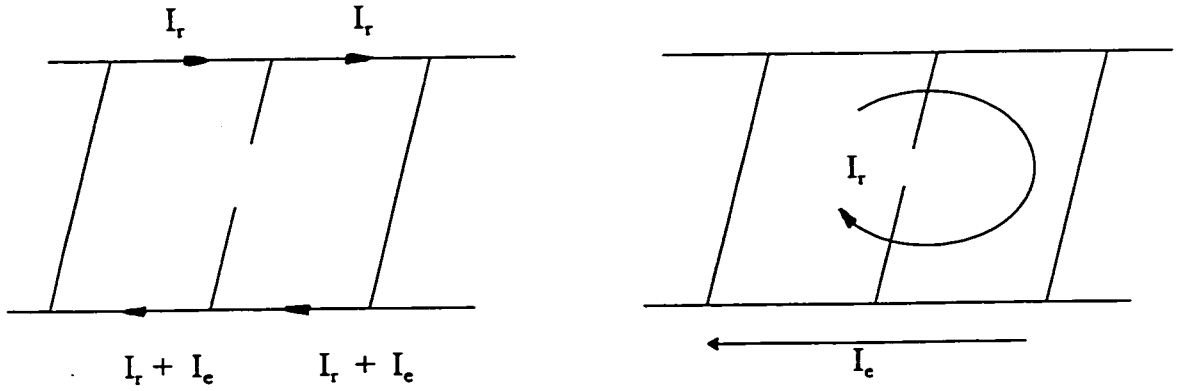

a) Broken Bar

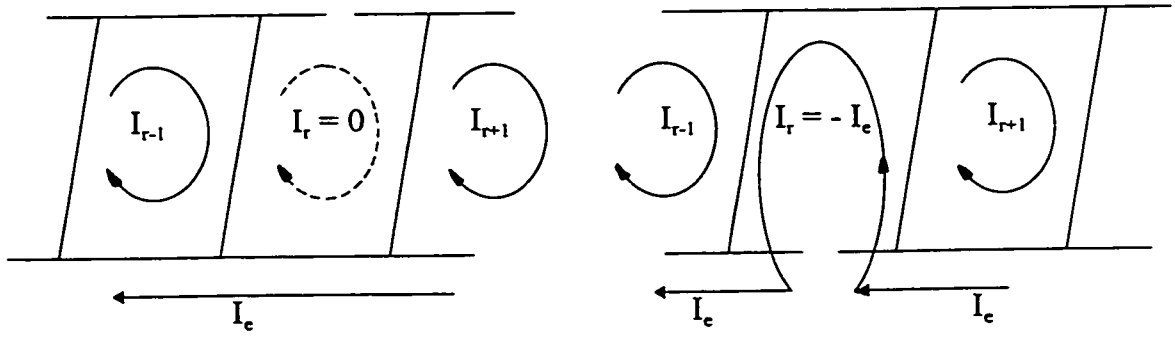

b) Broken End Rings

Figure 5.7: Broken Rotor Bar and End Rings and Current Distributions

can experience excessive vibration, noise and arcing during motor starting. It is important to ensure that the stray flux on the rotor shaft is minimum. Excessive amount of this homopolar flux can cause localized bearing currents in the journal-bearing region. These effects become noticeable when the incipient fault grows to involve several broken bars.

A broken bar may be distinguished from a rotating asymmetry by analysis of the high frequency content. An asymmetry will typically result in smooth variation of the air gap flux density and hence the upper harmonic content will be low. On the other hand, a broken bar, a localized effect, will result in large upper harmonics [57, 58]. The fundamental component of broken bar fields is always two pole. This fundamental component may be resolved into oppositely directed traveling waves of 2 pole length and slip frequency. For 2 pole motor, the fundamental forward rotating wave will have the same speed as the normal slip rotor current wave and will be lost in the normal line frequency components. The counter-rotating wave will be traveling at slip speed in the opposite direction, giving rise to twice slip frequency lower side-band of the line frequency. For a machine with 4 or more poles, the fundamental fault flux waves will be traveling much slower than the normal fluxes and will appear as a lower side-band near line frequency.

The rotor fault analysis by Itzhak Kerszenbaum [59] and Deleroi [60] are important to the understanding of the effects of rotor conditions on shaft current and are repeated in this chapter.

5.5.1 ITZHAK KERSZENBAUM'S ANALYSIS [59]

The proposed analysis of electromagnetic asymmetries is based on the unbalance in the rotor currents giving rise to positive and negative sequence components. The fundamental stator space MMF wave of wavelength λ^{l}_{s} rotates with a speed U_{is} relative to the stator. Then the speed of the k^{th} space harmonic field is

$$U_{ks} = \frac{U_{is}}{k} \qquad (5.20)$$

As the rotor moves with the speed U_r with respect to the stator, the relative speed of the stator produced "k" harmonic fields with respect to the rotor will be

$$U_{kr} = \frac{U_{is}}{k} - U_r \qquad (5.21)$$

These stator harmonic fields will induce electromotive forces (EMFs) and hence currents in the rotor circuit. These currents will have frequencies given by:

$$f_{kr} = \frac{U_{kr}}{\lambda^{l}_{k}} \qquad (5.22)$$

where $\lambda^{l}_{k} = \frac{\lambda^{l}_{s}}{k}$, the wavelength of the harmonic field.

If the rotor is completely symmetrical the forward rotating fields add while the backward rotating fields cancel. These rotor currents will not be balanced when there is imbalance in the rotor cage, for example if a broken bar exists. Hence, the unbalanced rotor currents will contain both the positive and negative sequence components. The positive sequence components produce some fields that rotate in the direction of the rotation and some fields

that rotate backwards. The negative sequence field components will produce fields that rotate in the opposite rotation to the positive sequence produced fields. The speed of these components relative to the rotor is given as

$$U_{zr} = \pm \frac{U_{kr}}{z} \qquad (5.23)$$

where z, the rotor harmonic order, is equal to 6g + 1 and g equals 0, ± 1, ±2, ±3...

With respect to the stator the speeds of these waves are:

$$U_{zrs} = U_r \pm U_{zr} \qquad (5.24)$$

The +/- signs take account of the respective direction of rotation of the field due to the positive and negative sequence rotor currents. These currents in the rotor circuit will induce EMF and hence current back into the stator primary winding. These induced currents will have frequencies given by

$$f_i = \frac{U_r \pm U_{zr}}{\lambda_k^l}$$

or

$$f_i = \frac{|k|}{\lambda_s^l} \frac{\left[k(z \mp 1)(1-s) \pm 1 \right]}{z\,k} U_{is} \qquad (5.25)$$

Considering the case of space harmonics of stator magnetomotive force (MMF) to be equal to the rotor harmonics, a condition necessary for the production of torque, the frequencies of the induced currents in the stator winding due to both positive and negative sequence currents in the rotor circuit are by equation (5.26).

$$f_I = f\,\frac{k(z \mp 1)(1-s) \pm 1}{z}$$

$$= f\,(z \mp 1)(1-s) \pm 1$$

$$= f\left[z(1-s) \pm s\right] \qquad (5.26)$$

where $f = U_{is} / \lambda l_s$.

The frequencies given in equation (5.26) are similar to frequencies of the spectral components in the air gap flux as given by Deleroi [60]:

$$f_{broken} = \left(\frac{v(1-s)}{p} \pm s\right) f \qquad (5.27)$$

where $v = (6g + 1)\,p$ and $g = 0, \pm 1, \pm 2, \pm 3$, etc.

5.5.2 DELEROI'S ANALYSIS [60]

In his analysis, Deleroi describes the rotor as a set of meshes, each mesh having identical impedances. Each mesh consists of resistance and leakage reactance of the rotor bars, end-ring sections as well as air gap field inductances. He further assumes that the stator currents are decoupled from the rotor, that is, there is no reaction on or from the stator current distribution. He assumes that the air gap is smooth on both sides, that is slot permeance variation is neglected. Skew is assumed to be zero and end effects are neglected. All the magnetics are assumed to be linear, that is no saturation, so that superposition applies. By the principle of superposition, the current in the broken bar is assumed to be the sum of the currents in that bar if it were not damaged, and a fault current

of equal magnitude but in the opposite direction. The fault current will have the effect of setting the current in the broken bar to zero and increasing the currents in the two adjacent bars. There is a phase shift between adjacent bars. The rotor MMF will then be the sum of the main forward rotating waves and the MMF waves derived from the circulating current due to the broken bar.

The air gap flux density caused by the additional fault current will pulsate at slip frequency. Neglecting the slight phase difference between the two loop currents, Fourier decomposition of the air gap flux density waveform yields

$$B^{bb}(\theta_r) = \sum_{n=1}^{\infty} B_{bb} \cos\left(s\omega t - \alpha_{bb}\right) \cos\left(n\Omega_r + n\kappa\right) \qquad (5.28)$$

where α_{bb} = the phase angle between the stator air gap field and the rotor air gap field,

κ = the spatial position of the bar,

$\Omega_r = \Omega - \omega_r t$

The flux density when transposed back to the stator frame is

$$B_r^{bb}(\Omega) = \sum_{n=1}^{\infty} B_{rbb} \cos\left(s\omega t - \alpha_{bb}\right) \cos\left(n\left[\Omega - \frac{\{1-s\}}{p}\omega t\right] + n\kappa\right)$$

$$= \sum_{n=1}^{\infty} \frac{B_{rbb}}{2} \left[\begin{array}{l} \cos\left(\left[s + \frac{n}{p}(1-s)\right]\omega t - n\Omega - \alpha_{bb} - n\kappa\right) \\ + \cos\left(\left[s - \frac{n}{p}(1-s)\right]\omega t + n\Omega - \alpha_{bb} + n\kappa\right) \end{array}\right] \qquad (5.29)$$

The components of this expression of air gap harmonic flux density distribution will induce EMFs in the stator winding when the spatial flux harmonic matches the spatial

winding harmonic. The main winding harmonic pole pair is p and hence equation (5.29) simplifies to equation (5.30).

$$B_r^{bb}(\Omega) = \frac{B_{rbb}}{2}\left[\begin{array}{l}\cos\left(\omega t - p\Omega - \alpha_{bb} - p\kappa\right) \\ + \cos\left(\left(1-2s\right)\omega t + p\Omega - \alpha_{bb} + p\kappa\right)\end{array}\right] \qquad (5.30)$$

Equation (5.30) indicates that (1-2s) f sideband currents are produced in the stator winding. The sideband current has a magnitude that is proportional to the air gap flux and hence the line voltage at a set speed. Torque ripple and saturation effects are considered negligible in the analysis. This equation verifies the research by Williamson [61] who showed that in neglecting saturation, the lower sidebands are dominant.

With low inertia, the torque ripple effect must be considered. As reported by Dorrell [62], the effect of the torque ripple at twice the slip frequency results in the production of lower and upper sideband currents of the same frequency as shown in equation (5.31)

$$\begin{aligned} B^f(\Omega) &= B_r^f \cos\left(\omega t - p\Omega - \alpha\right) \\ &\quad - \frac{p\Delta B_r^f}{4s^2\omega}\left[\begin{array}{l}\cos\left[\left\{1-2s\right\}\omega t - p\Omega - \alpha_r + \alpha_g + \alpha_{bb} - p\kappa\right] \\ + \cos\left[\left\{1+2s\right\}\omega t - p\Omega - \alpha_r - \alpha_g - \alpha_{bb} + p\kappa\right]\end{array}\right] \end{aligned} \qquad (5.31)$$

When the line voltage is high or when the inertia is low, this torque ripple will attenuate the lower side-band current in the stator winding. The upper side-band current will dominate. In the case of low voltage or high inertia the lower side-band current dominates. Thomson et. al. [63, 64] and Tavner [65] arrived at the same conclusion of upper and lower side-bands given in equation (5.31).

When core saturation and tooth saturation effects as described in section 4.5 are considered the rotor air gap field is defined by equation (5.32).

$$B_r^{bb}(\Omega) = \sum_{n=1}^{\infty} \frac{B_{rbb}}{2} \left[\begin{array}{l} \cos\left(\left[3s + \frac{n}{p}(1-s) \right] \omega t - n\Omega - \alpha_{bb} - n\kappa \right) \\ + \cos\left(\left[3s - \frac{n}{p}(1-s) \right] \omega t + n\Omega - \alpha_{bb} + n\kappa \right) \end{array} \right] \qquad (5.32)$$

When n equals p, upper side-band currents with frequencies of (1+2s) f and (1+4s)f are obtained. Air gap harmonics due to tooth or core saturation can also develop the upper side-band (1+2s)f. For higher stator winding harmonics such that n = 5p, 7p, etc. a series of side-band currents with frequencies (5-4s)f, (5-6s)f, (7-6s)f, etc. is formed. Taking the slot harmonics into account, the rotor asymmetry modulated air gap field is given as:

$$B_r^{bb}(\Omega) = \sum_{n=1}^{\infty} \frac{B_{rbb}}{2} \left[\begin{array}{l} \cos\left(\left[\frac{qR(1-s)}{p} + n_{ws}\, s + \frac{n}{p}(1-s) \right] \omega t - n\Omega - \alpha_{bb} - n\kappa \right) \\ + \cos\left(\left[\frac{qR(1-s)}{p} + n_{ws} s - \frac{n}{p}(1-s) \right] \omega t + n\Omega - \alpha_{bb} + n\kappa \right) \end{array} \right]$$

(5.33)

where n_{ws} is the saturation factor and n = p, 5p, 7p, 11p,...

5.6 SUMMARY

In this chapter, rotor eccentricity and asymmetry have been shown to introduce harmonic pole pairs and corresponding frequencies as shown in Table 5.1. Furthermore, these rotor anomalies result in net circulating flux around the shaft in machines with or without the segmental joints in either the stator or rotor. Stator current spectral analysis is

commonly used to detect the presence of these anomalies. In Chapter 6, the spectral analyses of the measured shaft voltage, current and flux will be used as indications of the rotor fault conditions. From Table 5.1 it is clear that as the number of poles increases the effect of rotor eccentricity on the magnitude of shaft current decreases.

Origin of Fields	Primary Fields	Harmonic Fields Caused by Damping Rotor Currents	
		Pole Pairs	Frequency
Eccentricity Equation (5.9)	$B(\Omega, t) = B_{P+1}\cos\left(\left[1+n_e\frac{(1-s)}{p}\right]\omega t - (p+1)\Omega\right)$ $+ B_{P-1}\cos\left(\left[1-n_e\frac{(1-s)}{p}\right]\omega t - (p-1)\Omega\right)$ $n_e = 0$ static eccentricity $n_e = 1$ dynamic eccentricity	$1 \pm n_e/p + [K_j R/p]$ $K_j = 1, 2, 3,..$	$[1+\{[K_j R/p] \pm n_e/p\}(1-s)]f$ $K_j = 1, 2, 3,\ldots$
Eccentricity and Saturation Equation (5.19)	$B(\Omega, t) = B_{P+1}\cos\left(\left[1+2n_s+n_e\frac{(1-s)}{p}\right]\omega t - (p+1+2n_s)\Omega\right)$ $+ B_{P-1}\cos\left(\left[1-2n_s-n_e\frac{(1-s)}{p}\right]\omega t - (p-1-2n_s)\Omega\right)$ $n_s = 1, 2, 3,\ldots$	$k_i + 1 + (\pm n_e/p) + K_j R/p$ $K_j = 1, 2, 3,\ldots$ $k_i = 3, 5, 7$	$[k_i+1+\{[K_j R/p] \pm n_e/p\}(1-s)]f$ $K_j = 1, 2, 3,\ldots$ $k_i = 3, 5, 7$
Eccentricity and MMF Phase belt and Saturation Equation (5.19)	$B(\Omega, t) = B_{P+1}\cos\left(\left[1+2n_s+n_e\frac{(1-s)}{p}\right]\omega t - (n_{st}\,p+1+2n_s)\Omega\right)$ $+ B_{P-1}\cos\left(\left[1-2n_s-n_e\frac{(1-s)}{p}\right]\omega t - (n_{st}\,p-1-2n_s)\Omega\right)$ $n_s = 1, 2, 3,\ldots$	$K_j R/p \pm 2n_s \pm n_e/p \pm n_{st}$ $n_s = 1, 2, 3,\ldots$ $n_{st} = 2mK_i \pm 1$ $K_i, K_j = 1, 2, 3,\ldots$	$[k_i+1+\{[K_j R/p] \pm n_e/p\}(1-s)]f$ $K_j = 1, 2, 3,\ldots$ $k_i = 3, 5, 7$

Table 5.1: Air Gap Fields of Induction Motor Under Rotor Fault Conditions

Eccentricity and MMF Phase belt, Stator Slots and Saturation Equation (5.19)	$B(\Omega, t) = B_{p-1}\cos\left(\left[1+2n_s+n_e\frac{(1-s)}{p}\right]\omega t-(n_{st}\,p+1+2n_s+hS)\Omega\right)$ $+B_{p+1}\cos\left(\left[1-2n_s-n_e\frac{(1-s)}{p}\right]\omega t-(n_{st}\,p-1-2n_s+hS)\Omega\right)$ $h = 1, 2, 3..,\ n_s = 1, 2, 3..$ $n_{st} = 2mK_i \pm 1$ $K_i, K_j = 1, 2, 3\ldots$	$K_jR/p \pm 2n_s \pm n_e/p \pm n_{st} \pm hS$ $h = 1, 2, 3..$ $n_s = 1, 2, 3..$ $n_{st} = 2mK_i \pm 1$ $K_i, K_j = 1, 2, 3\ldots$	$[k_i+1+\{[K_jR/p] \pm n_e/p\}(1-s)]f$ $K_j = 1, 2, 3....$ $k_i = 3, 5, 7$
Eccentricity and MMF Phase belt, Stator Slots and Saturation Equation (5.19)	$B(\Omega, t) = B_{p+1}\cos\left(\left[1+2n_s+n_e\frac{(1-s)}{p}\right]\omega t-(n_{st}\,p+1+2n_s+hS)\Omega\right)$ $+B_{p-1}\cos\left(\left[1-2n_s-n_e\frac{(1-s)}{p}\right]\omega t-(n_{st}\,p-1-2n_s+hS)\Omega\right)$ $h = 1, 2, 3$ $n_s = 1, 2, 3$ $n_{st} = 2mK_i \pm 1$ $K_i, K_j = 1, 2, 3\ldots$	$K_jR/p \pm 2n_s \pm n_e/p \pm n_{st} \pm hS$ $h = 1, 2, 3$ $n_s = 1, 2, 3$ $n_{st} = 2mK_i \pm 1$ $K_i, K_j = 1, 2, 3..$	$[k_i+1+\{[K_jR/p] \pm n_e/p\}(1-s)]f$ $K_j = 1, 2, 3....$ $k_i = 3, 5, 7$
Rotor Asymmetry Equation (5.29)	$B(\Omega, t) = B_{nu}\cos\left(\left[s+n\frac{(1-s)}{p}\right]\omega t - n\Omega\right)$ $+ B_{nu}\cos\left(\left[s-n\frac{(1-s)}{p}\right]\omega t - n\Omega\right)$ $n = p, 5p, 7p, 11p,\ldots$	-	-

(Continuation) Table 5.1: Air Gap Fields of Induction Motor Under Rotor Fault Conditions

CHAPTER 6

DESIGN OF EXPERIMENT AND RESULTS

6.0 INTRODUCTION

It has been well known since the 1900's that shaft current exists in electrical machines. Many authors [5-14] have described the causes and preventive methods as outlined in Chapter 2. However, the experimental results of many of these authors were not presented. In the limited number of experimental results presented, the shaft current measurement was carried out by inserting an ammeter in the circuit or using a shaft riding shunt. A novel method of shaft current measurement as described by the authors [66 - 67] in Chapter 3 was used in the experimental work. This method was demonstrated to be accurate compared to the conventional methods such as the ammeter method or the shunt method. The conventional methods disturb the conducting circuit.

Previously, the limited number of experimental results were based on research work on small ac machines operating on grease lubricated anti-friction bearing systems. There were no experimental results on large oil lubricated machines. The experimental work carried out in this chapter addresses this. A large oil ring lubricated machine, Appendix 1, was used. Also, the measurement was done based on steady state running conditions. The transient condition was not considered. The importance of oil film development during the transient condition will be demonstrated in this chapter.

The objective of each of the tests is given and the results of each test are fully discussed in relation to the hypotheses given in Chapters 4 and 5.

6.1 PURPOSE OF THE EXPERIMENTAL WORK

A large 3 phase, 8 pole, 2611 kW, 4000V and 60 Hz induction motor with segmental punchings on the stator and ring punchings on the rotor was used in the experimental work. This machine exhibits symptoms of shaft currents as demonstrated by the damage to the babbitt of both bearings of Figure 6.1 and the rub marks on the shaft journal of Figure 6.2 (a). Visual inspection of the lead-based bearing babbitt reveals spark tracks, stitch tracks and scotch marks in the circled areas numbered 1 to 5 of Figures 6.1 (a) and (b). Figure 6.2 (b) shows the discolored oil that may possibly be due to oxidation or contamination by arc debris. Further investigation of the circled areas of the bearing babbitt under the microscope by the metallurgist confirms the spark track and also the pitting of the bearing babbitt. The damages observed under 60X microscopic view were photographed as shown in Figures 6.3 - 6.7. Figure 6.3 is an example of pitting-type damage to this large induction machine's bearings. Pitting has round shiny bottoms. Figure 6.4 is an example of spark tracks with molten craters. Figures 6.5 - 6.7 are example of stitch tracks caused possibly by intermittent arcings. A possible consequence of arcing across the shaft journal and the bearing is the deterioration of the lubrication oil and the contamination of the lubrication oil by the arc debris. The lubrication oil is discolored with contamination observed at the bottom of the oil sump. As such a set of experiments were designed to determine the possible causes of the bearing damage - mechanical or electrical in nature.

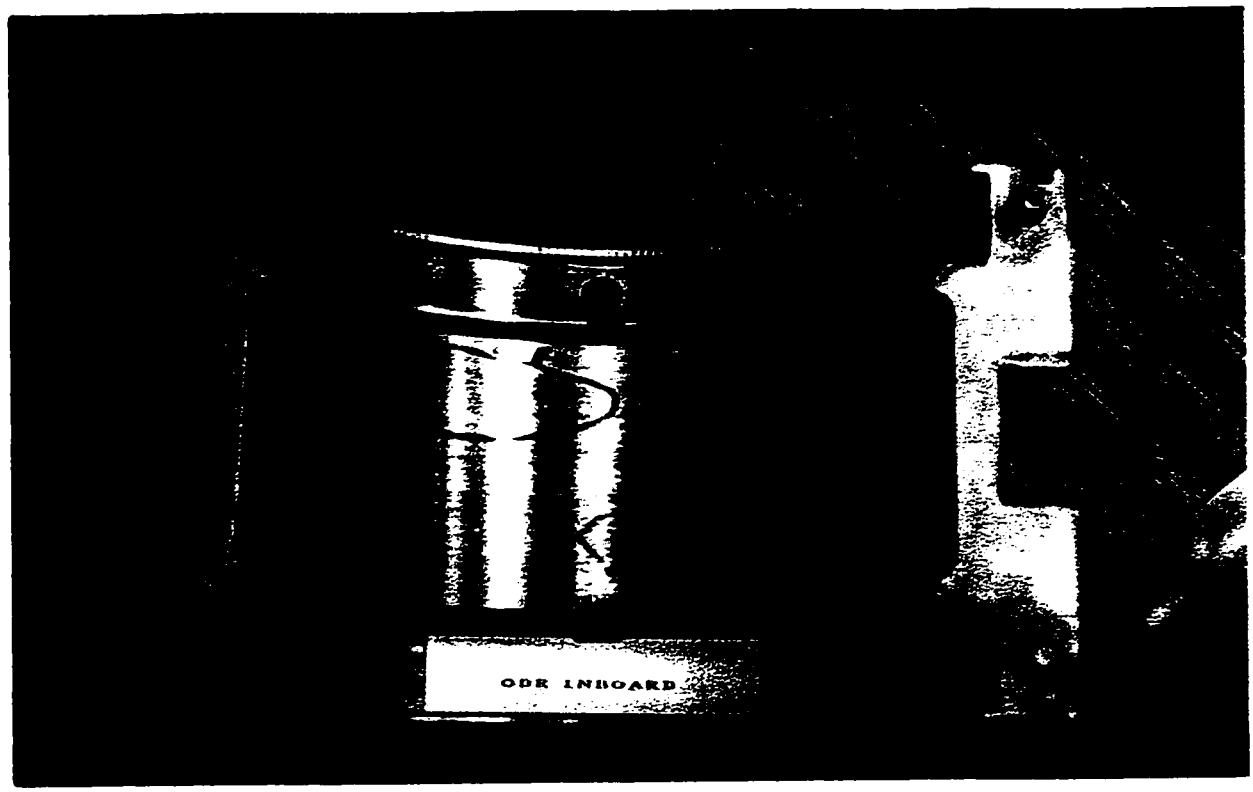

a) ODE Bearing

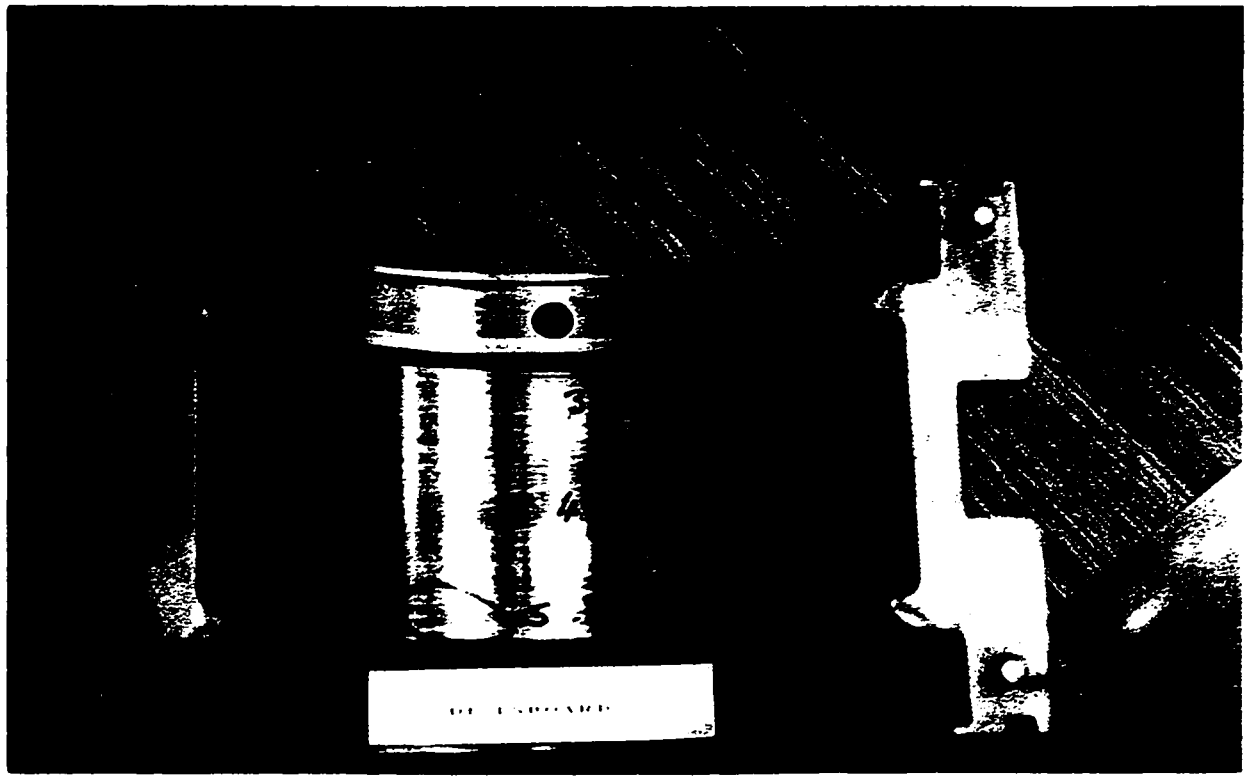

b) DE Bearing

Figure 6.1: Bearing Babbitt Damage.

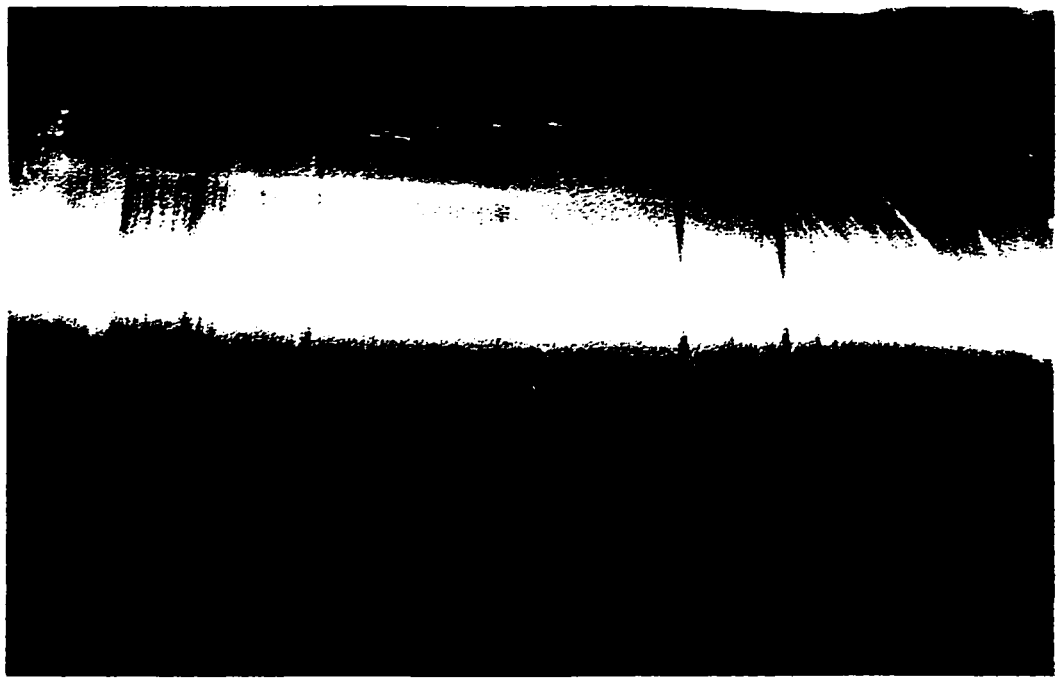

a) Rub Marks On the Shaft Journal.

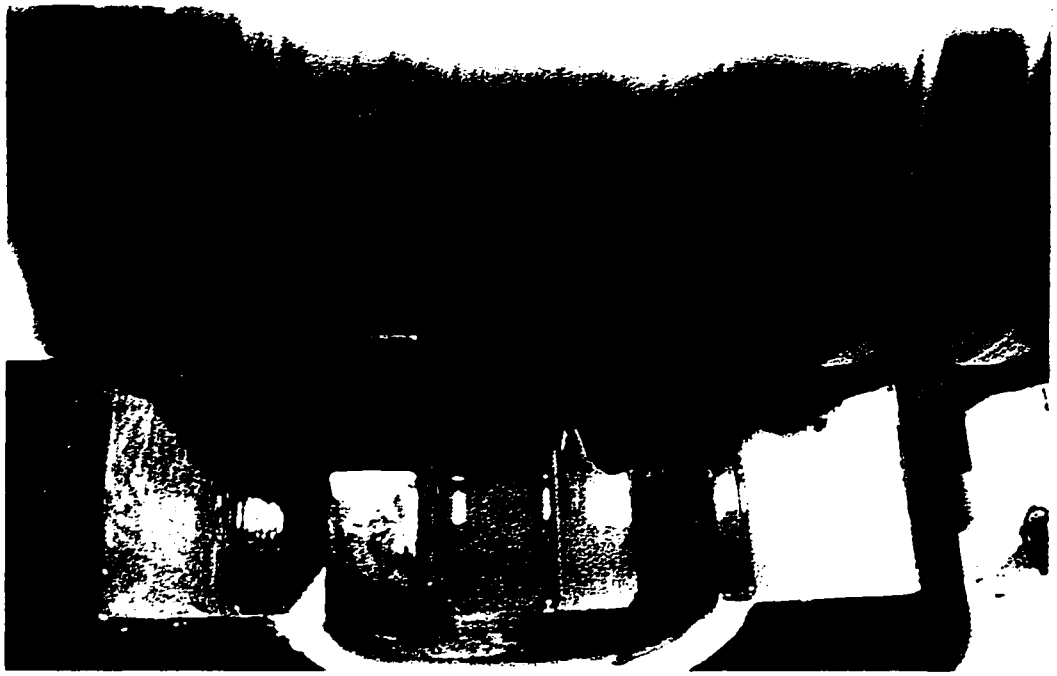

b) Darkened Colored Oil.

Figure 6.2: Rub Marks on the Shaft Journal and Darkend Colored Oil

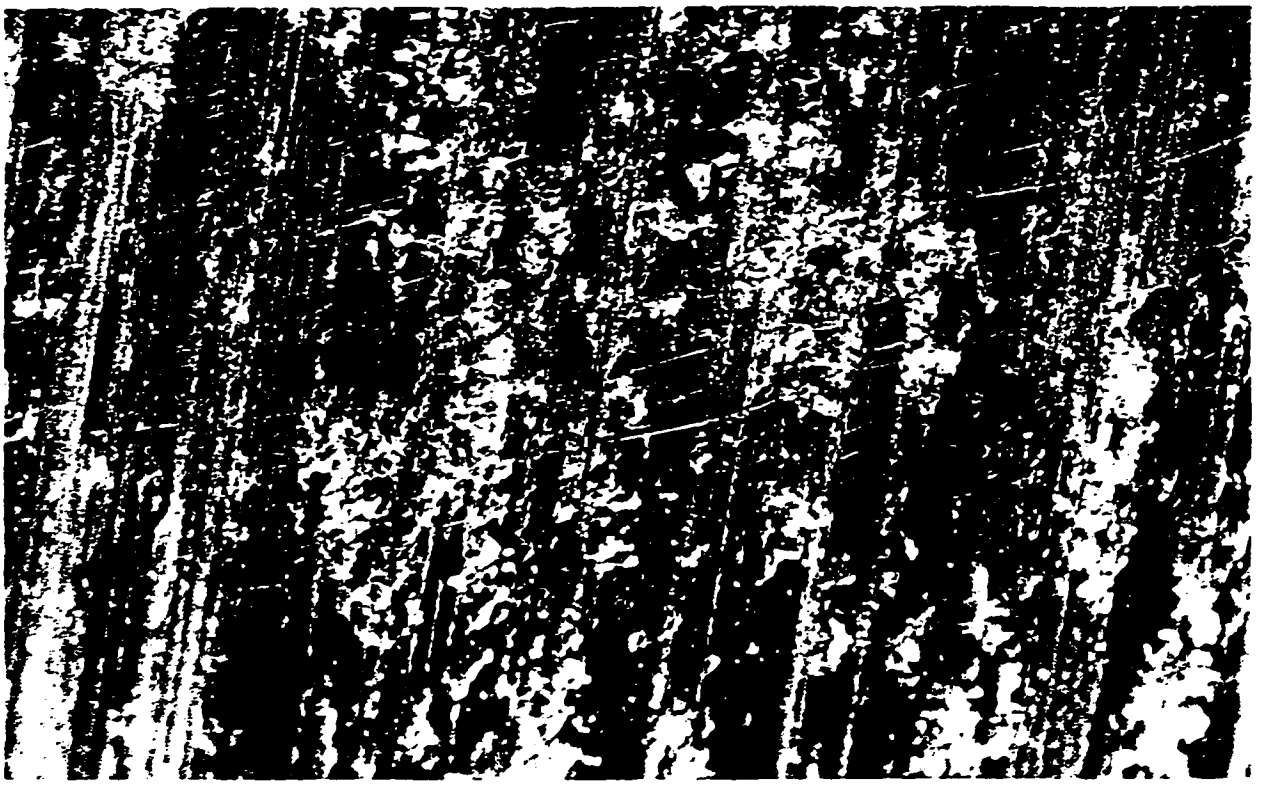

Figure 6.3: Microscopic View of the Area 1 in Figure 6.1

Figure 6.4: Microscopic View of the Area 2 in Figure 6.1

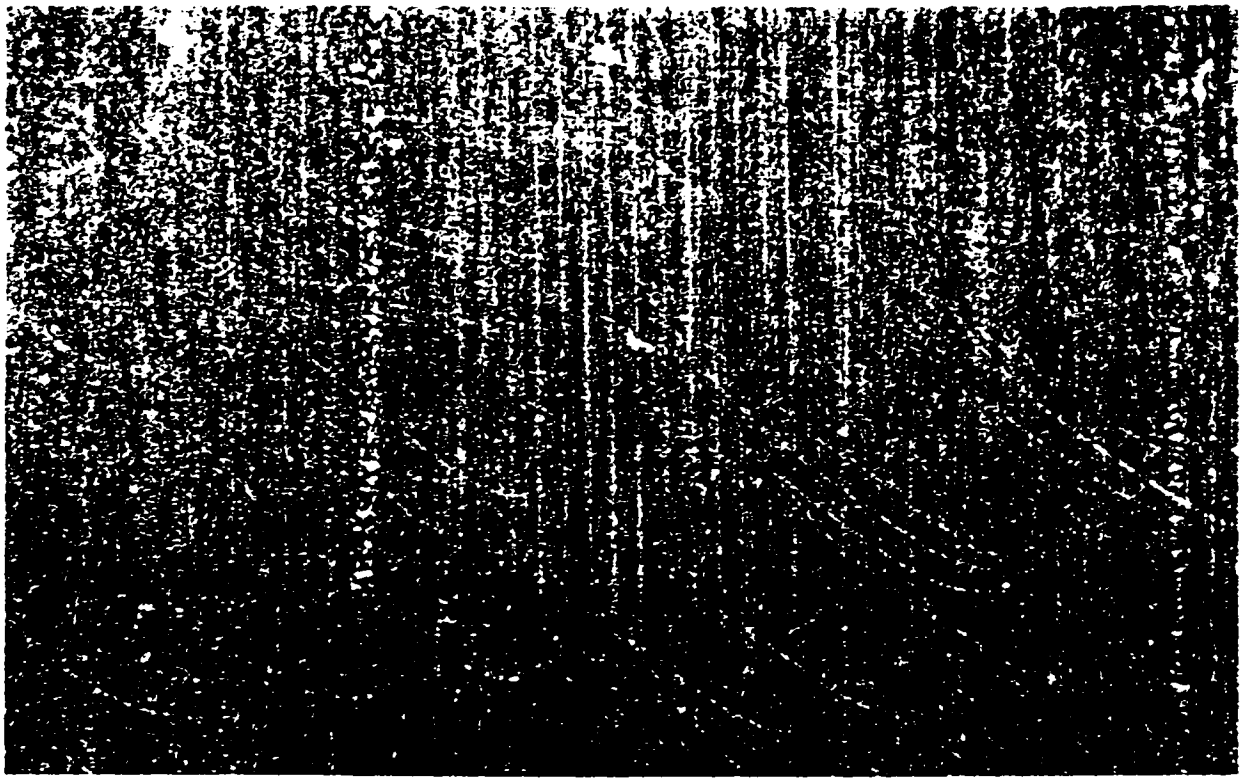

Figure 6.5: Microscopic View of the Area 3 in Figure 6.1

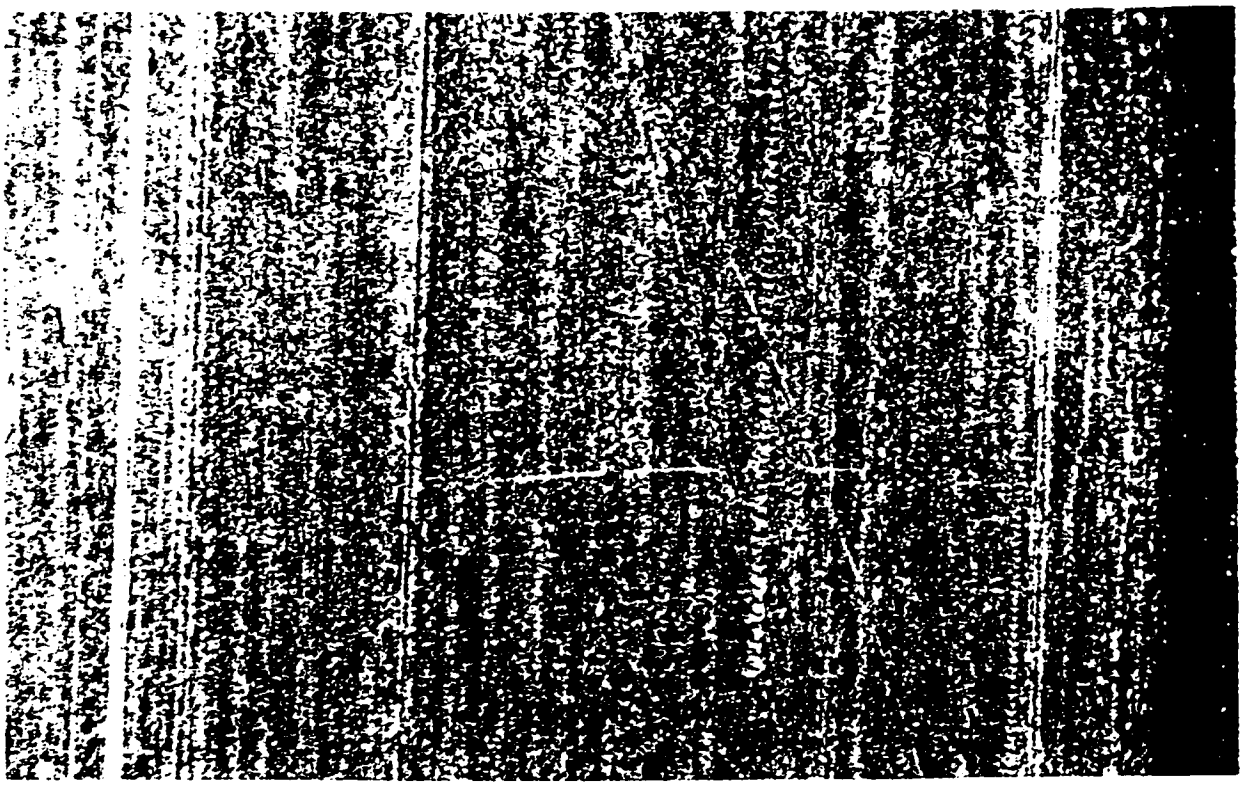

Figure 6.6: Microscopic View of the Area 4 in Figure 6.1

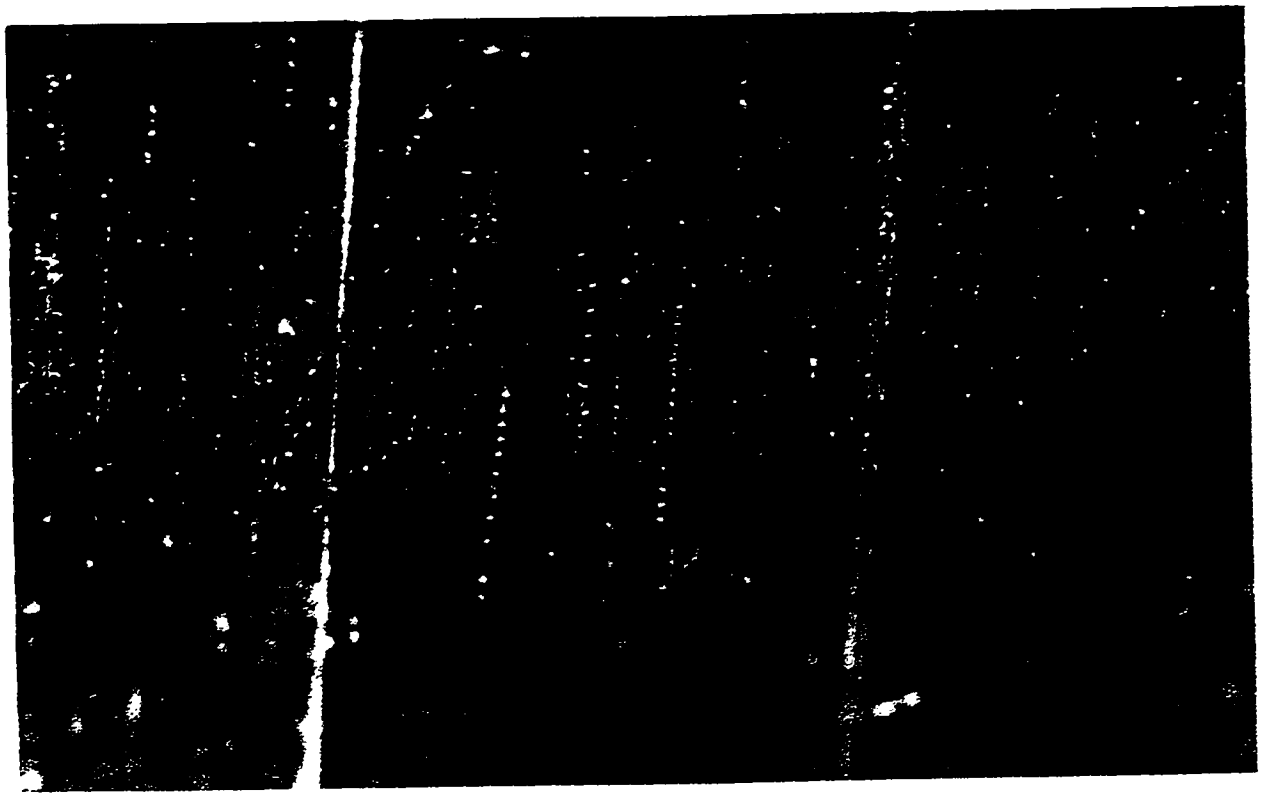

Figure 6.7: Microscopic View of the Area 5 in Figure 6.1

6.2 DESIGN OF EXPERIMENT

The experimental work consists of determining the cause of the bearing damage - mechanical or electrical in nature and determining the factors contributing to the cause(s) of the bearing damage:

6.2.1 Mechanical Test

A mechanical no-load test was conducted to determine whether the cause of the bearing damage was mechanical in nature. In this test, the test machine is brought up to no-load steady state running condition using a dc motor. The test machine is de-energized throughout the test. An oil sample was collected and an oil analysis was conducted to determine possible oxidation of oil. The bearings are inspected to determine any damage.

6.2.2 Acceleration Tests

In this series of tests, the magnitude and harmonic components of shaft current were measured. These tests provide useful information on the possible causes of shaft current - joints, eccentricity, saturation, etc.

1. Determining the magnitude and harmonic components of shaft voltage and current in the test motor with non-insulated oil ring lubricated sleeve bearings. In this test, the shaft current was measured from start of acceleration to no-load steady state running condition. The measurement provides information on the magnitude of shaft current prior to oil film development and following oil film development and steady state running condition. This information assists in the assessment of the performance of the oil ring to deliver

sufficient oil to lubricate the bearing and build up an oil film to open circuit the shaft current path.

2. Determining the magnitude and harmonic components of shaft current in the test motor with insulated oil ring lubricated sleeve bearings; only the opposite drive end (ODE) bearing is insulated. The motor accelerates to no load speed with the rotor held at magnetic center throughout the speed range. A dc motor is coupled to the test motor in order that the rotor is held at magnetic center throughout the speed range. An insulated spacer is installed between the two shaft ends to ensure no closed circuit for shaft current flow. This test, together with the test with allowed shaft end play movement, helps in the understanding of the effect of end play motion prior to machine running at its magnetic center, on the occurrence and magnitude of shaft current.
3. Determining the magnitude and harmonic components of shaft current in the test motor with insulated oil ring lubricated sleeve bearings; only the opposite drive end (ODE) bearing is insulated. The motor initially is de-energized; a dc motor is used to accelerate the test motor to no load speed. The dc motor is de-energized and the test motor decelerates to around 50 rpm at which time the test motor is energized. Throughout the test the dc motor is coupled to the test induction machine. A tachometer was installed on the ODE of the drive motor to monitor the speed of the test machine. The test results enable the determination of the effectiveness of this method of built-up of oil film prior to start of acceleration of the test motor.
4. Determining the magnitude and harmonic components of shaft currents in the test motor with insulated oil ring lubricated sleeve bearings and shaft end play movement. Only the

opposite drive end bearing is insulated. This test will provide an indication of the effectiveness of the insulation used.

5. Determining the magnitude of shaft current in the test motor with forced lubricated sleeve bearings, oil rings installed, DE bearing non-insulated and ODE bearing insulated. This test will demonstrate that forced lubrication is not necessary as long as the bearing insulation is effective.

6.2.3 Locked Rotor Tests

1. Determining the magnitude and harmonic components of shaft current in the test motor with insulated oil ring lubricated sleeve bearing; only the opposite drive end bearing is insulated. The insulated drive end bearing is shorted through a shorting pin.
2. Determining the locked rotor torque and current. This test will provide an indication of the saturation of the machine during transient condition.

6.2.4 Bearing Insulation Thickness Tests

1. Determining the magnitude and harmonic components of shaft current in the test motor with insulated oil ring lubricated sleeve bearing; only the opposite drive end bearing is insulated. The insulated drive end bearing is shorted through a shorting pin. The bearing insulation thickness was varied in this test. Initially, the insulation test was performed on the machine with 0.762 mm bearing insulation design. Material was removed from the bearing insulation to obtain 0.381 mm and 0.254 mm bearing insulation designs. Metallic shims were used to replace the material removed. Tests was conducted at 60%, 80% and 100% of rated voltage.

6.3 INITIAL EXPERIMENTAL CONTROL CONDITIONS

Initial experimental conditions were rigorously controlled to ensure that consistent results are obtained, minimizing as much as possible the influence of randomness in the controllable factors. These conditions are:

1) A new set of bearings was used in the experimental work since any wear in the bearing babbitt can lead to bearing failure.
2) Initially the machine sits at its magnetic center position prior to acceleration of the machine. There is a complete circuit ring on the opposite drive end of the machine. Each phase of the machine has four parallel circuits which are connected to the circuit ring. The magnitude of shaft flux will be influenced by the initial position of the shaft.
3) Clean new ISO VG 68 turbine oil from the same oil drum was used for each test. Contamination in the oil may cause the bearing damage, enhancing the probability of shaft current flow.
4) All sensor leads are shielded with shields connected to a common grounding point.
5) All tests were conducted using the same 60 Hz sinusoidal supply source with negligible harmonic contents. This condition is necessary to ensure that the supply is not a factor in the bearing damage.
6) The Rogowski coil installed on the shaft was calibrated prior to the test. This is to ensure that the correct proportionality constant is available for accurate shaft current measurement.

6.4 EXPERIMENTAL RESULTS

6.4.1 AIR GAP MEASUREMENT

During the set-up of the machine for test, the air gap of the test machine was measured. The air gap of the test machine was measured at four locations, 90 degrees apart and at both ends of the machine. Then the machine was rotated 90 degrees manually and the air gap measured again. In this manner, the nominal air gap value could be obtained. The designed air gap value is 2.54 mm.

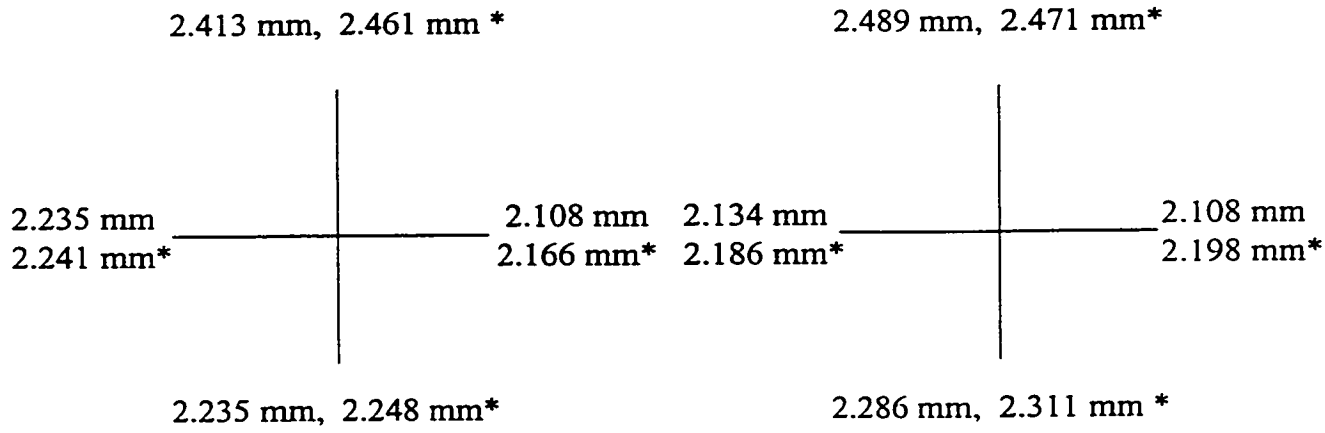

Figure 6.8: Air Gap Measurements at Drive End and Opposite Drive End Sections as Viewed From the Drive End.

The eccentricity of the machine is determined as a measure of air-gap symmetry deviation based on the direct measurement carried out at the end sections of the stator bore, the formula being as in equation (6.1)

$$\varepsilon = \frac{\delta_{max} - \delta_0}{\delta_0} \times 100\ \% \qquad (6.1)$$

δ_{max} is the maximum air gap measured and δ_0 the average air gap.

Based on equation (6.1) the drive end measurement indicates average air gap of 2.248 mm and air gap eccentricity of 7.34 % while the opposite drive end measurement shows average air gap of 2.254 mm and air gap eccentricity of 7.04%. A feeler gauge is used to determine the air gap. The thickness of the feeler gauge was determined to be accurate to within ± 0.00254 mm. Due to the epoxy layer on the rotor surface and stator bore surface, the errors on the air gap measurements at the four positions cannot be specifically stated. Hence, it is necessary to rotate the rotor 90 degrees manually and then measure the air gap again. The drive end average air gap is 2.279 mm and the opposite drive end average air gap is 2.292 mm. The air gap eccentricities are 7.95% and 7.83%, respectively.

The effect of eccentricities on the magnitude of shaft current in this test machine is negligible. As was determined in Chapter 5, the effect of eccentricities is a factor in the magnitude of shaft current only when the air gap eccentricities is at least 50%. Also, in Chapter 5, it was determined that as the number of poles of machine increases the effect of eccentricities decreases. The test machine is an 8 pole induction motor with 120 stator slots and 142 rotor slots. From Figure 5.4, considering static eccentricity or dynamic eccentricity, the effect of 7.95% eccentricity is negligible with permeance of orders of 14 or (S-R-2p) and 22 or (S-R). Hence, variation in the slot harmonics due to static eccentricity or side-bands due to dynamic eccentricity were not observed in the motor line current. Eccentricity is not a factor in the development of the shaft voltage.

6.4.2 OIL AND BEARING DAMAGE ANALYSIS

Clean oil samples and discolored oil samples were collected and analyzed to determine the possibility of oxidation of the lubrication oil and the constituents of the contamination [66,67]. The analysis results are given in Table 6.1.

The contaminants in the oil were separated by centrifuge and washed with petroleum ether to remove the oil. The material was then fired to burn off the organic matter. Finally the residue was analyzed using Scanning Electron Microscopy/Energy Dispersive Spectrometer. The residue was observed under microscope and photographed.

		Test Motor			
		Test 1		Test 2	
Type of Analysis	New Oil	DE Oil	ODE Oil	DE Oil	ODE Oil
Neutralization Number (ASTM D974-87) (mg KOH/g)	0.077	0.079	0.081	0.079	0.081
Saybolt Viscosity (SUS)	319	294	324	308	321
Kinematic Viscosity(mm^2/s) (ASTM D88-81)	68	63	69	66	67
ISO Viscosity Grade	ISO VG 68	ISO VG 68	ISO VG 68	ISO VG 68	ISO VG 68
Elemental Analysis	Ca, Si, Al, Na, S, Cl	Pb, Fe, Na, Ca, Si, Al, Cl,	Fe, Pb, Cu, Ca, Na, Si, Al, Cl	Ca, Al, Si, Pb, Cl, Na	Fe, Pb, Cu, Ca, Si, Al, Cl, Na

Table 6.1 : Oil Analysis of Clean Oil Sample and Discolored Oil Samples Taken From the Test Motor; DE - Drive End and ODE - Opposite Drive End.

Prior to test, a direct current motor was used to drive the induction machine up to rated no-load speed. The induction machine was not energized. The steady state running test (Test 1 in Table 6.1) lasted for four hours. Following the test, the oils in the DE and ODE oil sump were found to be milky colored. The oil was collected from both sumps and analyzed. The contaminants in the oil as shown in Figures 6.9 and 6.10 were also analyzed. The bearings were not damaged. It can be concluded that the cause of the bearing damage is not of mechanical nature; rather it is due to the presence of shaft current. The test was repeated for six hours until the oil in the oil sump was no longer discolored and there were no contaminants found in the oil. This test serves to minimize the influence of mechanical design on the validity of the test proper to determine the existence of shaft current.

Following the above test procedure, the induction machine with its ODE bearing insulated was started at 60%V and accelerated to the steady state no-load condition. The steady state no-load condition (Test 2 in Table 6.1) lasted for an hour. The oil was found to be " darkened " in color and contained contaminants as shown in Figures 6.11 and 6.12. The bearings were inspected and the bearing babbitts were found to be damaged. The damage on the bearing babbitt was viewed under microscope. The bearing damage is electrical in nature, pointing to shaft current as the cause of the damage. This is so in spite of the conclusion of the oil analysis in the next paragraph that indicates there was no oxidation of oil.

The maximum neutralization value for the ISO VG 68 oil used is 0.2 mg KOH/g. Its viscosity range at 40°C is 61.0 to 75.0 mm^2/s. The oil analysis from both tests indicates no oxidation of oil, otherwise the neutralization number would increase beyond 0.2 mg KOH/g and kinematic visosity above 75.0 mm^2/s. Calcium and silicon present as silicates may

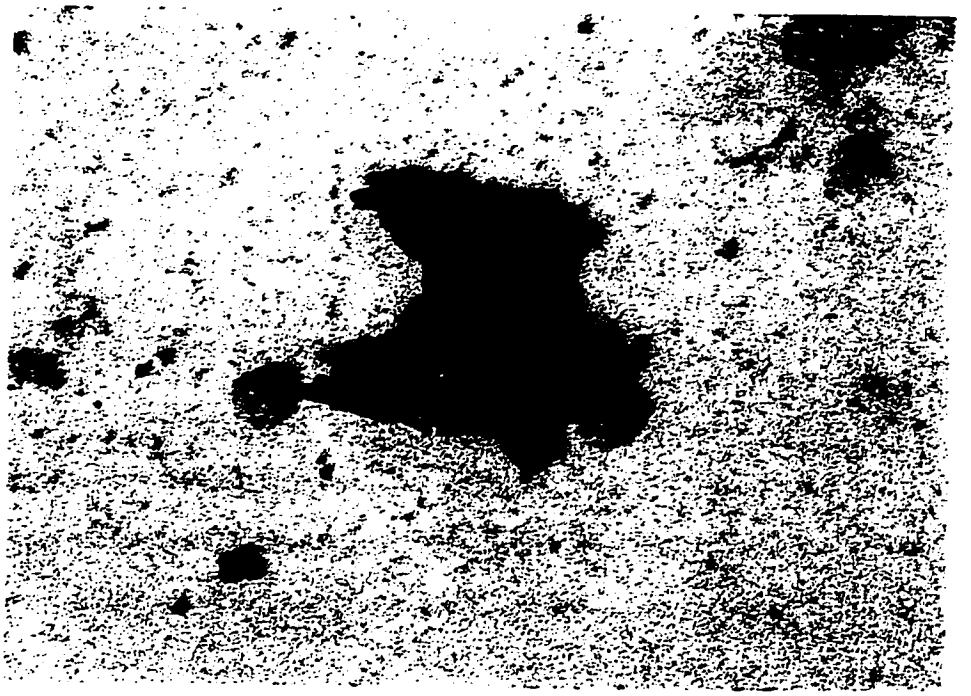

Figure 6.9: Contaminants in DE Bearing Housing; Induction Machine Driven Unenergised for Four Hours.

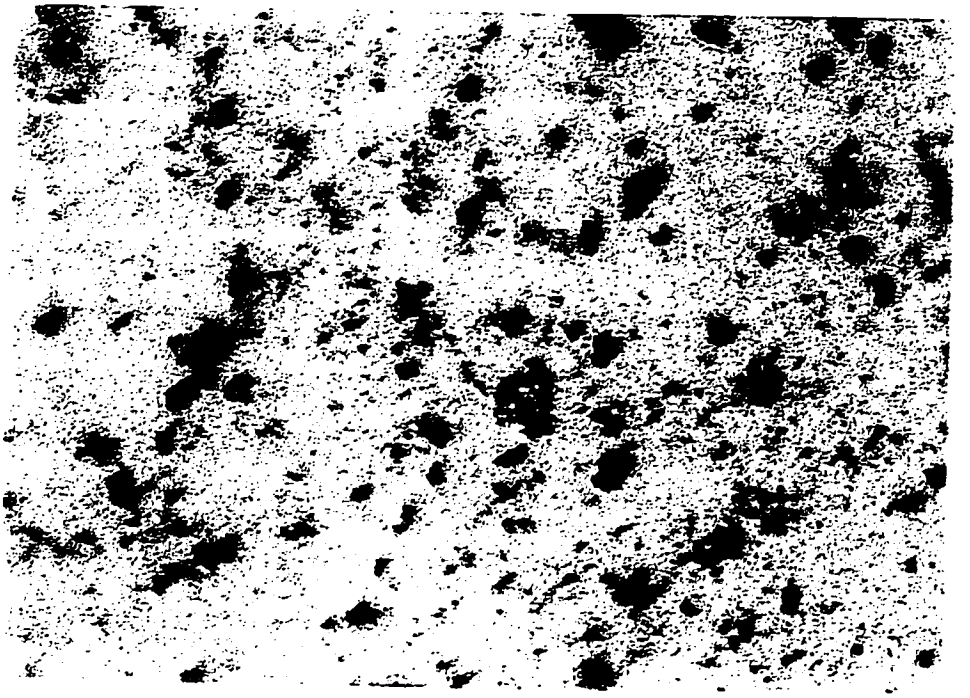

Figure 6.10: Contaminants in ODE Bearing Housing; Induction Machine Driven Unenergised for Four Hours.

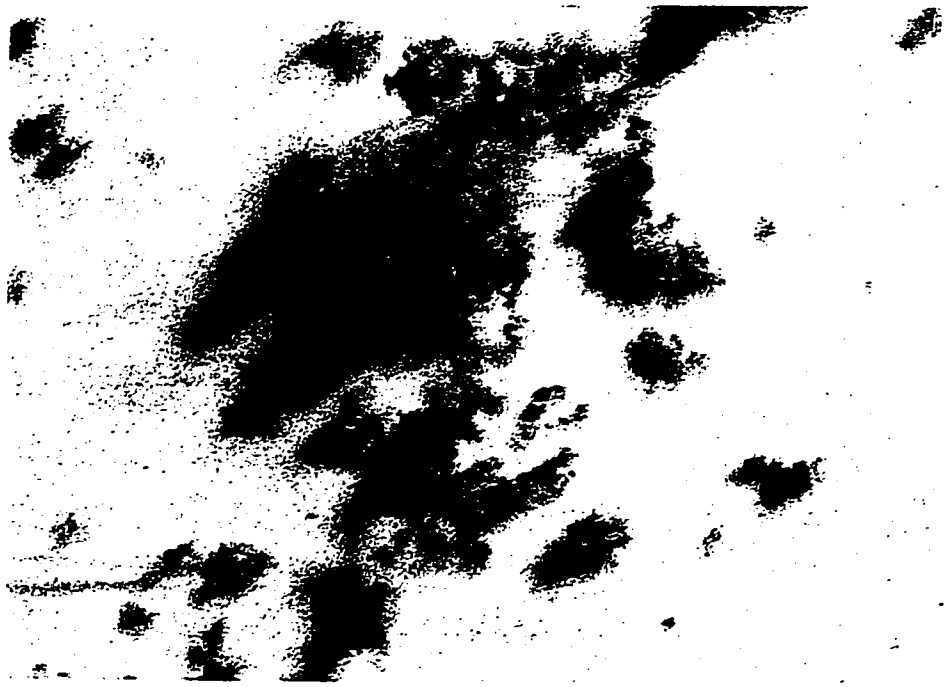

Figure 6.11: Contaminants in DE Bearing Housing; Induction Machine Energised at 60% Rated Line Voltage and Ran for an Hour.

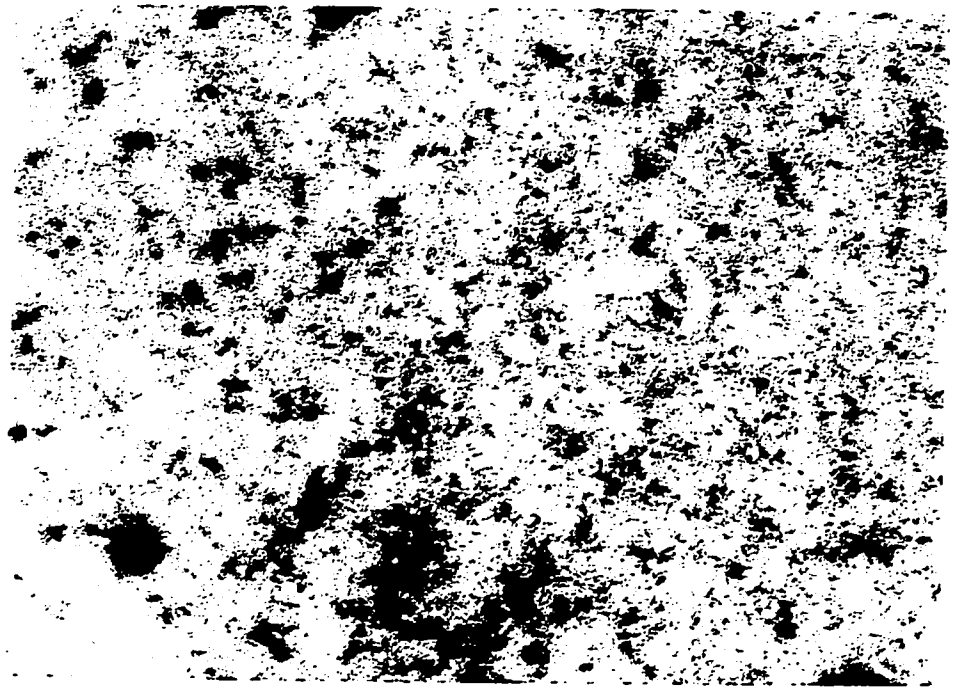

Figure 6.12: Contaminants in ODE Bearing Housing; Induction Machine Energised at 60% Rated Line Voltage and Ran for an Hour.

originate from the bearing insulation. Aluminum was present in all the oil samples including the clean unused oil. The presence of aluminum may be due to the oil itself or as an oxide from the sample container. The lead rich particles likely comes from the lead base babbitt. The copper particles originate from the bronze oil ring. These contaminants caused the oil to have "darkened " color.

6.4.3 SHAFT CURRENT MEASUREMENT

6.4.3.1 Both Bearings Non-Insulated, End-Play Movement, No-Load Condition, Oil Ring Lubrication.

The large induction machine has both bearings insulated. In this test, the grounding pins at both the DE and ODE housing were screwed down, touching the metallic base of the bearings and hence bypassing the insulating materials of the bearings. Then the large induction machine, both bearings non-insulated, is accelerated at no load rated condition to rated speed. The Rogowski coil induced voltage waveform shown in Figure 6.13 indicates that prior to partial development of an oil film, the average value of shaft current is 90A. Note that power is applied at time t = 1.61s. The shaft current occurs in the period t =1.61s to t = 1.90s with subsequent reduction in the current following development of the oil film. At close to standstill condition, there is metal-to-metal contact between the shaft journal and the bearing surface. An oil film had not developed. Figures 6.14 (a, i) and (b, i) show the expanded scale of the DE and ODE shaft current waveform prior to the development of the oil film. The DE Rogowski coil has a calibration scale of 11.02 mV/A while the ODE Rogowski coil has a calibration scale of 13.72 mV/A. As expected, both Rogowski coils produce similar

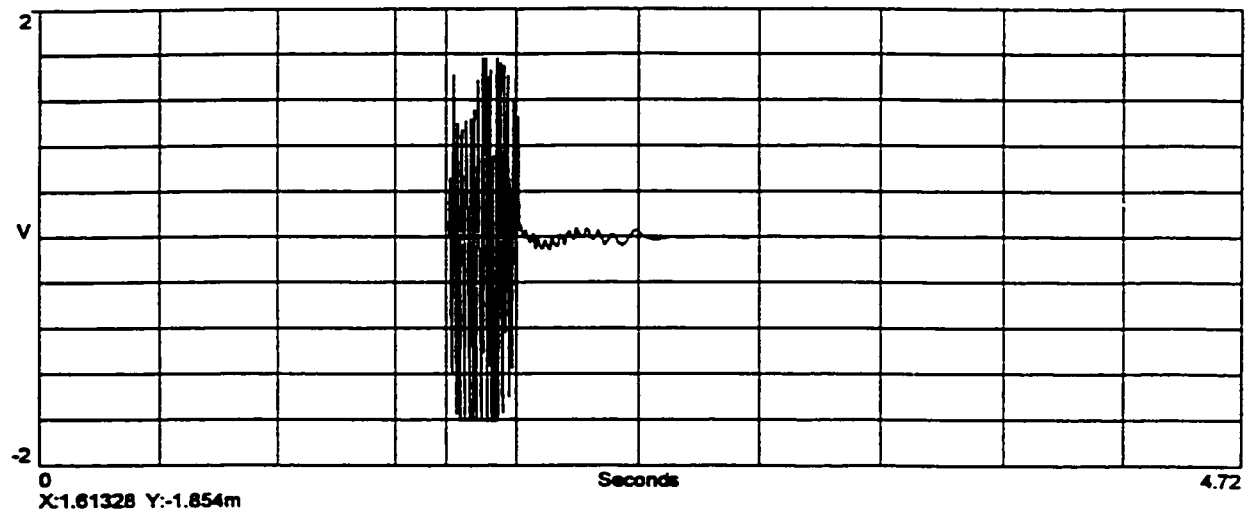

a) DE Rogowski Coil Shaft Current Measurement.

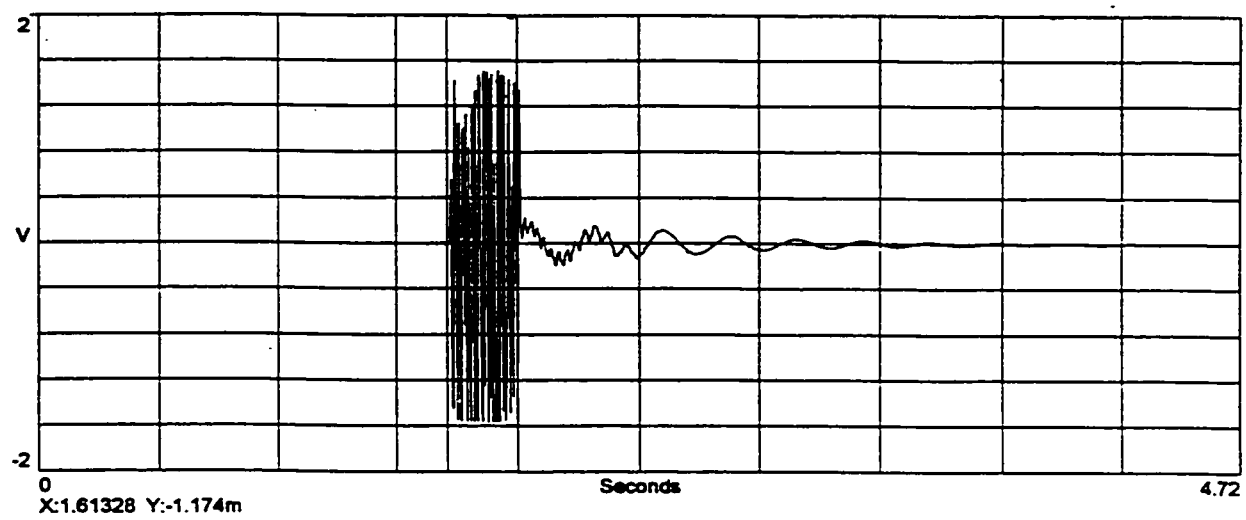

b) ODE Rogowski Coil Shaft Current Measurement

Figure 6.13: Waveform of Rogowski Coil Shaft Current Measurement at Rated Motor Line Voltage, Shaft End Play Movement, Both Bearings Non-Insulated, Oil Ring Lubrication.

waveforms of equal magnitude of current. Figures 6.14 (a, ii) and (b, ii) show the spectral plots of the waveforms, indicating 60 Hz, 120 Hz, 180 Hz and 240 Hz components. The 180 Hz component, three times the line frequency component, is due to the joints in the stator segments, verifying Alger's criterion [5] as shown in Table 6.7. Figure 6.15 indicates that at 20% of motor rated line voltage (20%V), when the motor is unsaturated, the 180 Hz component predominates, suggesting that the saturation effect is not the main cause of existence of the shaft current . Instead the shaft current is due to the joints between stator core segmented laminations.

The even multiples of line frequency could be explained by considering that the stator core has strong 120 and 240 Hz mechanical vibrations. These vibrations vary the air gap and thus modulate the yoke flux. The 120 Hz and 240 Hz components, due to stator core vibration, increase as the motor voltage is increased, the reason being that the stator core vibration created by the fundamental force wave is proportional to the square of the air gap flux density, and flux density is proportional to voltage.

As the oil ring, which hangs down into the oil sump and rides on the shaft journal begins to rotate, the ring starts to lift the oil from the oil sump to the shaft journal. The shaft journal carries the oil into the bearing and develops a wedge of oil between the journal and the bearing. The shaft rides on the film of oil so there is no metal-to-metal contact. The oil film is partially developed. The motor has not reached the no load speed. For each voltage starting condition, the oil film development begins at different speeds as indicated in Table 6.2. In this partial oil development region, the average magnitude of shaft current decreases to a level of 9A as shown in Figure 6.13. Examination of the DE Rogowski coil shaft current spectrum in

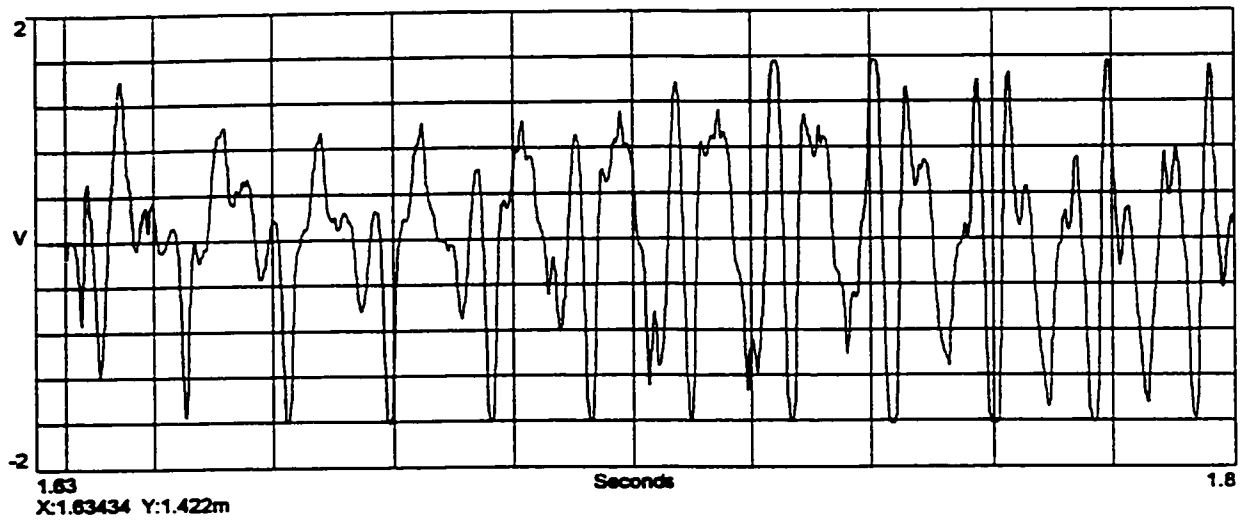

i) Shaft Current Waveform

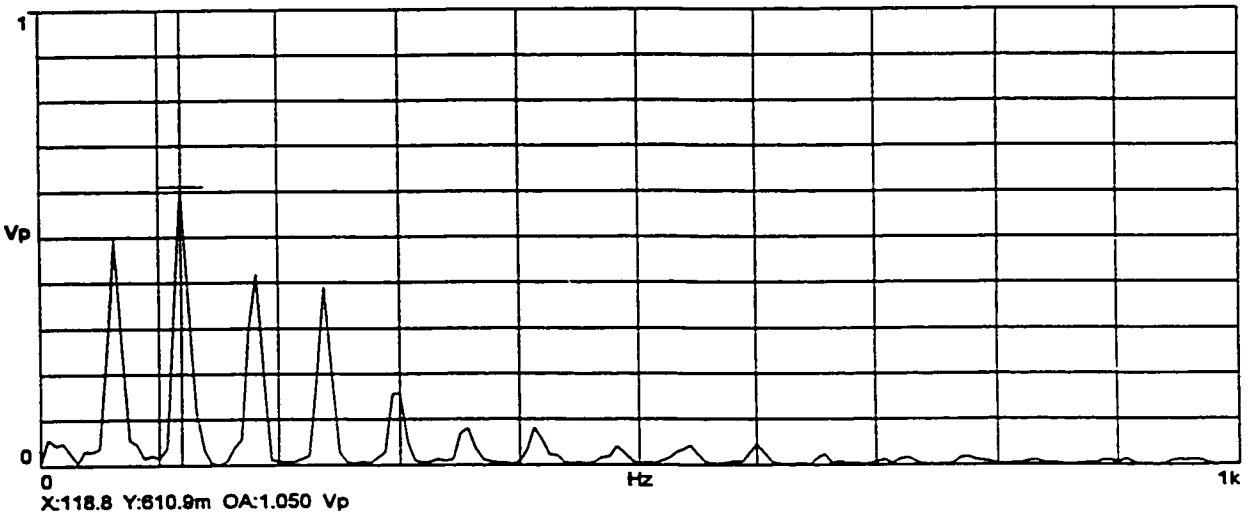

ii) Spectrum Plot

a) DE Rogowski Coil Shaft Current Waveform and Spectrum Plot

Figure 6.14: Waveform and Spectrum Plot of Shaft Current Measured During Initial Start of Acceleration and Prior to Oil Film Development.

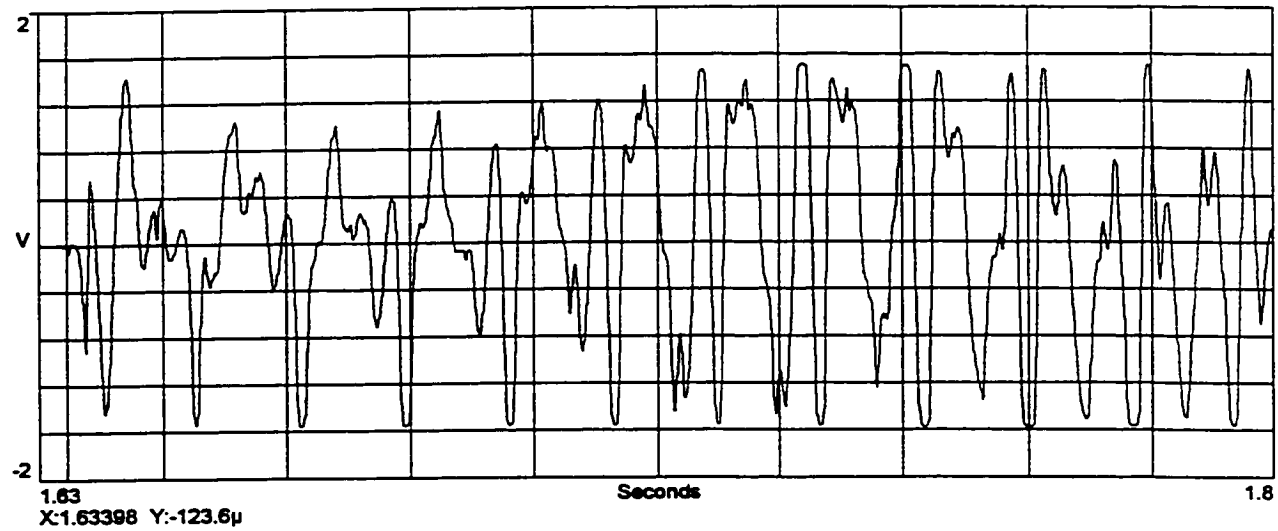

i) Shaft Current Waveform

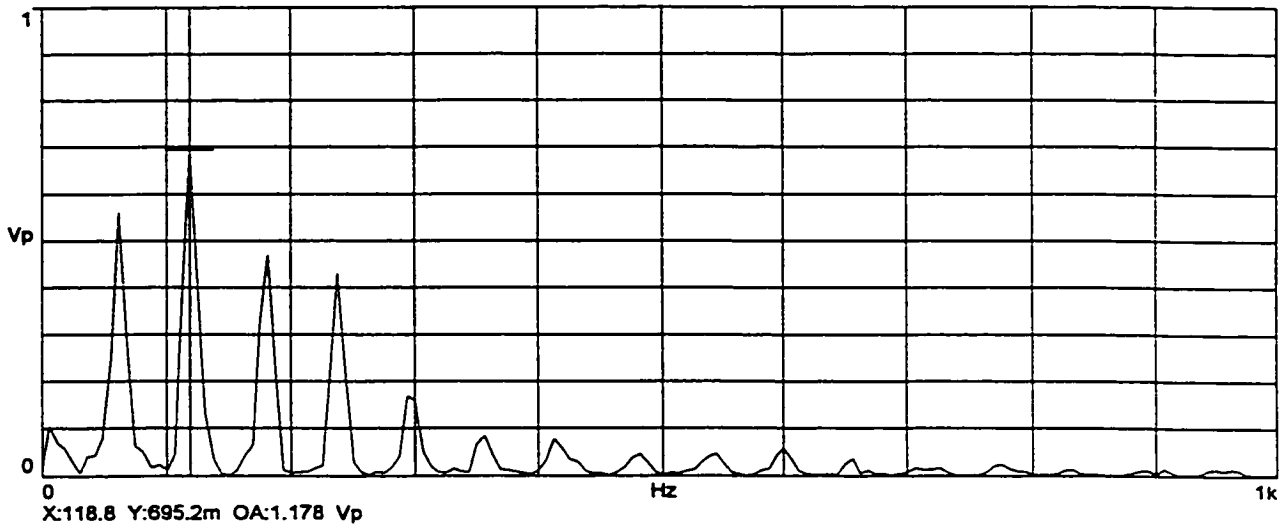

ii) Spectrum Plot

b) ODE Rogowski Coil Shaft Current Waveform and Spectrum Plot

Figure 6.14: Waveform and Spectrum Plot of Shaft Current Measured During Initial Start of Acceleration and Prior to Oil Film Development.

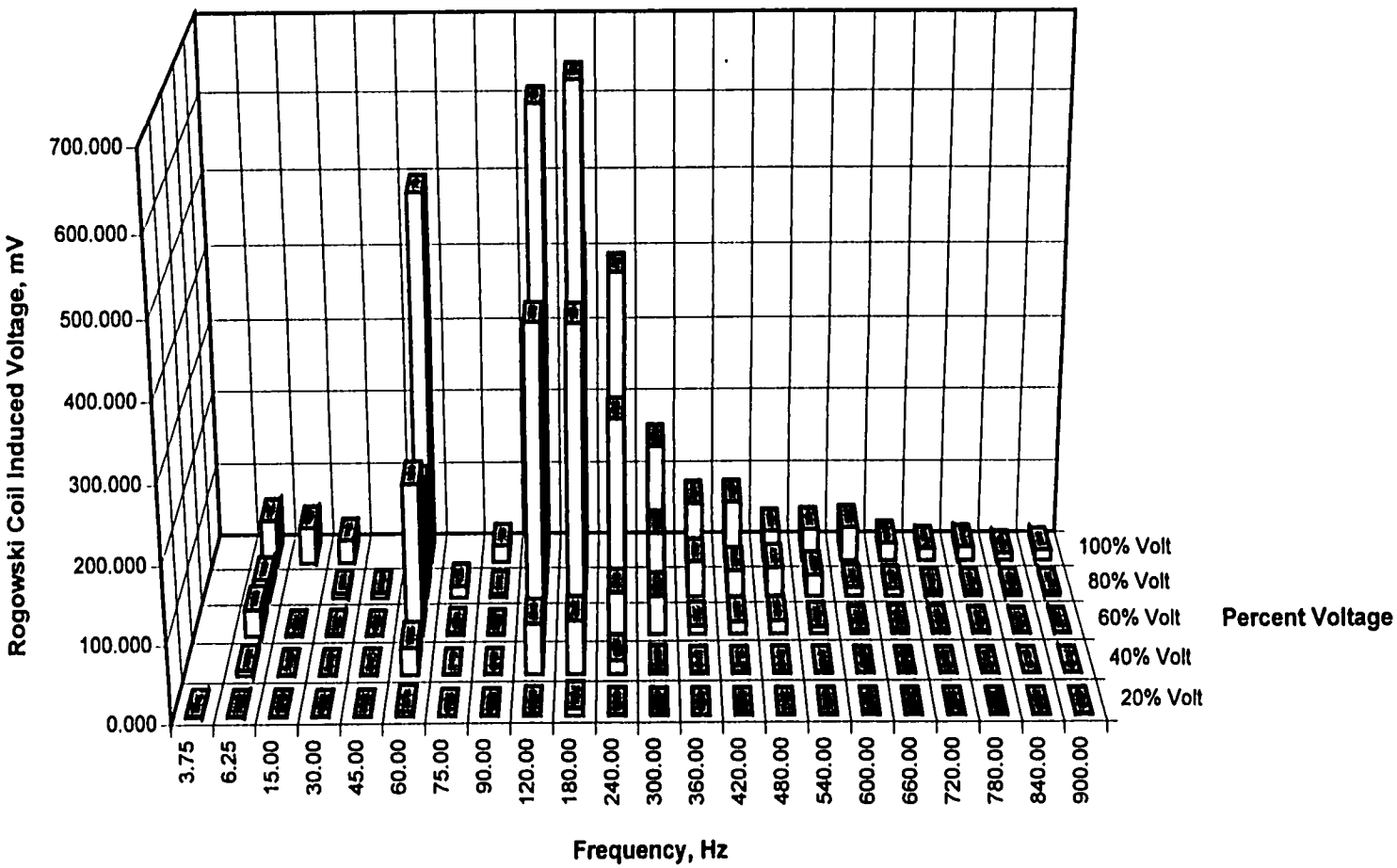

Figure 6.15: Spectrum Plot of DE Rogowski Coil Shaft Current Waveform During Initial Start of Acceleration and Prior to Oil Film Development, Shaft End Play Movement, Both Bearings Non-Insulated, Oil Ring Lubrication.

Figure 6.16 shows that the partial oil film reduces the high frequency components considerably. At steady state no-load condition, the average magnitude of the shaft current is reduced to 0.22A. The shaft current spectrum is presented in Figure 6.17 which shows the dominant frequency to be 15 Hz. This frequency is the rotor running frequency. The oil film is sufficiently developed at steady state rated no-load speed. This is the full oil film region. The oil film impedance is effective in reducing the average magnitude of the shaft current. It is thus important that consistent oil film be developed sufficiently. In this way, the extent of the bearing damage can be minimized.

Figure 6.16, a spectral plot of the DE Rogowski coil shaft current waveform, shows that when there is partial oil film development and the oil film thickness is consistent, the high frequency components are reduced to negligible magnitudes, see for example frequencies of 540 Hz and above. However, if there is a make-and-break of oil film phenomenon resulting in inconsistent oil film thickness, the high frequency shaft current components remain significant but at reduced values. See for example the 180 Hz, 240 Hz and 300 Hz components at 80%V. The insulating effectiveness of the inconsistent oil film is reduced. At steady state no-load conditions, when a full oil film condition exists, the reduced high frequency components, for example 180 Hz, 240 Hz and 300 Hz, are further reduced as shown in Figure 6.17.

At 20%V, the oil ring speed follows the shaft speed and there is no slippage of the oil ring. Oil is delivered consistently to the bearings. Hence, current spikes were not observed in Figures 6.18 (a) and (b). The Rogowski coil-induced voltage waveforms at 80%V as shown in Figures 6.18 (c) and (d) indicate spikes in the period t = 0.57s to t =1.34s as a result of

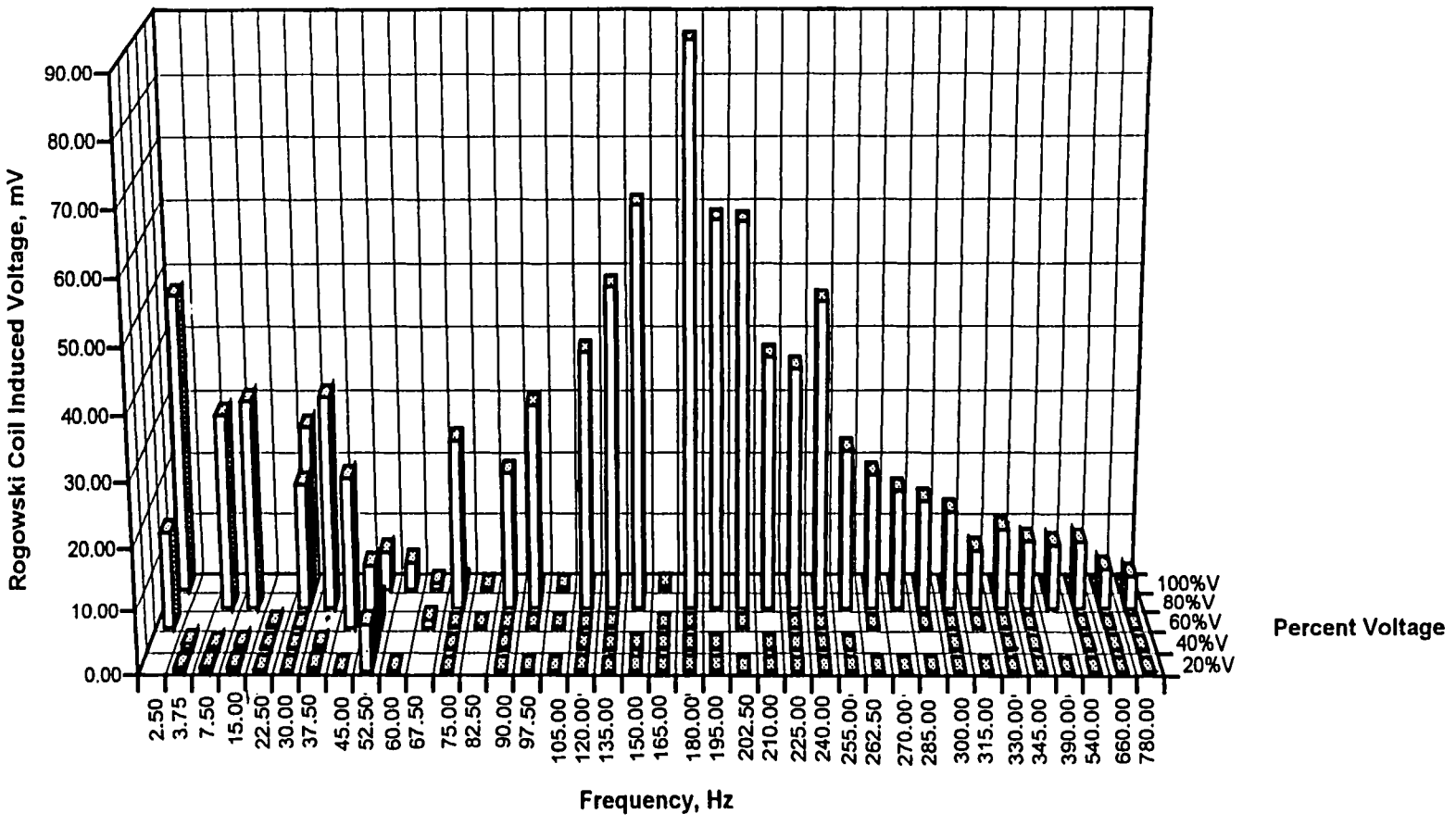

Figure 6.16: Spectrum Plot of DE Rogowski Coil Shaft Current Waveform Following Oil Development & Prior to Rated Speed, Shaft End Play Movement, Both Bearings Non-Insulated, Oil Ring Lubrication.

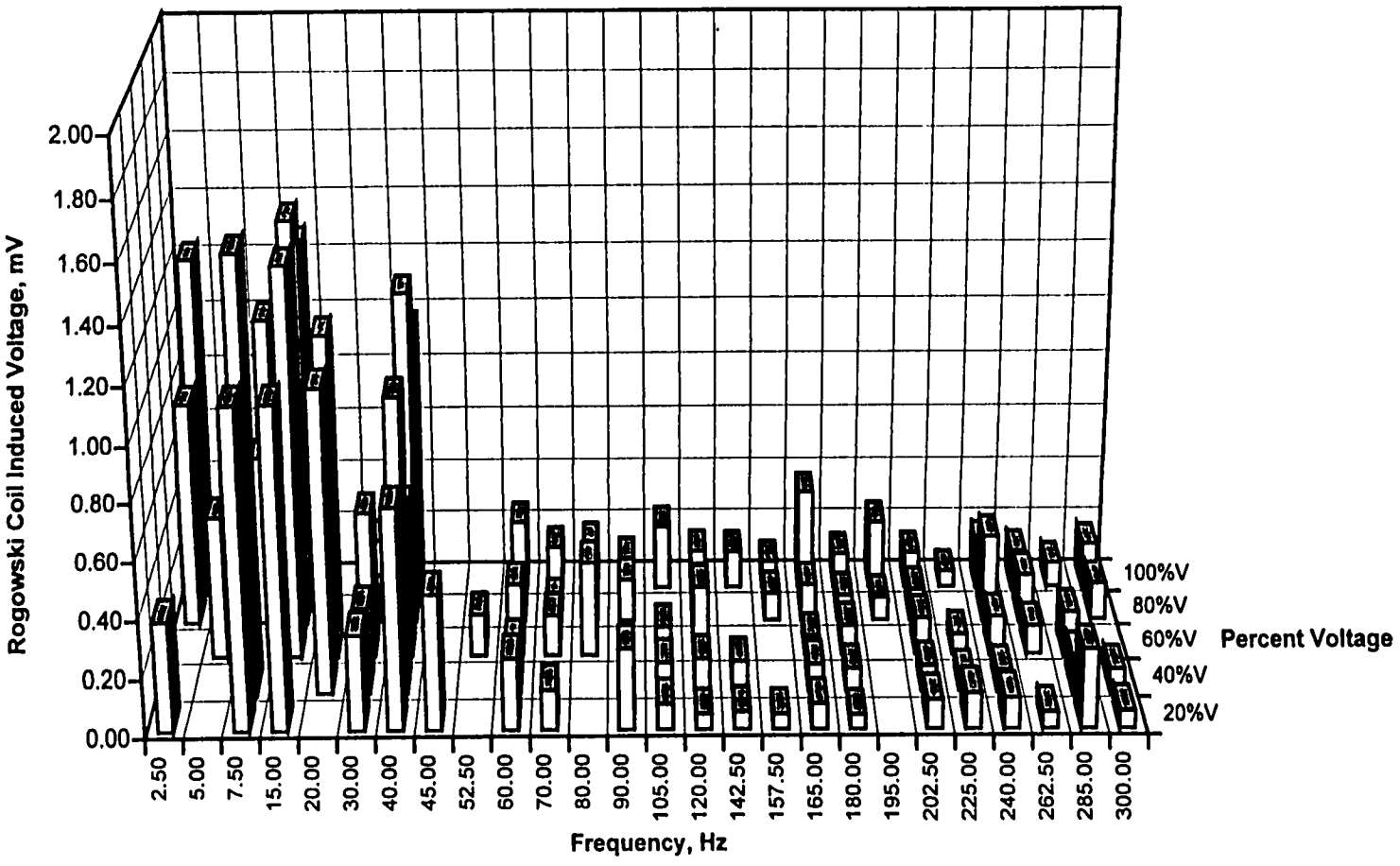

Figure 6.17: Spectrum Plot of DE Rogowski Coil Shaft Current Waveform During Steady State No-Load Condition, Shaft End Play Movement, Both Bearings Non-Insulated, Oil Ring Lubrication.

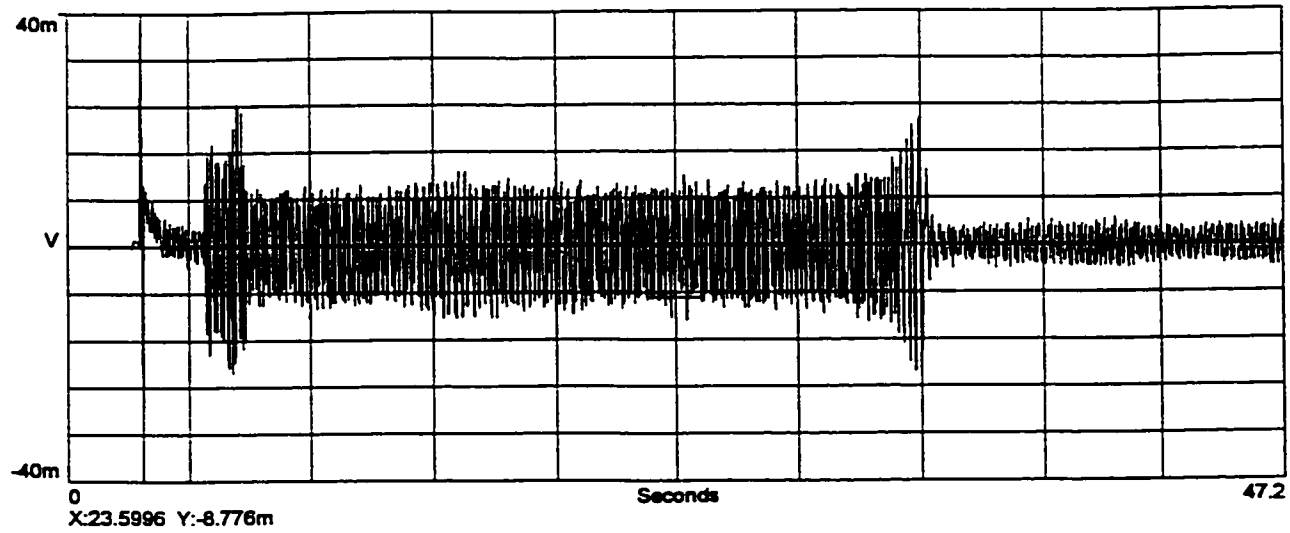

a) DE Rogowski Coil Shaft Current Measurement, 20% of Motor Rated Line Voltage.

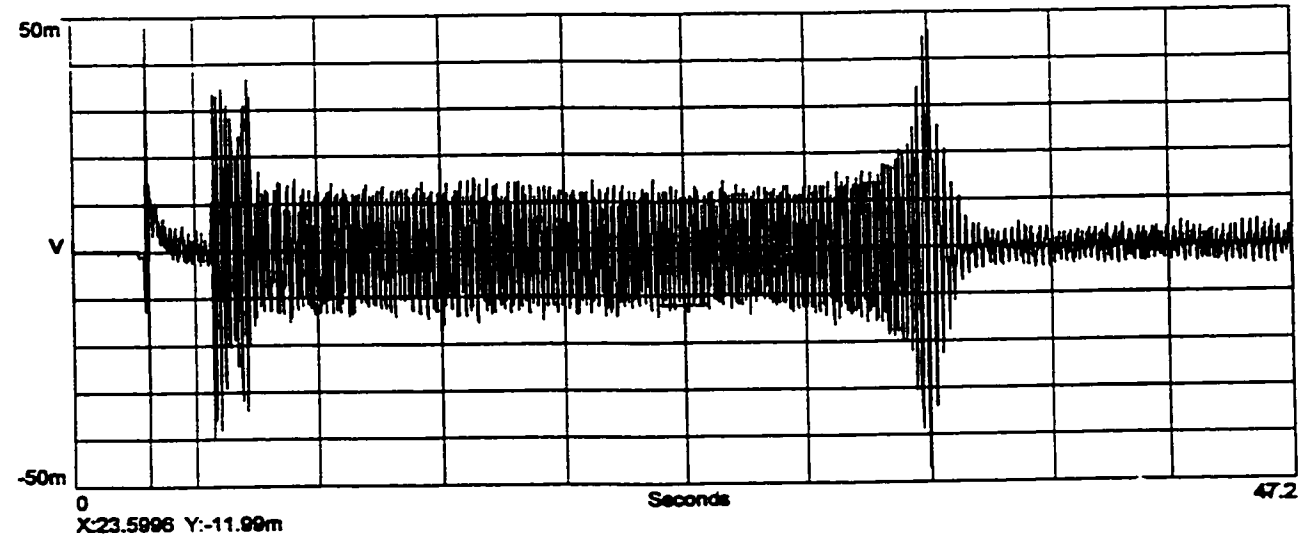

b) ODE Rogowski Coil Shaft Current Measurement, 20% of Motor Rated Line Voltage.

Figure 6.18: Waveforms of DE Rogowski Coil Shaft Current Measurement At 20% and 80% of Motor Rated Line Voltage, Shaft End Play Movement, Both Bearings Non-Insulated, Oil Ring Lubrication.

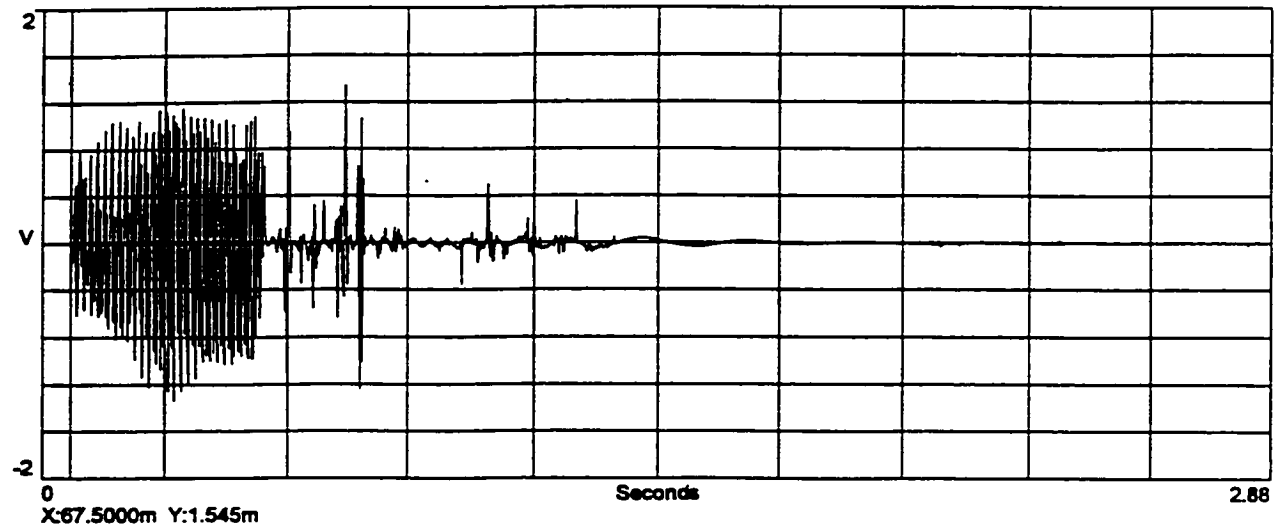

c) DE Rogowski Coil Shaft Current Measurement, 80% of Motor Rated Line Voltage.

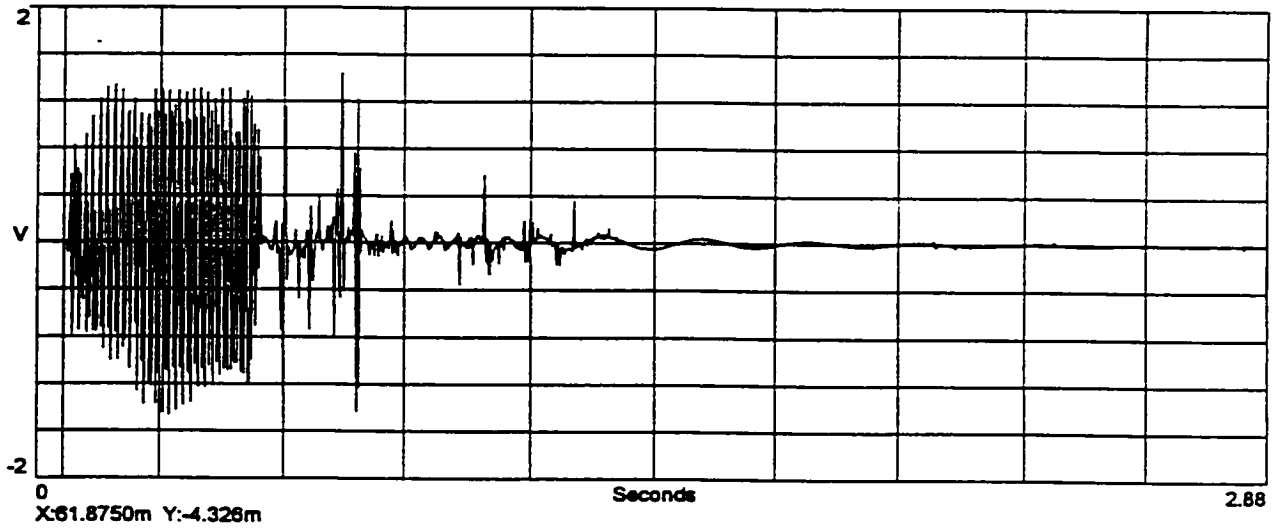

d) ODE Rogowski Coil Shaft Current Measurement, 80% of Motor Rated Line Voltage.

Figure 6.18: Waveforms of DE Rogowski Coil Shaft Current Measurement At 20% and 80% of Motor Rated Line Voltage, Shaft End Play Movement, Both Bearings Non-Insulated, Oil Ring Lubrication.

the make and-break of oil film phenomenon discussed previously. This phenomenon is a result of the oil ring slippage with respect to the shaft and hence inconsistent oil film thickness.

Figure 6.19 summarizes the rms shaft current measured in the three oil film development regions. The measurements in the no oil film region and the partial oil film region were averaged over a range of speed. Table 6.3 shows the range of speed over which the measurements were averaged.

	100%V	80%V	60%V	40%V	20%V
Speed at Which Oil Film Begins to Develop, rpm	167.14	204.5	88.71	51.43	32.53

Table 6.2: Shaft Speeds At Which Oil Film Begins to Develop for Different Voltage Start Conditions.

Region	Speed Range (rpm)				
	100%V	80%V	60%V	40%V	20%V
No Oil Film	0 - 119.97	0 - 80.6	0 - 88.71	0 - 38.78	0 - 18.20
Partial Oil Film	167.14 - 674.4	204.5 - 518.72	88.71 - 249.98	51.43 - 115.89	32.53 - 58.14

Table 6.3: Speed Range Over Which Shaft Current Measurement are Averaged.

6.4.3.2 DE Bearing Non-Insulated, ODE Bearing Insulated, End-Play Movement, No-Load Condition, Oil Ring Lubrication

With the ODE bearing insulated and bearing oil ring lubricated, at close to standstill condition, the magnitudes of shaft currents at all voltages except 20%V were reduced, as shown in Figures 6.20 (a) - (f). The shaft current waveforms at 20%V as shown in Figures 6.20 (a) and (b) resemble those obtained in the partial oil development region of the test with non-insulated bearings of Figures 6.18 (a) and (b). At low voltage starting conditions,

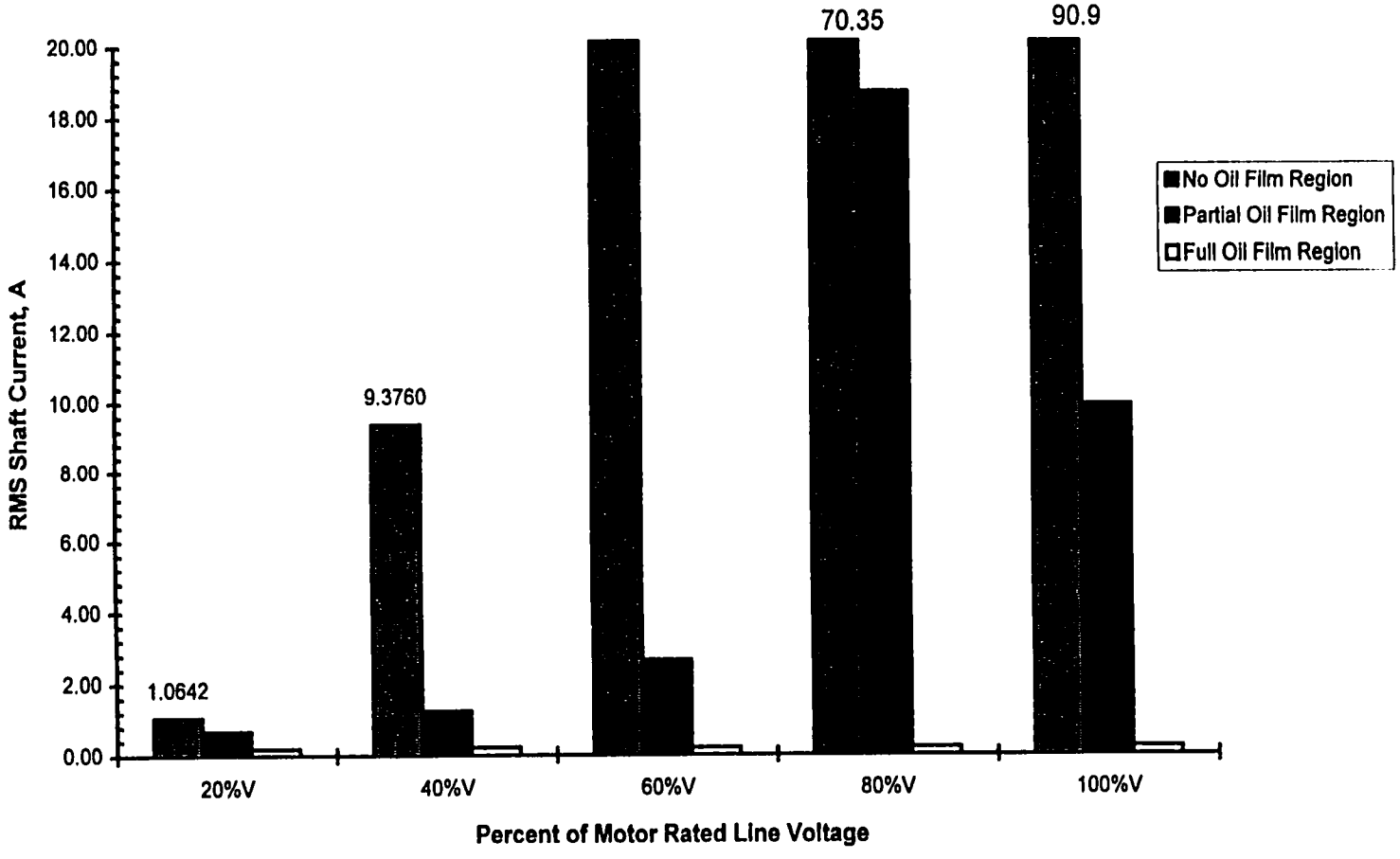

Figure 6.19: DE Rogowski Coil Shaft Current Measurement: Three Oil Film Development Regions, Shaft End Play Movement, Both Bearings Non-Insulated, Oil Ring Lubrication.

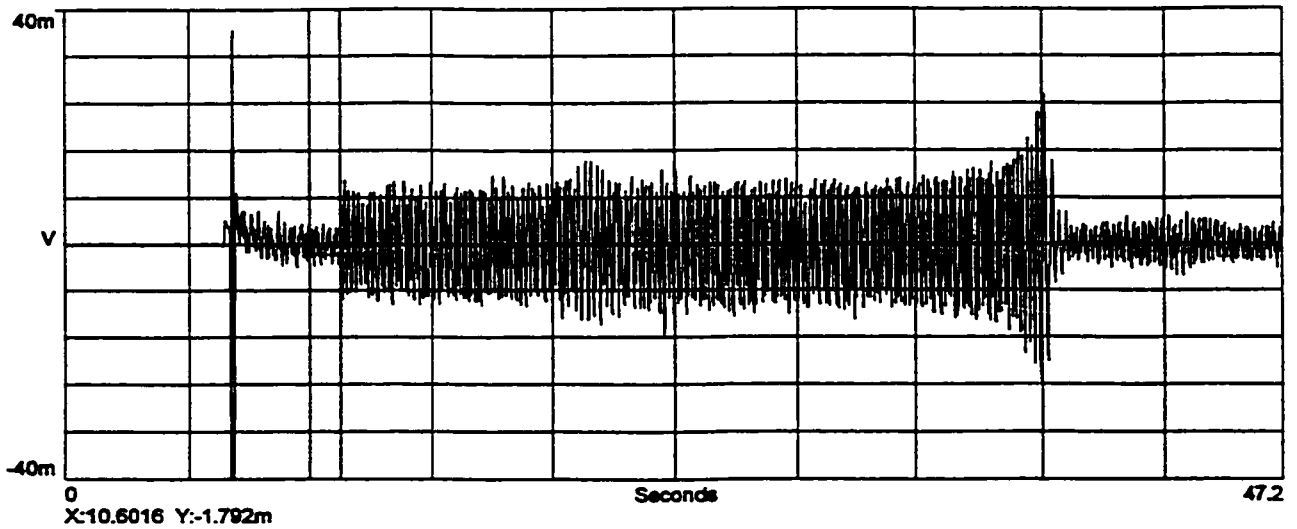

a) DE Rogowski Coil Shaft Current Measurement, 20% of Motor Rated Line Voltage.

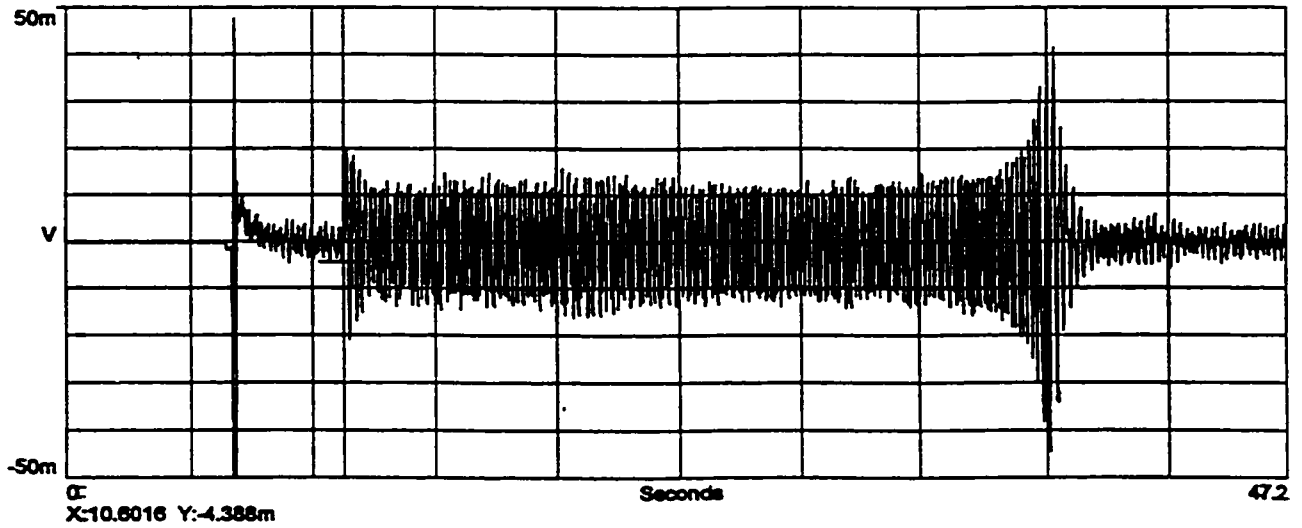

b) ODE Rogowski Coil Shaft Current Measurement, 20% of Motor Rated Line Voltage.

Figure 6.20: Waveforms of DE Rogowski Coil Shaft Current Measurement at 20%, 80% and 100% of Motor Rated Line Voltage, Shaft End Play Movement, DE Bearing Non-Insulated, ODE Bearing Insulated, Oil Ring Lubrication.

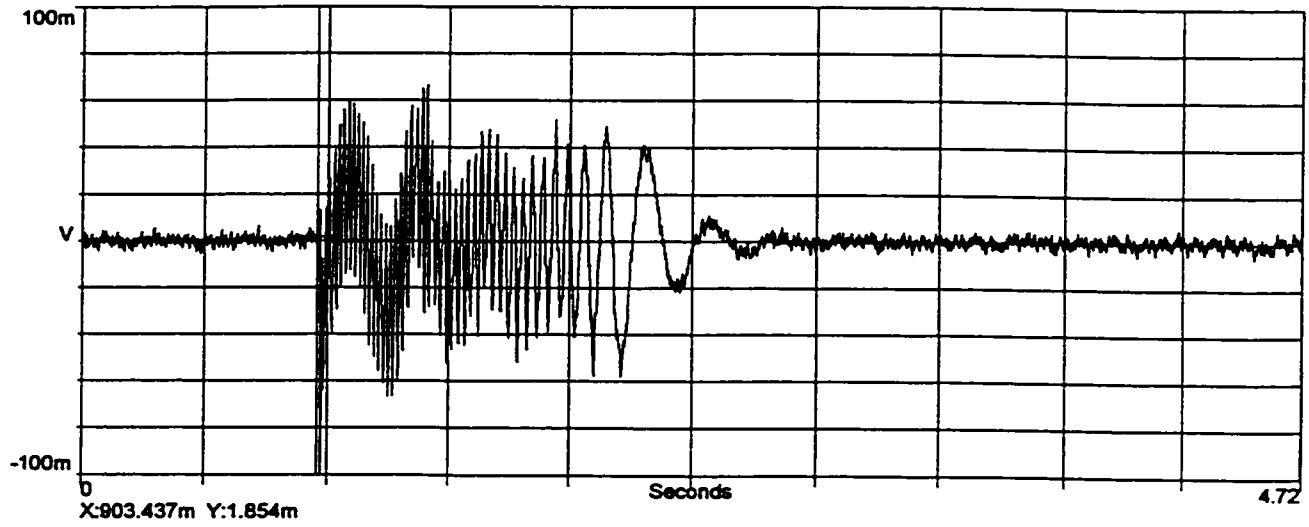

c) DE Rogowski Coil Shaft Current Measurement, 80% of Motor Rated Line Voltage.

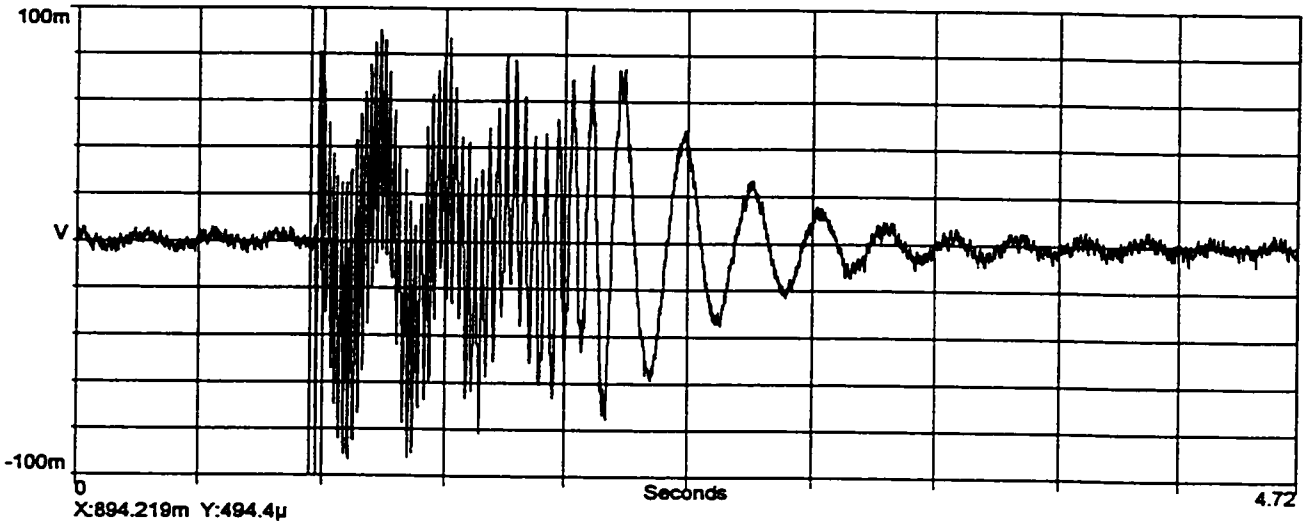

d) ODE Rogowski Coil Shaft Current Measurement, 80% of Motor Rated Line Voltage.

Figure 6.20: Waveforms of DE Rogowski Coil Shaft Current Measurement at 20%, 80% and 100% of Motor Rated Line Voltage, Shaft End Play Movement, DE Bearing Non-Insulated, ODE Bearing Insulated, Oil Ring Lubrication.

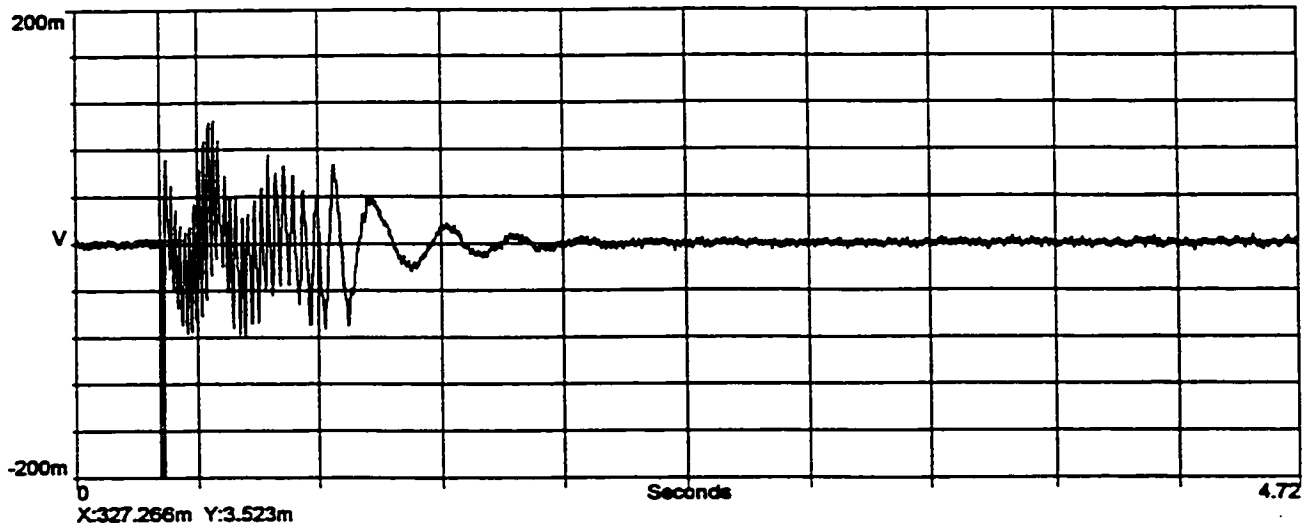

e) **DE Rogowski Coil Shaft Current Measurement, 100% of Motor Rated Line Voltage.**

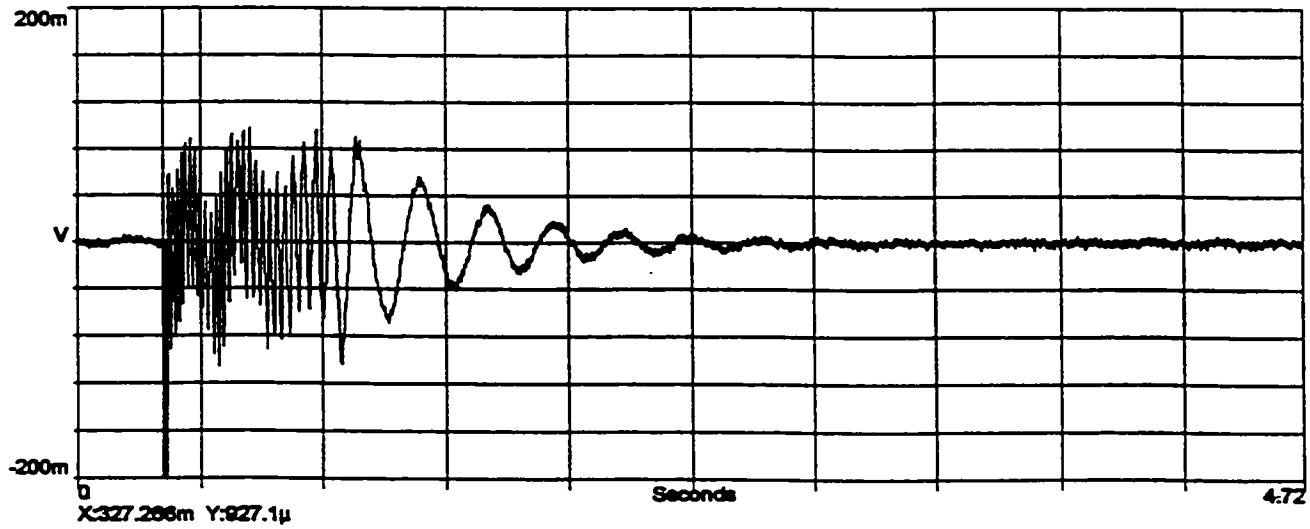

f) **ODE Rogowski Coil Shaft Current Measurement, 100% of Motor Rated Line Voltage.**

Figure 6.20: Waveforms of DE Rogowski Coil Shaft Current Measurement at 20%, 80% and 100% of Motor Rated Line Voltage, Shaft End Play Movement, DE Bearing Non-Insulated, ODE Bearing Insulated, Oil Ring Lubrication.

the oil ring speed follows the shaft speed and delivers oil to the bearing. Besides, the magnitude of shaft current at low voltage due to joints in the segmented laminations is small. The consistent oil film developed is sufficient to reduce the shaft current. Hence, we can say that at low voltage starting conditions, bearing insulation may not be required and bearing damage due to shaft current is minimal. The shaft current waveforms at 80%V as shown in Figures 6.20 (c) and (d) show no current spikes that were observed in Figures 6.18 (c) and (d). We may conclude that the bearing insulation prevented these spikes from occurring. Hence, it can be said that the bearing insulation is more effective than the oil film in reducing the shaft current. Relying on the oil film alone to prevent bearing damage due to shaft current is not recommended especially for starting conditions of 40%V and above.

The magnitude of shaft currents measured during transient conditions for across-the-line rated voltage start as shown in Figures 6.20 (e) and (f), are smaller than those obtained in the partial oil development region of the test with non-insulated bearings of Figures 6.13 (a) and (b). The average value of the shaft current is 3.6A, approximately forty percent of the value obtained with both bearings non-insulated and during partial oil development as shown in Figure 6.13. Furthermore, this 3.6A shaft current is small compared to the 90A shaft current obtained with both bearings non-insulated and prior to oil development. This finding reaffirms the recommendation that bearing insulation is required to reduce shaft current. The spectrum plot of the shaft current waveform during acceleration (transient phase) as shown in Figure 6.21, shows negligible high harmonic components. The 180 Hz component, also known as the zero sequence component, has been reduced to a negligible magnitude. Also, at 80%V when the shaft voltage is at its maximum, the zero sequence component of the shaft

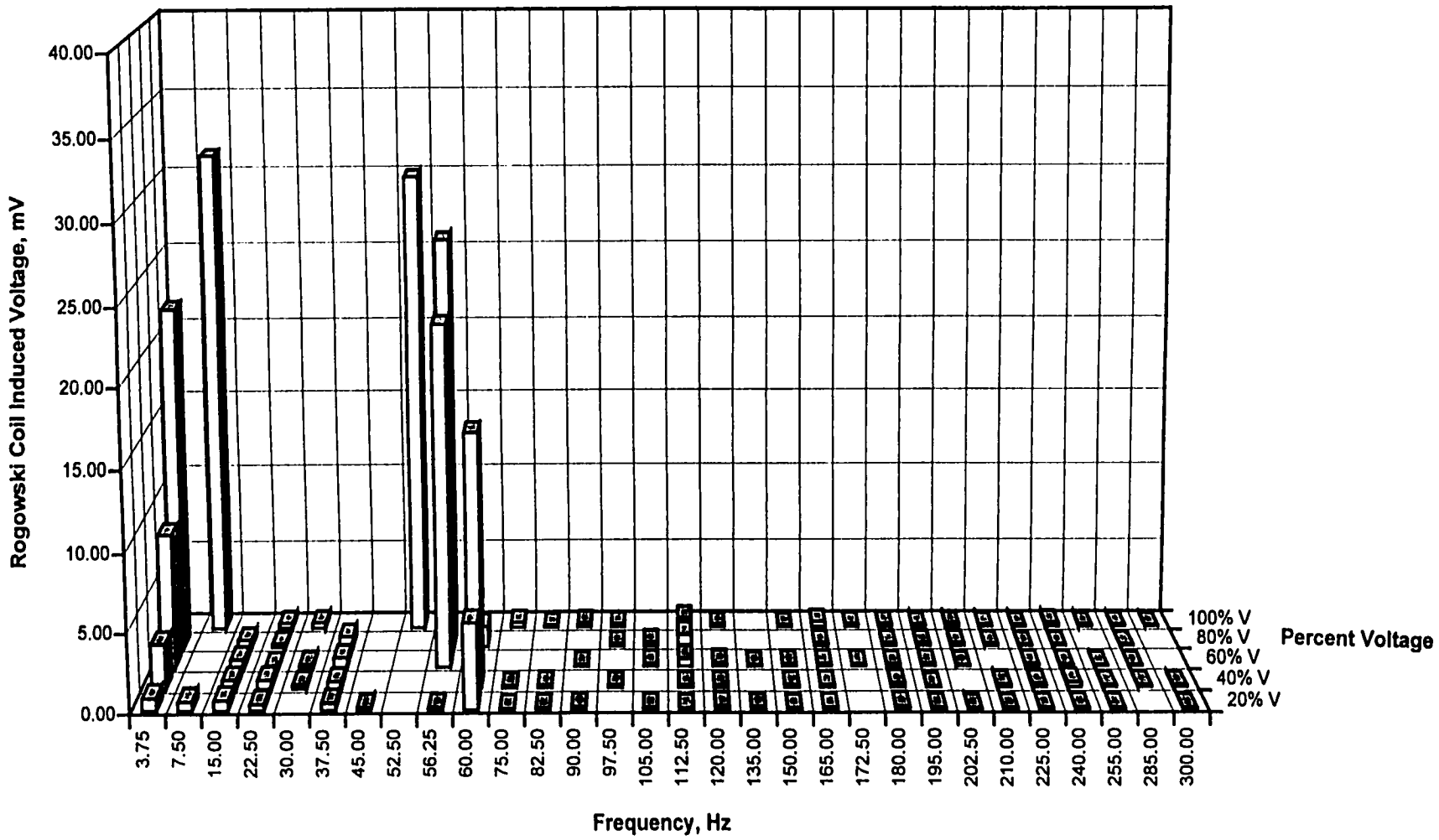

Figure 6.21: Spectrum Plot of DE Rogowski Coil Shaft Current Waveform During Initial Start of Acceleration, Shaft End Play Movement, DE Bearing Non-Insulated, ODE Bearing Insulated, Oil Ring Lubrication

current has been reduced considerably by the bearing insulation. The insulation at the ODE bearing breaks the shaft current circuit and hence the through path for the zero sequence component.

At rated no load speed and rated voltage, the peak magnitude of the shaft current waveform is reduced to 0.18A as shown in Figures 6.20 (e) and (f), approximating the value obtained with both bearings non-insulated and full oil film development. This indicates that during the steady state running condition when the oil film is fully developed to a consistent thickness, the oil film is sufficient to act as an insulator of shaft current. However, it is possible that a variation in the load condition may cause a corresponding variation in oil film thickness and thus lead to the possibility of large shaft currents and the resultant bearing damage. The shaft current spectrum shown in Figure 6.22 indicates a dominant 15 Hz component which is the rotor running frequency. The 180 Hz component and its odd multiples are negligible.

Figure 6.23 demonstrates that bearing damage, if any, will be more likely to occur during the transient condition than during the steady state running condition, the reason being that at transient condition the magnitude of shaft current is large compared to that obtained at steady state running condition. It is thus recommended that frequent starts at rated voltage be limited to reduce the probability of bearing damage.

6.4.3.3 DE Bearing Non-Insulated, ODE Bearing Insulated, End-Play Movement, No-Load Condition, Forced Lubrication

With forced lubricated sleeve bearings, oil ring installed and the ODE bearing insulated, the magnitudes of the measured shaft currents as shown in Figure 6.24 during transient and steady state conditions are approximately equal to the corresponding values obtained with oil

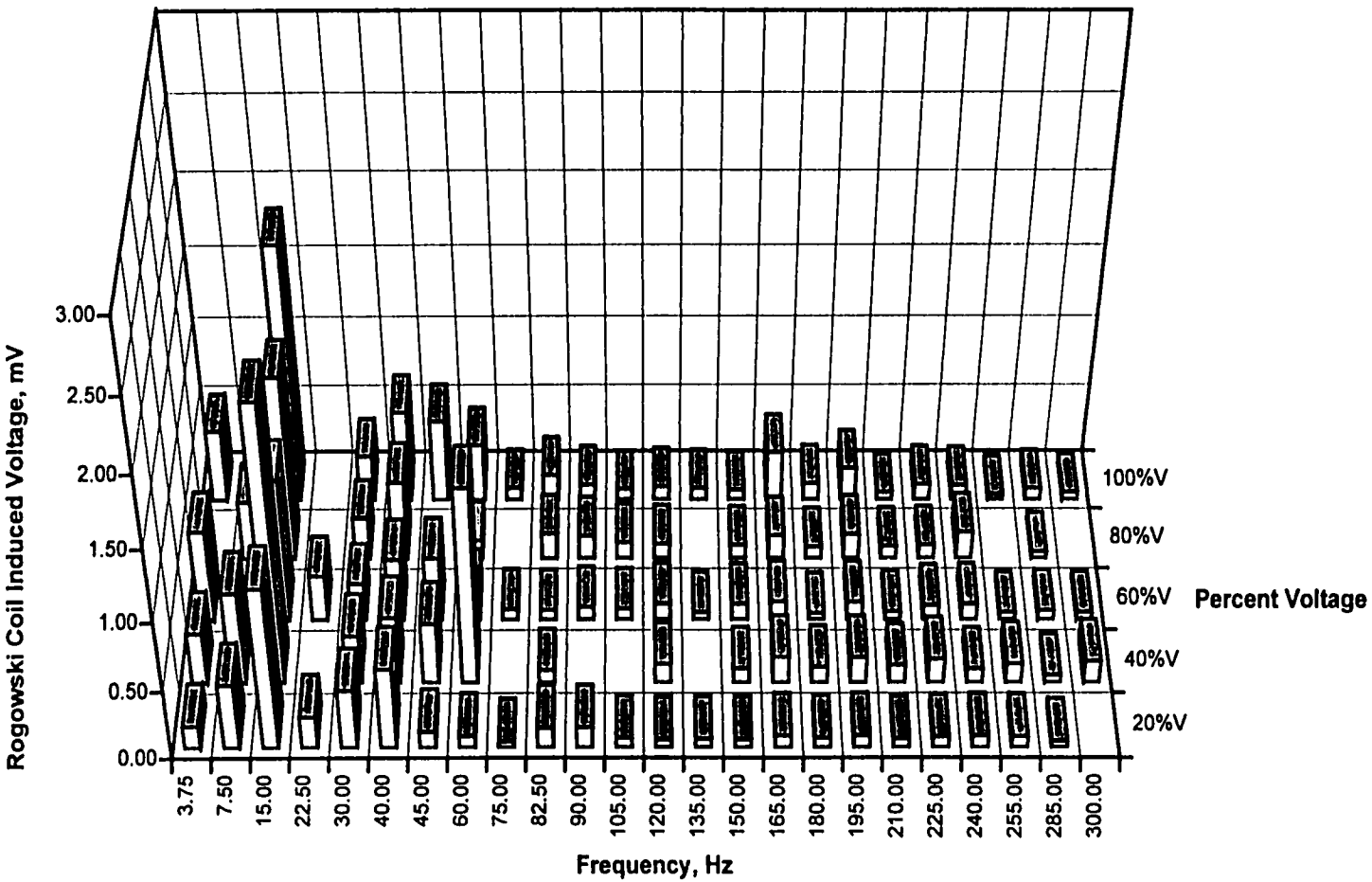

Figure 6.22: Spectrum Plot of DE Rogowski Coil Shaft Current Waveform During Steady State No-Load Condition, End Play Movement, DE Bearing Non-Insulated, ODE Bearing Insulated, Oil Ring Lubrication.

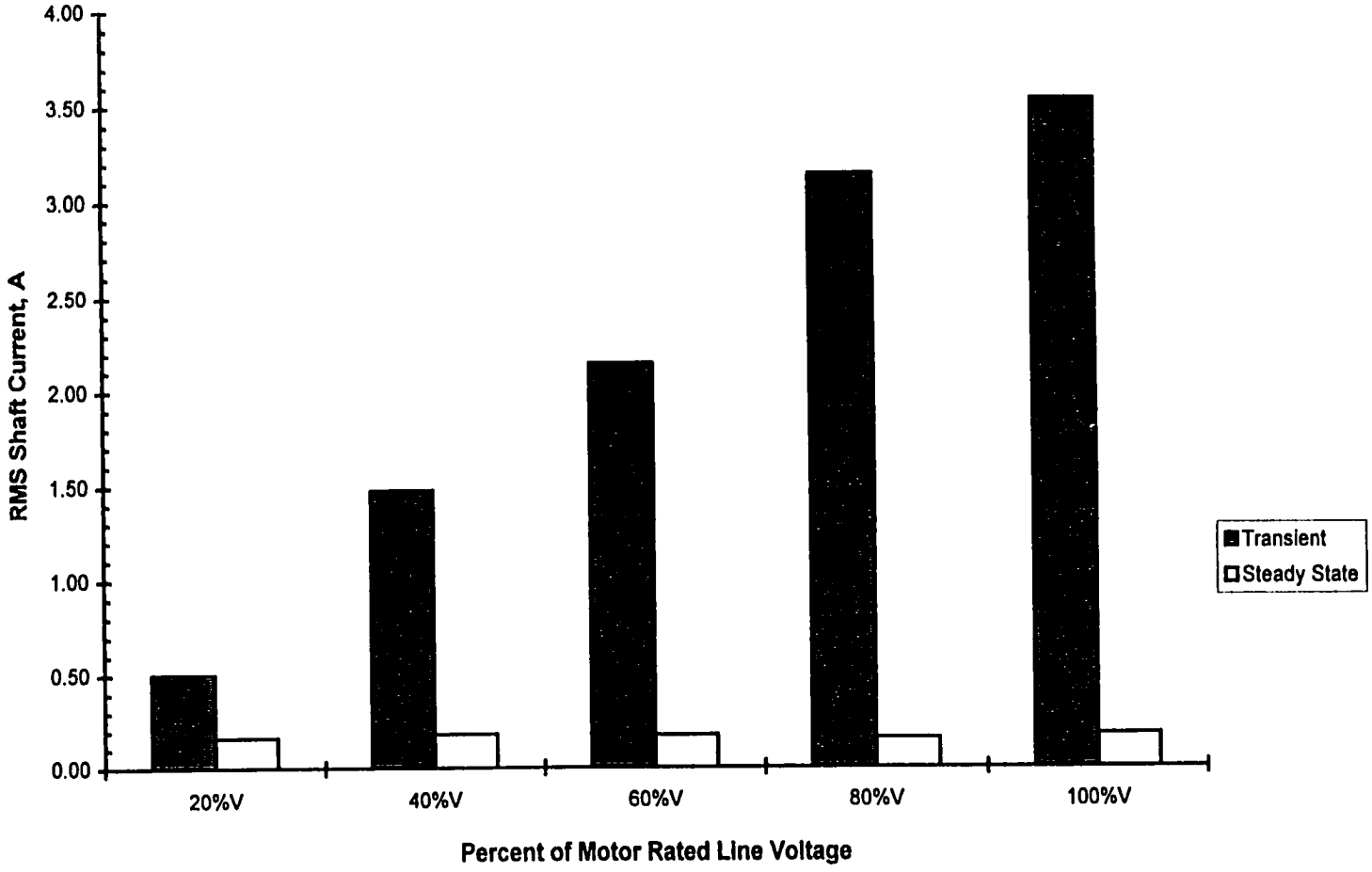

Figure 6.23: DE Rogowski Coil Shaft Current Measurement: Transient versus Steady State, Shaft End Play Movement, DE Bearing Non-Insulated, ODE Bearing Insulated, Oil Ring Lubrication.

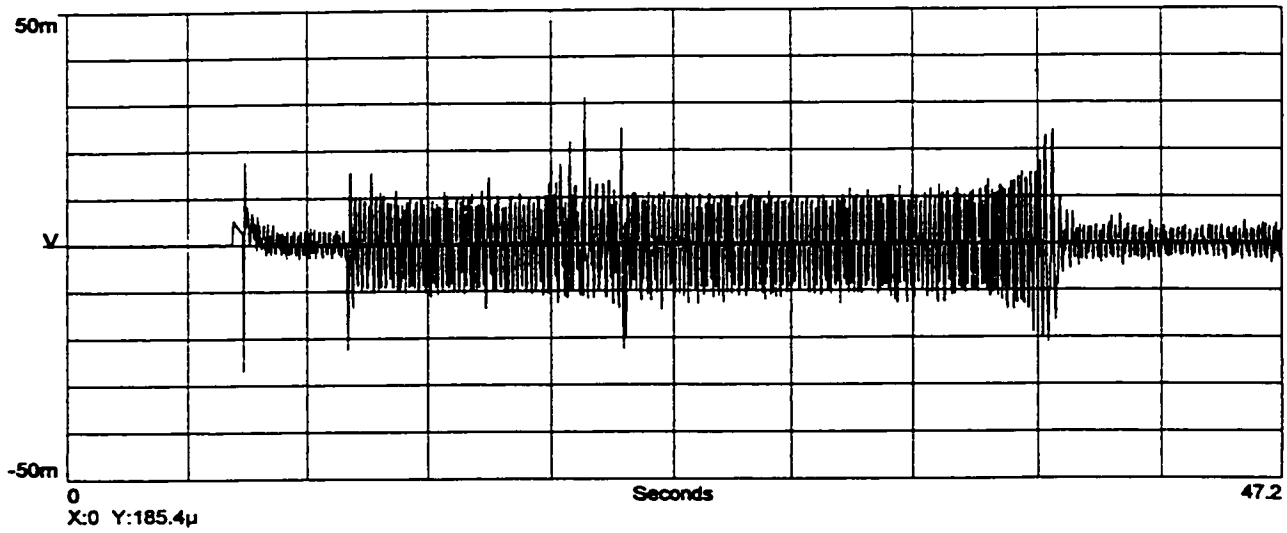

a) **DE Rogowski Coil Shaft Current Measurement, 20% of Motor Rated Line Voltage.**

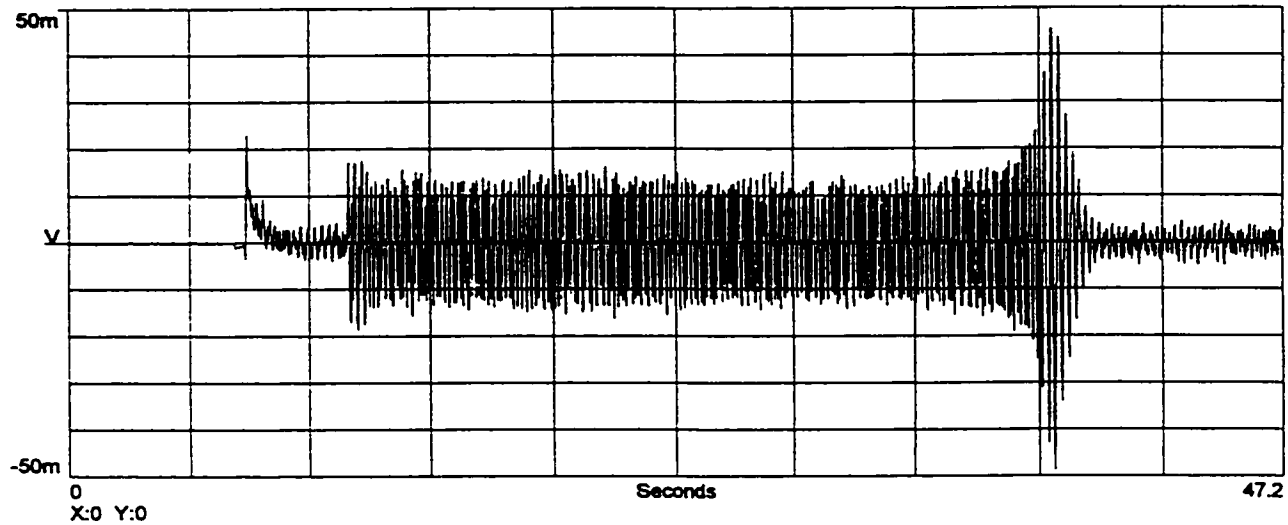

b) **ODE Rogowski Coil Shaft Current Measurement, 20% of Motor Rated Line Voltage.**

Figure 6.24: Waveforms of DE Rogowski Coil Shaft Current Measurement at 20%, 80% and 100% of Motor Rated Line Voltage, Shaft End Play Movement, DE Bearing Non-Insulated, ODE Bearing Insulated, Forced Lubrication.

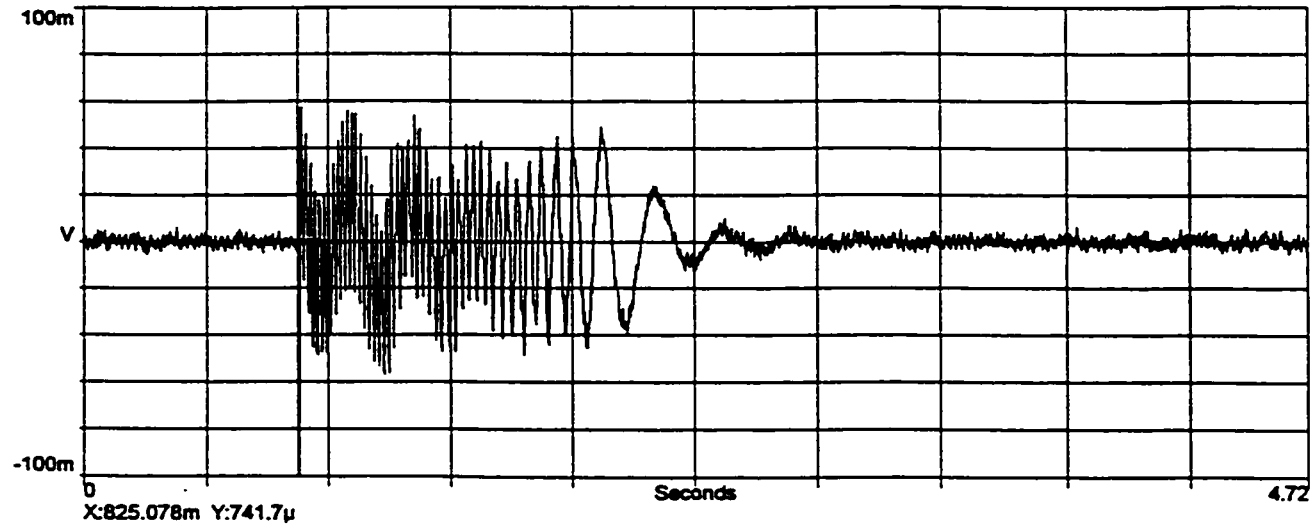

c) **DE Rogowski Coil Shaft Current Measurement, 80% of Motor Rated Line Voltage.**

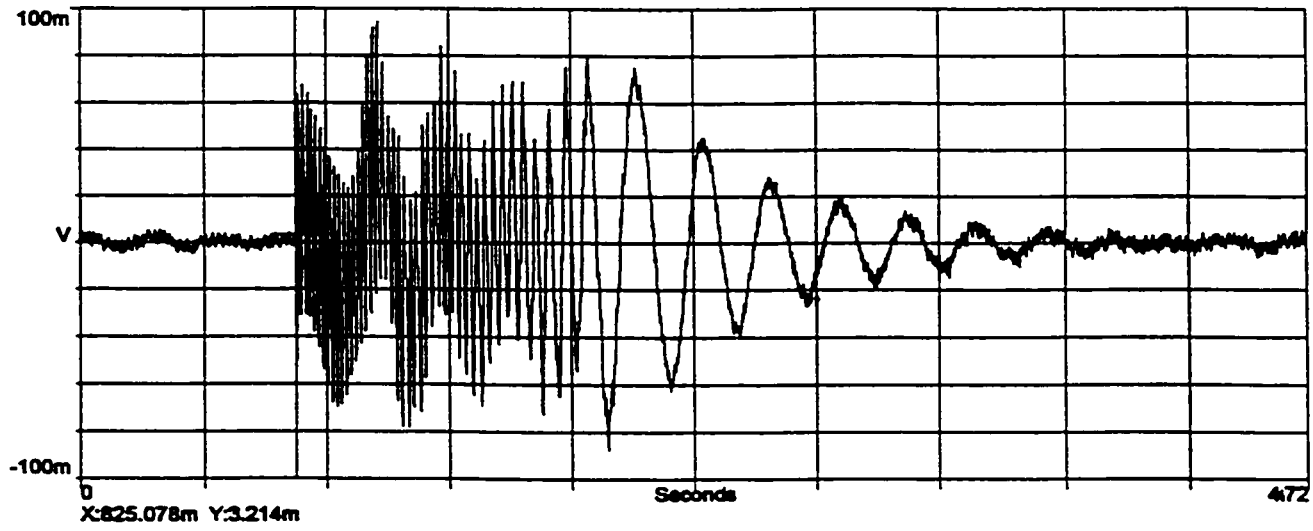

d) **ODE Rogowski Coil Shaft Current Measurement, 80% of Motor Rated Line Voltage.**

Figure 6.24: Waveforms of DE Rogowski Coil Shaft Current Measurement at 20%, 80% and 100% of Motor Rated Line Voltage, Shaft End Play Movement, DE Bearing Non-Insulated, ODE Bearing Insulated, Forced Lubrication.

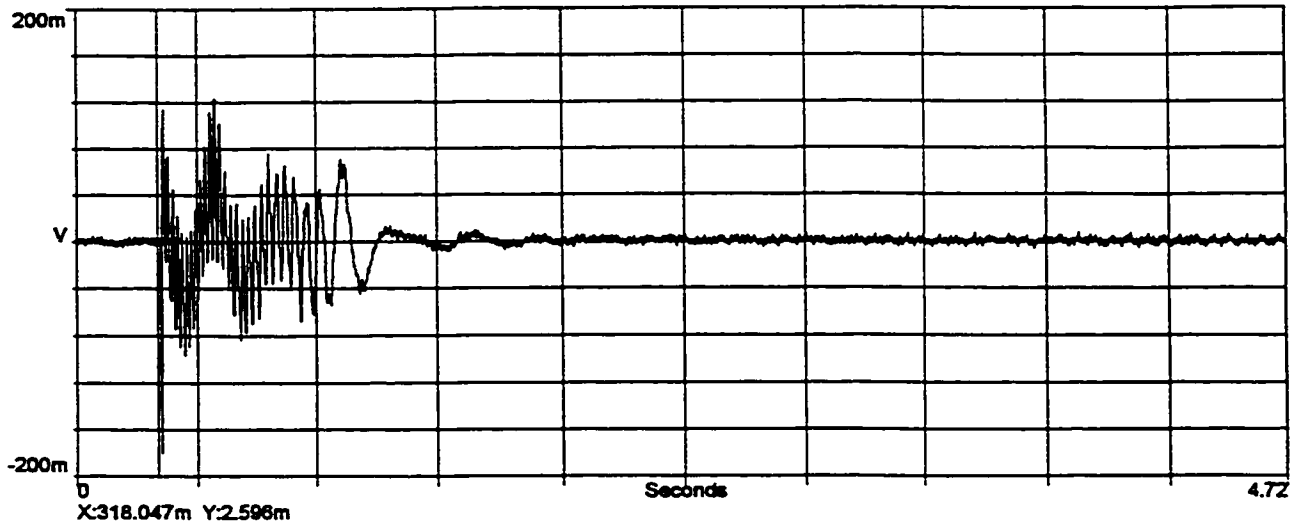

e) DE Rogowski Coil Shaft Current Measurement, 100% of Motor Rated Line Voltage.

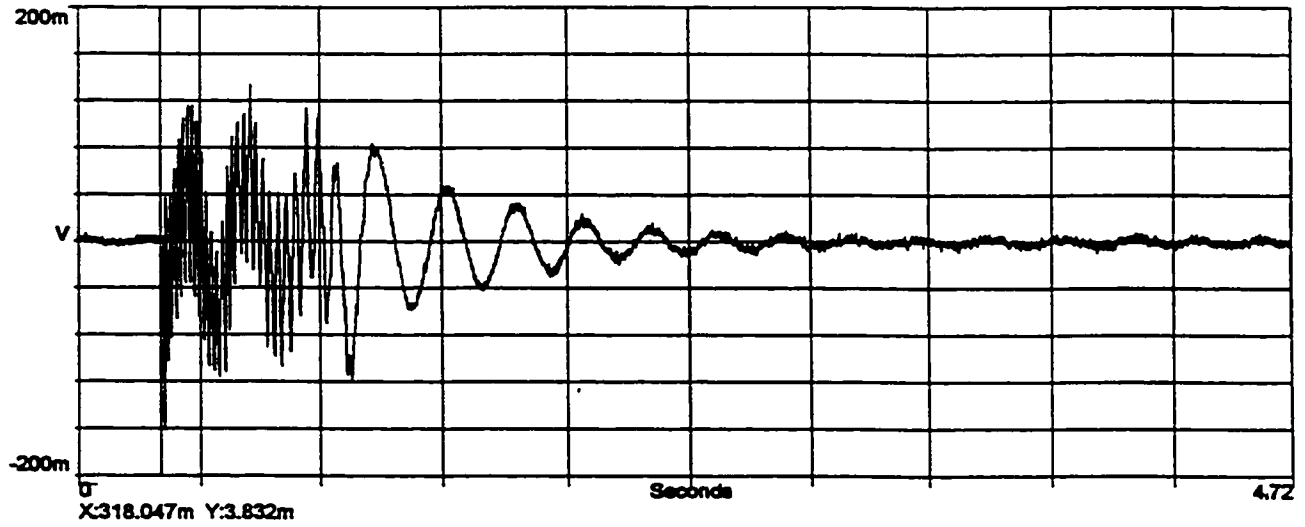

f) ODE Rogowski Coil Shaft Current Measurement, 100% of Motor Rated Line Voltage.

Figure 6.24: Waveforms of DE Rogowski Coil Shaft Current Measurement at 20%, 80% and 100% of Motor Rated Line Voltage, Shaft End Play Movement, DE Bearing Non-Insulated, ODE Bearing Insulated, Forced Lubrication.

ring lubricated sleeve bearings of Figure 6.20. This shows that as long as the bearings are well insulated, the magnitude of the shaft current can be considered to be independent of the type of oil lubrication system.

Figures 6.25 and 6.26 clearly show the magnitude of the zero sequence current to be negligible. In forced oil lubrication system, the lubrication unit pumps oil into the clearance between the shaft journal and the bearing. In this way, a thin oil film is developed prior to start-up. As the shaft rotates, the oil film thickness builds up and acts as insulator against the shaft current. Compared to the oil ring lubrication system which relies on the oil ring to lift the oil onto the journal, the forced lubrication system does ensure that there is a consistent oil film thickness. With this consistency in the oil film thickness, the probability of the bearing damage due to shaft current is minimized. In industry, the motor is usually started across the line at 100%V with a maximum voltage dip of 20%. At 80%V and 100%V, the shaft currents during transient condition are approximately thirty times the magnitudes obtained during steady state conditions. Thus, Figure 6.27 shows that bearing damage, if it does occur, is likely to happen during the transient condition especially at 60%V and above. This result verifies the findings observed in the insulated oil ring lubricated bearing case.

6.4.3.4 DE Bearing Non-Insulated, ODE Bearing Insulated, Locked Rotor Condition, Oil Ring Lubrication

A device [68] consisting of a fixed torque arm length, a calibrated load cell, low friction bearings and a coupling was used to directly measure the locked rotor torque. The device was insulated from the ground by placing an insulated shim under the motor frame feet. The

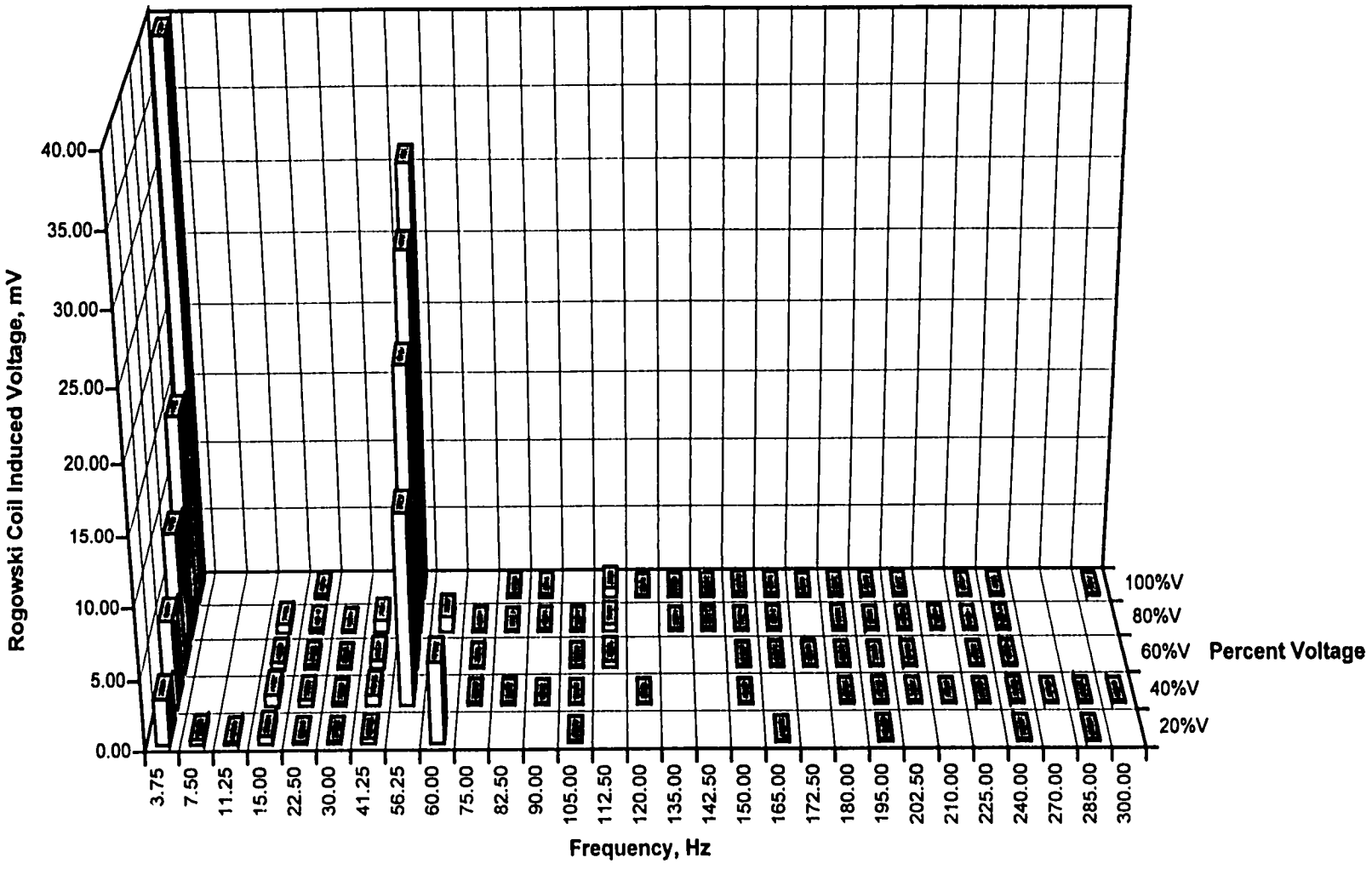

Figure 6.25: Spectrum Plot of DE Rogowski Coil Shaft Current Waveform During Initial Start of Acceleration, Shaft End Play Movement, DE Bearing Non-Insulated, ODE Bearing Insulated, Forced Lubrication.

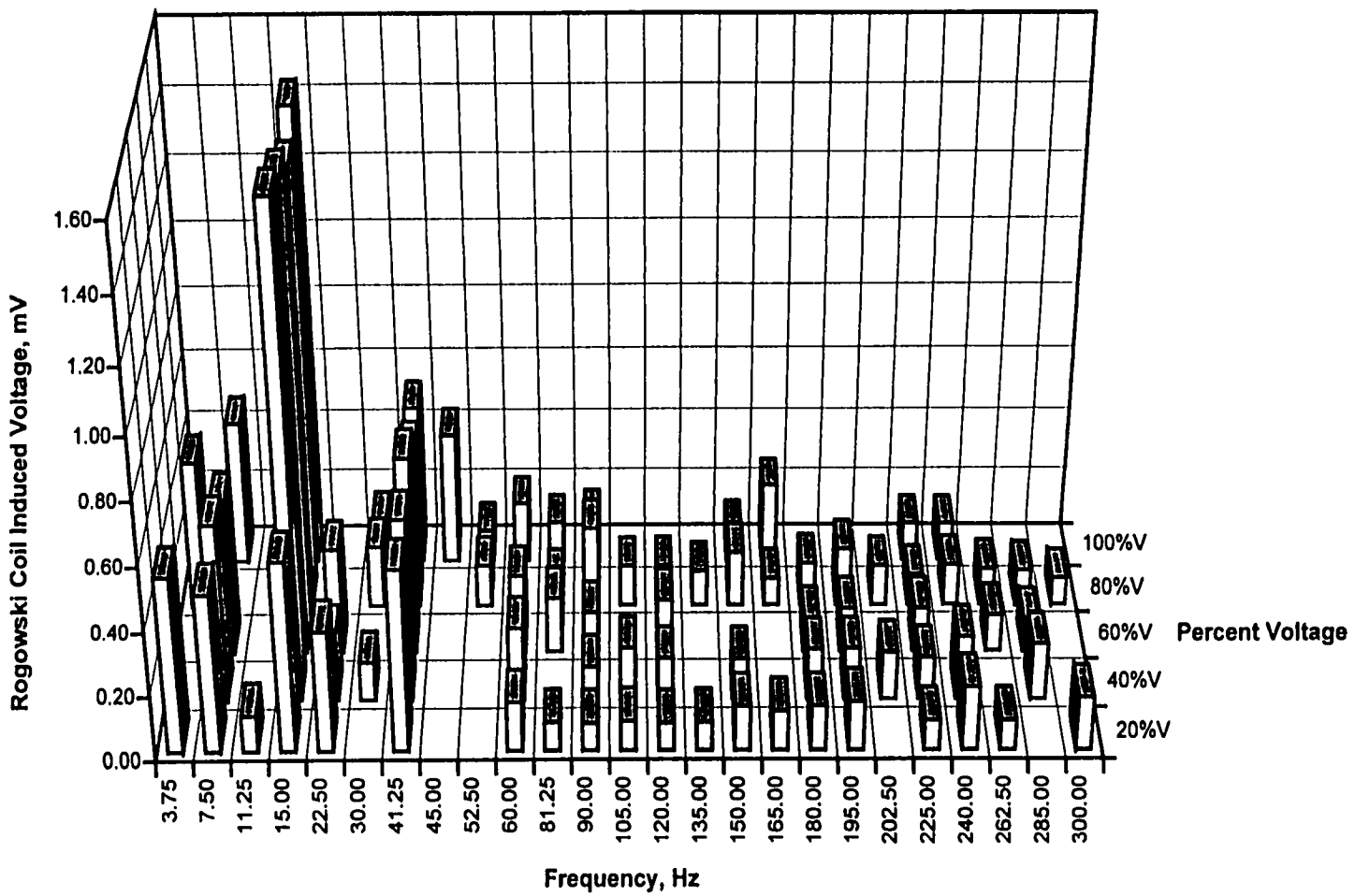

Figure 6.26: Spectrum Plot of DE Rogowski Coil Shaft Current Wavefrom During Steady State No-Load Condition, Shaft End Play Movement, DE Bearing Non-Insulated, ODE Bearing Insulated, Forced Lubrication.

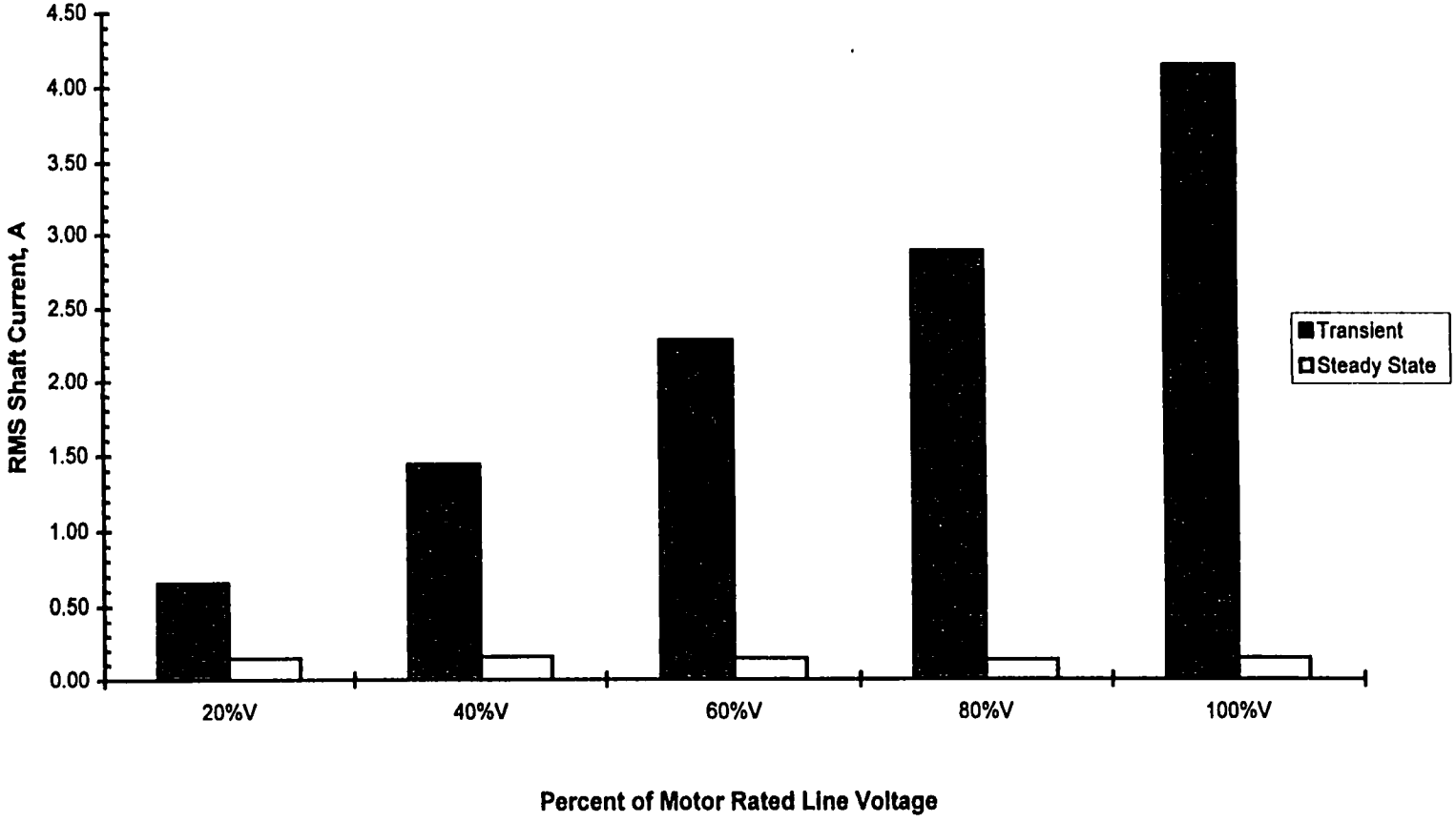

Figure 6.27: DE Rogowski Coil Shaft Current Measurement:Transient versus Steady State, Shaft End Play Movement, DE Bearing Non-Insulated, ODE Bearing Insulated, Forced Lubrication.

locked rotor torque test was conducted at various voltages. To allow for voltage ramp-up plus time for the voltage, current, torque and power readings to stabilize, a minimum test time of eight to ten seconds is required. The shaft current and shaft voltage were measured during this time period. Figures 6.28 (a) - (c) show the shaft current measured at 20%, 80%V and 100%V. Figures 6.29 (a, i) - (c, i) show a close-up view of the shaft current waveform obtained at locked rotor condition. The spectrum plots of these shaft current waveforms as shown in Figures 6.29 (a, ii) - (c, ii) indicate a dominant 60 Hz component. The zero sequence current is negligible, limited by the bearing insulation. The magnitudes of these 60 Hz shaft current components at various voltages as shown in Figure 6.30 are approximately equal to those obtained during the initial start-up of motor acceleration with either oil ring lubrication or forced lubrication and ODE bearing insulated of Figures 6.23 and 6.27.

6.4.4 SHAFT VOLTAGE MEASUREMENT

Shaft voltages are measured end to end, drive end to ground and opposite drive end to ground. A voltmeter is used in the measurement. At the same time the shaft voltage waveforms are stored in a spectrum analyzer. The time and frequency domains of these waveforms obtained at 20%V, 80%V and 100%V are presented in Figure 6.31. The voltage from one end of the shaft to the other end was measured. In addition, voltages from the DE of the shaft to ground and the ODE of the shaft to ground were measured. In the three cases, the 180 Hz voltage component was the dominant frequency component. The presence of the 180 Hz shaft voltage component at 20%V as shown in Figures 6.31 (a, ii) - (c, ii) indicates that the flux surrounding the shaft and causing the shaft voltage, is due to the presence of joints in

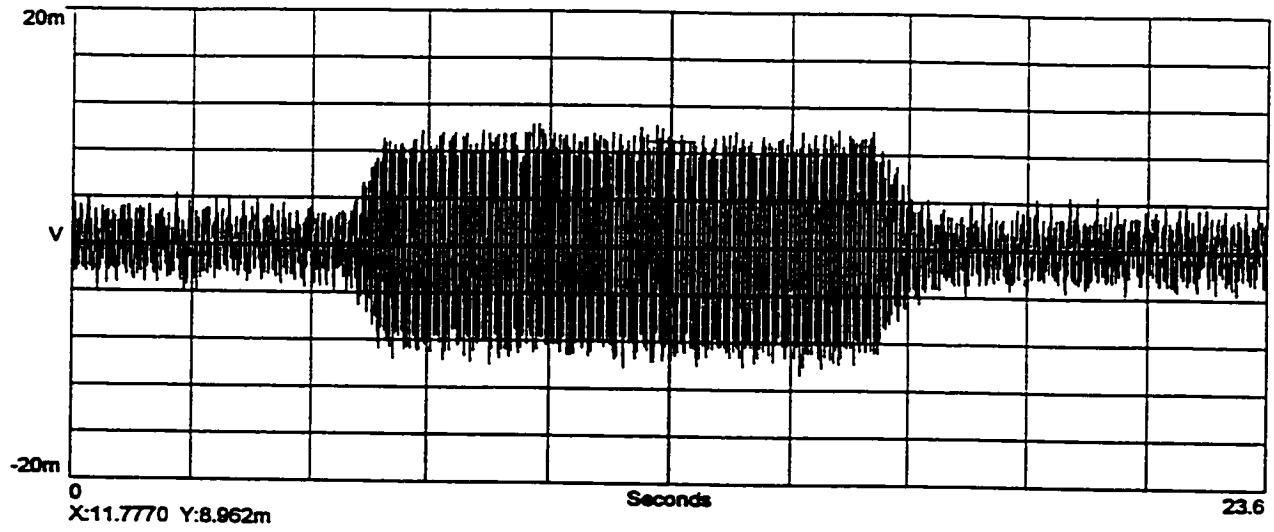

a) 20% of Motor Rated Line Voltage.

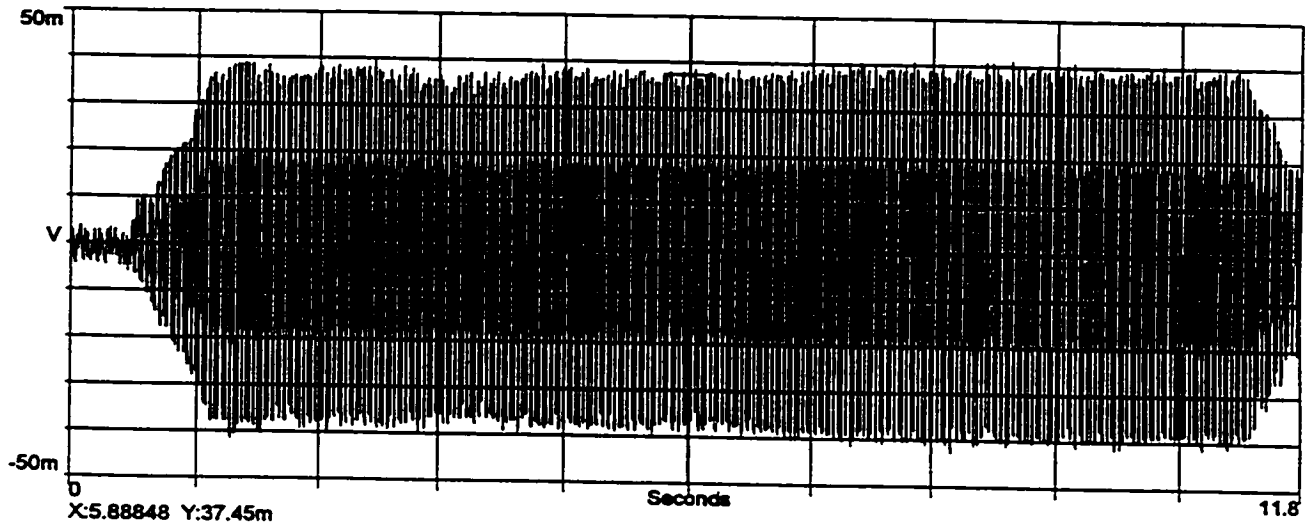

b) 80% of Motor Rated Line Voltage.

Figure 6.28: Waveforms of DE Rogowski Coil Shaft Current Measurement At 20%, 80% and 100% of Motor Line Voltage, Locked Rotor Condition, DE Bearing Non-Insulated, ODE Bearing Insulated, Oil Ring Lubrication.

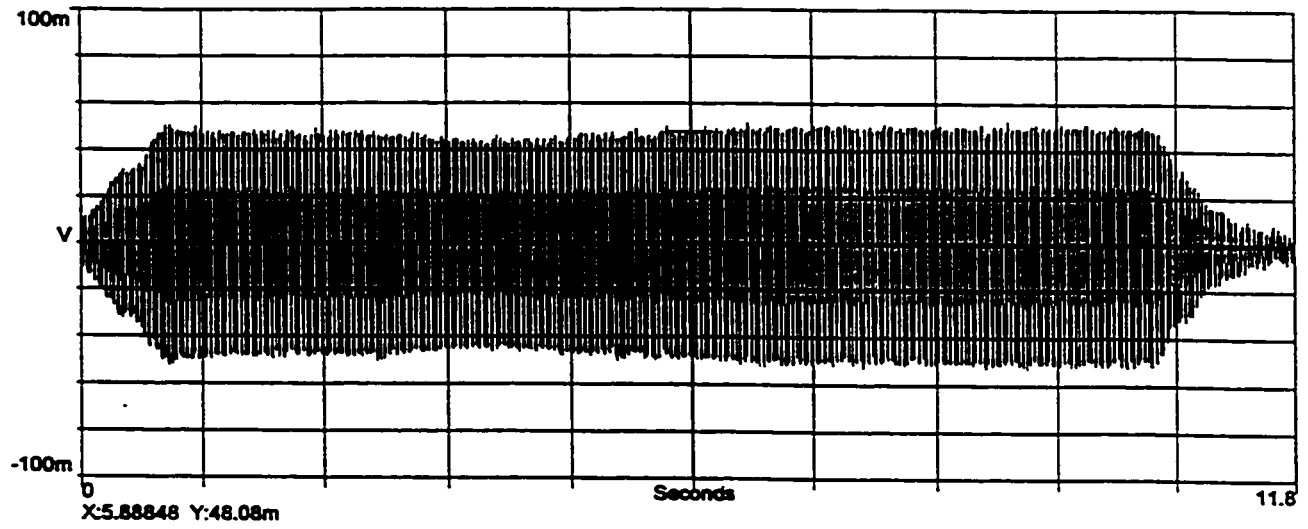

c) 100% of Motor Rated Line Voltage

Figure 6.28: Waveforms of DE Rogowski Coil Shaft Current Measurement At 20%, 80% and 100% of Motor Line Voltage, Locked Rotor Condition, DE Bearing Non-Insulated, ODE Bearing Insulated, Oil Ring Lubrication.

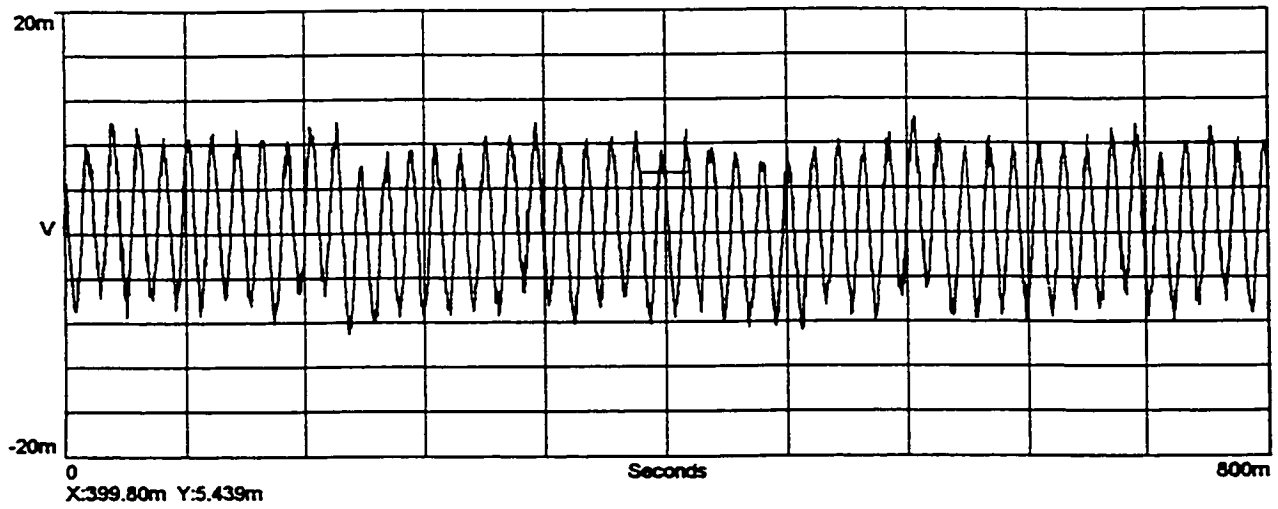

i) Shaft Current Waveform

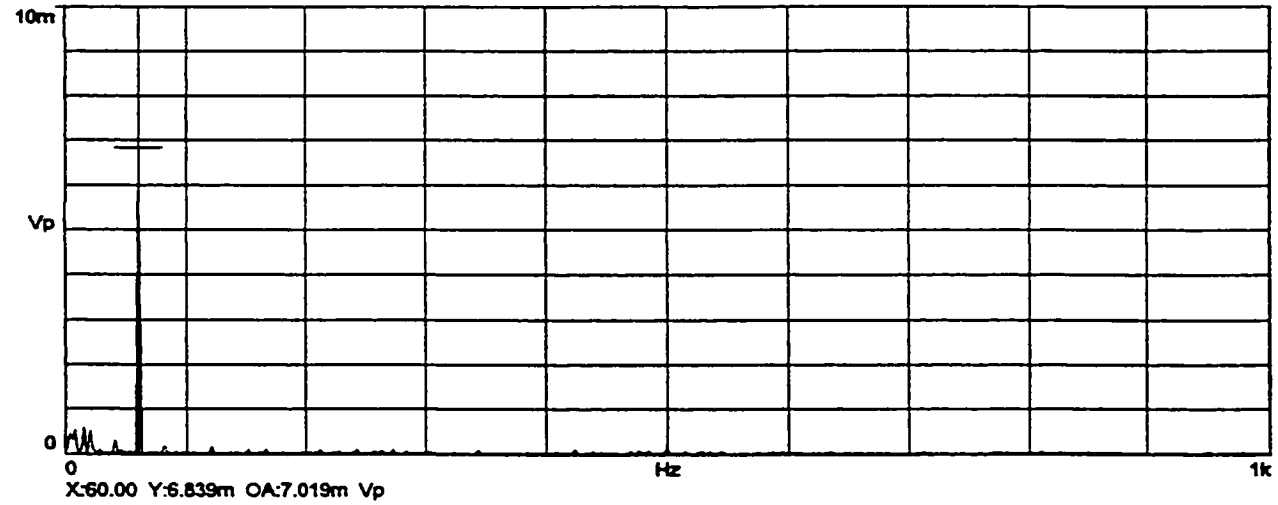

ii) Spectrum Plot

a) Close-Up View of the Shaft Current Waveform and Spectrum Plot, 20% of Motor Rated Line Voltage.

Figure 6.29: Close-Up View of the Shaft Current Waveform and Spectrum Plot, 20%, 80% and 100% of Motor Line Voltage, Locked Rotor Condition, DE Bearing Non-Insulated, ODE Bearing Insulated, Oil Ring Lubrication.

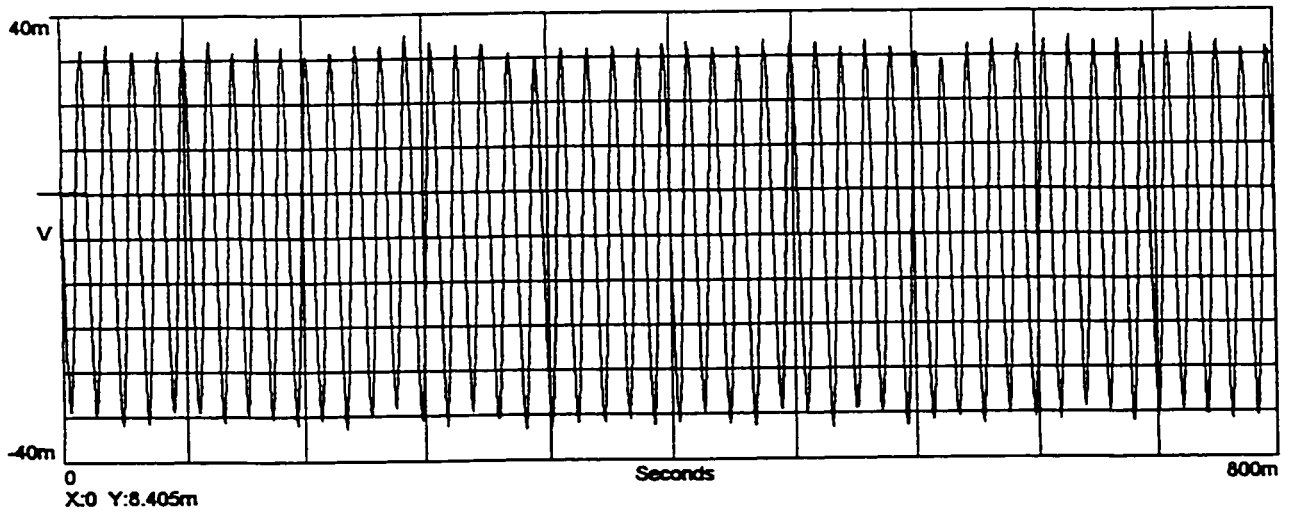

i) Shaft Current Waveform

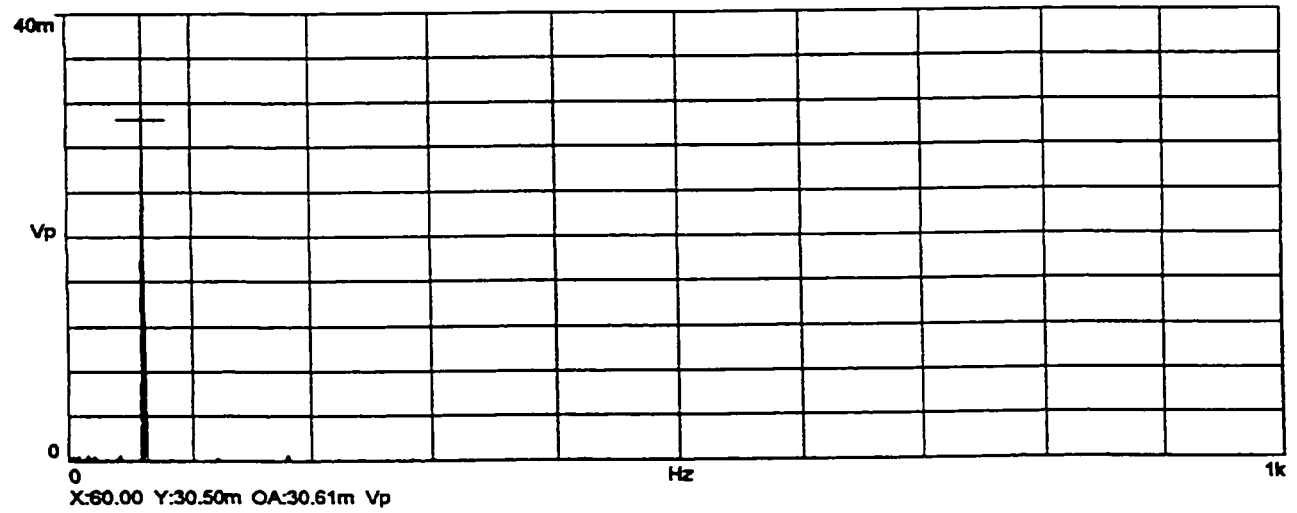

ii) Spectrum Plot

b) Close-Up View of the Shaft Current Waveform and Spectrum Plot, 80% of Motor Rated Line Voltage.

Figure 6.29: Close-Up View of the Shaft Current Waveform and Spectrum Plot, 20%, 80% and 100% of Motor Line Voltage, Locked Rotor Condition, DE Bearing Non-Insulated, ODE Bearing Insulated, Oil Ring Lubrication.

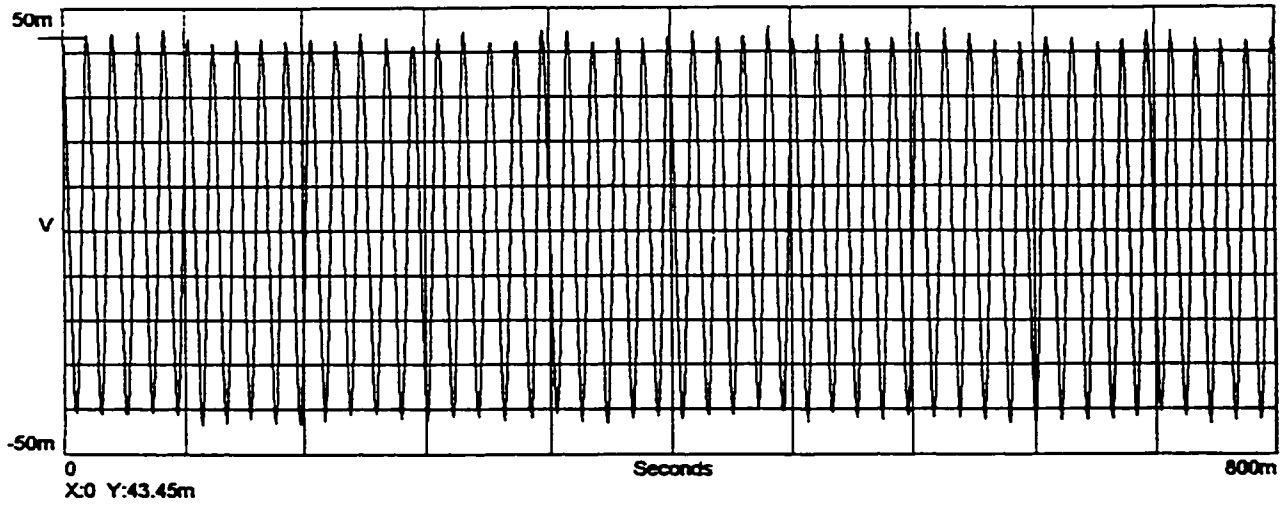

i) Shaft Current Waveform

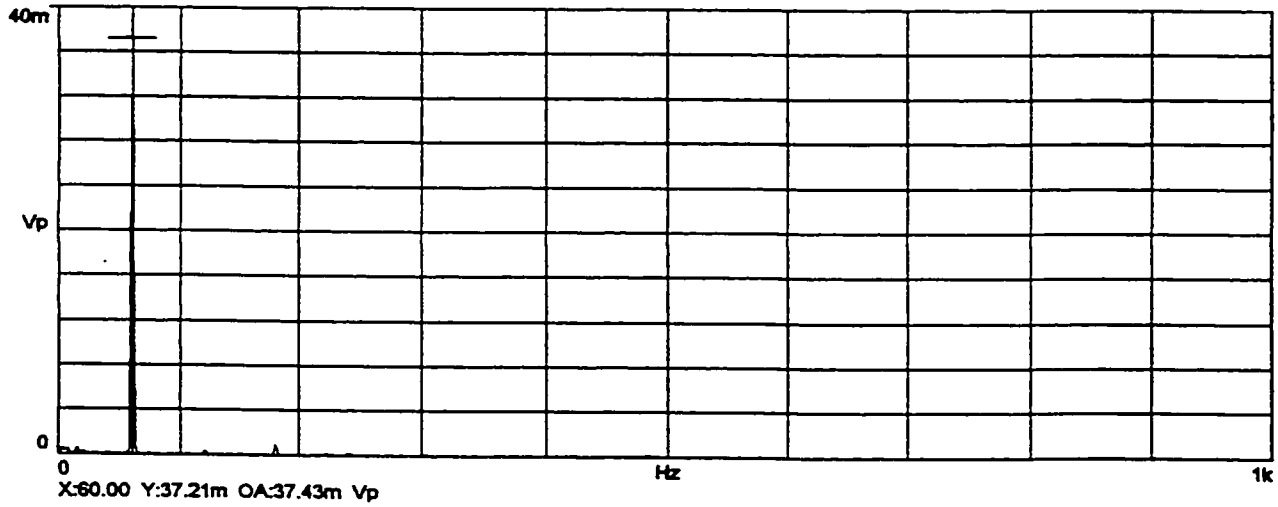

ii) Spectrum Plot

c) Close-Up View of the Shaft Current Waveform and Spectrum Plot, 100% of Motor Rated Line Voltage.

Figure 6.29: Close-Up View of the Shaft Current Waveform and Spectrum Plot, 20%, 80% and 100% of Motor Line Voltage, Locked Rotor Condition, DE Bearing Non-Insulated, ODE Bearing Insulated, Oil Ring Lubrication.

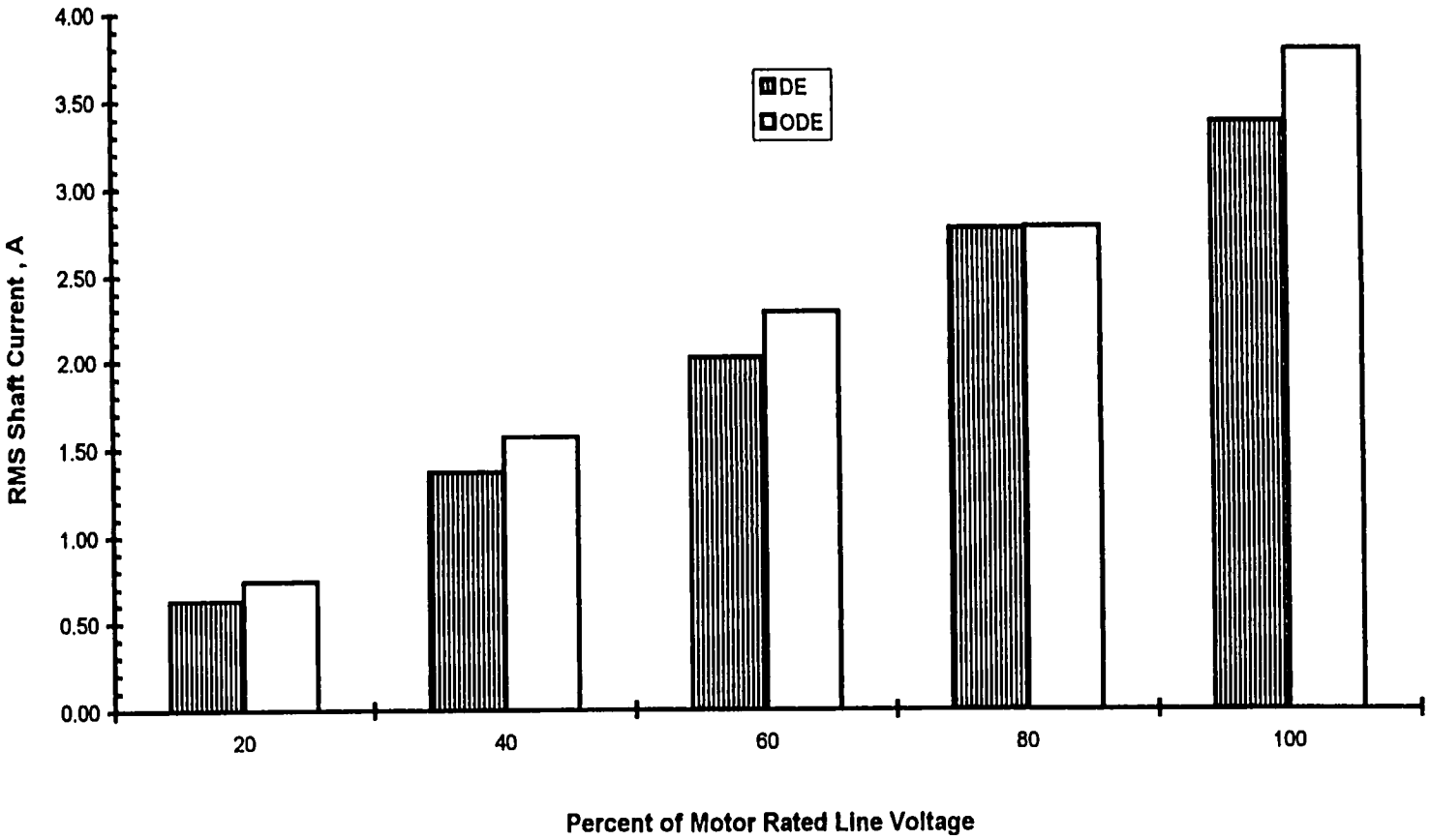

Figure 6.30: Rogowski Coil Shaft Current Measurement During Locked Rotor Condition, 60 Hz Component, DE Bearing Non-Insulated, ODE Bearing Insulated, Oil Ring Lubrication.

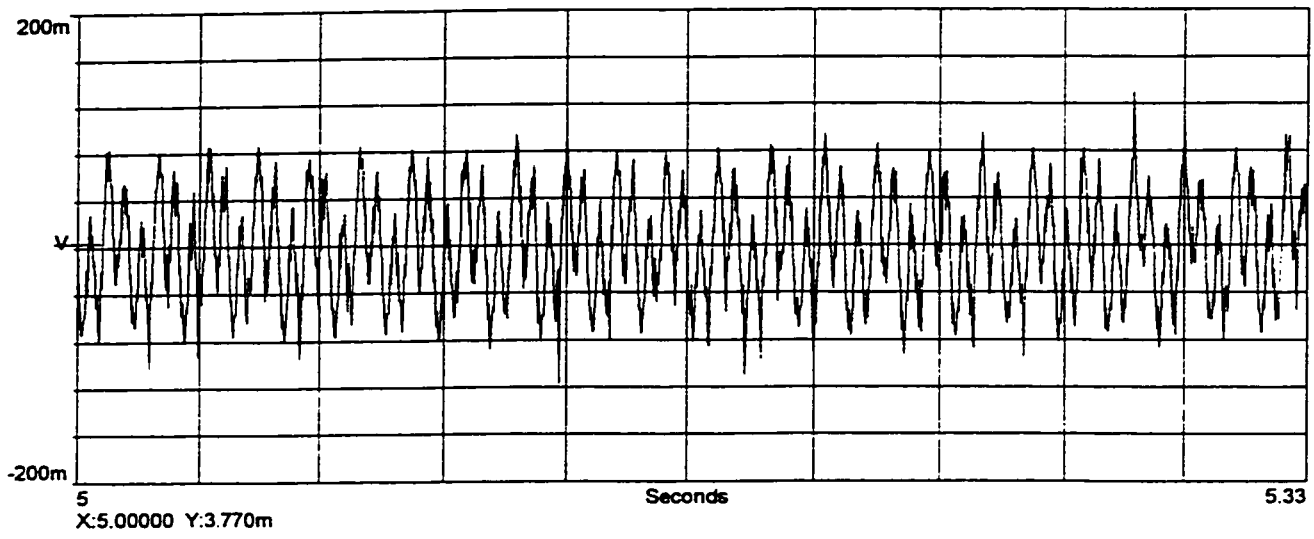

i) Shaft Voltage Waveform

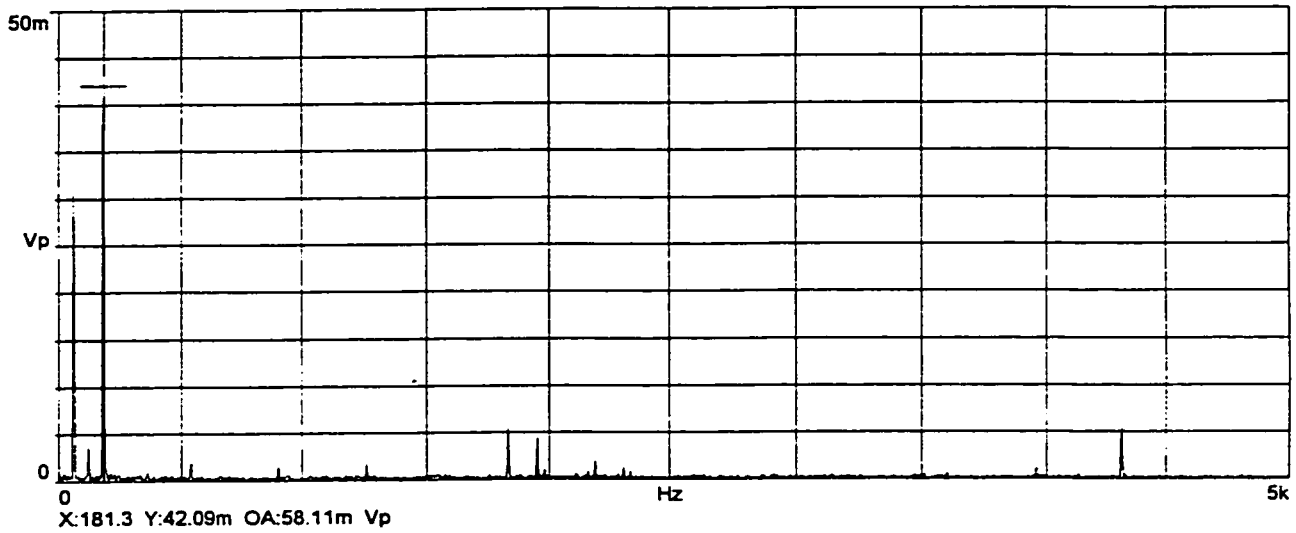

ii) Spectrum Plot

a) Shaft Voltage Waveform and Spectrum Plot, End-End Measurement, 20% of Motor Rated Line Voltage.

Figure 6.31: Shaft Voltage Measurement At 20%, 80% and 100% of Motor Line Voltage, Steady State No-Load Condition, DE Bearing Non-Insulated, ODE Bearing Insulated, Oil Ring Lubrication.

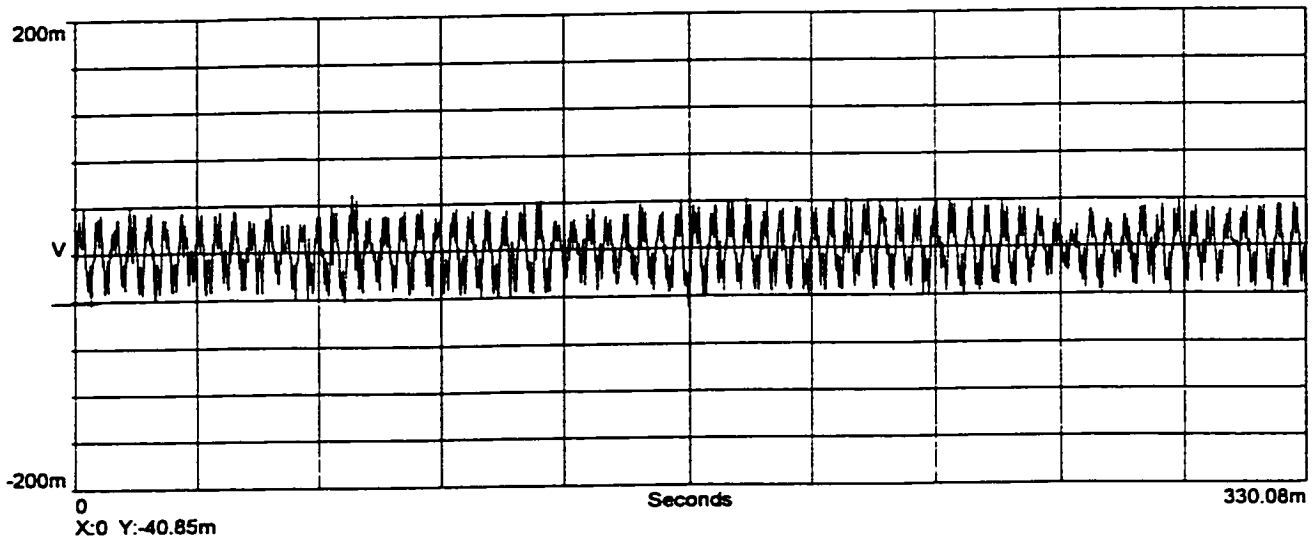

i) Shaft Voltage Waveform

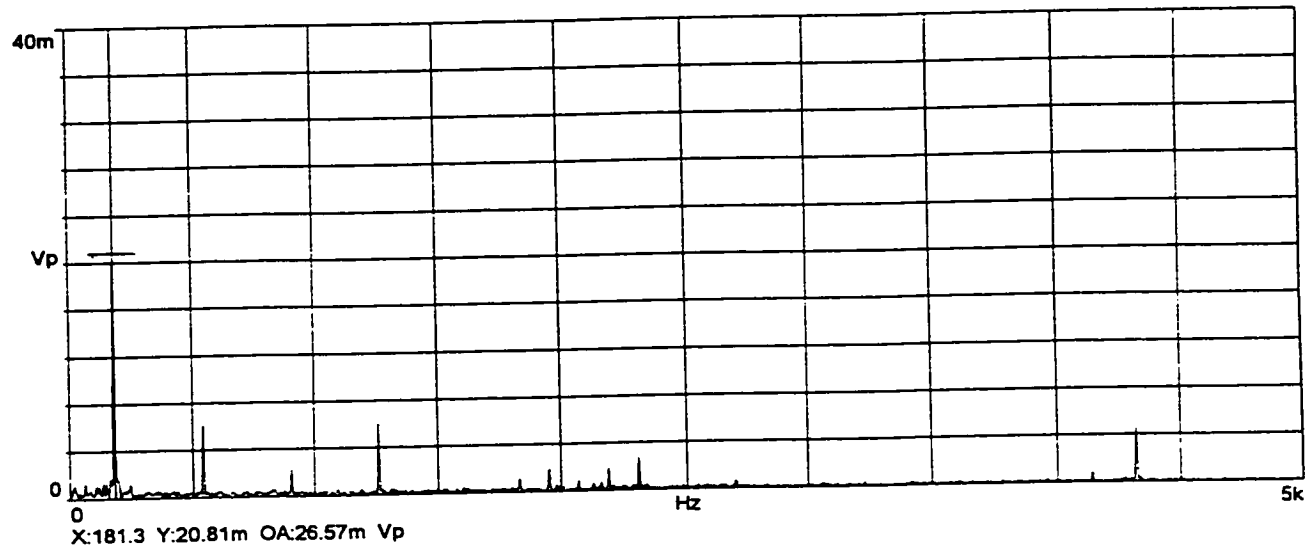

ii) Spectrum Plot

b) Shaft Voltage Waveform and Spectrum Plot, DE-GND Measurement, 20% of Motor Rated Line Voltage.

Figure 6.31: Shaft Voltage Measurement At 20%, 80% and 100% of Motor Line Voltage, Steady State No-Load Condition, DE Bearing Non-Insulated, ODE Bearing Insulated, Oil Ring Lubrication.

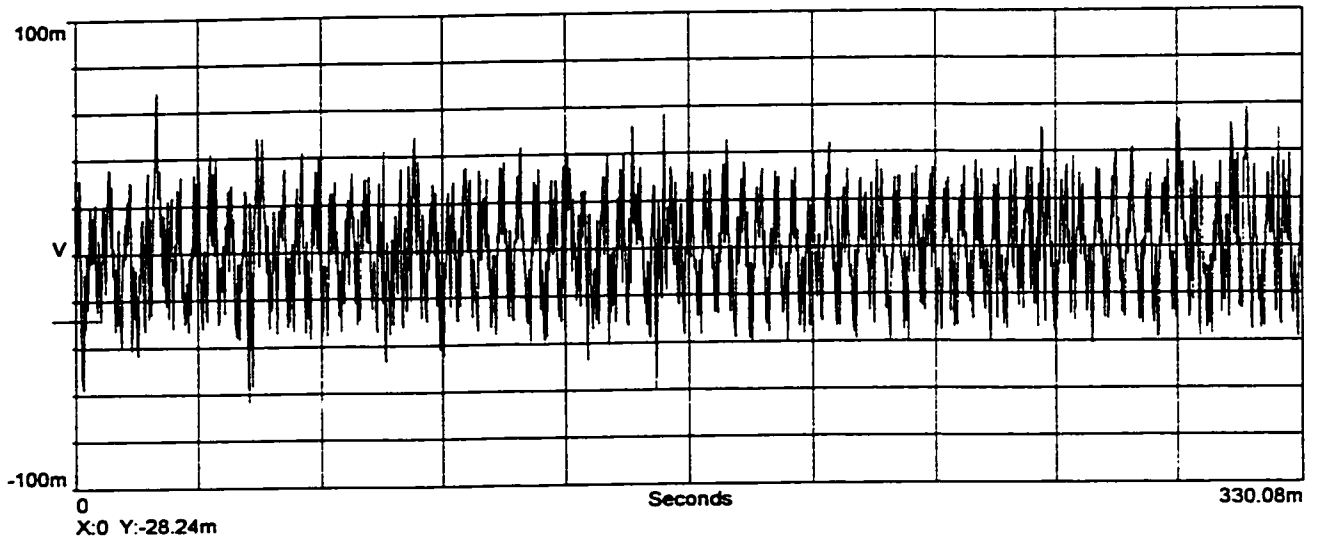

i) Shaft Voltage Waveform

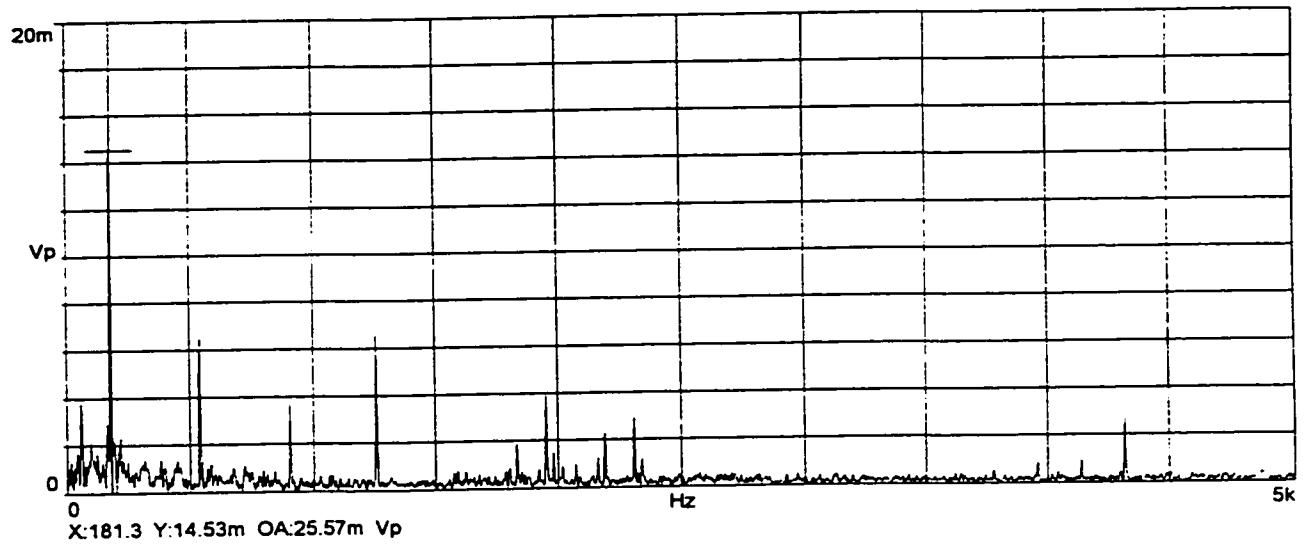

ii) Spectrum Plot

c) Shaft Voltage Waveform and Spectrum Plot, ODE-GND Measurement, 20% of Motor Rated Line Voltage.

Figure 6.31: Shaft Voltage Measurement At 20%, 80% and 100% of Motor Line Voltage, Steady State No-Load Condition, DE Bearing Non-Insulated, ODE Bearing Insulated, Oil Ring Lubrication.

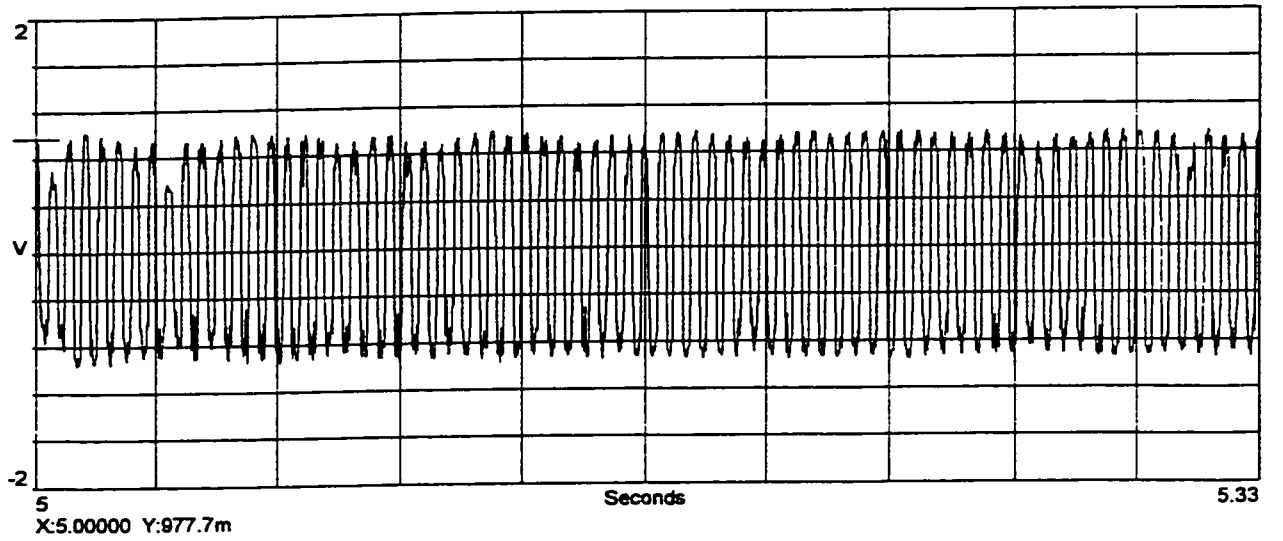

i) Shaft Voltage Waveform

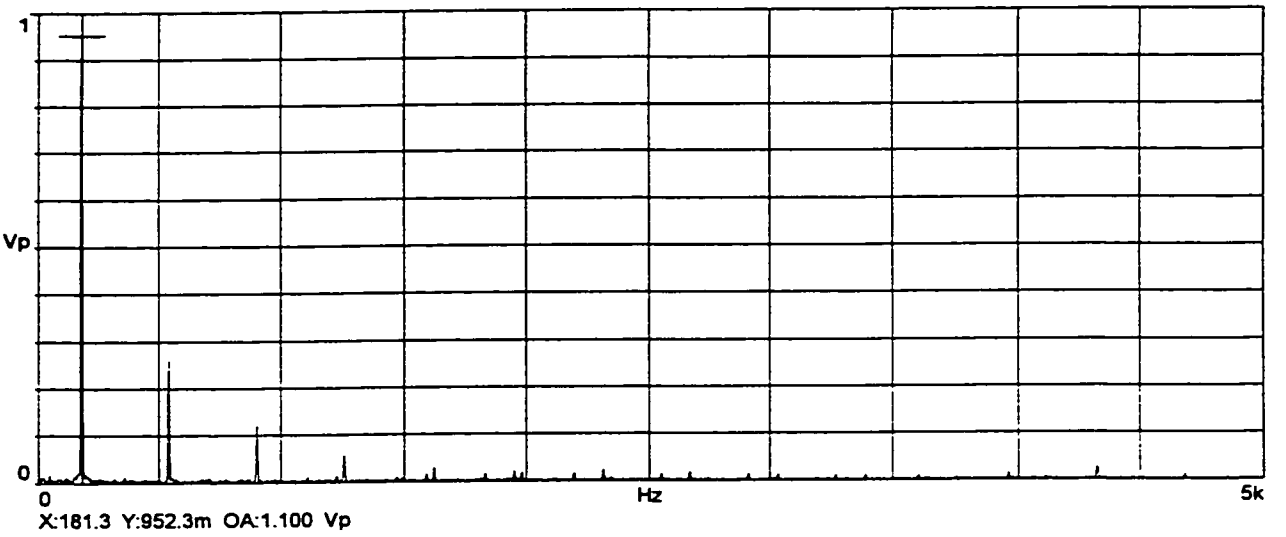

ii) Spectrum Plot

d) Shaft Voltage Waveform and Spectrum Plot, End-End Measurement, 80% of Motor Rated Line Voltage.

Figure 6.31: Shaft Voltage Measurement At 20%, 80% and 100% of Motor Line Voltage, Steady State No-Load Condition, DE Bearing Non-Insulated, ODE Bearing Insulated, Oil Ring Lubrication.

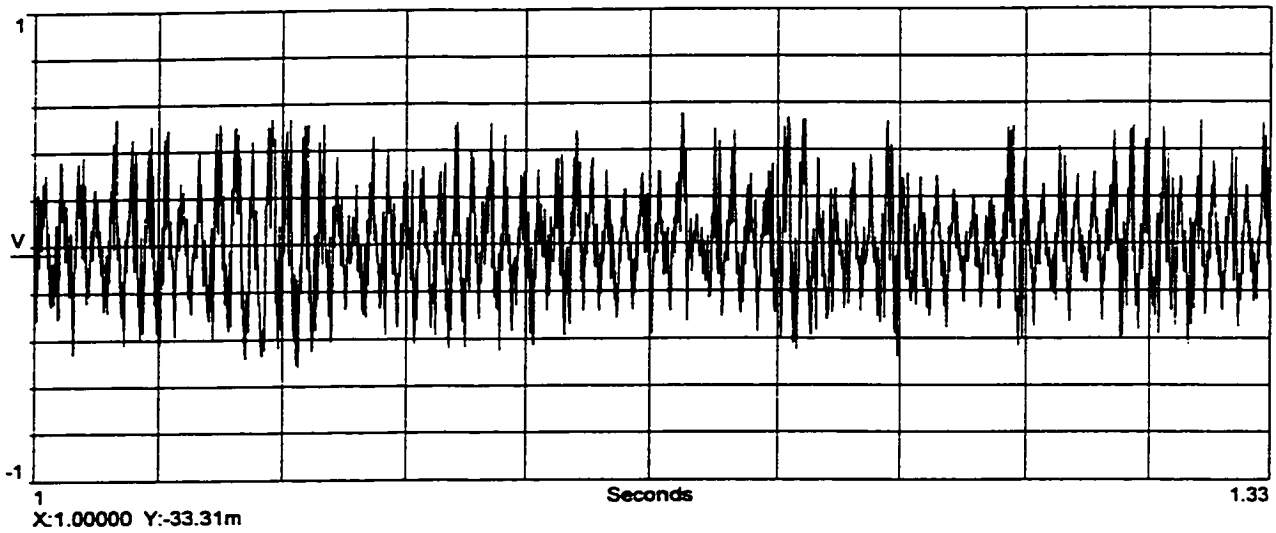

i) Shaft Voltage Waveform

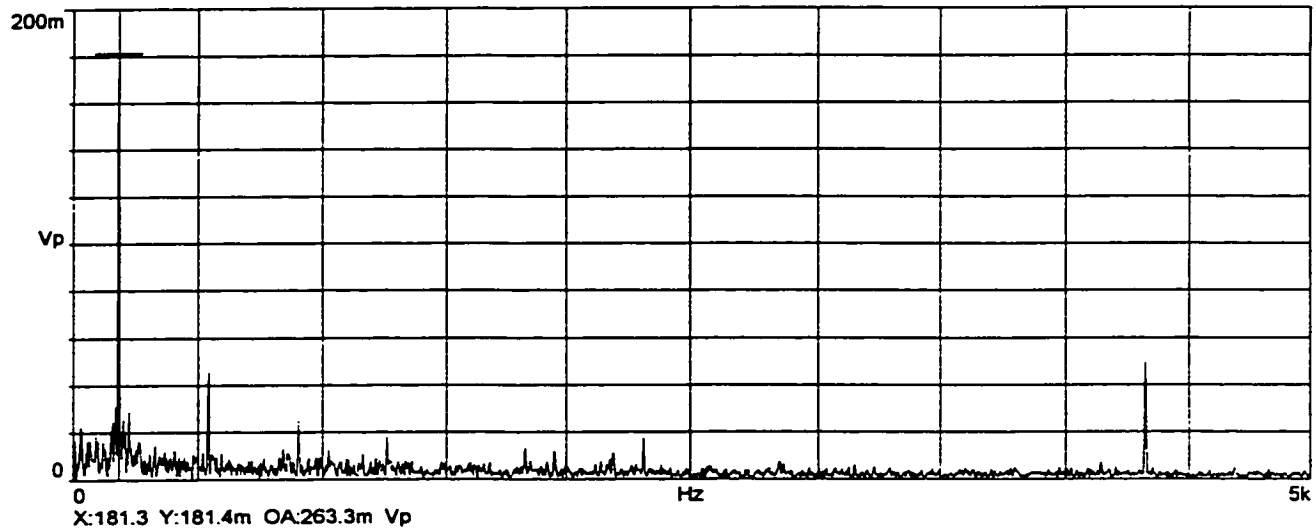

ii) Spectrum Plot

e) Shaft Voltage Waveform and Spectrum Plot, DE-GND Measurement, 80% of Motor Rated Line Voltage.

Figure 6.31: Shaft Voltage Measurement At 20%, 80% and 100% of Motor Line Voltage, Steady State No-Load Condition, DE Bearing Non-Insulated, ODE Bearing Insulated, Oil Ring Lubrication.

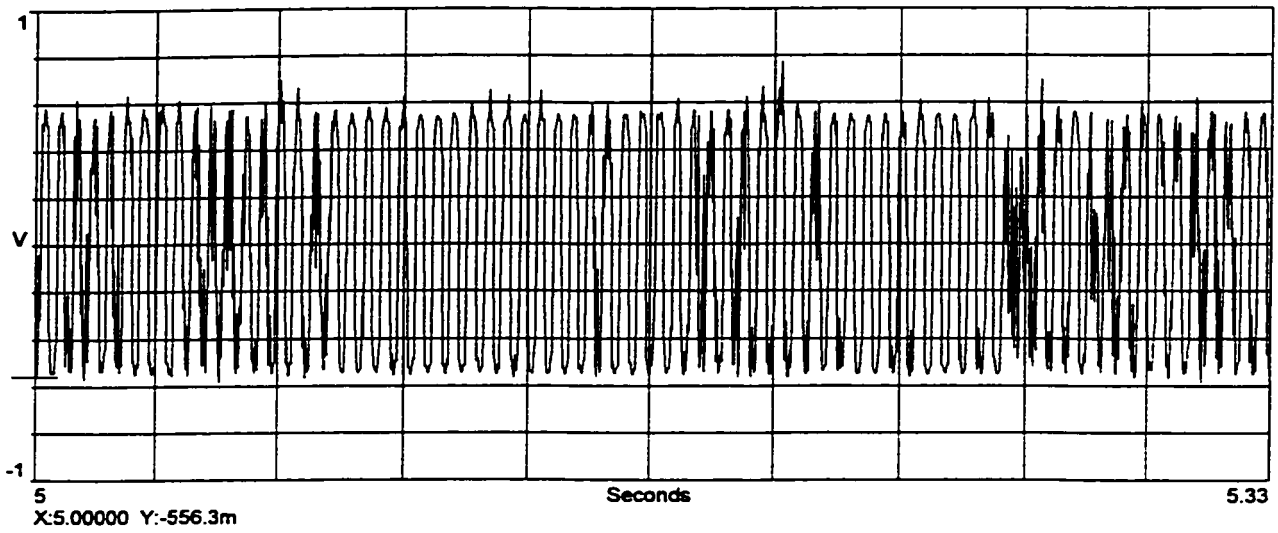

i) Shaft Voltage Waveform

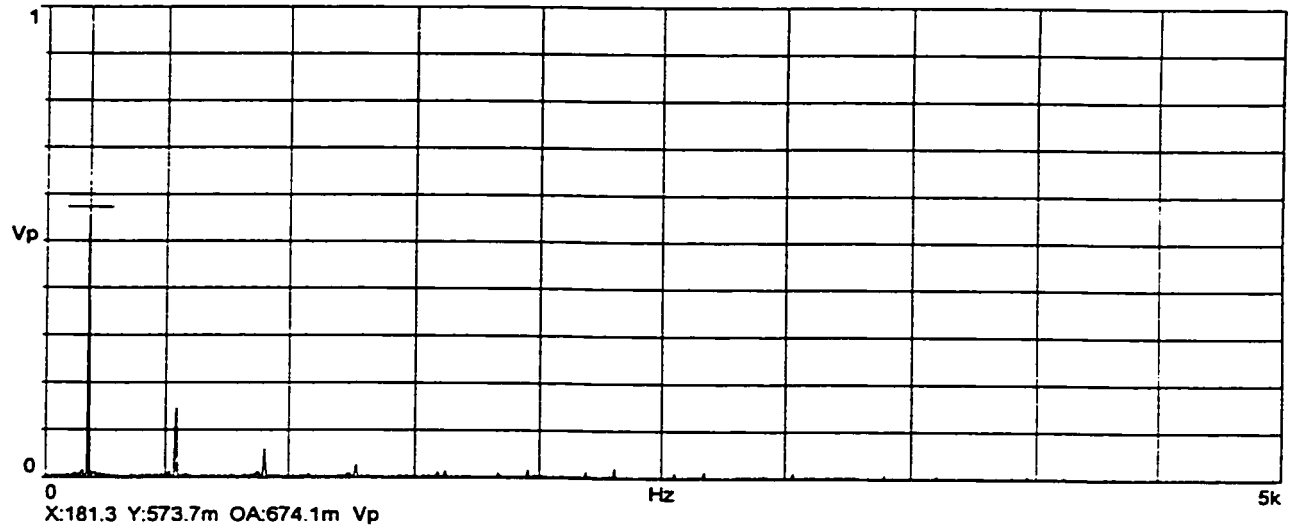

ii) Spectrum Plot

f) Shaft Voltage Waveform and Spectrum Plot, ODE-GND Measurement, 80% of Motor Rated Line Voltage.

Figure 6.31: Shaft Voltage Measurement At 20%, 80% and 100% of Motor Line Voltage, Steady State No-Load Condition, DE Bearing Non-Insulated, ODE Bearing Insulated, Oil Ring Lubrication.

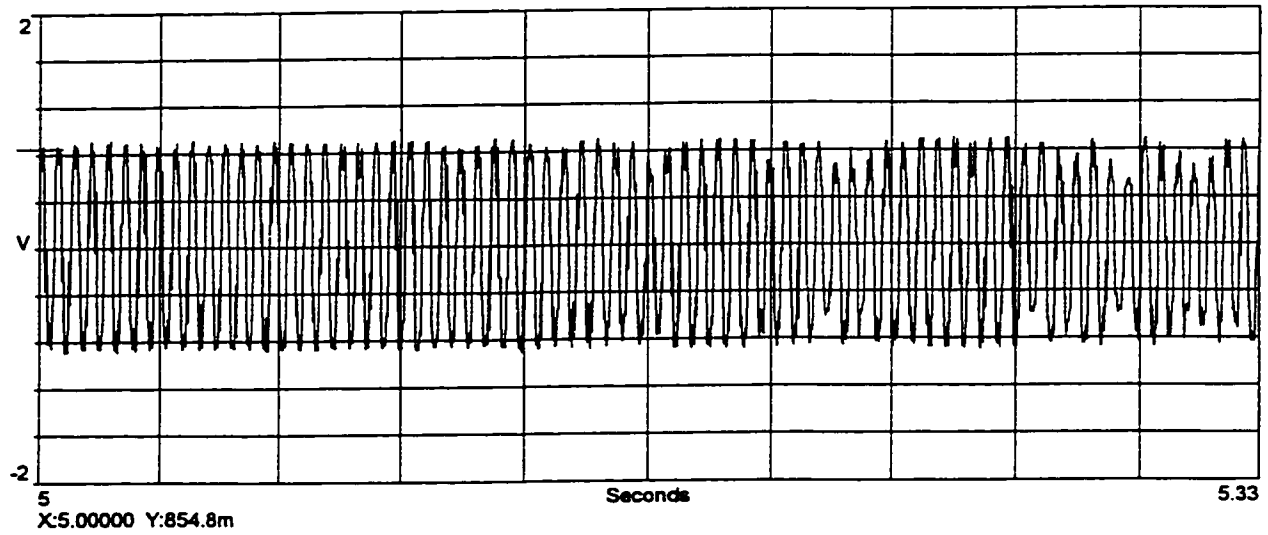

i) Shaft Voltage Waveform

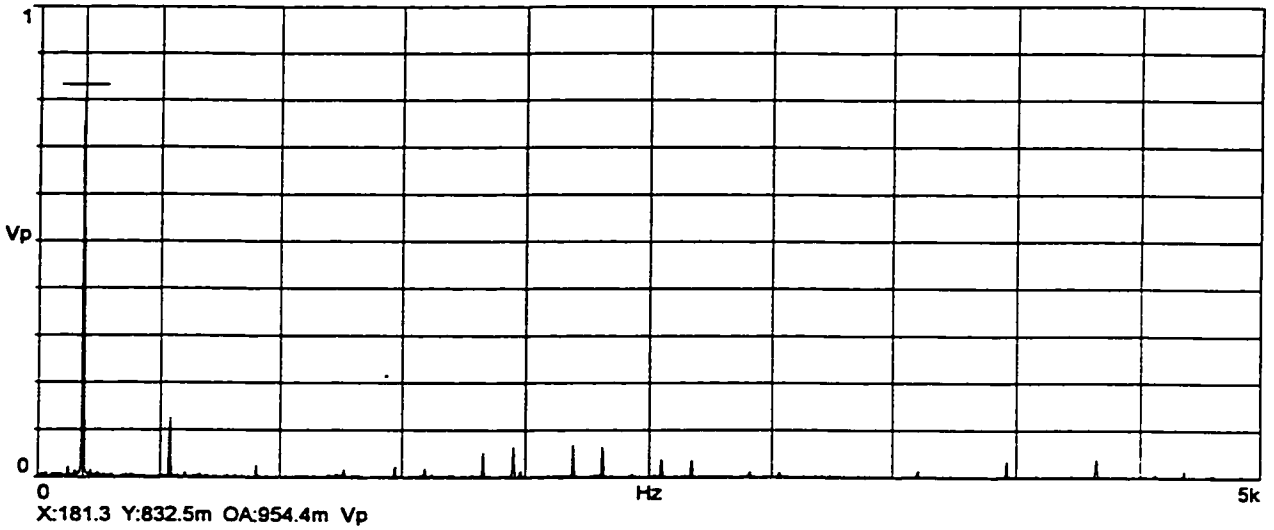

ii) Spectrum Plot

g) Shaft Voltage Waveform and Spectrum Plot, End-End Measurement, 100% of Motor Rated Line Voltage.

Figure 6.31: Shaft Voltage Measurement At 20%, 80% and 100% of Motor Line Voltage, Steady State No-Load Condition, DE Bearing Non-Insulated, ODE Bearing Insulated, Oil Ring Lubrication.

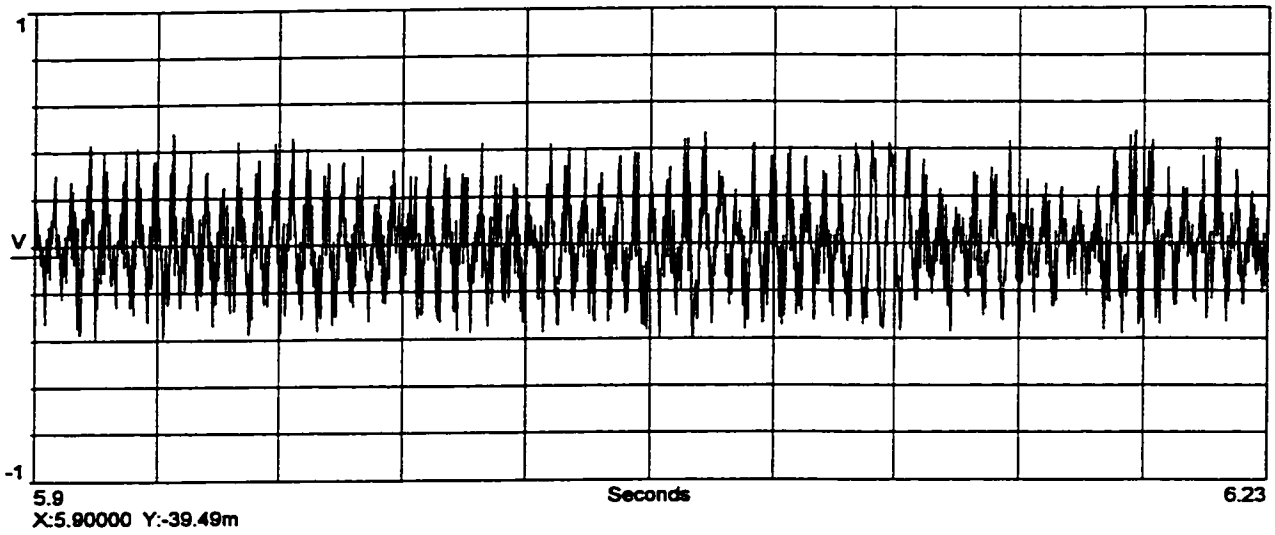

i) Shaft Voltage Waveform

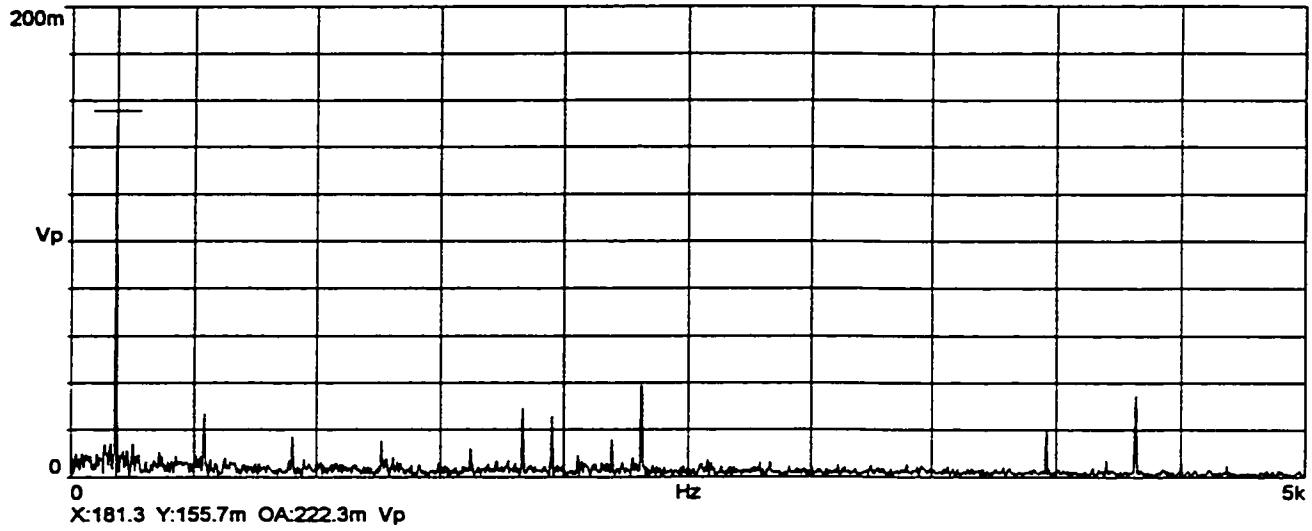

ii) Spectrum Plot

h) Shaft Voltage Waveform and Spectrum Plot, DE-GND Measurement, 100% of Motor Rated Line Voltage.

Figure 6.31: Shaft Voltage Measurement At 20%, 80% and 100% of Motor Line Voltage, Steady State No-Load Condition, DE Bearing Non-Insulated, ODE Bearing Insulated, Oil Ring Lubrication.

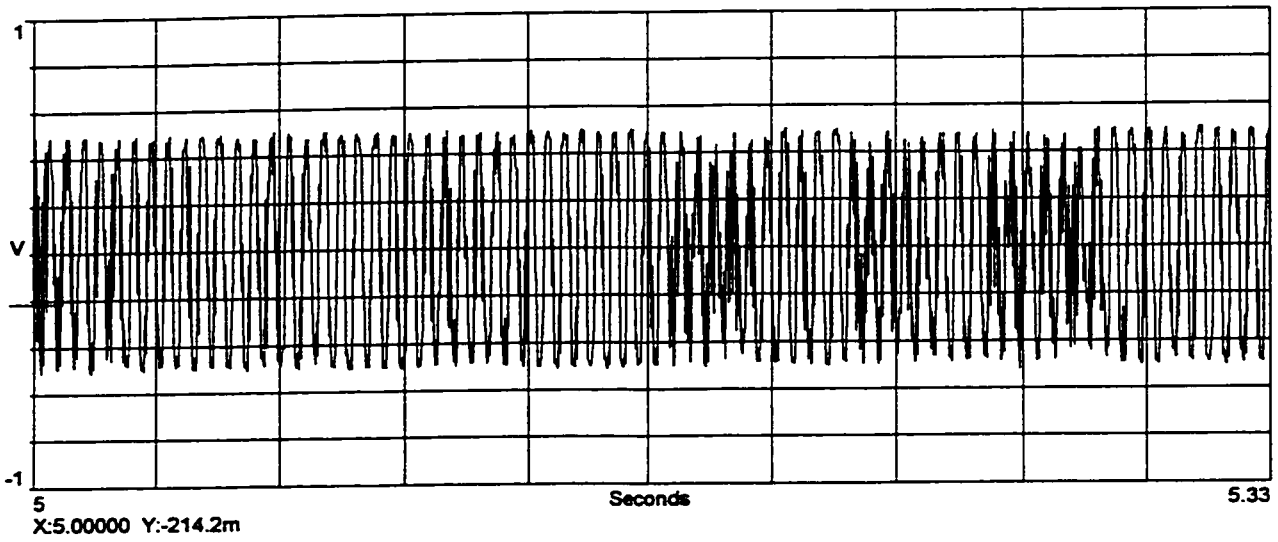

i) Shaft Voltage Waveform

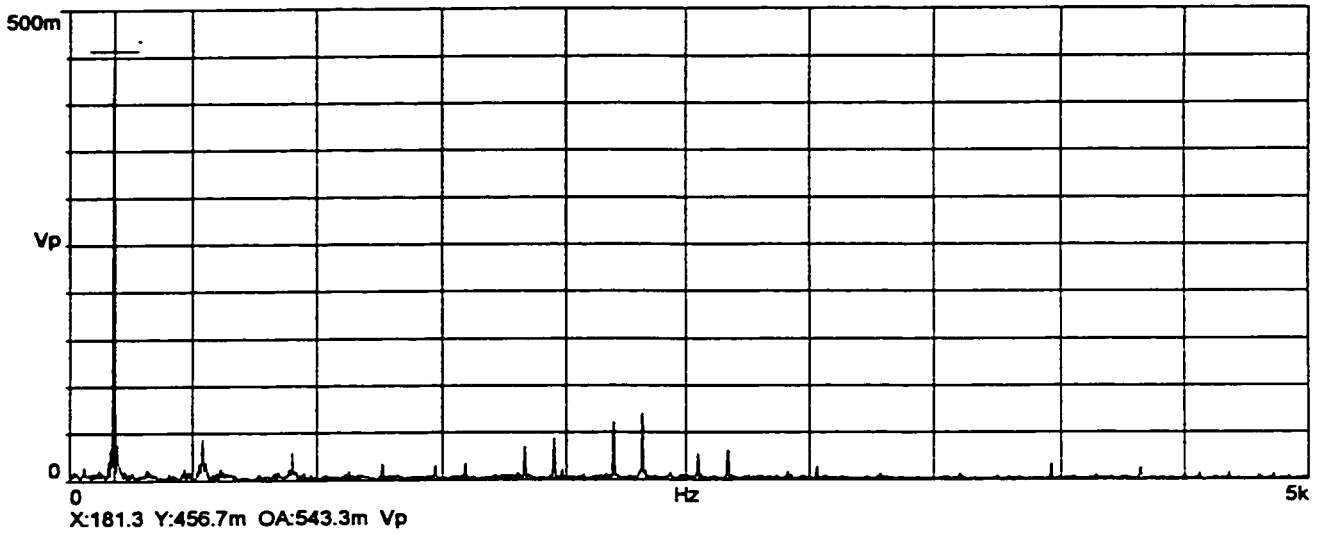

ii) Spectrum Plot

i) Shaft Voltage Waveform and Spectrum Plot, ODE-GND Measurement, 100% of Motor Rated Line Voltage.

Figure 6.31: Shaft Voltage Measurement At 20%, 80% and 100% of Motor Line Voltage, Steady State No-Load Condition, DE Bearing Non-Insulated, ODE Bearing Insulated, Oil Ring Lubrication.

the stator laminations and not due to saturation. The motor teeth do not saturate at 20%V. This finding is consistent with the Rogowski coil shaft current measurement conducted with both bearings non-insulated. At 60%V and higher of Figures 6.31 (d ,ii) - (r, ii), odd multiples of 180 Hz were also observed, indicating the effect of saturation. In Figure 6.32 (a), the shaft voltage initially increases with voltage, peaks at 80%V and decreases as the motor line voltage is further increased. The test machine is operating in saturation condition at this voltage. From 20%V to 40%V the rate of rise of shaft voltage is small. From 40%V to 60%V, the rate of rise of shaft voltage measured end to end is the highest. Thereafter, the rate of rise of shaft voltage decreases. Figures 6.32 (b) - (d) summarize the frequency components of the shaft voltage, listing the 180 Hz as the dominant frequency followed by 540 Hz and 900 Hz. The magnitude of shaft voltage measured from the drive end of the shaft to ground as shown in Figures 6.32 (a) and (c) is expected to be much smaller than that measured from the opposite drive end of the shaft to ground of Figures 6.32 (a) and (d). The reason is that the drive end bearing is non-insulated while the opposite drive end bearing is insulated.

The shaft voltage was also measured when the machine was operating with forced bearing lubrication. The shaft voltages measured end to end at different voltage levels, illustrated in Figure 6.33, did not differ much from those in Figure 6.32 (a). As seen in Figure 6.33, both the DE to ground voltage and ODE to ground voltage increase gradually from 40%V to 80%V. The voltages measured at 80%V and 90%V in both cases of bearing lubrications are approximately the same. In the forced bearing lubrication case, after 90%V the ODE to ground voltage decreases substantially from approximately 0.38V to 0.20V. The ODE bearing

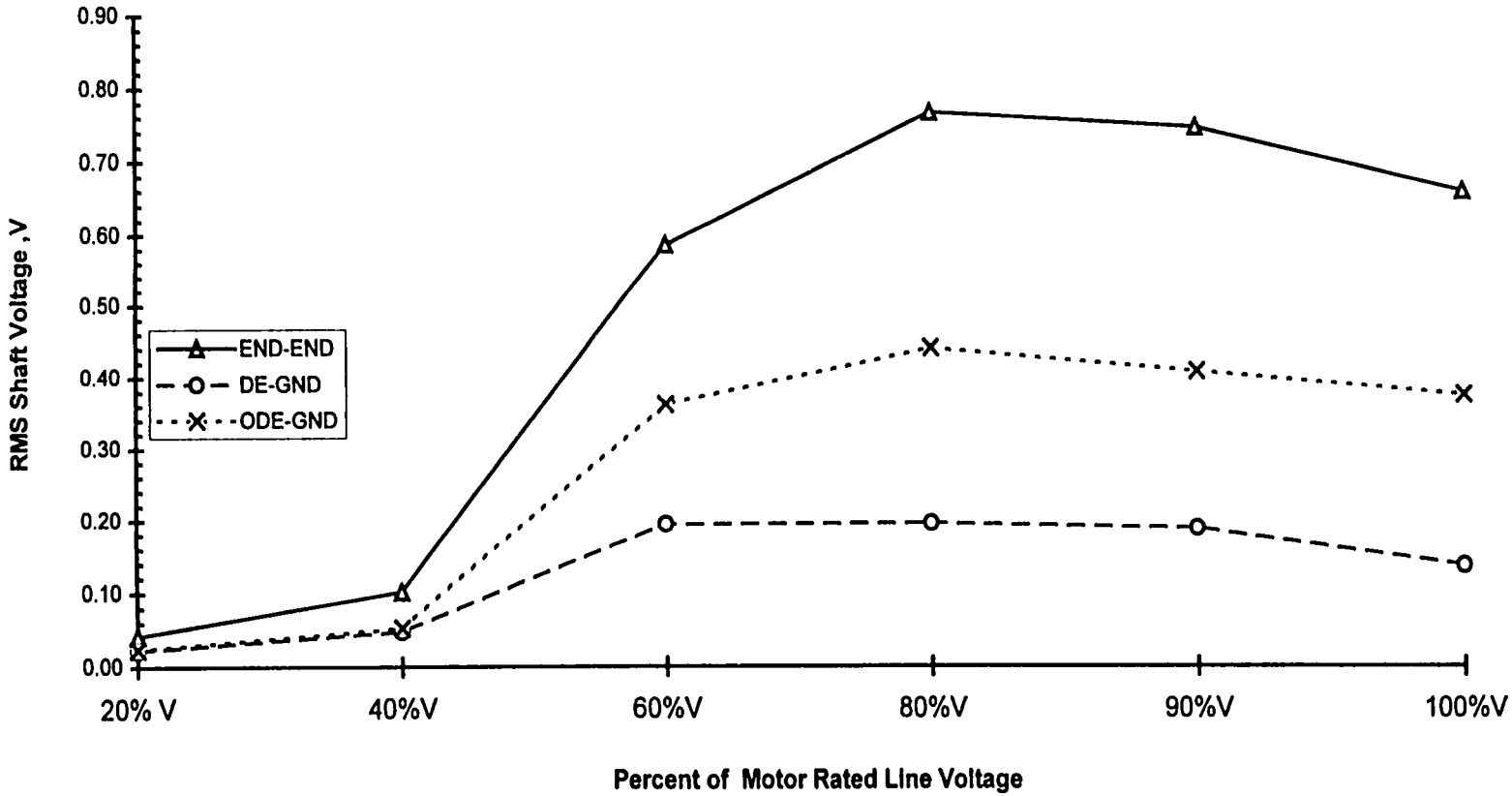

a) Magnitude

Figure 6.32: Shaft Voltage Measurement At Steady State No-Load Condition, DE Bearing Non-Insulated, ODE Bearing Insulated, Oil Ring Lubrication.

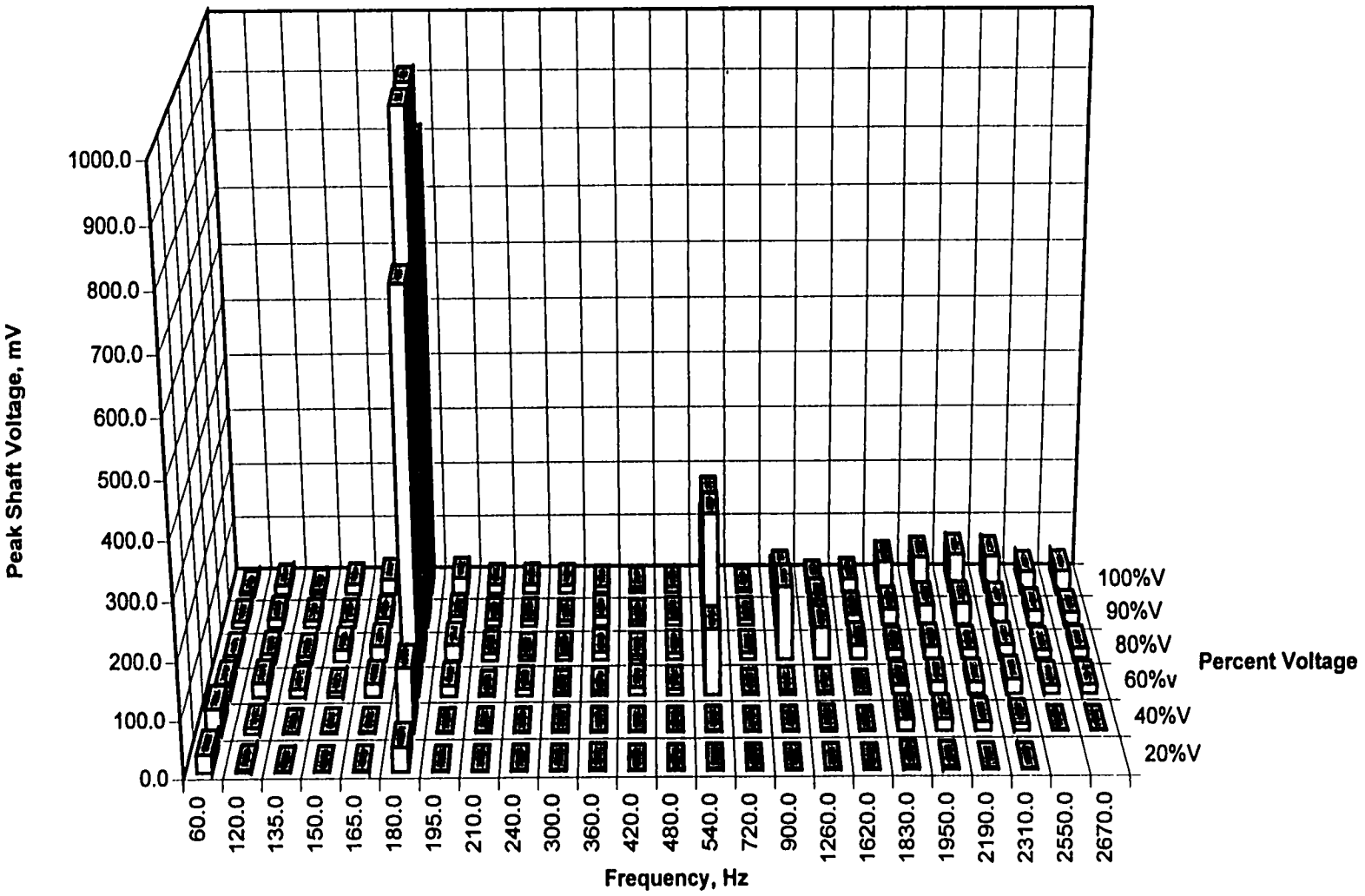

b) End-to-End Measurement

Figure 6.32: Shaft Voltage Measurement At Steady State No-Load Condition, DE Bearing Non-Insulated, ODE Bearing Insulated, Oil Ring Lubrication.

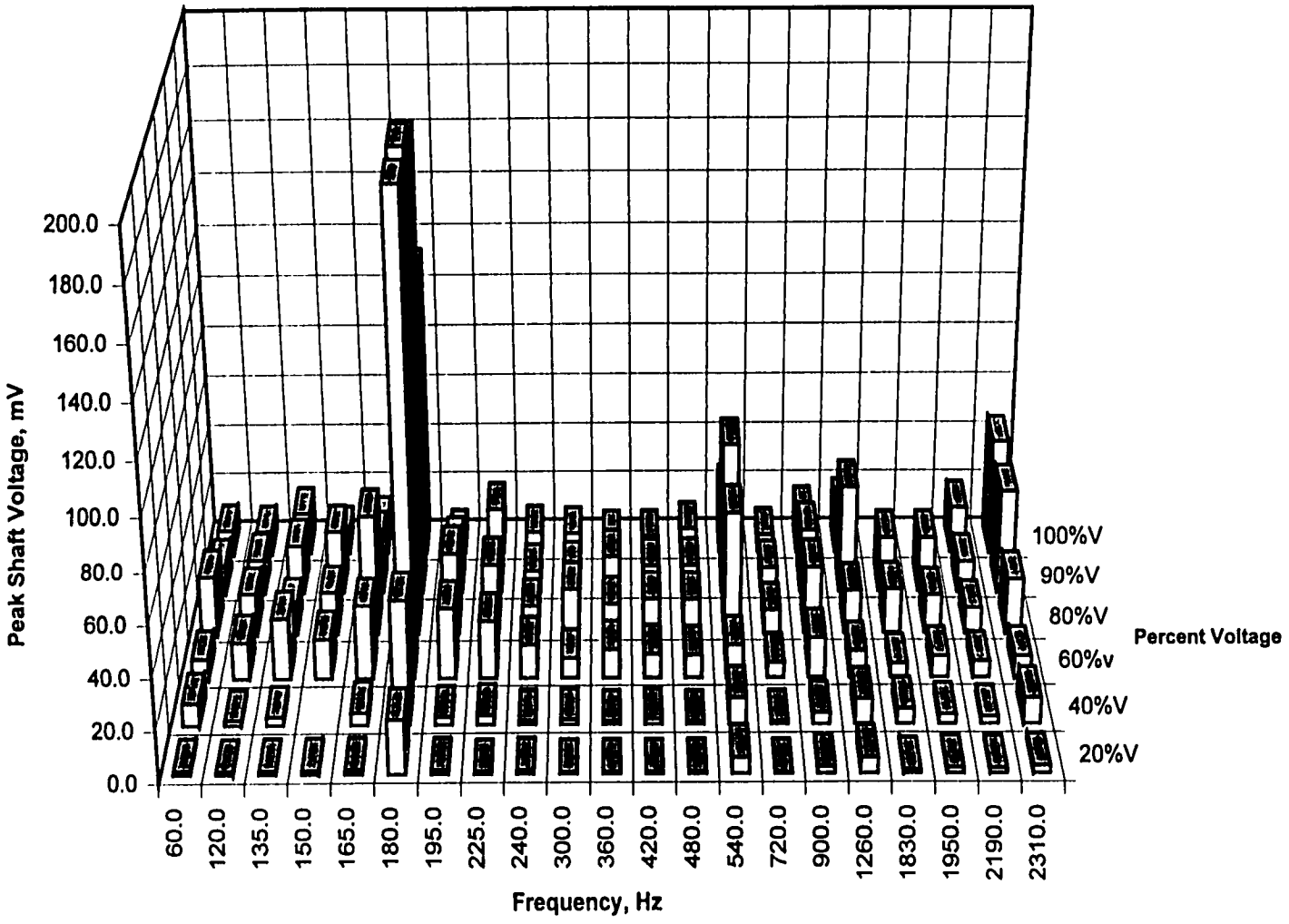

c) Drive End to Ground Measurement

Figure 6.32: Shaft Voltage Measurement At Steady State No-Load Condition, DE Bearing Non-Insulated, ODE Bearing Insulated, Oil Ring Lubrication.

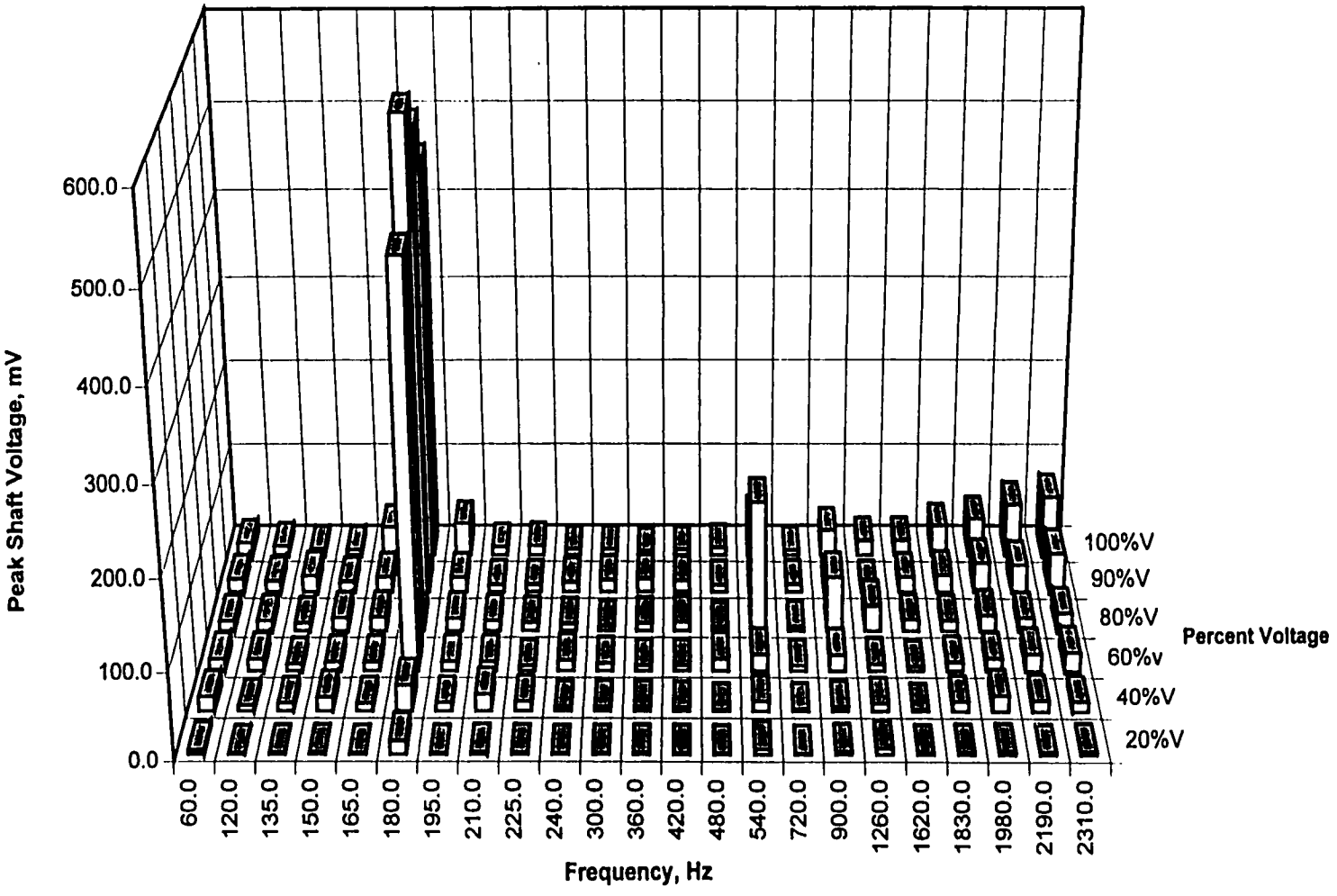

d) Opposite Drive to Ground Measurement

Figure 6.32: Shaft Voltage Measurement At Steady State No-Load Condition, DE Bearing Non-Insulated, ODE Bearing insulated, Oil Ring Lubrication.

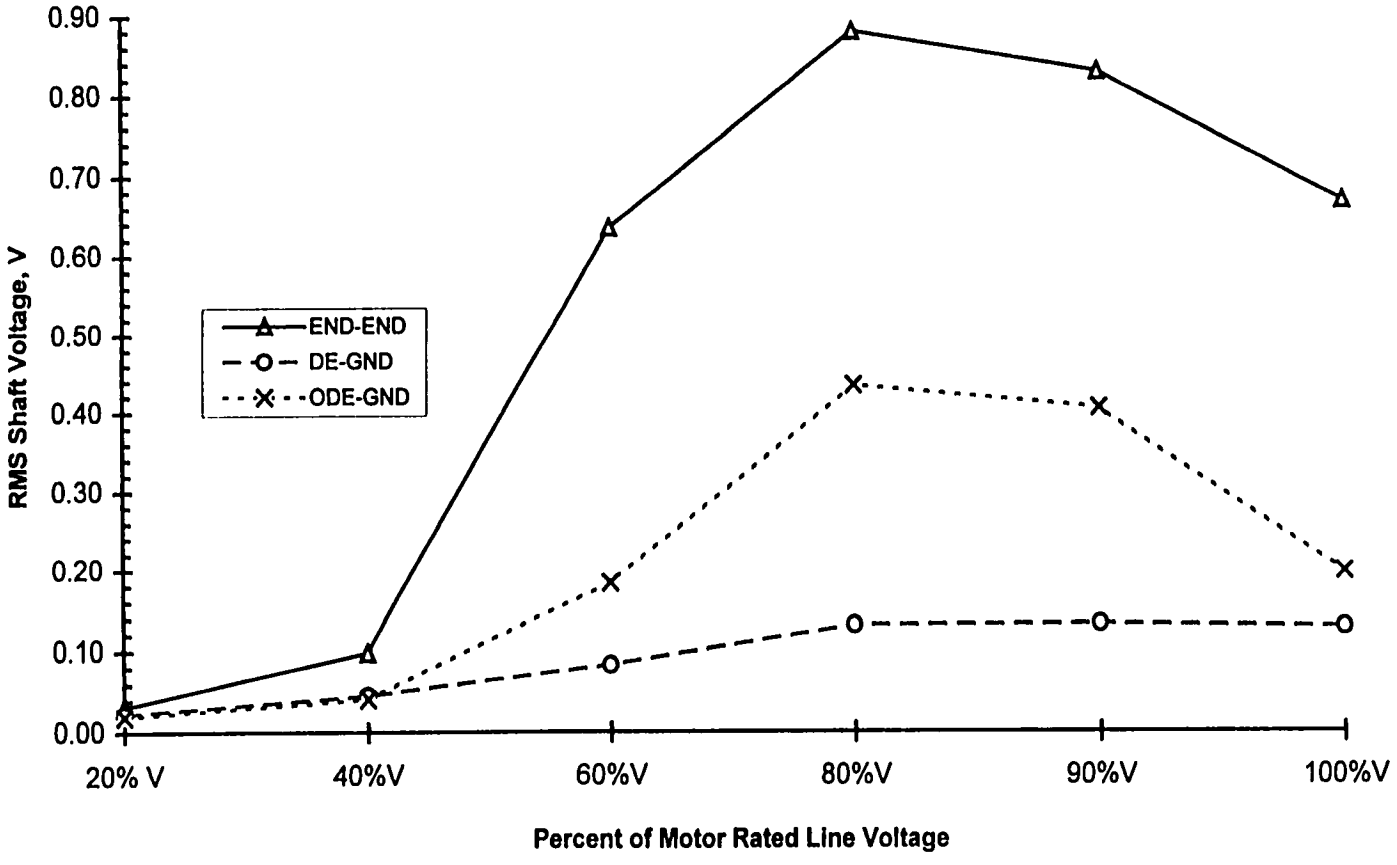

Figure 6.33: Shaft Voltage Measurement At Steady State No-Load Condition, DE Bearing Non-Insulated, ODE Bearing Insulated, Forced Lubrication.

is insulated, and there is a counter-acting voltage built-up due to the oil film from the forced lubrication. This may have reduced the voltage level.

In 1989, following the procedure explained by Alger [5], a new machine of similar design (except that the stator core has twice times the number of joints) was built. The shaft voltage results are compared with the results obtained from this test machine as shown in Figure 6.34. Figure 6.34 indicated that the shaft voltage measured end to end and ODE to ground have decreased by a factor of 2 for the rebuilt stator core. The DE to ground voltage remains approximately constant. When the number of joints was doubled, the numerator of the equation (2.1) becomes even and hence shaft current will not appear.

As expected in Figure 6.35 (a), the spectral plot of the shaft voltage measured during locked rotor, showed 180 Hz condition as the dominant frequency. Comparing Figure 6.35 (b) with Figure 6.32 (a) or Figure 6.33, the shaft voltage measured during locked rotor condition is smaller than during no-load running condition. This reduction is attributed to the reaction of the rotor current in reducing the higher harmonics.

6.4.5 SHAFT FLUX MEASUREMENT

Shaft flux coils are installed on the DE and ODE of the shaft at the inboard of the bearing housing. Figures 6.36 (a) - (f) show the shaft flux induced voltage waveform of the DE and ODE shaft flux coil in the test machine with non-insulated bearings at 20%V, 80%V and 100%V. These figures reveal that the magnitude of shaft flux during the transient running condition is at least seventy times larger than that during the steady state running condition. Also, the magnitude of shaft flux measured at the ODE is greater than that measured at the

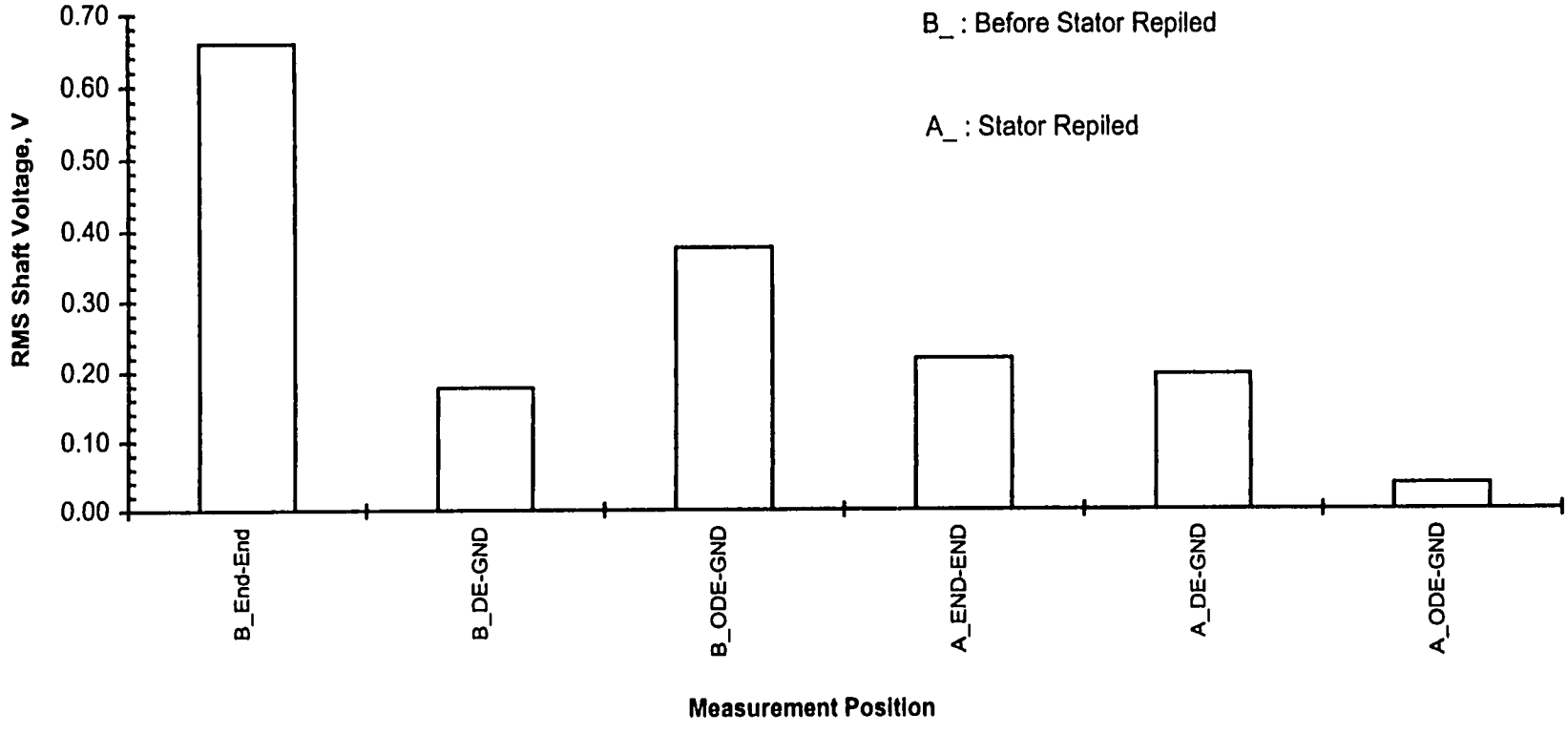

Figure 6.34: Shaft Voltage Measurement At Motor Rated Line Voltage, Steady State No-Load Condition, DE Bearing Non-Insulated, ODE Bearing Insulated, Oil Ring Lubrication: Before and After Stator Repiled.

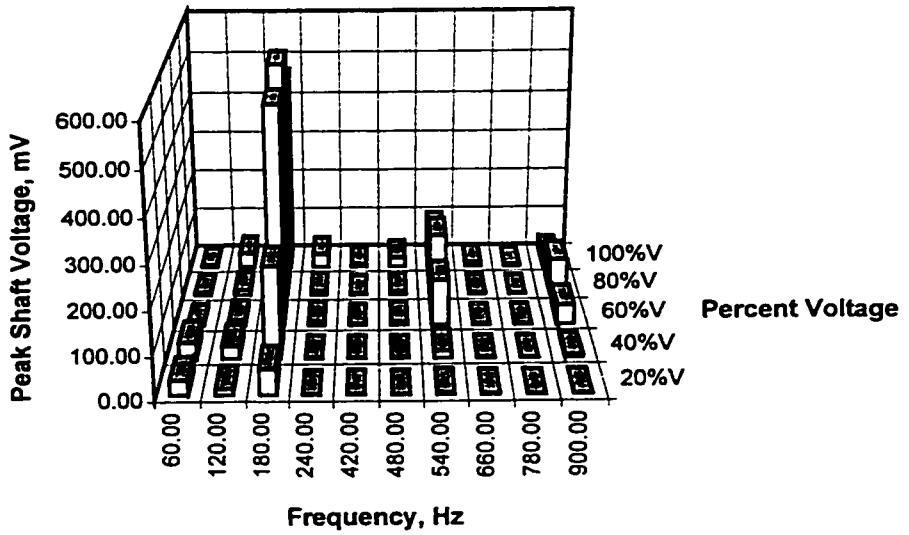

a) Shaft Voltage Spectrum

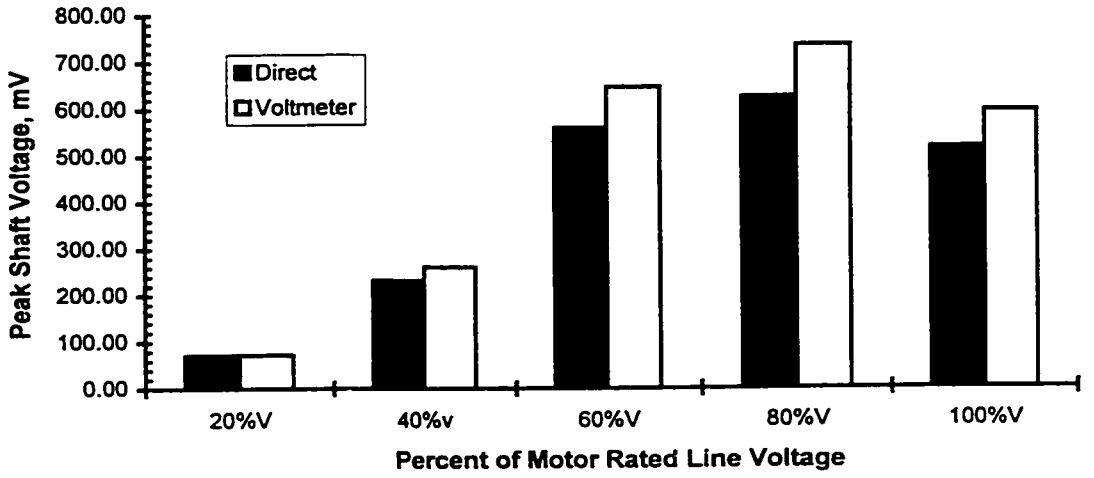

b) Peak Magnitude

Figure 6.35: Shaft Voltage Measured End to End During Locked Rotor Condition, DE Bearing Non-Insulated, ODE Bearing Insulated, Oil Ring Lubrication.

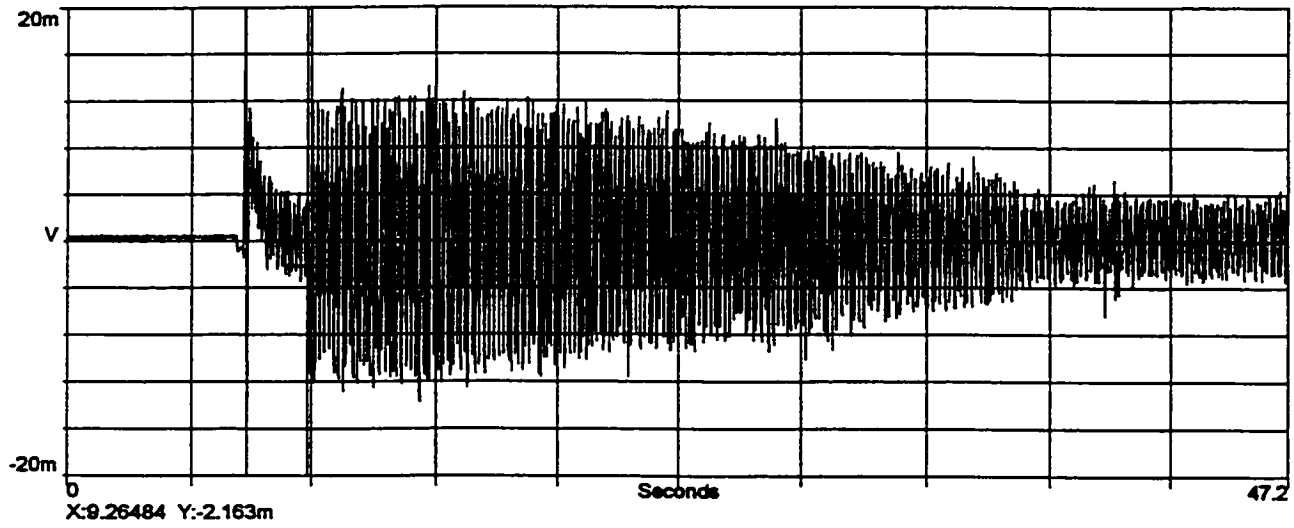

a) DE Shaft Flux Coil Induced Voltage, 20% of Motor Rated Line Voltage.

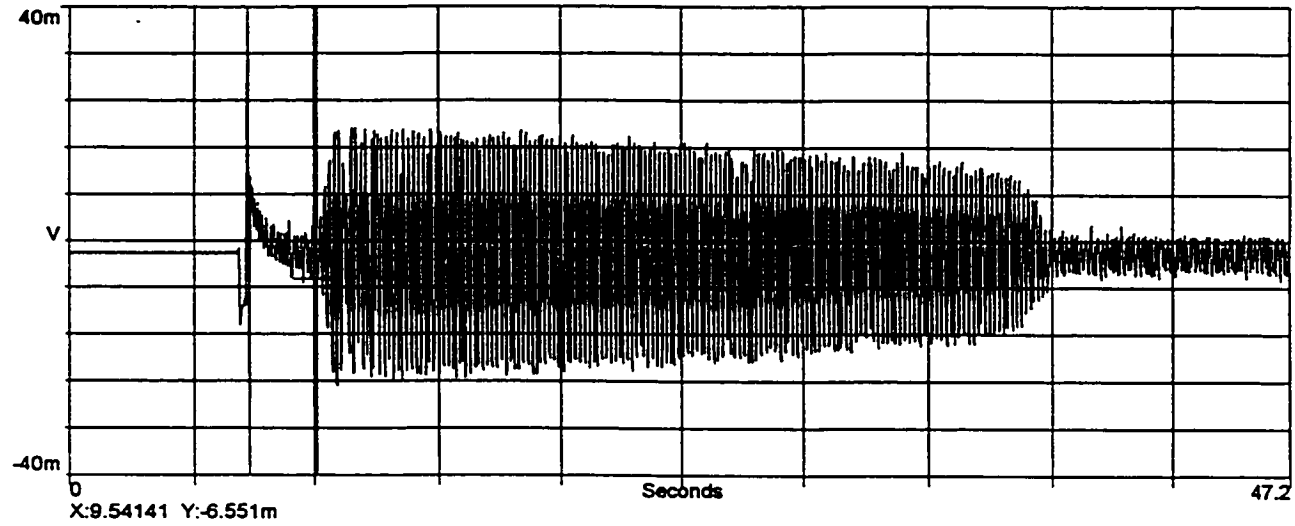

b) ODE Shaft Flux Coil Induced Voltage, 20% of Motor Rated Line Voltage.

Figure 6.36: Shaft Flux Coil Induced Voltage Measurement, Both Bearings Non-Insulated, Shaft End Play Movement, Oil Ring Lubrication.

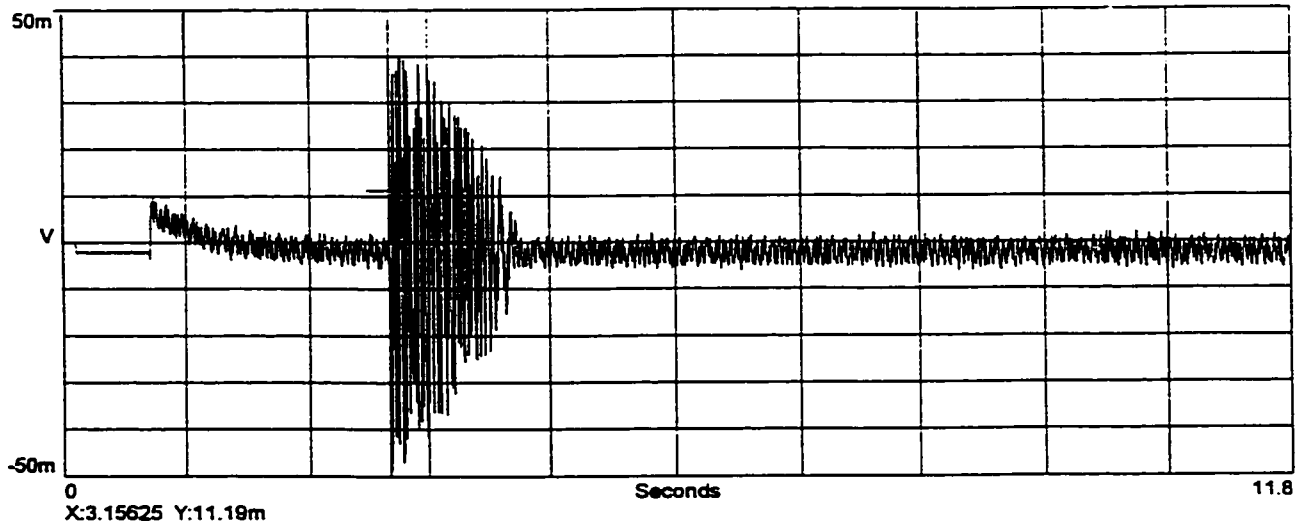

c) DE Shaft Flux Coil Induced Voltage, 80% of Motor Rated Line Voltage.

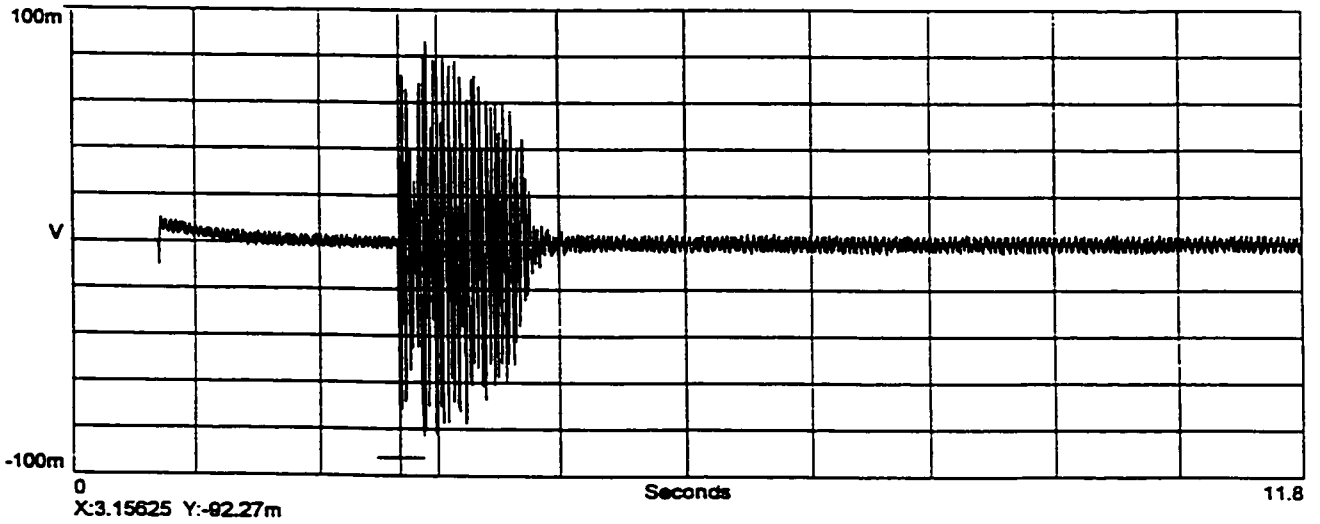

d) ODE Shaft Flux Coil Induced Voltage, 80% of Motor Rated Line Voltage.

Figure 6.36: Shaft Flux Coil Induced Voltage Measurement, Both Bearings Non-Insulated, Shaft End Play Movement, Oil Ring Lubrication

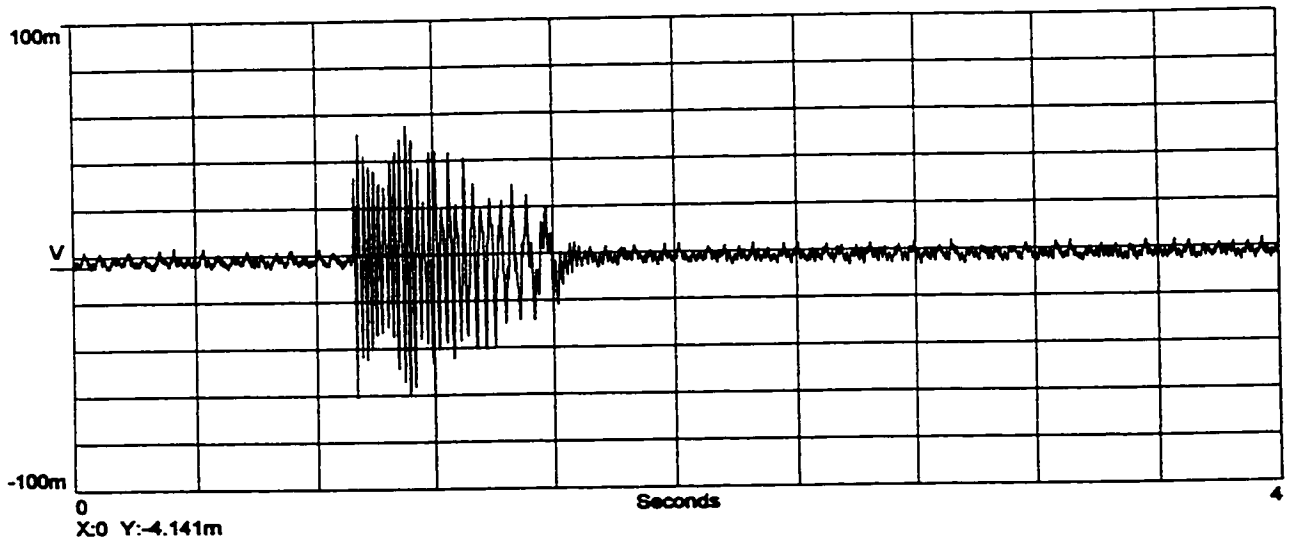

e) DE Shaft Flux Coil Induced Voltage, 100% of Motor Rated Line Voltage.

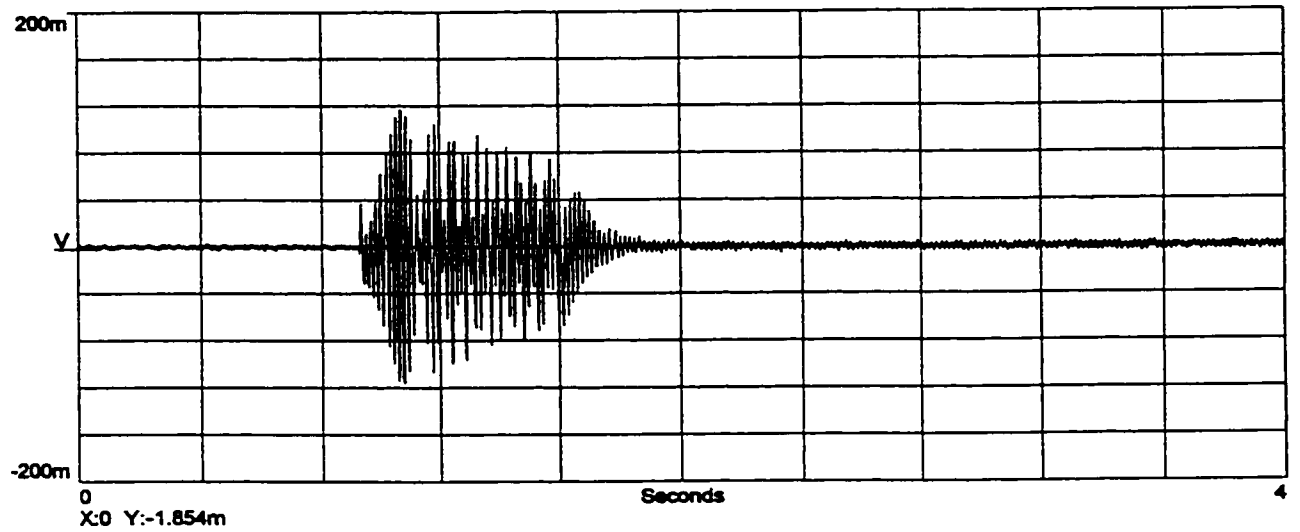

f) ODE Shaft Flux Coil Induced Voltage, 100% of Motor Rated Line Voltage.

Figure 6.36: Shaft Flux Coil Induced Voltage Measurement, Both Bearings Non-Insulated, Shaft End Play Movement, Oil Ring Lubrication

DE. John Sohre [17] and Michael Costello [18] indicated that the maximum shaft residual flux density should not be more than 0.0003 Tesla. They based their work on high speed turbo-machinery. However, in our case, peak values of shaft flux densities of 0.000758 Tesla and 0.000479 Tesla were measured at the DE and ODE respectively during the transient running condition. These values exceeded the maximum residual flux density suggested by Sohre et al. Figures 6.37 (a) - (l) show the DE and ODE shaft flux coil induced voltage waveforms and their corresponding spectrum plots during transient condition and steady state no-load condition at 20% V, 80%V and 100%V. The spectrum plots of the flux coil induced voltage waveforms indicate a fundamental component only, that is 60 Hz and the test machine is operating at medium speed. There is no requirement to demagnetize the shaft. During steady state no-load conditions, the magnitude of the fundamental component of shaft flux density is less than the maximum residual flux density. Figures 6.38 (a) - (d) summarize the spectrum analyses of the shaft flux waveforms measured during transient and steady state running conditions. Figures 6.38 (e) and (f) show that the shaft flux at the ODE measures at a higher magnitude than that at the DE. This difference is attributed to the circulation of currents in the complete circuit rings which surround the shaft and are located at the ODE.

Comparing Figure 6.38 (e) with Figure 6.38 (f), it is observed that at steady state no-load condition, the difference between the DE and ODE shaft flux is not as significant as the difference obtained during the transient condition.

At locked rotor condition of Figure 6.39, as expected, the magnitudes of shaft fluxes are close to those measured during the transient acceleration condition (close to locked rotor condition) of the test machine.

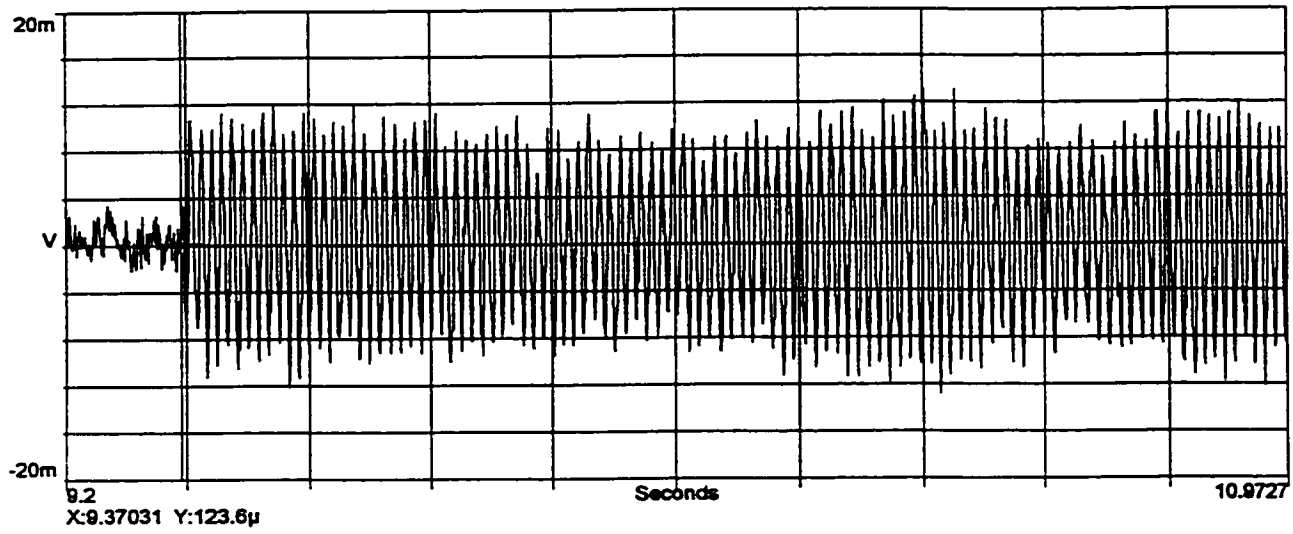

i) Shaft Flux Coil Induced Voltage Waveform

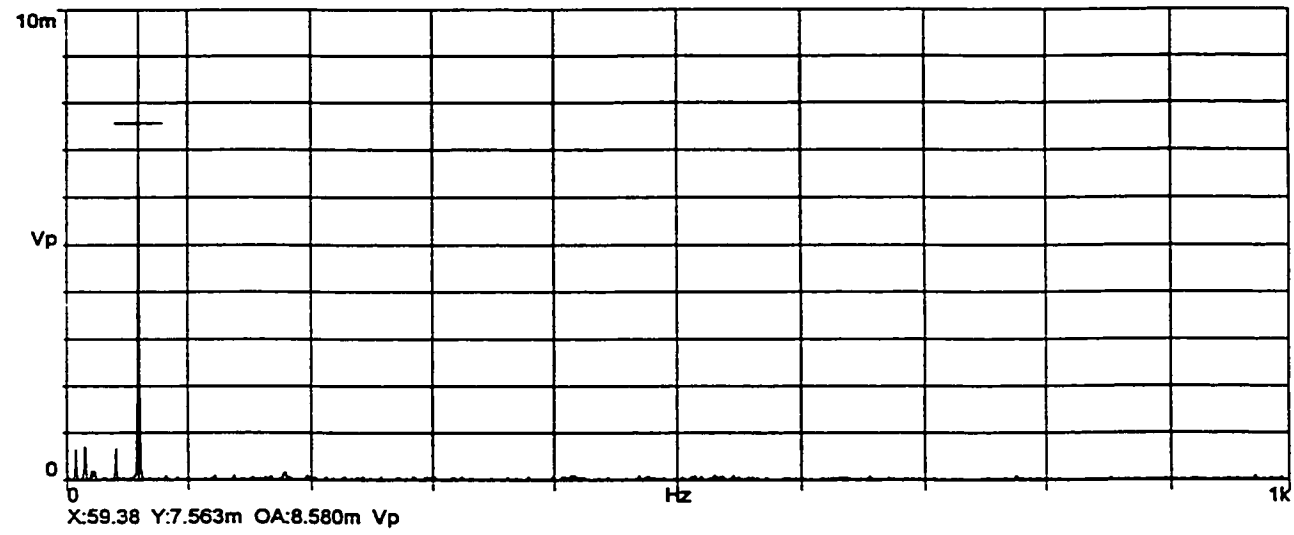

ii) Spectrum Plot

a) DE Shaft Flux Coil Induced Voltage, Transient Condition, 20% of Motor Rated Line Voltage.

Figure 6.37: Spectrum of Shaft Flux Coil Induced Voltage Waveform of Fig. 6.36 During Initial Start of Acceleration and Steady State No-Load Condition.

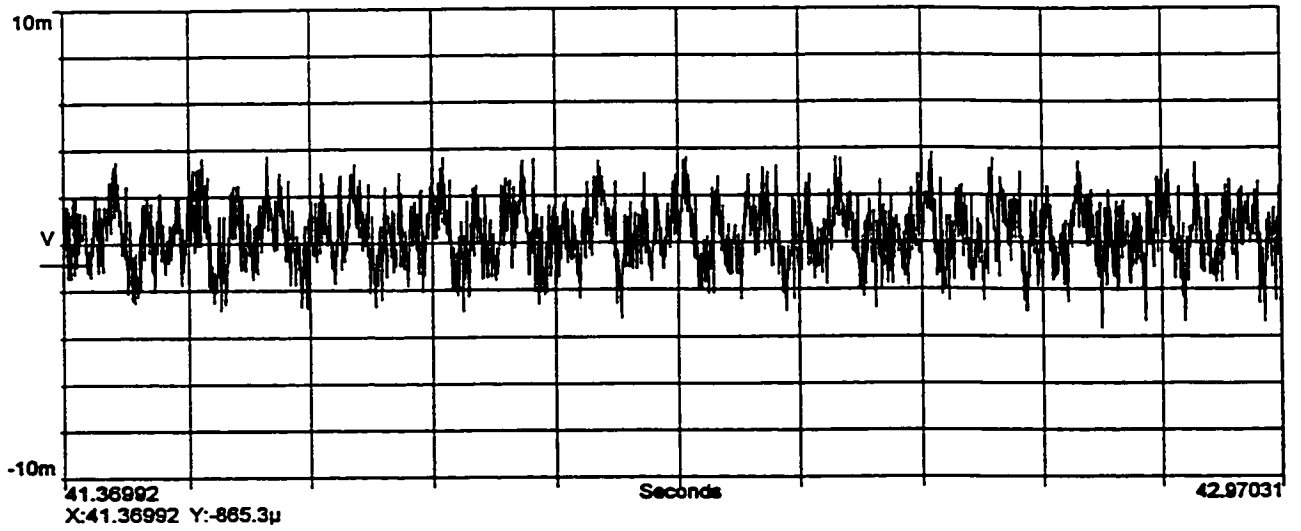

i) Shaft Flux Coil Induced Voltage Waveform

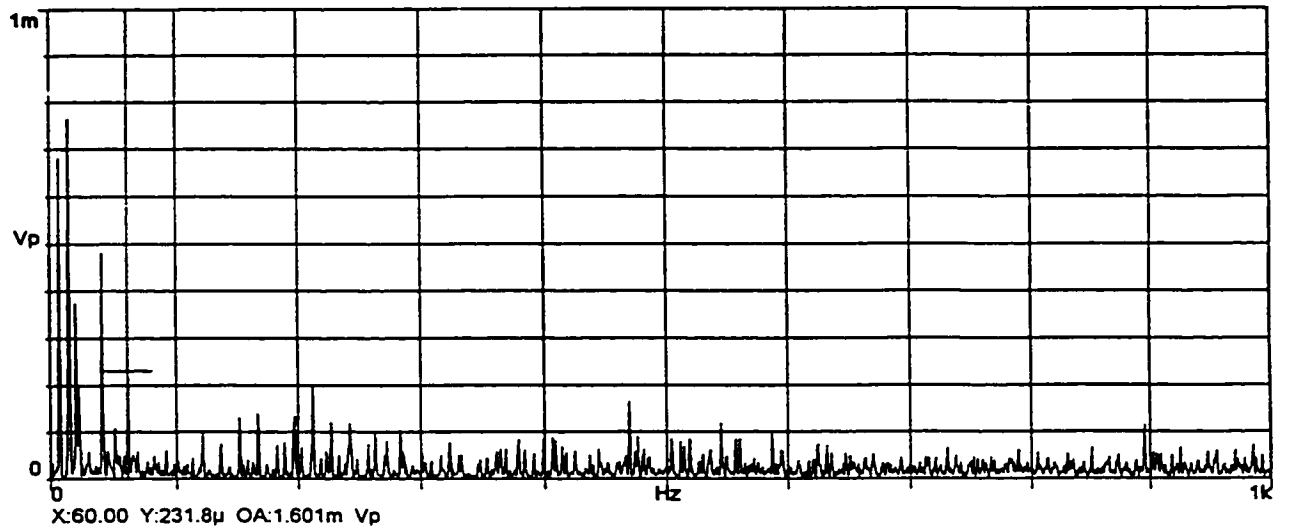

ii) Spectrum Plot

b) DE Shaft Flux Coil Induced Voltage, Steady State No-Load Condition, 20% of Motor Rated Line Voltage.

Figure 6.37: Spectrum of Shaft Flux Coil Induced Voltage Waveform of Fig. 6.36 During Initial Start of Acceleration and Steady State No-Load Condition.

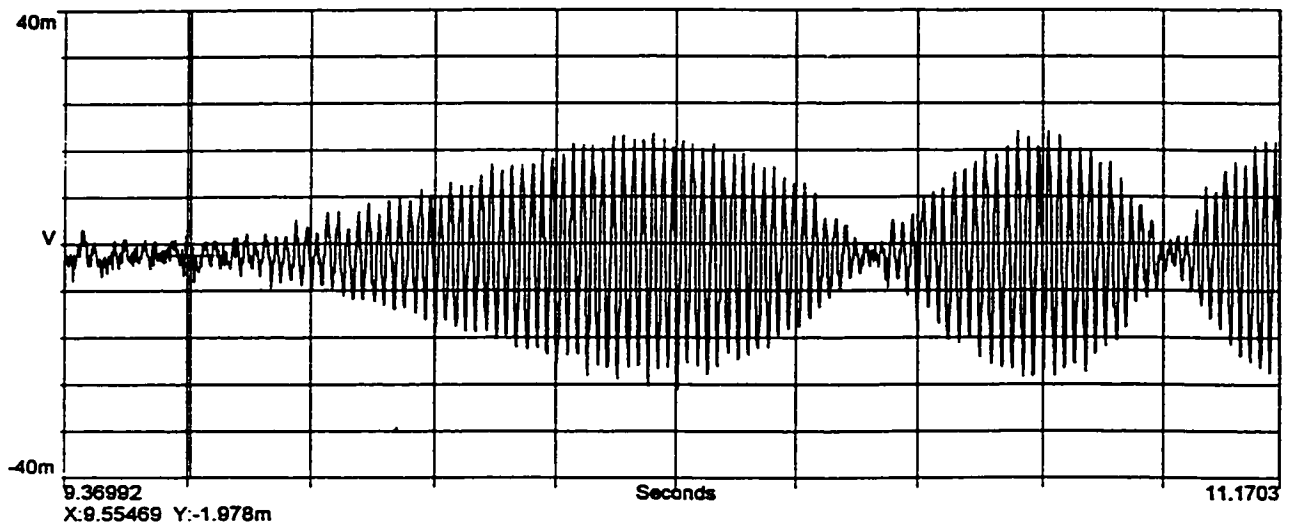

i) Shaft Flux Coil Induced Voltage Waveform

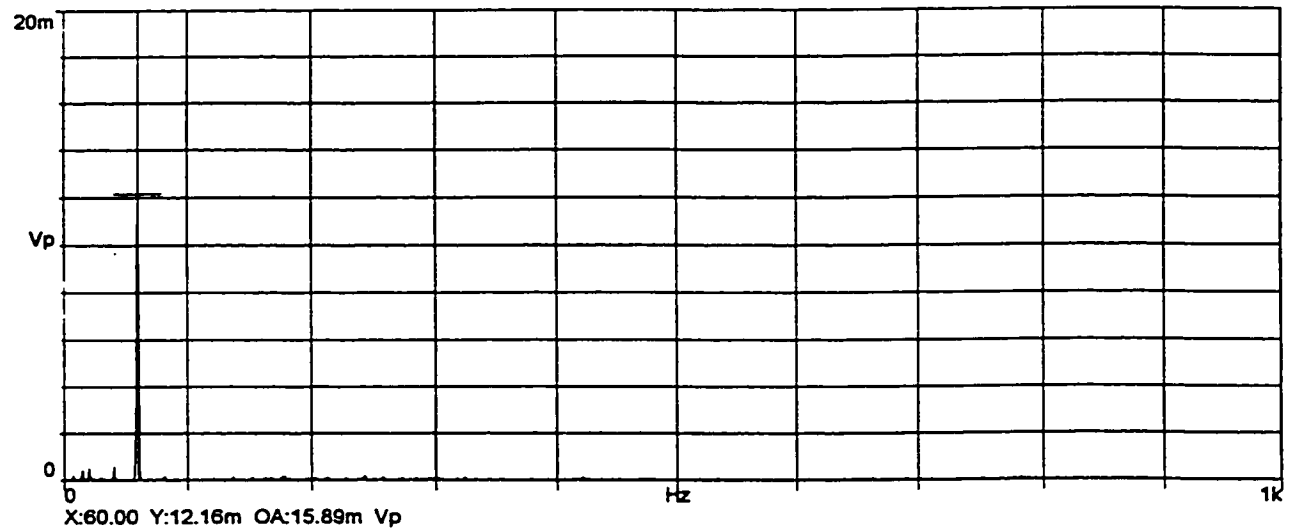

ii) Spectrum Plot

c) ODE Shaft Flux Coil Induced Voltage, Transient Condition, 20% of Motor Rated Line Voltage.

Figure 6.37: Spectrum of Shaft Flux Coil Induced Voltage Waveform of Fig. 6.36 During Initial Start of Acceleration and Steady State No-Load Condition.

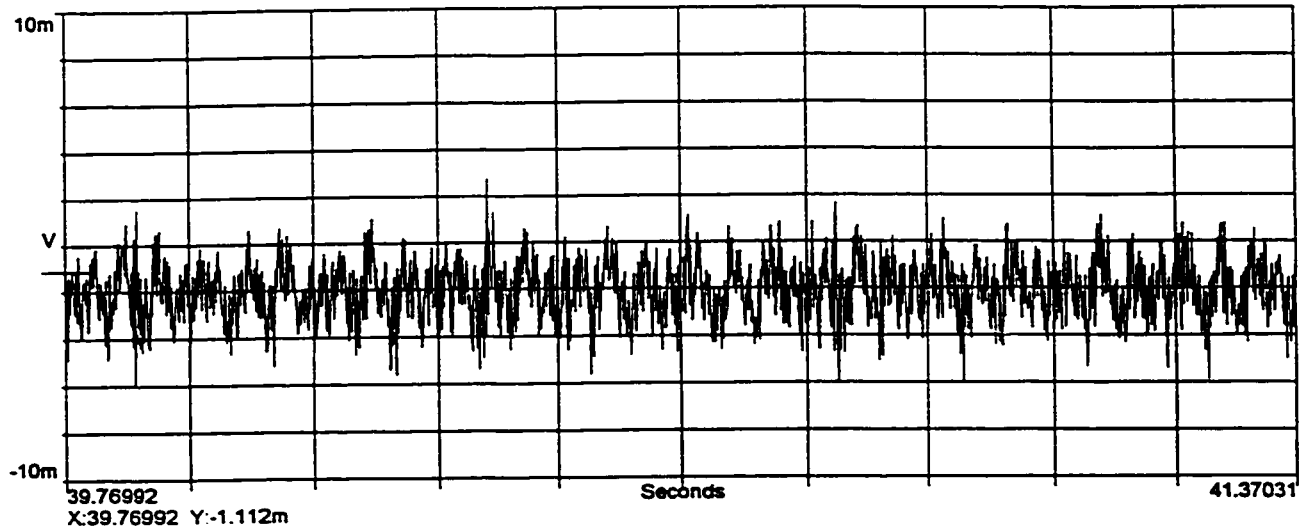

i) Shaft Flux Coil Induced Voltage Waveform

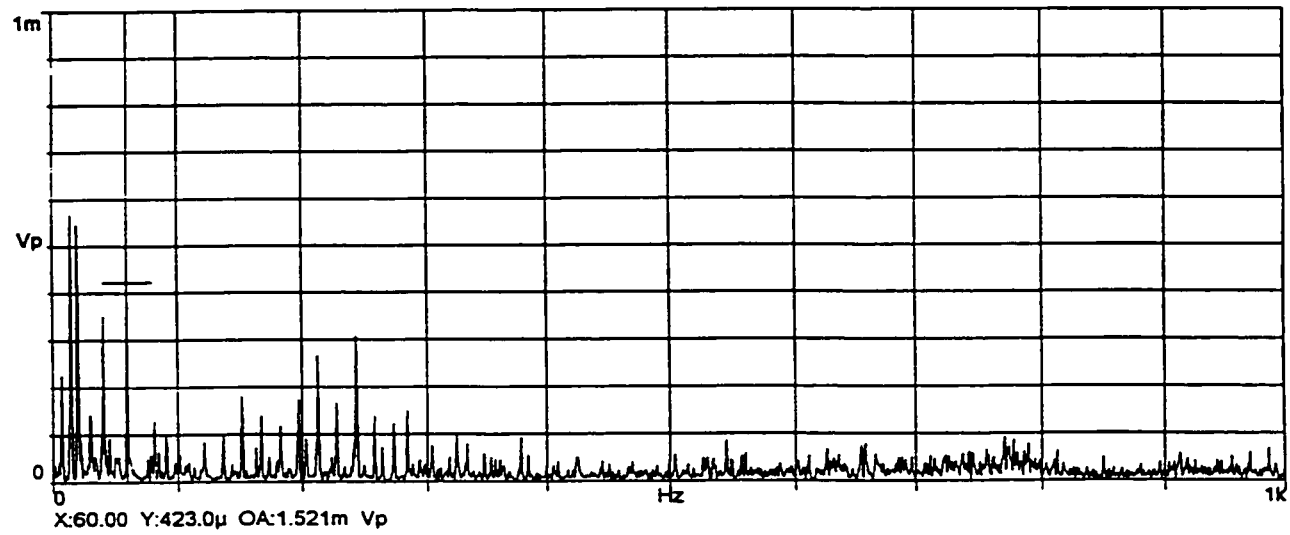

ii) Spectrum Plot

d) ODE Shaft Flux Coil Induced Voltage, Steady State No-Load Condition, 20% of Motor Rated Line Voltage.

Figure 6.37: **Spectrum of Shaft Flux Coil Induced Voltage Waveform of Fig. 6.36 During Initial Start of Acceleration and Steady State No-Load Condition.**

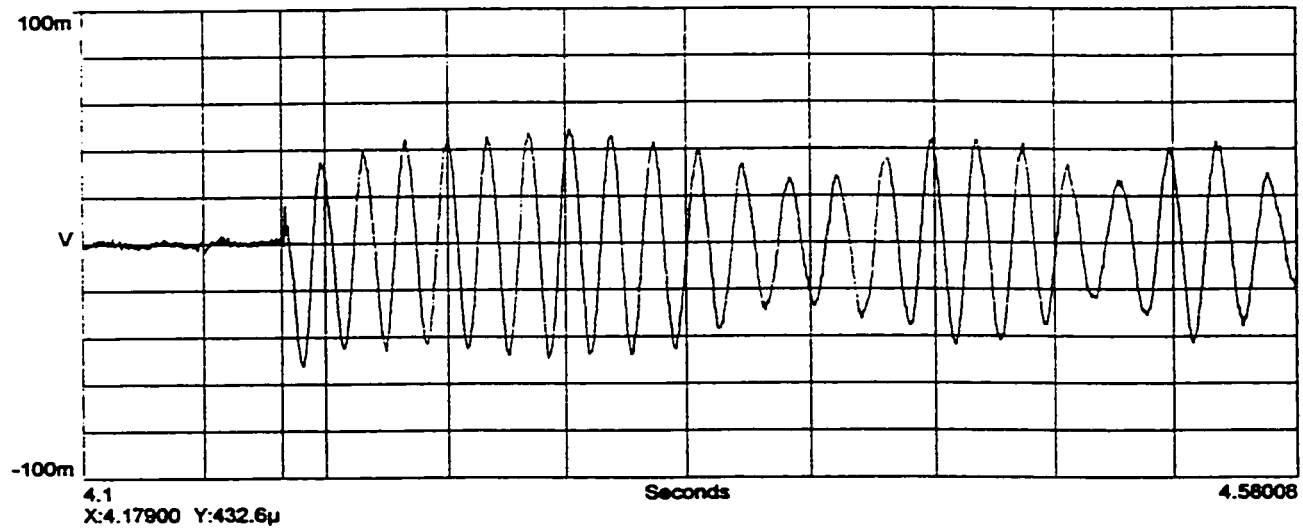

i) Shaft Flux Coil Induced Voltage Waveform

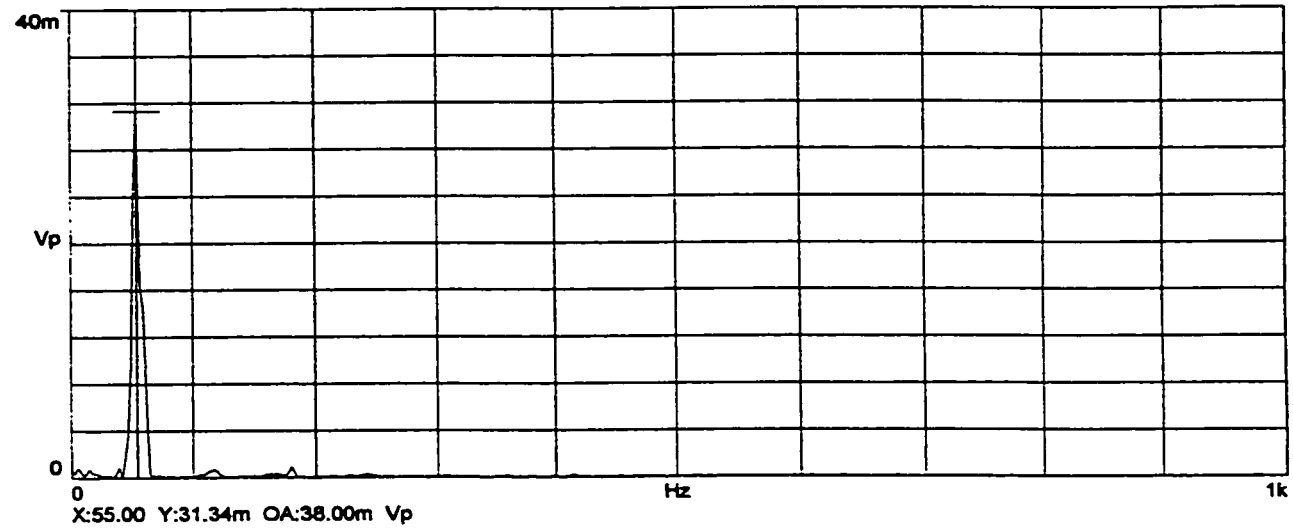

ii) Spectrum Plot

e) DE Shaft Flux Coil Induced Voltage, Transient Condition, 80% of Motor Rated Line Voltage.

Figure 6.37: Spectrum of Shaft Flux Coil Induced Voltage Waveform of Fig. 6.36 During Initial Start of Acceleration and Steady State No-Load Condition.

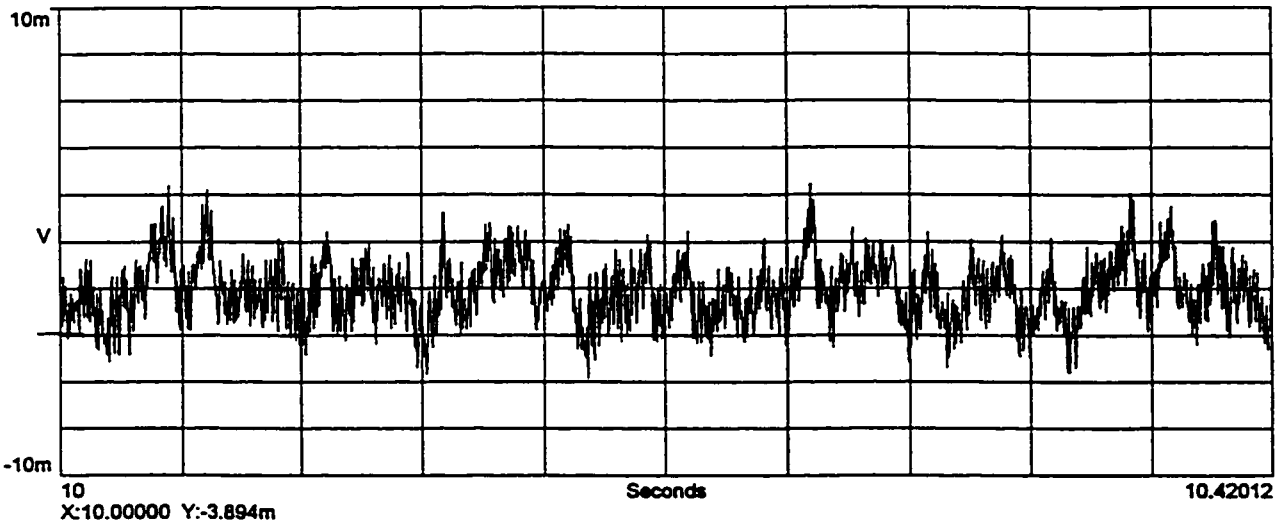

i) Shaft Flux Coil Induced Voltage Waveform

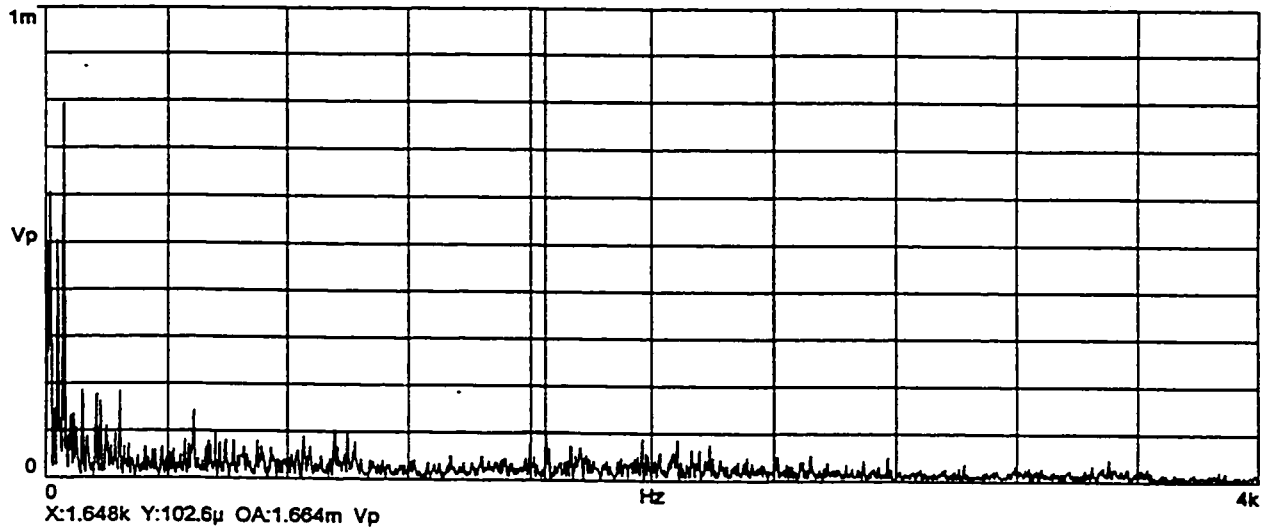

ii) Spectrum Plot

f) DE Shaft Flux Coil Induced Voltage, Steady State No-Load Condition, 80% of Motor Rated Line Voltage.

Figure 6.37: Spectrum of Shaft Flux Coil Induced Voltage Waveform of Fig. 6.36 During Initial Start of Acceleration and Steady State No-Load Condition.

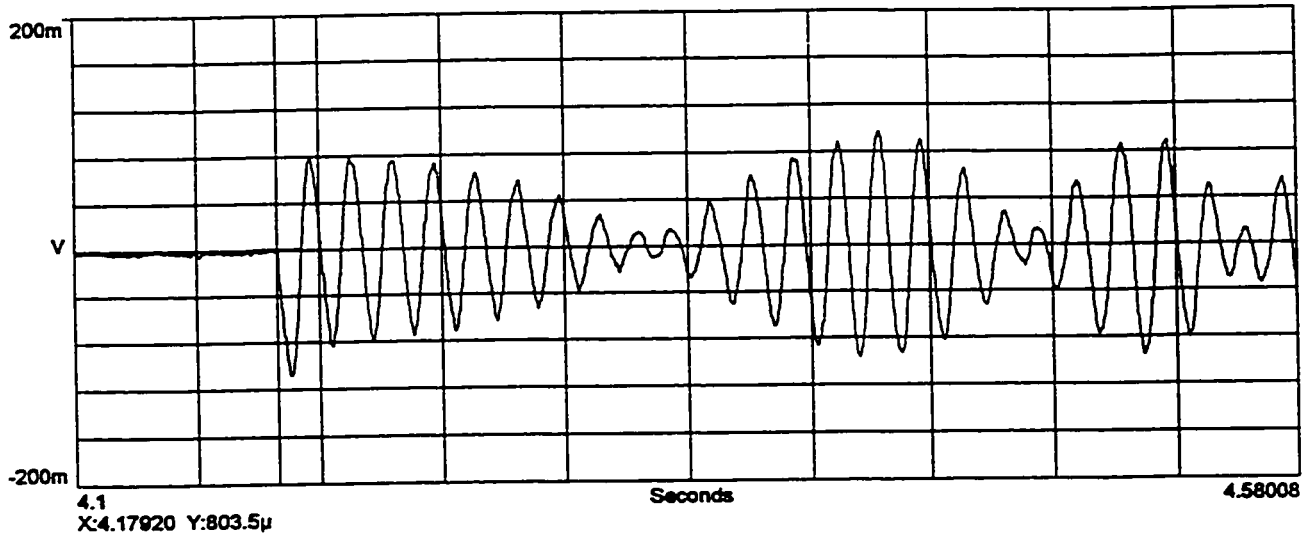

i) Shaft Flux Coil Induced Voltage Waveform

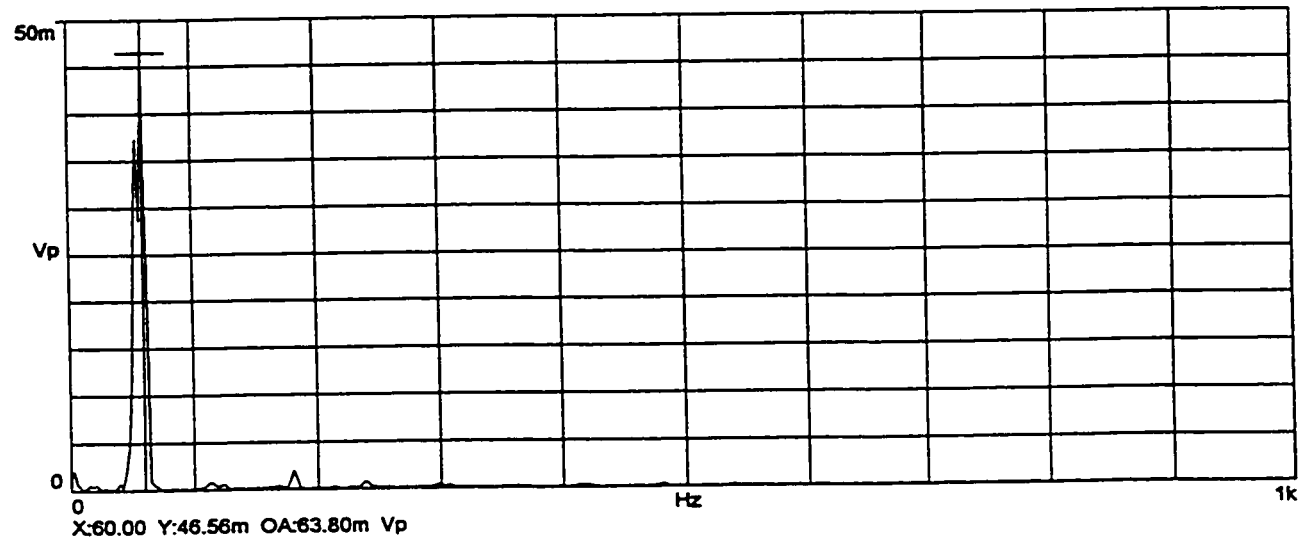

ii) Spectrum Plot

g) ODE Shaft Flux Coil Induced Voltage, Transient Condition, 80% of Motor Rated Line Voltage.

Figure 6.37: Spectrum of Shaft Flux Coil Induced Voltage Waveform of Fig. 6.36 During Initial Start of Acceleration and Steady State No-Load Condition.

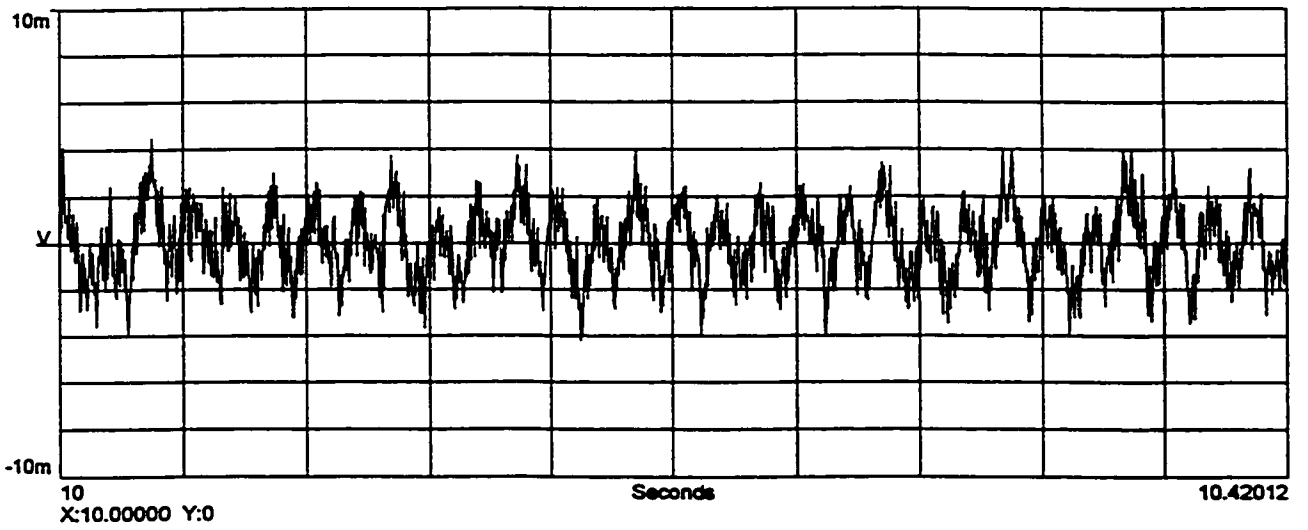

i) Shaft Flux Coil Induced Voltage Waveform

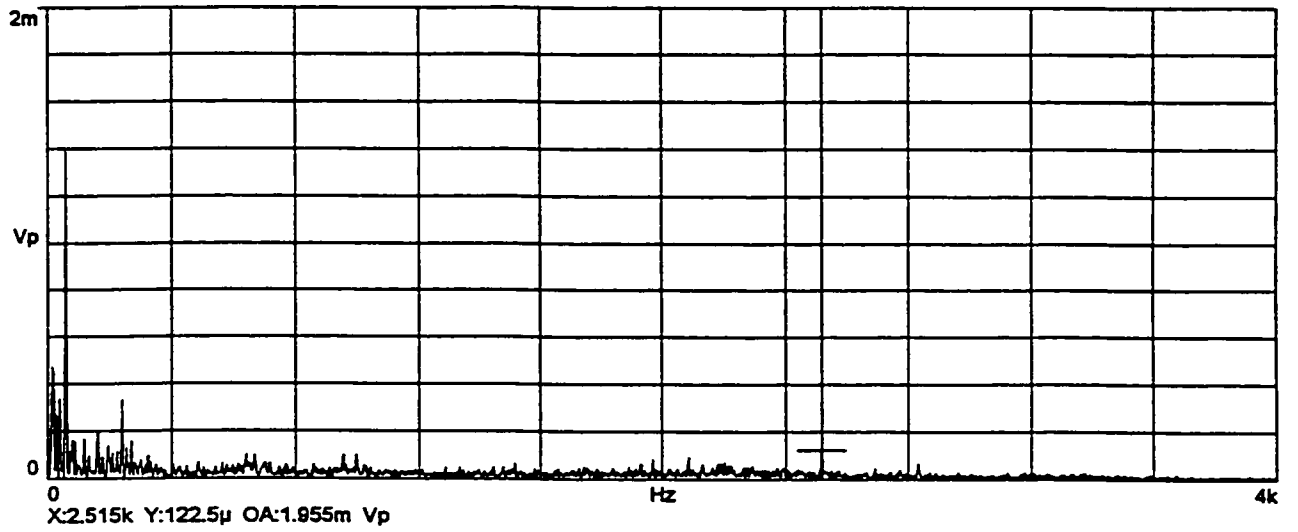

ii) Spectrum Plot

h) ODE Shaft Flux Coil Induced Voltage, Steady State No-Load Condition, 80% of Motor Rated Line Voltage.

Figure 6.37: Spectrum of Shaft Flux Coil Induced Voltage Waveform of Fig. 6.36 During Initial Start of Acceleration and Steady State No-Load Condition.

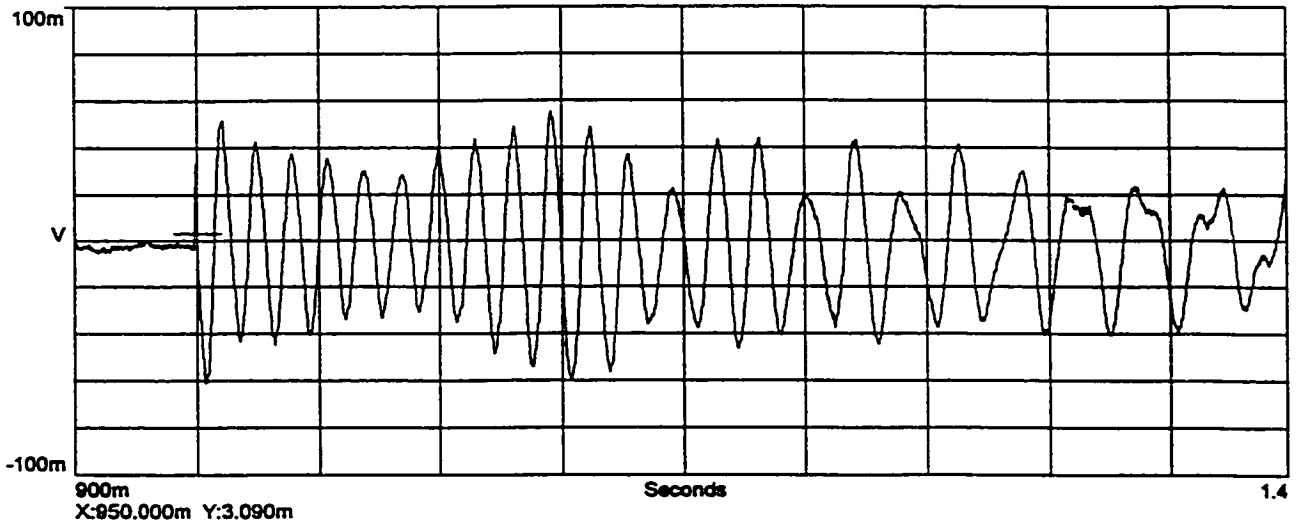

i) Shaft Flux Coil Induced Voltage Waveform

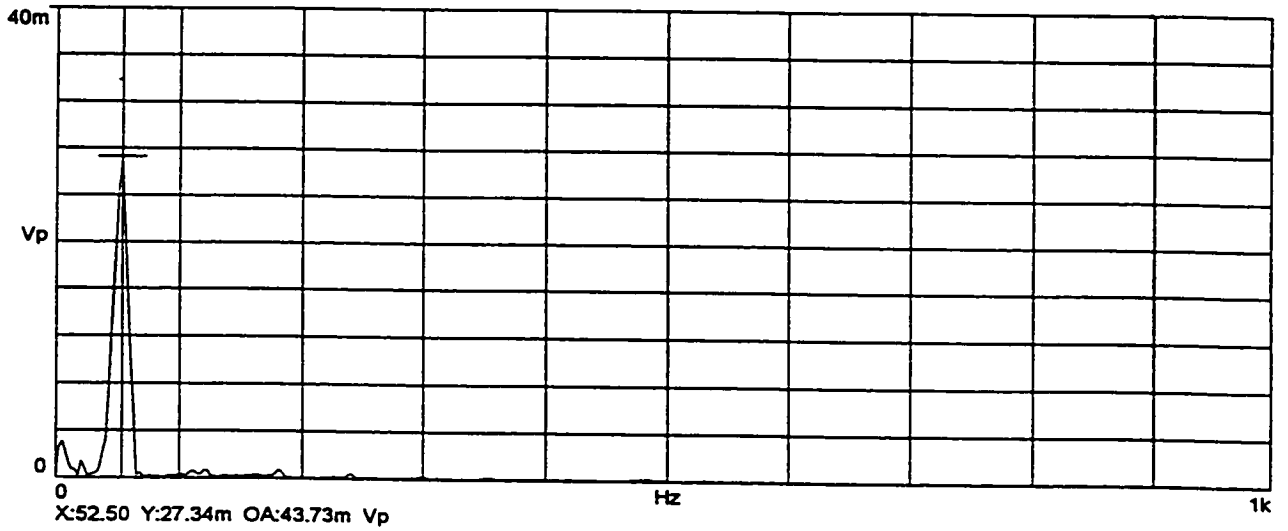

ii) Spectrum Plot

i) DE Shaft Flux Coil Induced Voltage, Transient Condition, 100% of Motor Rated Line Voltage.

Figure 6.37: Spectrum of Shaft Flux Coil Induced Voltage Waveform of Fig. 6.36 During Initial Start of Acceleration and Steady State No-Load Condition.

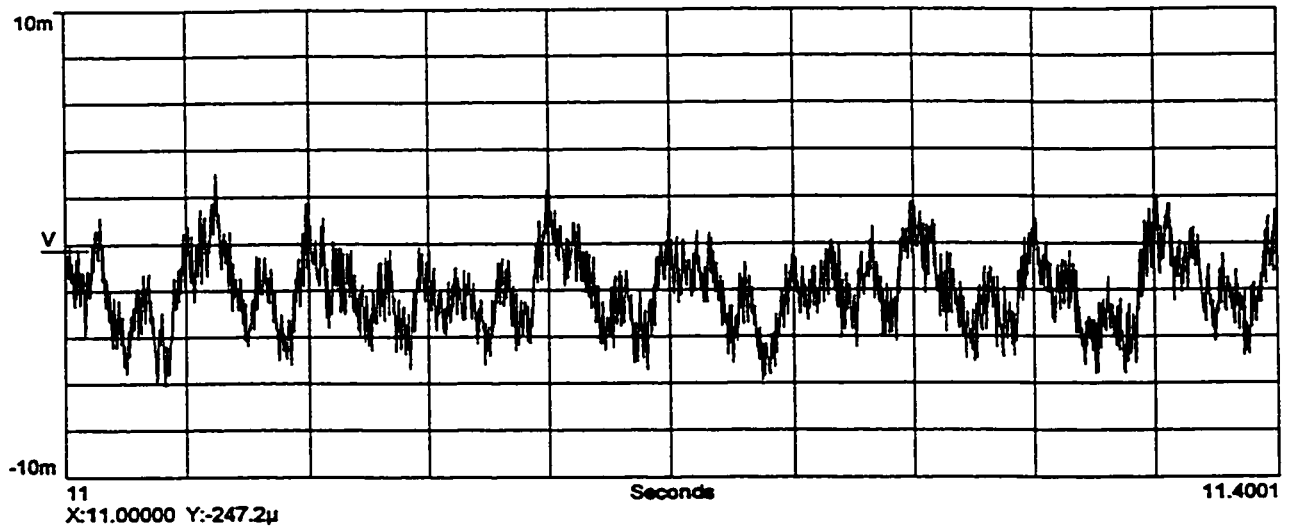

i) Shaft Flux Coil Induced Voltage Waveform

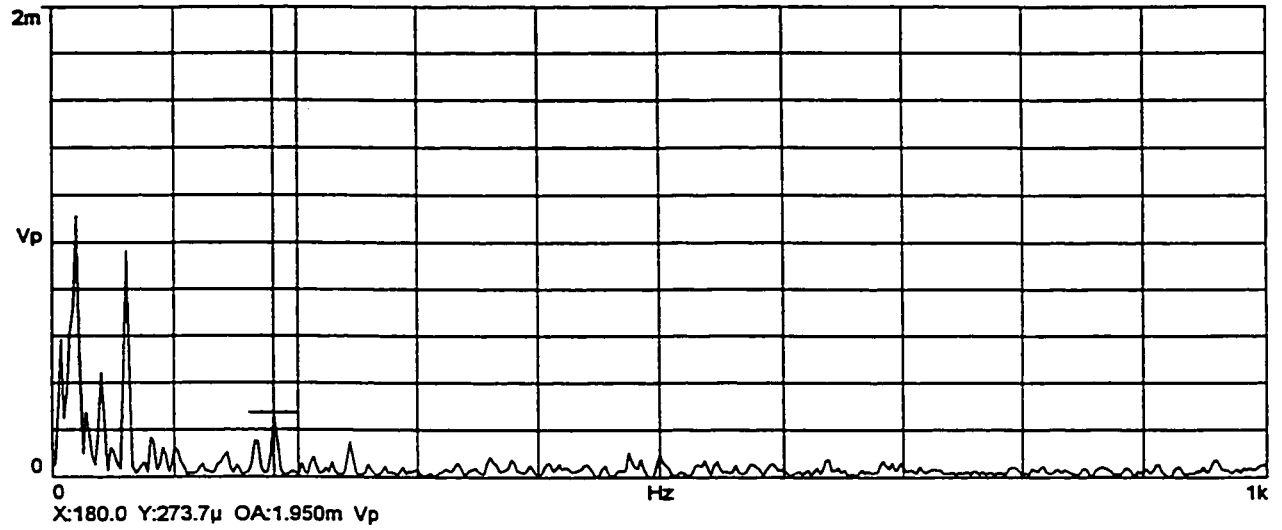

ii) Spectrum Plot

j) DE Shaft Flux Coil Induced Voltage, Steady State No-Load Condition, 100% of Motor Rated Line Voltage.

Figure 6.37: Spectrum of Shaft Flux Coil Induced Voltage Waveform of Fig. 6.36 During Initial Start of Acceleration and Steady State No-Load Condition.

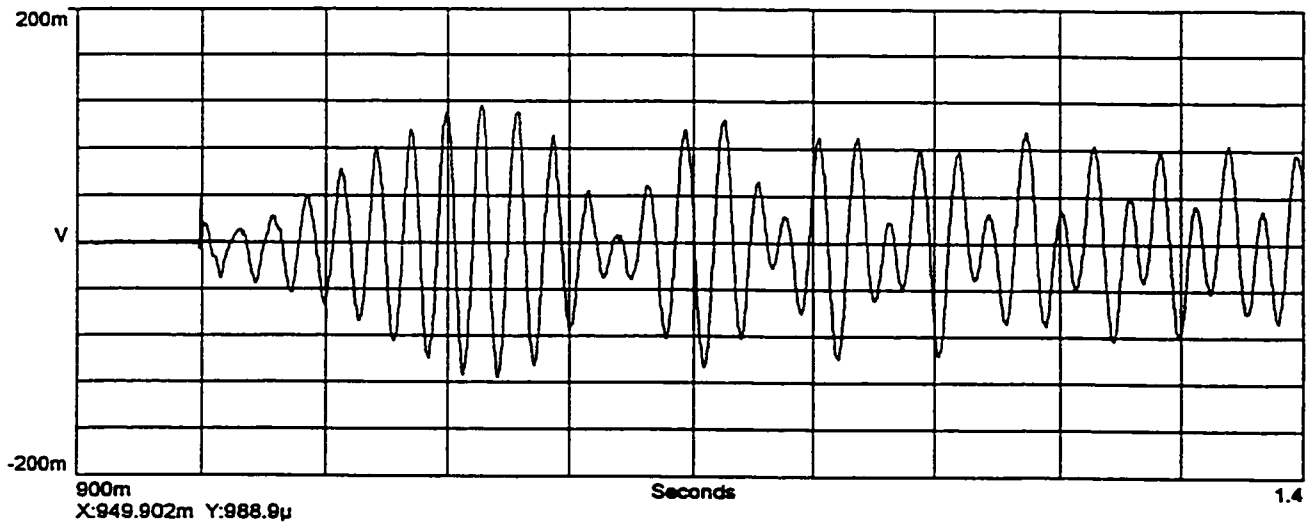

i) Shaft Flux Coil Induced Voltage Waveform

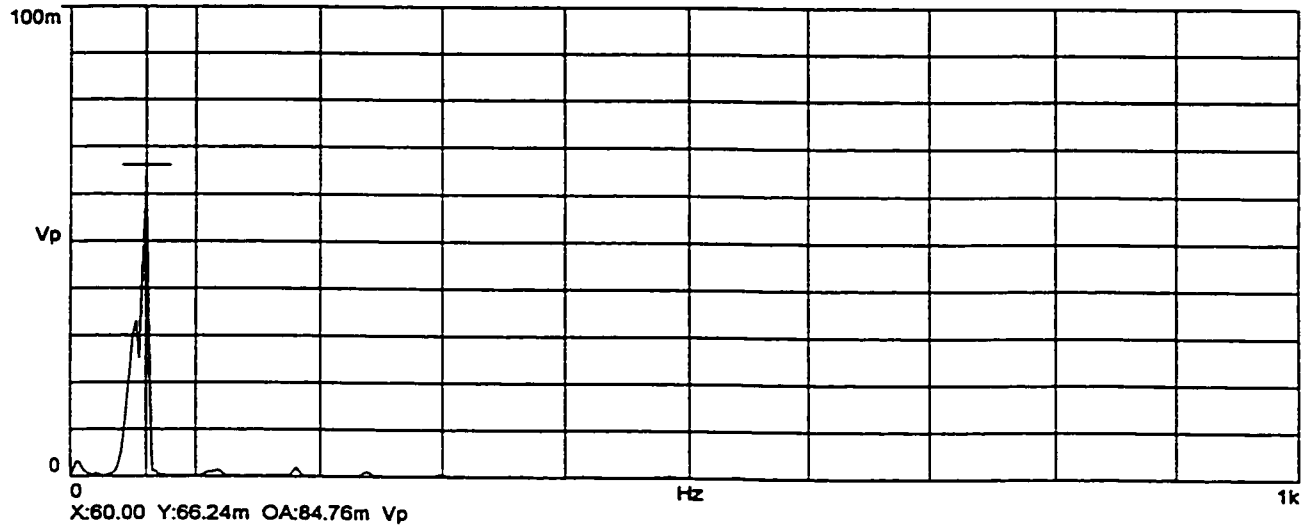

ii) Spectrum Plot

k) ODE Shaft Flux Coil Induced Voltage, Transient Condition, 100% of Motor Rated Line Voltage.

Figure 6.37: **Spectrum of Shaft Flux Coil Induced Voltage Waveform of Fig. 6.36 During Initial Start of Acceleration and Steady State No-Load Condition.**

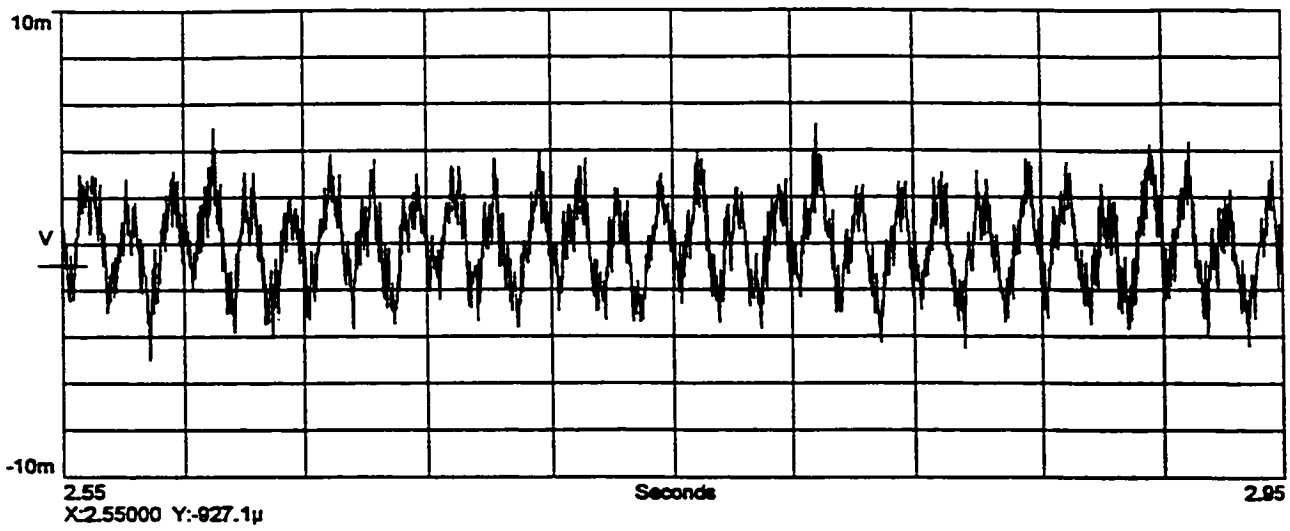

i) Shaft Flux Coil Induced Voltage Waveform

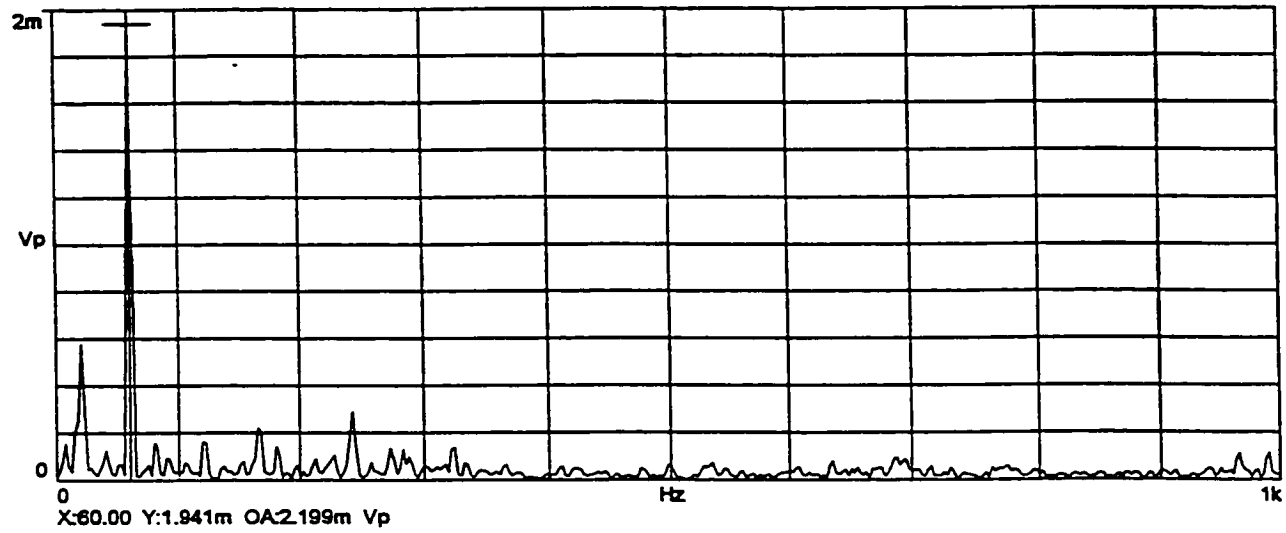

ii) Spectrum Plot

l) ODE Shaft Flux Coil Induced Voltage, Steady State No-Load Condition, 100% of Motor Rated Line Voltage.

Figure 6.37: Spectrum of Shaft Flux Coil Induced Voltage Waveform of Fig. 6.36 During Initial Start of Acceleration and Steady State No-Load Condition.

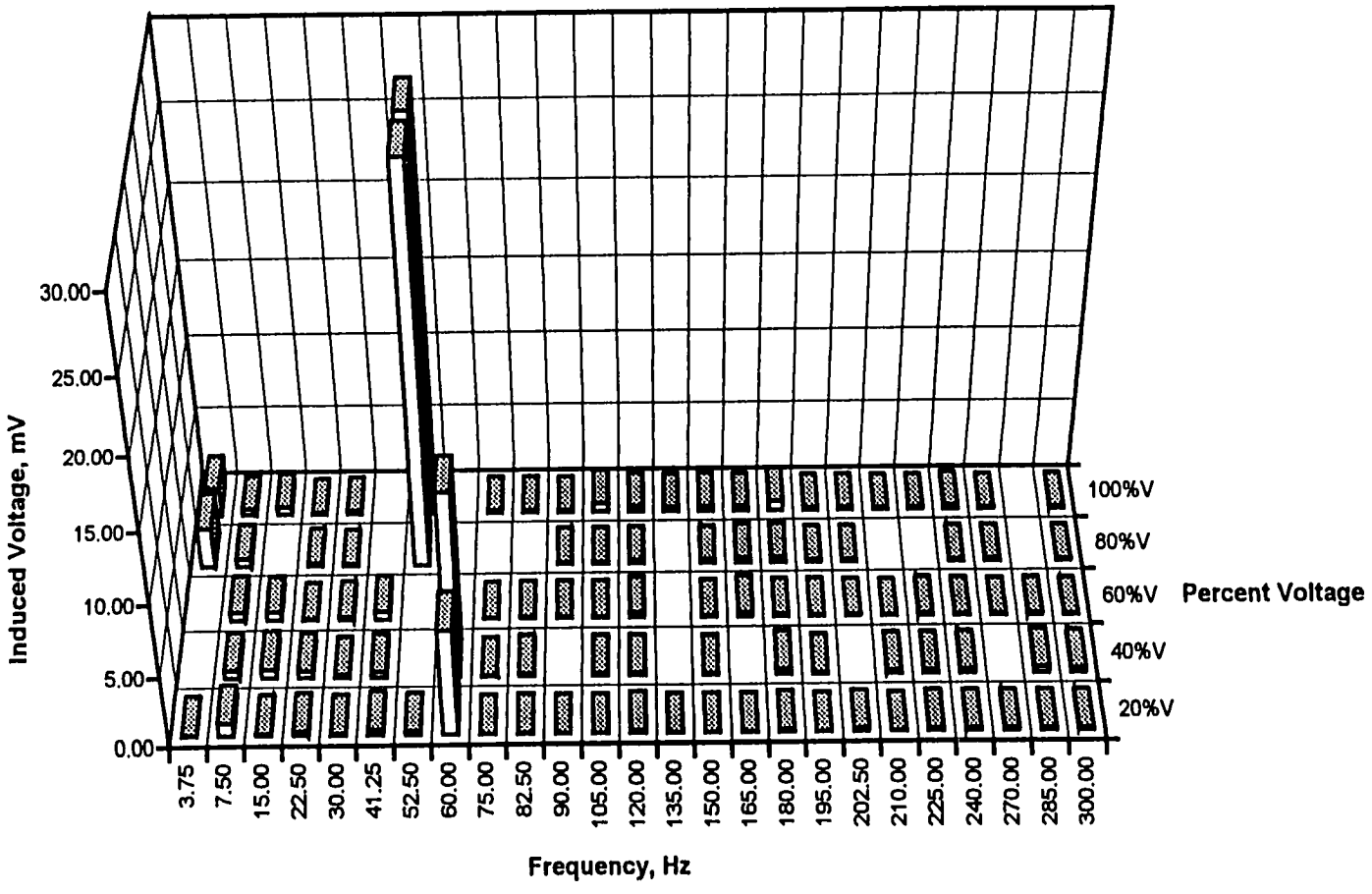

a) Drive End, Spectral Analysis, Transient Condition

Figure 6.38: Shaft Flux Coil Induced Voltage, Shaft End Play Movement, DE Bearing Non-Insulated, ODE Bearing Insulated, Oil Ring Lubrication.

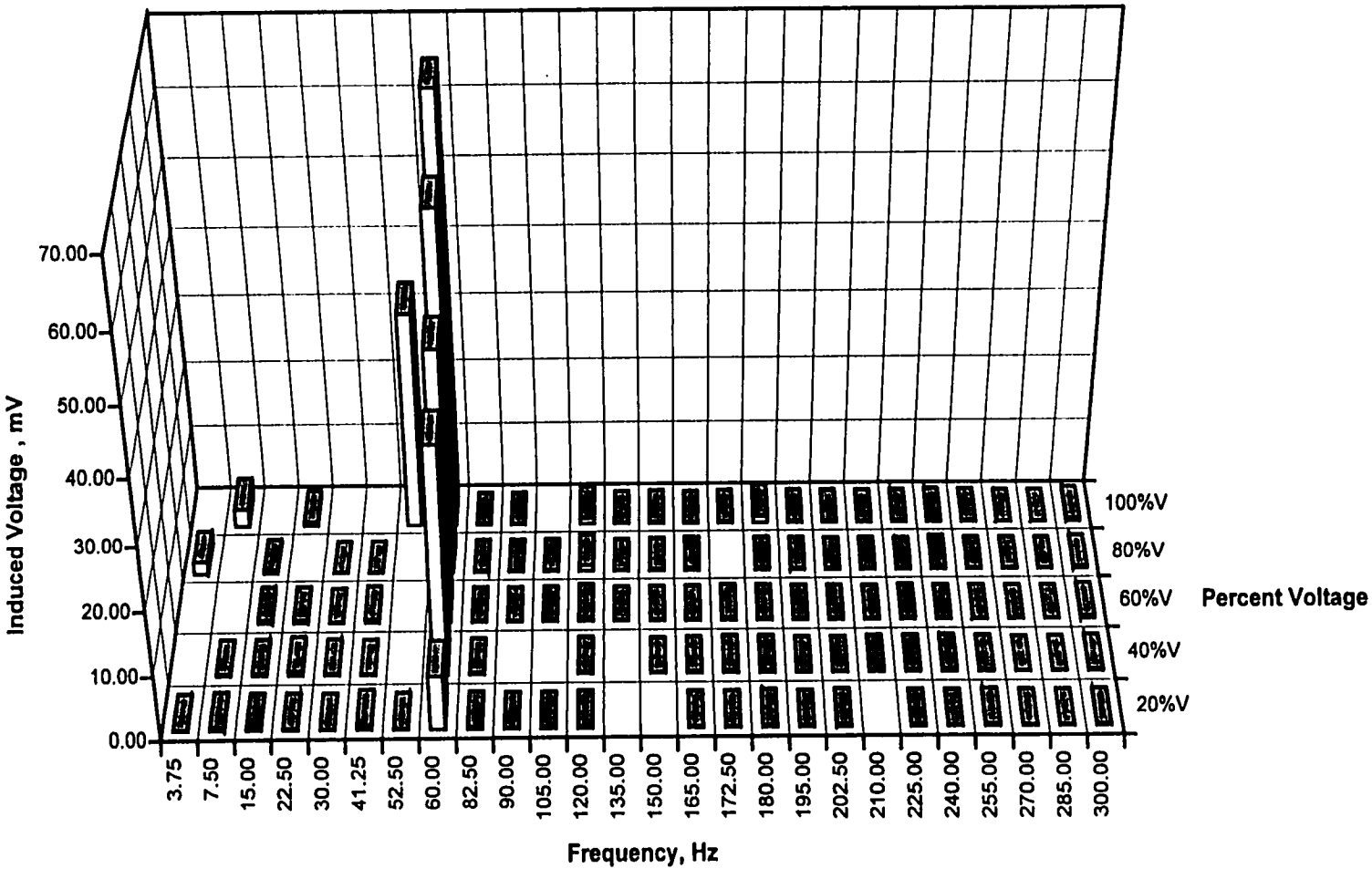

b) Opposite Drive End, Spectral Analysis, Tansient Condition

Figure 6.38: Shaft Flux Coil Induced Voltage, Shaft End Play Movement, DE Bearing Non-Insulated, ODE Bearing Insulated,Oil Ring Lubrication.

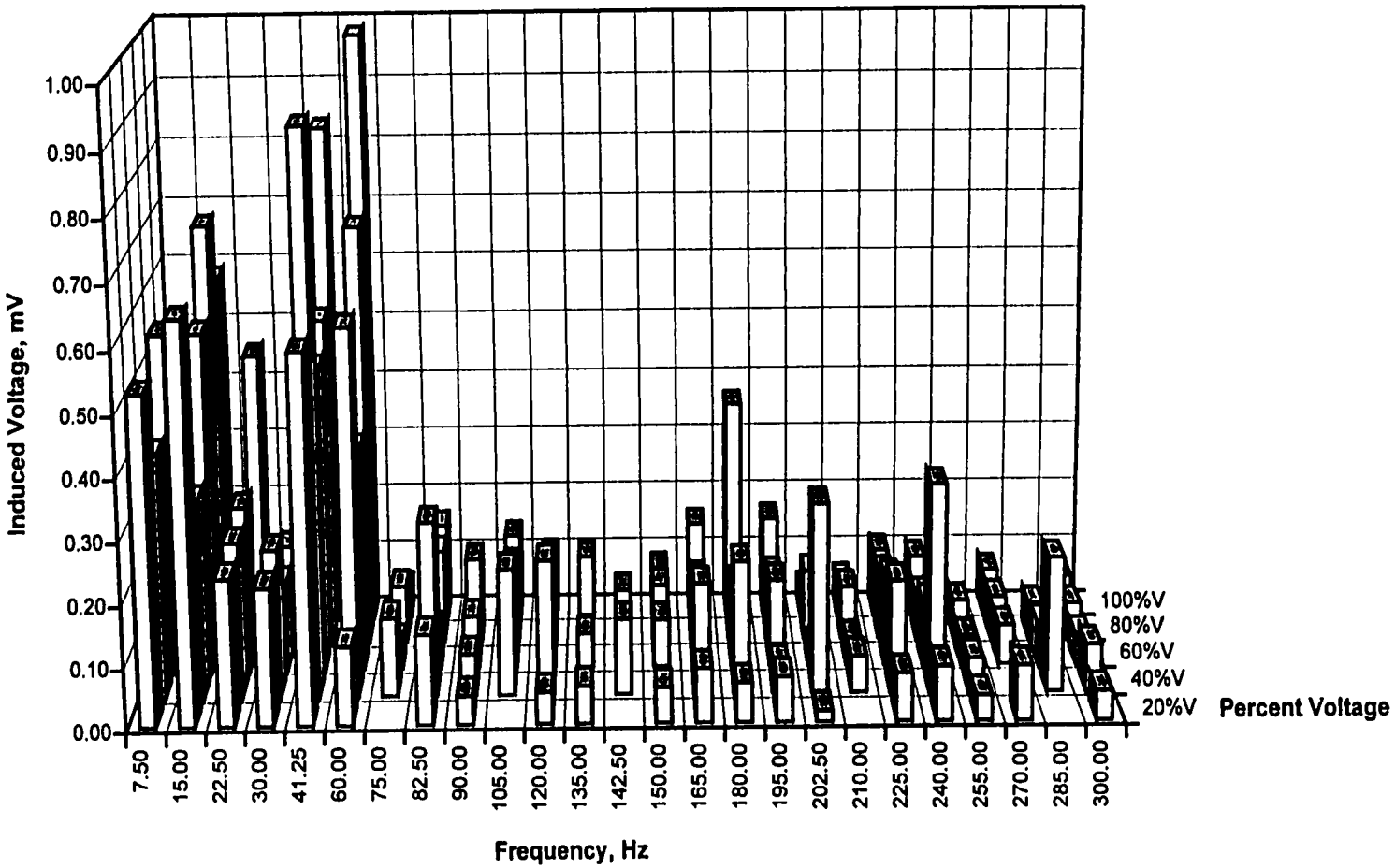

c) Drive End, Spectral Analysis, Steady State No-Load Condition

Figure 6.38: Shaft Flux Coil Induced Voltage, Shaft End Play Movement, DE Bearing Non-Insulated, ODE Bearing Insulated, Oil Ring Lubrication.

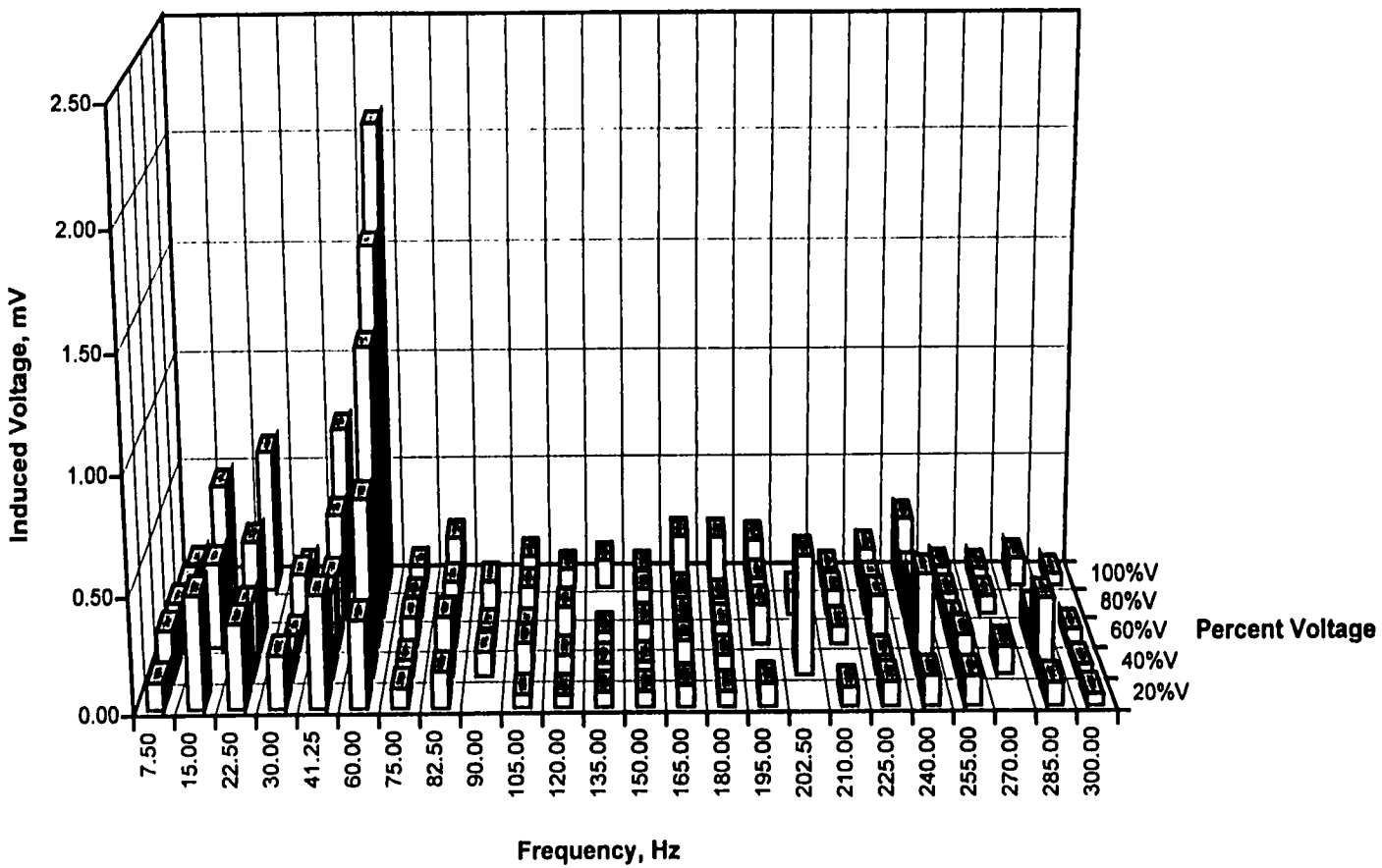

d) Opposite Drive End, Spectral Analysis, Steady State No-Load Condition

Figure 6.38: Shaft Flux Coil Induced Voltage, Shaft End Play Movement, DE Bearing Non-Insulated, ODE Bearing Insulated, Oil Ring Lubrication.

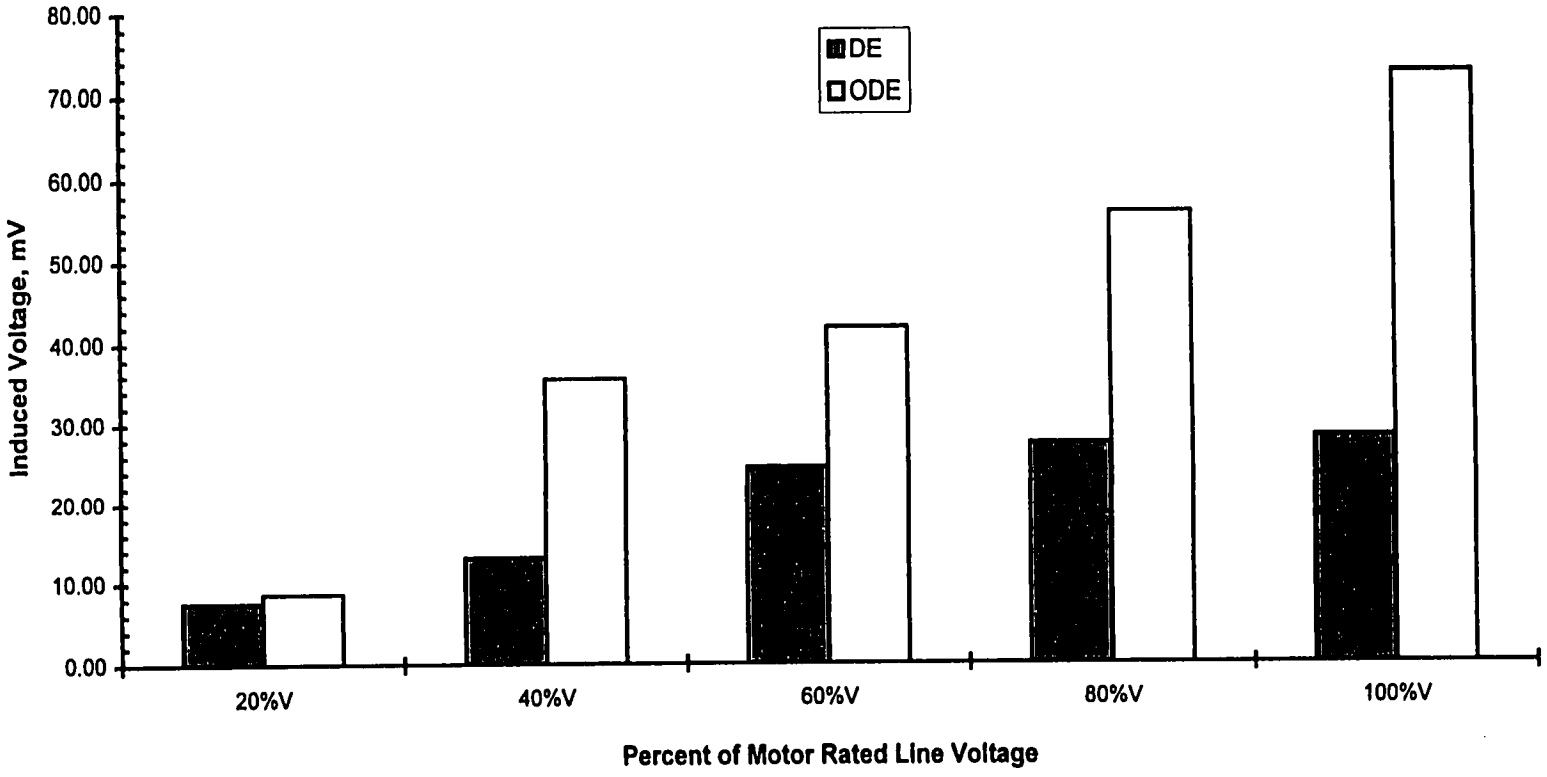

e) Magnitude, Transient Condition

Figure 6.38: Shaft Flux Coil Induced Voltages, Shaft End Play Movement, DE Bearing Non-Insulated, ODE Bearing Insulated, Oil Ring Lubrication.

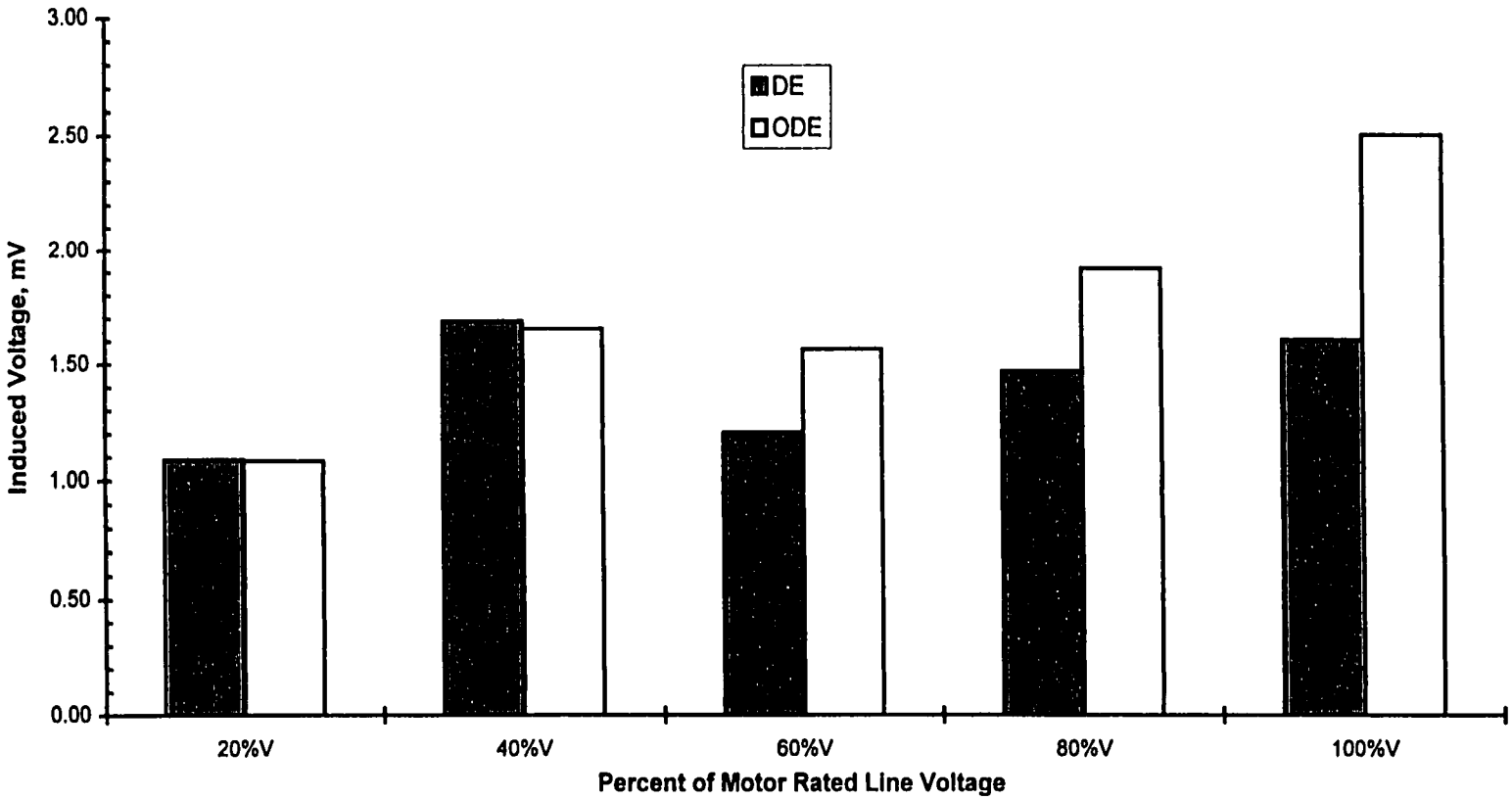

f) Magnitude, Steady State No-Load Condition.

Figure 6.38: Shaft Flux Coil Induced Voltages, Shaft End Play Movement, DE Bearing Non-Insulated, ODE Bearing Insulated, Oil Ring Lubrication

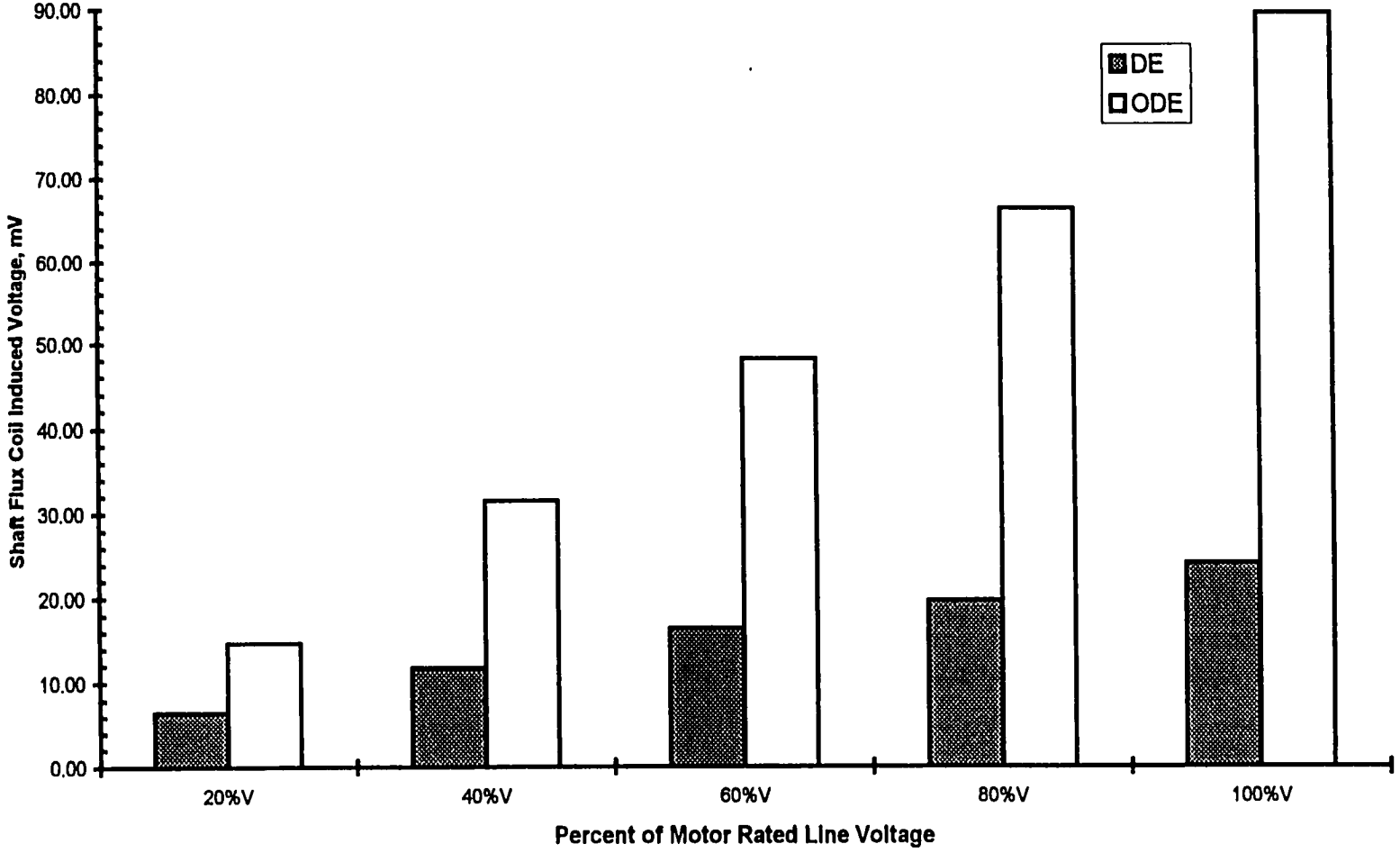

Figure 6.39: Shaft Flux Coil Induced Voltage Measurement, Locked Rotor Condition, 60Hz Component, DE Bearing Non-Insulated, ODE Bearing Insulated, Oil Ring Lubrication.

When the motor is held at magnetic center, spectral analyses of the measured shaft fluxes at both the DE and ODE as shown in Figures 6.40 (a) - (d), reveal harmonic components similar to the spectral analyses of the measurements performed when the motor is allowed the limited shaft end play movement. Furthermore, the magnitudes of the shaft flux coil induced voltages at magnetic center condition and shaft end-play movement condition of Figures 6.40 (e) and (f) are comparatively similar. It can be concluded that shaft end play movement which occurs during the acceleration of the motor had negligible effect on the magnitude of shaft flux. The shaft end play is measured to be 22.86 mm

6.4.6 VARIATION WITH BEARING INSULATION THICKNESS

Figure 6.41 shows the variation of magnitude of shaft current with bearing insulation thickness. As a result of this investigation, we can conclude that in this test machine, the bearing insulation thickness could be reduced to half its value with minimal detrimental consequence. Further investigation is required for a definitive conclusion of bearing insulation thickness that is required for all machine ratings.

6.4.7 SHAFT END-PLAY MOVEMENT FACTOR

In Chapter 2, it was mentioned that with end play movement and without bearing insulation, the probability of shaft current will increase due to the contact of the shaft journal with the bearing housing. However, in an oil ring lubricated machine with insulated bearing, end play movement assists in the build-up of the oil film. This results in a reduced increase of shaft current when the oil ring slippage occurs and a faster decay of the shaft current as the

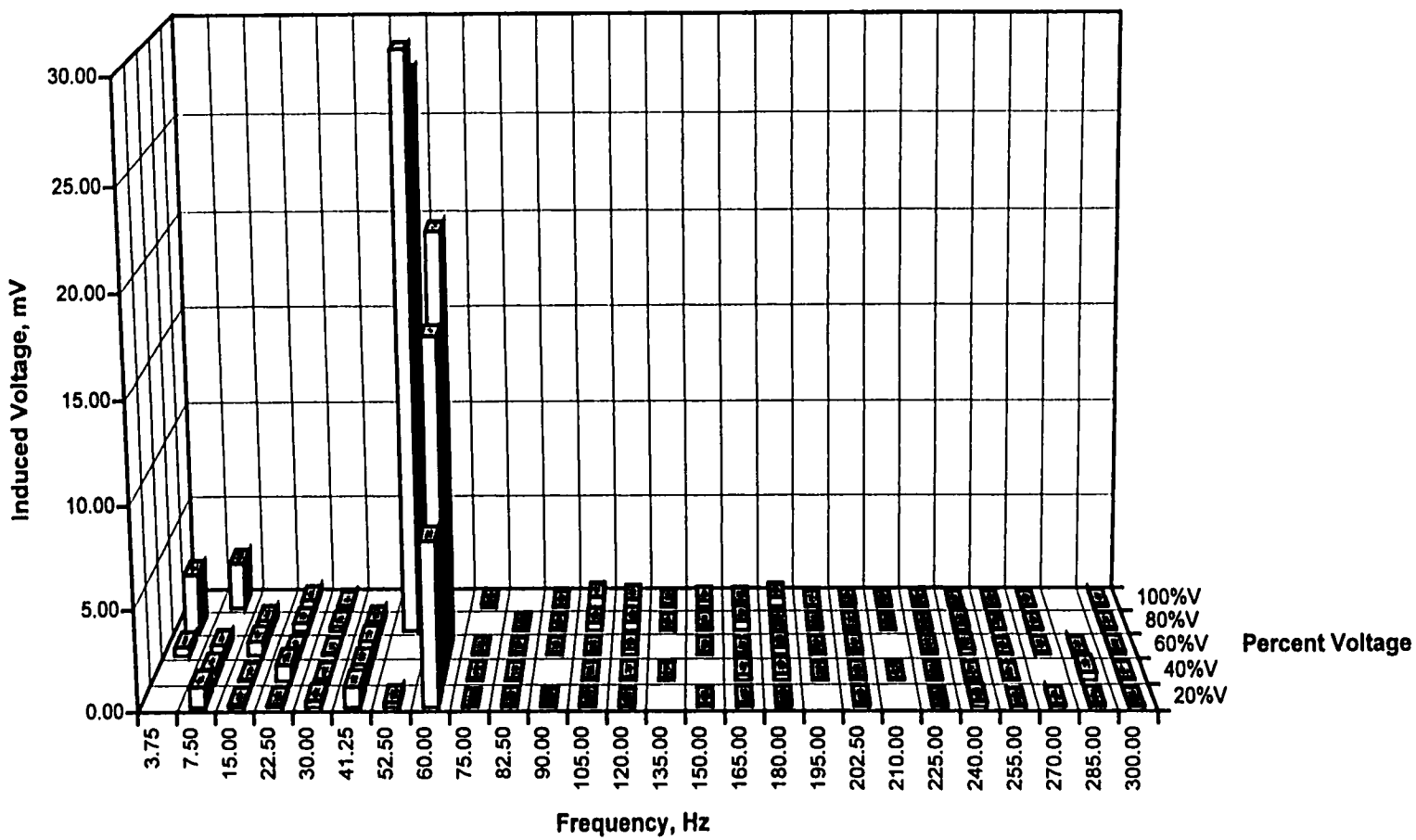

a) Drive End, Spectral Analysis,Transient Condition

Figure 6.40: Shaft Flux Coil Induced Voltage, Machine at Magnetic Centre, DE Bearing Non-Insulated, ODE Bearing Insulated, Oil Ring Lubrication.

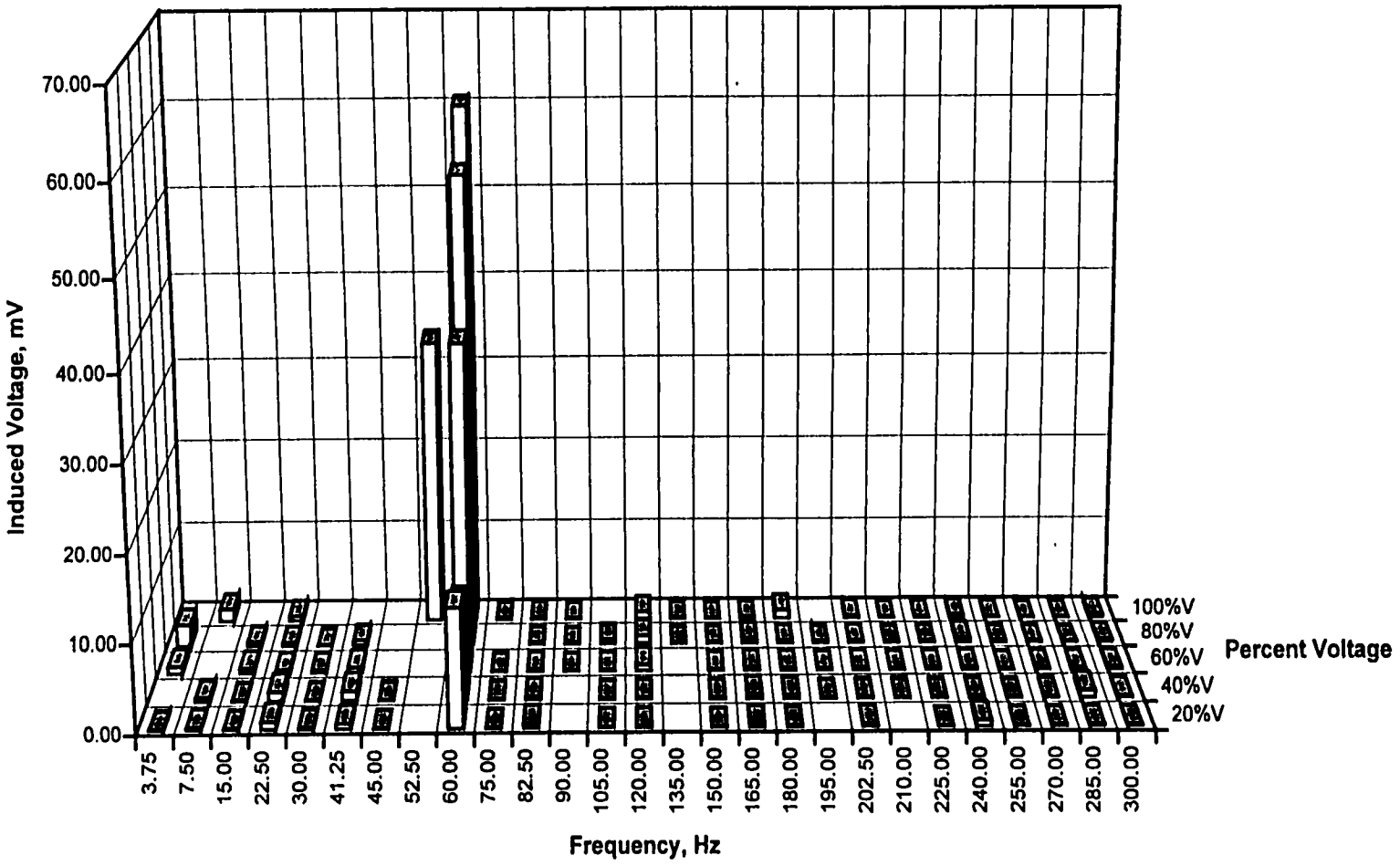

b) Opposite Drive End, Spectral Analysis,Transient Condition

Figure 6.40: Shaft Flux Coil Induced Voltage, Machine At Magnetic Centre, DE Bearing Non-Insulated, ODE Bearing Insulated, Oil Ring Lubrication.

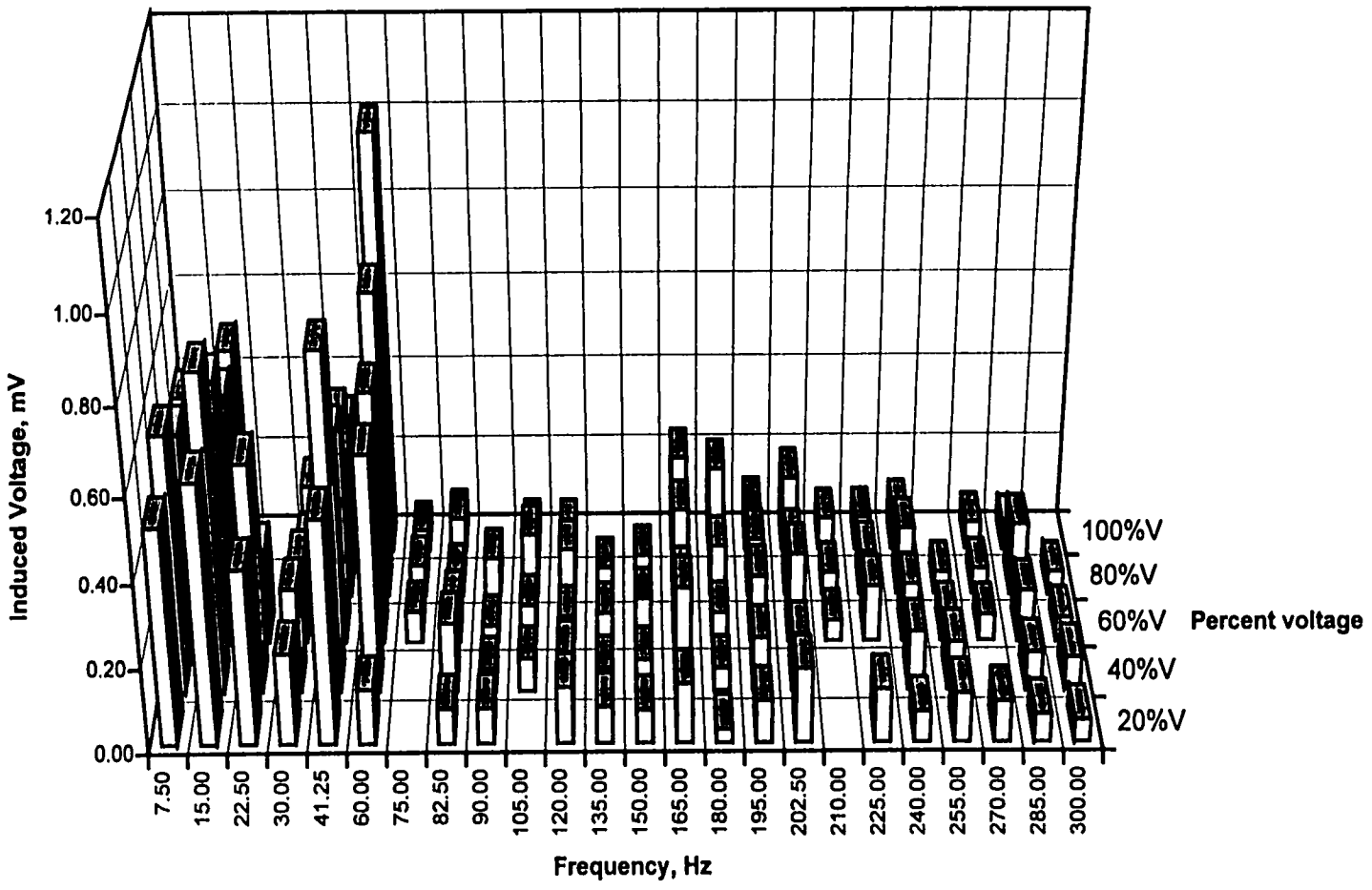

c) Drive End, Spectral Analysis, Steady State No-Load Condition

Figure 6.40: Shaft Flux Coil Induced Voltage, Machine At Magnetic Centre, DE Bearing Non-Insulated, ODE Bearing Insulated, Oil Ring Lubrication.

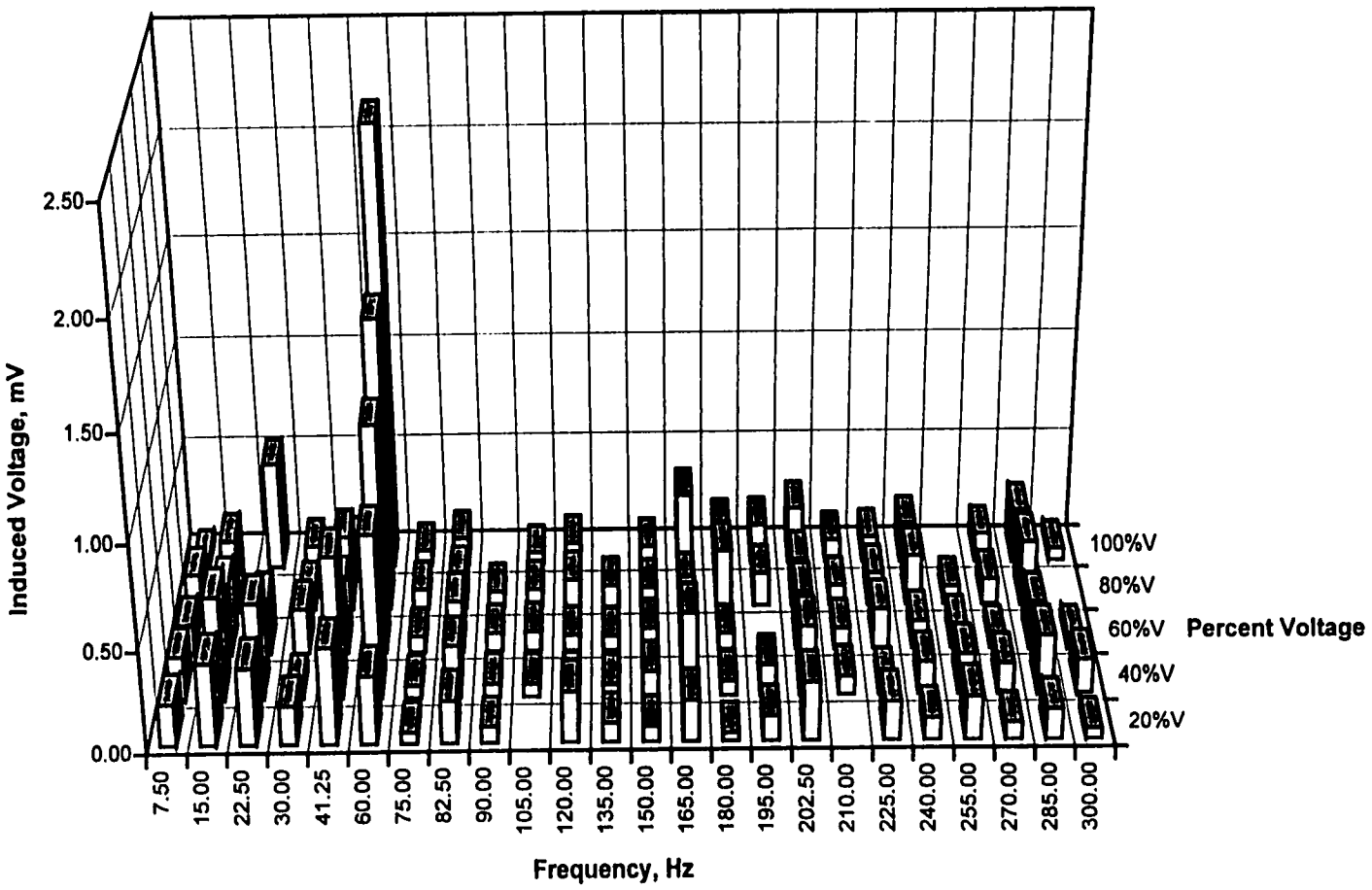

d) Opposite Drive End, Spectral Analysis, Steady State No-Load Condition

Figure 6.40: Shaft Flux Coil Induced Voltage, Machine At Magnetic Centre, DE Bearing Non-Insulated, ODE Bearing Insulated, Oil Ring Lubrication.

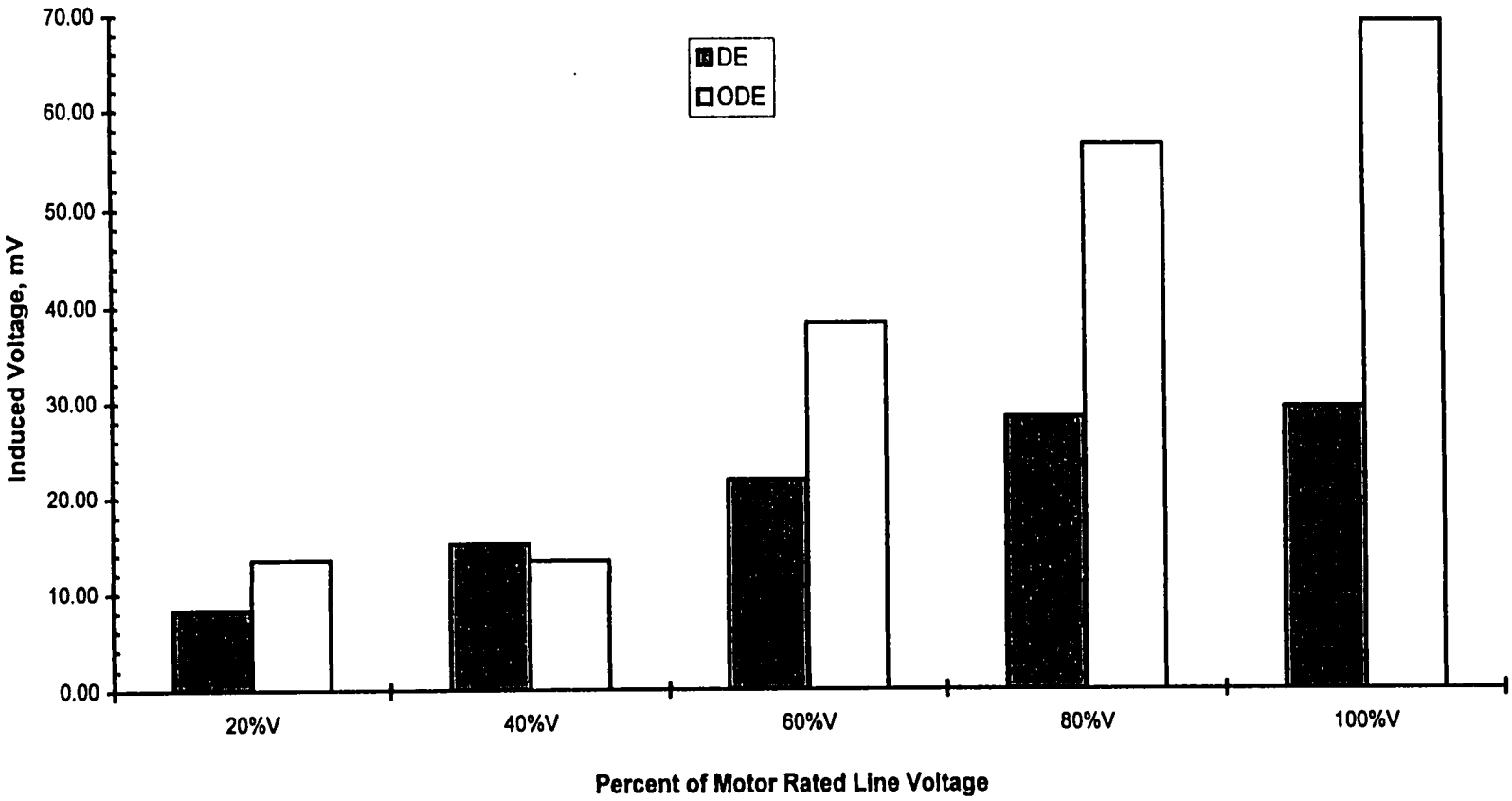

e) Magnitude, Transient Condition.

Figure 6.40: Shaft Flux Coil Induced Voltages, Machine At Magnetic Centre, DE Bearing Non-Insulated, ODE Bearing Insulated, Oil Ring Lubrication.

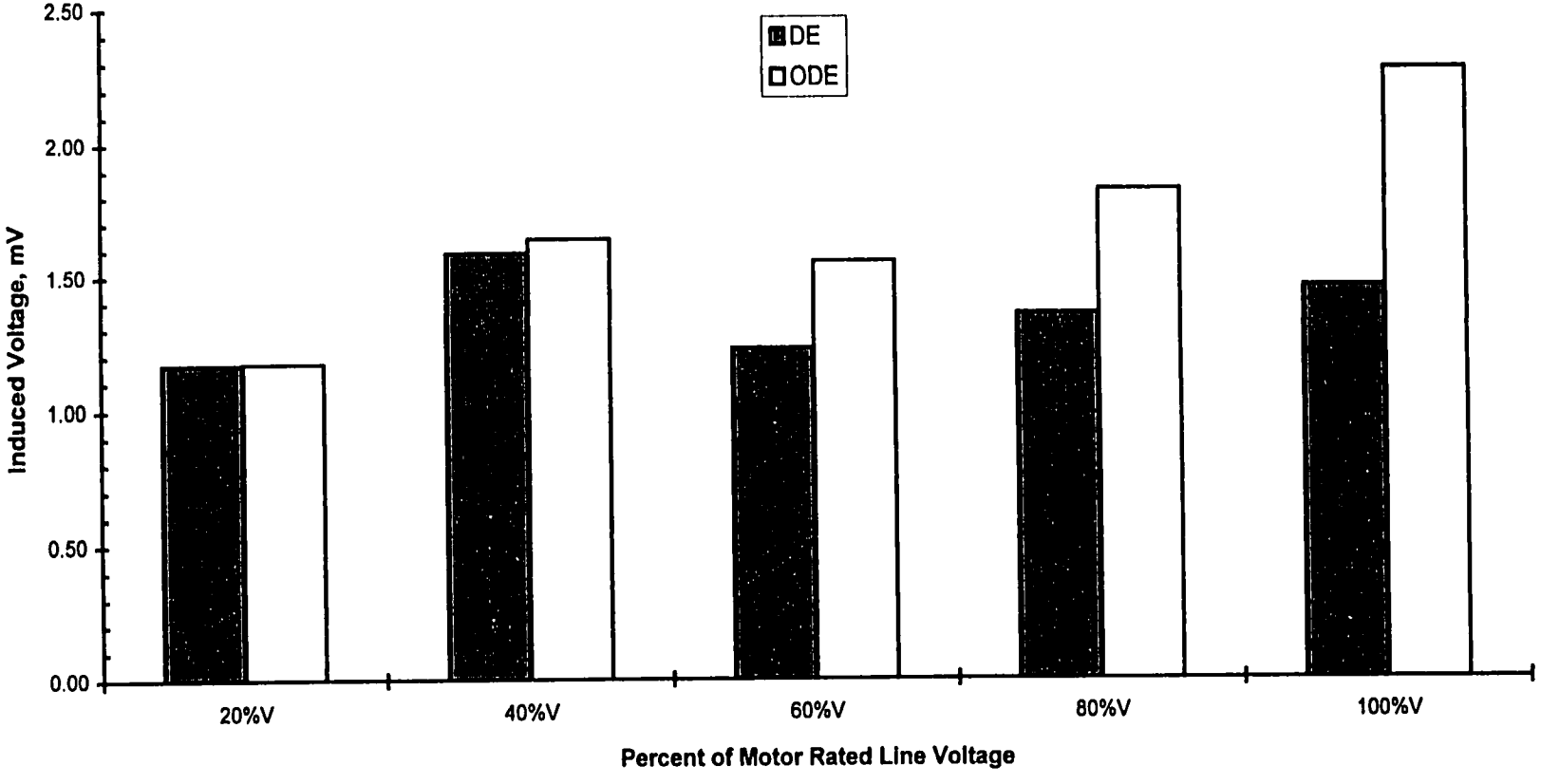

f) Magnitude, Steady State No-Load Condition.

Figure 6.40: Shaft Flux Coil Induced Voltages, Machine At Magnetic Centre, DE Bearing Non-Insulated, ODE Bearing Insulated, Oil Ring Lubrication

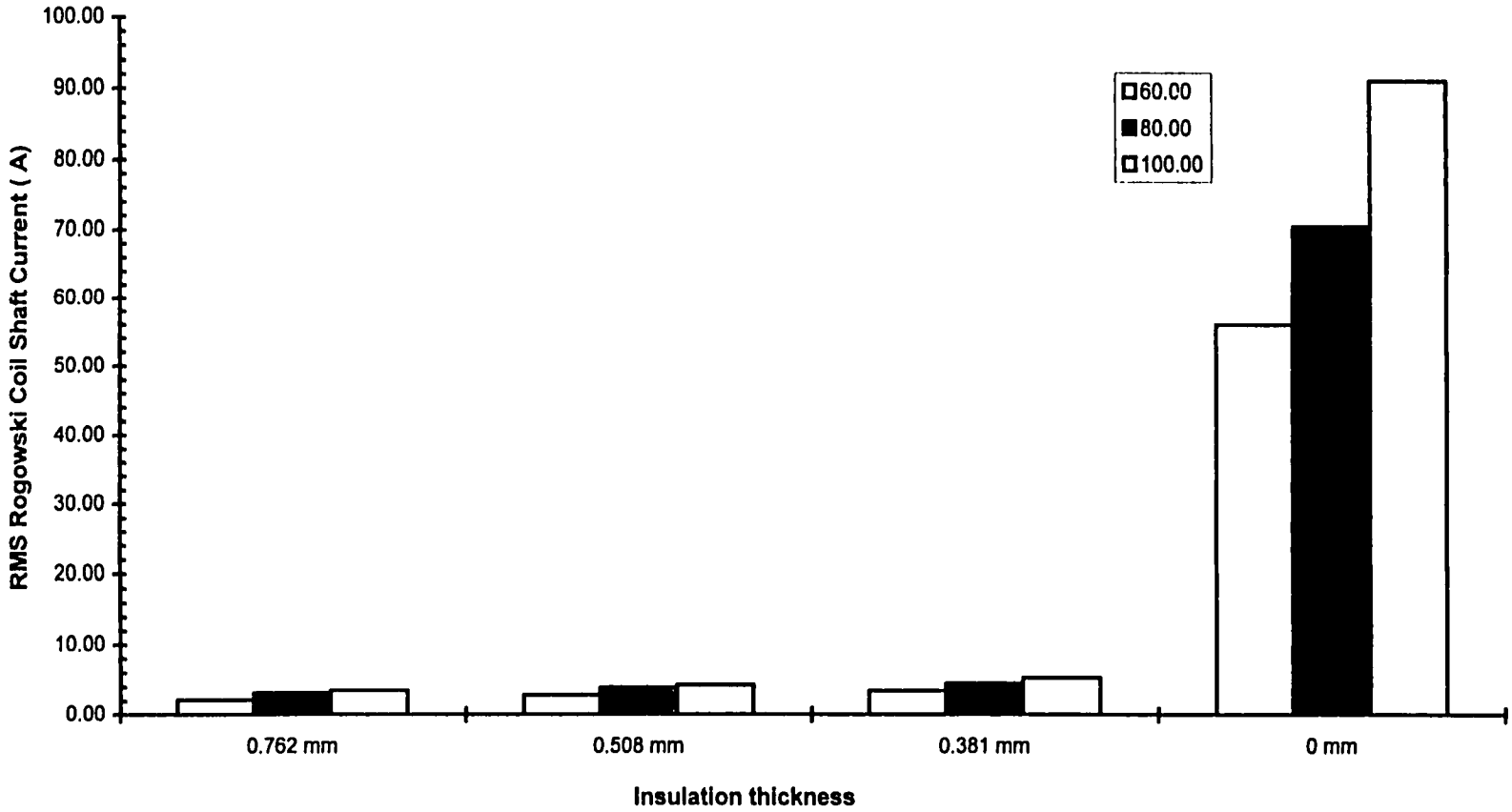

Figure 6.41: Shaft Current Measurement for Different Bearing Insulation Thickness, DE Bearing Non-Insulated,ODE Bearing Insulated, Shaft End Play Movement, Oil Ring Lubrication.

machine reaches steady state no-load speed. This finding is shown in Figures 6.42 (a) - (e). End play movement to some extent helps to reduce the slippage of the oil ring and hence oil is delivered quickly to the journal from the inside surface of the oil ring. However, the end play movement has the effect of thinning the oil film on the side of the bearing in the direction of motion and building up oil film in the opposite direction. As the shaft oscillates axially, this phenomenon of thinning and build up of the oil film increases the probability of breakdown of the oil film, resulting in shaft current. This effect is small in a machine with limited end play. The total end play of this machine is measured to be 22.86 mm. The axial shaft oscillation occurs during acceleration of the motor. A change of load can also cause this oscillation.

For all voltage starting conditions, at close to standstill condition, there is metal-to metal contact between the bearing and the shaft. Shaft current is detected in the closed circuit involving the shaft, the bearing and the machine frame. As the shaft speed increases, initially the oil ring speed follows the shaft speed. An oil film is developed. Shaft current decreases as shown in Figures 6.42 (a) - (e). On further increase of the shaft speed, the oil ring slips and the thickness of the oil film becomes inconsistent. Shaft current increases. When the machine reaches rated no-load speed, the oil film is sufficient to reduce the shaft current.

6.4.8 SATURATION EFFECT

Flux coils were located on the stator tooth closest to the air gap at the DE, center and ODE of the stator as shown in Figure 3.8. Each of the 3 coils was wrapped around a packet of laminations. Figure 6.43 shows the transient magnitudes of the flux coil induced voltage harmonics in per unit of the 20%V fundamental value. The third, fifth, seventh and ninth

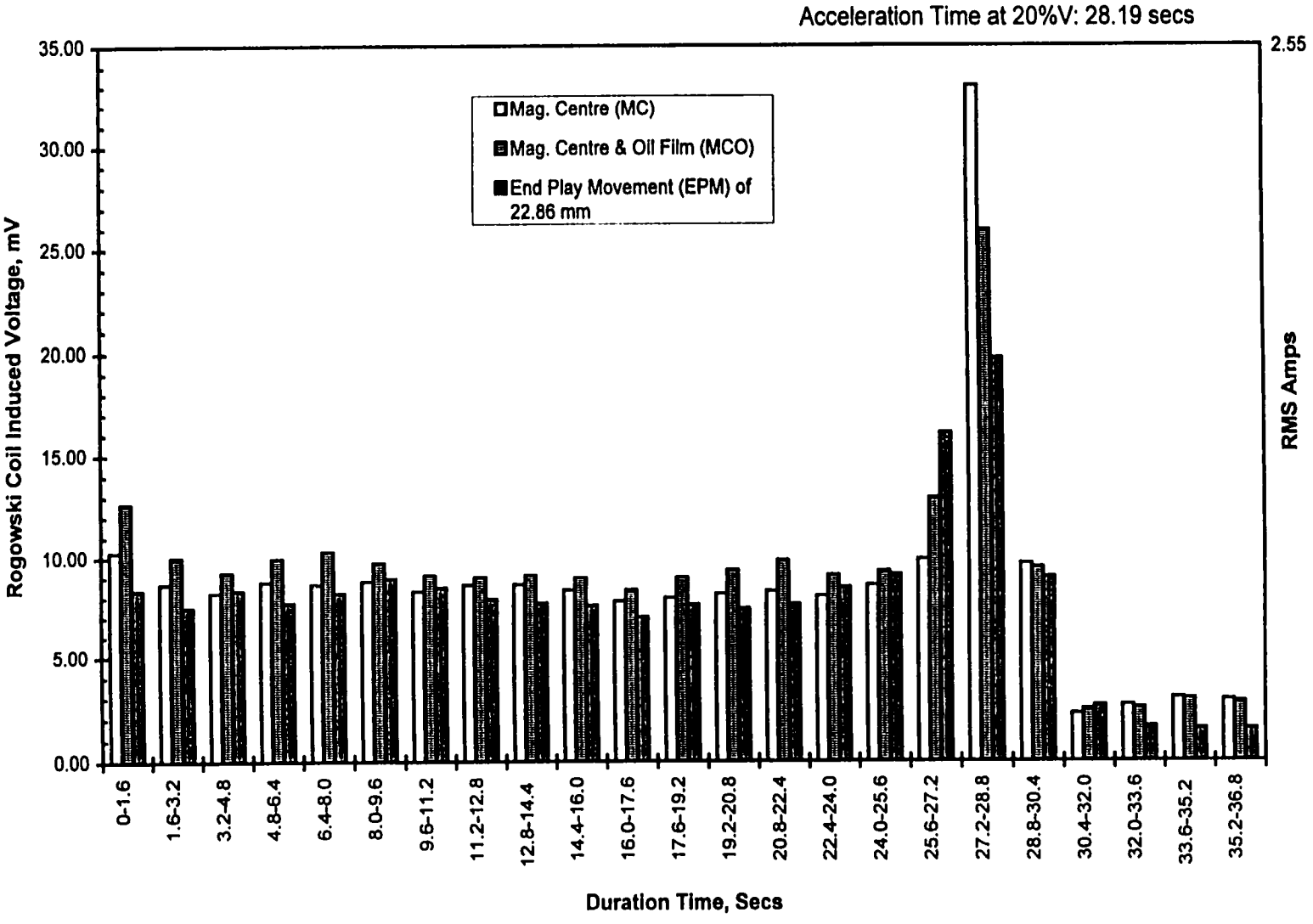

a) 20%V

Figure 6.42: Shaft Current Measurement For Different Machine Positions

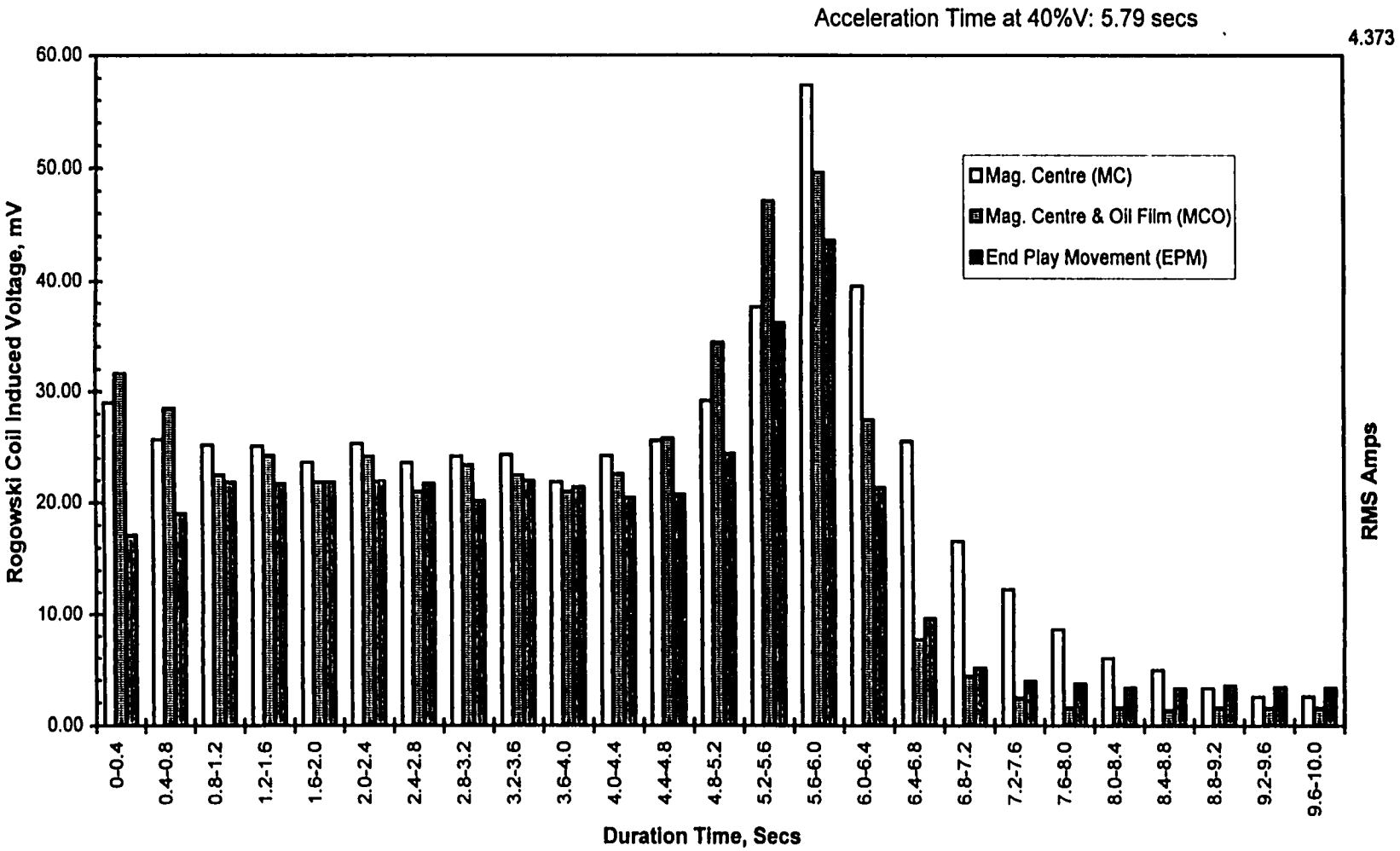

b) 40%V

Figure 6.42: Shaft Current Measurement For Different Machine Positions

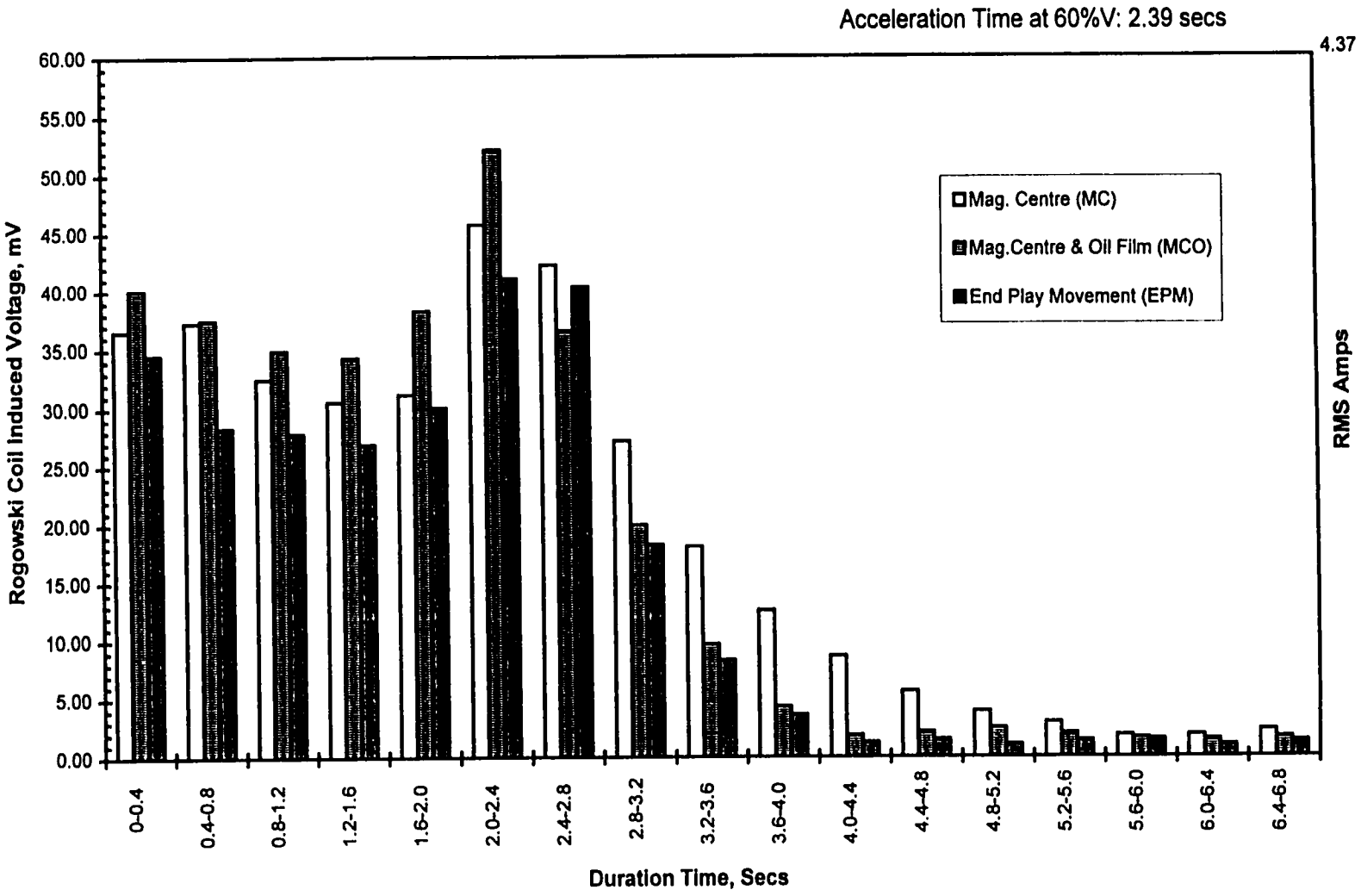

c) 60%V

Figure 6.42: Shaft Current Measurement For Different Machine Positions

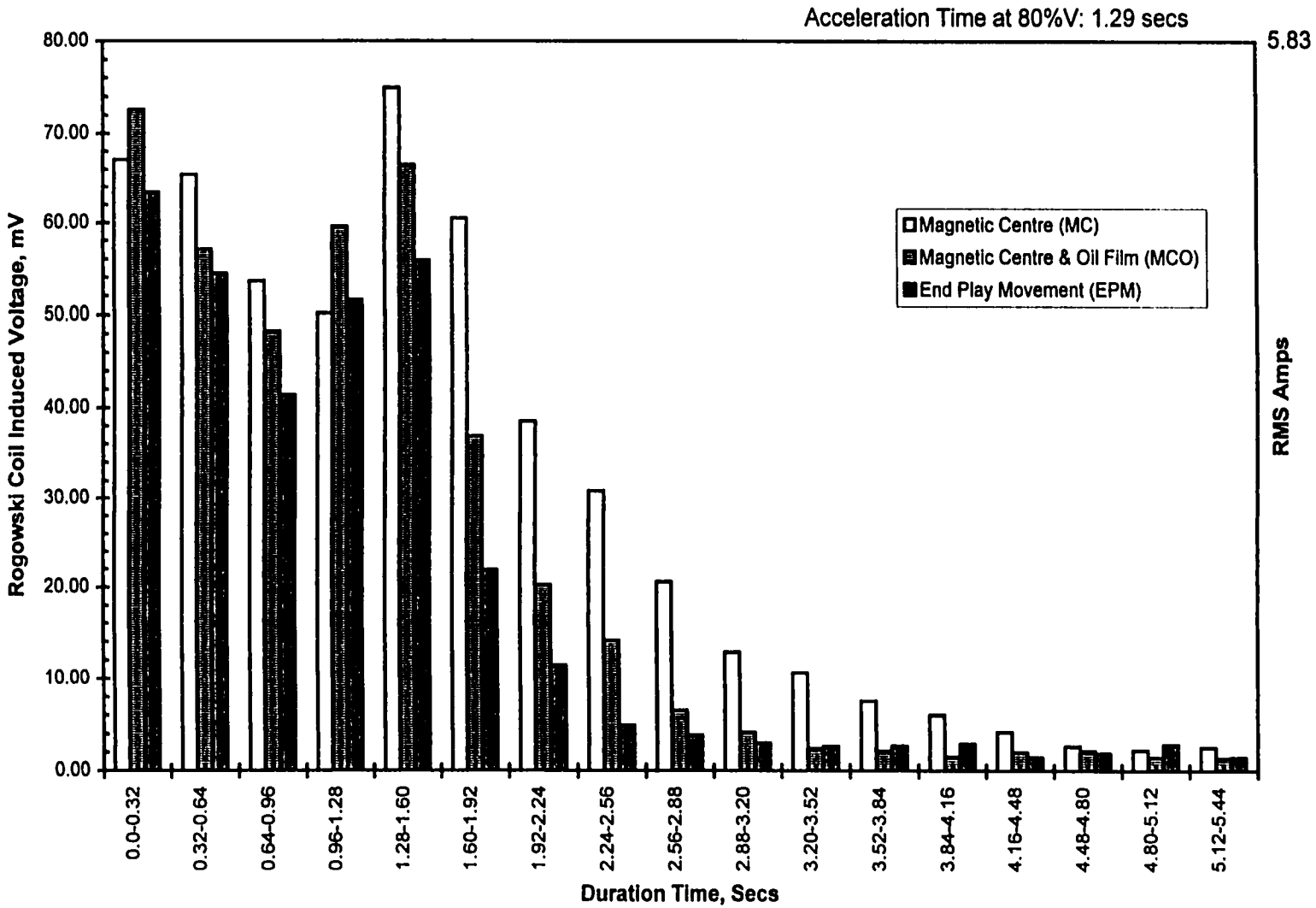

d) 80%V

Figure 6.42: Shaft Current measurement For Different Machine Positions

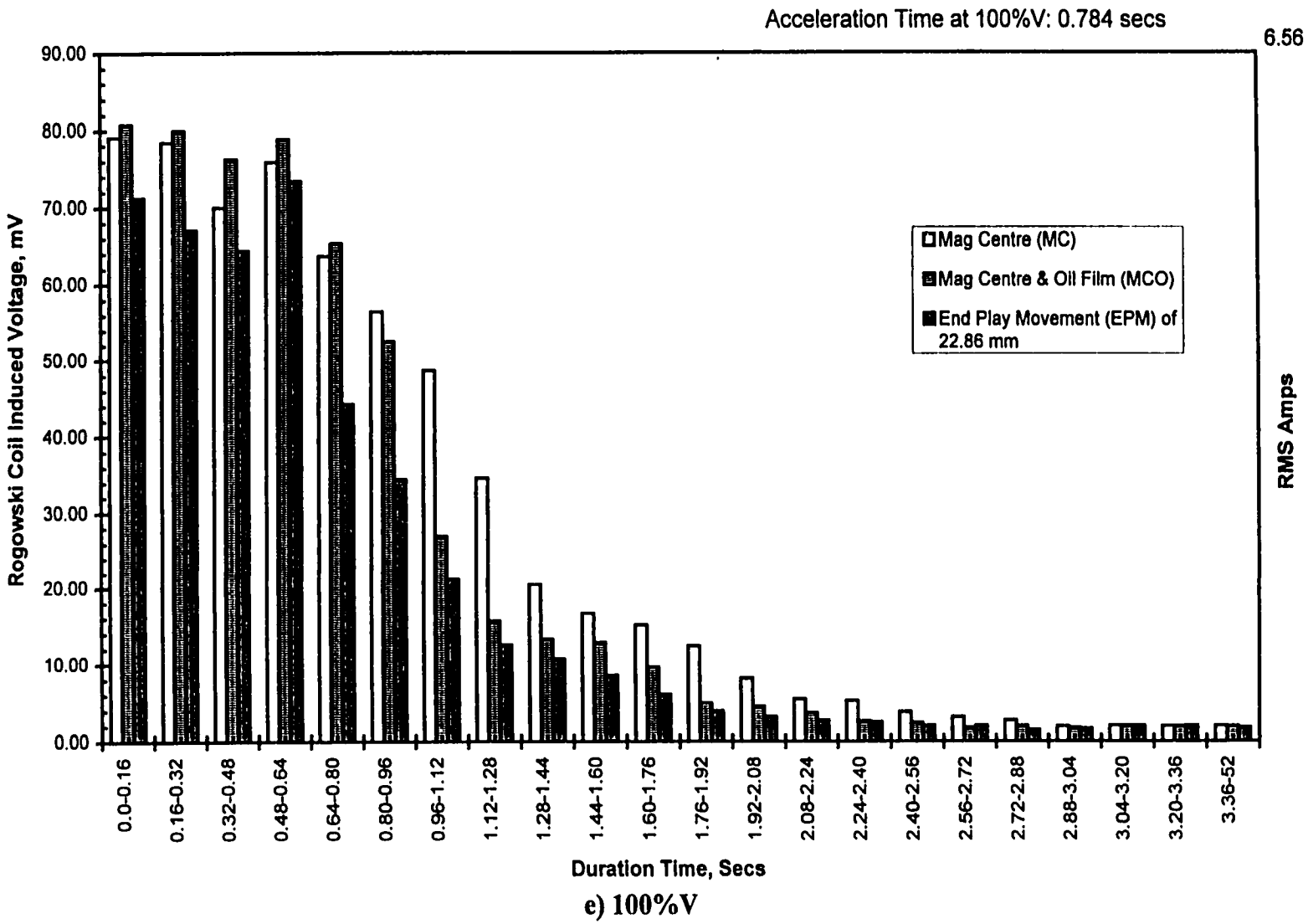

e) 100%V

Figure 6.42: Shaft Current Measurement For Different Machine Positions

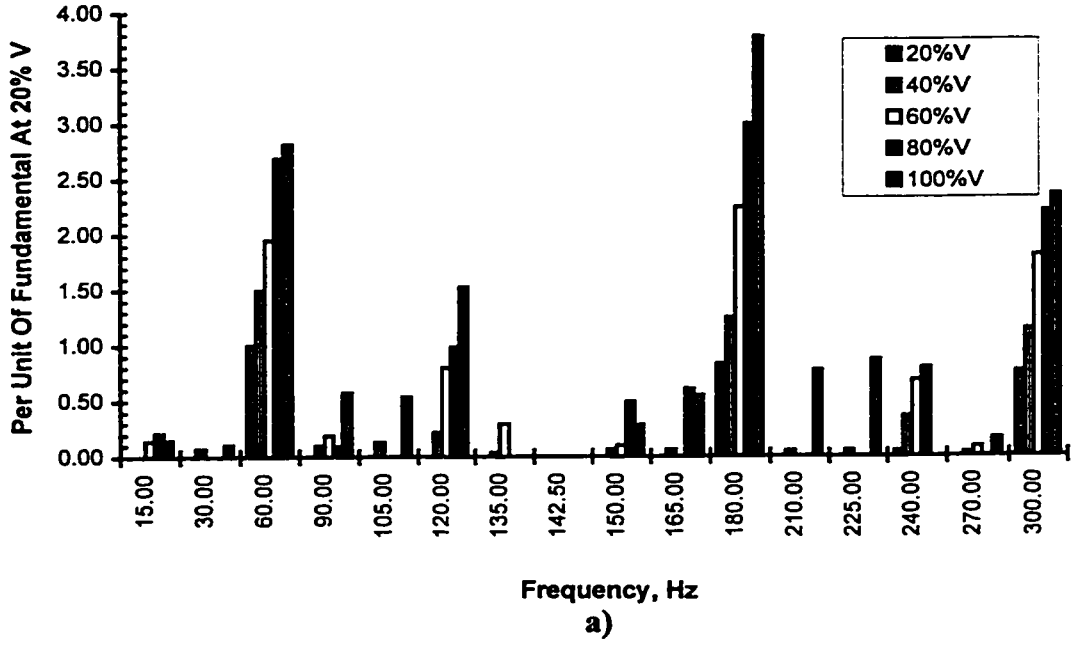

a)

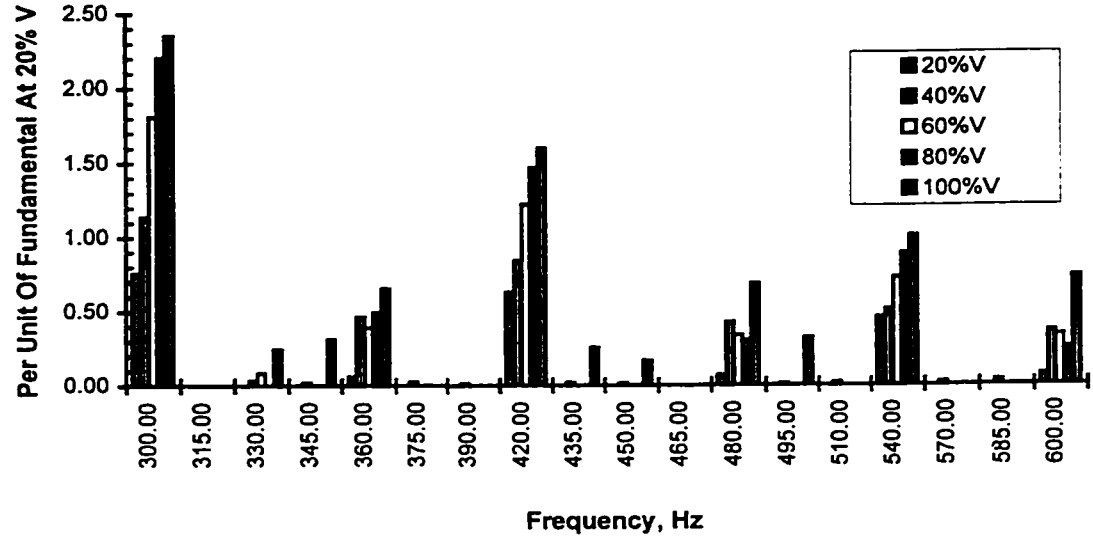

b)

Figure 6.43: Stator Tooth Flux Coil Induced Voltage, Transient Condition, Shaft End Play Movement, Both Bearings Non-Insulated, Oil Ring Lubrication.

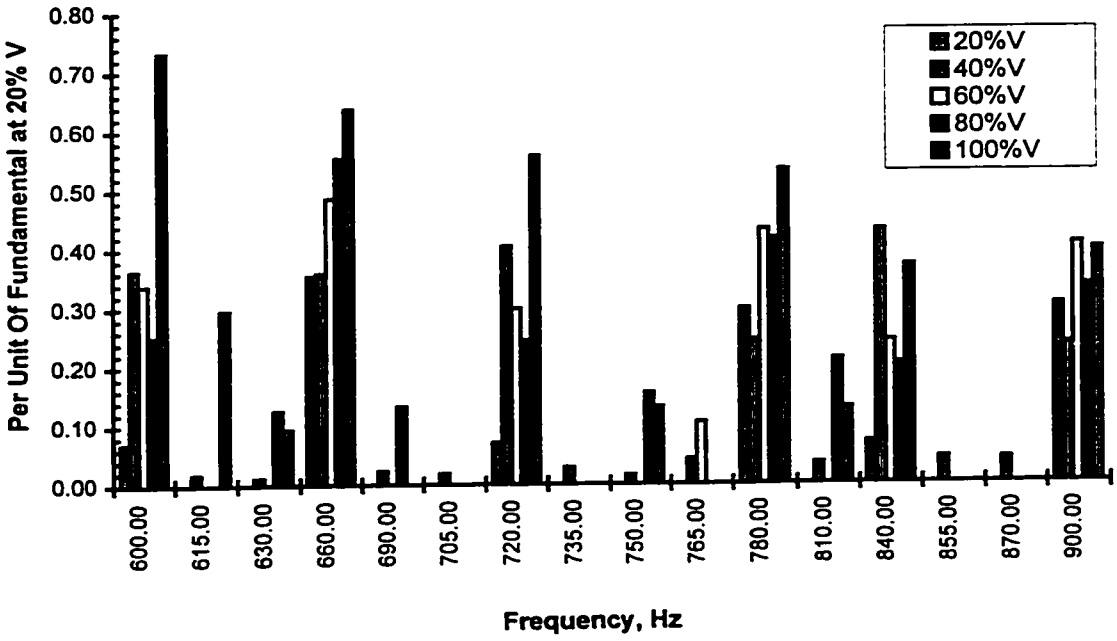

c)

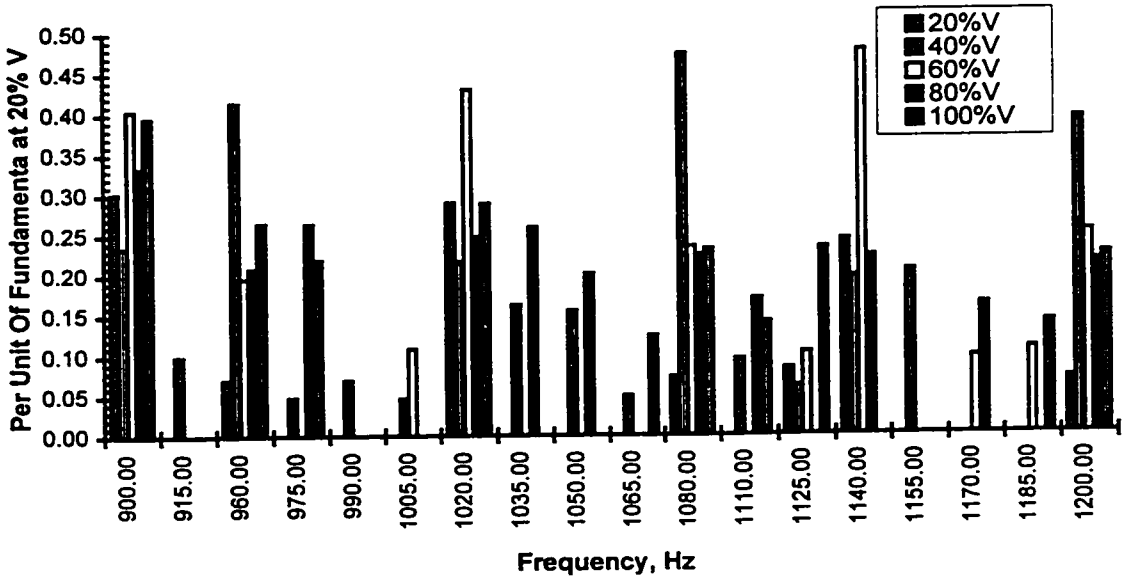

d)

Figure 6.43: Stator Tooth Flux Coil Induced Voltage, Transient Condition, Shaft End Play Movement, Both Bearings Non-Insulated, Oil Ring Lubrication.

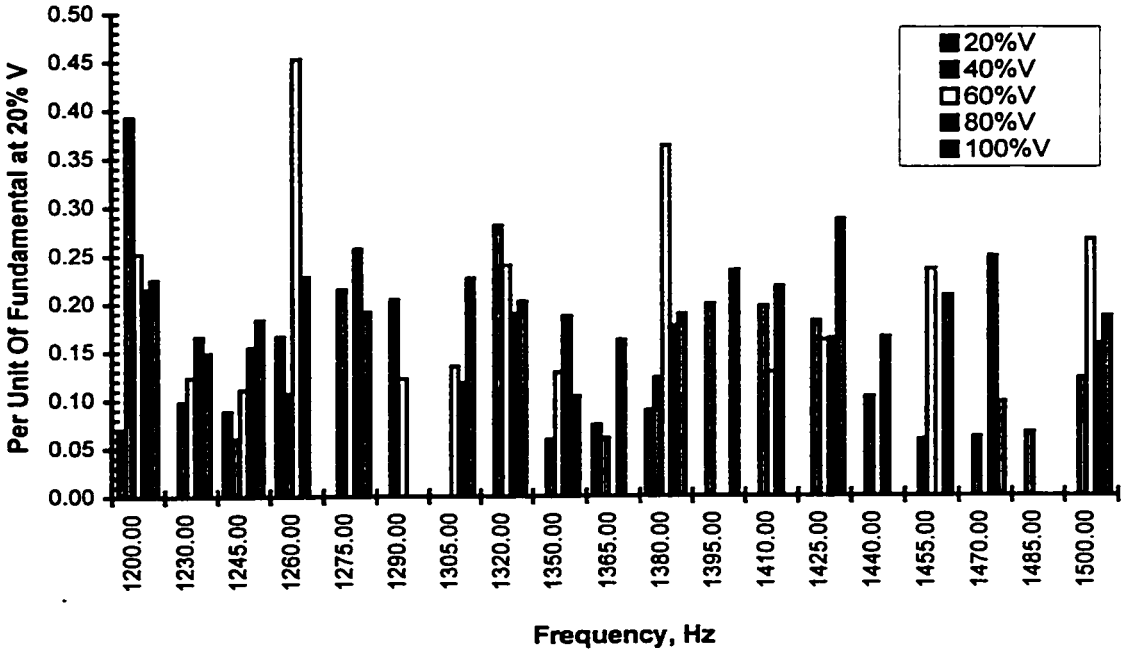

e)

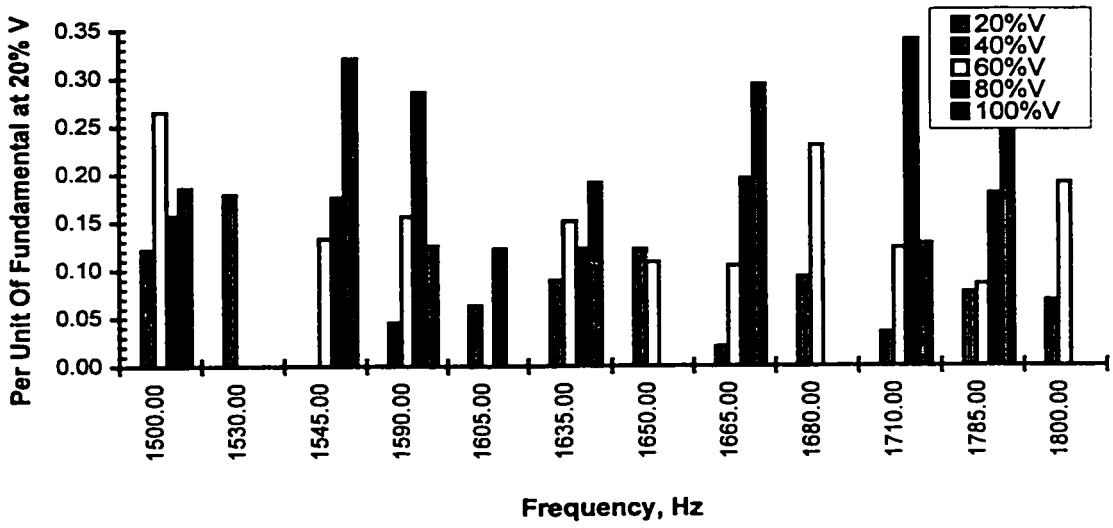

f)

Figure 6.43: Stator Tooth Flux Coil Induced Voltage, Transient Condition, Shaft End Play Movement, Both Bearings Non-Insulated, Oil Ring Lubrication.

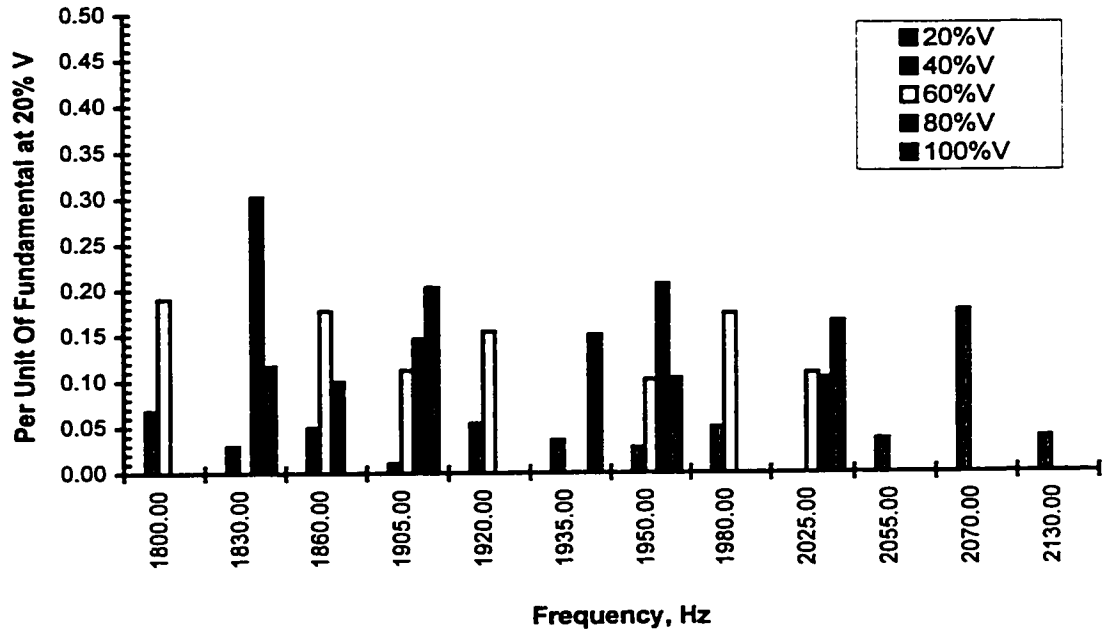

g)

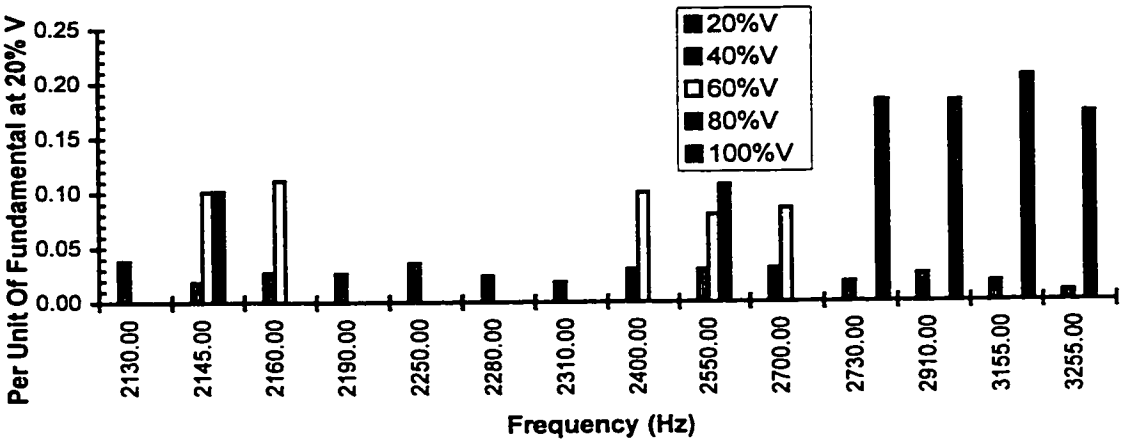

h)

Figure 6.43: Stator Tooth Flux Coil Induced Voltage, Transient Condition, Shaft End Play Movement, Both Bearings Non-Insulated, Oil Ring Lubrication.

harmonics are significant. The second, fourth, tenth, and twelfth harmonics are also observed, though negligible. As the voltages increase from 20%V to 100%V the significant harmonics increase, the exception being that the third harmonic increases initially but decreases after 80%V. At 60%V, the third harmonic and the fundamental are of comparable value.

During the steady state running condition as shown in Figure 6.44, the significant harmonics observed in the initial start of acceleration become negligible. Frequency components of about 1950, 2070 Hz and 2190 Hz are significant due to a combination of rotor slot harmonics, saturation harmonics and stator fundamental MMF, as indicated in Table 6.4.

6.4.9 SPIDER ARMS AND FRAME FLUX MEASUREMENTS

Flux coils each of 5 turns and covering an area of 50.8 mm by 939.8 mm, were mounted securely on three shaft spider arms, labeled "Arm A", "Arm B" and "Arm C" as shown in Figure 3.8 to measure the radial flux. From Figures 6.45 (a) - (f), it can be seen that at 20%V, 40%V and 60%V, there is a difference between the shaft flux on the spider arms opposite each other, that is Arm B and Arm C, when the machine accelerates at its magnetic center. This difference is not as large as it was when the measurement was conducted with the machine allowed shaft end play movement. The dc motor holding the machine at its magnetic center assists in minimizing the effects of radial magnetic pull. Radial magnetic pull is largest at the standstill condition. As well, eccentricity is reduced under these circumstances. At the steady state no-load condition, both the magnetic center case and the shaft end-play movement case have approximately the same difference.

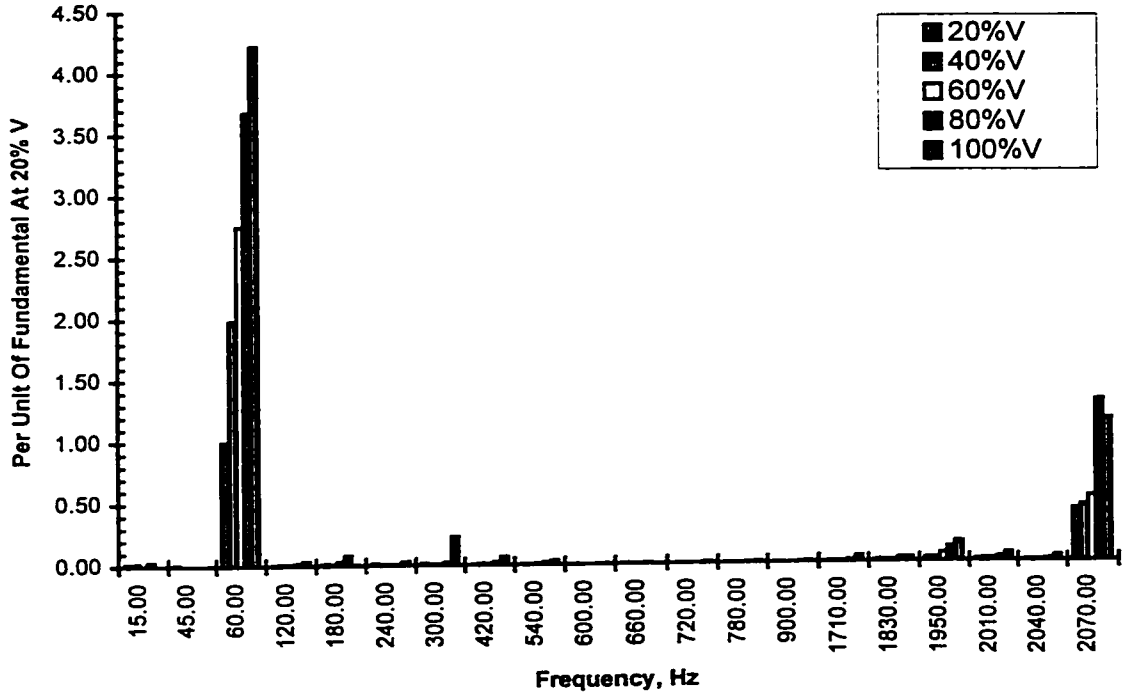

a)

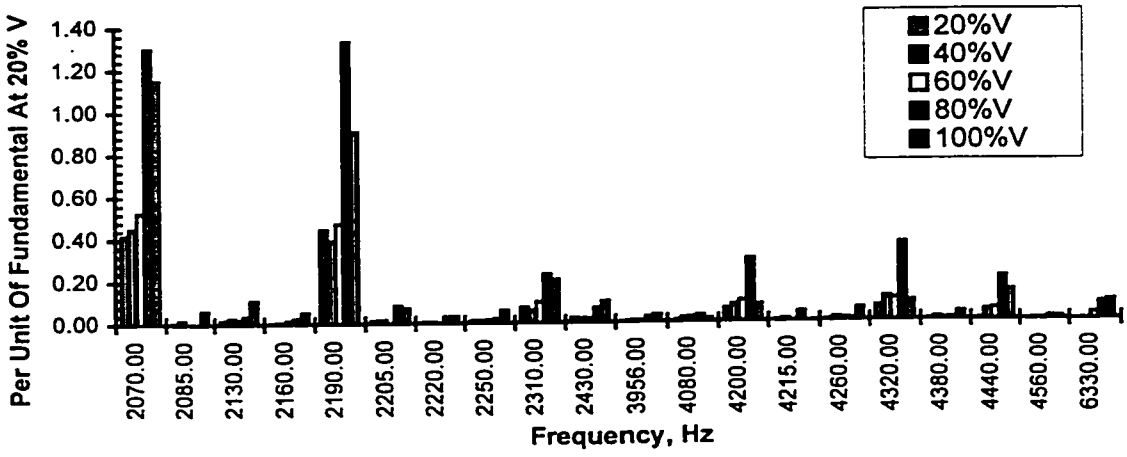

b)

Figure 6.44: Stator Tooth Flux Coil Induced Voltage, Steady State No-Load Condition, Shaft End Play Movement, Both Bearings Non-Insulated, Oil Ring Lubrication.

Causes	Frequency Components (Hz)
Rotor Slots Modulation	2067.63, 2187.63
Rotor Slots Modulation and Saturation (3^{rd})	1947.63, 2307.66
Dynamic Eccentricity (n_d=R ± S)	1738.0, 1858.0, 2517.27, 2397.27
Dynamic Eccentricity (n_d=R ± S±2p)	1618.14, 1738.14, 1857.87, 1977.87, 2277.40, 2397.40, 2517.14, 2637.14
Dynamic Eccentricity (n_d=R ± S) + Saturation (3^{rd})	1618.0, 1738.0, 1858.0, 1978.0, 2277.27, 2397.27, 2517.27, 2637.27
Dynamic Eccentricity (n_d= R ± S± 2p) + Saturation (3^{rd})	1498.14, 1618.14, 1738.14, 1857.87, 1977.87, 2097.87, 2157.40, 2277.40, 2397.40, 2517.40, 2757.14
Broken Bar	59.87, 60.13
Broken Bar and Saturation	60.13, 60.264
Broken Bar, Winding Harmonic (5^{th}) and Saturation (3^{rd})	299.76, 299.64

Table 6.4: Causes and Predicted Frequency Components, Steady State No-Load Condition (slip of 0.0011 p.u.)

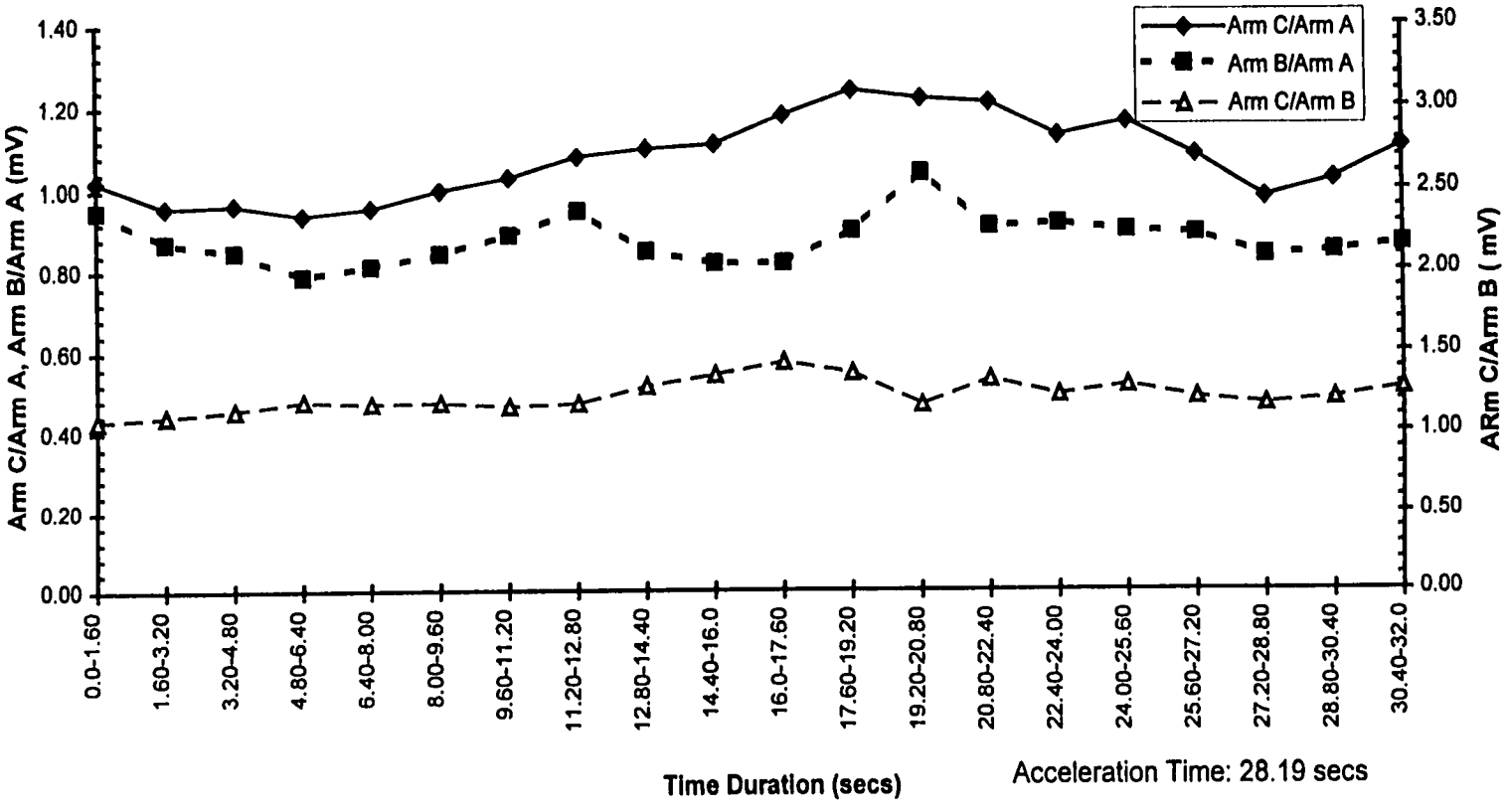

a) Shaft End Play Movement, 20%V

Figure 6.45: Shaft Spider Arm Flux Coil Induced VoltageRatio: Shaft End Play Versus Magnetic Center, DE Bearing Non-Insulated, ODE Bearing Insulated, Oil Ring Lubrication.

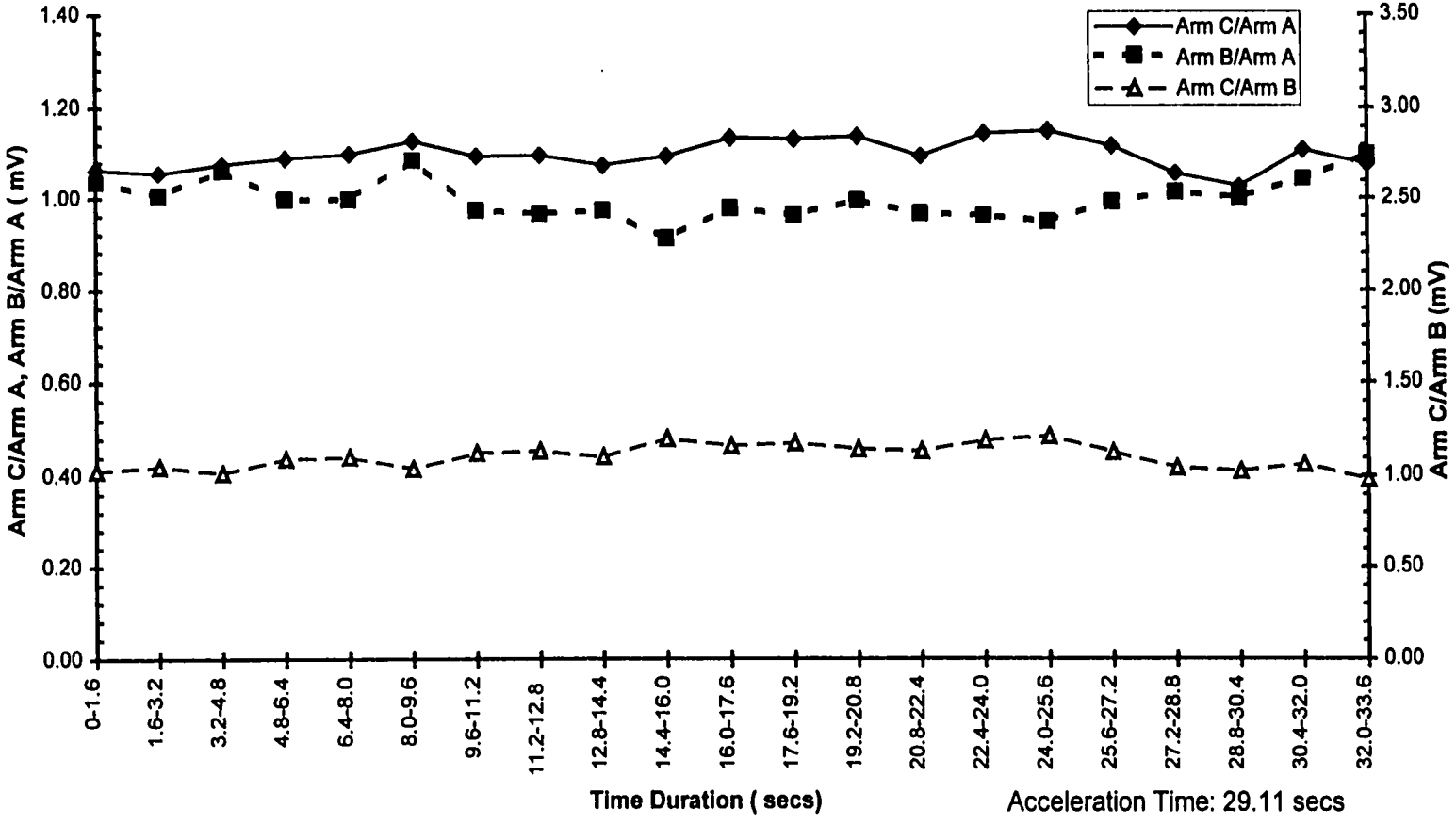

b) Magnetic Center, 20%V

Figure 6.45: Shaft Spider Arm Radial Flux Coil Induced Voltage Ratio: Shaft End Play Versus Magnetic Center, DE Bearing Non-Insulated, ODE Bearing Insulated, Oil Ring Lubrication.

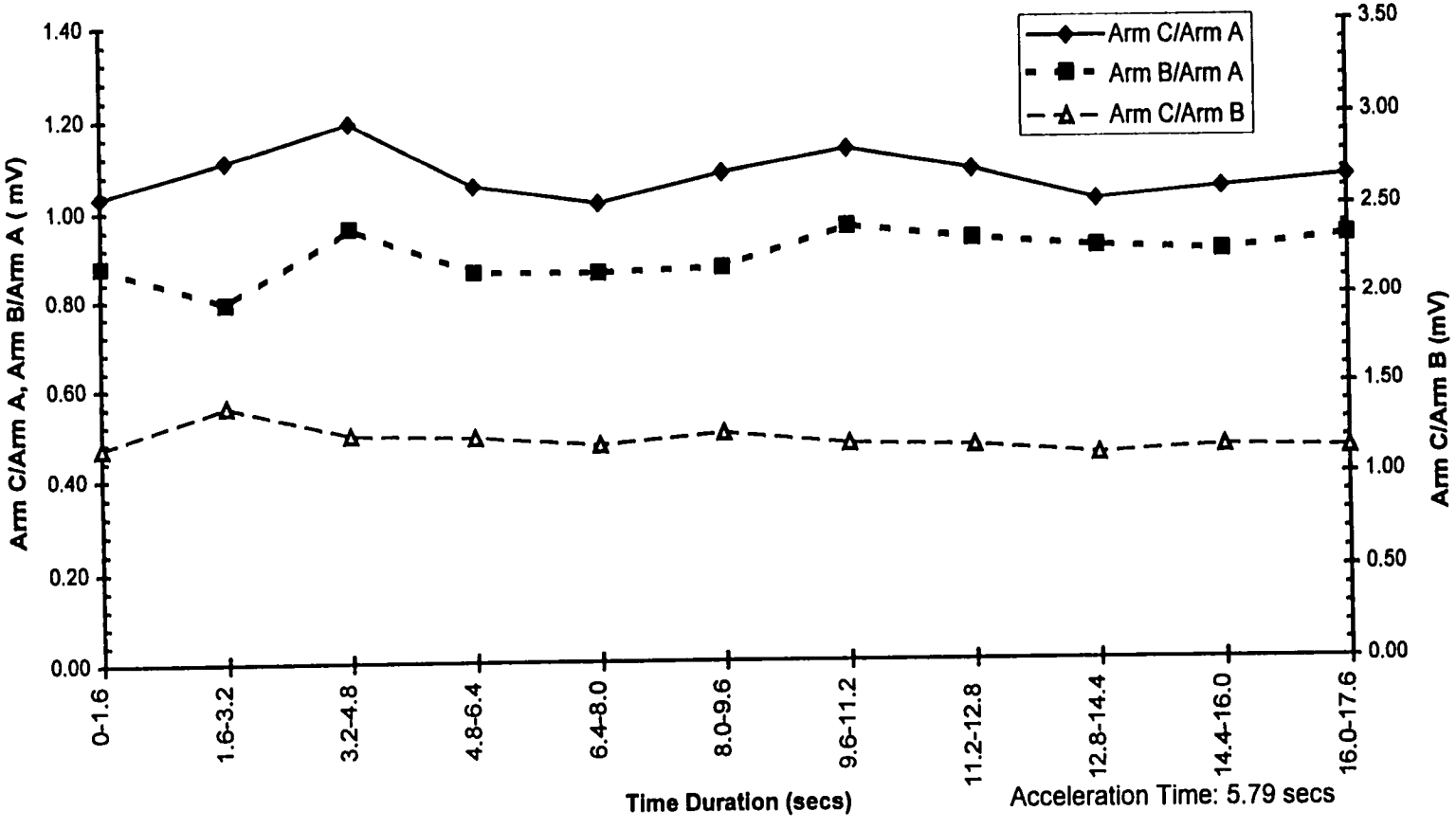

c) Shaft End Play Movement, 40%V

Figure 6.45: Shaft Spider Arm Radial Flux Coil Induced Voltage Ratio: Shaft End Play Versus Magnetic Center, DE Bearing Non-Insulated, ODE Bearing Insulated, Oil Ring Lubrication.

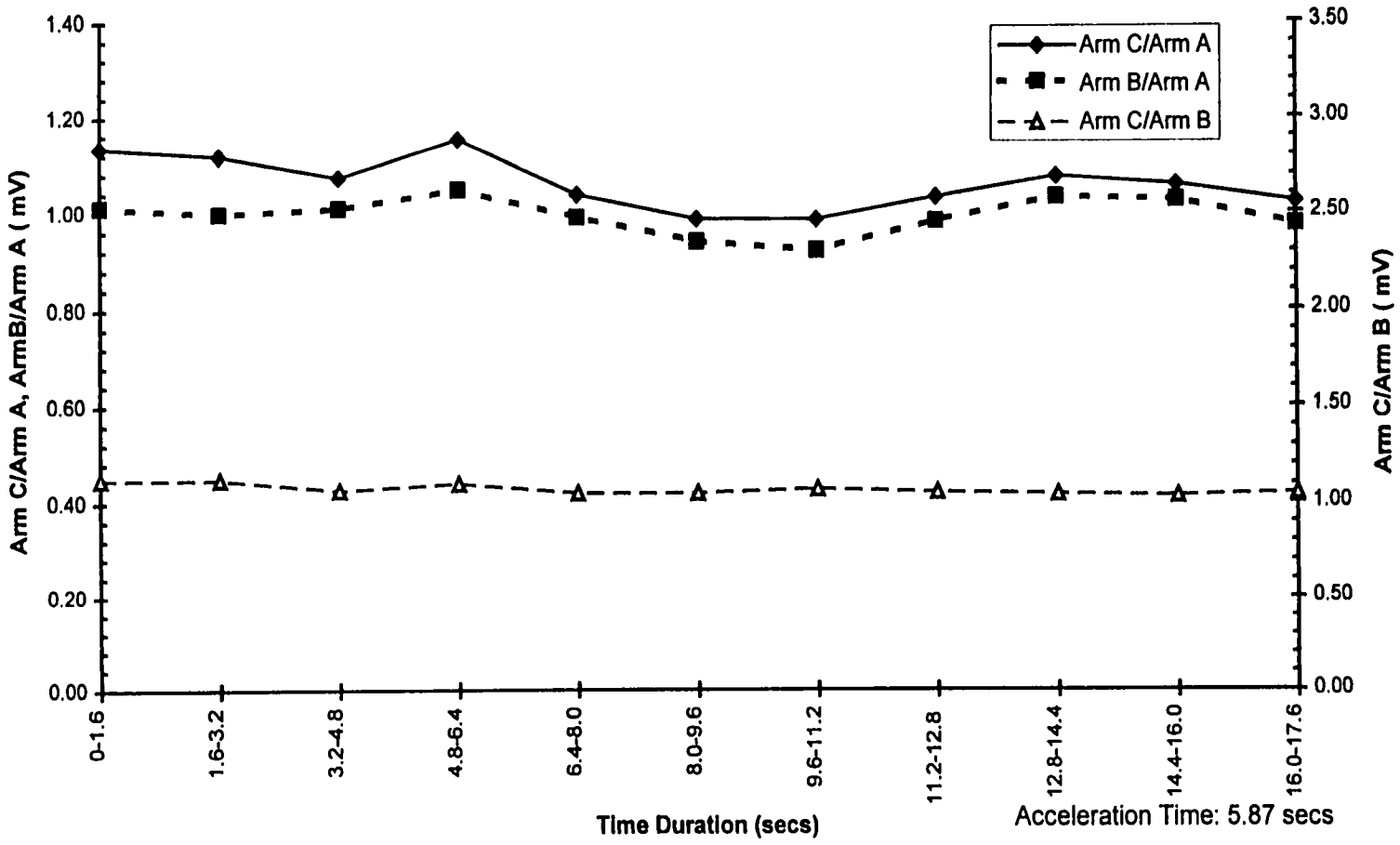

d) Magnetic Center, 40%V

Figure 6.45: Shaft Spider Arm Radial Flux Coil Induced Voltage Ratio: Shaft End Play Vesus Magnetic Center, DE Bearing Non-Insulated, ODE Bearing Insulated, Oil Ring Lubrication.

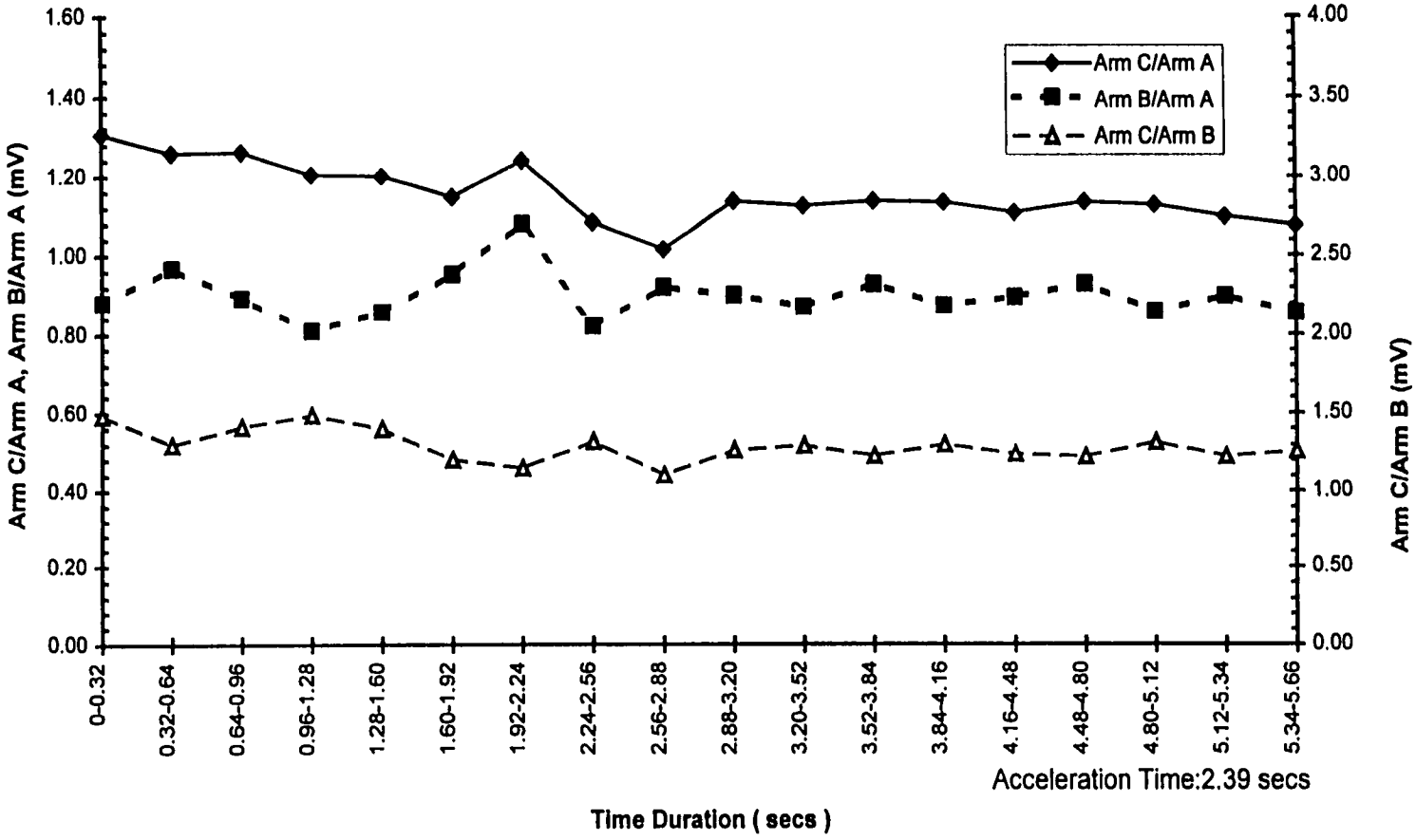

e) Shaft End Play Movement, 60%V

Figure 6.45: Shaft Spider Arm Radial Flux Coil Induced VoltageRatio: Shaft End Play Versus Magnetic Center, DE Bearing Non-Insulated, ODE Bearing Insulated, Oil Ring Lubrication.

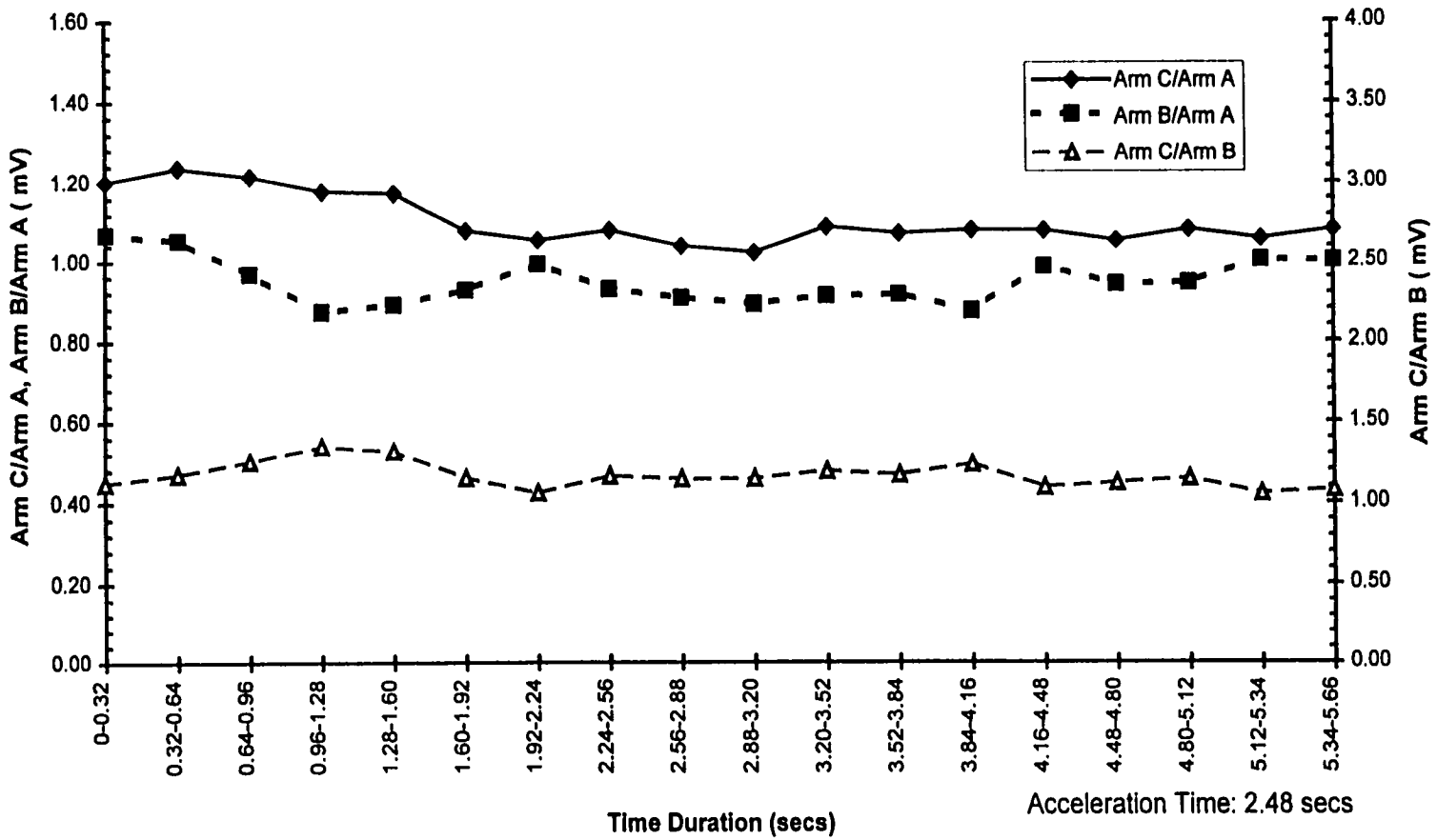

f) Magnetic Center, 60%V

Figure 6.45: Shaft Spider Arm Radial Flux Coil Induced Voltage Ratio: Shaft End Play Versus Magnetic Center, DE Bearing Non-Insulated, ODE Bearing Insulated, Oil Ring Lubrication.

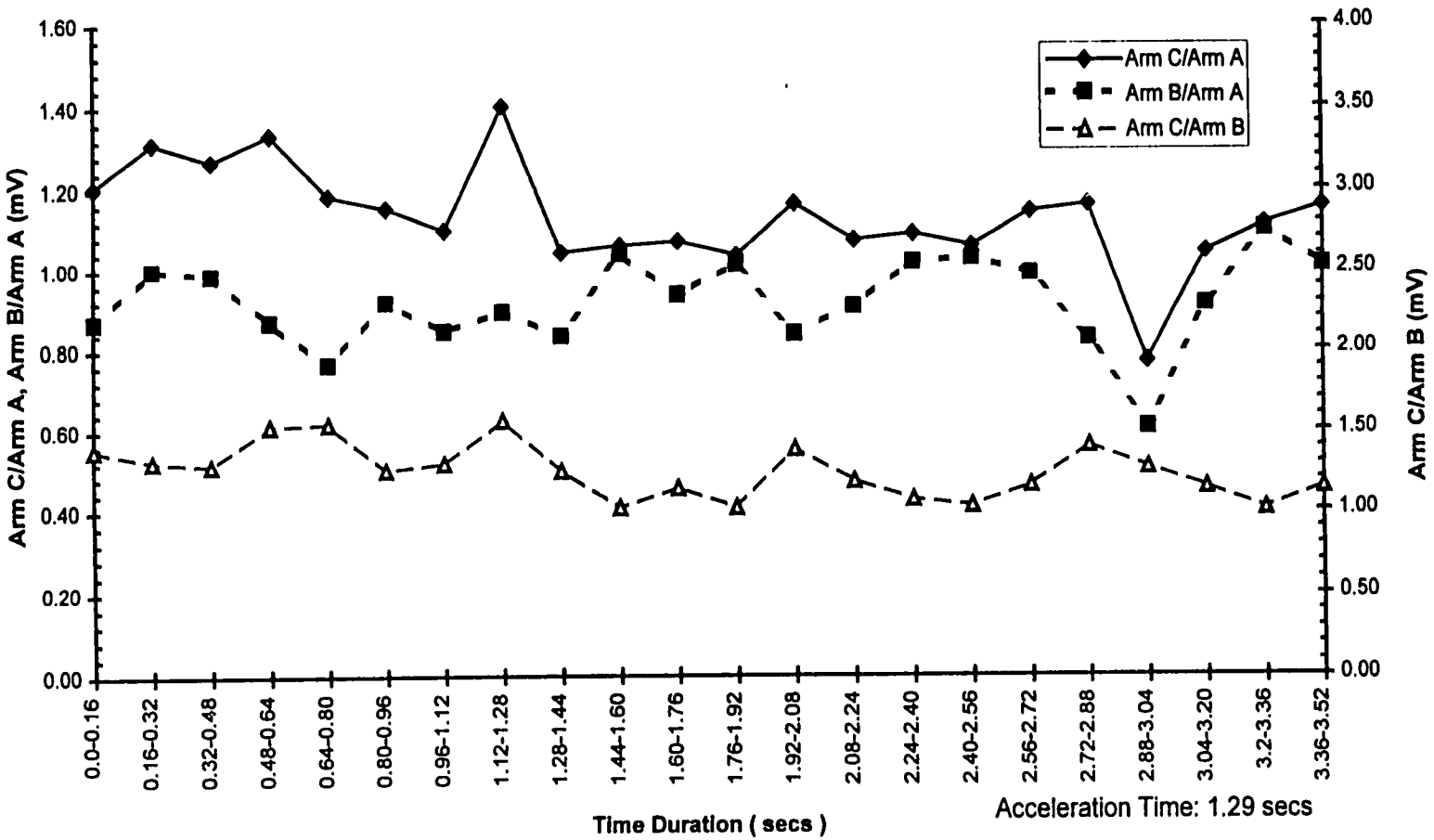

g) Shaft End Play Movement, 80%V

Figure 6.45: Shaft Spider Arm Radial Flux Coil Induced Voltage Ratio: Shaft End Play Versus Magnetic Center, DE Bearing Non-Insulated, ODE Bearing Insulated, Oil Ring Lubrication.

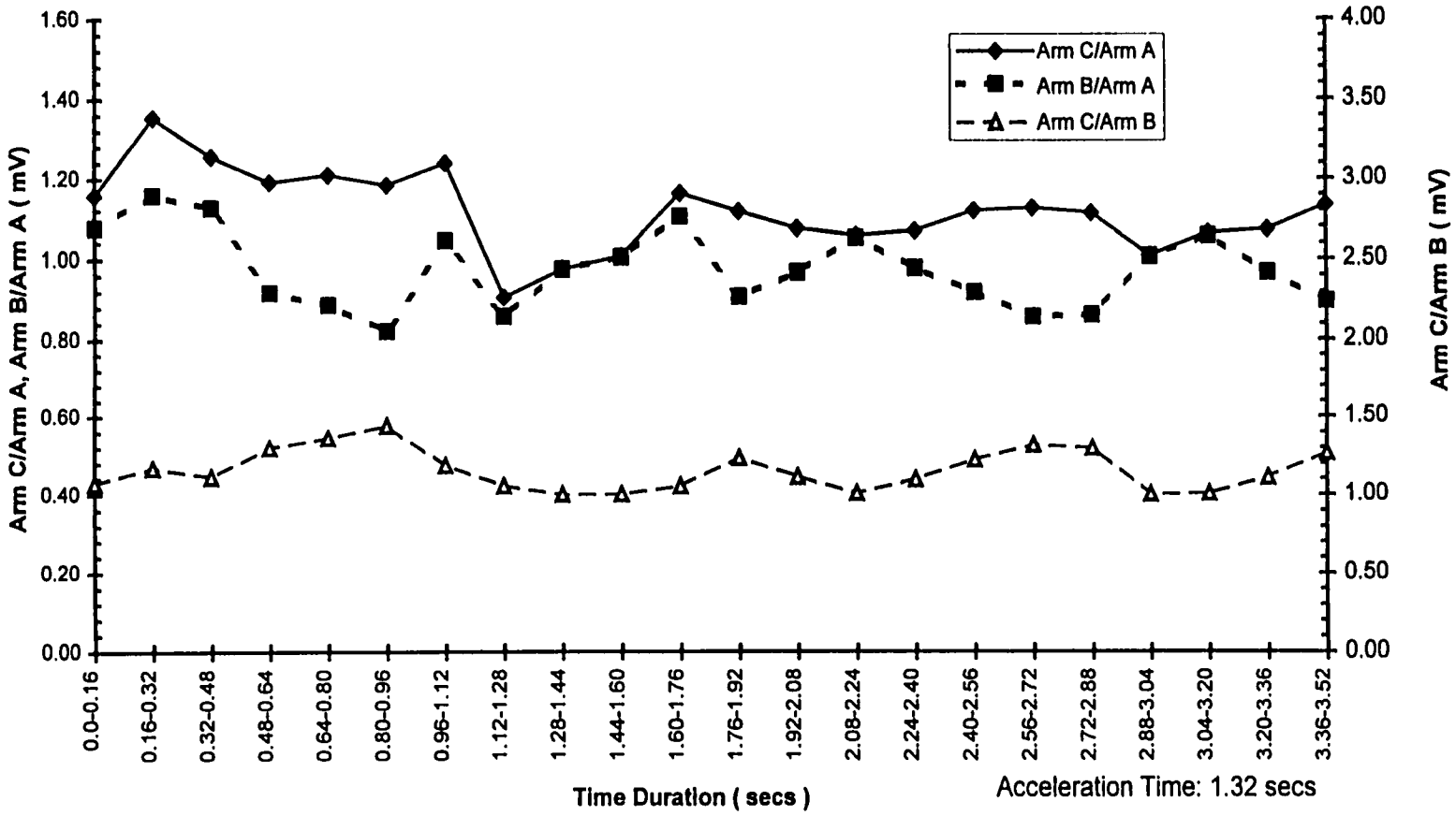

h) Magnetic Center, 80%V

Figure 6.45: Shaft Spider Arm Radial Flux Coil Induced Voltage Ratio: Shaft End Play Versus Magnetic Centre, DE Bearing Non-Insulated, ODE Bearing Insulated, Oil Ring Lubrication.

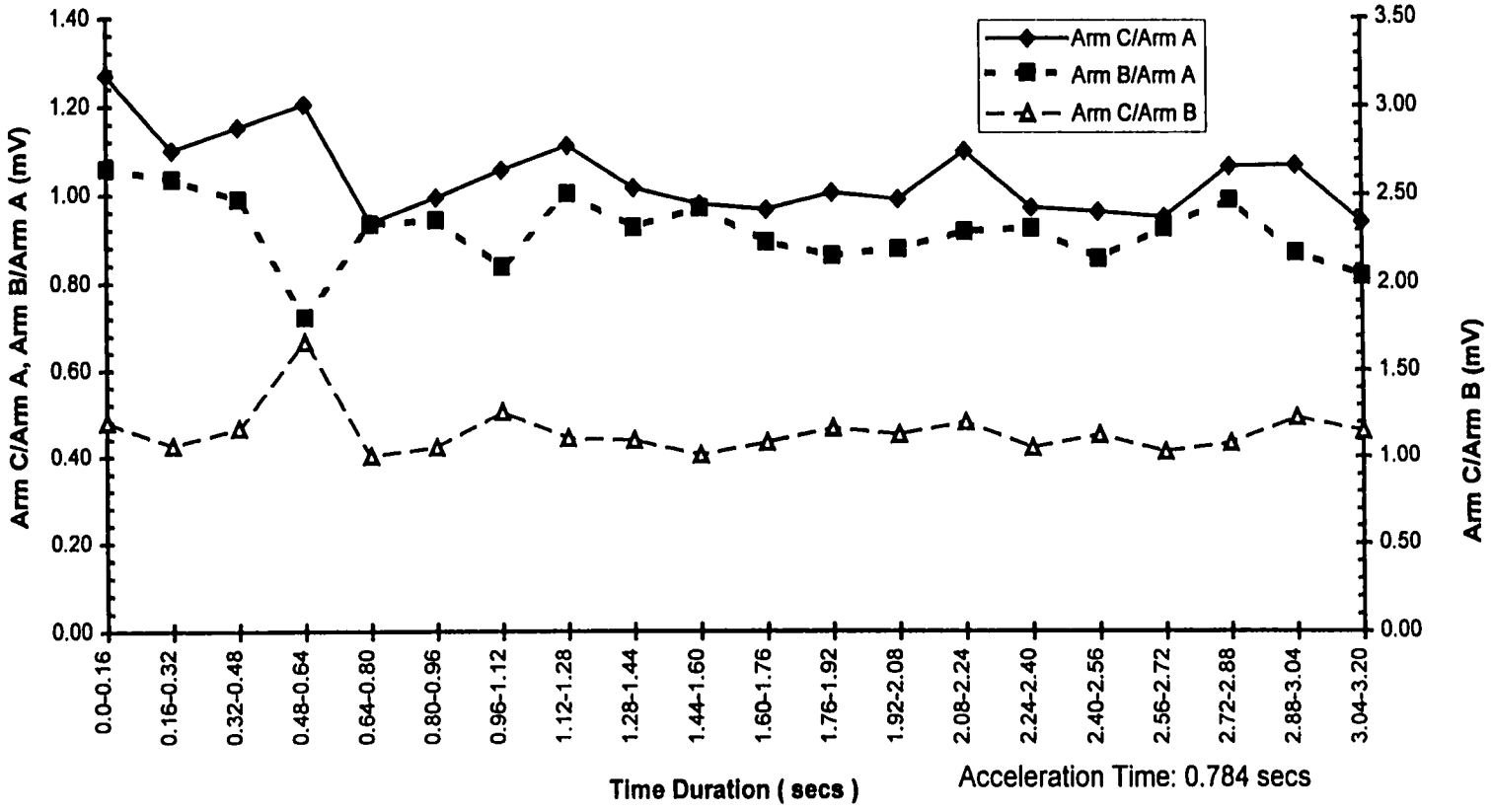

i) Shaft End Play Movement, 100%V

Figure 6.45: Shaft Spider Arm Radial Flux Coil Induced VoltageRatio: Shaft End Play Versus Magnetic Center, DE Bearing Non-Insulated, ODE Bearing Insulated, Oil Ring Lubrication.

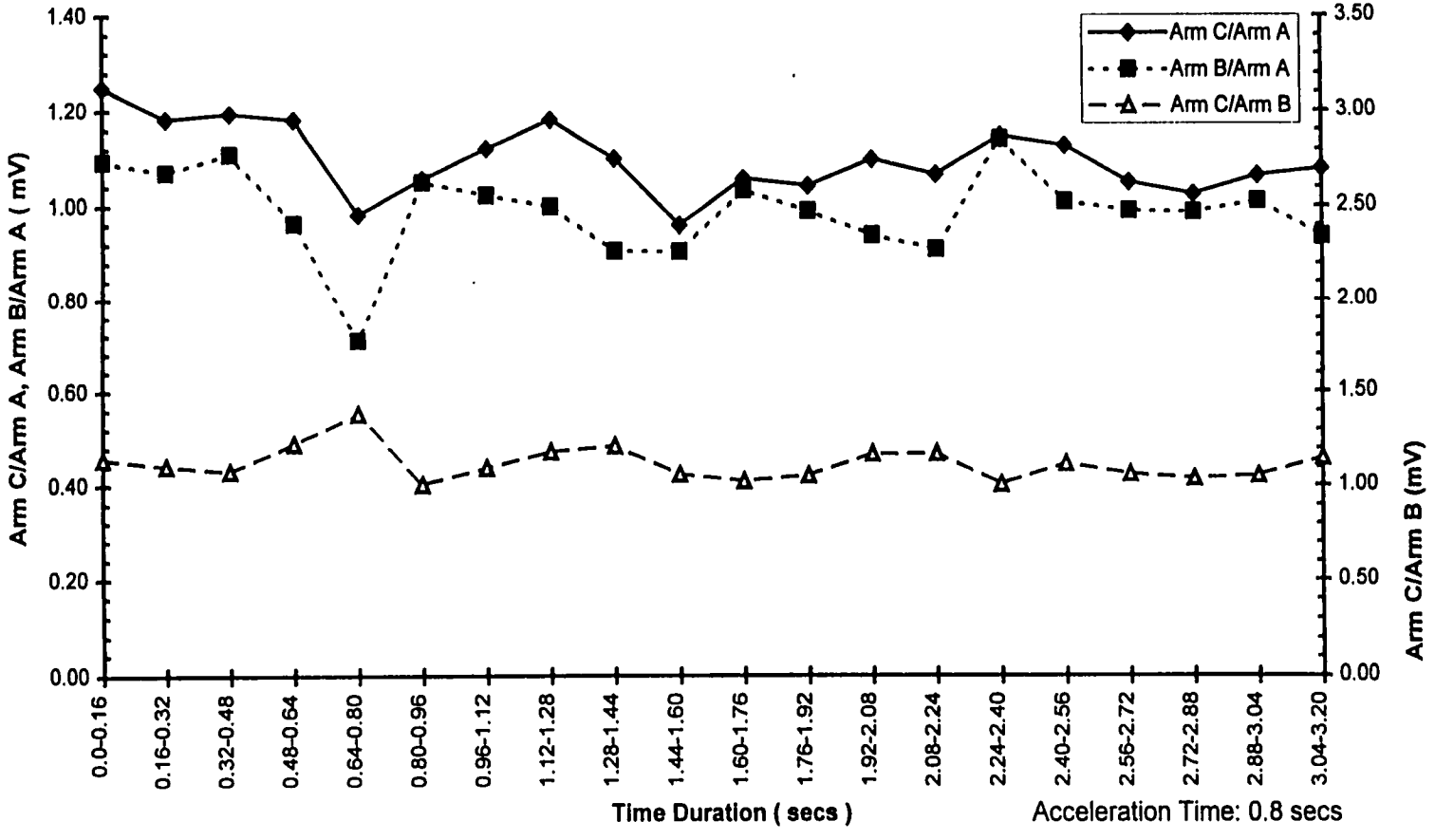

j) Magnetic Center, 100%V

Figure 6.45: Shaft Spider Arm Radial Flux Coil Induced Voltage Ratio: Shaft End Play Versus Magnetic Center, DE Bearing Non-Insulated, ODE Bearing Insulated, Oil Ring Lubrication.

At 80%V and 100%V, the dc motor is incapable of minimizing the effect of radial unbalanced magnetic pull. Hence, the difference between induced voltages of the flux coils on Arm B and Arm C is now larger. The differences at steady state conditions in both cases are approximately the same as those at 20%V to 60%V. The average difference is 20%, attesting to the presence of circulating flux around the shaft.

Frame fluxes at the opposite drive end of the machine were measured. Complete circuit rings carrying current and encircling the shaft are located at the opposite drive end of the machine. The flux at the bottom right of the frame is measured to be greater than the flux at the top left of the frame as shown in Figures 6.46 (a) and (b). There is apparently a net flux at the opposite drive end frame of the machine. This finding leads us to conclude that there could be a net flux encircling the shaft. The components of the fluxes at 120 Hz, 180 Hz, 240 Hz, 300 Hz and 420 Hz, though of small magnitude, are observed as shown in Figures 6.46 (d) - (i). The flux is mainly line frequency component. During steady state no-load conditions, spectral analyses of the frame fluxes at 20%V as shown in Figures 6.46 (j) and (k) indicate the main component is at 60 Hz with smaller components at 30 Hz, 120 Hz, 180 Hz and 300 Hz. Small flux components at modulated frequency of 180 Hz plus multiples of rotor running frequency of 15 Hz were also observed. The spectral analyses of the frame fluxes at 80%V and 100%V as shown in Figures 6.46 (l) - (o) indicate that the main component is at 60 Hz with smaller components at 180 Hz and 240 Hz. The spectral analyses of the frame fluxes at locked rotor condition as shown in Figures 6.46 (p) - (u) indicate components at 60 Hz, 120 Hz, 180 Hz, 240 Hz, 300 Hz and 420 Hz, similar to the spectral analyses during the transient condition.

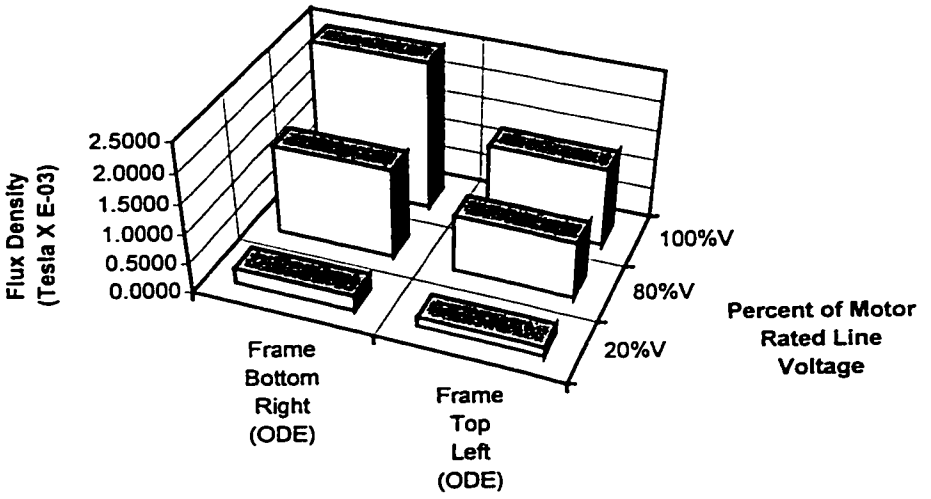

a) Frame Flux Density , Transient Condition

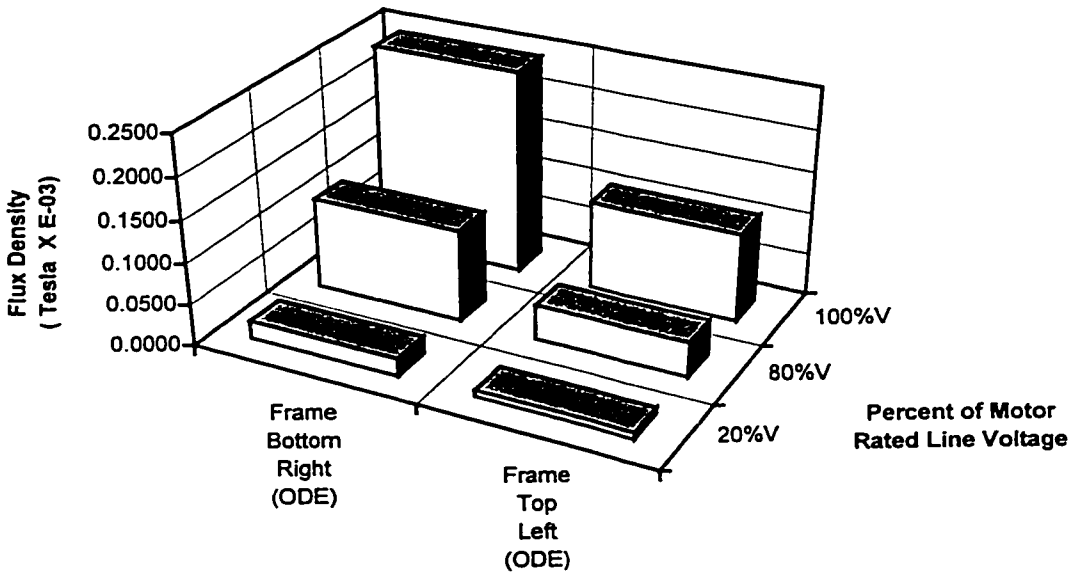

b) Frame Flux Density, Steady State No-Load Condition

Figure 6.46: Frame Flux Density, 60 Hz Component, DE Bearing Non-Insulated, ODE Bearing Insulated, Oil Ring Lubrication.

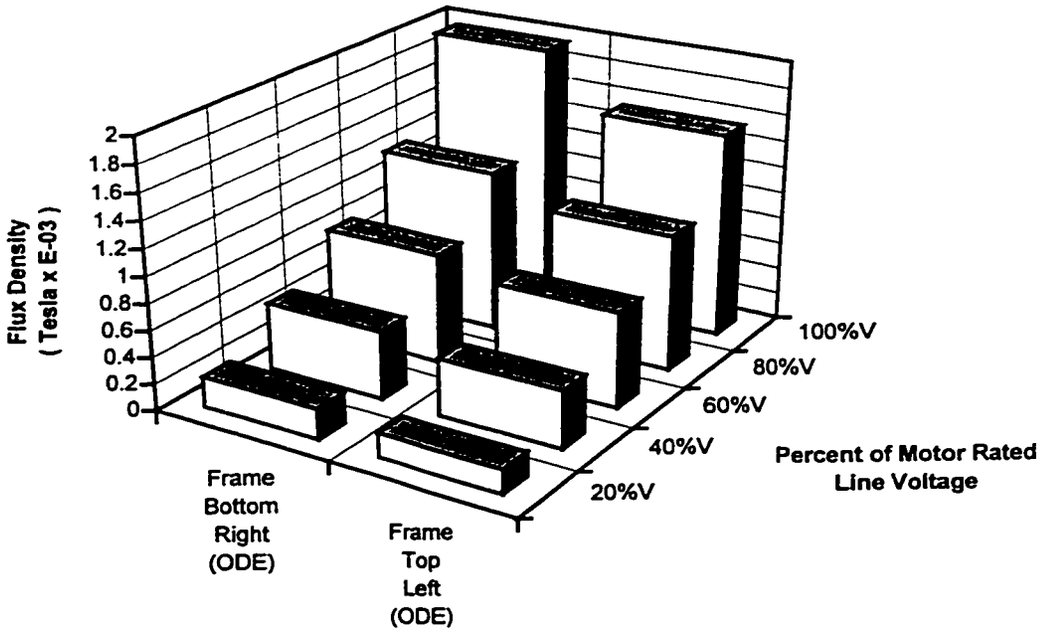

c) Frame Flux Density, Locked Rotor Condition

Figure 6.46: Frame Flux Density, 60 Hz Component, DE Bearing Non-Insulated, ODE Bearing Insulated, Oil Ring Lubrication.

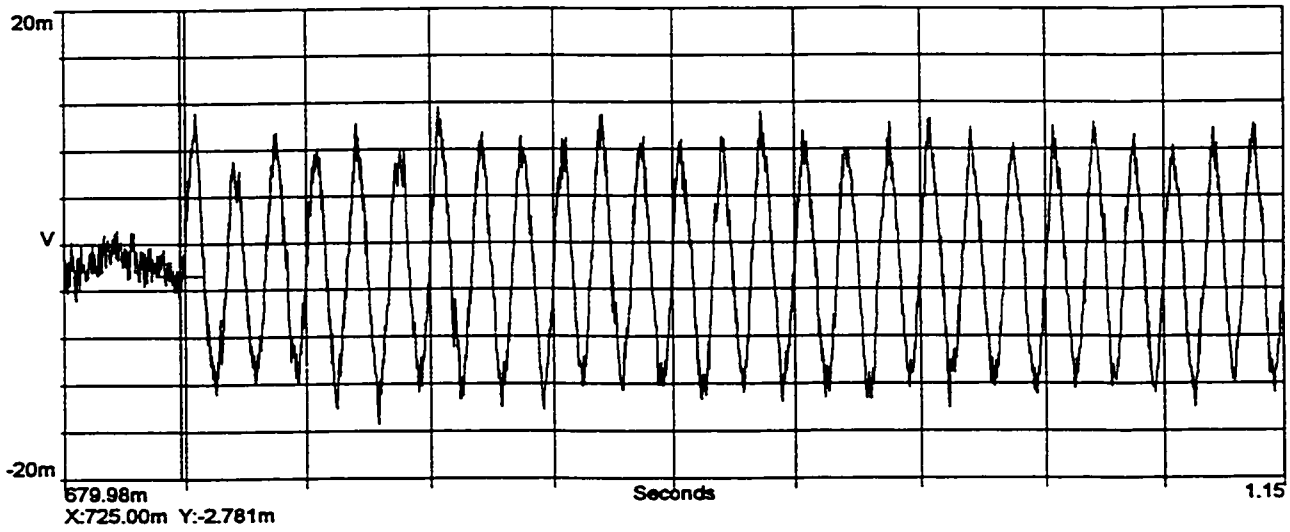

i) Frame Flux Coil Induced Voltage Waveform

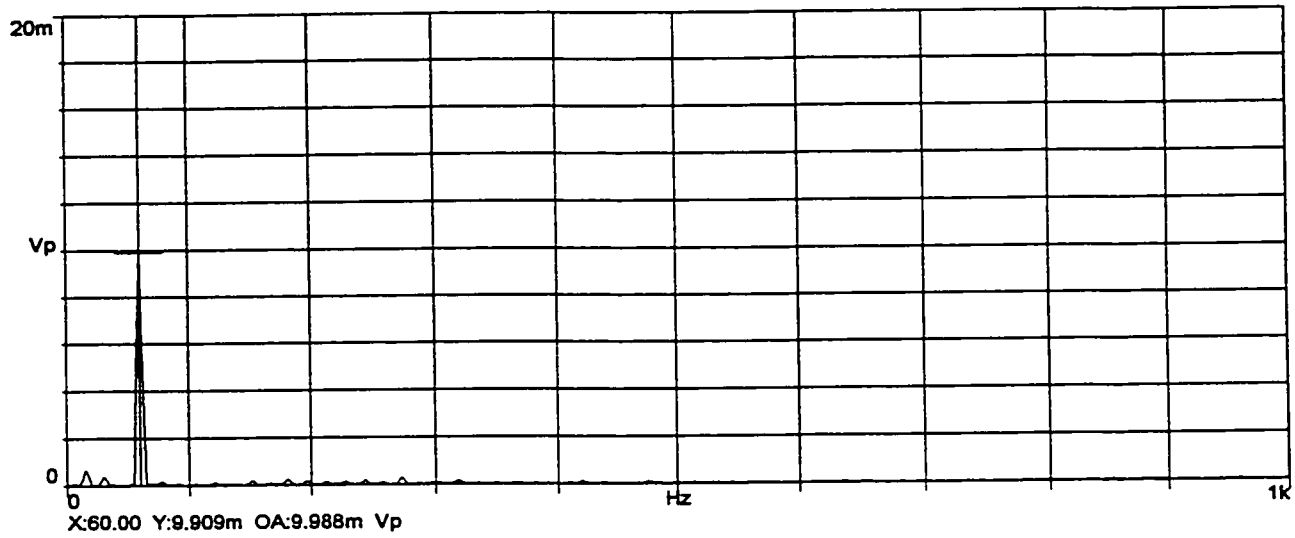

ii) Spectrum Plot

d) Frame Top Left, ODE, 20%V, Transient Condition.

Figure 6.46: Frame Flux Density, 60 Hz Component, DE Bearing Non-Insulated, ODE Bearing Insulated, Oil Ring Lubrication.

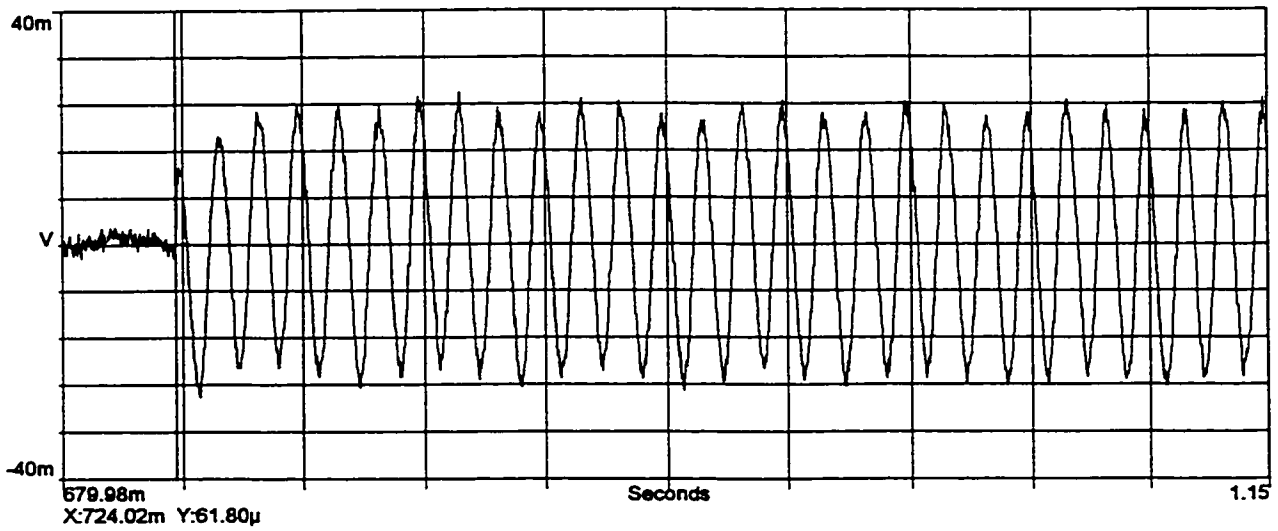

i) Frame Flux Coil Induced Voltage Waveform

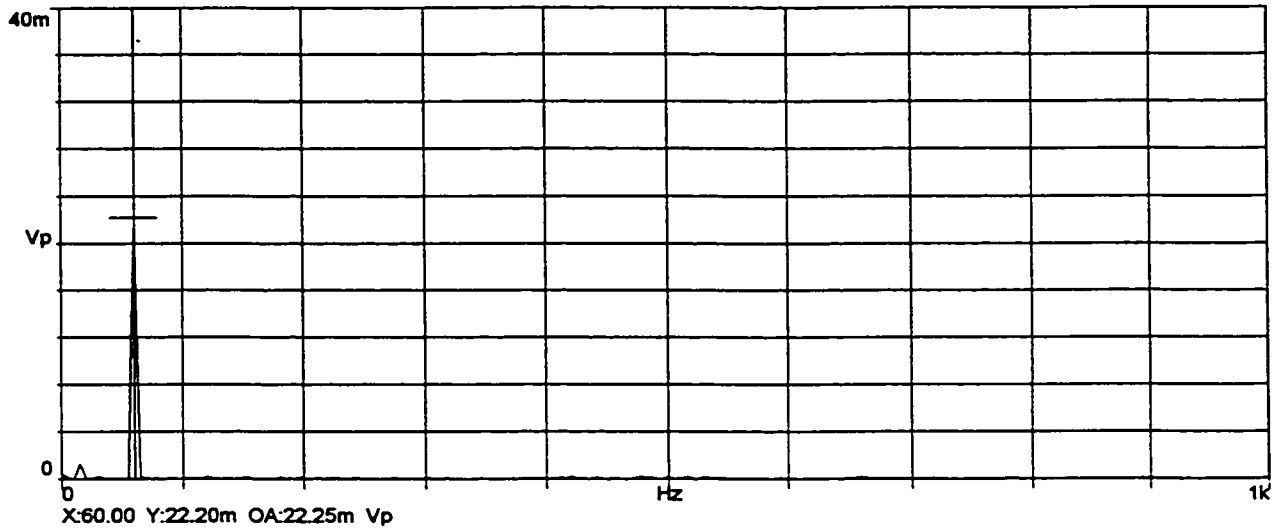

ii) Spectrum Plot

e) Frame Bottom Right, ODE, 20%V, Transient Condition.

Figure 6.46: Frame Flux Density, 60 Hz Component, DE Bearing Non-Insulated, ODE Bearing Insulated, Oil Ring Lubrication.

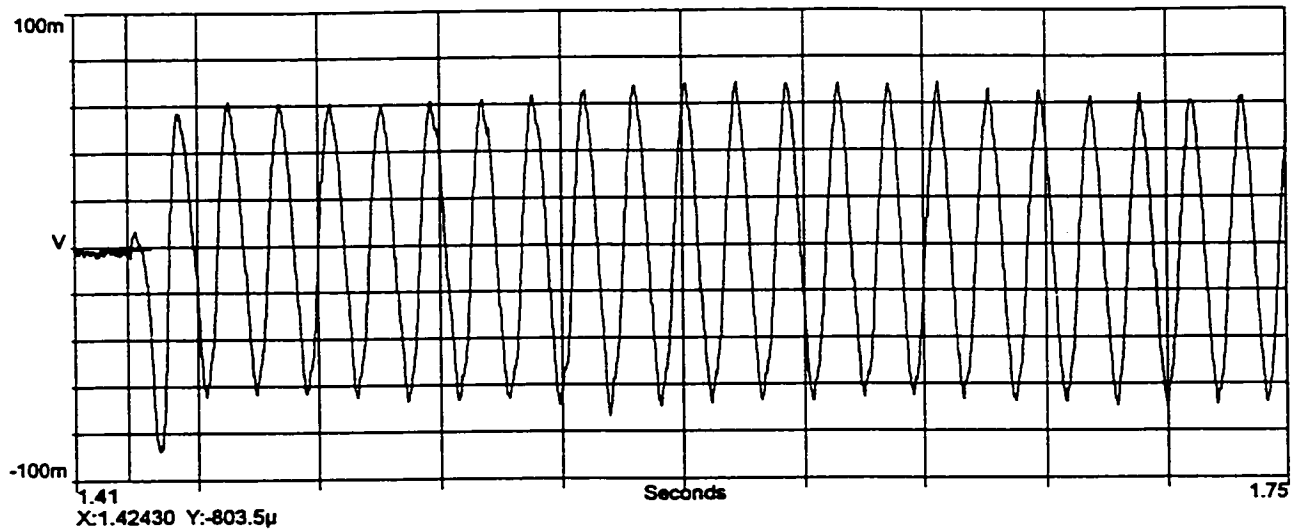

i) Frame Flux Coil Induced Voltage Waveform

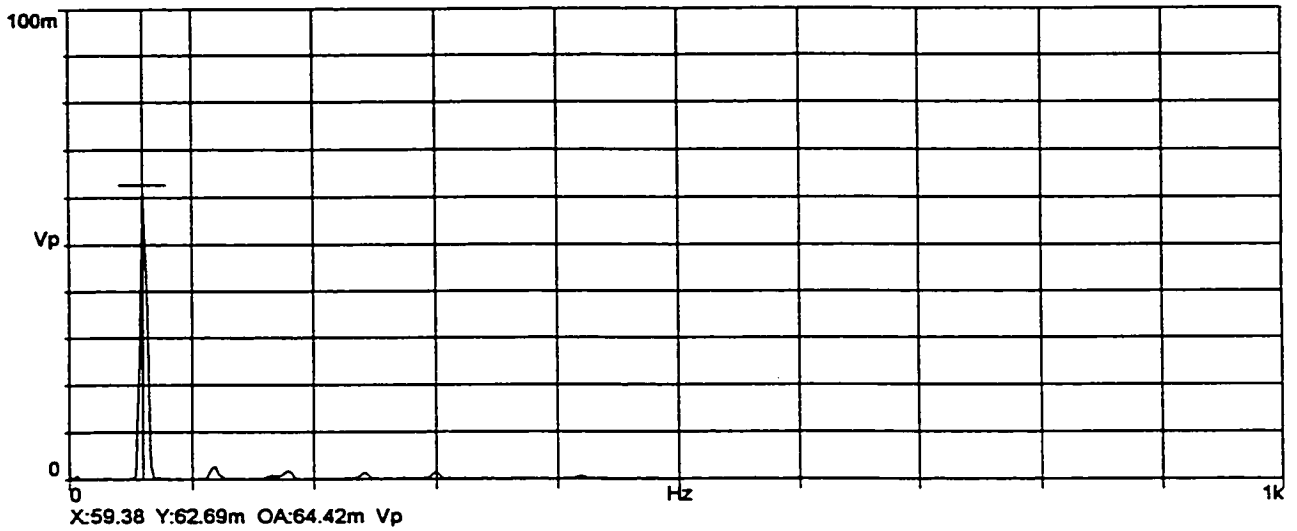

ii) Spectrum Plot

f) Frame Top Left, ODE, 80%V, Transient Condition.

Figure 6.46: Frame Flux Density, 60 Hz Component, DE Bearing Non-Insulated, ODE Bearing Insulated, Oil Ring Lubrication.

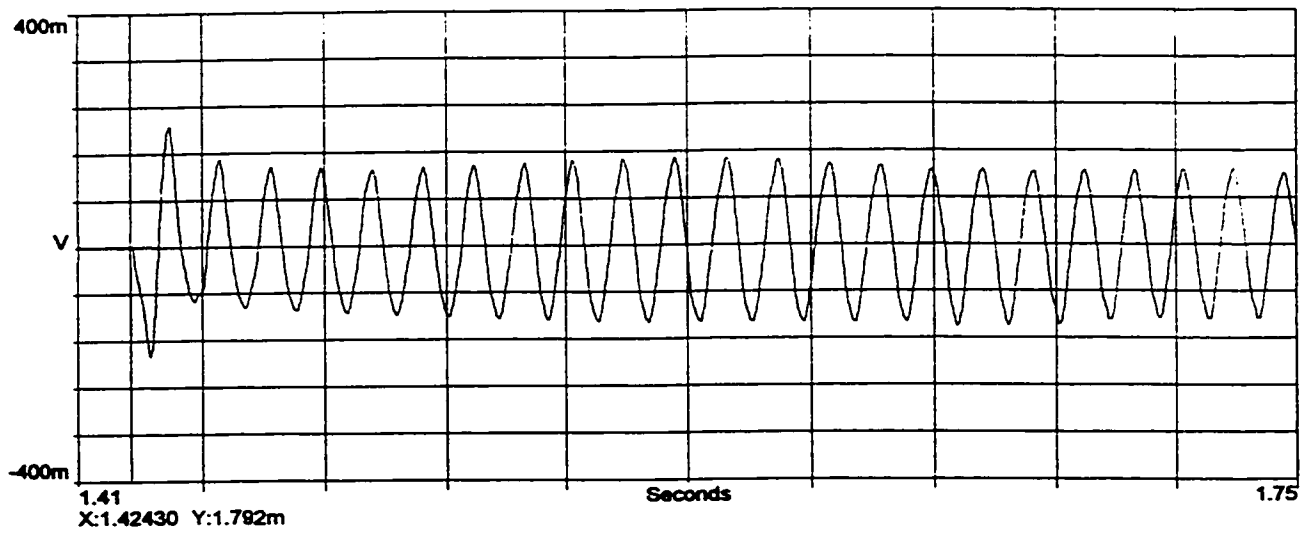

i) Frame Flux Coil Induced Voltage Waveform

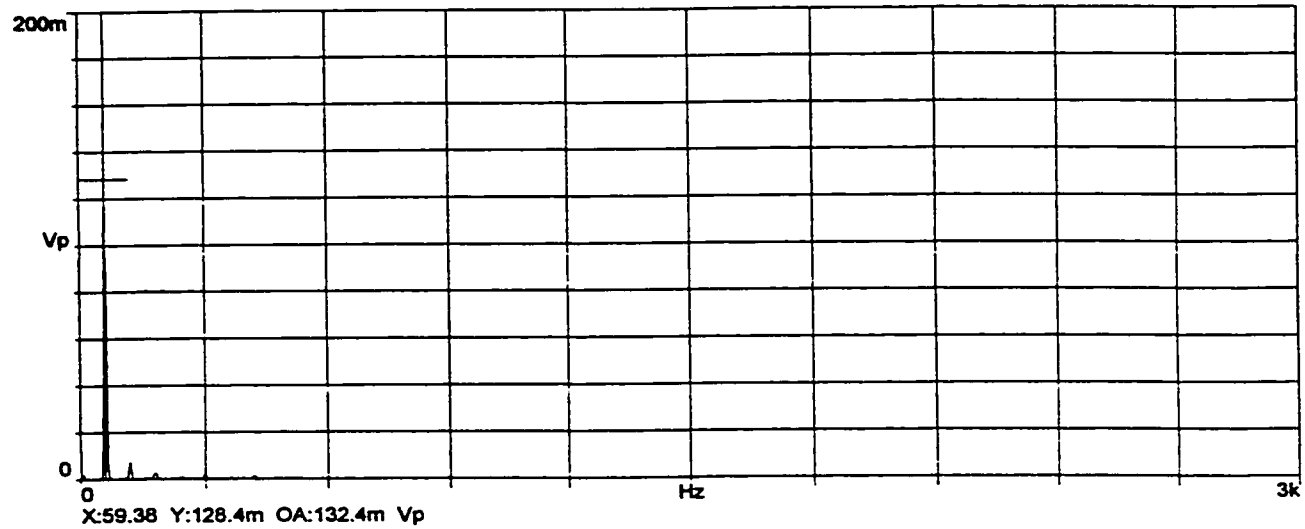

ii) Spectrum Plot

g) Frame Bottom Right, ODE, 80%V, Transient Condition.

Figure 6.46: Frame Flux Density, 60 Hz Component, DE Bearing Non-Insulated, ODE Bearing Insulated, Oil Ring Lubrication.

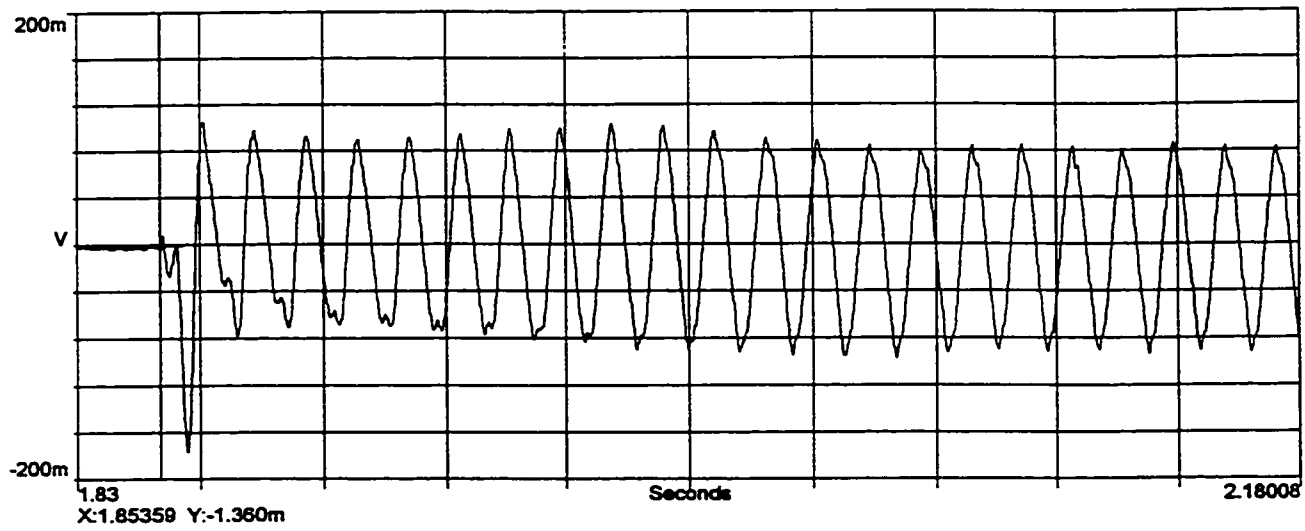

i) Frame Flux Coil Induced Voltage Waveform

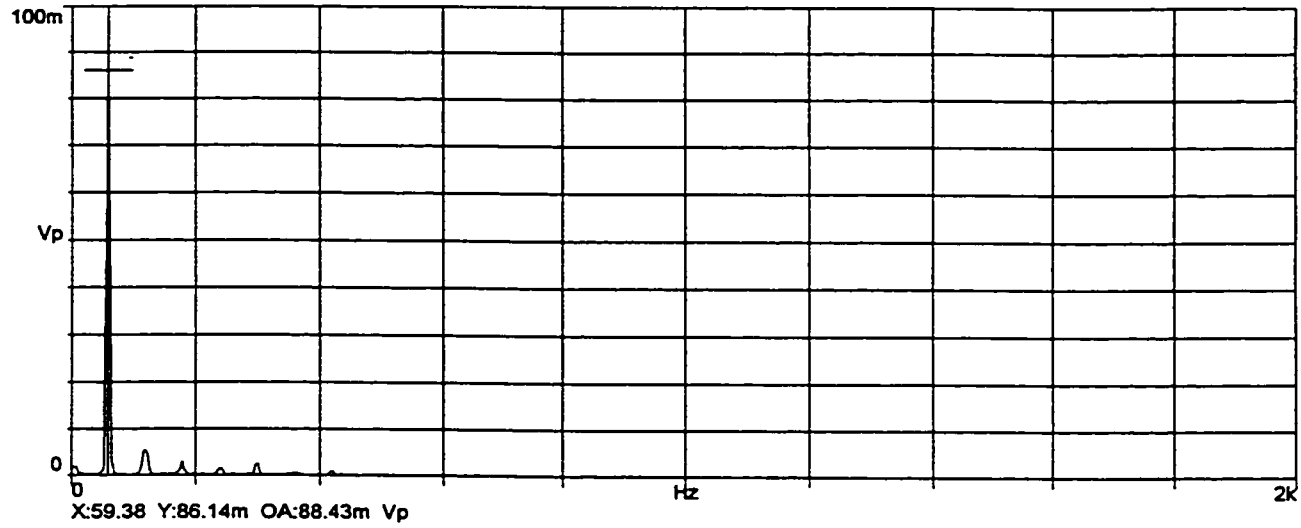

ii) Spectrum Plot

h) Frame Top Left, ODE, 100%V, Transient Condition.

Figure 6.46: Frame Flux Density, 60 Hz Component, DE Bearing Non-Insulated, ODE Bearing Insulated, Oil Ring Lubrication.

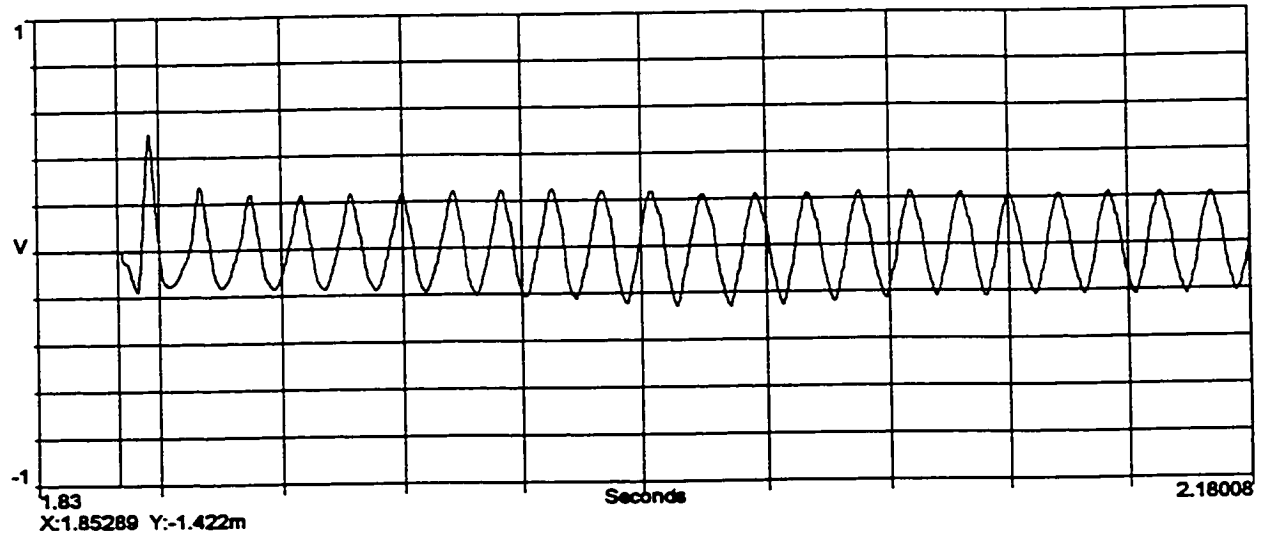

i) Frame Flux Coil Induced Voltage Waveform

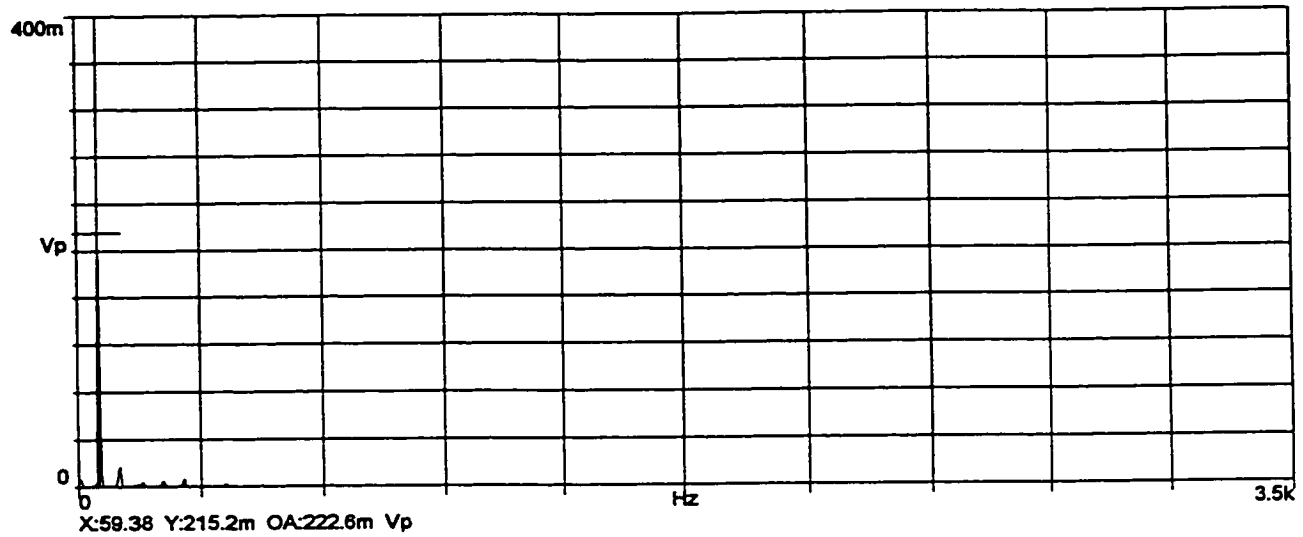

ii) Spectrum Plot

i) Frame Bottom Right, ODE, 100%V, Transient Condition.

Figure 6.46: Frame Flux Density, 60 Hz Component, DE Bearing Non-Insulated, ODE Bearing Insulated, Oil Ring Lubrication.

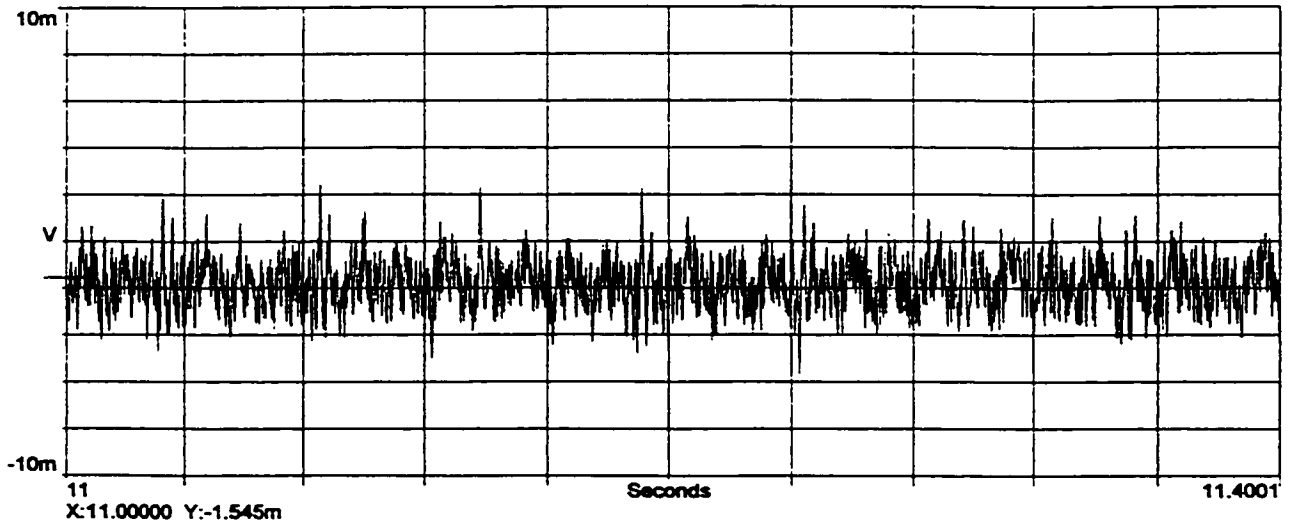

i) Frame Flux Coil Induced Voltage Waveform

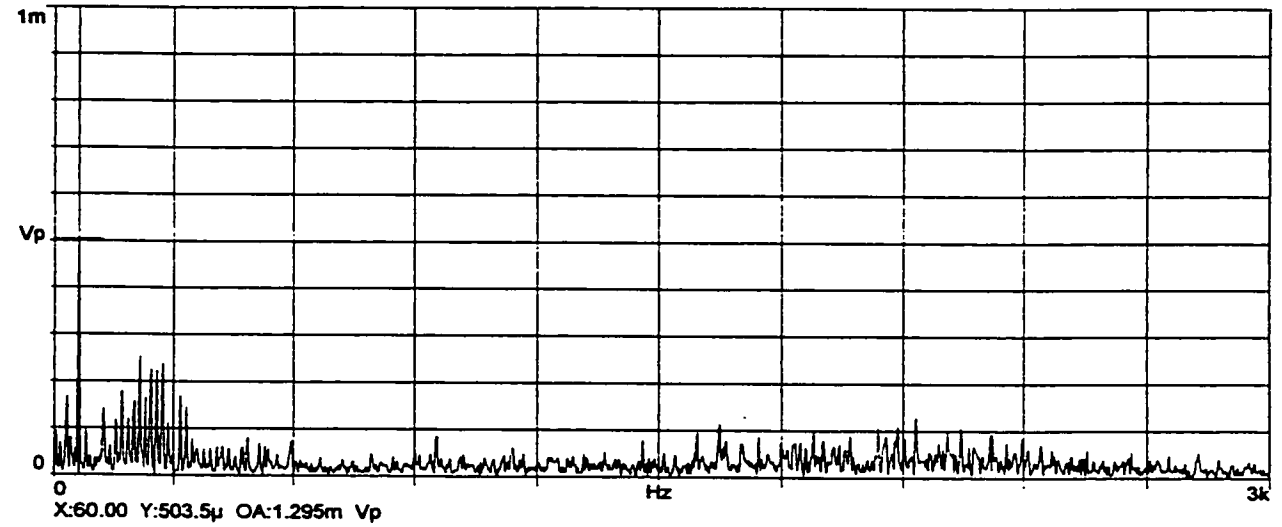

ii) Spectrum Plot

j) Frame Top Left, ODE, 20%V, Steady State No-Load Condition.

Figure 6.46: Frame Flux Density, 60 Hz Component, DE Bearing Non-Insulated, ODE Bearing Insulated, Oil Ring Lubrication.

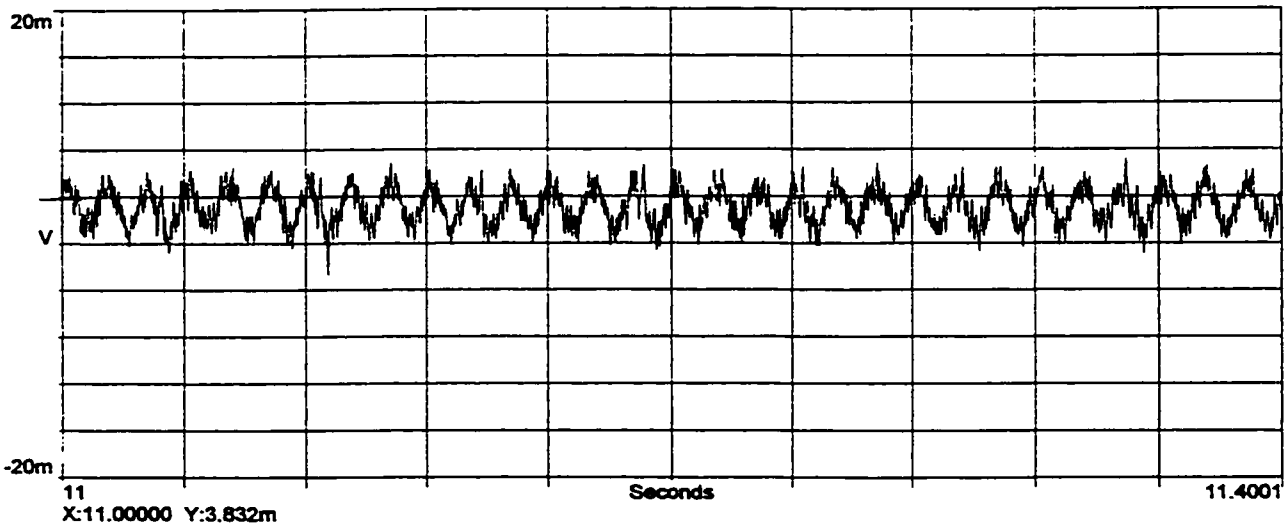

i) Frame Flux Coil Induced Voltage Waveform

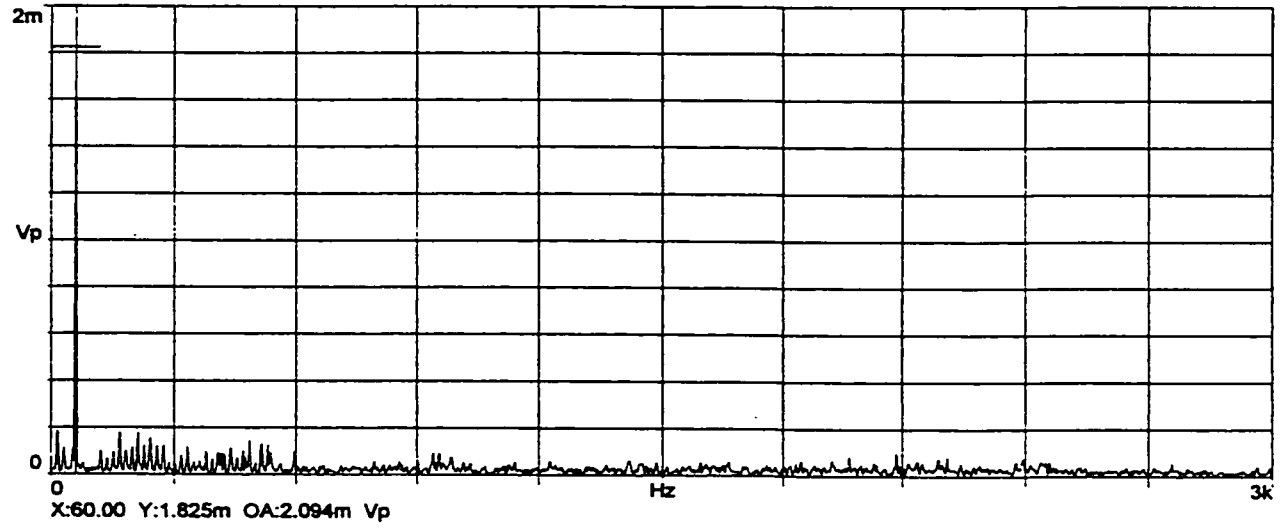

ii) Spectrum Plot

k) Frame Bottom Right, ODE, 20%V, Steady State No-Load Condition.

Figure 6.46: Frame Flux Density, 60 Hz Component, DE Bearing Non-Insulated, ODE Bearing Insulated, Oil Ring Lubrication.

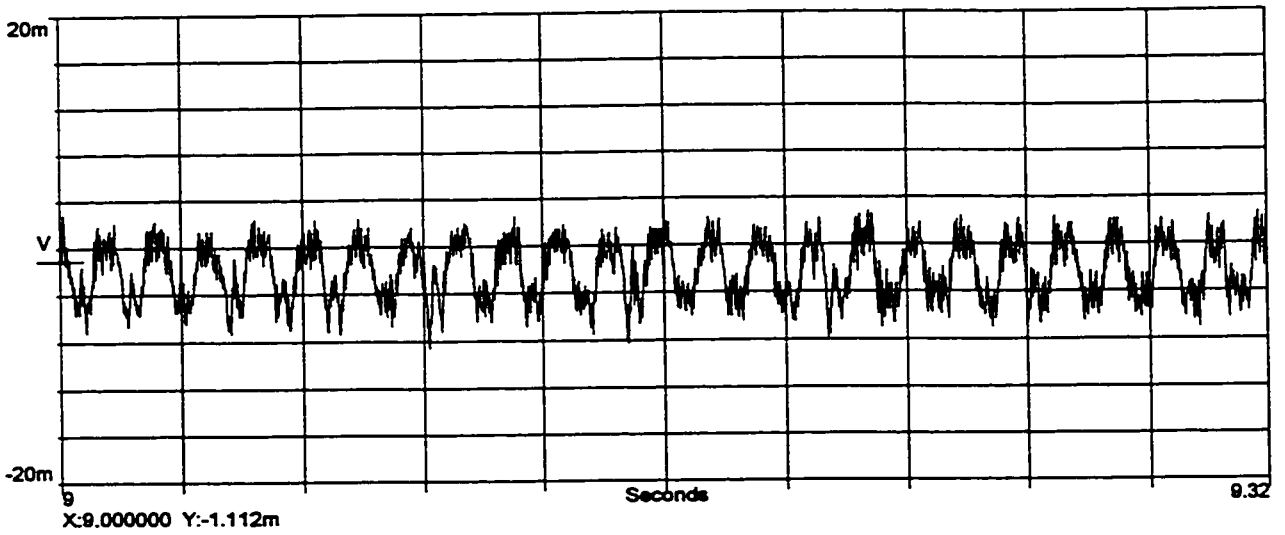

i) Frame Flux Coil Induced Voltage Waveform

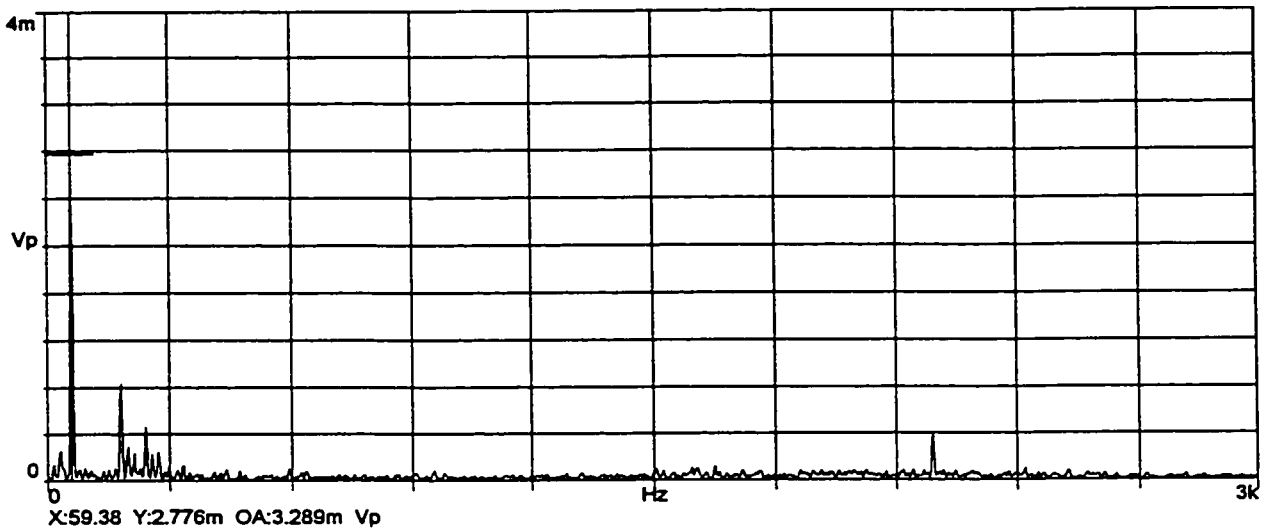

ii) Spectrum Plot

l) Frame Top Left, ODE, 80%V, Steady State No-Load Condition.

Figure 6.46: Frame Flux Density, 60 Hz Component, DE Bearing Non-Insulated, ODE Bearing Insulated, Oil Ring Lubrication.

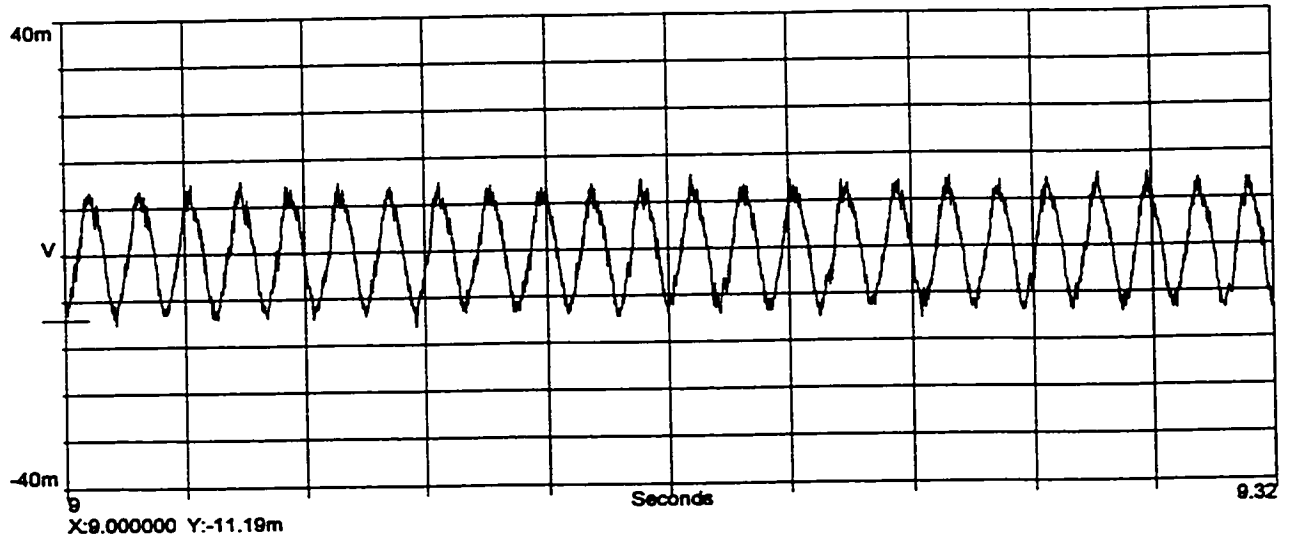

i) Frame Flux Coil Induced Voltage Waveform

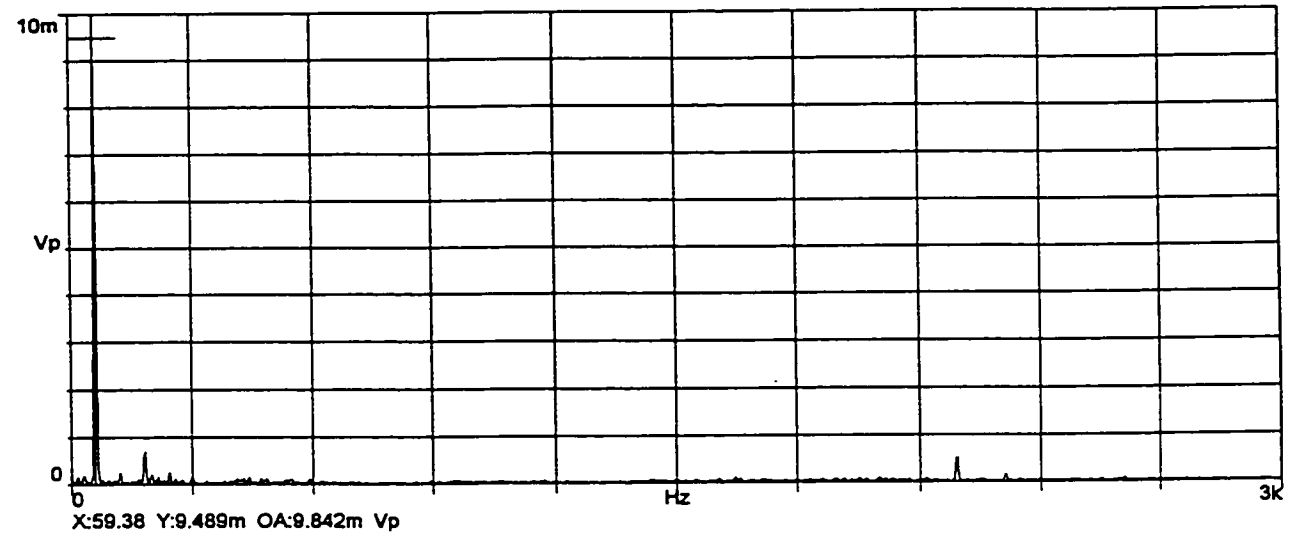

ii) Spectrum Plot

m) Frame Bottom Right, ODE, 80%V, Steady State No-Load Condition.

Figure 6.46: Frame Flux Density, 60 Hz Component, DE Bearing Non-Insulated, ODE Bearing Insulated, Oil Ring Lubrication.

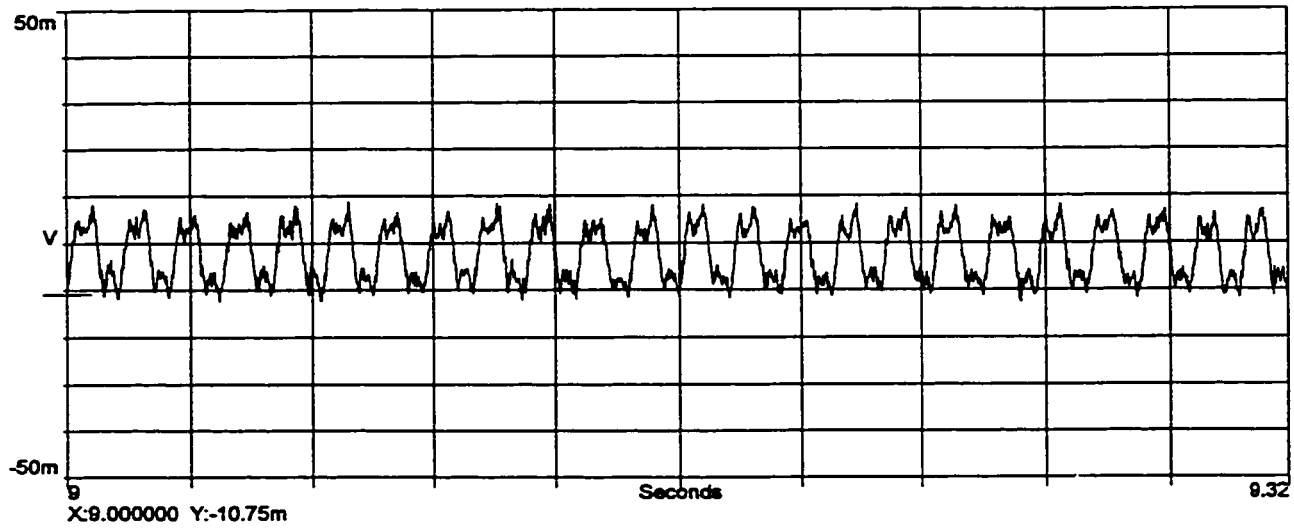

i) Frame Flux Coil Induced Voltage Waveform

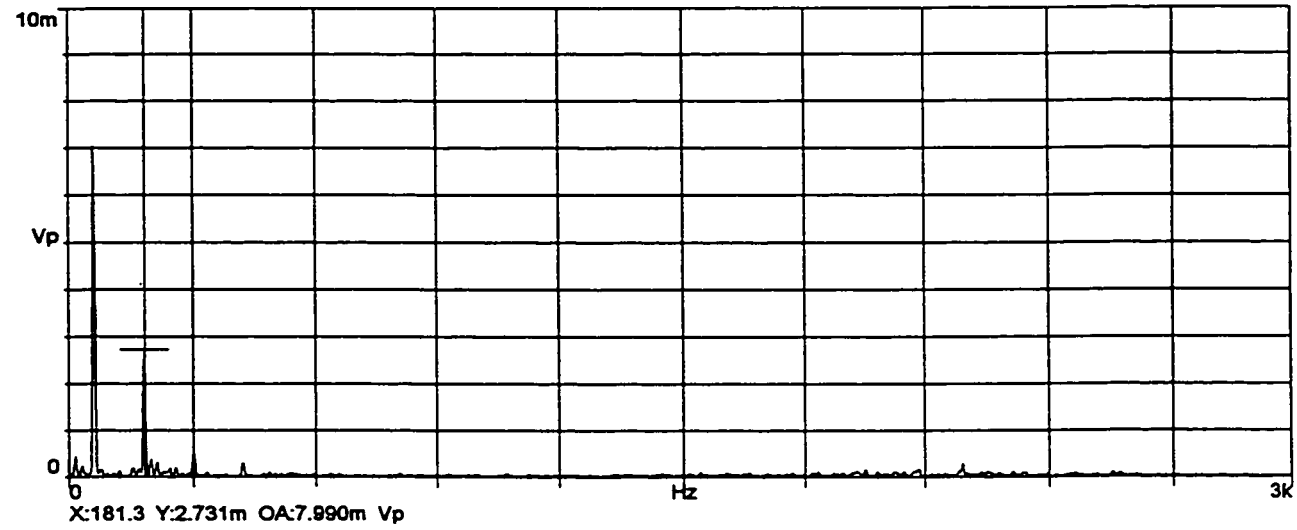

ii) Spectrum Plot

n) Frame Top Left, ODE, 100%V, Steady State No-Load Condition.

Figure 6.46: Frame Flux Density, 60 Hz Component, DE Bearing Non-Insulated, ODE Bearing Insulated, Oil Ring Lubrication.

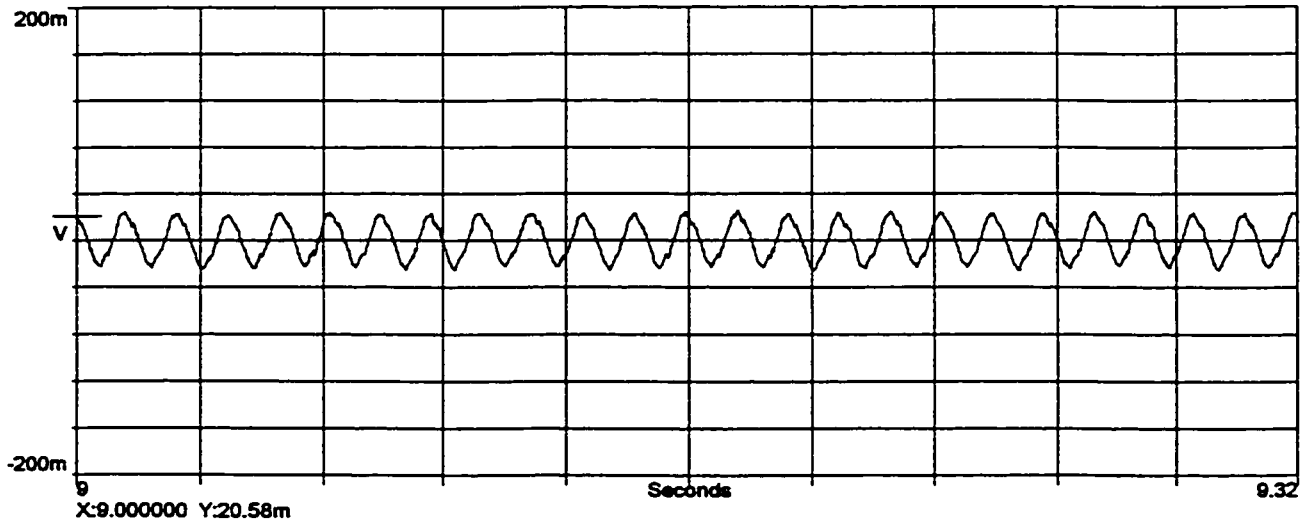

i) Frame Flux Coil Induced Voltage Waveform

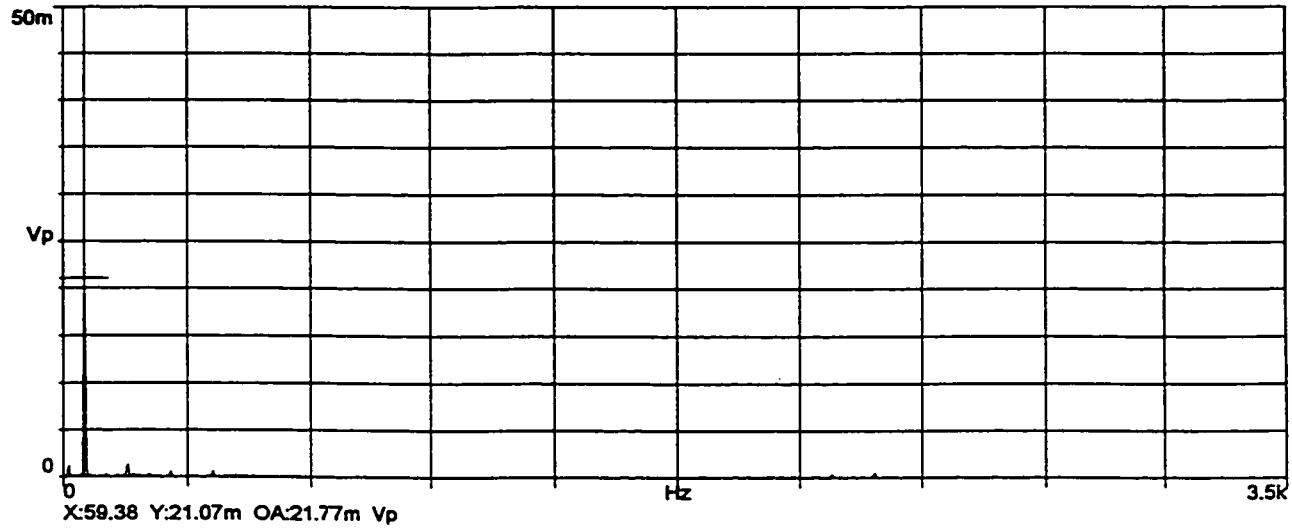

ii) Spectrum Plot

o) Frame Bottom Right, ODE, 100%V, Steady State No-Load Condition.

Figure 6.46: Frame Flux Density, 60 Hz Component, DE Bearing Non-Insulated, ODE Bearing Insulated, Oil Ring Lubrication.

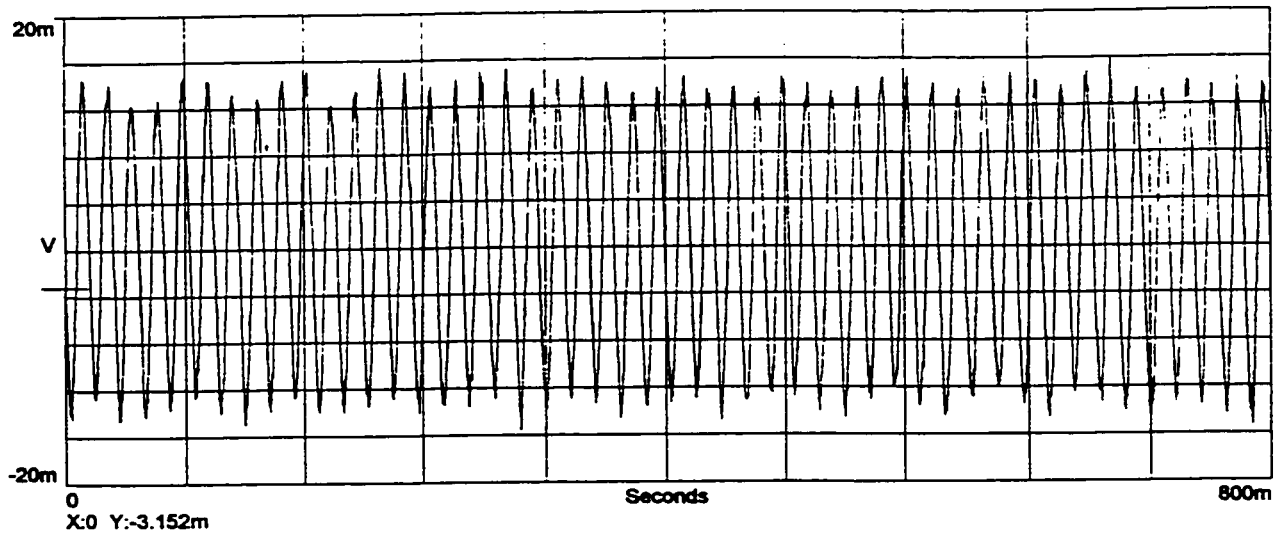

i) Frame Flux Coil Induced Voltage Waveform

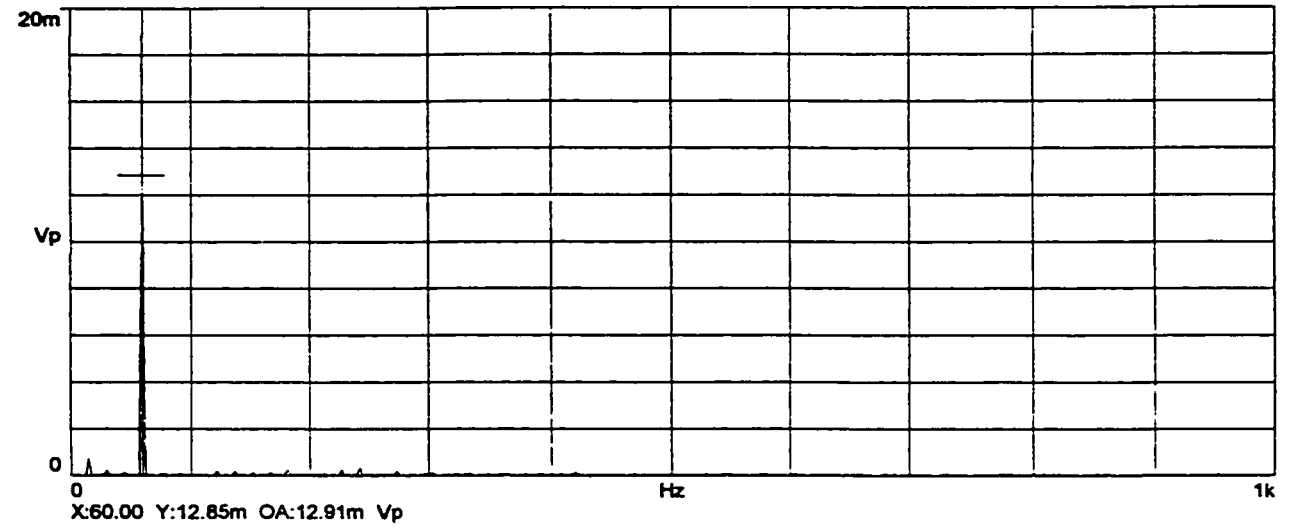

ii) Spectrum Plot

p) Frame Top Left, ODE, 20%V, Locked Rotor Condition.

Figure 6.46: Frame Flux Density, 60 Hz Component, DE Bearing Non-Insulated, ODE Bearing Insulated, Oil Ring Lubrication.

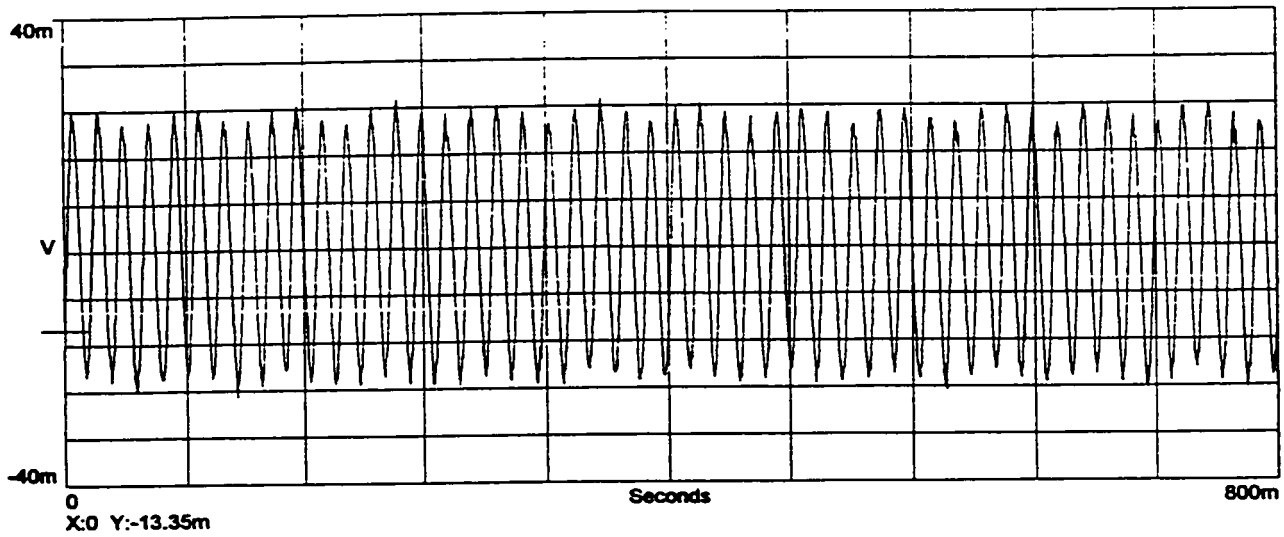

i) Frame Flux Coil Induced Voltage Waveform

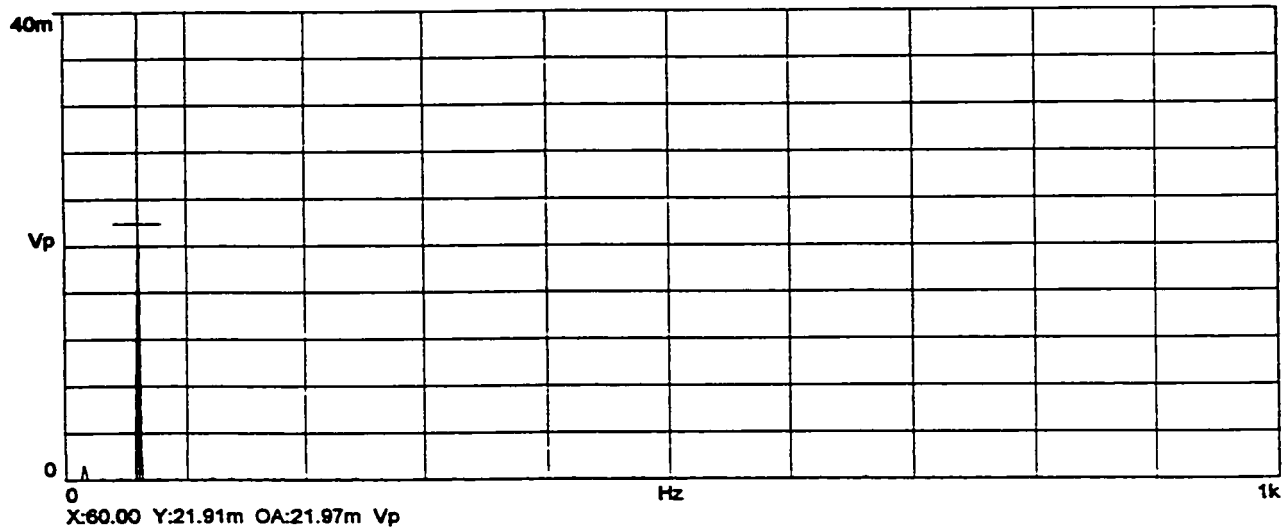

ii) Spectrum Plot

q) Frame Bottom Right, ODE, 20%V, Locked Rotor Condition.

Figure 6.46: Frame Flux Density, 60 Hz Component, DE Bearing Non-Insulated, ODE Bearing Insulated, Oil Ring Lubrication.

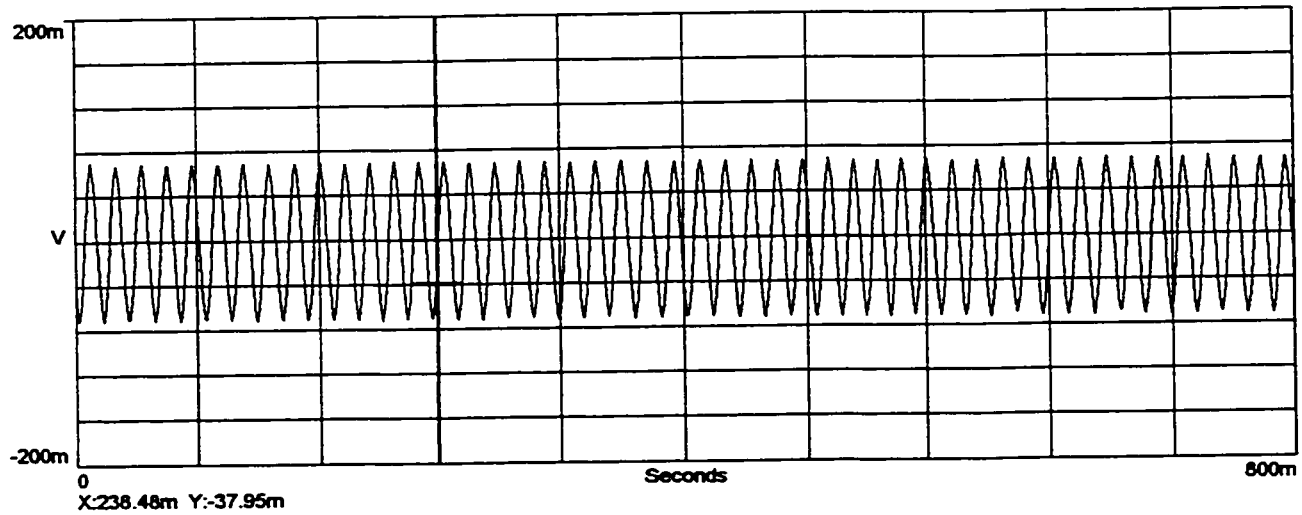

i) Frame Flux Coil Induced Voltage Waveform

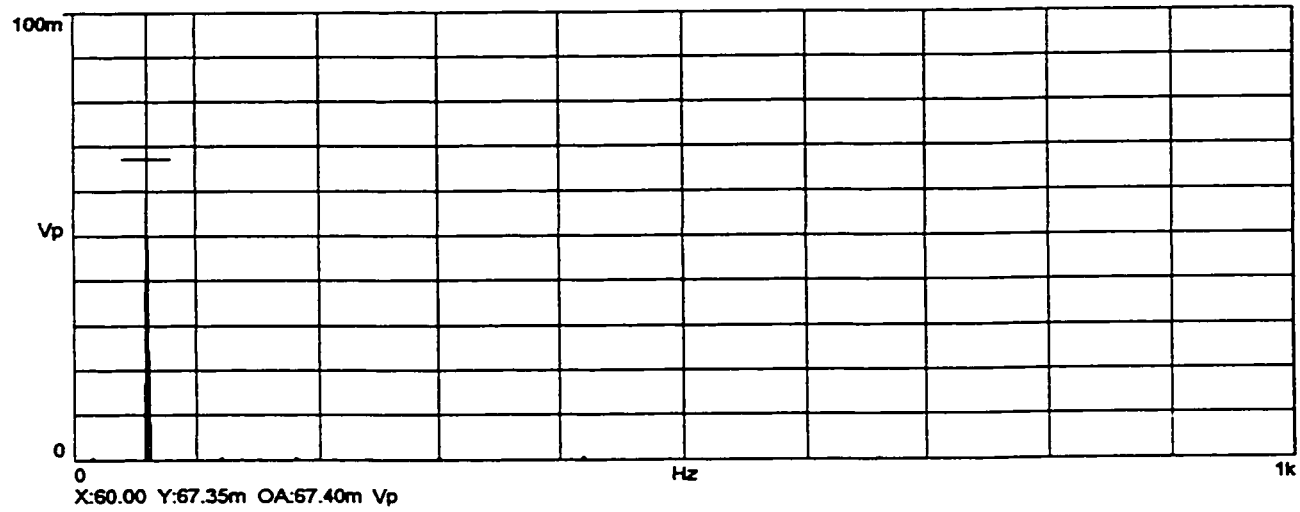

ii) Spectrum Plot

r) Frame Top Left, ODE, 80%V, Locked Rotor Condition.

Figure 6.46: Frame Flux Density, 60 Hz Component, DE Bearing Non-Insulated, ODE Bearing Insulated, Oil Ring Lubrication.

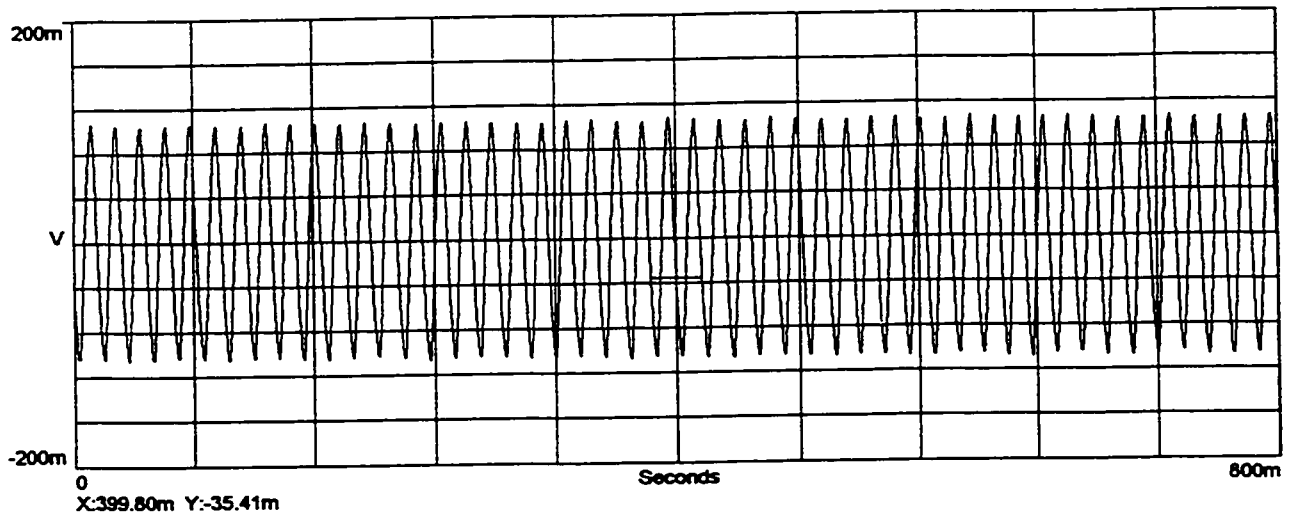

i) Frame Flux Coil Induced Voltage Waveform

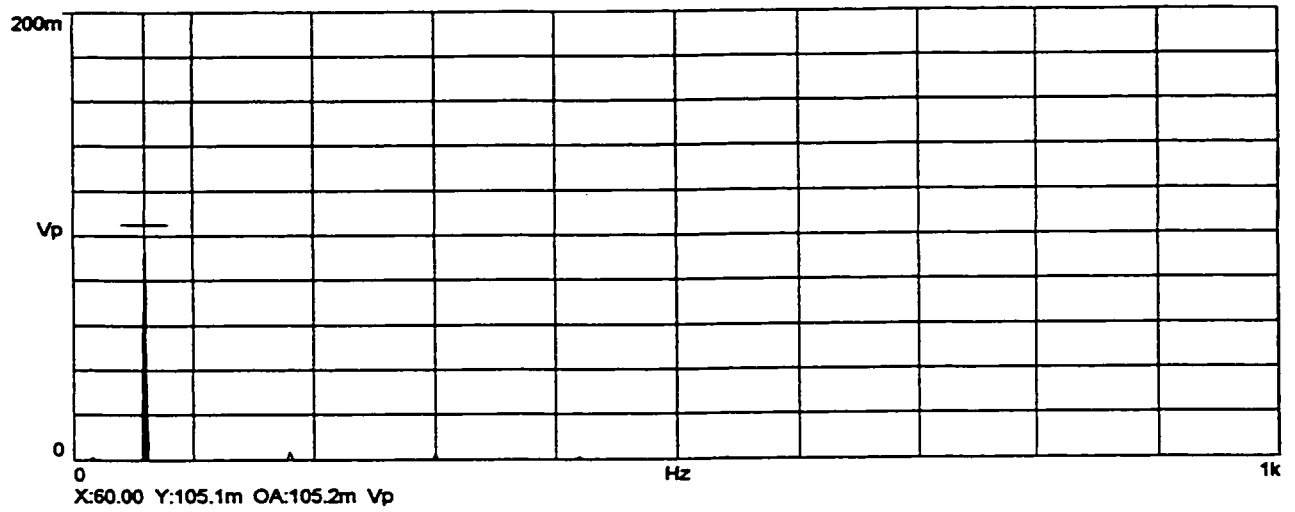

ii) Spectrum Plot

s) Frame Bottom Right, ODE, 80%V, Locked Rotor Condition.

Figure 6.46: Frame Flux Density, 60 Hz Component, DE Bearing Non-Insulated, ODE Bearing Insulated, Oil Ring Lubrication.

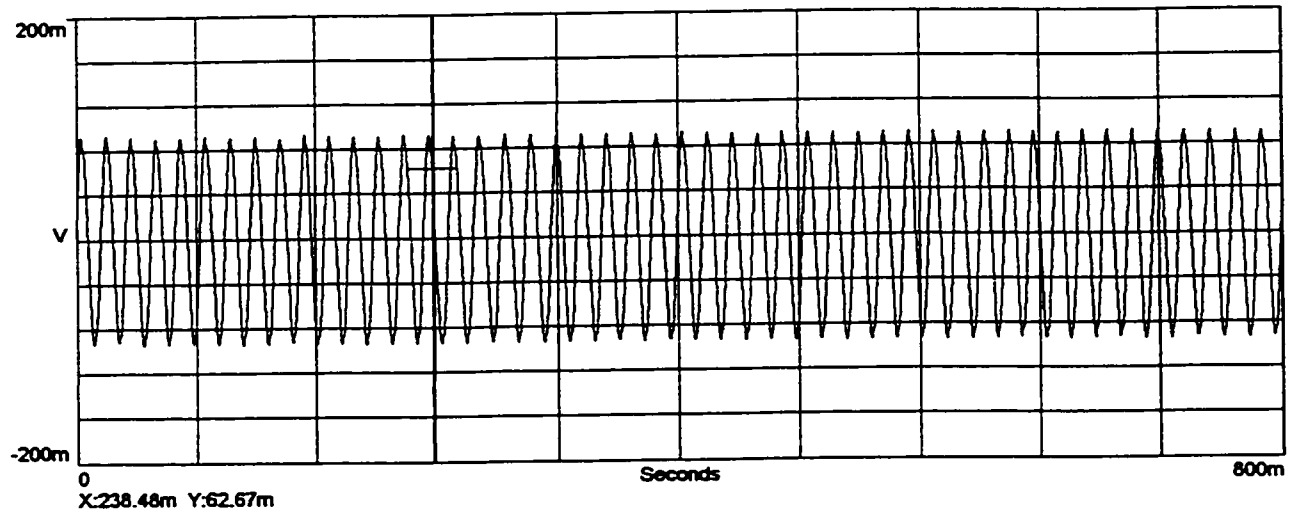

i) Frame Flux Coil Induced Voltage Waveform

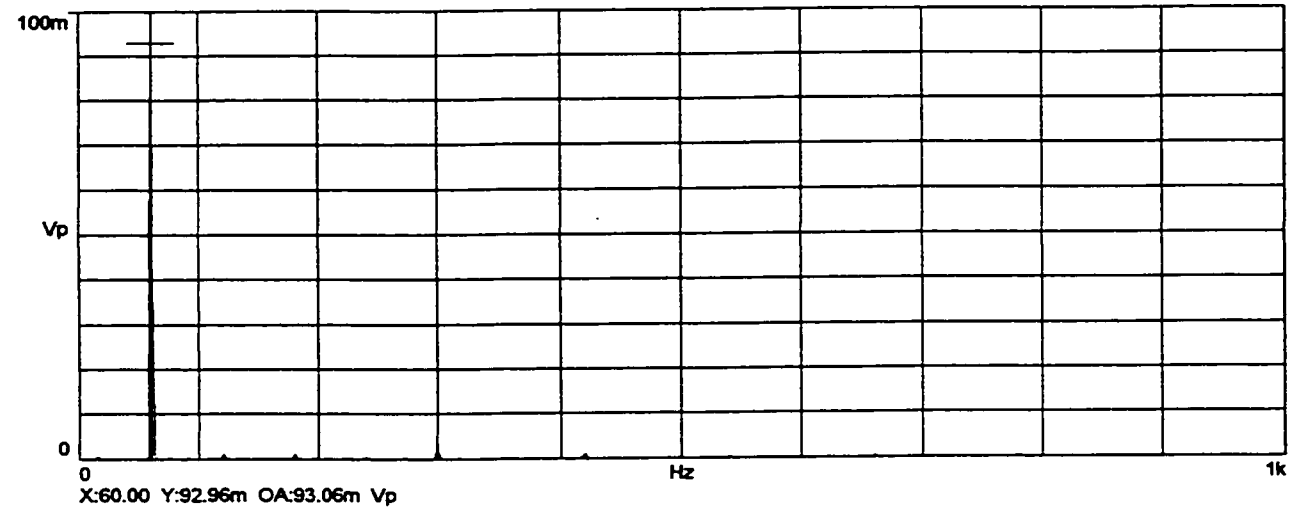

ii) Spectrum Plot

t) Frame Top Left, ODE, 100%V, Locked Rotor Condition.

Figure 6.46: Frame Flux Density, 60 Hz Component, DE Bearing Non-Insulated, ODE Bearing Insulated, Oil Ring Lubrication.

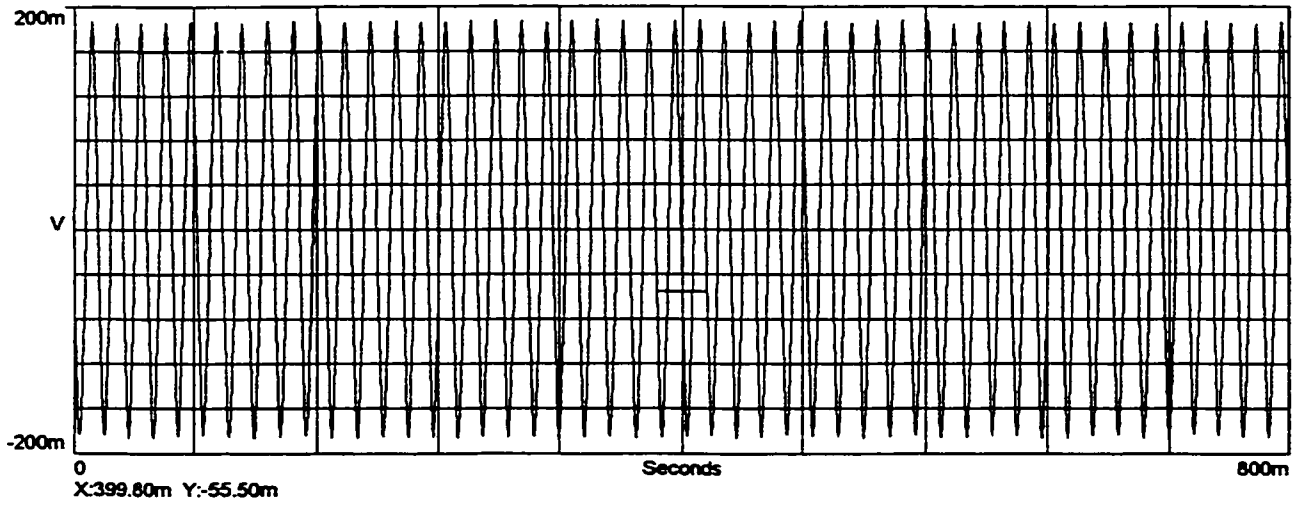

i) Frame Flux Coil Induced Voltage Waveform

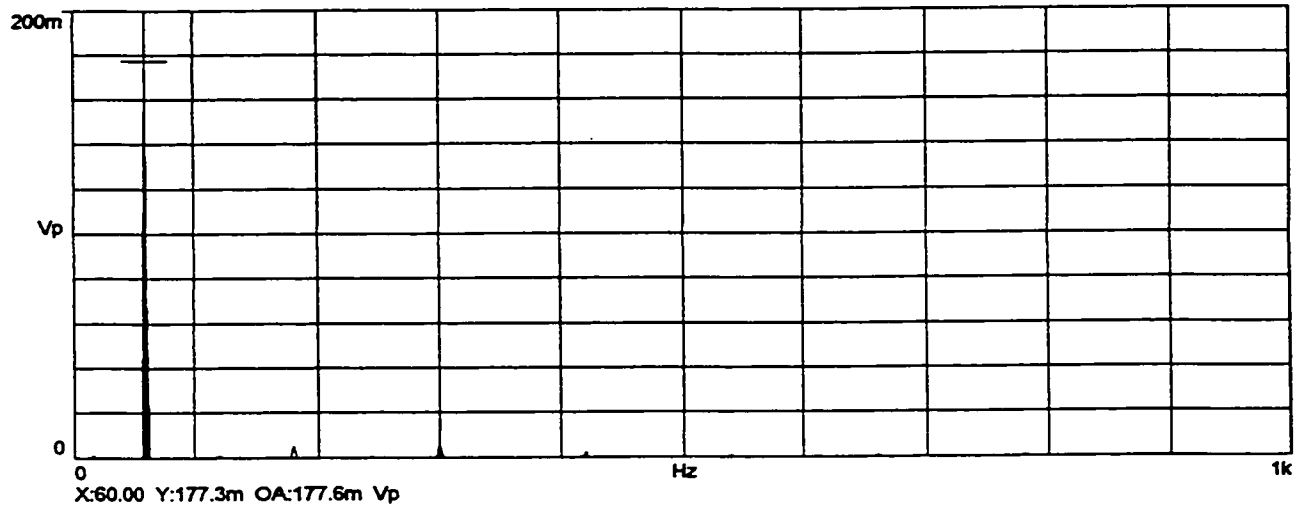

ii) Spectrum Plot

u) Frame Bottom Right, ODE, 100%V, Locked Rotor Condition.

Figure 6.46: Frame Flux Density, 60 Hz Component, DE Bearing Non-Insulated, ODE Bearing Insulated, Oil Ring Lubrication.

6.4.10 LOCKED ROTOR TORQUE AND CURRENT MEASUREMENT [68]

Locked rotor torque and current were measured at different voltages and plotted in Figure 6.47. From Figure 6.47 the slopes of the curves for the locked rotor torque and current were determined and found to be 2.44 and 1.14, respectively. Theoretically, without saturation, the slope of the torque curve is 2.0 (torque is proportional to the square of the voltage) and that of the current is 1.0 (current is proportional to the voltage). Saturation begins to occur at 40%V as seen in Figure 6.48. Saturation needs to be considered in the determination of the occurrence of shaft current especially during starting of the motor. It is during starting of the motor that the probability of bearing damage due to shaft current is highest. The higher the harmonic content present as a result of saturation, the higher the probability of the shaft current punching through the bearing insulation. In Section 6.4.7, during transient conditions, the main harmonic component was determined to be the zero sequence component.

6.4.11 OIL RING PERFORMANCE [69- 72]

Each bearing in the tested machine had an oil ring riding on the shaft journal as shown in Figure 2.3. The oil ring had an inner diameter of 254.0 mm and width of 19.05 mm. The oil ring weighs 758.2 grams and rides on a shaft journal of 165.1 mm with fifteen percent of the oil ring diameter immersed in oil which has kinematics viscosity of 63.0 mm^2/s. The shaft journal peripheral velocity is 7.8 m/s, less than the practical oil ring upper limit of 14 m/s [71], above which oil ring bearing design is not used. All the data are substituted into equations (A2-2), (A2-7) and (A2-10) and the results are tabulated in Table 6.5.

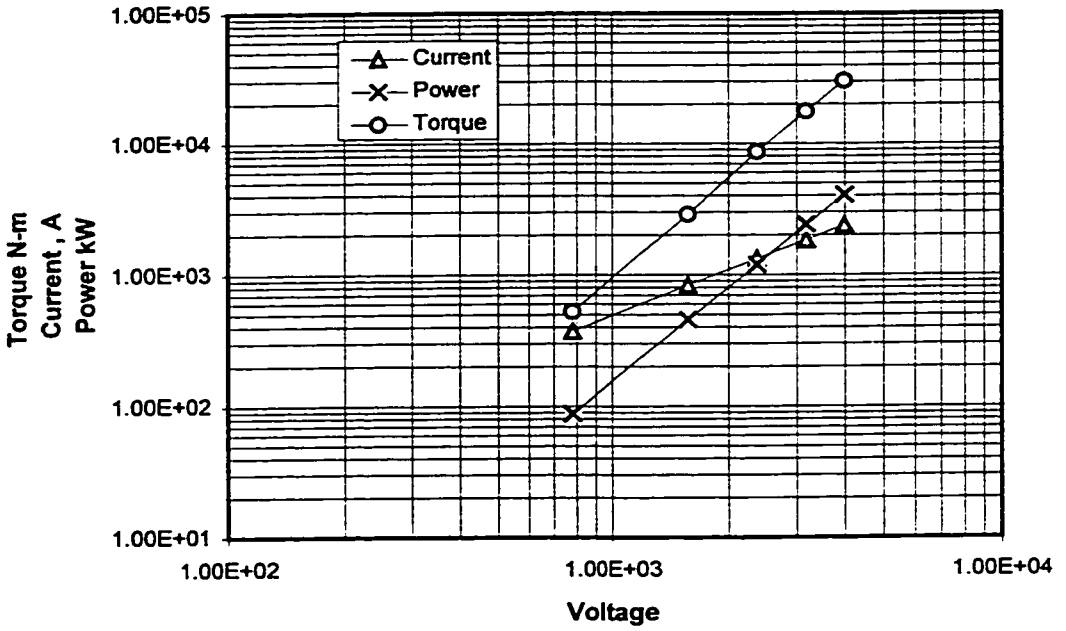

Figure 6.47: Log-log Scale of Locked Rotor Torque, Current and Power Versus Voltage.

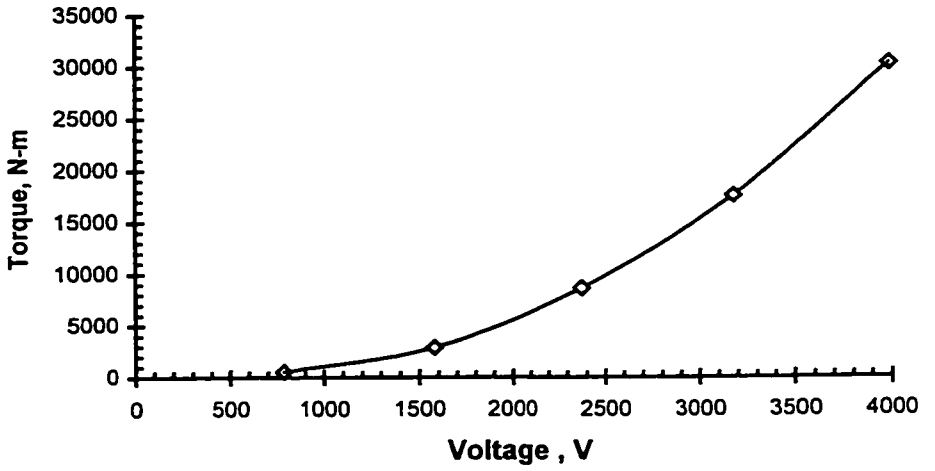

Figure 6.48: Linear Scale of Locked Rotor Torque Versus Voltage

Shaft Speed At Start Of Ring Slip Region (a)	96 RPM
Shaft Speed At Start of Full Film Ring Drive (b)	282 RPM
Ratio of (b) to (a)	2.94
Lemon et al [69] Ratio	2.90

Table 6.5: Calculated Shaft Speed At Start of Ring Slip Region and Full Film Ring Drive

D. C. Lemon and E.R. Booser [69], R. Baudry and L. M. Tichvinsky [70] and G. B. Karelitz [73] provided some details of the elaborate experimental apparatus set-up designed to duplicate as closely as possible the normal operation of the oil ring in a bearing housing. Generally, the speed of the ring was determined by counting and timing the passages of a white mark on the ring and the speed of the journal was measured by a stroboscope. An alternative method of measuring the shaft speed at different lubrication regions is to measure the shaft speed and the shaft current of the machine during different motor line voltage starts, as the machine accelerates from zero speed to no load speed. A tachometer was installed on the shaft end to measure the speed during the starting condition. A stroboscope was used to determine the no load speed.

At low motor line voltage start, the motor accelerates slowly. The oil ring speed is able to follow the shaft speed and oil film develops quickly between the shaft journal and the bearing. The shaft current measured during the initial start of the motor will decrease when the oil film is developed between the shaft journal and the bearing. There is a linear relationship between the shaft speed at which oil film develops and the motor line voltage in this low motor line-voltage region.

At higher motor line-voltage starts, the motor will accelerate faster, and a condition will be reached when the oil ring slips and the oil film develops much later. There is no longer a linear relationship between the motor line voltage and the shaft speed at which the oil film first develops.

As the shaft speed increases the degree of slippage between the ring and the journal increases until a point is reached when a complete lubricating oil film is built up to support the ring. At this condition the shaft speed at which an oil film first develops peaks at a particular motor line voltage start.

For any motor line voltage start beyond this voltage level, the shaft speed at which the oil film develops will drop. Shaft speeds at which the oil film first develops at different motor line voltage starts are plotted against the motor line voltages in Figure 6.49. The start of slip of the oil rings occurs when the motor is started across the line at around 2200V. The full film occurs when the motor is started across the line at around 3326 volts. The test shaft speed in the two lubricating regions are given in Table 6.6.

Shaft Speed At Start Of Ring Slip Region (a)	72.74 rpm
Shaft Speed At Start of Full Film Ring Drive (b)	205.02 rpm
Ratio of (b) to (a)	2.81

Table 6.6: Test Shaft Speed At Start of Ring Slip Region and Full Film Ring Drive

The start of the oil ring slip region occurs at a much reduced shaft speed than the calculated speed. Hence, the oil delivery of the oil ring to the bearings is reduced. The probability of a closed shaft current circuit is thus increased. This method of determination of the performance characteristic of the oil ring is more accurate than the conventional way of

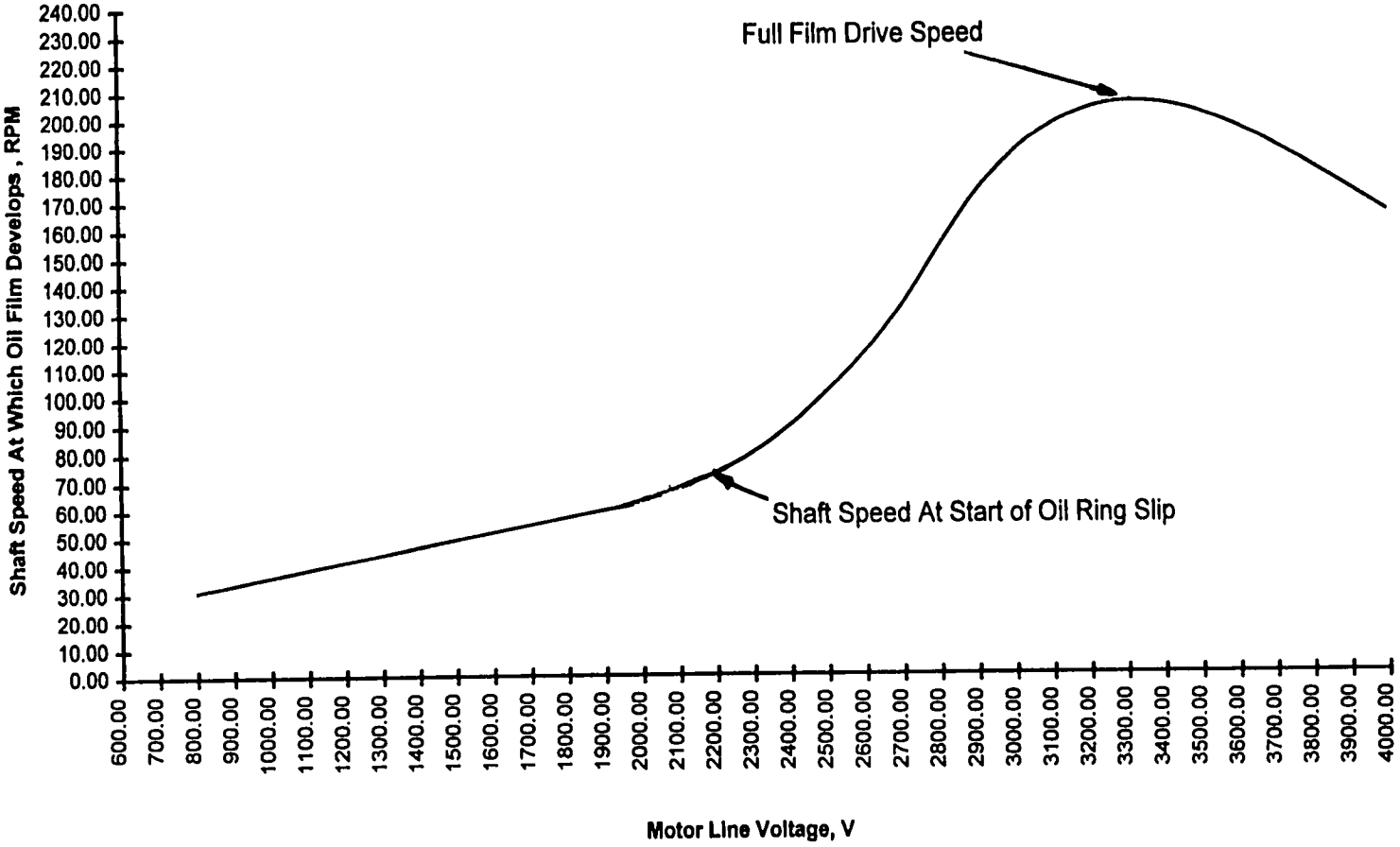

Figure 6.49: Shaft Speed At Which Oil Film Begins to Develop For Different Motor Line Voltage Starts

determining the full film ring drive speed which is counting the number of revolutions of the oil ring and timing the counts. The ring slip region speed is calculated from Lemon's ratio [68].

6.5 STATOR CURRENT MEASUREMENT.

Many diagnostic techniques to detect machine faults are based on stator current spectral analysis. In this thesis, spectral analyses of shaft current and voltage and shaft flux were utilized as alternatives to the current spectral analysis. In order to verify further the conclusions reached in the alternative analyses, the stator current was measured and analyzed. Figures 6.50 (a) - (c) are the measured stator current waveforms at 20%, 80% and 100% of motor rated line voltage. Each of these waveforms were analyzed at three conditions - close to standstill condition, mid-way of transient condition and steady state condition, as shown in Figures 6.50 (d) - (l). These figures clearly indicate 60 Hz component. Frequencies caused by eccentricity and broken bar were not detected, confirming the conclusions reached from the shaft voltage and current measurements, shaft flux measurement and air gap measurement.

6.5 SHAFT VOLTAGE PREDICTION RULES

From Table 6.7, it is now clear that the shaft current in this machine is clearly due to the joints between the lamination segment. The resulting flux circulation around the shaft can be explained in a simplified step-by step representation of flux as illustrated in Figure 6.51. There is no circulating flux at zero load angle as defined in Figure 6.51 (a). The net circulating flux rotates clockwise as the load angle is increased. Figures 6.51 (b) - (e)

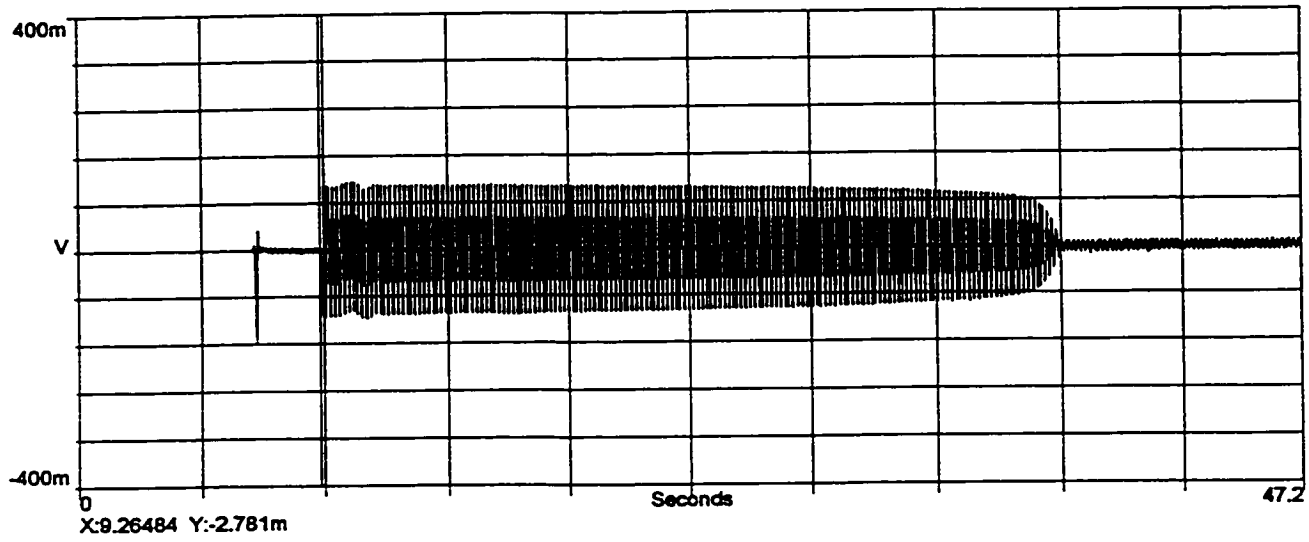

a) Stator Current Waveform, 20% of Motor Rated Line Voltage

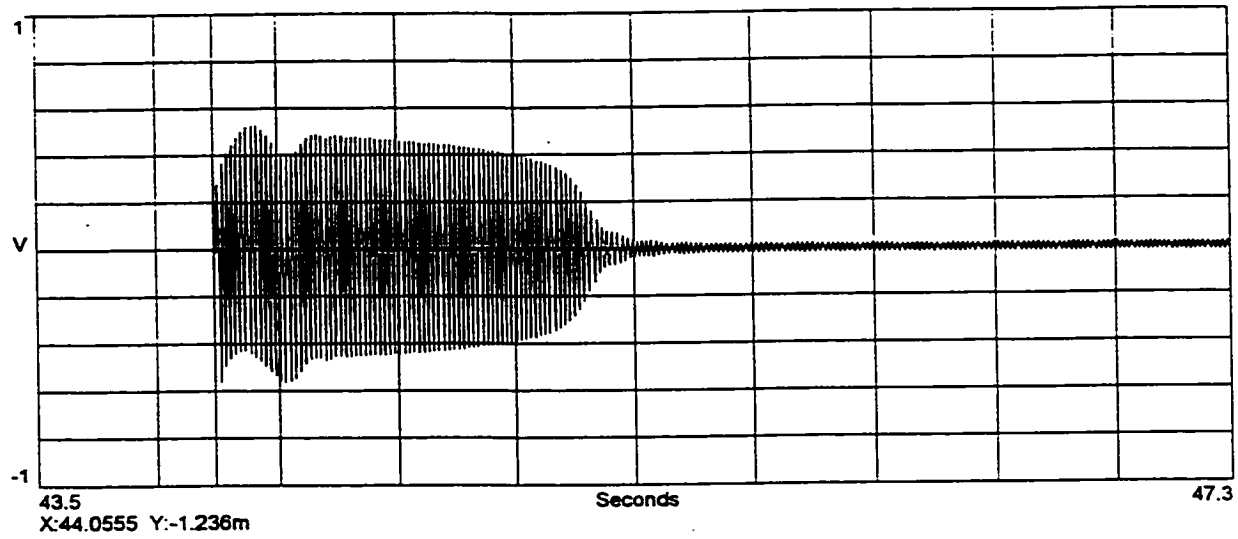

b) Stator Current Waveform, 80% of Motor Rated Line Voltage

Figure 6.50: Motor Phase Current Waveform At 20%, 80% and 100% of Motor Rated Line Voltage and Spectral Analyses.

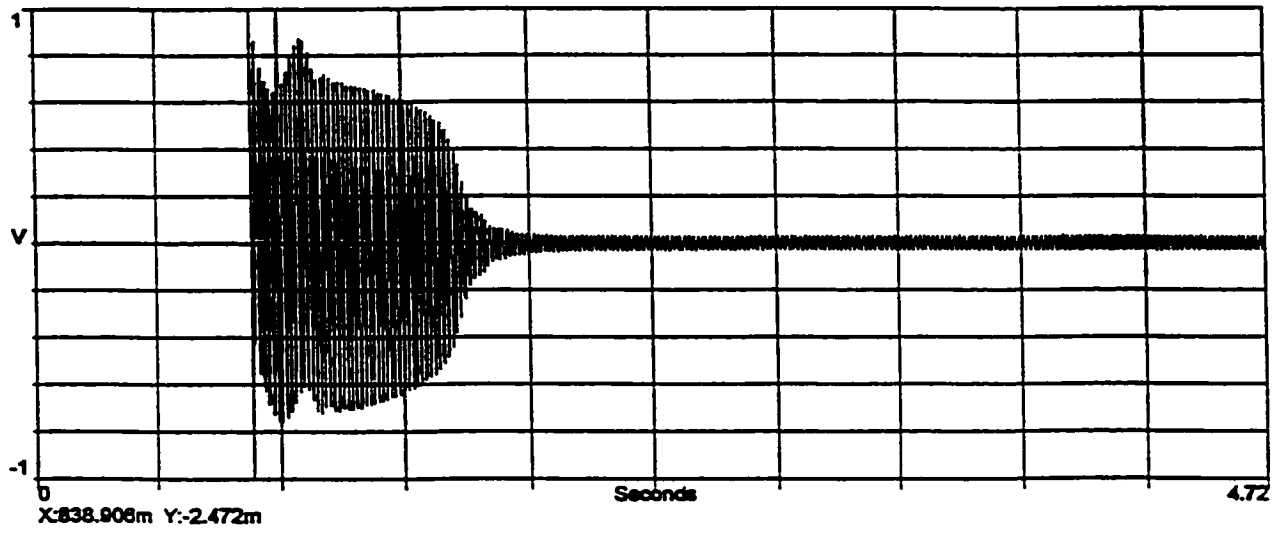

c) Stator Current Waveform, 100% of Motor Rated Line Voltage

Figure 6.50: Motor Phase Current Waveform At 20%, 80% and 100% of Motor Rated Line Voltage and Spectral Analyses.

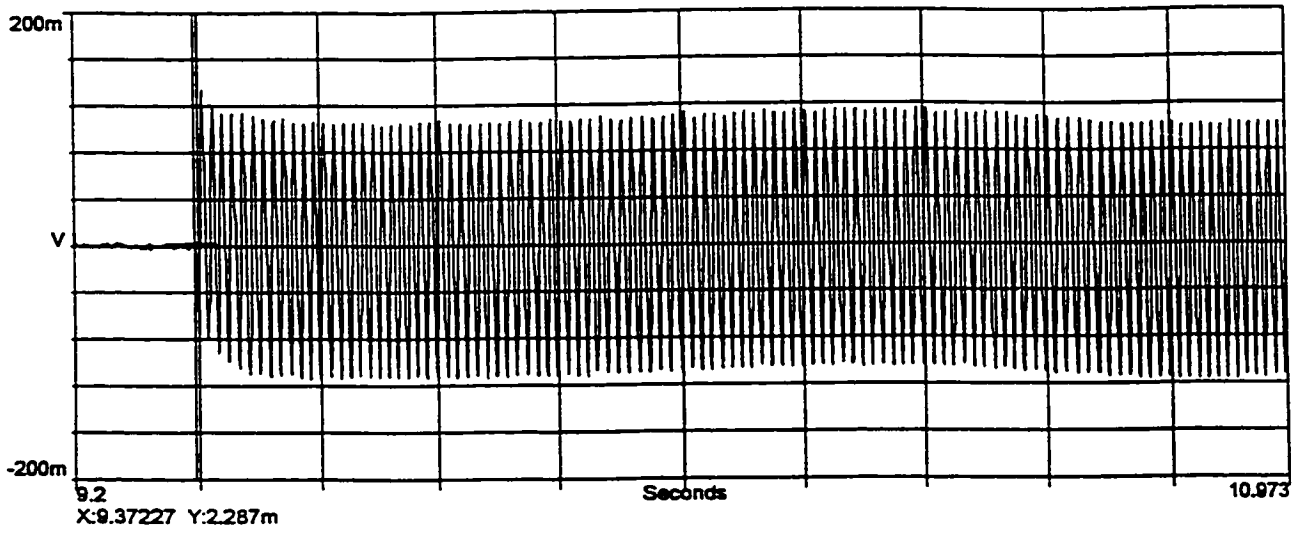

i) Stator Current Waveform

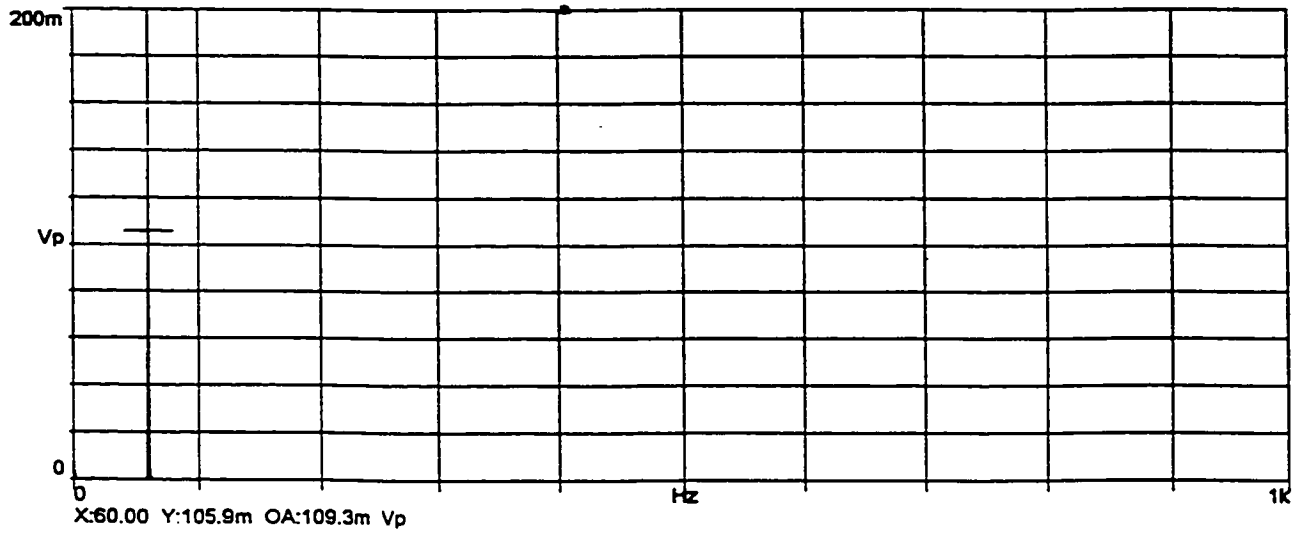

ii) Spectrum Plot

d) Stator Current, Close to Standstill Condition, 20% of Motor Rated Line Voltage

Figure 6.50: Motor Phase Current Waveform At 20%, 80% and 100% of Motor Rated Line Voltage and Spectral Analyses.

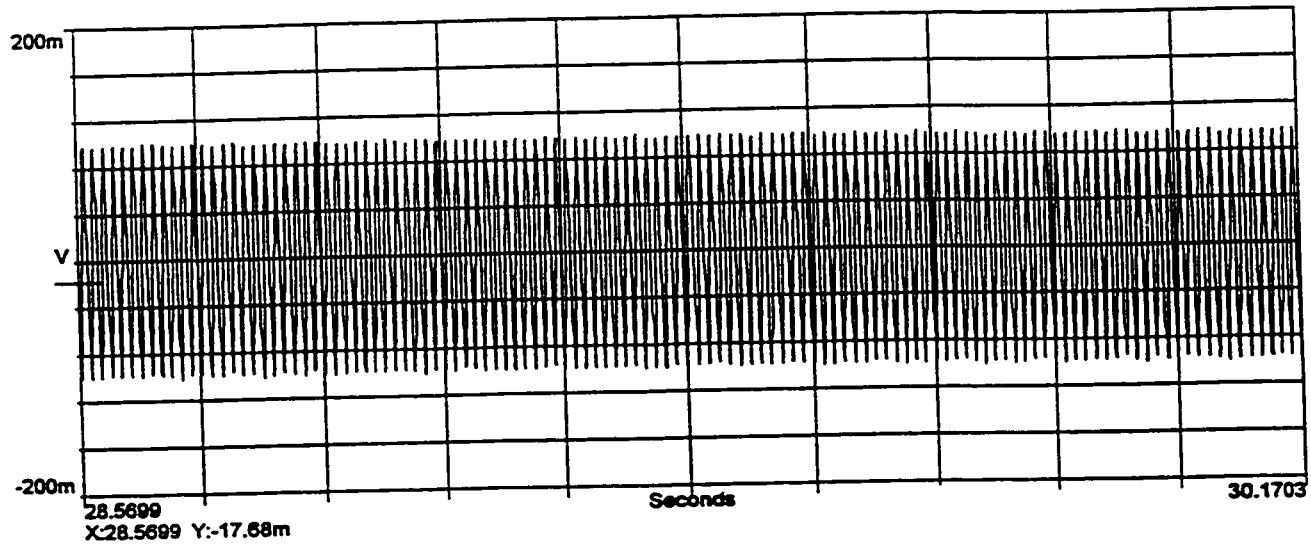

i) Stator Current Waveform

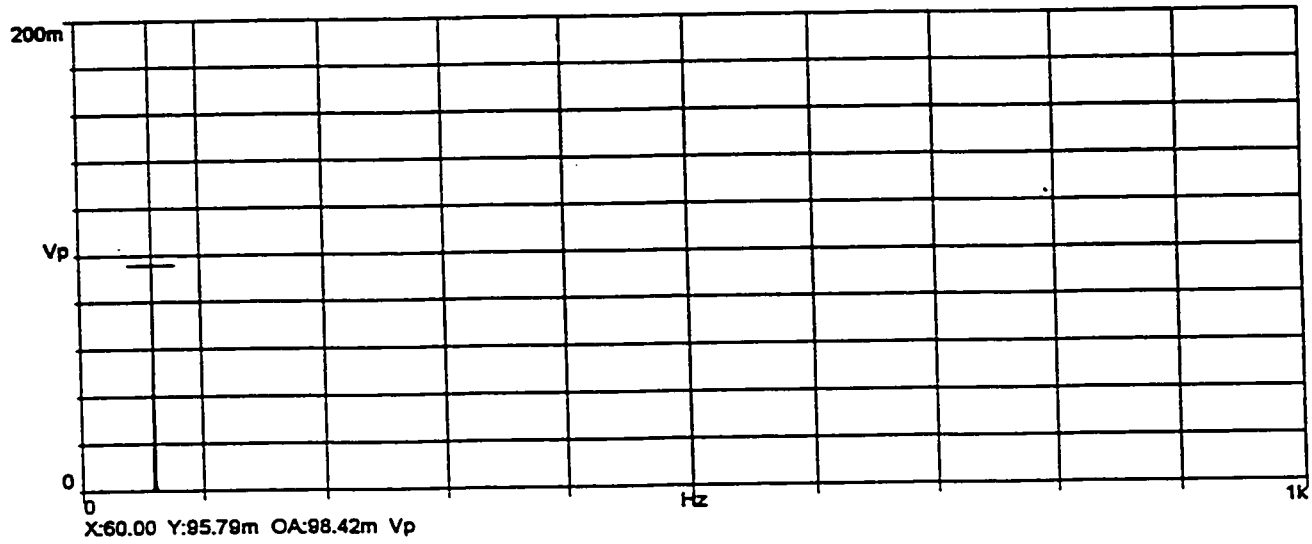

ii) Spectrum Plot

e) Stator Current, Mid-Way of Transient Condition, 20% of Motor Rated Line Voltage

Figure 6.50: Motor Phase Current Waveform At 20%, 80% and 100% of Motor Rated Line Voltage and Spectral Analyses.

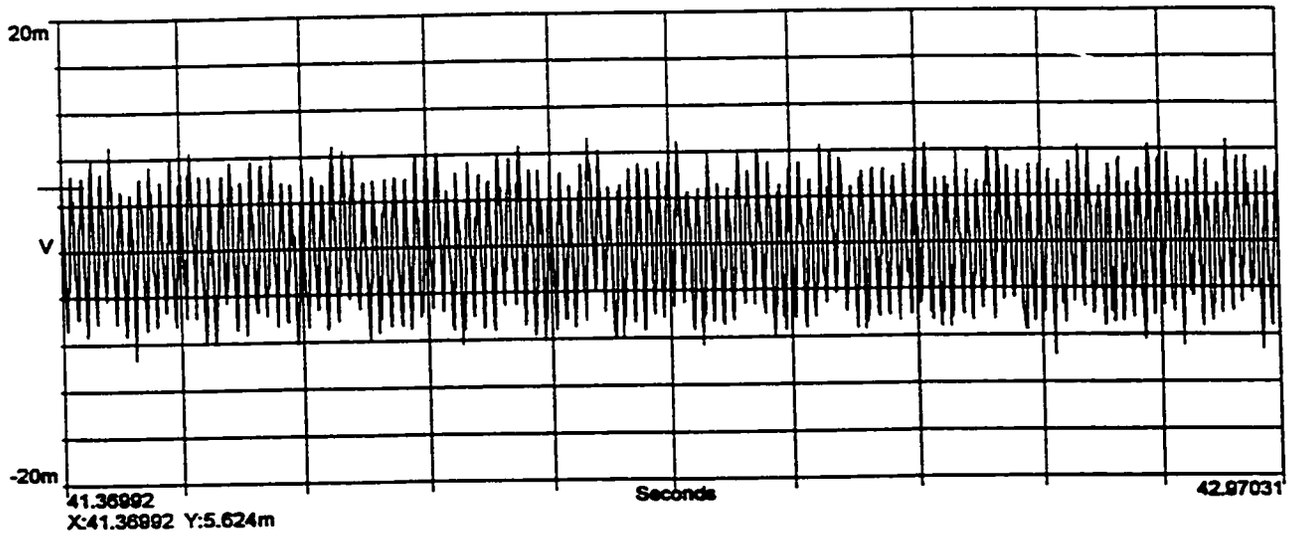

i) Stator Current Waveform

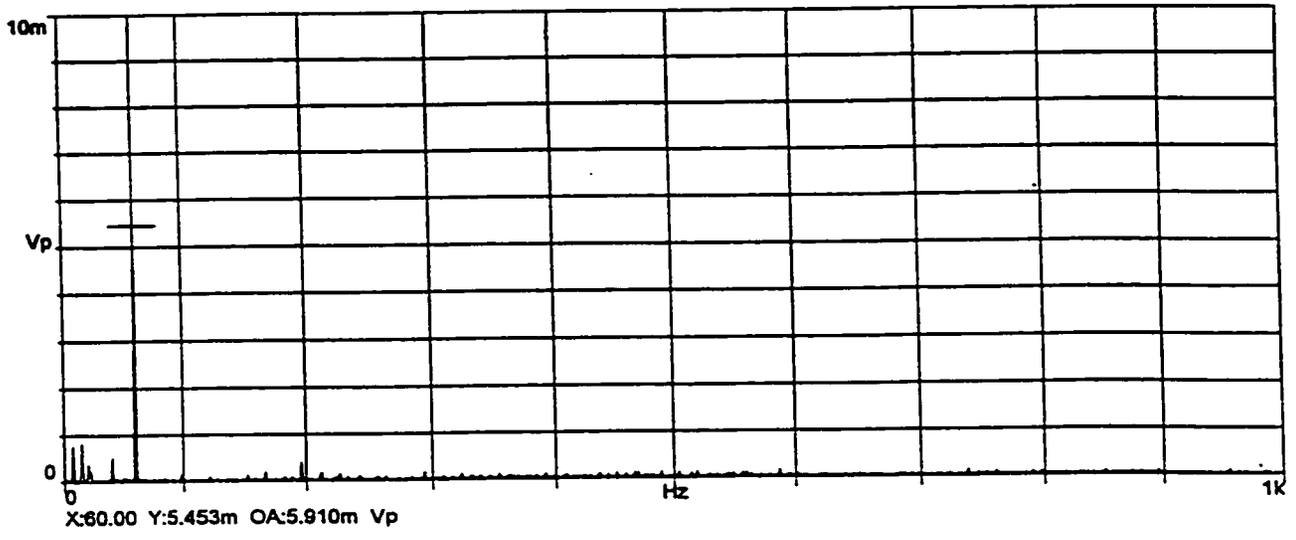

f) Stat ii) Spectrum Plot

f) Stator Current, Steady State No-Load Condition, 20% of Motor Rated Line Voltage

Figure 6.50: Motor Phase Current Waveform At 20%, 80% and 100% of Motor Rated Line Voltage and Spectral Analyses.

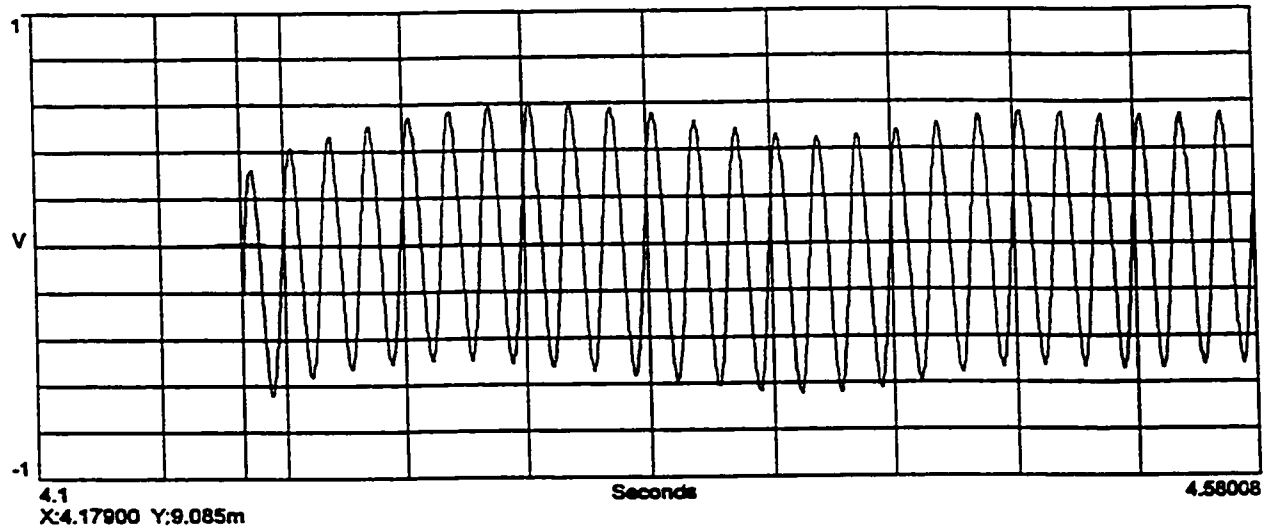

i) Stator Current Waveform

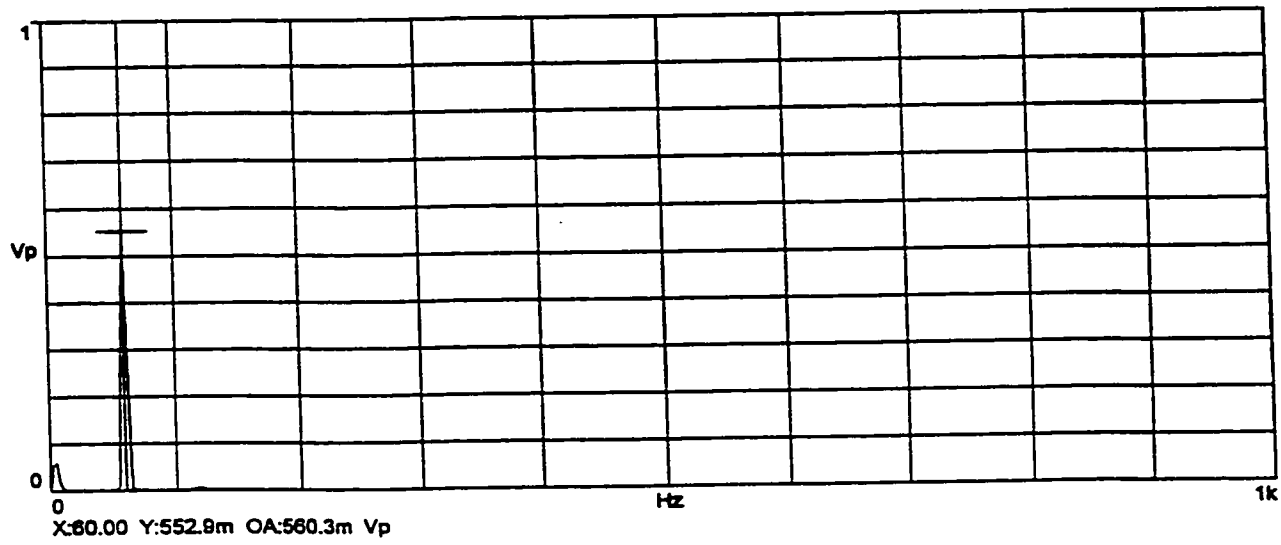

ii) Spectrum Plot

g) Stator Current, Close to Standstill Condition, 80% of Motor Rated Line Voltage

Figure 6.50: Motor Phase Current Waveform At 20%, 80% and 100% of Motor Rated Line Voltage and Spectral Analyses.

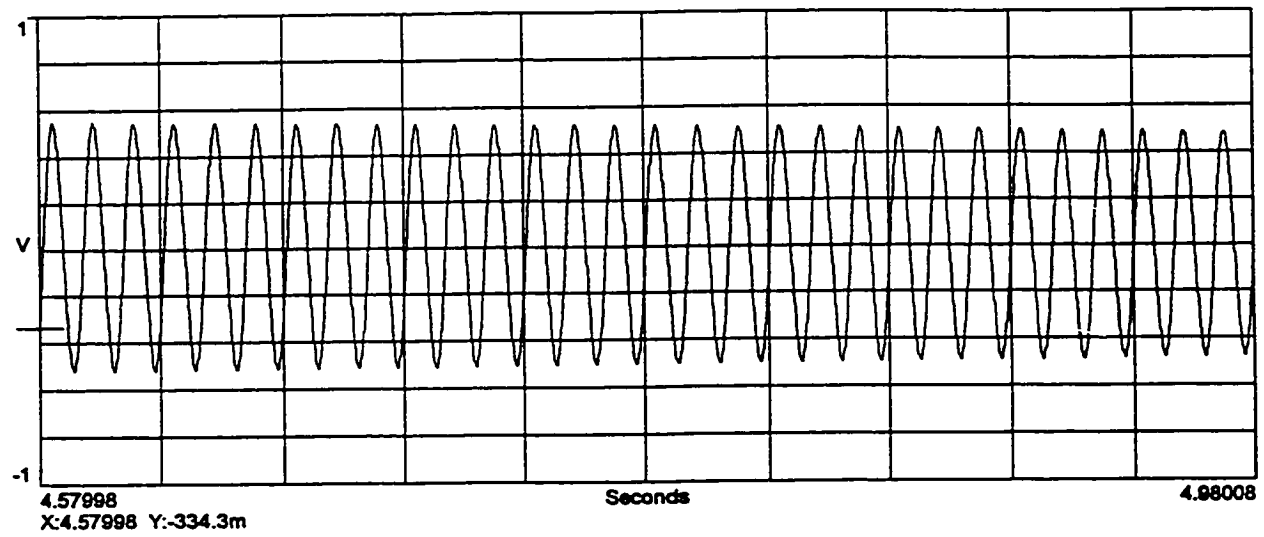

i) Stator Current Waveform

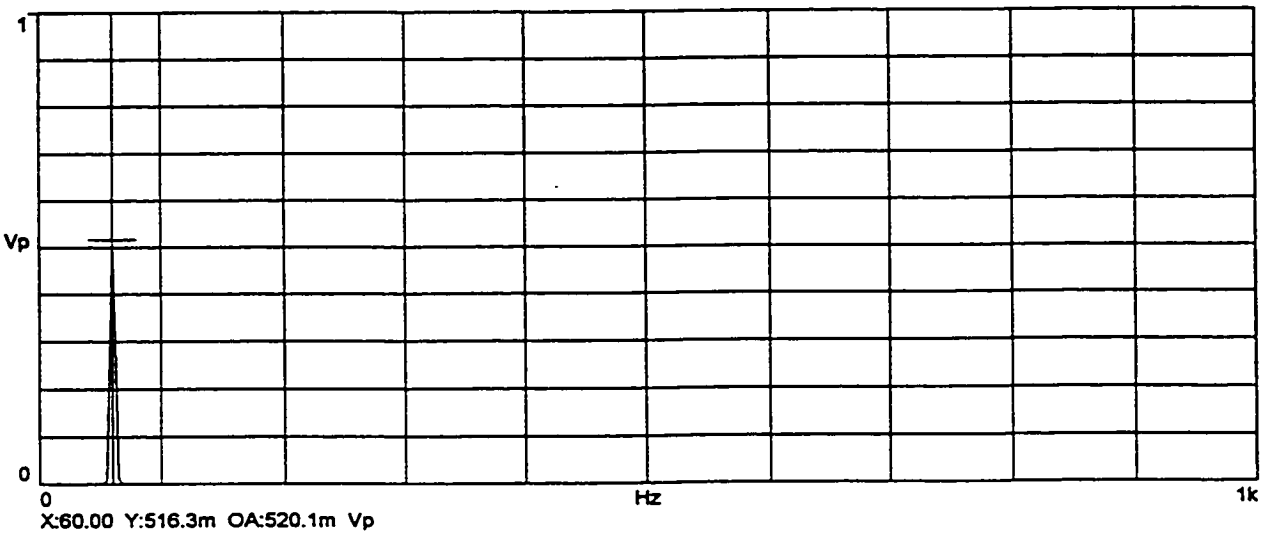

ii) Spectrum Plot

h) Stator Current, Mid-Way of Transient Condition, 80% of Motor Rated Line Voltage

Figure 6.50: Motor Phase Current Waveform At 20%, 80% and 100% of Motor Rated Line Voltage and Spectral Analyses.

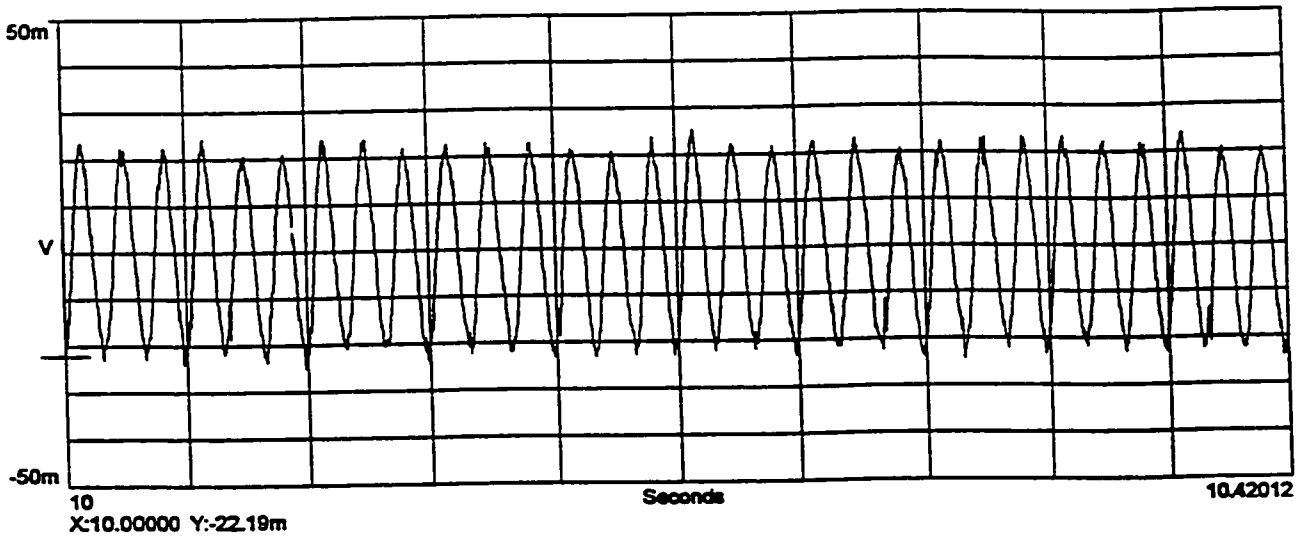

i) Stator Current Waveform

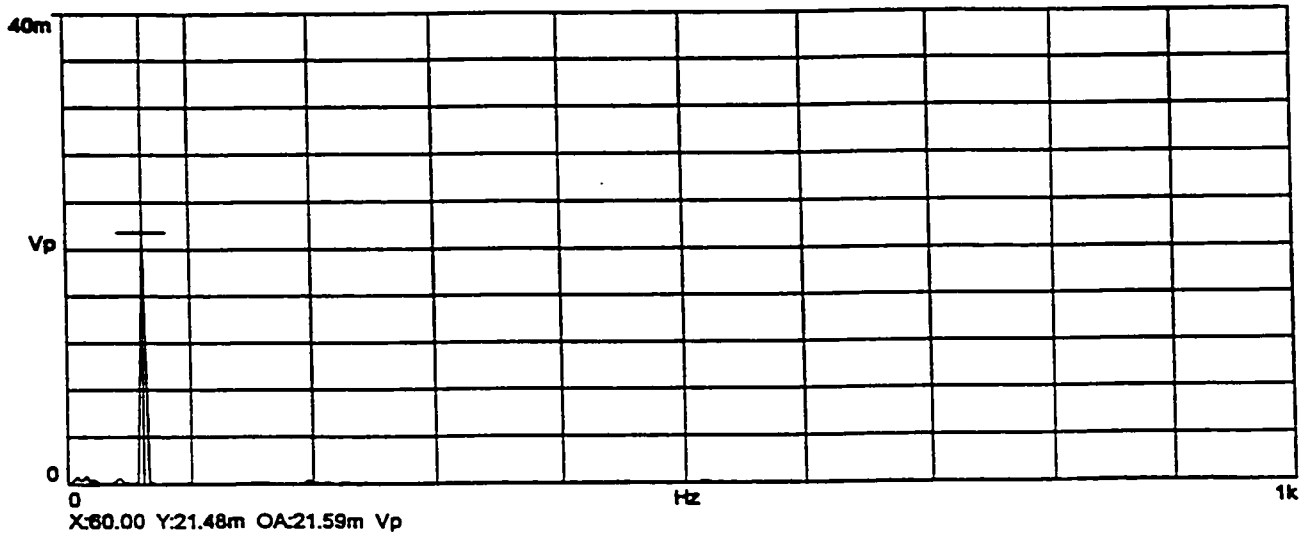

ii) Spectrum Plot

i) Stator Current, Steady State No-Load Condition, 80% of Motor Rated Line Voltage

Figure 6.50: Motor Phase Current Waveform At 20%, 80% and 100% of Motor Rated Line Voltage and Spectral Analyses.

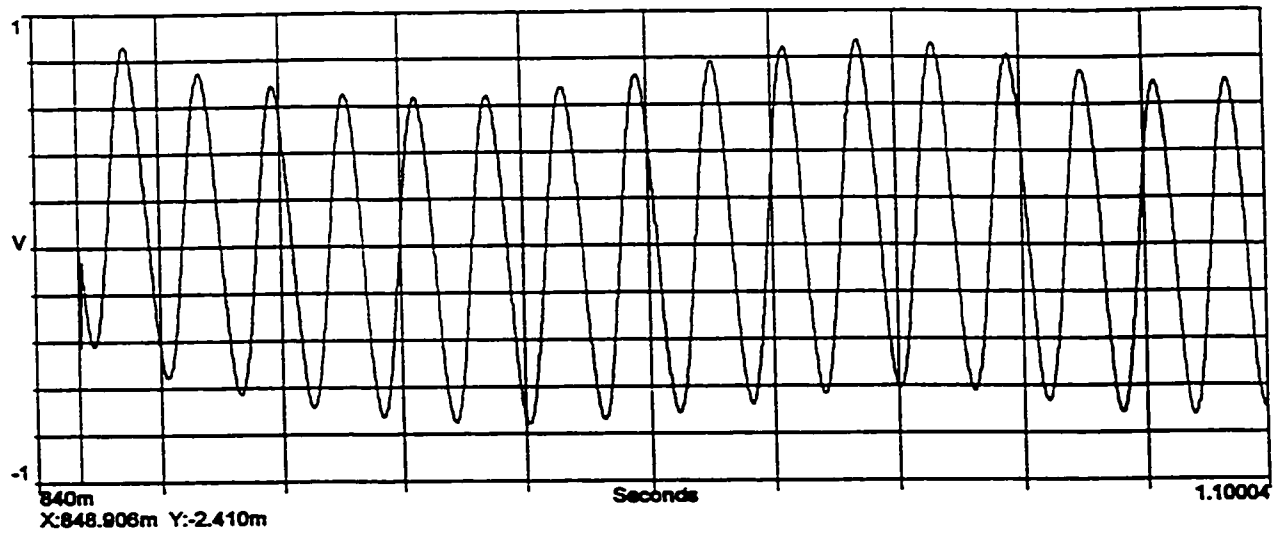

i) Stator Current Waveform

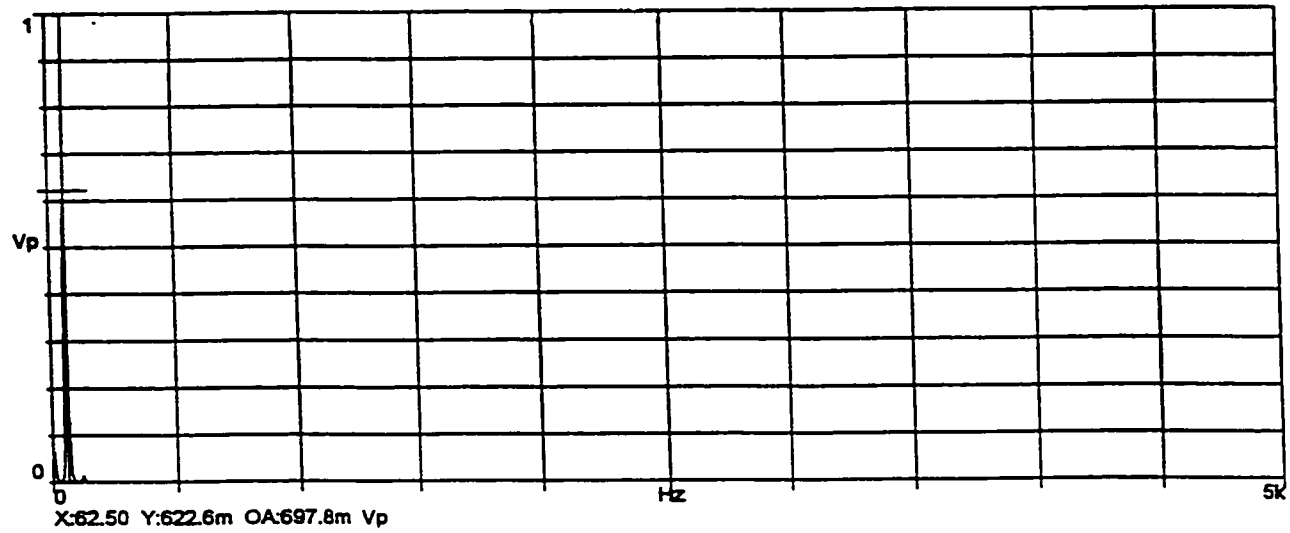

ii) Spectrum Plot

j) Stator Current, Close to Standstill Condition, 100% of Motor Rated Line Voltage

Figure 6.50: Motor Phase Current Waveform At 20%, 80% and 100% of Motor Rated Line Voltage and Spectral Analyses.

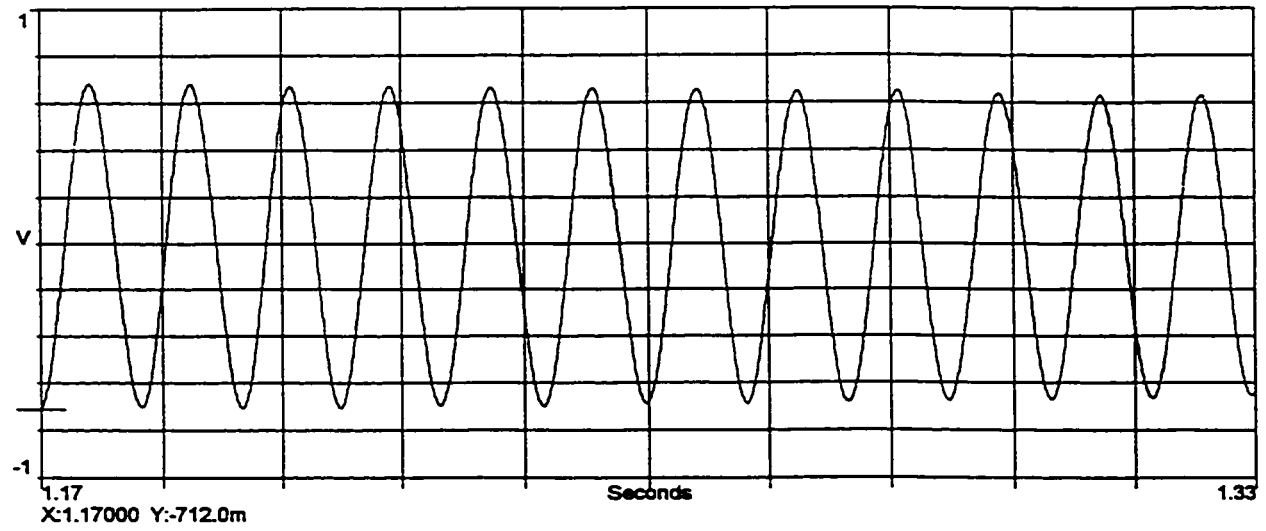

i) Stator Current Waveform

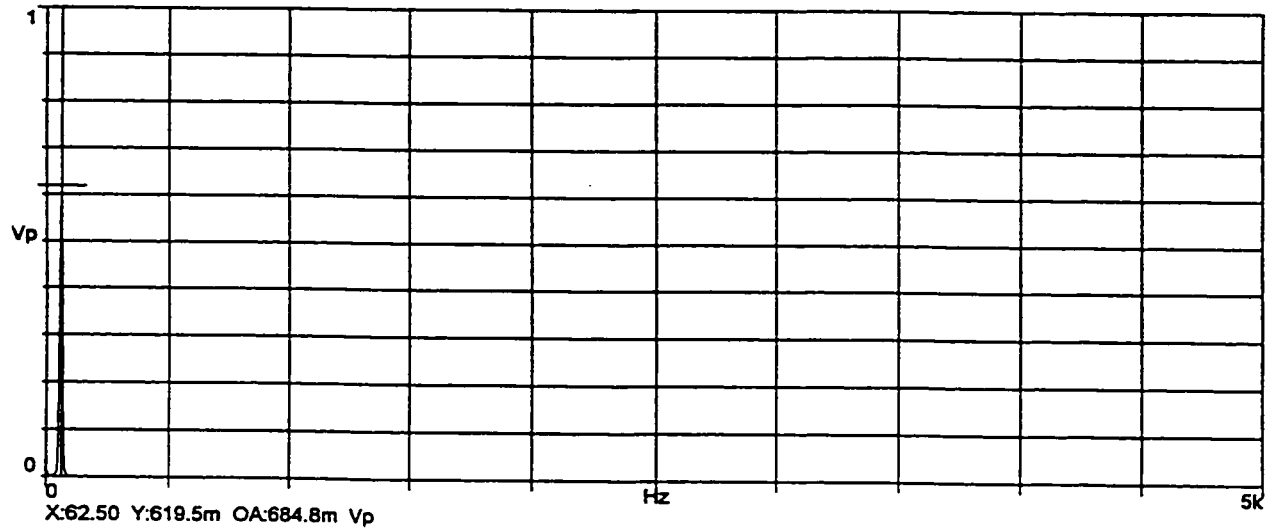

ii) Spectrum Plot

k) Stator Current, Mid-Way of Transient Condition, 100% of Motor Rated Line Voltage

Figure 6.50: Motor Phase Current Waveform At 20%, 80% and 100% of Motor Rated Line Voltage and Spectral Analyses.

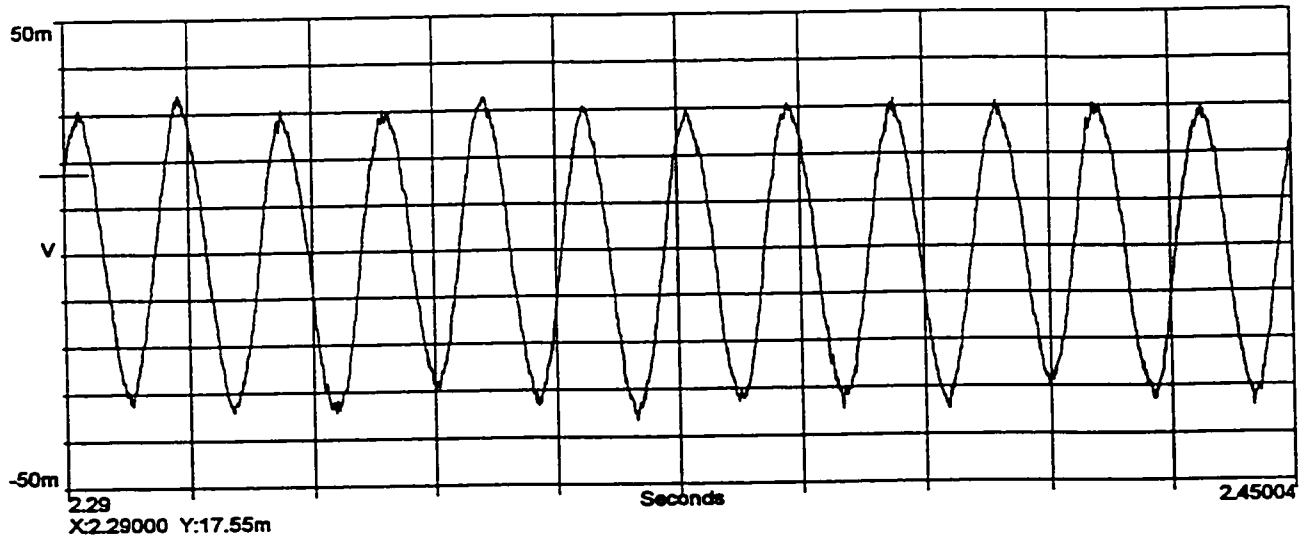

i) Stator Current Waveform

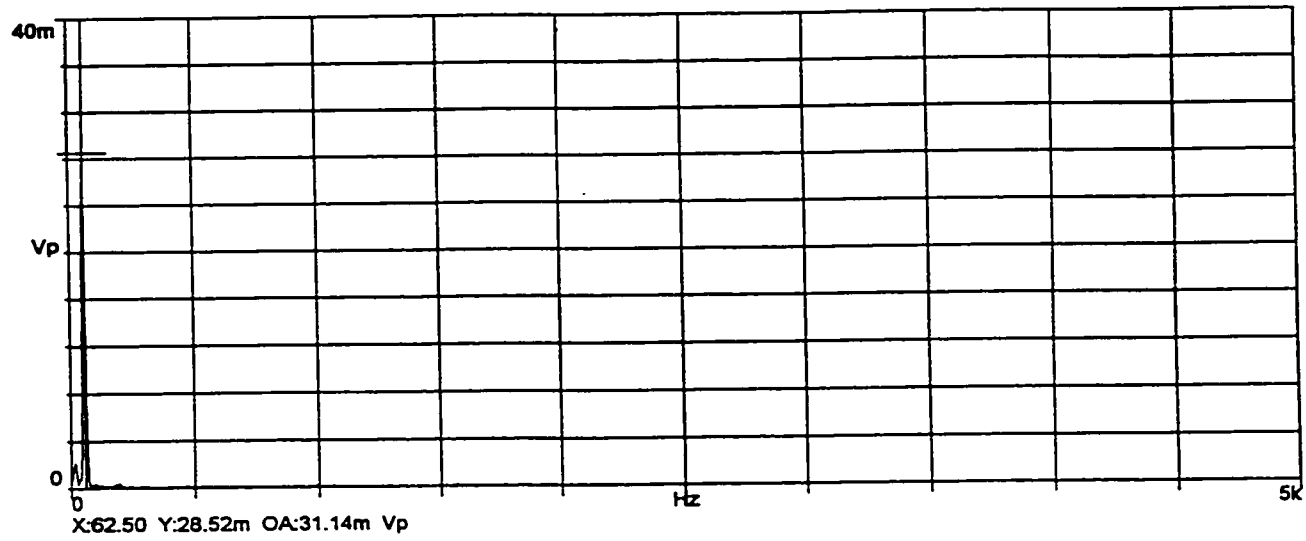

ii) Spectrum Plot

l) Stator Current, Steady State No-Load Condition, 100% of Motor Rated Line Voltage

Figure 6.50: Motor Phase Current Waveform At 20%, 80% and 100% of Motor Rated Line Voltage and Spectral Analyses.

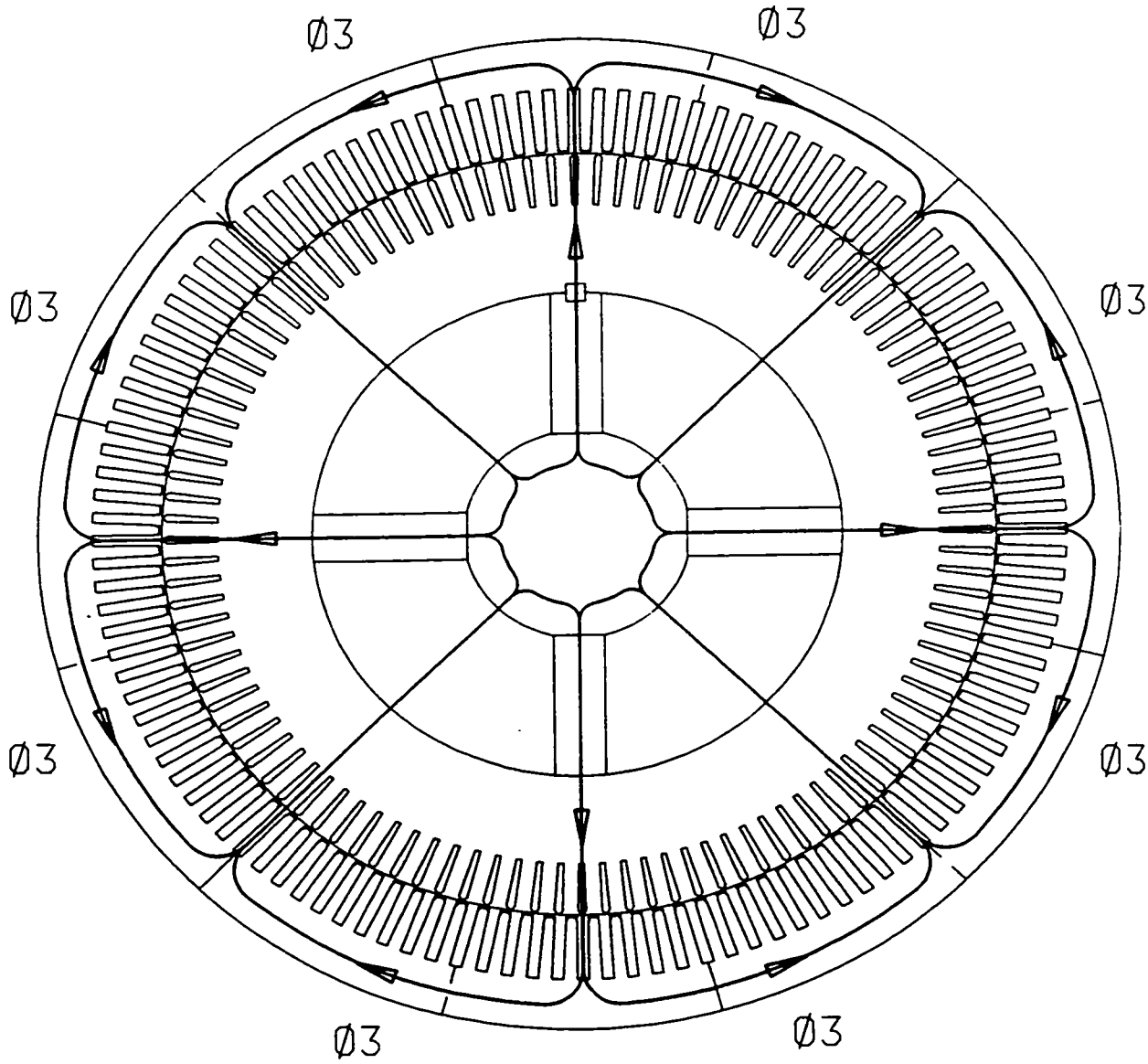

No Circulation of Flux Around the Shaft

(a) : Angular Position: Zero Degrees

Figure 6.51: Simplified Step-by Step Pictorial Representation of Circulating Flux.

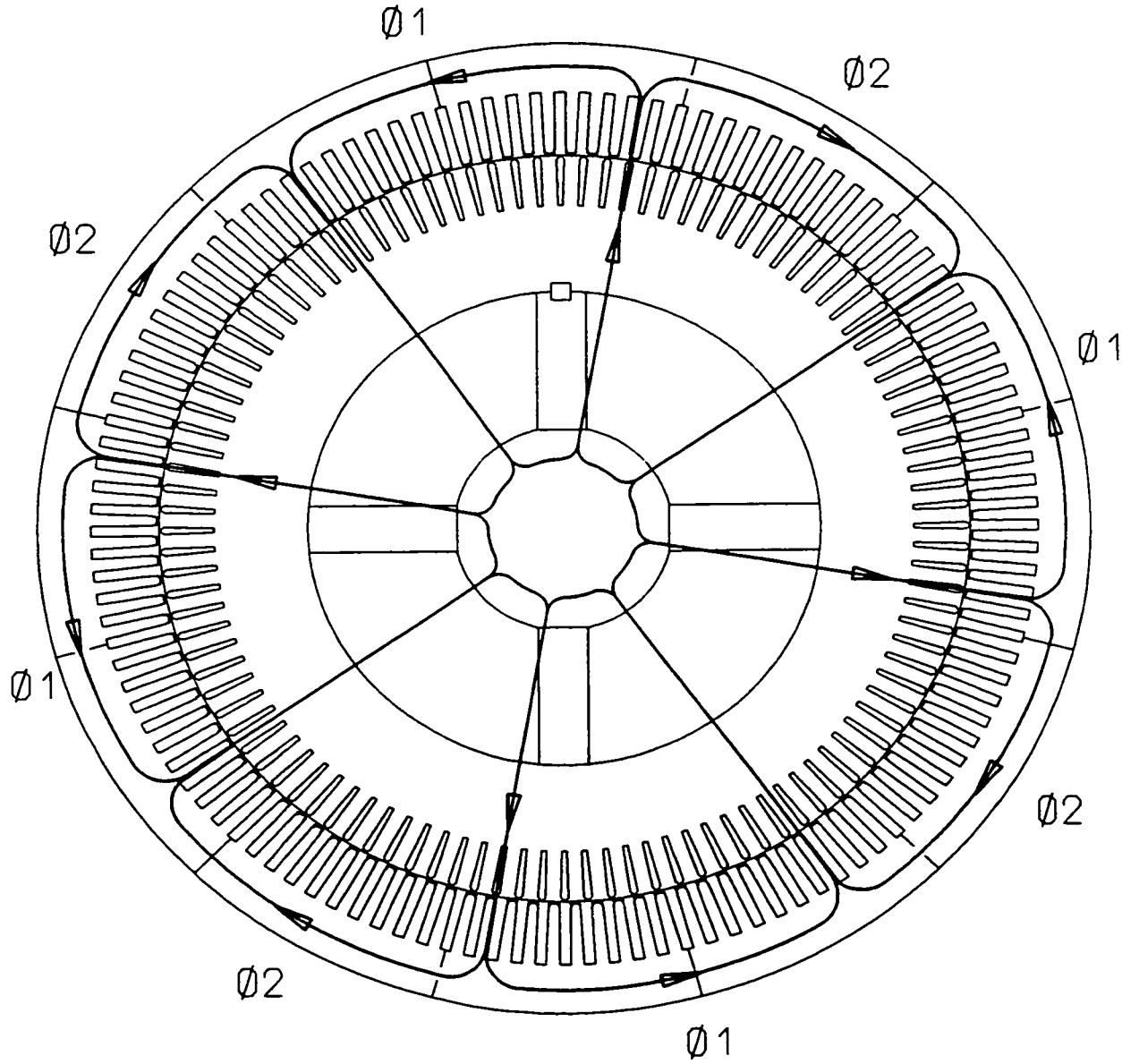

Figure 6.51 (b): Figure 6.51 (c) + Figure 6.51 (d)

(b) : Angular Position: Ten Degrees

Figure 6.51: Simplified Step-by Step Pictorial Representation of Circulating Flux.

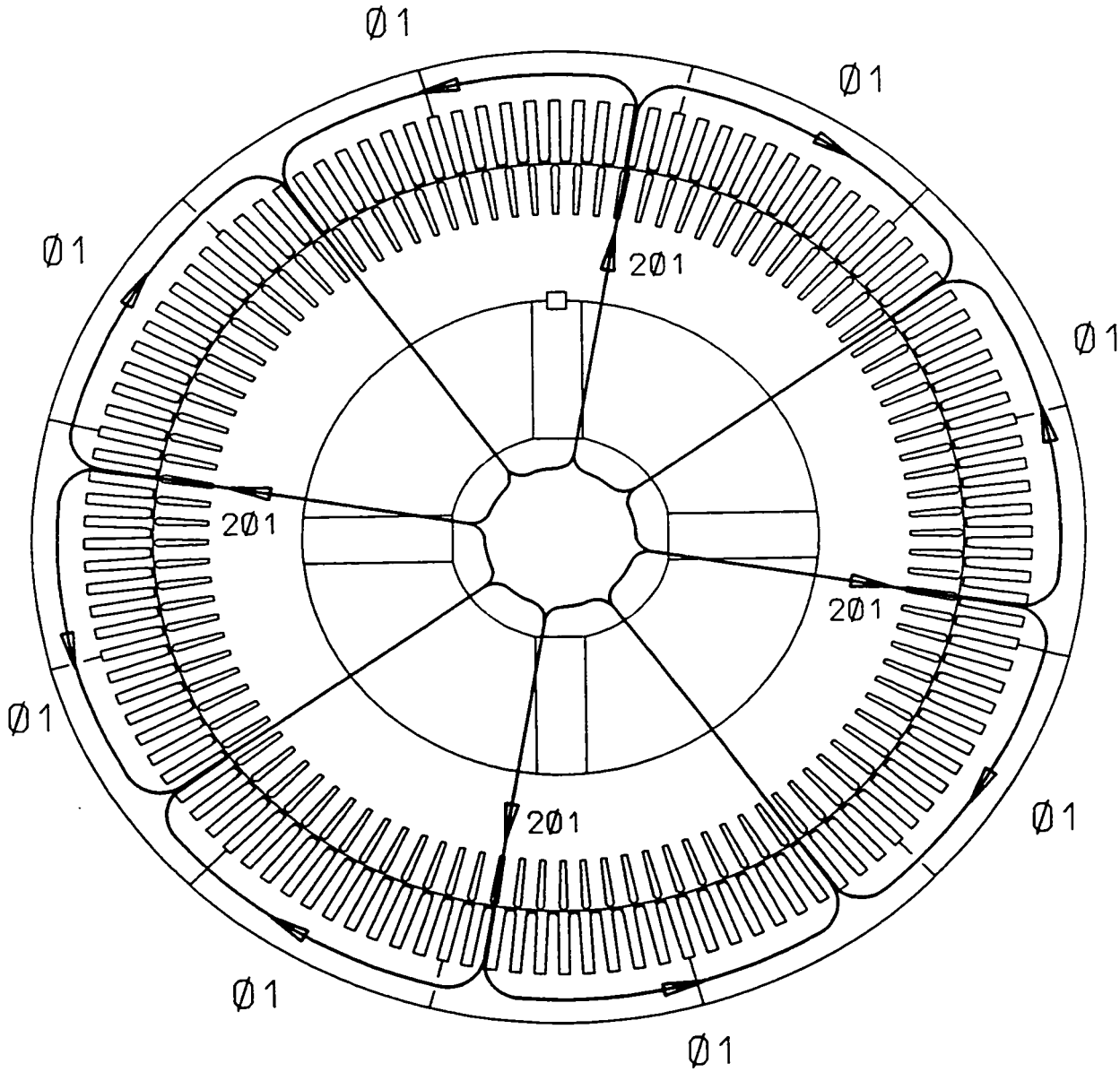

(c) : Angular Position: Ten Degrees

Figure 6.51: Simplified Step-by Step Pictorial Representation of Circulating Flux.

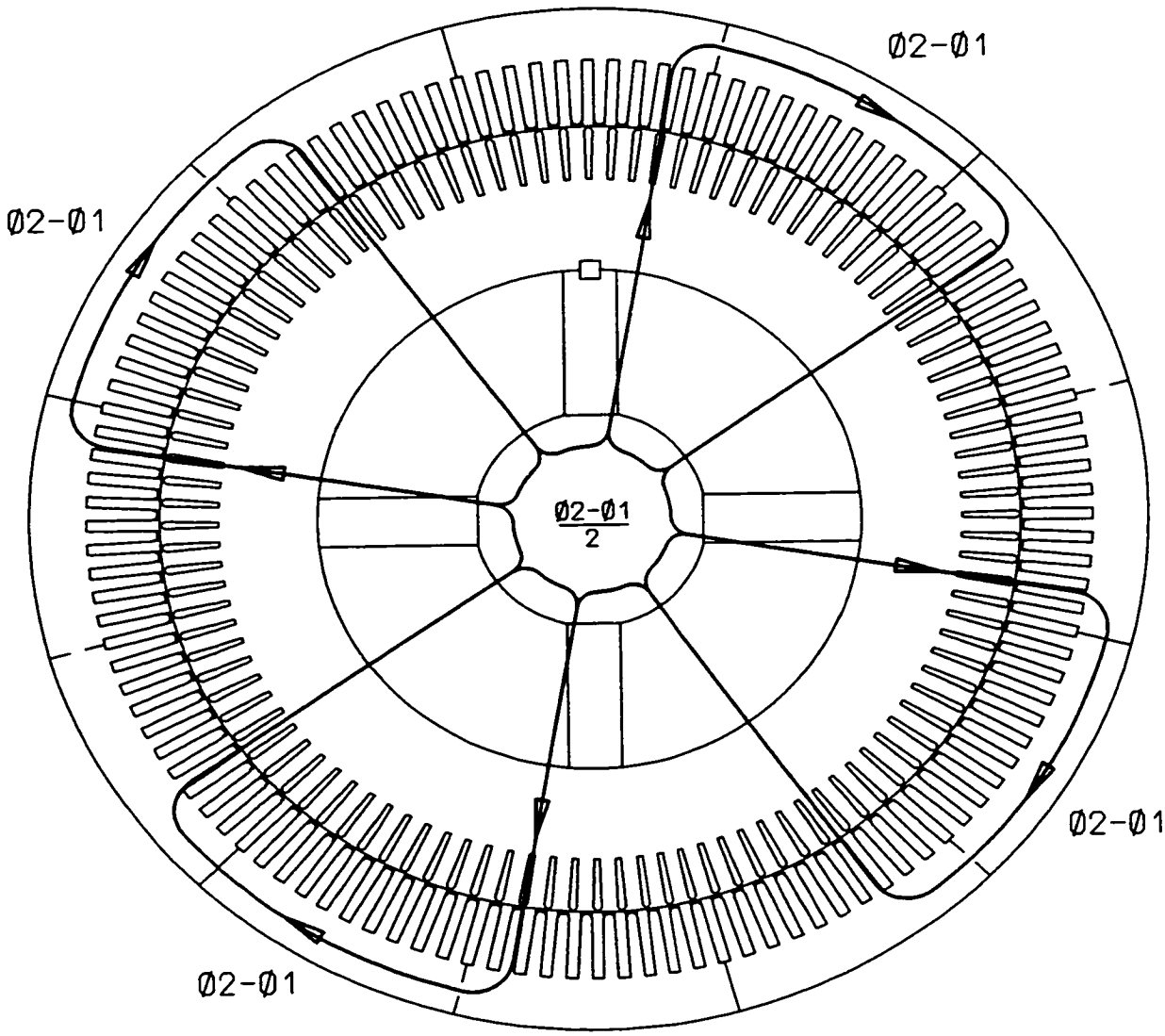

Figure 6.51 (d): Figure 6.51 (e) + Figure 6.51 (f)

(d) : Angular Position: Ten Degrees

Figure 6.51: Simplified Step-by Step Pictorial Representation of Circulating Flux.

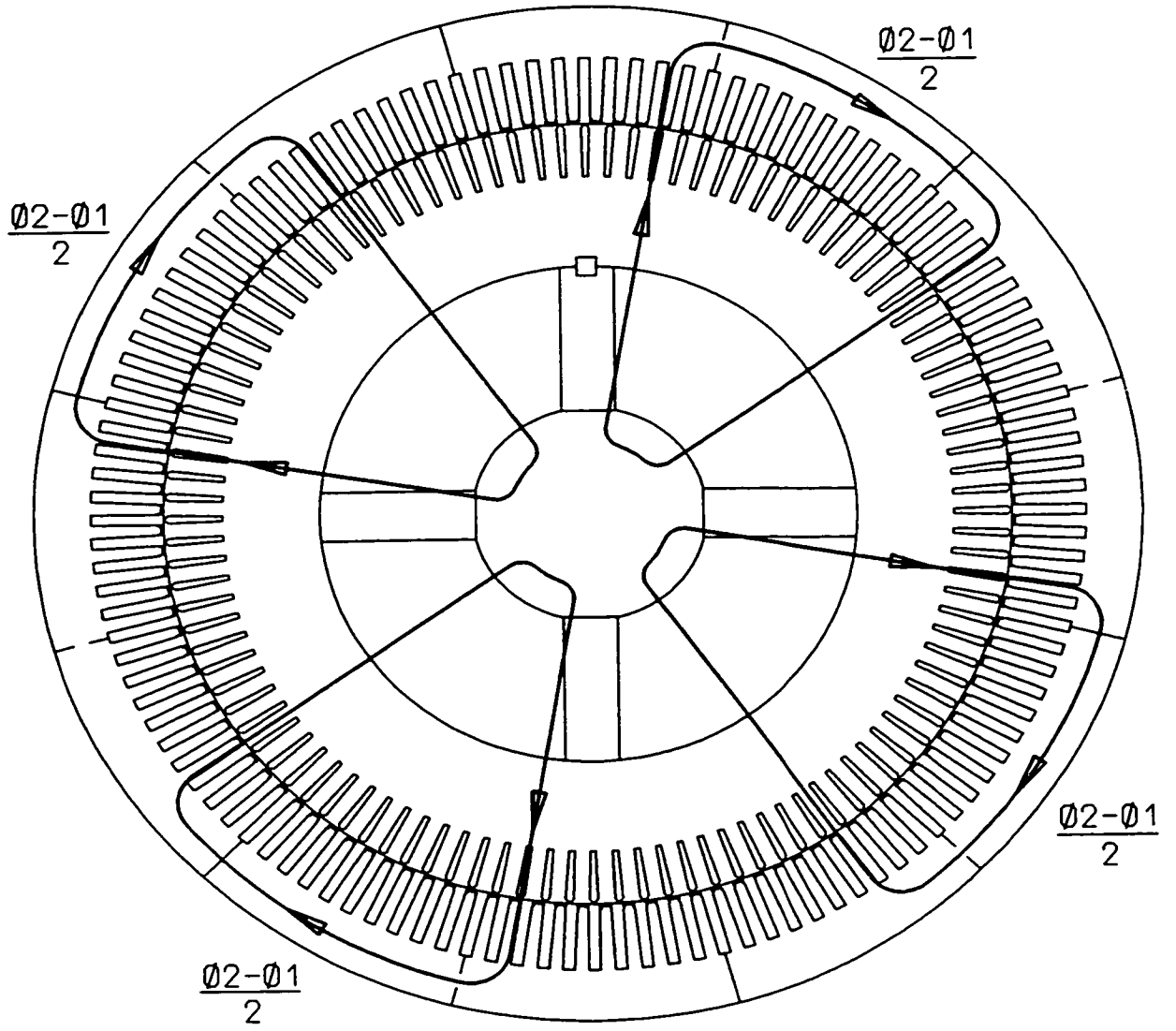

(e) :Angular Position: Ten Degrees

Figure 6.51: Simplified Step-by Step Pictorial Representation of Circulating Flux.

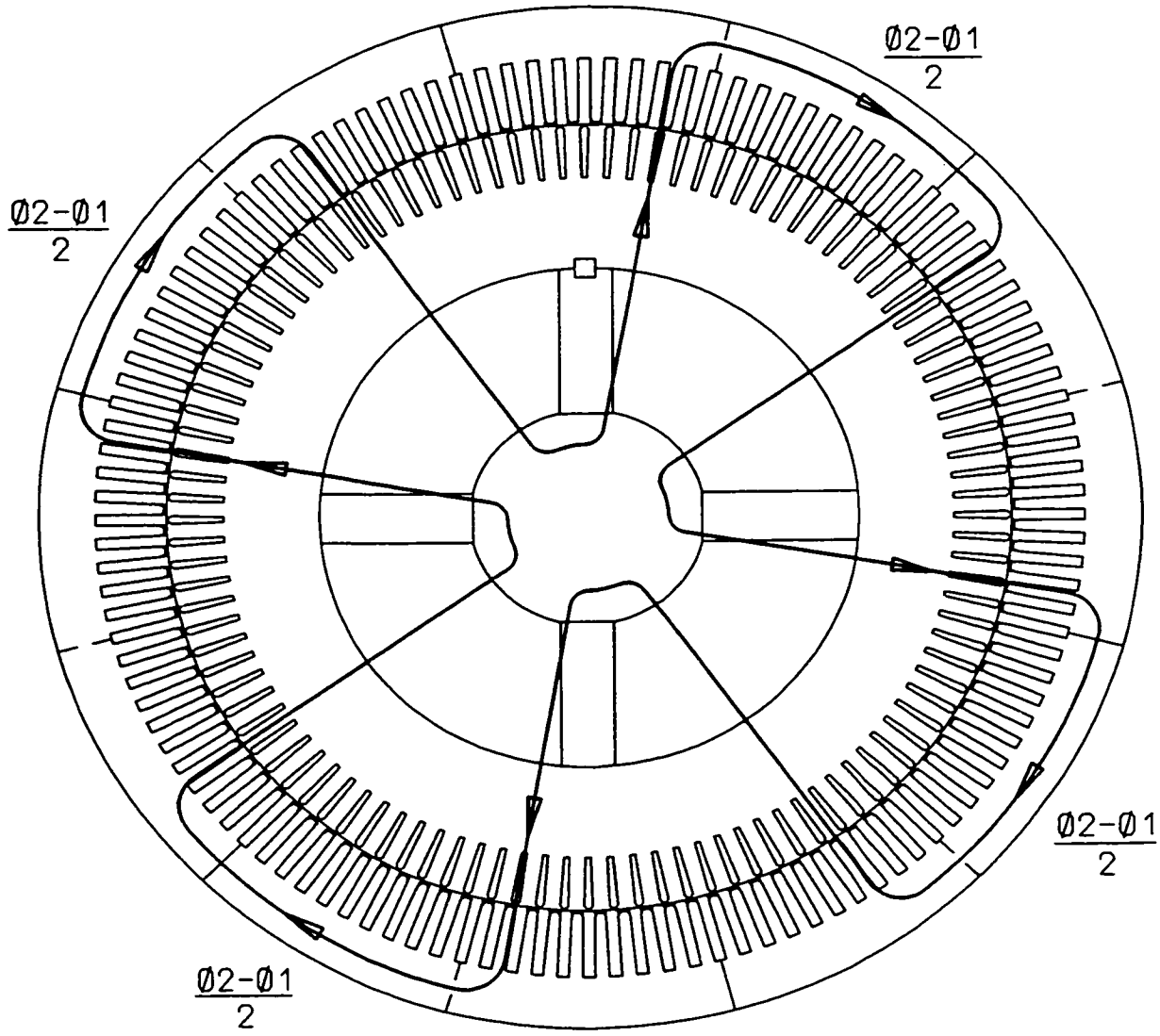

Clockwise Circulation of Flux Around the Shaft

(f) :Angular Position: Ten Degrees

Figure 6.51: Simplified Step-by Step Pictorial Representation of Circulating Flux.

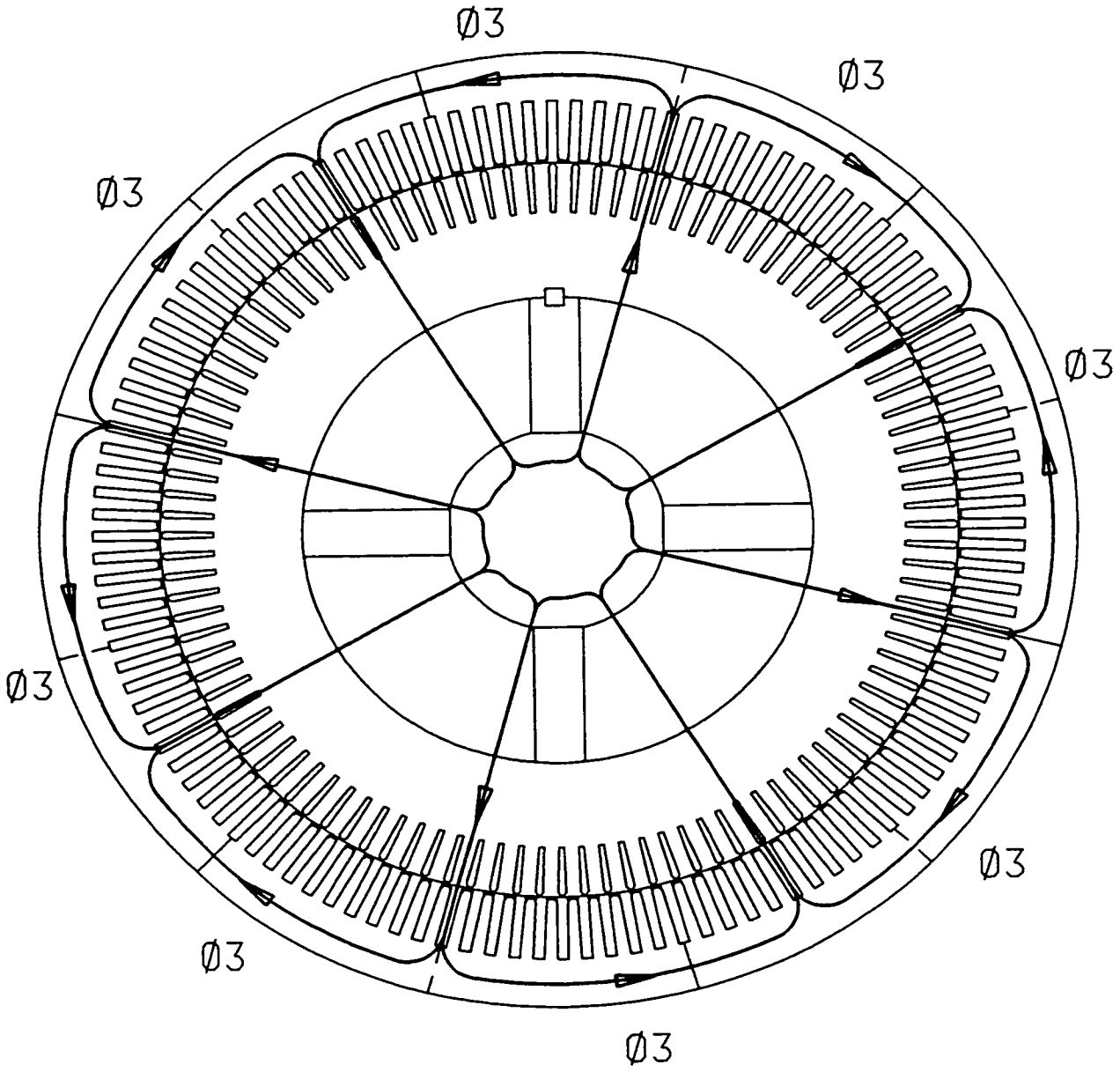

No Circulation of Flux Around the Shaft

(g) : Angular Position: Fifteen Degrees

Figure 6.51: Simplified Step-by Step Pictorial Representation of Circulating Flux.

illustrate how net circulating flux arises. At a load angle of 15 degrees as shown in Figure 6.51 (f), the net flux is zero. On further increase of load angle as shown in Figure 6.51 (g), there is net circulating flux, but in the counter clockwise direction. The net zero flux repeats at multiples of 15 degrees. The rate of change of flux during acceleration of the machine is high. The induced shaft voltage is high. As the machine approaches rated no load speed, the rate of change of flux decreases and hence the shaft voltage and shaft current reduce.

The preceding discussion indicates that shaft current is pronounced during acceleration of the motor and hence implies that a speedy development of oil film is required. The oil ring must carry sufficient oil from the oil reservoir for built up of oil film.

6.6 SUMMARY

The experiment was conducted systematically to separate the mechanical cause from the electrical cause of bearing damage as shown in Figure 6.52. The bearing damage was determined to be due to shaft current. Based on the analyses in Chapters 4 and 5 and applying Alger's rule as given by equation (2.2), shaft voltage and current prediction rules are formulated as shown in Table 6.7. Shaft current of 180 Hz was determined. Review of Tables 4.1, 4.2, 5.1, 6.4 and 6.7 indicates that the shaft current component of three times the line frequency is due to joints of the segmental punching. Eccentricity is small and the effect is small in this 8 pole induction machine. The magnitude of shaft current is small with oil ring lubricated or forced lubricated sleeve bearing provided the bearing is well insulated. Also, it has been shown that the probability of bearing damage due to shaft current is the highest during initial start of acceleration. During the start-up condition, the oil film has a high

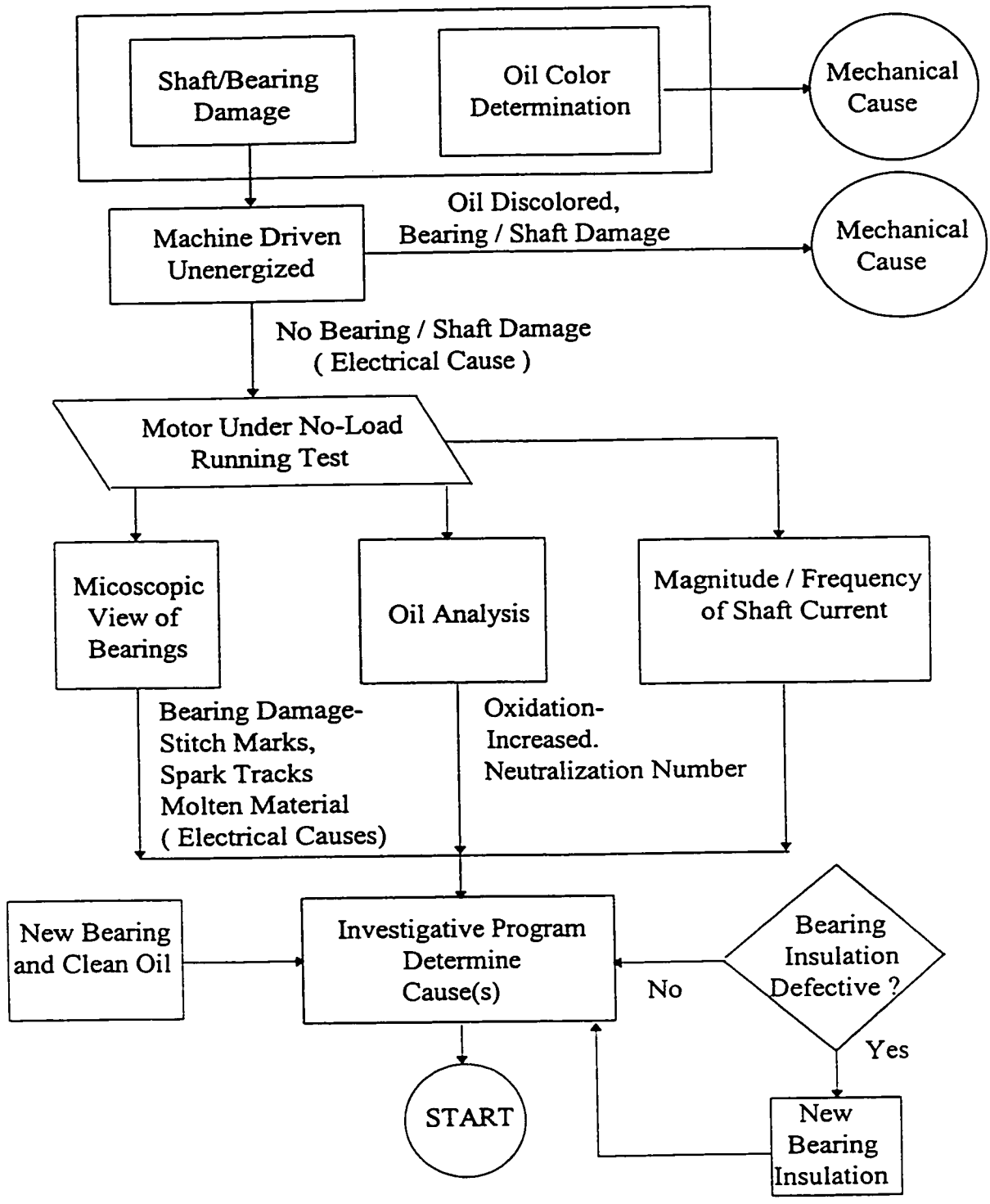

Figure 6.52: Design of Experiments to Determine the Cause(s) of Bearing Damage.

Fields	Frequency	Shaft Voltage Prediction Rule
Fundamental	f	D /p
Eccentricity	$\{ 1 + n_e (1-s)/p \} f$	D/ | p+1| D/ | p-1 |
Stator Slots (S)	f	D/ | S+p |, D/ | S-p |
Rotor Slots (R)	$\{ R(1-s)/p \pm 1 \} f$	D/ | R+p |, D / | R-p |
Stator and Rotor Slots (S, R)	$\{ R(1-s)/p \pm 1 \} f$	D/ | R-S+p | , D/ | R-S-p |, D/ | R+S-p |
Shaft Spider(SS)	$\{ SS (1-s)/p \pm 1 \} f$	D/ | SS + p |, D/ | SS - p |
Saturation	$(2n_s+1) f$	D / | $(2n_s +1)p$ |
Stator Slots and Saturation	$(2n_s+1) f$	D/ | S + [$2n_s$ +1]p | , D / | S- [$2n_s$ +1] p |
Stator Slots and Saturation and MMF Phase belts	$(2n_s + 1) f$	D/ | S+ $n_{st}p + 2n_s p$ |, D/ | S-[$n_{st}p + 2n_s p$] |
Stator and Rotor Slots and Saturation and MMF Phase Belt	$\{ R(1-s)/p + (2n_s +1) \} f$	D/ | R+ S+ $n_{st}p + 2n_s p$ |, D/ | R+ S-[$n_{st}p + 2n_s p$] | D/ | R- S+ $n_{st}p + 2n_s p$ |, D/ | R-S -[$n_{st}p + 2n_s p$] |

Table 6.7: Shaft Voltage Prediction Rules

tendency to make and break and hence result in arcs from the shaft to the bearing. Hence, it is important that the design of the oil ring be considered to obtain sufficient build up of oil film between the shaft and the bearing and the oil film thickness is sufficient that the make and break of oil film phenomenon does not arise. End play movement is not a factor in the development of the shaft voltage. In fact, as long as the bearing insulation is effective, end play movement hastens the decay of the transient shaft current. Based on the results obtained in this Chapter, the following remedies for avoidance of shaft current are proposed:

1. The combination of poles and joints as indicated by the shaft current prediction rule must be followed to determine the potential of occurrence of shaft current.
2. Allow for reasonable end play of the shaft so that metallic contact between the shaft and the bearing lining does not arise. The oil films in the two bearings are then electrically in series thus reducing the shaft current value. It was determined in the experiment that the end play, in fact has a damping effect on the magnitude of the shaft current in the case of insulated bearings.
3. If segments alone are the cause of shaft currents, the most desirable method of avoiding the currents is to use offset segments. This is accomplished by piling the first layer of punchings with lap joints in the usual way and then piling the next layer of punchings in the manner that this layer's lap joints are located one quarter of the punching segment arc from the first layer's lap joints. For the next two layers, the same process is repeated with the punchings piled upside down. If the dovetail tags are set at 1/8 and 5/8 positions, the number of slots per segments must be a multiple of 4 for the offset

segment method to be workable. The offset segment method is a preferred method as it gives better core loss, lower yoke reluctance and a more solid core construction.

4. A highly polished bearing will give a very low coefficient of friction. This is very important in high speed machines. Any increase in the roughness of the shaft will increase this coefficient and may result in bearing currents and hence bearing failure.
5. It is important to insulate all machine parts that have the high probability of contact with the shaft journal including bearing and connection to the bearings such as oil piping and bearing resistance temperature detector connection. This will break any shaft circuit that could develop.
6. Where possible, the oil film thickness is increased to reduce the wear rate substantially.

Other measures that are effective in the reduction of the magnitude of shaft current include the following:

1. A copper collar encircles the shaft with the collar wound with a ring winding being fed with suitable line frequency voltage such that an alternating flux is set up whose phase opposes the circulating flux. This method removes the fundamental frequency component but does not remove the higher frequency components.
2. Non-magnetic bearing housing or equivalent may be used to increase the reluctance of the flux path. However, this remedy may not be cost effective to the motor manufacturer. This measure was carried out on another machine.
3. A ring wound coil encircling the stator yoke is fed with a line frequency current of such a phase angle as to nearly cancel the magnetic field set up by the joints.

4. Low contact resistance brushes with ample capacity may be used. The use of brush riding may be limited by space. Furthermore, maintenance of the brush is required. The use of brush riding is considered the last resort.

Chapter 7

CONCLUSIONS

7.0 INTRODUCTION

Motor bearing failures traditionally were presumed to be related to mechanical factors. The high rate of bearing failure due to shaft current has driven continuing research to establish the causes of shaft current and non-invasive on-line motor diagnostics. An understanding of the physical origin of the shaft current is essential if induction machines are to be designed with minimal probability of shaft current and without bearing damage. Furthermore, a proper understanding of the causes of the shaft current can assist in the development of non-invasive on-line motor diagnostics. For this purpose, a 2611 kW induction machine exhibiting symptoms of shaft current was studied. In this chapter, the research objectives are reviewed, the major achievements and contributions are summarized, and suggestions for future research are presented.

7.1 SUMMARY OF THE THESIS

The main objective of this thesis was to investigate the causes of the shaft current in a large squirrel cage induction motor. In surveying the literature, it became evident that the method of measurement of shaft current is inadequate, as the conventional method as outlined in IEEE 112 standard [4] disturbs the circulating current loop between the shaft

and the ground. The conventional method does not measure the current in the path involving the shaft, the bearing and the frame. Also, the survey indicates that the shaft voltage prediction does not take into the account the effects of slotting, eccentricity, broken bars or inter-bar currents. Furthermore, the survey indicates that much of the research work was done on small induction machines operating on grease-lubricated anti-friction bearing systems. The previous research work was carried out during steady state operating condition. The transient condition was neglected.

The new method of shaft current measurement discussed in this work is reliable, requiring no maintenance, unlike the shaft ground brush method. The new method provides for reasonably accurate prediction of the magnitudes and frequencies of the shaft currents. The Rogowski coil method, described in detail in Chapter 3, is also not load-dependent unlike the ammeter method. This proposed method of shaft current measurement, when used with a spectrum analyzer and a video recording system, provides for a reliable on-line monitoring system. In Chapters 4 and 5, the analytical method based on the interaction of the MMF and permeance waves and taking into account the effects of slotting, eccentricity, broken bars and inter-bar currents, etc. has been developed to produce prediction rules to determine the occurrence of shaft current. The understanding gained by investigating these effects led to the development of a diagnostic procedure for detecting shaft current and determining its causes. The diagnostic procedure recommended for an on-line monitoring system includes the measurement of the spectra of both the shaft current and the stator current.

The shaft current measurement results outlined in Chapter 6 confirmed that the shaft current phenomenon is a serious problem during the transient condition. During the transient condition, when the oil film has not fully developed to a consistent thickness, the probability of bearing damage due to the shaft current is increased. The experimental results, shown in Chapter 6, indicated the importance of oil film development and the consequence of variation of oil film thickness. The performance of the oil ring to deliver oil to the bearing is essential for the proper operation and life expectancy of the bearing. In Chapter 6, an important characteristic of the oil ring was determined in a novel inexpensive manner using the Rogowski coil method. This method is the subject of a patent application. The experimental result from the novel test indicates that the empirical calculation currently used tends to be optimistic. This method of determination of oil ring performance is much more accurate than the conventional method. The conventional method is the determination of the full film drive shaft speed by measuring the time it takes for a specified number of revolutions of the oil ring. Then, the oil ring slip region shaft speed is calculated from Lemon's ratio [69].

7.2 MAJOR CONTRIBUTIONS OF THE THESIS

In this work, a wide range of issues relevant to the understanding of the shaft current phenomenon and shaft current measurement techniques were studied. Improved analysis and measuring technique were developed. The major contributions may be summarized as follows:

1. An alternative accurate method of measuring shaft current had been proposed. This method is the first known application of the Rogowski coil to the shaft current measurement. The method was presented at the IEEE Power Engineering Society Meeting in February 2-6 1997 in New York and subsequently published in the IEEE Transactions on Energy Conversion [31]. The Rogowksi coil method is accurate, having a linear input-output relationship. Error from strong magnetic field due to sources other than the current to be measured, is eliminated. Furthermore, this method of shaft current measurement does not disturb the circulating current loop. The method is maintenance free and can be used as part of an on-line monitoring system. The method is being pursued for use in alternating current adjustable speed drives within General Electric. Furthermore, the method has generated great interest among the members of NEMA working group on standards for such drives.
2. A magnetomotive force-permeance approach was proposed to account for effects due to armature reaction, slotting, saturation, eccentricity and broken bars. As a result, shaft voltage prediction rules were proposed.
3. A method of minimizing the shaft current, especially during the transient condition was proposed. There has been a brief but pertinent discussion of this method. A patent application based on the method is being filed.
4. An alternative novel inexpensive method of determining the performance characteristics of the oil ring is proposed. This novel method utilizes the proposed

shaft current measurement technique. A patent application for this method is being filed.

5. An on-line monitoring system incorporating the Rogowski coil is proposed. The system is based on the analysis of stator phase current spectra and the shaft voltage and current spectra. Where it is possible to install a shaft flux coil, the shaft flux is to be measured as it also provides indication of the machine faults.

7.3 SUGGESTIONS FOR FUTURE RESEARCH

A number of aspects relevant to the shaft current phenomenon and shaft current measurement technique need to be explored in the future. The following suggestions are made based on the developments in this thesis research:

1. The various causes of shaft current have been surveyed in this project. A finite element modeling of the electrical machine should be carried out to provide for accurate determination of the magnitude of the shaft current. The amplitudes of the harmonic waves predicted by the magnetomotive force-permeance approach is not sufficiently accurate given the series approximation. The finite element modeling will provide the design engineer prior knowledge of the probability of occurrence of shaft current and the current magnitude before the machine is built.
2. The Rogowski coil used in the shaft current measurement has a -3 dB frequency response of 8 Hz to 100 kHz. In order to use this method in an ac adjustable speed

drive. the frequency response needs to be extended to at least 5 MHz. This work is underway and progressing.

3. In Chapter 6, it was determined that the bearing insulation thickness could be reduced. However, it is necessary to carry out more tests over a wide range of machines before a definitive conclusion on the reduction of insulation thickness can be reached. Also, one type of bearing insulation was used. The bearing insulation system used is labor intensive. Tests on other types of insulation systems are required for determination of an effective low cost bearing insulation system.
4. Oil ring performance is a function of temperature and viscosity of the oil, oil ring immersion level, thickness of the oil ring, solid or split design oil ring, oil ring groove and oil ring material. The Rogowski method should be used to design a much improved oil ring which will deliver the required amount of oil to the bearing.

APPENDIX 1

TEST MACHINE

A1.0 MACHINE DATA

MACHINE DATA	
kW	2611
NO. POLES	8
VOLTAGE	4000
PHASES	3
FREQUENCY	60
NO. OF STATOR SLOTS	120
NO. OF ROTOR SLOTS	142
AIR GAP	2.54 MM
NO. OF PARALLEL CIRCUITS	4
WINDING CONNECTION	WYE
SKEW	NONE
STATOR LAMINATION	6 SEGMENTS
ROTOR LAMINATION	COMPLETE CIRCLE
NO. OF SPIDER ARMS	4
CIRCUIT RING (AT ODE)	COMPLETE RING
LUBRICATION	OIL RING TYPE
BEARING	SPLIT SLEEVE
NO LOAD SPEED	899.9 RPM

APPENDIX 2

BEARING AND LUBRICATION

A2.0 TYPES OF OIL LUBRICATION

Hydrodynamic lubrication, also called full film or fluid lubrication, is the phenomenon of the load carrying surfaces of the bearing being separated by a relatively thick film of lubricant so as to prevent metal-to-metal contact. This lubrication requires the existence of an adequate supply at all times. In this form of lubrication the moving surface pulls the lubricant into a wedge -shaped zone at a velocity sufficiently high to create the pressure necessary to separate the surfaces against the load on the bearing. The oil film between the shaft journal and the bearing serves not only as a lubricant but as an insulator against shaft current. It is important to maintain continuous oil film; any make and break of oil film will result in arcing from the shaft journal to the bearing. Hence, the bearing can be pitted. The damaged bearing will cause the motor bearing vibration to increase and in turn the bearing temperature will increase. Increase in the bearing temperature will reduce the viscosity of the oil and the motor bearing vibration will increase further. This domino effect can be catastrophic.

Two types of hydrodynamic lubrication systems are available - self contained bearing lubrication system [69, 70]and pressure-fed bearing lubrication system. The self

contained bearing lubrication system is characterized as a single unit comprising the bearing housing, hydrodynamic journal, lubricant circulating system and a heat exchanger unit. The self contained bearing lubrication system is limited to modest machine shaft speeds whereas the pressure fed bearing lubrication system is widely used in high speed machinery. Also, the minimum oil film thickness between the shaft surfaces and self lubricated bearings is much smaller than in the pressure-fed bearings. Of the lubrication circulating systems commonly used in self contained system, the oil ring lubrication system is most popular. In such system the preferred bearing proportions [71] are as follows:

1. Ratio of net bearing working length to shaft journal diameter, L/d is between 0.6 and 1.1.
2. Ratio of oil ring bore diameter to shaft journal diameter, D/d , is between 1.5 and 2.0.

A2.1 PERFORMANCE CHARACTERISTICS OF BEARING OIL RING

Oil rings have been used for the lubrication of the bearing for many years. Its simplicity and ruggedness make it economical and it requires little maintenance. An adequate lubricant supply [72] is one of the requisites for satisfactory operation of a fluid film bearing. It is thus important to consider the factors affecting oil delivery of the oil ring bearing. The speed of the oil ring is the most important factor affecting the oil delivery in an oil ring lubrication system.

At very low speed the ring follows the journal. The amount of oil delivered increases with speed in this low speed region called the solid friction region. In this region the oil delivery is a function of the ring velocity V and oil viscosity ν [71].

$$Q = 2.74\,\rho\,\nu^{0.65}\,V^{1.5}$$

$$= 2.74\,\rho\,\nu^{0.65}(DN)^{1.5} \qquad (A2\text{-}1)$$

where Q is the volume of oil delivered, m^3/s,

D is the inside diameter of the oil ring, m,

ρ is the length of periphery of oil ring cross section from which the oil is delivered, (width of ring riding on the journal), m,

ν is kinematics viscosity, m^2/s

and N is the rotational speed of the oil ring, rps.

Several factors were not considered in the above equation. They are the surface tension of the oil, the oil ring centrifugal action, variations in ring immersion and the weight of the ring. In the "no-slip" range the ring speed (N) and the shaft journal speed (n) are simply related as follows:

$$N = n\frac{d}{D} \qquad (A2\text{-}2)$$

where d is the shaft journal diameter, m

and D is the inside diameter of the oil ring, m

When the viscous oil drag on the lower arc of the ring begins to exceed the driving friction force from the rotating journal the oil ring begins to slip. The slip speed of the oil

ring is derived from the balance of the static driving force and the viscous drag force as follows:

$$f W = k \mu V_s D \qquad \text{(A2-3)}$$

where f is the coefficient of friction between the journal and the ring,

W is the weight of the ring in kg,

μ is the absolute viscosity of the oil in Pa s,

V_s is the maximum peripheral velocity of the oil ring for no-ring slip operation, m/s

and D is the inside diameter of the oil ring, m.

Equation (A2-3) is rearranged as

$$V_s = \frac{f W}{k \mu D} \qquad \text{(A2-4)}$$

$$\approx 0.0015 \frac{W}{\mu D} \text{ m/s} \qquad \text{(A2-5)}$$

The peripheral velocity of the oil ring is given as

$$V_s = \pi D N_s \quad \text{m/s} \qquad \text{(A2-6)}$$

Equating equation (A2-6) with equation (A2-5) results in 'no slip' oil ring speed given by

$$N_s = 0.00048 \frac{W}{\mu D^2} \text{ r/s} \qquad \text{(A2-7)}$$

As oil ring speed increases, oil delivery drops immediately, this being the region of semi-fluid friction. In this region the centrifugal force flings the oil off the ring and it is

lost for lubrication purposes. As the ring speed increases further, a transition ring speed will be reached when the oil delivery of the oil ring no longer follows equation (A2-1). This transition speed is given as follows:

$$V_t = \sqrt{1.9E\text{-}06}\, g^{5/6} D^{3/2}\, \nu^{-2/3} \qquad \text{m/s} \qquad \text{(A2-8)}$$

$$N_t = 446E\text{-}06\, g^{5/6} D^{1/2}\, \nu^{-2/3} \qquad \text{r/s} \qquad \text{(A2-9)}$$

As the journal speed increases, the partial oil film generated between the ring and the journal reduces the coefficient of friction and hence decreases the driving force. A point will be reached when the full lubricating oil film is built up to support the oil ring. This full film drive ring speed can be calculated from Lemmon and Booser [69]

$$N_f = K_d\, \nu^{0.2}\, \frac{\left(n_f\, d^2\right)^{0.8}}{D^2} \qquad \text{r/s} \qquad \text{(A2-10)}$$

where N_f is the full film drive ring speed, rps,

n_f is the full film drive shaft journal speed, rps,

d is the shaft journal diameter, m,

D is the oil ring inner diameter, m,

K_d is the correction factor for the different oil immersion depths

and ν is the oil absolute viscosity in Pa. s.

Lemmon et al [69] determined that the full film drive shaft journal speed is 2.9 times the shaft speed at start of oil ring slip, N_s.

A2.2 FACTORS AFFECTING THE PERFORMANCE OF OIL RING

The amount of oil delivered by the oil ring decreases rapidly with an increase in temperature of the oil. This can be explained by the fact that the viscosity of the hot oil decreases and hence the friction force exerted by the oil film on the oil ring decreases correspondingly. The oil is thrown off the ring by the centrifugal force before it is entered in the radial clearance between the shaft journal and the bearing surface.

As shown by Karelitz [73] , the transition speed at which slip of the ring begins is higher with heavier rings and more oil is delivered in the spray by the oil ring to the bearing. A heavier ring results in thinner oil film between the ring and the shaft journal with more oil consequently being squeezed out from the inner surface of the ring to the bearing.

An increase in submersion of the oil ring tends to decrease the oil delivery and the ring speed though not significantly as shown by Lemmon et al [69] .

A2.3 CHARACTERISTICS OF BEARING, LUBRICATION OIL AND OIL RING USED IN THE TEST

Bearing L/d ratio	0.523
Bearing D/d ratio	1.6667
Bearing Babbitt	Lead Base
Oil Ring Material	Leaded Brass (Bronze)
Oil Ring	Split Smooth Design; No grooves
Lubrication Oil	ISO VG 68

A2.3.1 SPECIFICATION OF LEAD BASED BABBITT

Element	Specification
Arsenic (As)	0.76-1.25 %
Antimony (Sb)	18.0 – 19.0 %
Copper (Cu)	0.15 - 0.50 %
Tin (Sn)	1.0 - 2.0 %
Lead	Remainder

A2.3.2 SPECIFICATION OF OIL RING MATERIAL - BRONZE

Element	Specification
Copper (Cu)	55.0 –60.0 %
Zinc (Zn)	Remainder
Lead (Pb)	2.0-3.8 %
Iron (Fe)	0.35 %
Other Impurities	0.50 %

A2.4 FACTORS AFFECTING THE LIFE OF BEARING

The life of a bearing assembly is dependent upon an number of inter-related factors

- Loading
- Temperature
- Type of Oil
- Quality of Oil
- Maintenance practices

Bearing overloading accelerates the bearing wear if the design limit is exceeded. Higher bearing temperature can reduce the viscosity of the oil and may affect the lubrication of the bearing. Higher temperature may also promote oxidation and other chemical change in the oil.

A2.5 PHYSICAL AND CHEMICAL PROPERTIES OF INDUSTRIAL MINERAL OILS AFFECTING LUBRICATION [74 - 79]

The physical properties of lubricants are attributable primarily to the structure of the lubricant base oil stock. The chemical properties of the finished or formulated lubricants are due to the additive packages and the response of the base stocks to the additive package.

Lubrication oils have long chain hydrocarbon structures. Viscosity may be visualized as a result of physical interaction of molecules when subjected to flow. Viscosity is the property of a fluid that causes it to resist flow. It is by far the most significant property for establishing the thickness, pressure and temperature of an oil film in hydrodynamic lubrication. The oil film thickness increases with viscosity. Viscosity is also in equations for calculating the Sommerfeld number and power loss for hydrodynamic bearings. Viscosity decreases as the temperature increases because the molecules vibrate more and interact less. ASTM D445 covers the method of determining the oil viscosity. Viscosity is useful in identifying the grades of oil and for following the performance of oils in service. An increase in viscosity usually indicated that the oil has deteriorated somewhat through oxidation.

The viscosity index (VI) [75] is a commonly used expression of the lubricating oil's change of viscosity with temperature. The higher the viscosity index the smaller the relative change in viscosity with temperature. Viscosity increases with pressure because the molecules are squeezed together forcing greater interaction. The higher the temperature the lower the viscosity increases due to pressure. Lubricating oils are subjected to wide ranges of temperature in service. At high temperature the viscosity of an oil may drop to point where the lubricating film strength is insufficient to carry the load and breaks down, allowing some form of metal-to-metal contact and severe wear. Any make and break of metal-to-metal contact between the shaft journal and bearing can lead to arcing between the bearing surface and the shaft journal due to shaft current passage. At other extreme of temperature the oil may become too viscous for proper circulation of the oil in the clearance between the journal and the bearing. In this case a thick oil film develops which leads to more bearing friction loss. This loss translates to higher temperature of the oil and thus oil thinning. Finally a stable oil film condition will be reached. During the initial unstable oil film condition the variation in the oil film to some extent is similar to a make and break of metal-to-metal contact. There is that possibility of arc between the bearing surface and the shaft journal. Hence a wide variation in viscosity with temperature is to be avoided.

Depending on its source, additive content and refining procedures a lubricating oil will exhibit certain acid or alkaline (base) characteristics. A measure of the acidic or alkaline constituents in the lubricating oil may be derived from the product's neutralization

number. The neutralization number is widely used as one criterion of used oil quality. The used oil's neutralization number must be compared with the number of new oil. The neutralization number may be determined colorimetrically (ASTM D974) or potentiometrically (ASTM D664). ASTM D974 gives the total acid number (TAN) only. ASTM D664 gives both total acid number and total base number (TBN). TBN provides a measure of the remaining amount of protective alkaline agents place in the oil to neutralize the acids. The amount and the rate of change of this number will provide an indication of oxidation and the rate of oxidation. A high value of TAN and low value of TBN when compared to the value for fresh oil, is generally indicative of oxidation. Acids are formed during oxidation of the oil.

Contaminants such as water, dirt and metallic particles are common in lubricating oils. Contaminant particles are discrete objects ranging in size from sub-micron to well above 100 micron-meter.

APPENDIX 3

CALIBRATION OF ROGOWSKI COIL

A3.0 Calibration Procedure and Result

Calibration of the Rogowski coil was done following installation on the shaft. The calibration procedure involved the use of a current generator, replacing the ammeter in the circuit as shown in Figure 3.6. The Rogowski coil was calibrated at a number of frequencies as shown in Tables A6.1 and A6.2. The drive end Rogowski coil had a calibration value of 11.02 millivolts per ampere at all frequencies from 8 Hz to 4 kHz. The opposite drive end Rogowski coil had a calibration value of 13.72 millivolts per ampere at the same range of frequencies.

mV	Amperes	Hz	mV/A/Hz	mV/A
11.000	1	60	0.18333	11.000
21.990	2	60	0.18325	10.995
43.9800	4	60	0.18325	10.995
65.960	6	60	0.18322	10.993
87.960	8	60	0.18325	10.995
109.950	10	60	0.18325	10.995
11.010	1	120	0.09175	11.010
22.030	2	120	0.09179	11.015
44.040	4	120	0.09175	11.010
66.070	6	120	0.09176	11.012
88.090	8	120	0.09176	11.011
110.110	10	120	0.09176	11.011
11.030	1	180	0.06128	11.030
22.060	2	180	0.06128	11.030
44.110	4	180	0.06126	11.028
66.167	6	180	0.06127	11.028
88.230	8	180	0.06127	11.029
110.280	10	180	0.06127	11.029
11.042	1	240	0.04601	11.042
22.082	2	240	0.04600	11.041
44.150	4	240	0.04599	11.038
66.230	6	240	0.04599	11.038
88.310	8	240	0.04599	11.039
110.390	10	240	0.04600	11.039
11.043	1	1K	0.01104	11.043
22.089	2	1 K	0.01104	11.045
44.16	4	1 K	0.01104	11.040
66.21	6	1 K	0.01104	11.035
88.32	8	1 K	0.01104	11.040
110.400	10	1 K	0.01104	11.040
11.045	1	4K	0.00276	11.045
22.091	2	4 K	0.00276	11.046
44.18	4	4 K	0.00276	11.045
66.24	6	4 K	0.00276	11.040
88.34	8	4 K	0.00276	11.043
110.400	10	4 K	0.00276	11.040
			average	**11.020**

Table A3.1 : DE Rogowski Coil Calibration Data

mV	Amperes	Hz	mV/A/Hz	mV/A
13.72	1	60	0.22952	13.771
27.49	2	60	0.22908	13.745
41.305	3	60	0.22947	13.768
68.809	5	60	0.22936	13.762
96.330	7	60	0.22936	13.761
137.368	10	120	0.22947	13.768
13.720	1	120	0.11433	13.720
27.440	2	120	0.11433	13.720
41.190	3	120	0.11442	13.730
68.630	5	120	0.11438	13.726
96.080	7	120	0.11438	13.726
137.290	10	120	0.11441	13.729
13.708	1	180	0.07616	13.708
27.423	2	180	0.07618	13.712
41.200	3	180	0.07630	13.733
68.620	5	180	0.07624	13.724
96.020	7	180	0.07621	13.717
137.200	10	180	0.07622	13.720
13.720	1	240	0.05717	13.720
27.425	2	240	0.05716	13.718
41.141	3	240	0.05714	13.714
68.563	5	240	0.05714	13.713
96.010	7	240	0.05715	13.716
137.160	10	240	0.05715	13.716
13.695	1	1 K	0.01370	13.695
27.380	2	1 K	0.01369	13.690
41.150	3	1 K	0.01372	13.717
68.540	5	1 K	0.01371	13.708
95.930	7	1 K	0.01370	13.704
137.07	10	1 K	0.01371	13.707
13.680	1	4 K	0.00340	13.680
27.350	2	4 K	0.00342	13.675
41.040	3	4 K	0.00342	13.680
68.400	5	4 K	0.00342	13.680
95.760	7	4 K	0.000342	13.680
136.800	10	4 K	0.00342	13.680
			average	**13.718**

Table A3.2 : ODE Rogowski Coil Calibration Data

APPENDIX 4

WINDING FACTOR

A4.0 DISTRIBUTION AND PITCH FACTORS

When the winding has more than one coil, the total MMF for a given harmonic cannot be found simply by multiplying the value of the MMF produced by one coil with the number of coils in the winding. In distributed winding the MMFs of adjacent coils have equal amplitudes when the number of turns are equal but they are shifted to each other in the air gap by an angle, α_s. The total MMF for a given harmonic can be obtained by the vector addition of the corresponding harmonic produced by each coil. The winding factor is defined as the ratio between the effective and the total number of turns in a winding. This factor [35, 36] is written as

$$k_{w,n} = \sin\left\{\frac{n\pi y}{2\tau_p}\right\} \frac{\sin\frac{q\, n\alpha_s}{2}}{q\sin\left(\frac{n\,\alpha_s}{2}\right)} \qquad (A4\text{-}1)$$

$$= \sin\left\{\frac{n\,\alpha_c}{2}\right\} \frac{\sin\frac{q\,n\,\alpha_s}{2}}{q\,\sin\left(\frac{n\,\alpha_s}{2}\right)}$$

where q = number of slot per poles per phase,

α_s = electrical angle between the slots, radians

y = coil pitch, m

τ_p = pole pitch, m

and $\alpha_c = \pi y/\tau_p$, coil pitch, radians.

The angle α_s , the electrical angle between the slots , is defined as

$$\alpha_s = \frac{\pi \tau_s}{\tau_p} = \frac{2 \pi p}{S} = \frac{\pi}{bq} \qquad (A4\text{-}2)$$

where S is the number of stator slots,

b is the number of phase belts,

p is the pole pairs,

and τ_s = slot pitch, m.

The pitch factor for slot harmonics follows from first term in equation (A4-1) by substituting $S_p \pm 1$ for n where S_p is the number of stator slots per pole pair:

$$k_{p.n} = \sin\left[(S_p \pm 1)\frac{\pi y}{2 \tau_p}\right] \qquad (A4\text{-}3)$$

$$= \sin\left[\frac{\pi y}{2 \tau_p}\right]$$

The pitch factor for the slot harmonics is equal to the pitch factor for the fundamental. Hence the winding factor for the slot harmonics is equal to the winding factor for the fundamental.

The distribution factor for slot harmonics follows from second term in equation (A4-1) by substituting $S_p \pm 1$ for n where S_p is the number of stator slots per pole pair

$$k_{d,n} = \frac{\sin \frac{q\,(S_p \pm 1)\alpha_s}{2}}{q \sin\left(\frac{(S_p \pm 1)\,\alpha_s}{2}\right)} \qquad \text{(A4-4)}$$

$$= \frac{\sin\left[\frac{q\alpha_s}{2}\right]}{q \sin\left[\frac{\alpha_s}{2}\right]}$$

The distribution factor for the slot harmonics is equal to the distribution factor for the fundamental.

APPENDIX 5

UNBALANCED MAGNETIC PULL

A5.0 DETERMINATION OF AVOIDANCE CONDITION

Unbalanced magnetic pull is defined as the net radial force between the stator and rotor of an electric machine resulting from a difference in the air gap flux densities on opposite sides of the machine. For example, if the rotor and stator slot numbers differ by only one, radial magnetic pull can occur during the starting period. In this case when a rotor tooth is centered on a stator tooth, at the diametrically opposite point a rotor tooth is centered on a stator slot. Hence, a one slot difference between rotor and stator should be avoided. This can be verified by reviewing the radial force wave created by multiplying the harmonic permeance air gap flux density and the constant average permeance air gap flux density.

The permeance wave of a slotted stator is the sum of the average permeance and the harmonic permeance, desribed as:

$$\wp_{ss} = \wp_o + \wp_{ss} \cos(hS\Omega) \qquad (A5\text{-}1)$$

where $\wp_o$ is the constant average permeance and

$\wp_{ss}$ is the half amplitude permeance variation due to stator slot openings.

Similarly, if there are R rotor slots and taking the center of a stator tooth as the reference point the permeance wave of the slotted rotor is given as:

$$\wp_{sr} = \wp_o + \wp_{sr} \cos\left(qR[\Omega - \omega_r t]\right) \qquad (A5\text{-}2)$$

The combined air gap permeance wave due to the slotted stator and rotor is

$$\wp_{ssr} = \wp_o \left(1 + \frac{\wp_{sr}}{\wp_o} \cos(qR[\Omega - \omega_r t])\right)\left(1 + \frac{\wp_{ss}}{\wp_o} \cos[hS\Omega]\right)$$

$$= \wp_o \left(1 + \frac{\wp_{sr}}{P_o} \cos(qR[\Omega - \omega_r t]) + \frac{\wp_{ss}}{\wp_o} \cos[hS\Omega] + \frac{\wp_{ss}\wp_{sr}}{2P_o} \{\cos([qR - hS]\Omega - qR\omega_r t) + \cos([qR + hS]\Omega - qR\omega_r t)\} \right)$$

(A5-3)

The air gap MMF considering spatial harmonic up to 7th harmonic and stator slot harmonics is given as:

$$\Im = A\cos(p\Omega - \omega t) + B\cos(5p\Omega + \omega t) + C\cos(7p\Omega - \omega t) + D\cos\left(\left[\frac{hS}{p} - 1\right]p\Omega + \omega t\right) + E\cos\left(\left[\frac{hS}{p} + 1\right]p\Omega + \omega t\right) \qquad (A5\text{-}4)$$

The air gap flux density is given as the product of the air gap permeance and the air gap MMF.

$$B_g = \wp_{ssr} \left\{ \begin{array}{l} A\cos(p\Omega - \omega t) + B\cos(5p\Omega + \omega t) + C\cos(7p\Omega - \omega t) \\ + D\cos\left(\left[\frac{hS}{p} - 1\right]p\Omega + \omega t\right) + E\cos\left(\left[\frac{hS}{p} + 1\right]p\Omega + \omega t\right) \end{array} \right\} \qquad (A5\text{-}5)$$

The first major component of equation (A5-5) is the product of the fundamental MMF and the uniform component of air gap permeance. The next group of the components are the product of the mmf harmonics and the uniform component of air gap permeance. The other group of components are the products of the fundamental MMF and the air gap permeance.

The components of flux which are the products of fundamental mmf and the permeance harmonics are:

$$
\begin{aligned}
B_{gfh} = & \frac{A}{2}\wp_{ss}\{\cos([hS+p]\Omega-\omega t)+\cos([hS-p]\Omega+\omega t)\} \\
& +\frac{A}{2}\wp_{sr}\{\cos([qR+p]\Omega-[qR\omega_r+\omega]t)+\cos([qR-p]\Omega-[qR\omega_r-\omega]t)\} \\
& +\frac{A}{4\wp_o}\wp_{sr}\wp_{ss}\{\cos([qR-hS+p]\Omega-[qR\omega_r+\omega]t)+\cos([qR-hS-p]\Omega-[qR\omega_r-\omega]t)\} \\
& +\frac{A}{4\wp_o}\wp_{sr}\wp_{ss}\{\cos([qR+hS+p]\Omega-[qR\omega_r+\omega]t)+\cos([qR+hS-p]\Omega-[qR\omega_r-\omega]t)\}
\end{aligned}
\qquad (A5\text{-}6)
$$

The components of flux which are the products of MMF harmonics and the uniform (average) components of permeance are:

$$
\begin{aligned}
B_{gfa} = & A\wp_o\{\cos(p\Omega-\omega t)\} + B\wp_o\{\cos(5p\Omega+\omega t)\} \\
& + C\wp_o\{\cos(7p\Omega-\omega t)\} + D\wp_o\{\cos([hS-p]\Omega-\omega t)\} \\
& + E\wp_o\{\cos([hS+p]\Omega+\omega t)\}
\end{aligned}
\qquad (A5\text{-}7)
$$

The magnetic pull is proportional to square of air gap flux density. The terms of interest in the force wave created by multiplying the two flux density expressions, B_{gfh} and B_{gha} are given in equation (A5-8).

$$F(\Omega, t) = \left\{ \begin{array}{l} \frac{A}{4}\frac{\wp_{ss}\wp_{sr}}{P_o}\cos\left[(qR - hS + p)\Omega - \frac{R}{p}(1-s)\omega t - \omega t\right] \\ + \frac{A}{4}\frac{\wp_{ss}\wp_{sr}}{\wp_o}\cos\left[(qR - hS - p)\Omega - \frac{R}{p}(1-s)\omega t + \omega t\right] \end{array} \right\} X\, A\wp_o \cos(p\Omega - \omega t)$$

(A5-8)

The force wave equation is simplified as

$$F(\Omega, t) = \frac{A^2}{8}\wp_{ss}\wp_{sr}\left\{ \begin{array}{l} \cos\left[(qR - hS + 2p)\Omega - \frac{R}{p}(1-s)\omega t - 2\omega t\right] \\ + \cos\left[(qR - hS)\Omega - \frac{R}{p}(1-s)\omega t\right] \\ + \cos\left[(qR - hS - 2p)\Omega - \frac{R}{p}(1-s)\omega t + 2\omega t\right] \\ + \cos\left[(qR - hS)\Omega - \frac{R}{p}(1-s)\omega t\right] \end{array} \right\}$$

(A5-9)

From equation (A5-9) it can be seen that a 2 pole wave will exist if

$$\begin{array}{lll} qR - hS + 2p & = & \pm 1 \\ qR - hS & = & \pm 1 \\ qR - hS - 2p & = & \pm 1 \end{array}$$

(A5-10)

To avoid the existence of 2 pole force the following condition is necessary

$$qR \neq hS \pm 1 \pm p$$

(A5-11)

APPENDIX 6

AIR GAP ECCENTRICITY

A6.0 CALCULATION OF THE AIR-GAP OF AN ECCENTRIC ROTOR.

In Figure A6.1, the stator core is considered as a circle with the equation

$$(\Delta + x)^2 + y^2 = R_1^2 \qquad (A6\text{-}1)$$

This equation is expanded to obtain

$$x^2 + y^2 = R_1^2 - 2\Delta x - \Delta^2 \qquad (A6\text{-}2)$$

Let $z^2 = x^2 + y^2$ (A6-3)

Also, $x = z \cos \Omega$ (A6-4)

Hence, equation (A6-2) is rearranged as

$$z^2 + 2\Delta z \cos \Omega + \Delta^2 \cos^2 \Omega = R_1^2 - \Delta^2 (1 - \cos^2 \Omega) \qquad (A6\text{-}5)$$

$$z + \Delta \cos \Omega = R_1 \sqrt{1 + \Delta^2/R_1^2 (\cos^2 \Omega - 1)}$$

Induction machine is normally designed with the center of the rotor at or very close to the center of the stator core, i.e. $\Delta << R_1$

Therefore $\sqrt{1 + \Delta^2/R_1^2 (\cos^2 \Omega - 1)} \approx 1$ (A6-6)

and hence $z \approx R_1 - \Delta \cos \Omega$ (A6-7)

The radial distance between the stator bore and the rotor, $\delta(\Omega)$ is approximated by equation (A6-8).

$$\begin{aligned} \delta(\Omega) &\approx z - R_2 \\ &\approx R_1 - R_2 - \Delta \cos\Omega \\ &\approx \delta_{av}\,(1 - \Lambda \cos\Omega) \end{aligned} \qquad \text{(A6-8)}$$

where $\Delta = \Lambda \,.\, \delta_{av}$, $\delta_{av} = R_1 - R_2$, and R_2 is the radius of the rotor

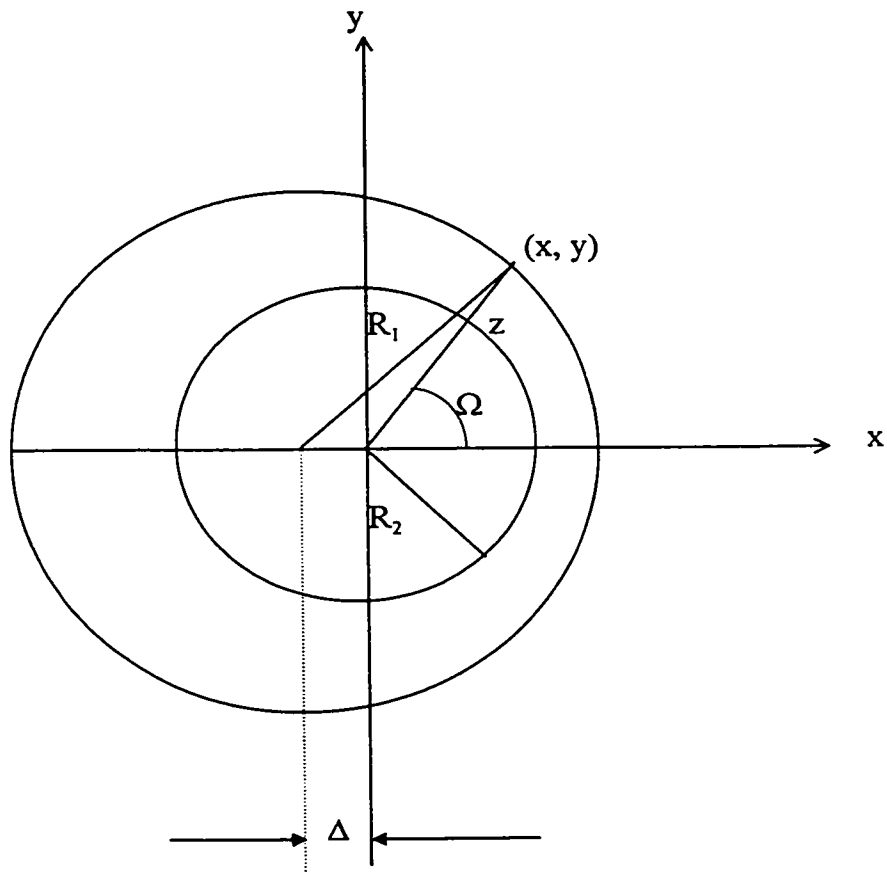

Figure A6.1 Air Gap Eccentricity

APPENDIX 7

PUBLISHED PAPERS/PATENTS/AWARDS

A7.0 PUBLISHED PAPERS

1. R. Ong, J. H. Dymond, R. D. Findlay, " A Comparison of Techniques For Measurement of Shaft Currents in Rotating Machines, " IEEE Transactions on Energy Conversion, Vol. 12, No. 4, Dec. 1997, Pages 363-367.

2. R. Ong, J. H. Dymond, R. D. Findlay, B. Szabados, " Shaft Current Measurement of a Large Induction Motor Using the Rogowski Coil Method, " IEEE International Symposium on Diagnostics for Electrical Machines, Power Electronics and Drives, Carry-le-Rouet, France, Sept. 1-3 1997, Pages 23-26.

3. R. Ong, J. H. Dymond, R. D. Findlay, B. Szabados, " Shaft Current Phenomenon: Experimental Testing and Analysis of a Large Induction Machine, " Proceedings of the IASTED International Conference on High Technology in the Power Industry '97, Oct. 27-30 1997, Orlando, Florida, Pages 241-246.(Approved for publication in International Journal of Power and Energy Systems; Paper No. 203-2126)

4. R.D. Findlay, R.Ong, J.H. Dymond, " Some Aspects of Determination of Shaft Current in Large Induction Motors, " 4th International Workshop on Electrical and Magnetic Fields, Marseille, France, 12-15 May 1998, Pages 27-32.

5. J. H. Dymond, Raymond Ong, Peter McKenna, " Locked Rotor and Acceleration Testing of Large Induction Machines - Methods, Problems and Interpretation of the Results, " IEEE Petroleum and Chemical Industry Conference, Sept. 1998, Paper No. PCIC-98-07 (Approved for publication in IEEE Transactions on Industry Applications).

6. R. Ong, J. H. Dymond, J. V. Kay, R. D. Findlay, B. Szabados, " Impact of Oil Lubrication on the Magnitude of Shaft Current in a Large Oil Ring Lubricated Induction Machine, " ICEM' 98, Istanbul, Turkey, 2-4 Sept 1998.

7. R. Ong, J. H. Dymond, R. D. Findlay, B. Szabados, " Systematic Practical Approach to the Study of Bearing Damage in a Large Oil Ring Lubricated Induction Machine," Accepted for Presentation at IEEE Petroleum and Chemical Industry Conference 1999, San Diego, U.S.A. (Approved for publication in IEEE Transactions on Industry Applications).

8. R. Ong, J. H. Dymond, R. D. Findlay, B. Szabados, " Significance of Joints Due to Lamination Segmentation on Shaft Currents in Induction Machine," Submitted for Presentation at IEEE International Electrical Machines and Drives Conference 1999, Seattle, Washington (Submitted for publication in IEEE Transaction on Energy Conversion)

A7.1 PATENTS

1. Minimizing Shaft Currents in Dynamoelectric Machines, Patent Filing Reference No. GECAN 3182, Filed Nov 25 1998.

2. Rogowski Method to Determine Performance of Oil Ring, Patent Filing Reference No. GECAN 3183, Filed Feb 22 1999.

A7.2 AWARDS

1. Minimizing Shaft Currents in Dynamoelectric Machines, Patent Filing Reference No. GECAN 3182, Filed Nov 25 1998, Judged the Best Patent in the First Inventor Category in General Electric Industrial Systems' Patent Competition.

REFERENCES

[1] A. Bonnett, G. C. Soukup, " Cause and Analysis of Stator and Rotor Failures in Three-Phase Squirrel-Cage Induction Motors, " IEEE Trans. On Industry Applications, Vol. 28, No. 4, July/Aug. 1992, Pages 921-936.

[2] A. Bonnett, G. C. Soukup, " Analysis of Rotor Failures in Squirrel-Cage Induction Motors, " IEEE Trans. On Industry Applications, Vol. 24, No. 6, Nov/Dec 1988, Pages 1124-1130.

[3] O. V. Thorsen, M. Dalva, " A Survey of Faults on Induction Motors In Offshore Oil Industry, Petrochemical Industry, Gas Terminals and Oil Refineries, " IEEE PCIC 1994, Paper No. PCIC-94-01, Pages 1-9.

[4] IEEE Standard 112 - 1991, *IEEE Standard Test Procedure for Polyphase Induction Motors and Generators*, IEEE Standard, 1991.

[5] P. L. Alger, H. W. Samson, " Shaft Currents in Electric Machines, " Transactions AIEE, Feb. 1924, Vol. 43, Pages 235- 245.

[6] E. G. Merrick, " Bearing Currents, " General Electric Review, Oct. 1914, Pages 936-941.

[7] W. Buchanan, " Currents in Bearings of Electric Generators, " The Electrician, May 1915, Pages 266-267.

[8] L. Adler, " The Origin and Prevention of Currents in Bearings, " The Electrician, Vol. 65, June 1910, Pages 315-317.

[9] C. T. Pearce, " Bearing Currents - Their Origin and Prevention, " The Electric Journal, Vol. XXIV, No. 8, Aug. 1927, Pages 372-376.

[10] M. E. Wagner, " Bearing Currents - Their Causes and Means of Prevention, " Power, Vol. 72, Nov. 1930, Pages 798-801.

[11] F. Barozzi, " Shaft Currents in Electric Machines, " Elettrotecnica,Vol. 26, No. 11, June 1939, Pages 402-407 (In Italian) , (The Electrical Research Association Ref. Trans. IB2111).

[12] L. W. Riggs, " How Much Shaft Current Can a Bearing Carry Safely, " Power, Vol. 88, Feb. 1944, Pages 103-105.

[13] A. H. Lauders, " Shaft Currents in Engine Driven Generators, " Diesel Power and Diesel Transportation, Feb. 1950, Pages 56-60.

[14] O. Haus, " Shaft Voltages and Bearing Currents, Their Cause, Effect and Remedial Measures, " Elektrotech. Z. (ETZ), (A), Vol. 85, No. 4, Feb. 1964, Pages 106-112, (In German), (The Electrical Research Association Ref. Trans. IB2194).

[15] P. J. Tavner, J. Penman, R. L. Stoll, H. O. Lorch, " Influence of Winding Design on the Axial Flux in Laminated Stator Cores, " IEE Proceedings, Pt. B, Vol. 125, Oct 1978, Pages 948-956.

[16] J. S. Sohre, P. I. Nippes, " Electromagnetic Shaft Currents and Demagnetization of Rotors of Turbine and Compressors, " 7th Turbomachinery Symposium, Dec. 1978, Texas A & M University, College Station, Texas.

[17] J. S. Sohre, P. I. Nippes, " Electromagnetic Shaft Currents in Turbomachinery - An Update, Part II : Magnetics and Demagnetization, " 25th Symposium on Safety in Ammonia Plants and Related Facilities, American Institute of Chemical Engineers, Portland, Oregon, Aug 17-20, 1978.

[18] Michael J. Costello, " Shaft Voltages and Rotating Machinery, " IEEE Transaction on Industry Applications, Vol. 29, No. 2, Mar./Apr. 1993, Pages 419-426.

[19] C. Ammann, K. Reichert, R. Joho, Z. Posedel, " Shaft Voltages in Generators with Static Excitation Systems - Problems and Solution, " IEEE Transactions on Energy Conversion, Vol. 3, No. 2, Jun. 1988, Pages 409-419.

[20] C. Ammann, K. Reichert, Z. Posedel, " Shaft Voltages in Turbosets: Operating Experience With RC-Grounding Device and New Possibilities For Monitoring the Condition of Turbogenerators, " International Conference on Evolution of Synchronous Machine, Aug. 1991.

[21] S. P. Verma, R. S. Girgis, R. J. Fleming, " Shaft Potential and Bearing Currents in Modern Turbogenerators : Damages and Means of Prevention, " Canadian Electrical Association Spring Meeting 1981, Rotating Machines Subsection, Toronto.

[22] S. P. Verma, R. S. Girgis, R. J. Fleming, " The Problems and Failures Caused by Shaft Potentials and Bearing Currents in Turbogenerators, " International Conference on Large High Voltage Electric System, CIGRE Session, 1980, Paper 11-10.

[23] S. P. Verma, Vikas Gupta, " Shaft Potentials in Modern Turbogenerators With Particular Reference to Static Excitation, " Electrical Machines - Design and Application, IEE Publication No. 254, Sept. 1985, Pages 156-162.

[24] L. T. Rosenberg, " Eccentricity, Vibration and Shaft Currents in Turbine Generator, " Transaction AIEE, Vol. 74, Part III, 1955, Pages 38-41.

[25] J. Boyd, H. N. Kaufman, " The Conduction of Current in Bearings, " ASLE Transaction, Vol. 2, No. 1, 1959, Pages 67-77.

[26] J. Boyd, H. N. Kaufman, " The Causes and the Control of Electrical Currents in Bearings, " Lubrication Engineering, Jan. 1959, Pages 28-35.

[27] John S. Hsu, Jan Stein, " Effects of Eccentricities on Shaft Signals studied through Windingless Rotors, " IEEE Transactions on Energy Conversion, Vol. 9, No. 3, Sept. 1994, Pages 564-571.

[28] P. Von Kaehne, " Shaft Voltages and Bearing Currents - A Survey of Published Work, " The Electrical Research Association Report No. 5030, 1964.

[29] R.L Stoll, " Method of Measuring Alternating Currents Without Disturbing the Conducting Current, " Proceedings IEE, Vol. 122, No. 10, Oct.1975, Pages 1166-1168.

[30] Signal Processing Systems, " Installation and Operation Manual- ProSeries Model SA390 Dynamic Signal Analyser, " Publication No. 22623 Rev. A, Jun. 5, 1996.

[31] R. Ong, J. H. Dymond, R. D. Findlay, " A Comparison of Techniques For Measurement of Shaft Currents in Rotating Machines, " IEEE Transactions on Energy Conversion, Vol. 12, Dec. 1997, Pages 363-367.

[32] Paul L. Cochran, " Polyphase Induction Motors, " Marcel Dekker Inc., 1989.

[33] P. L. Alger, " Induction Machines, " Gordon and Breach Science Publishers, 2nd Edition, 1970.

[34] K. Oberretl, " The Field Harmonic Theory of the Squirrel Cage Motor, Taking Multiple Armature Reaction into account, " Archiv Für Elektrotechnik, Vol. 49, 1965, Pages 343-364 (in German).

[35] K. Oberretl, " Field Harmonic Theory of the Slip Ring Motor Taking Multiple Armature Reaction into Account, " IEE Proceedings., Vol. 117, No. 8, Aug. 1970, Pages 1667-1674.

[36] V. Ostovic, " Computer-Aided Analysis of Electric Machines, " Prentice Hall, 1994.

[37] B. Heller and V. Hamata, " Harmonic Field Effects in Induction Machines, " Czechoslovak Academy of Sciences, Prague 1977.

[38] C. H. Lee, " Saturation Harmonics of Polyphase Induction Machines, " Transactions AIEE, Vol. 80, Oct. 1961, Pages 597-603.

[39] B. J. Chalmers, R. Dogson, " Waveshapes of Flux Density in Polyphase Induction Motor Under Saturated Conditions, " IEEE Transactions on Power Apparatus and Systems, Vol. 90, No. 2, Mar/Apr 1971, Pages 564-569.

[40] Y. Liao, T. Lipo, " Effect of Saturation Third Harmonic on the Performance of Squirrel Cage Induction Machines, " Electric Machines and Power Systems, Vol. 22, 1994, Pages 155-171.

[41] J. Hsu, S. P. Liou, B. T. Lin, W.F. Weldon, " Losses Influenced by Third Harmonic Flux in Induction Motors, IEEE Transactions on Energy Conversion, Vol. 6, No. 3, Sept. 1991, Pages 461-468.

[42] A. Bonnett, G. C. Soukup, " Analysis of Rotor Failures in Squirrel Cage Induction Motors, " IEEE Transactions on Industrial Applications, Vol. 24, No. 6, 1988 Pages 1124-1130.

[43] S. Salon, M. DeBortoli, D. Burrow, C. Slavic, " Calculation of Circulating Current Between Parallel Windings in Induction Motors with Eccentric Rotors by Finite Element Method, " Proceedings of ICEM '92, Manchester, UK, Pages 371-375.

[44] A. Stavrou, J. Penman, " The On-Line Quantification of Air-Gap Eccentricity in Induction Machines, " Proceedings of ICEM '94, Paris, France, Sept. 1994, Pages 261-266.

[45] M. Bradford, " Unbalanced Magnetic Pull in a 6-pole Induction Motor, " IEE Proceedings, Vol. 115 (11), 1968, Pages 1619-1627.

[46] D. G. Dorrell, " The Effects of Dynamic Rotor Eccentricity in Cage Induction Motors, " Proceedings of UPEC '94, University College Galway, Galway, Ireland, Sept. 1994, Pages 402-405.

[47] D. G. Dorrell, W. T. Thomson, S. Roach, " Combined Effects of Static and Dynamic Eccentricity on Air Gap Flux Waves and the Application of Current Monitoring to Detect Dynamic Eccentricity in 3-Phase Induction Motors, " IEE Electrical Machines and Drive, Conference Publication No. 412, Sept 1995, Pages 151-155.

[48] R.C. Robinson, " Line Frequency Magnetic Vibration of AC Machines, " AIEE Trans. on Power Apparatus and Systems, Vol. 81, 1963, Pages 675 - 679.

[49] P. Von Kaehne, " Unbalanced Magnetic Pull in Rotating Electrical Machines, " Electrical Research Association Report No. Z/T142, 1963.

[50] A. J. Ellison, S. J. Yang, " Effects of Rotor Eccentricity on Acoustic Noise from Induction Machines, " Proceedings IEE, Vol. 118, No. 1, 1971, Pages 174-184.

[51] J. R. Cameron, W. T. Thomson, A. B. Dow, " Vibration and Current Monitoring for Detecting air gap eccentricity in Large Induction Motors, " Proceedings IEE, Vol. 133, Pt. B, No. 3, 1986, Pages 155 - 163.

[52] J. R. Cameron, W. T. Thomson, A. B. Dow, " On Line Current Monitoring of Induction Motors- A Method for Calculating the level of Air Gap Eccentricity, " Proceedings IEE Conf. EMDA, 1987, Pages 173-178.

[53] N. Christofides, " Origins of Load Losses in Induction Motors with Cast Aluminum Rotors, " Proceeding IEE, Vol. 112, No. 12, 1965, Pages 2317-2332.

[54] R. Weppler, " Influence of Inter-bar Rotor Currents on the Performance of Single Phase and Polyphase Induction Motors, " Siemens Forsch. U. Entwickl. Ber. Bd. 4, 1975, Nr. 2, Pages 84-89.

[55] I. Kerszenbaum, C. F. Landy, " The Existence of Large Inter-bar Currents in the Three Phase Squirrel Cage Motors with Rotor Bar and/or End-Ring Faults, " IEEE Transactions on Power Apparatus and Systems, Vol. 103, No. 7, 1984, Pages 1854-1862.

[56] R. F. Walliser, C. F. Landy, " Determination of Inter-bar Current Effects in the Detection of Broken Bars in Squirrel Cage Induction Motors, " IEEE Transactions on Energy Conversion, Vol. 9, No. 1, 1994, Pages 152-158.

[57] C. Hargis, B. G. Gaydon, K. Kamash, " The Detection of Rotor Defects in Induction Motors, " IEE International Conference on Electrical Machines Design and Applications, 1982, Pages 216-220.

[58] G. B. Kliman, R. A. Koegl, J. Stein, R. D. Endicott, M. W. Madden, " Noninvasive Detection of Broken Bars in Operating Induction Motors," IEEE Transactions on Energy Conversion, Vol. 3, No. 4, 1988, Pages 873-879.

[59] I. Kerszenbaum, " The Behaviour of Three-Phase Squirrel Cage Induction Motors with Unbalance in the Rotor Impedance; In Particular Two Pole Motors, " Ph.D. Dissertation, Johannesburg, S. Africa, 1983.

[60] W. Deleroi, " Squirrel Cage Motor with Broken Bar in the Rotor - Physical Phenomena and their Experimental Assessment, " Proceedings of ICEM '82, Budapest, Hungary, Sept. 1982, Pages 767-770.

[61] S. Williamson, A. C. Smith, " Steady State Analysis of Three Phase Cage Motors with Rotor Bar and End Ring Faults,," IEE Proceedings, Pt. B, Vol. 129, May 1982, Pages 93-100.

[62] D. G. Dorrell, N. C. Patterson, J. F. Watson, " The Causes and Quantification of Sideband Currents for Use in Rotor Fault Detection Systems for Cage Induction Motors, " Proceedings of ICEM '96, Virgo, Spain, Pages 414 - 419.

[63] W. T. Thomson, D. R. Rankin, " Case Histories of Rotor Winding Fault Diagnosis in Induction Motors," 2nd International Condition Monitoring Conference, University College Swansea, March 1987.

[64] W. T. Thomson, " On Line Current Monitoring To Diagnose Shaft Misalignment in Three Phase Induction Motor Drive Systems, " Proceedings of ICEM '94, Vol. 2, Paris, France, Sept. 1994, Pages 238-243.

[65] P. J. Tavner, J. Penman, " Condition Monitoring of Electrical Machines, " John Wiley & Sons Inc., 1987.

[66] R. Ong, J. H. Dymond, R. D. Findlay, B. Szabados, " Shaft Current Measurement of a Large Induction Motor Using the Rogowski Coil Method, " IEEE International Symposium on Diagnostics for Electrical Machines, Power Electronics and Drives, Carry-le-Rouet, France, Sept. 1997, Pages 23-26.

[67] R. Ong, J. H. Dymond, R. D. Findlay, B. Szabados, " Shaft Current Phenomenon: Experimental Testing and Analysis of a Large Induction Machine," Proceedings of the IASTED International Conference on High Technology in the Power Industry '97, Oct. 27-30 1997, Orlando, Florida, Pages 241-246.

[68] J. H. Dymond, Raymond Ong, Peter McKenna, " Locked Rotor and Acceleration Testing of Large Induction Machines - Methods, Problems and Interpretation Of the Results, " IEEE Petroleum and Chemical Industry Conference, 1998, Paper No. PCIC-98-07.

[69] D. C. Lemon, E. R. Booser, " Bearing Oil Ring Performance, " Transactions of the ASME, Journal of Basic Engineering, Vol. 82, Series D, No. 2, June 1960, Pages 327-334.

[70] R. Baudry, L.M. Tichvinsky, " Performance of Oil Rings- Results of test on Various Special Types of Rings, " Mechanical Engineering, Feb. 1927, Pages 89-92.

[71] R. C. Elwell, " Self Contained Bearing Lubrication: Rings, Disks and Wicks, " CRC Handbook of Lubrication & Tribology, Volume III, Chapter 9, Pages 515-532.

[72] H. J. Connors, " An Analysis of the Effect of Lubricant Supply Rate on the Performance of the 360° Journal Bearing, " ASLE Transactions, No. 5, 1962, Pages 404-417.

[73] G. B. Karelitz, " Performance of Oil Ring Bearings, " Transaction ASME, Vol. 52, 1930, Pages 57-70.

[74] Imperial Oil Limited, " Product Information- Lubricants and Specialties, " 4th Edition, 1980.

[75] D. Godfrey, W. R. Herguth, " Physical and Chemical Properties of Industrial Mineral Oils Affecting Lubrication, Part 1, " Lubrication Engineering, Vol. 51, No. 5, May 1995, Pages 397-400.

[76] D. Godfrey, W. R. Herguth, " Physical and Chemical Properties of Industrial Mineral Oils Affecting Lubrication, Part 2, " Lubrication Engineering, Vol. 51, No. 6, June 1995, Pages 493-496.

[77] D. Godfrey, W. R. Herguth, " Physical and Chemical Properties of Industrial Mineral Oils Affecting Lubrication, Part 3, " Lubrication Engineering, Vol. 51, No. 10, Oct. 1995, Pages 825-828.

[78] D. Godfrey, W. R. Herguth, " Physical and Chemical Properties of Industrial Mineral Oils Affecting Lubrication, Part 4, " Lubrication Engineering, Vol. 51, No. 12, Dec. 1995, Pages 977-979.

[79] D. Godfrey, W. R. Herguth, " Physical and Chemical Properties of Industrial Mineral Oils Affecting Lubrication, Part 5, " Lubrication Engineering, Vol. 52, No. 2, Feb. 1996, Pages 145-148.